

# A COMBINED MICROWAVE AND OPTICAL SENSOR SYSTEM WITH APPLICATION IN CANCER DETECTION



*A thesis submitted to Cardiff University in the candidature for the degree of*

***Doctor of Philosophy***

by

**May Fadheel Estephan Estephan**

MSc. Medical Physics & BSc. Physics

Cardiff School of Engineering

Cardiff University

United Kingdom

**March 2021**



## DEDICATION

\* \* \*

*This thesis is dedicated to my*

*“Beloved family, late Father” Fadheel Estephan”,  
mother” Basima”, late Brother” Father Fawaz”,  
sister” Dr Maha”, and Brother’s family “Faris,  
Selvana, Fadi and Mariam” with all love and  
respect”.*

\* \* \*

# ACKNOWLEDGEMENT

Firstly, I would like to thank and praise the Lord my God through Jesus Christ, who encouraged me, supported me, and helped me in all the complicated steps of my study. I lift this research for his use, and I hope he may use it in his way for initial accurate and quick application in cancer detection. It is the preparation step to start animal and then human samples for the next generation to help people suffering from cancer.

Sincerely, I feel a great urge to present my most profound appreciation and gratitude to my supervisor, Dr Richard Perks, for his suggestions and supervision of this research and his endless support, patience, guidance, encouragement, and advice to complete this research.

I want to express my gratitude and deep appreciation to Professor Adrian Porch for his enrichment of this research through his remarkable ideas, advice, and encouragement.

I want to give a big thank you to the Director of Postgraduate Research Studies, Dr Roger Grosvenor, my tutor Dr Andrew Crayford and all the staff in the research office (in particular the Postgraduate Research Office Manager, Mrs Aderyn Reid) for supporting me during my difficulties with the former supervision for two and a half years.

Very special thanks are due to Very Rev Dr Gareth Jones (Fr. Sebastian Jones), the Chaplin of Cardiff University, for his support, advice, encouragement and for helping me with his spiritual guidance during my struggles.

I would like to express my heartfelt thanks from the bottom of my heart to my late Brother Father Fawaz Estephan for his prayer, encouragement, advice, and for helping me with his spiritual guidance during my struggles before passing away by sudden death on 25/12/2017. I am sure he is keeping me in his prayer.

I would like to thank my lovely family, my mother, my sister and my brother's family for their prayers, love, and support through the long days and nights that have witnessed the birth of this thesis.

A big thank to Al-Nahrain University / School of Medicine for allowing me to finish my PhD in the UK and for the Iraqi culture Attaché in London for all support.

My thanks to Prof. David Barrow who gave me the chance to use the microscope in his laboratory for inspecting the polishing steps of the optical probe.

My thanks to Andrew Rankmore and his team in the mechanical workshop, particularly Paul Malpas, who helped with some steps of Optical Probe fabrication.

My thanks also go to the staff in the clear room for the use of the electronic balance during my

sample preparation.

I am deeply grateful to the staff of Trevithick Library and the IT - School of engineering - Cardiff University for their help and support.

Finally, Thanks to my colleagues Dr Mohammad Alnajideen, Dr Azam Al-Rawachy, and Dr Balsam Shallal for their support. Also, I would like to thank the team at C<sub>3.11</sub> (Richard Gumbleton, Dr Samuel Hefford and Robert Batson) for their recommendations for the microwave part. Thank you very much Dr Abdalla Eblabla for helping in Au plating as well.



# ABSTRACT

Cancer remains a significant health problem, despite great scientific advances in recent years. Biomedical imaging procedures are commonly used to facilitate the diagnosis and treatment of different types of cancer. However, there are still many limitations to these diagnostic techniques. To overcome some of these issues, new approaches are urgently needed.

This study aims to establish potential new techniques to improve disease staging diagnosis through more accurate detection and allow real-time monitoring of sample characteristics to help the surgeons reduce the number of biopsies for making a diagnosis.

An optical probe has been fabricated in our laboratory with specific characteristics resulting from modelling and experimental exploration. This probe produced encouraging results from a tissue phantom with an ability to distinguish between different particle sizes 2, 0.8 and 0.413  $\mu\text{m}$  with various polystyrene spheres in suspension (PS) concentrations.

A Microwave cavity resonator showed the ability to distinguish between different saline dilutions for two types of preparation and different PS concentrations with some limitations. Many correction techniques were developed to enhance the quality of the data obtained.

A novel T- Structure and capacitive coupling technique enabled a more robust  $S_{21}$  measurement to be made utilising a resonant coaxial probe at microwave frequencies between around 0.1 GHz and 6 GHz. This structure was modelled and used in experimental scenarios leading to the ability to distinguish between various saline dilutions and different concentrations of PS. Additional correction techniques showed a significant improvement in PS detection limits.

Some difficulties have been overcome, relating to settling the PS particles in suspension, corrosion of the microwave probe, and signal processing. All of this has led to a novel system design by combined the optical and microwave sensor system to facilitate effective and efficient tumour detection. This novelty demonstrated that this new system could distinguish between different particles sizes by optical detection and dielectric properties by microwave characterisation.

The concluding section of this thesis presents the simultaneous detection of PS samples of different concentrations optically and with the microwave probe. This represents the first time such simultaneous measurements have been carried out using a combined probe such as that described here.

## LIST OF ABBREVIATION

ADS	Advance Design System Software
AUC	Area Under the Curve
BW	Bandwidth
CCRs	Cylindrical Cavity Resonators
CF	Central Frequency
COMSOL	Software for Multiphysics Simulation
CT	Computed Tomography
DI_W	Deionized Water
DRS	Diffuse Reflectance Spectroscopy
ELSS	Elastic Light Scattering Spectroscopy
ELSSS	Elastic Light Single-Scattering Spectroscopy
FNAB	Fine Needle Aspiration Biopsy
FS	Fluorescence Spectroscopy
FWHM	Full Width at Half Maximum
IR	Infrared
LabVIEW	Laboratory Virtual Instrument Engineering Workbench
LED	Light Emitting Diode
M	Molarity
MATLAB	Matrix Laboratory
MUT	Material Under Test
NA	Numerical Aperture
NaCl	Sodium Chloride
NADH	Nicotinamide Adenine Dinucleotide
nm	Nanometre
NPV	Negative Predictive Value
OH	Hydroxyl
PDF	Probability Density Function
ppt	Part Per Thousand
PPV	Positive Predictive Value
PS	Polystyrene Spheres in Suspension
PTFE	Polytetrafluoroethylene
Q factor	Quality Factor
RS	Raman Spectroscopy
$S_{11}$	Reflection
$S_{21}$	Insertion Loss
SE	Standard Error
SPC	Silver Plated Copper
SPCW	Silver Plated Copper Clad Steel
SPCW	Silver-Plated Copper Wire
TE	Transverse Electric
TG	Tungsten Halogen
TM	Transverse Magnetic
US	Ultrasound
UV	Ultraviolet

VNA	Vector Network Analyser
VNA	Vector Network Analyzer

### Symbols

$\mu_a$	Absorption coefficient
$\theta_a$	Acceptance angle
$\varepsilon'$	Real part
$\varepsilon''$	Imaginary part
$n_0$	Ambient refractive index
$A_s$	Actual cross-section
$R(\lambda)_{bg}$	Background spectrum
$R(\lambda)_c$	Spectrum of spectralon
$R(\lambda)_s$	Suspension of monodisperse polystyrene microspheres
$n_m$	Refractive index of the medium
$n_s$	Surrounding medium
$\varepsilon_{air}$	Real permittivity of the air
$\varepsilon_{eff}$	Effective permittivity
$\varepsilon_w$	Real permittivity of water
$\mu'_s$	Scattering function
$\mu_s$	Scattering coefficient
$\rho_s$	Density of the scattering particles
$\sigma_s$	Scattering cross-section
$\varepsilon$	Relative permittivity
$P(\theta, \varphi)$	Scattering function
$P(\cos\theta)$	Scattering phase function
$\varepsilon(\infty)$	Extrapolated high-frequency permittivity
$\varepsilon(0)$	Low-frequency permittivity
$\tau$	Relaxation time

# TABLE OF CONTENTS

<b>DEDICATION</b> .....	<b>I</b>
<b>ACKNOWLEDGEMENT</b> .....	<b>II</b>
<b>ABSTRACT</b> .....	<b>V</b>
<b>LIST OF ABBREVIATION</b> .....	<b>VI</b>
<b>TABLE OF CONTENTS</b> .....	<b>VIII</b>
<b>LIST OF FIGURES</b> .....	<b>XII</b>
<b>LIST OF TABLES</b> .....	<b>XXIV</b>
<b>1 INTRODUCTION AND THESIS OVERVIEW</b> .....	<b>1</b>
<b>1.1 Background of Clinical Problem</b> .....	<b>1</b>
<b>1.2 Optical and Microwave non-destructive techniques</b> .....	<b>2</b>
<b>1.3 Aim and objectives</b> .....	<b>2</b>
<b>1.4 Hypothesis</b> .....	<b>3</b>
<b>1.5 Tumour Biology</b> .....	<b>3</b>
1.5.1 Normal Tissues .....	3
1.5.2 Benign and Malignant Tumour.....	4
<b>1.6 Thesis Scope</b> .....	<b>7</b>
<b>1.7 Thesis Overview</b> .....	<b>8</b>
1.7.1 Original Contributions .....	8
<b>1.8 Presentations</b> .....	<b>9</b>
<b>2 DIAGNOSTIC TECHNIQUES</b> .....	<b>10</b>
<b>2.1 Optical Diagnostic Technologies</b> .....	<b>10</b>
2.1.1 Diffuse Reflectance Spectroscopy (DRS) .....	10
2.1.2 Fluorescence Spectroscopy (FS) .....	13
2.1.3 Raman Spectroscopy (RS).....	14
2.1.4 Elastic Light Scattering Spectroscopy (ELSS) .....	16
<b>2.2 Microwave Techniques</b> .....	<b>29</b>
2.2.1 Resonant Techniques .....	30
2.2.2 Non-Resonant Methods .....	31
<b>2.3 Other Technique for Cancer Diagnosis</b> .....	<b>36</b>
<b>2.4 Chapter Summary</b> .....	<b>36</b>
<b>3 ELSS OPTICAL DETECTION</b> .....	<b>37</b>
<b>3.1 Transportation of Light in Tissue</b> .....	<b>37</b>
3.1.1 Optical Properties of Biological Tissues.....	37
<b>3.2 Scattering</b> .....	<b>40</b>

<b>3.3</b>	<b>Elastic Light Scattering Spectroscopy (ELSS) Principle .....</b>	<b>42</b>
<b>3.4</b>	<b>Mathematical Model .....</b>	<b>43</b>
3.4.1	Definition and Objective .....	43
3.4.2	Equations of the Mathematical Model .....	44
3.4.3	Effect of Some Parameters on the Mathematical Model.....	46
<b>3.5</b>	<b>Chapter Summary .....</b>	<b>52</b>
<b>4</b>	<b><i>FABRICATION AND EXPERIMENTAL RESULTS FOR THE OPTICAL PROBE .....</i></b>	<b>54</b>
<b>4.1</b>	<b>Geometrical Design and Fabrication .....</b>	<b>54</b>
4.1.1	Selecting the Optical Fibre .....	54
4.1.2	Fabrication and Geometrical Design .....	55
<b>4.2</b>	<b>Tissue Phantom Preparation .....</b>	<b>57</b>
4.2.1	Optical tissue phantom .....	57
<b>4.3</b>	<b>Analysing Data.....</b>	<b>58</b>
<b>4.4</b>	<b>Instruments .....</b>	<b>58</b>
<b>4.5</b>	<b>Configuration Types.....</b>	<b>59</b>
<b>4.6</b>	<b>Experimental Results .....</b>	<b>60</b>
4.6.1	Effect of the Particle Size (Tissue Phantom Polystyrene Spheres in DI-W) .....	60
4.6.2	Effect of the Dimension of the Core Diameter and the Separation between Fibre Optics on the Measurements of no- Absorbing Tissue Phantoms. Polystyrene in DI- W .....	62
4.6.3	Conclusion for of the Particle Size (Tissue Phantom Polystyrene Spheres in DI-W) of the first conf.....	64
<b>4.7</b>	<b>Light Source, Light-Emitting Diode (LED) .....</b>	<b>64</b>
<b>4.8</b>	<b>Spliced Fibre Configuration .....</b>	<b>65</b>
4.8.1	Conclusion for Spliced Fibre Configuration .....	68
<b>4.9</b>	<b>Chapter Summary .....</b>	<b>68</b>
<b>5</b>	<b><i>Microwave Theory, Theoretical Calculation and Simulation Work.....</i></b>	<b>69</b>
<b>5.1</b>	<b>Introduction .....</b>	<b>69</b>
<b>5.2</b>	<b>Interaction between Different Materials and an Alternating Electric Field .....</b>	<b>70</b>
<b>5.3</b>	<b>The Debye Model for Water .....</b>	<b>73</b>
<b>5.4</b>	<b>Effective Permittivity (<math>\epsilon_{eff}</math>) .....</b>	<b>76</b>
<b>5.5</b>	<b>Theoretical Measurements of the Effective Permittivity of Polystyrene Spheres in a Water Host .....</b>	<b>77</b>
<b>5.6</b>	<b>Experimental Works for Non- Resonant Method.....</b>	<b>79</b>
<b>5.7</b>	<b>Comparison between Theoretical and Experimental Work .....</b>	<b>82</b>
<b>5.8</b>	<b>Method Selection in Our Measurements .....</b>	<b>82</b>
<b>5.9</b>	<b>Resonant Coaxial Probe .....</b>	<b>83</b>
5.9.1	Introduction .....	83
5.9.2	Theory of Coaxial Cable .....	83
5.9.3	Electromagnetic Resonators .....	94

<b>5.10 Simulation of Novel 'tee' Structure and Capacitive Coupling. ....</b>	<b>97</b>
5.10.1 Design Setup.....	99
<b>5.11 The Effect of Circuit Parameters on the Bandwidth (BW), Q Factor and <math>S_{21}</math> .....</b>	<b>99</b>
5.11.1 Effect of Symmetry in the Coupling Capacitances.....	100
5.11.2 Effect of Asymmetry in the Coupling Capacitances .....	102
5.11.3 Effect of Coaxial Cable Length on the Bandwidth, Central Frequency, Quality Factor, and Insertion loss.....	106
5.11.4 Sample Effect.....	108
<b>5.12 Resonance Skew .....</b>	<b>111</b>
5.12.1 Resonance Skew and Correction .....	115
<b>5.13 Experiment of De-Skew.....</b>	<b>117</b>
<b>5.14 Chapter Summary .....</b>	<b>120</b>
<b>6 MICROWAVE CAVITY TECHNIQUE.....</b>	<b>122</b>
<b>6.1 Introduction .....</b>	<b>122</b>
<b>6.2 Basic Principle of the Cavity Resonator .....</b>	<b>122</b>
<b>6.3 Cavity Perturbation Theory .....</b>	<b>123</b>
<b>6.4 Experimental Measurements Using Cylindrical Cavity Resonators .....</b>	<b>125</b>
6.4.1 Introduction .....	125
<b>6.5 Sample Preparation, Correction Solutions and Measurements .....</b>	<b>126</b>
6.5.1 Measurements on Commercially Obtained Saline .....	126
6.5.2 Detection Limits and Sample Classification.....	137
6.5.3 Measurements of Lab Prepared Saline Dilutions .....	142
<b>6.6 Comparison between Preparation Types .....</b>	<b>149</b>
<b>6.7 Converting the Microwave Parameters to the Permittivity.....</b>	<b>151</b>
6.7.1 Introduction .....	151
6.7.2 Methodology.....	152
6.7.3 Results .....	152
<b>6.8 Enhanced Exponential Correction.....</b>	<b>153</b>
<b>6.9 Polystyrene Results by Using the Eppendorf Tube Sample.....</b>	<b>155</b>
6.9.1 Conclusion for Polystyrene Results by Using the Eppendorf Tube Sample.....	161
<b>6.10 Results by Using Thin and Long Eppendorf Tube Sample. ....</b>	<b>161</b>
6.10.1 Results for Saline Samples.....	161
6.10.2 Comparison between Our Experimental Work and Earlier Publications for the Saline	164
6.10.3 Polystyrene Results Using Thin and Long Eppendorf Tube Sample .....	165
6.10.4 Conclusion for Saline and Polystyrene Results Using Thin and Long Eppendorf Tube Sample	168
6.10.5 Comparison between the Permittivity of the Experimental and the Theoretical (the Effective Permittivity) Work for the Polystyrene .....	169
<b>6.11 Chapter Summary .....</b>	<b>170</b>
<b>7 RESONANT COAXIAL PROBE .....</b>	<b>172</b>
<b>7.1 Introduction .....</b>	<b>172</b>

<b>7.2</b>	<b>Methodology</b> .....	<b>173</b>
7.2.1	Results of Coaxial Resonator (first set of frequencies).....	173
7.2.2	A second Set frequencies detection .....	179
<b>7.3</b>	<b>Coaxial Cable and Polystyrene Experiments</b> .....	<b>190</b>
7.3.1	Microwave Measurements at 2 $\mu\text{m}$ Polystyrene Spheres in Suspension .....	190
7.3.2	Microwave Measurements at 0.8 $\mu\text{m}$ Polystyrene Spheres in Suspension .....	204
7.3.3	Microwave Measurements at 0.413 $\mu\text{m}$ of Polystyrene Spheres in Suspension ...	210
7.3.4	Discussion of Polystyrene Spheres in Suspension .....	210
<b>7.4</b>	<b>Chapter Summary</b> .....	<b>212</b>
<b>8 OVERCOMING CHALLENGES AND A NOVEL TECHNIQUE FOR SIMULTANEOUSLY DETECTING MICROWAVE AND ELSS SIGNALS</b> .....		<b>214</b>
<b>8.1</b>	<b>Introduction</b> .....	<b>214</b>
<b>8.2</b>	<b>Overcoming the Corrosion of the Probe</b> .....	<b>214</b>
8.2.1	The 'Crimp Cut' Protruding Probe .....	214
8.2.2	Gold (Au) Coating of the Internal Conductor (flat shape) .....	229
8.2.3	Silver Plated Copper (SPC) of Centre Conductor Coax Cable .....	233
8.2.4	Discussion for the Overcoming the Corrosion of the Probe.....	237
<b>8.3</b>	<b>A Combined Microwave / Optical spectroscopy system</b> .....	<b>238</b>
8.3.1	A combined BW Microwave/ Optical results at 2 $\mu\text{m}$ of PS .....	240
8.3.2	A combined BW Microwave/ Optical results at 0.8 $\mu\text{m}$ of PS .....	244
8.3.3	A combined BW Microwave/ Optical results at 0.413 $\mu\text{m}$ of PS .....	246
8.3.4	Discussion for the Combined System .....	247
<b>8.4</b>	<b>Chapter Summary</b> .....	<b>250</b>
<b>9 CONCLUSIONS AND FUTURE WORK</b> .....		<b>252</b>
<b>9.1</b>	<b>Chapter Conclusions</b> .....	<b>252</b>
<b>9.2</b>	<b>Future Work</b> .....	<b>256</b>
<b>APPENDICES</b> .....		<b>258</b>
<b>APPENDIX (A) MATHEMATICAL MODEL FOR GEOMETRICAL PROBE CHARACTERISATION</b> .....		<b>258</b>
<b>APPENDIX (B) DE-SKEWED RESONANCE</b> .....		<b>262</b>
<b>APPENDIX (C) ENHANCED EXPONENTIAL CORRECTION</b> .....		<b>264</b>
<b>APPENDIX (D) RESONANT COAXIAL PROBE RESULTS</b> .....		<b>266</b>
<b>REFERENCES</b> .....		<b>279</b>

# LIST OF FIGURES

FIGURE 1-1: COMPARISON OF A BENIGN AND A MALIGNANT TUMOUR OF THE THYROID [14].	5
FIGURE 1-2: FOLLICULAR ADENOMA. THE HISTOLOGIC APPEARANCE OF THE THYROID GLAND'S BENIGN TUMOUR CELLS SHOWS TUMOUR CELLS THAT ARE MONOMORPHIC IN SHAPE AND COLOUR [16].	5
FIGURE 1-3: MICROSCOPIC APPEARANCE OF A PAPILLARY ADENOCARCINOMA OF THE THYROID. THE FRONDS OF TISSUE HAVE THIN FIBROVASCULAR CORES [17].	6
FIGURE 1-4: MICROSCOPIC APPEARANCE IN A SAMPLE OF THE HOBNAIL VARIANT OF PAPILLARY THYROID CARCINOMA, TUMOUR CELLS HAVE NUCLEI LOCATED TOWARD THE MIDDLE OR APICAL PORTION OF THE CELL, PRODUCING A SURFACE BULGE IMPARTING THE SO-CALLED "HOBNAIL" APPEARANCE (ARROWS). OCCASIONALLY, THE CELLS CAN APPEAR TALL AND COLUMNAR. NOTE THE AMPLE, EOSINOPHILIC, AND SLIGHTLY GRANULAR CYTOPLASM, WHICH IS REMINISCENT OF ONCOCYTIC CELLS (H&E STAIN, ORIGINAL MAGNIFICATION 360) [19].	6
FIGURE 2-1: DIFFUSE REFLECTANCE SPECTROSCOPY SET UP [31].	11
FIGURE 2-2: FLUORESCENCE SPECTROSCOPY SETUP [45].	13
FIGURE 2-3: RAMAN SPECTROSCOPY SET UP	15
FIGURE 2-4: ELSS SETUP [20].	17
FIGURE 2-5: TM010 CAVITY IS COMMONLY USED FOR PERTURBATION MEASUREMENTS OF UP TO 10 GHz [96].	30
FIGURE 2-6: (A) THE REFLECTION SCHEME OF THE SIGNAL; (B) ILLUSTRATION OF THE APPARATUS USED FOR MICROWAVE PROBE LIQUID MEASUREMENTS [101].	32
FIGURE 2-7: (A) TRANSMISSION LINE METHOD; WAVEGUIDE AND COAXIAL LINE CASE; (B) A PRACTICAL EXAMPLE OF THE TRANSMISSION LINE ( WAVEGUIDE) SETUP FOR MICROWAVE MEASUREMENTS UNDER TEMPERATURE CONTROL [103, 104].	33
FIGURE 2-8: FREE SPACE SETUP [105]	34
FIGURE 3-1: INTERACTION OF LIGHT INCIDENT WITH THE TISSUE.	37
FIGURE 3-2: ANISOTROPY IN SCATTERING.	39
FIGURE 3-3: OPTICAL PROPERTIES ( $\mu_s$ , $g$ AND $\mu'_s$ ) OF THREE PARTICLE SIZES OF PS, 2, 0.8 AND 0.4 $\mu\text{m}$ .	39
FIGURE 3-4: EFFECT OF THE PARTICLE SIZE ON THE SCATTERING TYPES.	41
FIGURE 3-5: SCHEMATIC SET UP OF THE ELSS	43
FIGURE 3-6: SCHEMATIC DIAGRAM ILLUSTRATING THE OVERLAP BETWEEN THE EMISSION CONES OF BOTH FIBRES GIVING RISE TO THE SENSING VOLUME AND THE FIBRE SEPARATION $D_s$ .	44
FIGURE 3-7: SCHEMATIC DIAGRAM ILLUSTRATING THE POSITION-DEPENDENT FWHM, $\sigma$ AS A FUNCTION OF DISTANCE FROM THE FIBRE FACE.	45
FIGURE 3-8: THE EFFECT OF CORE DIAMETER AND THE ACCEPTANCE ANGLE $\theta_a$ AND $\theta_c$ IS THE CRITICAL ANGLE FOR THE TOTAL INTERNAL REFLECTION.	45
FIGURE 3-9: THE INTENSITY PROFILE FOR THE DIFFERENT NUMBER OF SIGMA ( $N-\sigma$ ).	46
FIGURE 3-10: THE ACCEPTANCE ANGLE AND THE INCIDENT RAY.	47
FIGURE 3-11: THE EFFECT OF ACCEPTANCE ANGLE ON THE SCATTERING INTENSITY	48
FIGURE 3-12: THE EFFECT OF THE SCATTER ON THE SCATTERING INTENSITY	48
FIGURE 3-13: THE EFFECT OF THE SEPARATION ON THE SCATTERING INTENSITY	49
FIGURE 3-14: THE EFFECT OF THE DIAMETER ON THE SCATTERING INTENSITY	50
FIGURE 3-15: 3-D INTENSITY PROFILES FOR DIFFERENT DISTANCES FROM THE FIBRE FACES. (LAMBERTIAN EMITTER MODEL.), $Z$ .	51
FIGURE 3-16: COUPLING INTENSITY AS A FUNCTION OF THE DISTANCE BETWEEN THE FIBRES FOR TWO DIFFERENT ACCEPTANCE ANGLES (15 AND 25 DEGREES). (LAMBERTIAN EMITTER MODEL.).	52
FIGURE 4-1: FABRICATION STEPS 1-GLUING TWO FIBRE OPTICS AFTER ADJACENT BOTH OF THEM.2- GLUE AND HOUSE THE ADJACENT FIBRES IN A RIGID STAINLESS STEEL NEEDLE.3- DRYING ALL GLUING PARTS.4- FIX AND SEPARATE TWO FIBRES, ONE AS A SOURCE AND THE SECOND AS A RECEIVER.	56
FIGURE 4-2: POLISHING STEPS FOR THE SMA905 FIBRE CONNECTORS.1-HANG THE CONNECTOR IN A SAFE SPOT AFTER INSERTING FIBRE INTO EPOXIED CONNECTOR.2- PROTRUDE FIBRE TO MAKE READY FOR POLISHING. 3- FIBRE AFTER POLISHING.	56
FIGURE 4-3: THE DESIGN OF THE OPTICAL PROBE.	56

FIGURE 4-4: THE PHYSICAL OPTICAL PROBE .....	57
FIGURE 4-5: POLYSTYRENE PREPARATION .....	58
FIGURE 4-6: SET UP OF THE EXPERIMENT .....	59
FIGURE 4-7: SCHEMATIC DIAGRAM OF THE FIRST SET-UP.....	59
FIGURE 4-8: THE DIAGRAM OF THE SECOND SET-UP .....	60
FIGURE 4-9: COMPARISON BETWEEN THREE PARTICLE SIZES AT 0.625 % PS CONCENTRATION BY USING AN OPTICAL PROBE WITH 100 $\mu\text{M}$ , EACH PARTICLE SIZE WITH A DIFFERENT SIGNATURE. ....	61
FIGURE 4-10: DERIVATIVES OF THE SPECTRA IN FIGURE 4.9.....	61
FIGURE 4-11: PARTICLE DIAMETER AS A FUNCTION OF THE TOTAL NUMBER OF MAXIMA AND MINIMA OF THE ELASTIC SCATTER SPECTRUM DERIVATIVES BETWEEN 450 AND 800 NM. ....	62
FIGURE 4-12: COMPARING THE CORE DIAMETER 100 AND 200 $\mu\text{M}$ FOR THREE PARTICLES 2, 0.8 AND 0.413(A, B AND C) MICRON WITH CONCENTRATION (2.5%) STOCK PS CONCENTRATION.....	63
FIGURE 4-13: THE SPECTRUM FOR THREE PARTICLES 2, 0.8 AND 0.413 $\mu\text{M}$ (A, B AND C) WITH VARIOUS CONCENTRATIONS 2.5%, 1.25% AND 0.625% PS CONCENTRATION, RESPECTIVELY, BY USING THE PROBE OF 100 $\mu\text{M}$ CORE DIAMETER.....	64
FIGURE 4-14: COMPARING TG AND LED THREE PARTICLES' SIZES 2, 0.8 AND 0.413 $\mu\text{M}$ (A, B AND C) AT 2.5 % PS CONCENTRATION WITH 200 $\mu\text{M}$ CORE DIAMETER.....	65
FIGURE 4-15: COMPARISON BETWEEN THE FIRST (PROBE 1 WITH 200 FOR THE TWO IDENTICAL CORE DIAMETER) AND A SECOND CONFIGURATION SET UP FOR THREE PARTICLES SIZES 2, 0.8 AND 0.413 $\mu\text{M}$ (A, B AND C) AT 2.5 % PS CONCENTRATION.....	66
FIGURE 4-16: COMPARISON BETWEEN THE FIRST (PROBE 1 WITH 200 FOR THE TWO IDENTICAL CORE DIAMETER) AND A SECOND CONFIGURATION SET UP FOR THREE PARTICLES SIZES 2, 0.8 AND 0.413 $\mu\text{M}$ (A, B AND C) AT 1.25 % PS CONCENTRATION.....	66
FIGURE 4-17: COMPARISON BETWEEN THE FIRST (PROBE 1 WITH 200 FOR THE TWO IDENTICAL CORE DIAMETER) AND A SECOND CONFIGURATION SET UP FOR THREE PARTICLES SIZES 2, 0.8 AND 0.413 $\mu\text{M}$ (A, B AND C) AT 0.625 % PS CONCENTRATION.....	67
FIGURE 4-18: A NUMBER OF MAXIMA AND MINIMA AMONG THREE DIFFERENT DESIGNS. ....	67
FIGURE 5-1: ELECTRIC FIELD BETWEEN OPPOSITELY CHARGED PLATES. ....	70
FIGURE 5-2: WATER MOLECULE DIPOLES RANDOMLY ORIENTATED IN THE ABSENCE OF AN APPLIED ELECTRIC FIELD. ....	70
FIGURE 5-3: POLARISED (ALIGNED) WATER DIPOLES OPPOSING THE APPLIED ELECTRIC FIELD. ....	71
FIGURE 5-4: CORRECTED LOW FREQUENCY PERMITTIVITY $\epsilon(0)$ WITH THE RANGE OF THE TEMPERATURE (15 TO 35) $^{\circ}\text{C}$ . 74	74
FIGURE 5-5: CORRECTED EXTRAPOLATED HIGH-FREQUENCY PERMITTIVITY $\epsilon(\infty)$ WITH THE RANGE OF THE TEMPERATURE (15 TO 35) $^{\circ}\text{C}$ .....	74
FIGURE 5-6: CORRECTED RELAXATION TIME $\tau$ WITH THE RANGE OF THE TEMPERATURE (15 TO 35) $^{\circ}\text{C}$ .....	75
FIGURE 5-7: MATHEMATICAL DEBYE MODEL FROM OUR WORK, PERMITTIVITY REAL AND IMAGINARY WITH THE RANGE OF FREQUENCY (1E8-1E12) HZ AT RANGE TEMPERATURE (15 TO 35) $^{\circ}\text{C}$ . ....	75
FIGURE 5-8: OUR CALCULATOR LABORATORY FOR MEASURING THE REAL AND IMAGINARY PERMITTIVITY FOR SPECIFIC FREQUENCY AND TEMPERATURE. ....	75
FIGURE 5-9: MAGNITUDE COMPLEX EFFECTIVE PERMITTIVITY FOR DI-W AND DIFFERENT CONCENTRATION OF SUSPENSION POLYSTYRENE (2.5%, 2.25%, 2%, 1.75%, 1.5% AND 1.25%) AT FREQUENCY RANGE (0.1 TO 3) GHZ. ....	78
FIGURE 5-10: TANGENT $\delta$ FOR DI-W AND DIFFERENT CONCENTRATION OF SUSPENSION POLYSTYRENE (2.5%, 2.25%, 2%, 1.75%, 1.5% AND 1.25%) AT FREQUENCY RANGE (0.1 TO 3) GHZ. ....	78
FIGURE 5-11: EFFECTIVE REAL PERMITTIVITY FOR DI-W AND DIFFERENT CONCENTRATION OF SUSPENSION POLYSTYRENE (2.5%, 2.25%, 2%, 1.75%, 1.5% AND 1.25%) AT FREQUENCY RANGE (0.1 TO 3) GHZ. ....	79
FIGURE 5-12: EFFECTIVE IMAGINARY PERMITTIVITY FOR DI-W AND DIFFERENT CONCENTRATION OF SUSPENSION POLYSTYRENE (2.5%, 2.25%, 2%, 1.75%, 1.5% AND 1.25%) AT FREQUENCY RANGE (0.1 TO 3) GHZ. ....	79
FIGURE 5-13: THE REFLECTION $S_{11}$ AS A FUNCTION TO THE RANGE OF THE FREQUENCY (0.1 TO 3) GHZ FOR THE DI-W (CALIBRATION CURVE) AND THE CONCENTRATIONS RANGE (2.5% TO 1.25%) AT 0.413 MM PARTICLE SIZE. ....	80
FIGURE 5-14: THE REFLECTION $S_{11}$ AS A FUNCTION TO THE RANGE OF THE FREQUENCY (100 TO 200) MHZ FOR THE DI- W (CALIBRATION CURVE) AND THE CONCENTRATIONS RANGE (2.5% TO 1.25%) AT 0.413 MM PARTICLE SIZE. 81	81
FIGURE 5-15: THE REFLECTION $S_{11}$ AS A FUNCTION TO THE RANGE OF THE FREQUENCY (100 TO 200) MHZ FOR THE DI- W (CALIBRATION CURVE) AND THE CONCENTRATIONS RANGE (2.5% TO 1.25%) AT 0.8 MM PARTICLE SIZE. ....	81

FIGURE 5-16: THE REFLECTION $S_{11}$ AS A FUNCTION TO THE RANGE OF THE FREQUENCY (100 TO 200) MHZ FOR THE DI-W (CALIBRATION CURVE) AND THE CONCENTRATIONS RANGE (2.5% TO 1.25%) AT 2 MM PARTICLE SIZE. ....	81
FIGURE 5-17: THE COMPARISON BETWEEN THE THEORETICAL CALCULATION AND THE EXPERIMENTAL RESULTS FOR NON-RESONANT METHOD AT FREQUENCY RANGE 100 TO 200 MHZ FOR THE DI-W AND THE CONCENTRATIONS RANGE 2.5% TO 1.25%. ....	82
FIGURE 5-18: LINE TRANSMISSION MODEL.....	84
FIGURE 5-19: LOSS TRANSMISSION MODEL. ....	84
FIGURE 5-20: LOSING FEATURES.....	86
FIGURE 5-21: SERIES RLC RESONATOR CIRCUIT. ....	87
FIGURE 5-22: INPUT IMPEDANCE VERSUS FREQUENCY OF THE SERIOUS RESONANT.....	88
FIGURE 5-23: PARALLEL RLC RESONATOR CIRCUIT. ....	89
FIGURE 5-24: INPUT IMPEDANCE VERSUS FREQUENCY OF THE PARALLEL RESONANT. ....	89
FIGURE 5-25: REGIONS FOR CARRYING CURRENT. ....	91
FIGURE 5-26: LOSING FEATURES.....	95
FIGURE 5-27: CALCULATION OF THE Q FACTOR. ....	96
FIGURE 5-28: THE SCHEMATIC OF THE COAXIAL PROBE SIMULATION. ....	98
FIGURE 5-29: EXPERIMENTAL PHYSICAL SET-UP. ....	98
FIGURE 5-30: THE MEASURED BW FOR ALL MODES IN THE RANGE OF THE FREQUENCY (0.1 TO 6) GHZ WITH SYMMETRIC VALUES OF THE CAPACITORS (0.0075, 0.01, 0.05, 0.075 AND 0.1) GHZ. ....	100
FIGURE 5-31: CENTRAL FREQUENCY MEASUREMENTS FOR THE RANGE OF THE FREQUENCY (0.1 TO 6) GHZ WITH SYMMETRIC VALUES OF THE CAPACITORS (0.0075, 0.01, 0.05, 0.075 AND 0.1) PF.....	101
FIGURE 5-32: THE MEASURED Q FACTOR FOR THE RANGE OF THE FREQUENCY (0.1 TO 6) GHZ WITH SYMMETRIC VALUES OF THE CAPACITORS (0.0075, 0.01, 0.05, 0.075 AND 0.1) PF. ....	101
FIGURE 5-33: $S_{21}$ MEASUREMENTS FOR THE RANGE OF THE FREQUENCY (0.1 TO 6) GHZ WITH SYMMETRIC VALUES OF THE CAPACITORS (0.0075, 0.01, 0.05, 0.075 AND 0.1) PF. ....	102
FIGURE 5-34: COMPARISON BETWEEN BW MEASURED OF ASYMMETRIC CAPACITORS (0.1 AND 0.05) PF AND THE OPPOSITE, SYMMETRIC CAPACITORS (0.05, 0.1 AND 0.075 (THE AVE. VALUE OF THE ASYMMETRICAL CAPACITORS) PF FOR THE RANGE OF THE FREQUENCY (0.1 TO 6) GHZ. ....	103
FIGURE 5-35: COMPARISON BETWEEN CF MEASURED OF ASYMMETRIC CAPACITORS (0.1 AND 0.05) PF AND THE OPPOSITE, SYMMETRIC CAPACITORS (0.05, 0.1 AND 0.075 (THE AVE. VALUE OF THE ASYMMETRICAL CAPACITORS) PF FOR THE RANGE OF THE FREQUENCY (0.1 TO 6) GHZ. ....	103
FIGURE 5-36: COMPARISON BETWEEN Q FACTOR MEASURED OF ASYMMETRIC CAPACITORS (0.1 AND 0.05) PF AND THE OPPOSITE, SYMMETRIC CAPACITORS (0.05, 0.1 AND 0.075 (THE AVE. VALUE OF THE ASYMMETRICAL CAPACITORS) PF FOR THE RANGE OF THE FREQUENCY (0.1 TO 6) GHZ. ....	104
FIGURE 5-37: COMPARISON BETWEEN $S_{21}$ MEASURED OF ASYMMETRIC CAPACITORS (0.1 AND 0.05) PF AND THE OPPOSITE, SYMMETRIC CAPACITORS (0.05, 0.1 AND 0.075 (THE AVE. VALUE OF THE ASYMMETRICAL CAPACITORS) PF FOR THE RANGE OF THE FREQUENCY (0.1 TO 6) GHZ. ....	104
FIGURE 5-38: COMPARISON BETWEEN DIFFERENT ASYMMETRICAL (0.05 & 0.1 PF, 0.06 & 0.09 PF, 0.07 & 0.08, AND VICE VERSA) PF AND THE SYMMETRICAL 0.075 PF CASE FOR THE ACTUAL FIRST MODE (LOWER FREQUENCY). .	105
FIGURE 5-39: COMPARISON BETWEEN $S_{21}$ MEASURED OF ASYMMETRIC CAPACITORS (0.1 AND 0.05) PF AND THE OPPOSITE, SYMMETRIC CAPACITORS (0.05, 0.1 AND 0.075 (THE AVE. VALUE OF THE ASYMMETRICAL CAPACITORS) PF FOR THE RANGE OF THE FREQUENCY (0.1 TO 6) GHZ. ....	105
FIGURE 5-40: COMPARISON BETWEEN BW MEASUREMENTS AT SYMMETRIC CAPACITORS 0.0075 PF WITH DIFFERENT COAXIAL LENGTHS (255, 180 AND 105) MM. ....	106
FIGURE 5-41: COMPARISON BETWEEN RESONANT FREQUENCY MEASUREMENTS AT SYMMETRIC CAPACITORS 0.0075 PF WITH DIFFERENT COAXIAL LENGTHS (255, 180 AND 105) MM. ....	107
FIGURE 5-42: COMPARISON BETWEEN Q FACTOR MEASUREMENTS AT SYMMETRIC CAPACITORS 0.0075 PF WITH DIFFERENT COAXIAL LENGTHS (255, 180 AND 105) MM. ....	107
FIGURE 5-43: COMPARISON BETWEEN $S_{21}$ MEASUREMENTS AT SYMMETRIC CAPACITORS 0.0075 PF WITH DIFFERENT COAXIAL LENGTHS (255, 180 AND 105) MM. ....	108

FIGURE 5-44: COMPARISON BETWEEN $S_{21}$ MEASURED FOR DIFFERENT SAMPLES (AIR AND DI-W) AT STEP SIZE 0.1GHZ, SYMMETRIC CAPACITORS (0.0075) PF AND (0.0073) PF FOR AIR AND WATER, RESPECTIVELY FOR THE WHOLE RANGE OF FREQUENCY (0.1 TO 6) GHZ .....	109
FIGURE 5-45: COMPARISON BETWEEN $S_{21}$ MEASURED FOR DIFFERENT SAMPLE (AIR AND DI-W) AT SYMMETRIC CAPACITORS (0.0075) PF AND (0.0073) PF FOR AIR AND WATER RESPECTIVELY AT THE FIRST MODE AT RESONANT FREQUENCY 0.382 GHZ.....	109
FIGURE 5-46: COMPARISON BETWEEN $S_{21}$ MEASURED FOR DIFFERENT SAMPLE (AIR AND DI-W) AT SYMMETRIC CAPACITORS (0.0075) PF AND (0.0073) PF FOR AIR AND WATER RESPECTIVELY AT THE LAST MODE AT RESONANT FREQUENCY 5.433 GHZ.....	110
FIGURE 5-47: COMPARISON BETWEEN $S_{21}$ MEASURED FOR DIFFERENT OF NORMAL SALINE SAMPLE CONCENTRATIONS (STOCK= 0.154 M, FIRST CONCENTRATIONS ( $C_1=0.077M$ ) AND SECOND CONCENTRATIONS ( $C_2=0.039 M$ )) AT THE FIRST RESONANT FREQUENCY (0.76 GHZ).....	111
FIGURE 5-48: SKEW EXAMPLES OWING TO INDUCTIVE, CAPACITIVE CROSS-COUPLING AND NEARBY MODES .....	112
FIGURE 5-49: RESISTIVE CAPACITIVE AND INDUCTIVE ELEMENTS THAT REPRESENT A LOSSY RESONANT CIRCUIT. ....	112
FIGURE 5-50: THE EQUIVALENT CIRCUIT OF A TWO-PORT, LOOP- COUPLED RESONATOR. THE RESONATOR IS MODELLED AS A SERIES LRC CIRCUIT OF IMPEDANCE Z .....	113
FIGURE 5-51: MICROWAVE RESONATOR MODEL WITH AN ARBITRARY NUMBER FOR RESONANCE OR CROSSTALK TERMS. ....	115
FIGURE 5-52: $ S_{21} $ SHOWN THE NO SKEW CASE ( $S_{21}$ —LINE) AND FOR INCREASING SKEW RATIO. ....	117
FIGURE 5-53: $ S_{21} $ SHOWN THE NO SKEW CASE ( $S_{21}$ —BLUE) AND FOR INCREASING SKEW RATIO. ....	117
FIGURE 5-54: EXAMPLE OF A TYPICAL SKEWED RESONANCE CURVE. ....	118
FIGURE 5-55: THE POLAR PLOT OF THE RESONANCE ABOVE, THE POSITION OF THE PEAK IS HIGHLIGHTED WITH THE RED DOT AND THE CENTRE OF THE CIRCLE IS DENOTED WITH THE CROSS.....	118
FIGURE 5-56: DE-SKEWED RESONANCE (RED) AND ORIGINAL SKEWED RESONANCE (BLUE). ....	119
FIGURE 5-57: DE-SKEWED RESONANCE (RED) AND ORIGINAL SKEWED RESONANCE (BLUE). ....	119
FIGURE 6-1: THE PHYSICAL CAVITY PRINCIPLE. ....	123
FIGURE 6-2: THE PREPARATION DILUTION STEPS FROM COMMERCIAL OBTAINED SALINE.....	126
FIGURE 6-3: COMSOL SIMULATIONS OF E-FIELD DISTRIBUTIONS FOR TWO CAVITY MODES. A: $TM_{010}$ E-FIELD AT 2.45 GHZ, B: $TM_{210}$ E-FIELD AT 5.33 GHZ.....	127
FIGURE 6-4: $ S_{21} $ FOR THE CCR USED WITH SENSING AND REFERENCE MODES HIGHLIGHTED.....	128
FIGURE 6-5: RELATIONSHIP BETWEEN THE SIGNAL MODE (VERTICAL AXIS) AND THE REFERENCE MODE (HORIZONTAL AXIS) MEASURED OVER A PERIOD OF TIME WHERE THE TEMPERATURE OF THE CAVITY WAS ALLOWED TO CHANGE. CORRELATION COEFFICIENT 0.999. ....	128
FIGURE 6-6: FITTING CORRELATION BETWEEN THE $Q_{SENSE}$ AND $C_{REF}$ FOR DI-W. ....	129
FIGURE 6-7: CORRECTION LINEAR EQUATION. ....	129
FIGURE 6-8: AFFECTION CAVITY FREQUENCY CORRECTION OF Q FACTOR.....	131
FIGURE 6-9: EFFECT OF CAVITY TEMPERATURE CORRECTION FOR Q FACTOR AFTER FREQUENCY CORRECTION (Q FACTOR_F_CORR.). ....	132
FIGURE 6-10: EXPONENTIAL CHANGE OF THE TEMPERATURE. ....	133
FIGURE 6-11: RAW DATA, FREQUENCY, TEMPERATURE AND EXPONENTIAL CORRECTIONS FOR Q FACTOR MEASUREMENTS FOR DIFFERENT CONCENTRATIONS OF THE NORMAL SALINE (0.154 TO 9.400E-06) MOLARITY (COMMERCIAL OBTAINED SALINE) OF $TM_{010}$ CAVITY (EPPENDORF SAMPLE TUBE). ....	135
FIGURE 6-12: RAW DATA, FREQUENCY, TEMPERATURE AND EXPONENTIAL CORRECTIONS FOR $ S_{21} $ MEASUREMENTS FOR DIFFERENT CONCENTRATIONS OF THE NORMAL SALINE (0.154 TO 9.400E-06) MOLARITY (COMMERCIAL OBTAINED SALINE) OF $TM_{010}$ CAVITY (EPPENDORF SAMPLE TUBE). ....	135
FIGURE 6-13: RAW DATA, FREQUENCY, TEMPERATURE AND EXPONENTIAL CORRECTIONS FOR BW MEASUREMENTS FOR DIFFERENT CONCENTRATIONS OF THE NORMAL SALINE (0.154 TO 9.400E-06) MOLARITY (COMMERCIAL OBTAINED SALINE) OF $M_{010}$ CAVITY (EPPENDORF SAMPLE TUBE). ....	136
FIGURE 6-14: AVE. OF Q FACTOR OVER THE THREE SETS AFTER APPLYING ALL THE CORRECTIONS OF THE NORMAL SALINE (0.154 TO 9.400E-06) MOLARITY.....	136
FIGURE 6-15: AVERAGING $ S_{21} $ OVER THE THREE SETS AFTER APPLYING ALL THE CORRECTIONS OF THE NORMAL SALINE (0.154 TO 9.400E-06) MOLARITY.....	137

FIGURE 6-16: AVERAGING BW OVER THE THREE SETS AFTER APPLYING ALL THE CORRECTIONS OF THE NORMAL SALINE (0.154 TO 9.400E-06) MOLARITY.....	137
FIGURE 6-17: RANGES OF STDEV IN THE NORMAL PROBABILITY DENSITY FUNCTION. ....	138
FIGURE 6-18: THE CORRELATION BETWEEN THE CORRECTED Q FACTOR DATA WITH DIFFERENT CONCENTRATIONS AND STATISTICAL DETECTION $\pm(2\sigma(\text{RED})$ AND $3\sigma(\text{BLUE}))$ . ....	139
FIGURE 6-19: THE CORRELATION BETWEEN THE CORRECTED $ S_{21} $ DATA WITH DIFFERENT CONCENTRATIONS AND STATISTICAL DETECTION $\pm(2\sigma(\text{RED})$ AND $3\sigma(\text{BLUE}))$ . ....	139
FIGURE 6-20: THE CORRELATION BETWEEN THE CORRECTED BW DATA WITH DIFFERENT CONCENTRATIONS AND STATISTICAL DETECTION $\pm(2\sigma(\text{RED})$ AND $3\sigma(\text{BLUE}))$ . ....	140
FIGURE 6-21: AVERAGING OF Q FACTOR CORRECTIONS AFTER REPEATING THREE TIMES AT A CONCENTRATION BETWEEN (0.154 TO 9.400E-06) MOLARITY.....	140
FIGURE 6-22: AVERAGING OF $ S_{21} $ CORRECTIONS AFTER REPEATING THREE TIMES AT A CONCENTRATION BETWEEN (0.154 TO 9.400E-06) MOLARITY.....	141
FIGURE 6-23: AVERAGING OF BW CORRECTIONS AFTER REPEATING THREE TIMES AT A CONCENTRATION BETWEEN (0.154 TO 9.400E-06) MOLARITY. ....	141
FIGURE 6-24: AVERAGE RESONANT FREQUENCY $CF_{\text{SENSE}}$ AFTER REPEATING THREE TIMES AT A CONCENTRATION BETWEEN (0.154 TO 9.400E-06) MOLARITY.....	141
FIGURE 6-25: PREPARATION STEPS OF LAB PREPARED SALINE DILUTIONS. ....	142
FIGURE 6-26: FITTING TEMPERATURE CORRECTION FOR Q FACTOR.....	144
FIGURE 6-27: FITTING TEMPERATURE CORRECTION FOR $ S_{21} $ .....	144
FIGURE 6-28: FITTING TEMPERATURE CORRECTION FOR BW MEASUREMENTS. ....	144
FIGURE 6-29: RAW DATA BLACK, TEMPERATURE GREEN AND EXPONENTIAL IN RED CORRECTIONS FOR Q FACTOR MEASUREMENTS FOR VARIANCE CONCENTRATIONS (5.22E-05 TO 1.71) M (LAB PREPARED SALINE DILUTIONS) OF M010 CAVITY (EPPENDORF SAMPLE TUBE). ....	145
FIGURE 6-30: RAW DATA BLACK, TEMPERATURE GREEN AND EXPONENTIAL IN RED CORRECTIONS FOR $ S_{21} $ MEASUREMENTS FOR VARIANCE CONCENTRATIONS (5.22E-05 TO 1.71) M (LAB PREPARED SALINE DILUTIONS) OF M010 CAVITY (EPPENDORF SAMPLE TUBE). ....	145
FIGURE 6-31: RAW DATA BLACK, TEMPERATURE GREEN AND EXPONENTIAL IN RED CORRECTIONS FOR BW MEASUREMENTS FOR VARIANCE CONCENTRATIONS (5.22E-05 TO 1.71) M (LAB PREPARED SALINE DILUTIONS) OF M010 CAVITY (EPPENDORF SAMPLE TUBE). ....	146
FIGURE 6-32: AVE. OF Q FACTOR OVER THE FOUR SETS AFTER APPLYING ALL THE CORRECTIONS FOR VARIANCE CONCENTRATIONS (5.22E-05 TO 1.71) M.....	146
FIGURE 6-33: AVE. OF $ S_{21} $ OVER THE FOUR SETS AFTER APPLYING ALL THE CORRECTIONS FOR VARIANCE CONCENTRATIONS (5.22E-05 TO 1.71) M.....	147
FIGURE 6-34: AVE. OF BW OVER THE FOUR SETS AFTER APPLYING ALL THE CORRECTIONS FOR VARIANCE CONCENTRATIONS (5.22E-05 TO 1.71) M.....	147
FIGURE 6-35: THE CORRELATION BETWEEN THE CORRECTED Q FACTOR DATA WITH DIFFERENT CONCENTRATIONS AND STATISTICAL DETECTION $\pm(2\sigma(\text{RED})$ AND $3\sigma(\text{BLUE}))$ . ....	148
FIGURE 6-36: THE CORRELATION BETWEEN THE CORRECTED $ S_{21} $ DATA WITH DIFFERENT CONCENTRATIONS AND STATISTICAL DETECTION $\pm(2\sigma(\text{RED})$ AND $3\sigma(\text{BLUE}))$ . ....	148
FIGURE 6-37: THE CORRELATION BETWEEN THE CORRECTED BW DATA WITH DIFFERENT CONCENTRATIONS AND STATISTICAL DETECTION $\pm(2\sigma(\text{RED})$ AND $3\sigma(\text{BLUE}))$ . ....	149
FIGURE 6-38: COMPARISON BETWEEN COMMERCIALY OBTAINED SALINE AND LAB PREPARED SALINE DILUTIONS FOR Q FACTOR MEASUREMENTS. ....	150
FIGURE 6-39: COMPARISON BETWEEN COMMERCIALY OBTAINED SALINE AND LAB PREPARED SALINE DILUTIONS FOR $ S_{21} $ MEASUREMENTS. ....	150
FIGURE 6-40: COMPARISON BETWEEN COMMERCIALY OBTAINED SALINE AND LAB PREPARED SALINE DILUTIONS FOR BW MEASUREMENTS. ....	150
FIGURE 6-41: COMPARISON BETWEEN COMMERCIALY OBTAINED SALINE AND LAB PREPARED SALINE DILUTIONS FOR CF MEASUREMENTS. ....	151

FIGURE 6-42: THE COMPARISON AMONG THE REAL PERMITTIVITY AMONG THE LAB PREPARED SALINE DILUTIONS AT (1.00E+02, 5.00E+01-7.81E-01) PPT, COMMERCIAL OBTAINED SALINE AT (9.00E+00-5.49E-04) PPT., PENMAN’S RESULTS AT (2.73E+02, 1.64E+02, 5.47E+01, 2.73E+01, 1.09E+01AND 2.73E+00) PPT AND WEBSITE AT (35 TO 0) PPT. ....	153
FIGURE 6-43: THE COMPARISON AMONG THE IMAGINARY PERMITTIVITY AMONG THE LAB PREPARED SALINE DILUTIONS AT (1.00E+02, 5.00E+01-7.81E-01) PPT, COMMERCIAL OBTAINED SALINE AT (9.00E+00-5.49E-04) PPT., PEYMAN’S RESULTS AT (2.73E+02, 1.64E+02, 5.47E+01, 2.73E+01, 1.09E+01AND 2.73E+00) PPT AND WEBSITE AT (35 TO 0)PPT. ....	153
FIGURE 6-44: THE COMPARISON BETWEEN THE EXCEL AND MATLAB CORRECTIONS. ....	154
FIGURE 6-45: DEMONSTRATED THE COMPARISON BETWEEN THE AVERAGE FOR RAW DATA AND THE CORRECTIONS OF EXCEL AND MATLAB.....	154
FIGURE 6-46: COMPARISON BETWEEN THE EXCEL CORRECTIONS (A) AND MATLAB FOR DIFFERENT SETS (B), AVERAGING.....	155
FIGURE 6-47: AVERAGING CENTRAL FREQUENCY FOR SUSPENSION POLYSTYRENE (2 MM) WITH DIFFERENT CONCENTRATIONS (12.5 TO 0.195) PPT. ....	156
FIGURE 6-48: RAW DATA, FREQUENCY, TEMPERATURE AND EXPONENTIAL CORRECTIONS FOR Q FACTOR MEASUREMENTS OF DILUTIONS PREPARED FROM SUSPENSION POLYSTYRENE (2MM) WITH DIFFERENT CONCENTRATIONS (12.5 TO 0.195) PPT BY USING EPPENDORF TUBE SAMPLE (CAVITY TM010). ....	156
FIGURE 6-49: RAW DATA, FREQUENCY, TEMPERATURE AND EXPONENTIAL CORRECTIONS FOR $ S_{21} $ MEASUREMENTS OF DILUTIONS PREPARED FROM SUSPENSION POLYSTYRENE (2MM) WITH DIFFERENT CONCENTRATIONS (12.5 TO 0.195) PPT BY USING EPPENDORF TUBE SAMPLE (CAVITY TM010). ....	157
FIGURE 6-50: RAW DATA, FREQUENCY, TEMPERATURE AND EXPONENTIAL CORRECTIONS FOR BANDWIDTH MEASUREMENTS OF DILUTIONS PREPARED FROM SUSPENSION POLYSTYRENE (2MM) WITH DIFFERENT CONCENTRATIONS (12.5 TO 0.195) PPT BY USING EPPENDORF TUBE SAMPLE (CAVITY TM010). ....	157
FIGURE 6-51: AVERAGING OF Q FACTOR OVER THE TWO SETS AFTER APPLYING ALL THE CORRECTIONS FOR SUSPENSION POLYSTYRENE (2 MM) WITH DIFFERENT CONCENTRATIONS (12.5 TO 0.195) PPT BY USING EPPENDORF TUBE SAMPLE (CAVITY M010). ....	157
FIGURE 6-52: AVERAGING $ S_{21} $ OVER THE TWO SETS AFTER APPLYING ALL THE CORRECTIONS FOR SUSPENSION POLYSTYRENE (2 MM) WITH DIFFERENT CONCENTRATIONS (12.5 TO 0.195) PPT BY USING EPPENDORF TUBE SAMPLE (CAVITY M010). ....	158
FIGURE 6-53: AVERAGING BANDWIDTH OVER THE TWO SETS AFTER APPLYING ALL THE CORRECTIONS FOR SUSPENSION POLYSTYRENE (2 MM) WITH DIFFERENT CONCENTRATIONS (12.5 TO 0.195) PPT BY USING EPPENDORF TUBE SAMPLE (CAVITY M010). ....	158
FIGURE 6-54: THE CORRELATION BETWEEN THE CORRECTED Q FACTOR, CORRECTED DATA WITH DIFFERENT CONCENTRATIONS FOR SUSPENSION POLYSTYRENE OF 2 MM (12.5 TO 0.195) PPT AND STATISTICAL DETECTION $\pm(2\sigma(\text{RED})$ AND $3\sigma(\text{BLUE}))$ .....	158
FIGURE 6-55: THE CORRELATION BETWEEN THE CORRECTED $ S_{21} $ CORRECTED DATA WITH DIFFERENT CONCENTRATIONS FOR SUSPENSION POLYSTYRENE OF MM (12.5 TO 0.195) PPT AND STATISTICAL DETECTION $\pm(2\sigma(\text{RED})$ AND $3\sigma(\text{BLUE}))$ .....	159
FIGURE 6-56: THE CORRELATION BETWEEN THE CORRECTED BW CORRECTED DATA WITH DIFFERENT CONCENTRATIONS FOR SUSPENSION POLYSTYRENE OF 2 MM (12.5 TO 0.195) PPT AND STATISTICAL DETECTION $\pm(2\sigma(\text{RED})$ AND $3\sigma(\text{BLUE}))$ .....	159
FIGURE 6-57: AVERAGING QUALITY FACTOR FOR SUSPENSION POLYSTYRENE (2 MM) WITH CONCENTRATION RANGE 12.5 TO 0.195 PPT BY USING EPPENDORF TUBE SAMPLE (CAVITY TM010). ....	160
FIGURE 6-58: $ S_{21} $ MEASUREMENTS FOR SUSPENSION POLYSTYRENE (2 MM) WITH CONCENTRATION RANGE 12.5 TO 0.195 PPT BY USING EPPENDORF TUBE SAMPLE (CAVITY TM010).....	160
FIGURE 6-59: AVERAGING BANDWIDTH MEASUREMENTS FOR SUSPENSION POLYSTYRENE (2 MM) WITH CONCENTRATION RANGE12.5 TO 0.195 PPT BY USING EPPENDORF TUBE SAMPLE (TM010). ....	160
FIGURE 6-60: AVERAGING CENTRAL FREQUENCY MEASUREMENTS FOR SUSPENSION POLYSTYRENE (2MM) WITH CONCENTRATION RANGE12.5 TO 0.195 PPT BY USING EPPENDORF TUBE SAMPLE (TM010). ....	161

FIGURE 6-61: RAW DATA, TEMPERATURE AND EXPONENTIAL CORRECTIONS FOR Q FACTOR MEASUREMENTS OF LAB PREPARED SALINE DILUTIONS FOR VARIANCE CONCENTRATIONS (5.22E-05 TO 1.71E+00) M BY USING A LONG THIN EPPENDORF TUBE SAMPLE. ....	162
FIGURE 6-62: RAW DATA, TEMPERATURE AND EXPONENTIAL CORRECTIONS FOR $ S_{21} $ MEASUREMENTS OF LAB PREPARED SALINE DILUTIONS FOR VARIANCE CONCENTRATIONS (5.22E-05 TO 1.71E+00) M BY USING A LONG THIN EPPENDORF TUBE SAMPLE. ....	162
FIGURE 6-63: RAW DATA, TEMPERATURE AND EXPONENTIAL CORRECTIONS FOR BW MEASUREMENTS OF LAB PREPARED SALINE DILUTIONS FOR VARIANCE CONCENTRATIONS (5.22E-05 TO 1.71E+00) M BY USING A LONG THIN EPPENDORF TUBE SAMPLE. ....	163
FIGURE 6-64: THE CORRELATION BETWEEN THE CORRECTED Q FACTOR DATA WITH DIFFERENT CONCENTRATION FOR VARIANCE SALINE CONCENTRATION (5.22E-05 TO 1.71) M AND STATISTICAL DETECTION $\pm(2\sigma(\text{RED})$ AND $3\sigma(\text{BLUE}))$ BY USING A LONG THIN EPPENDORF TUBE SAMPLE. ....	163
FIGURE 6-65: THE CORRELATION BETWEEN THE CORRECTED $ S_{21} $ DATA WITH DIFFERENT CONCENTRATION FOR VARIANCE SALINE CONCENTRATION (5.22E-05 TO 1.71) M AND STATISTICAL DETECTION $\pm(2\sigma(\text{RED})$ AND $3\sigma(\text{BLUE}))$ BY USING A LONG THIN EPPENDORF TUBE SAMPLE. ....	164
FIGURE 6-66: THE CORRELATION BETWEEN THE CORRECTED BW DATA WITH DIFFERENT CONCENTRATION FOR VARIANCE SALINE CONCENTRATION (5.22E-05 TO 1.71) M AND STATISTICAL DETECTION $\pm(2\sigma(\text{RED})$ AND $3\sigma(\text{BLUE}))$ BY USING A LONG THIN EPPENDORF TUBE SAMPLE. ....	164
FIGURE 6-67: REAL PERMITTIVITY COMPARISON AMONG LAB PREPARED SALINE DILUTIONS BY USING EPPENDORF AND LONG THIN EPPENDORF TUBE SAMPLE AND COMMERCIALY OBTAINED SALINE, PREVIOUS AUTHORS WORK. ...	165
FIGURE 6-68: IMAGINARY PERMITTIVITY COMPARISON AMONG LAB PREPARED SALINE DILUTIONS BY USING EPPENDORF AND LONG THIN EPPENDORF TUBE SAMPLE AND COMMERCIAL OBTAINED SALINE AND PREVIOUS AUTHORS WORK. ....	165
FIGURE 6-69: THE AVERAGING CORRECTED QUALITY FACTOR OF THE SUSPENSION POLYSTYRENE 2 MM WITH VARIOUS CONCENTRATIONS 12.5 TO 0.195 PPT AND DI-W FOR A LONG THIN EPPENDORF TUBE. ....	166
FIGURE 6-70: THE AVERAGING CORRECTED $ S_{21} $ OF THE SUSPENSION POLYSTYRENE 2 MM WITH VARIOUS CONCENTRATIONS 12.5 TO 0.195 PPT AND DI-W FOR A LONG THIN EPPENDORF TUBE. ....	166
FIGURE 6-71: THE AVERAGING CORRECTED BW OF THE SUSPENSION POLYSTYRENE 2 MM WITH VARIOUS CONCENTRATIONS 12.5 TO 0.195 PPT AND DI-W FOR A LONG THIN EPPENDORF TUBE. ....	166
FIGURE 6-72: THE CORRECTED QUALITY FACTOR AND THE CONCENTRATION OF THE SUSPENSION POLYSTYRENE 12.5 TO 0.195 PPT AND DI-W FOR A LONG THIN EPPENDORF TUBE. ....	167
FIGURE 6-73: THE CORRECTED $ S_{21} $ AND THE CONCENTRATION OF THE SUSPENSION POLYSTYRENE 12.5 TO 0.195 PPT AND DI-W FOR A LONG THIN EPPENDORF TUBE ....	167
FIGURE 6-74: THE CORRECTED BW AND THE CONCENTRATION OF THE SUSPENSION POLYSTYRENE 12.5 TO 0.195 PPT AND DI-W FOR A LONG THIN EPPENDORF TUBE ....	168
FIGURE 6-75: THE RESONANT FREQUENCY AND THE CONCENTRATION OF THE SUSPENSION POLYSTYRENE 12.5 TO 0.195 PPT AND DI-W FOR A LONG THIN EPPENDORF TUBE. ....	168
FIGURE 6-76: REAL PERMITTIVITY COMPARISON BETWEEN THE EXPERIMENTAL AND THE THEORETICAL AT THE CONCENTRATION OF THE SUSPENSION POLYSTYRENE 12.5 TO 0.195 PPT. ....	169
FIGURE 6-77: IMAGINARY PERMITTIVITY COMPARISON BETWEEN THE EXPERIMENTAL AND THE THEORETICAL AT THE CONCENTRATION OF THE SUSPENSION POLYSTYRENE 12.5 TO 0.195 PPT. ....	170
FIGURE 7-1: SCHEMATIC DESIGN OF A NOVEL T- STRUCTURE AND CAPACITIVE COUPLING. ....	172
FIGURE 7-2: PHYSICAL DESIGN OF A NOVEL T- STRUCTURE AND CAPACITIVE COUPLING. ....	173
FIGURE 7-3: RAW AND AVERAGING DATA FOR Q FACTOR MEASUREMENTS OF COMMERCIAL OBTAINED SALINE FOR VARIANCE CONCENTRATIONS (0.154 TO 9.400E-06) M. ....	174
FIGURE 7-4: RAW AND AVERAGING DATA FOR $ S_{21} $ OF COMMERCIAL OBTAINED SALINE FOR VARIANCE CONCENTRATIONS (0.154 TO 9.400E-06) M. ....	174
FIGURE 7-5: RAW AND AVERAGING DATA FOR BW MEASUREMENTS OF COMMERCIAL OBTAINED SALINE FOR VARIANCE CONCENTRATIONS (0.154 TO 9.400E-06) M. ....	175
FIGURE 7-6: DETECTION LIMITS AT BW IN THE FIRST MODE 0.757 GHz OVER A RANGE OF DILUTIONS (0.154 TO 9.400E-06) M. ....	176

FIGURE 7-7: DETECTION LIMITS AT BW IN THE SECOND MODE 1.52 GHZ OVER A RANGE OF DILUTIONS (0.154 TO 9.400E-06) M. ....	176
FIGURE 7-8: DETECTION LIMITS AT BW IN THE THIRD MODE 2.3 GHZ OVER A RANGE OF DILUTIONS (0.154 TO 9.400E-06) M. ....	177
FIGURE 7-9: COMPARISON BETWEEN Q FACTOR OF DIFFERENT FREQUENCIES (0.757, 1.52, 2.3 AND 3) GHZ FOR VARIANCE CONCENTRATIONS (0.154 TO 9.400E-06) M. ....	177
FIGURE 7-10: COMPARISON BETWEEN $ S_{21} $ OF DIFFERENT FREQUENCIES (0.757, 1.52, 2.3 AND 3) GHZ FOR VARIANCE CONCENTRATIONS (0.154 TO 9.400E-06) M. ....	178
FIGURE 7-11: COMPARISON BETWEEN BW OF DIFFERENT FREQUENCIES (0.757, 1.52, 2.3 AND 3) GHZ FOR VARIANCE CONCENTRATIONS (0.154 TO 9.400E-06) M. ....	178
FIGURE 7-12: COMPARISON BETWEEN CF OF DIFFERENT FREQUENCIES (0.757, 1.52, 2.3 AND 3) GHZ FOR VARIANCE CONCENTRATIONS (0.154 TO 9.400E-06) M. ....	178
FIGURE 7-13: VARIATION IN THE QUALITY FACTOR AT 0.378 GHZ WITH THE PICO TEMPERATURE (T <sub>0</sub> ), WHICH IS A SIMPLE TERM INTERFACE BETWEEN THERMOCOUPLE AND THE PC, SAMPLE TEMPERATURE (T <sub>1</sub> ) AND AMBIENT TEMPERATURE (T <sub>2</sub> ). ....	180
FIGURE 7-14: CORRELATION OF THE CENTRAL FREQUENCY (CF_1) 0.378 GHZ WITH THE PICO TEMPERATURE (T <sub>0</sub> ), SAMPLE TEMPERATURE (T <sub>1</sub> ) AND AMBIENT TEMPERATURE (T <sub>2</sub> ). ....	180
FIGURE 7-15: THE AVERAGE Q FACTOR MEASUREMENTS OF LAB. PREPARED SALINE FOR VARIANCE CONCENTRATIONS (5.22 E-05 TO 1.71) M. ....	181
FIGURE 7-16: THE AVERAGE $ S_{21} $ MEASUREMENTS OF LAB. PREPARED SALINE FOR VARIANCE CONCENTRATIONS (5.22E-05 TO 1.7) M. ....	181
FIGURE 7-17: THE AVERAGE BW MEASUREMENTS OF LAB. PREPARED SALINE FOR VARIANCE CONCENTRATIONS (5.22E-05 TO 1.71) M. ....	182
FIGURE 7-18: DETECTION LIMITS AT BW IN THE FIRST MODE 0.378 GHZ OVER A RANGE OF DILUTIONS (5.22E-05 TO 1.71) M. ....	182
FIGURE 7-19: DETECTION LIMITS AT BW IN THE SECOND MODE 0.757 GHZ OVER A RANGE OF DILUTIONS (5.22E-05 TO 1.71) M. ....	183
FIGURE 7-20: DETECTION LIMITS AT BW IN THE THIRD MODE 1.14 GHZ OVER A RANGE OF DILUTIONS (5.22E-05 TO 1.71) M. ....	183
FIGURE 7-21: DETECTION LIMITS AT BW IN THE FOURTH MODE 1.52 GHZ OVER A RANGE OF DILUTIONS (5.22E-05 TO 1.71) M. ....	183
FIGURE 7-22: COMPARISON BETWEEN Q FACTOR OF DIFFERENT FREQUENCIES (0.378, 0.757, 1.14 AND 1.52) GHZ FOR VARIANCE CONCENTRATIONS (5.22E-05 TO 1.71) M. ....	185
FIGURE 7-23: COMPARISON BETWEEN $ S_{21} $ OF DIFFERENT FREQUENCIES (0.378, 0.757, 1.14 AND 1.52) GHZ FOR VARIANCE CONCENTRATIONS (5.22E-05 TO 1.71) M. ....	185
FIGURE 7-24: COMPARISON BETWEEN BW OF DIFFERENT FREQUENCIES (0.378, 0.757, 1.14 AND 1.52) GHZ FOR VARIANCE CONCENTRATIONS (5.22E-05 TO 1.71) M. ....	186
FIGURE 7-25: COMPARISON BETWEEN CF OF DIFFERENT FREQUENCIES (0.378, 0.757, 1.14 AND 1.52) GHZ FOR VARIANCE CONCENTRATIONS (5.22E-05 TO 1.71) M. ....	186
FIGURE 7-26: COMPARING BETWEEN THE Q FACTOR MEASUREMENTS OF DIFFERENT FREQUENCIES FOR VARIANCE CONCENTRATIONS OF COMMERCIALY OBTAINED SALINE (0.154 TO 9.4E-06) M AND LAB. PREPARED SALINE DILUTIONS (5.22E-05 TO 1.71) M. ....	187
FIGURE 7-27: COMPARING BETWEEN THE $ S_{21} $ MEASUREMENTS OF DIFFERENT FREQUENCIES FOR VARIANCE CONCENTRATIONS OF COMMERCIALY OBTAINED SALINE (0.154 TO 9.4E-06) M AND LAB. PREPARED SALINE DILUTIONS (5.22E-05 TO 1.71) M. ....	188
FIGURE 7-28: COMPARING BETWEEN BW MEASUREMENTS OF DIFFERENT FREQUENCIES FOR VARIANCE CONCENTRATIONS OF COMMERCIALY OBTAINED SALINE (0.154 TO 9.4E-06) M AND LAB. PREPARED SALINE DILUTIONS (5.22E-05 TO 1.71) M. ....	188
FIGURE 7-29: CORROSION OF THE STEEL CENTRE CONDUCTOR. ....	189
FIGURE 7-30: COMPARING BETWEEN REAL PERMITTIVITY OF DIFFERENT FREQUENCIES 0.378, 0.757, 1.14 AND 1.52 GHZ OF LAB. PREPARED SALINE DILUTIONS (5.22E-05 TO 1.71) M. ....	189

FIGURE 7-31: COMPARING BETWEEN IMAGINARY PERMITTIVITY OF DIFFERENT FREQUENCIES 0.378, 0.757, 1.14 AND 1.52 GHZ OF LAB. PREPARED SALINE DILUTIONS (5.22E-05 TO 1.71) M.....	190
FIGURE 7-32: RAW DATA FOR BW MEASUREMENTS OF POLYSTYRENE WITH 2 MM OF FOUR MODES FOR VARIANCE CONCENTRATIONS (25 TO 1.56) PPT. ....	191
FIGURE 7-33: RAW DATA FOR Q FACTOR OF POLYSTYRENE WITH 2 MM OF FOUR MODES FOR VARIANCE CONCENTRATIONS (25 TO 1.56) PPT. ....	191
FIGURE 7-34: RAW DATA FOR $ S_{21} $ OF POLYSTYRENE WITH 2 MM OF FOUR MODES FOR VARIANCE CONCENTRATIONS (25 TO 1.56) PPT. ....	192
FIGURE 7-35: RAW DATA-BLACK AND CORRECTED DATA IN RED OF POLYSTYRENE WITH 2 MM AT THE FIRST MODE (378 MHZ) FOR VARIANCE CONCENTRATIONS (25 TO 1.56) PPT. ....	193
FIGURE 7-36: FITTING AVERAGING RAW DATA AND TEMPERATURE (T) IN THE SECOND MODE (757 MHz).....	193
FIGURE 7-37: SCATTER IN THE BW FOR WATER FOR MODE 2 (RAW DATA- BLACK AND CORRECTED DATA-RED).....	194
FIGURE 7-38: SCATTER AND AVERAGING AFTER CORRECTION IN THE BW FOR THREE SETS FOR MODE 2 (RAW DATA - BLACK, CORRECTED DATA-ORANGE AND AVERAGING AFTER CORRECTIONS - RED).....	194
FIGURE 7-39: FITTING AVERAGING RAW DATA AND CF IN THE THIRD MODE (1.14 GHZ). ....	195
FIGURE 7-40: SCATTER IN THE BW FOR WATER FOR MODE 3 (RAW DATA-BLACK AND CORRECTED DATA-RED).....	195
FIGURE 7-41: SCATTER IN THE BW FOR WATER FOR MODE 3 (RAW DATA – BLACK, CF CORRECTED DATA RED – AND TEMPERATURE CORRECTED IN GREEN). ....	196
FIGURE 7-42: CORRECTED AND AVERAGED THE BW FOR ALL SAMPLES FOR MODE 3 (RAW DATA– BLACK, CF CORRECTED DATA-ORANGE, TEMPERATURE CORRECTED DATA- GREEN AND AVERAGING AFTER CORRECTIONS IN RED). ....	196
FIGURE 7-43: FITTING AVERAGING BW- RAW DATA AND CF OF THE FOURTH MODE (1.52 GHZ). ....	197
FIGURE 7-44: SCATTER IN THE BW FOR WATER FOR MODE 4 (1.52 GHZ) (RAW DATA - BLACK, CF CORRECTED DATA – RED AND TEMPERATURE CORRECTED DATA IN GREEN).....	197
FIGURE 7-45: CORRECTED AND AVERAGED THE BW FOR ALL SAMPLES FOR MODE 4 (RAW DATA- BLACK, CF CORRECTED DATA- ORANGE, TEMPERATURE CORRECTED DATA- GREEN AND AVERAGING AFTER CORRECTIONS IN RED). ...	198
FIGURE 7-46: RAW DATA, CORRECTIONS AND AVERAGING OF Q FACTOR MEASUREMENTS FOR ALL MODES AT VARIANCE CONCENTRATIONS (25 TO 1.56) PPT OF 2 MM (RAW DATA - BLACK, CORRECTED DATA - ORANGE AND GREEN AND AVERAGING IN RED). ....	198
FIGURE 7-47: RAW DATA, CORRECTIONS AND AVERAGING OF $ S_{21} $ MEASUREMENTS FOR ALL MODES AT VARIANCE CONCENTRATIONS (25 TO 1.56) PPT OF 2 MM (RAW DATA - BLACK, CORRECTED DATA-ORANGE AND GREEN AND AVERAGING IN RED).....	199
FIGURE 7-48: AVE. OF BW OVER THE THREE SETS AFTER APPLYING ALL THE CORRECTIONS FOR VARIANCE CONCENTRATIONS (25 TO 1.56) PPT AT 2 MM. ....	199
FIGURE 7-49: AVE. OF Q FACTOR OVER THE THREE SETS AFTER APPLYING ALL THE CORRECTIONS FOR VARIANCE CONCENTRATIONS (25 TO 1.56) PPT AT 2 MM. ....	200
FIGURE 7-50: AVE. OF $ S_{21} $ OVER THE THREE SETS AFTER APPLYING ALL THE CORRECTIONS FOR VARIANCE CONCENTRATIONS (25 TO 1.56) PPT AT 2 MM. ....	200
FIGURE 7-51: THE CORRELATION BETWEEN THE BANDWIDTH CORRECTED DATA WITH DIFFERENT CONCENTRATIONS AND STATISTICAL DETECTION ( $2\sigma$ AND $3\sigma$ ) AT 2 MM. ....	201
FIGURE 7-52: THE AVERAGE BW MEASUREMENTS AFTER CORRECTIONS FOR SUSPENSION POLYSTYRENE (2 MM) WITH A CONCENTRATION RANGE OF 25 TO 1.56 PPT.....	201
FIGURE 7-53: THE AVERAGE Q FACTOR MEASUREMENTS AFTER CORRECTIONS FOR SUSPENSION POLYSTYRENE (2 MM) WITH A CONCENTRATION RANGE OF 25 TO 1.56 PPT. ....	202
FIGURE 7-54: THE AVERAGE $ S_{21} $ MEASUREMENTS AFTER CORRECTIONS FOR SUSPENSION POLYSTYRENE (2 MM) WITH A CONCENTRATION RANGE OF 25 TO 1.56 PPT.....	202
FIGURE 7-55: THE AVERAGE CF MEASUREMENTS FOR SUSPENSION POLYSTYRENE (2 MM) WITH A CONCENTRATION RANGE OF 25 TO 1.56 PPT. ....	202
FIGURE 7-56: REAL PERMITTIVITY OF THE EXPERIMENTAL WORK FOR DIFFERENT MODE (0.377, 0.757, 1.14 AND 1.52) GHZ AT VARIANCE CONCENTRATIONS OF THE 2 MM FOR SUSPENSION POLYSTYRENE (25 TO 1.56) PPT.....	203
FIGURE 7-57: IMAGINARY PERMITTIVITY OF THE EXPERIMENTAL WORK FOR DIFFERENT MODES (0.377, 0.757, 1.14 AND 1.52) GHZ AT VARIANCE CONCENTRATIONS OF THE 2 MM FOR SUSPENSION POLYSTYRENE (25 TO 1.56) PPT.....	204

FIGURE 7-58: RAW DATA, CORRECTIONS AND AVERAGING OF BW MEASUREMENTS FOR ALL MODES AT VARIANCE CONCENTRATIONS (25 TO 1.56) PPT OF 0.8 MM (RAW DATA - BLACK, CORRECTED DATA - ORANGE AND GREEN AND AVERAGING IN RED) .....	205
FIGURE 7-59: RAW DATA, CORRECTIONS AND AVERAGING OF Q FACTOR MEASUREMENTS FOR ALL MODES AT VARIANCE CONCENTRATIONS (25 TO 1.56) PPT OF 0.8 MM (RAW DATA - BLACK, CORRECTED DATA - ORANGE AND GREEN AND AVERAGING IN RED) .....	205
FIGURE 7-60: RAW DATA, CORRECTIONS AND AVERAGING OF $ S_{21} $ MEASUREMENTS FOR ALL MODES AT VARIANCE CONCENTRATIONS (25 TO 1.56) PPT OF 0.8 MM (RAW DATA - BLACK, CORRECTED DATA - ORANGE AND GREEN AND AVERAGING IN RED) .....	206
FIGURE 7-61: THE CORRELATION BETWEEN THE CORRECTED BW DATA WITH DIFFERENT CONCENTRATIONS AND STATISTICAL DETECTION $\pm(2\sigma(\text{RED})$ AND $3\sigma(\text{BLUE}))$ AT 0.8 MM FOR ALL MODES. ....	206
FIGURE 7-62: AVE. BW MEASUREMENTS AFTER CORRECTIONS FOR SUSPENSION POLYSTYRENE (0.8 MM) WITH CONCENTRATION RANGE 25 TO 1.56 PPT OF ALL MODES. ....	207
FIGURE 7-63: AVE. Q FACTOR MEASUREMENTS AFTER CORRECTIONS FOR SUSPENSION POLYSTYRENE (0.8 MM) WITH CONCENTRATION RANGE 25 TO 1.56 PPT OF ALL MODES. ....	207
FIGURE 7-64: AVE. $ S_{21} $ MEASUREMENTS AFTER CORRECTIONS FOR SUSPENSION POLYSTYRENE (0.8 MM) WITH CONCENTRATION RANGE 25 TO 1.56 PPT OF ALL MODES. ....	208
FIGURE 7-65: AVE. CF MEASUREMENTS FOR SUSPENSION POLYSTYRENE (0.8 MM) WITH CONCENTRATION RANGE 25 TO 1.56 PPT. ....	208
FIGURE 7-66: REAL PERMITTIVITY OF THE EXPERIMENTAL WORK FOR DIFFERENT MODE (0.378, 0.757, 1.14 AND 1.52) GHZ AT VARIANCE CONCENTRATIONS OF 0.8 MM FOR SUSPENSION POLYSTYRENE (25 TO 1.56) PPT.....	209
FIGURE 7-67: IMAGINARY PERMITTIVITY OF THE EXPERIMENTAL WORK FOR DIFFERENT MODES (0.378, 0.757, 1.14 AND 1.52) GHZ AT VARIANCE CONCENTRATIONS OF 0.8 MM FOR SUSPENSION POLYSTYRENE (25 TO 1.56) PPT... ..	209
FIGURE 7-68: COMPARISON BETWEEN THE REAL PERMITTIVITY AT DIFFERENT MODES (0.378, 0.757, 1.14 AND 1.52) GHZ AT VARIANCE CONCENTRATIONS FOR THREE PARTICLE SIZES (2, 0.8 AND 0.413) MM (25 TO 1.56) PPT FOR 2 AND 0.8 MM AND (25 TO 3.12) PPT FOR 0.413 MM.....	211
FIGURE 7-69: COMPARISON BETWEEN THE IMAGINARY PERMITTIVITY AT DIFFERENT MODES (0.378, 0.757, 1.14 AND 1.52) GHZ AT VARIANCE CONCENTRATIONS FOR THREE PARTICLE SIZES (2, 0.8 AND 0.413) MM (25 TO 1.56) PPT FOR 2 AND 0.8 MM AND (25 TO 3.12) PPT FOR 0.413 MM. ....	212
FIGURE 8-1: PROTRUDING PROBE 'CUT BACK' .....	215
FIGURE 8-2: BANDWIDTH MEASURED FOR DIFFERENT CONCENTRATIONS OF 0.8 MM PS SPHERES AT THE FIRST 4 MODES OF THE PROBE RESONATOR.....	216
FIGURE 8-3: FITTING AVERAGING RAW DATA AND CENTRAL FREQUENCY (CF) IN THE FIRST MODE (432 MHz). ....	218
FIGURE 8-4: SCATTER IN THE BW FOR WATER FOR MODE 1 (RAW DATA _ BLUE AND CORRECTED DATA _ ORANGE)..	218
FIGURE 8-5: SCATTER IN THE BW FOR ALL SAMPLES FOR MODE 1 (RAW DATA _ BLUE AND CORRECTED DATA _ ORANGE). ....	219
FIGURE 8-6: AVERAGE OF THE BW FOR ALL SAMPLES FOR MODE 1 (RAW DATA _ BLUE AND CORRECTED DATA _ ORANGE). ....	219
FIGURE 8-7: THE CORRELATION BETWEEN THE CORRECTED DATA WITH DIFFERENT CONCENTRATIONS AND STATISTICAL DETECTION ( $2\sigma$ AND $3\sigma$ ) OF MODE1 (432) MHZ.....	220
FIGURE 8-8: FITTING AVERAGING RAW DATA AND TEMPERATURE OF THE ENVIRONMENT IN THE SECOND MODE (868 MHZ).....	220
FIGURE 8-9: SCATTER IN THE BW FOR WATER FOR MODE 2 (RAW DATA – BLUE AND CORRECTED DATA – ORANGE)..	221
FIGURE 8-10: SCATTER IN THE BW FOR WATER FOR MODE 2 (RAW DATA – BLUE, TEMPERATURE CORRECTED DATA – ORANGE AND CF CORRECTED IN GREEN).....	221
FIGURE 8-11: AVERAGE OF THE BW FOR ALL SAMPLES FOR MODE 2 (RAW DATA – BLUE, TEMPERATURE CORRECTED DATA – ORANGE AND CF CORRECTED IN GREEN). ....	222
FIGURE 8-12: THE CORRELATION BETWEEN THE CORRECTED DATA WITH DIFFERENT CONCENTRATIONS AND STATISTICAL DETECTION ( $2\sigma$ AND $3\sigma$ ) FOR MODE 2.....	223
FIGURE 8-13: FITTING AVERAGED RAW DATA AND TEMPERATURE OF THE ENVIRONMENT IN BW OF THE THIRD MODE (1.31 GHZ).....	223

FIGURE 8-14: SCATTER IN THE BW FOR WATER FOR MODE 3 (RAW DATA – BLUE, TEMPERATURE CORRECTED DATA – ORANGE AND CF CORRECTED IN GREEN).....	224
FIGURE 8-15: THE AVERAGE OF THE BW FOR ALL SAMPLES FOR MODE 3 (RAW DATA – BLUE, TEMPERATURE CORRECTED DATA – ORANGE AND CF CORRECTED IN GREEN). ....	224
FIGURE 8-16: THE CORRELATION BETWEEN THE CORRECTED DATA WITH DIFFERENT CONCENTRATIONS AND STATISTICAL DETECTION ( $2\sigma$ AND $3\sigma$ ). ....	225
FIGURE 8-17: FITTING AVERAGING ROW DATA AND TEMPERATURE OF THE ENVIRONMENT IN BW OF THE FOURTH MODE (1.76 GHz).....	226
FIGURE 8-18: ILLUSTRATED THE RAW DATA, CORRECTED OF CF, AND AMBIENT TEMPERATURE WITH CORRELATION COEFFICIENT (-0.8764). ....	226
FIGURE 8-19: SCATTER IN THE BW FOR WATER FOR MODE 4 (RAW DATA – BLUE, TEMPERATURE CORRECTED DATA – ORANGE AND CF CORRECTED IN GREY).....	227
FIGURE 8-20: AVERAGE OF THE BW FOR ALL SAMPLES FOR MODE 4 (RAW DATA – BLUE, CORRECTED DATA FROM FREQUENCY – ORANGE AND CORRECTED FREQUENCY DATA FROM TEMPERATURE - GREEN). ....	227
FIGURE 8-21: THE CORRELATION BETWEEN THE CORRECTED DATA WITH DIFFERENT CONCENTRATIONS AND STATISTICAL DETECTION ( $2\sigma$ AND $3\sigma$ ). ....	228
FIGURE 8-22: COATED FLAT COAXIAL CABLE WITH AU. ....	229
FIGURE 8-23: BANDWIDTH MEASURED FOR DIFFERENT CONCENTRATIONS OF 0.8 MM PS SPHERES AT THE FIRST 4 MODES OF THE PROBE RESONATOR AFTER COATING WITH AU. ....	230
FIGURE 8-24: THE CORRELATION BETWEEN THE CORRECTED DATA WITH DIFFERENT CONCENTRATIONS AND STATISTICAL DETECTION ( $2\sigma$ AND $3\sigma$ ) AT THE FIRST MODE.....	231
FIGURE 8-25: THE CORRELATION BETWEEN THE CORRECTED DATA WITH DIFFERENT CONCENTRATIONS AND STATISTICAL DETECTION ( $2\sigma$ AND $3\sigma$ ) AT THE SECOND MODE. ....	232
FIGURE 8-26: THE CORRELATION BETWEEN THE CORRECTED DATA WITH DIFFERENT CONCENTRATIONS AND STATISTICAL DETECTION ( $2\sigma$ AND $3\sigma$ ) AT THE THIRD MODE.....	233
FIGURE 8-27: BANDWIDTH MEASURED FOR DIFFERENT CONCENTRATIONS OF 0.8 MM PS SPHERES AT THE FIRST 4 MODES OF THE SPC PROBE RESONATOR. ....	234
FIGURE 8-28: THE CORRELATION BETWEEN THE CORRECTED DATA WITH DIFFERENT CONCENTRATIONS AND STATISTICAL DETECTION ( $2\sigma$ AND $3\sigma$ ) OF 0.8 MM PS SPHERES AT THE FIRST MODE OF THE SPC PROBE RESONATOR.....	235
FIGURE 8-29: THE CORRELATION BETWEEN THE CORRECTED DATA WITH DIFFERENT CONCENTRATIONS AND STATISTICAL DETECTION ( $2\sigma$ AND $3\sigma$ ) OF 0.8 MM PS SPHERES AT THE SECOND MODE OF THE SPC PROBE RESONATOR. ....	236
FIGURE 8-30: THE CORRELATION BETWEEN THE CORRECTED DATA WITH DIFFERENT CONCENTRATIONS AND STATISTICAL DETECTION ( $2\sigma$ AND $3\sigma$ ) OF 0.8 MM PS SPHERES AT THE THIRD MODE OF THE SPC PROBE RESONATOR.....	236
FIGURE 8-31: SCHEMATIC OF A COMBINED SYSTEM. ....	238
FIGURE 8-32: EXPERIMENTAL PHYSICAL SET-UP OF A COMBINED SYSTEM. ....	239
FIGURE 8-33: SCHEMATIC FOR COMBINED MICROWAVE/ OPTICAL SYSTEM TIP .....	239
FIGURE 8-34: THE PRESENTATION OF A COMBINED MICROWAVE/ OPTICAL CORRECTED DATA FOR PS (2 MM) WITH STOCK FROM THE MANUFACTURER (25) PPT AND DIFFERENT CONCENTRATIONS (12.5 TO 0.78) PPT OF FOUR MODES (0.378, 0.757, 1.14 AND 1.52) GHZ OF BW MEASUREMENTS AND OVER THE WAVELENGTH RANGE (400 TO 1000) NM FOR OPTICAL DETECTION. ....	241
FIGURE 8-35: THE AVERAGE CORRECTED OF A COMBINED MICROWAVE (BW)/ OPTICAL DETECTION AND THE CONCENTRATION OF THE PS (12.5 TO 0.78) PPT AND STOCK FROM THE MANUFACTURER (25) PPT AT 2 MM FOR ALL MODES SEPARATELY.....	242
FIGURE 8-36: THE AVERAGE CORRECTED OF A COMBINED MICROWAVE (BW)/ OPTICAL DETECTION AND THE CONCENTRATION OF THE PS (12.5 TO 0.78) PPT AND STOCK FROM THE MANUFACTURER (25) PPT AT 2 MM FOR ALL MODES TOGETHER.....	243
FIGURE 8-37: AREA UNDER CURVE (AUC) OF A COMBINED MICROWAVE (BW)/ OPTICAL DETECTION AND THE CONCENTRATION OF THE PS (12.5 TO 0.78) PPT AT 2 MM FOR ALL MODES TOGETHER.....	243
FIGURE 8-38: THE PRESENTATION OF A COMBINED MICROWAVE/ OPTICAL CORRECTED DATA FOR PS (0.8 MM) WITH STOCK FROM THE MANUFACTURER (25) PPT AND DIFFERENT CONCENTRATIONS (12.5 TO 0.78) PPT OF FOUR MODES (0.378, 0.757, 1.14 AND 1.52) GHZ OF BW MEASUREMENTS AND OVER THE WAVELENGTH RANGE (400 TO 1000) NM FOR OPTICAL DETECTION.....	244

FIGURE 8-39: THE AVERAGE CORRECTED OF A COMBINED MICROWAVE (BW)/ OPTICAL DETECTION AND THE CONCENTRATION OF THE PS (12.5 TO 0.78) PPT AND STOCK FROM THE MANUFACTURER (25) PPT AT 0.8 MM FOR ALL MODES TOGETHER.....	245
FIGURE 8-40: AREA UNDER CURVE (AUC) OF A COMBINED MICROWAVE (BW)/ OPTICAL DETECTION AND THE CONCENTRATION OF THE PS (12.5 TO 0.78) PPT AT 0.8 MM FOR ALL MODES TOGETHER.....	245
FIGURE 8-41: THE PRESENTATION OF A COMBINED MICROWAVE/ OPTICAL CORRECTED DATA FOR PS (0.413 MM) WITH STOCK FROM THE MANUFACTURER AND DIFFERENT CONCENTRATIONS (12.5 TO 0.78) PPT OF FOUR MODES (0.378, 0.757, 1.14 AND 1.52) GHZ OF BW MEASUREMENTS AND OVER THE WAVELENGTH RANGE (400 TO 1000) NM FOR OPTICAL DETECTION. ....	246
FIGURE 8-42: THE AVERAGING CORRECTED OF A COMBINED MICROWAVE (BW)/OPTICAL DETECTION AND THE CONCENTRATION OF THE PS (12.5 TO 0.78) PPT AND STOCK FROM THE MANUFACTURER (25) PPT AT 0.413 MM FOR ALL MODES TOGETHER.....	246
FIGURE 8-43: AREA UNDER CURVE (AUC) OF A COMBINED MICROWAVE (BW)/ OPTICAL DETECTION AND THE CONCENTRATION OF THE PS (12.5 TO 0.78) PPT AT 0.413 MM FOR ALL MODES TOGETHER.....	247
FIGURE 8-44: AREA UNDER CURVE (AUC) COMPARISON FOR ALL PARTICLES (2, 0.8 AND 0.413) MM AT WAVELENGTH DETECTING RANGE (400 TO1000) NM OVER VARIOUS DILATIONS (25 TO 0.78) PPT.....	248
FIGURE 8-45: THE CORRELATION BETWEEN THE CORRECTED BW DATA OF 2 MM WITH DIFFERENT CONCENTRATIONS (25 TO 0.78) PPT AND STATISTICAL DETECTION $\pm(2\sigma(\text{RED})$ AND $3\sigma(\text{BLUE}))$ . ....	249
FIGURE 8-46: THE CORRELATION BETWEEN THE CORRECTED BW DATA OF 0.8 MM WITH DIFFERENT CONCENTRATIONS (25 TO 0.78) PPT AND STATISTICAL DETECTION $\pm(2\sigma(\text{RED})$ AND $3\sigma(\text{BLUE}))$ . ....	249
FIGURE 8-47: THE CORRELATION BETWEEN THE CORRECTED BW DATA OF 0.413 MM WITH DIFFERENT CONCENTRATIONS (25 TO 0.78) PPT AND STATISTICAL DETECTION $\pm(2\sigma(\text{RED})$ AND $3\sigma(\text{BLUE}))$ . ....	250

# LIST OF TABLES

TABLE 1-1: COMPARISON OF BENIGN AND MALIGNANT TUMOUR PRODUCED FROM [14].	7
TABLE 2-1: OVERVIEW OF THE OPTICAL DETECTING TECHNIQUES WITH DIFFERENT TISSUE TYPES	21
TABLE 2-2: OVERVIEW OF THE TISSUE PHANTOM IN THE ELSS DETECTING.	27
TABLE 6-1: DILUTIONS PREPARED FROM COMMERCIALY OBTAINED SALINE (BOOT'S PHARMACY)	134
TABLE 6-2: SAMPLE LABELS AND RESPECTIVE CONCENTRATIONS.	143
TABLE 8-1: MEAN, STANDARD DEVIATION AND PERCENTAGE ERROR FOR FOUR MODES OF THE BW.	217
TABLE 8-2: MEAN, STANDARD DEVIATION AND PERCENTAGE ERROR FOR ROW AND CORRECTED FIRST MODE DATA (432 MHz).	218
TABLE 8-3: MEAN, STANDARD DEVIATION AND PERCENTAGE ERROR FOR RAW AND CORRECTED DATA OF SECOND MODE (686 MHz).	222
TABLE 8-4: MEAN, STANDARD DEVIATION AND PERCENTAGE ERROR FOR MODE THREE OF THE BW.	225
TABLE 8-5: MEAN, STANDARD DEVIATION AND PERCENTAGE ERROR FOR MODE 4 OF THE BW.	228
TABLE 8-6: MEAN, STANDARD DEVIATION AND PERCENTAGE ERROR IN THE BW FOR THE FOUR MODES.	230
TABLE 8-7: MEAN, STANDARD DEVIATION AND PERCENTAGE ERROR FOR FIRST MODE OF THE BW.	231
TABLE 8-8: MEAN, STANDARD DEVIATION AND PERCENTAGE ERROR FOR SECOND MODE OF THE BW.	231
TABLE 8-9: MEAN, STANDARD DEVIATION AND PERCENTAGE ERROR FOR THIRD MODE OF THE BW.	232
TABLE 8-10: MEAN, STANDARD DEVIATION AND PERCENTAGE ERROR IN THE BW AT THE FOUR MODES.	234
TABLE 8-11: MEAN, STANDARD DEVIATION AND PERCENTAGE ERROR IN THE BW AT THE FIRST MODE.	235
TABLE 8-12: MEAN, STANDARD DEVIATION AND PERCENTAGE ERROR IN THE BW AT THE SECOND MODE.	235
TABLE 8-13: MEAN, STANDARD DEVIATION AND PERCENTAGE ERROR IN THE BW AT THE THIRD MODE.	236
TABLE 8-14: MEAN, STANDARD DEVIATION AND PERCENTAGE ERROR IN THE BW FOR THE FOUR MODES.	240
TABLE 8-15: MEAN, STANDARD DEVIATION, PERCENTAGE ERROR AND SE FOR FIRST MODE OF THE BW.	240
TABLE 8-16: MEAN, STANDARD DEVIATION, PERCENTAGE ERROR AND SE FOR SECOND MODE OF THE BW.	240
TABLE 8-17: MEAN, STANDARD DEVIATION, PERCENTAGE ERROR AND SE FOR THIRD MODE OF THE BW.	241
TABLE 8-18: MEAN, STANDARD DEVIATION, PERCENTAGE ERROR AND SE FOR FOURTH MODE OF THE BW.	241

# CHAPTER 1

## INTRODUCTION AND THESIS OVERVIEW

### 1.1 BACKGROUND OF CLINICAL PROBLEM

Cancer is one of the most prevalent and fatal diseases across the globe. According to the Union for International Cancer Control, over 7 million people die from cancer, and more than 11 million new cases are diagnosed worldwide every year. The accurate diagnosis and treatment planning of different types of cancer have been achieved using biopsies. Various medical imaging modalities have been used to guide needle biopsies for tumour diagnosis to extract cells from a suspicious area, such as breast lumps and enlarged lymph nodes. Ultrasound (US) and Computed Tomography (CT) are used in image-guided procedures. Ultrasound is commonly used for counselling due to its flexibility, relatively low cost and capacity to provide real-time visualization with high image quality. However, this technique's image contrast may limit safe needle insertion accuracy, mainly when dealing with complex 3D anatomy [1]. Despite the use of CT imaging as guidance in the positioning of the biopsy, there is a limitation in the visualization of relevant structures due to thresholds in contrast and image resolution. The needle biopsy procedure lacks sensitivity and usually requires multiple sampling locations; the area of interest may be either missed or under-sampled. In some cases, although a biopsy needle is correctly localized in the lesion target, there is a probability for incorrect diagnostic because only necrotic tissue is sampled [2], it is estimated that between 4.3 and 17.9 % of cancer diagnoses are missed by "false-negative" biopsies despite the continuing evolution of imaging techniques in cancer detection. Furthermore, needle biopsies are repeated in 4% through 32% of cases due to the unspecified pathological analysis [3]. Between 75% and 80% of patients who undergo biopsy suffer from unnecessary anxiety and potential morbidity because of low specificity, representing a significant financial burden upon the healthcare system [4]. It is clear that the biopsy procedures are an invasive, complicated and time-consuming procedure; thus, there is an urgent need to develop a more efficient and effective minimally invasive method for an accurate predictive technique for diagnosis to reduce or even eliminate the emotional trauma to the patient waiting for a diagnosis and can speed the next stage of the surgical process. Additionally, to reduce health care costs and eliminate the need for a surgical biopsy [5]

---

## **1.2 OPTICAL AND MICROWAVE NON-DESTRUCTIVE TECHNIQUES**

In this study, two techniques have been used for detecting prior to the novelty of a combined Microwave/ Optical sensor system in the application of cancer detection.

Optical spectroscopy (the first technique) is a non-invasive or minimally invasive real-time diagnostic technique for tissue pathology using a specific wavelength of light. The optical spectrum interprets biochemical information by measuring absorption, fluorescence, or Raman scattering signals. Morphological and structure information can be obtained by techniques that assess the elastic scattering properties of tissue.

Regarding the second technique (Microwave measurements), it is a non-destructive diagnostic technique. Also, the use of Electromicrowave energy in the microwave spectrum plays a vital role in detecting as it can balance the competing requirements in resolution and penetration. The dielectric properties have an essential role in microwave measurements. It quantifies the proportion of energy that falls into three categories (reflected, transmission and absorbed) after the microwave radiation interacts with the material. Furthermore, the advantage gained by measuring the dielectric properties has an essential role in microwave measurements as it is tracking specific properties of the physical or chemical changes in the material. It also clarifies the basic physiological difference between the normal and cancerous tissue in biological systems. Water plays an essential role in detecting microwave measurements. At cancer tissue, the water content and vascular is high except when it becomes necrotic [6, 7]. Moreover, there is an approximate increase in the permittivity by 10% to 30% for high water content tissue, for instance, skin, liver, muscle and spleen [6]. On the other hand, a considerable increase in the dielectric constant and loss factor has been reported for breast tumours (4-10 times). The dielectric constant is the ratio between the permittivity of the material to the permittivity of the vacuum.

## **1.3 AIM AND OBJECTIVES**

The key aim of this research is to develop and combined an optical sensor and a coaxial microwave sensor and evaluate this system's application in cancer detection.

The key objectives of the project include:

- 1- Select the optical technique of Elastic Light Scattering Spectroscopy (ELSS) and develop a mathematical model for geometrical characterization, fabrication optical probe, and experimental work using an artificial tissue, polystyrene sphere in suspension (PS) with different spheres size particles.

- 2- Use of the non-resonant method (open-ended coaxial cable) for detecting by using the range of frequency (0.1 to 3) GHz as the first instance for detection of PS with different dilutions.
- 3- Utilize the resonant technique (cavity resonant) as a reference for detecting PS samples and normal saline with various dilutions.
- 4- Develop the resonant coaxial cable (Novel T-Structure and capacitive coupling technique), simulation by using Advance Design System and experiment work for distinguishing different concentrations normal saline and PS.
- 5- Design a combined system, Microwave (a Novel T-Structure and capacitive coupling technique), and optical sensors exploiting elastic light scattering Spectroscopy fabricated probe for the first time in the application of cancer detection.

## **1.4 HYPOTHESIS**

The hypothesis establishes two variables, Optical detection by elastic light scattering Spectroscopy and Microwave detection by developing a Novel T-Structure and capacitive coupling technique. A combined Microwave /Optical sensors system could be designed for application in cancer detection. Polystyrene spheres in suspension (PS) as a cancer phantom were the subject of both techniques to confirm the ability to detect separately.

## **1.5 TUMOUR BIOLOGY**

### **1.5.1 NORMAL TISSUES**

A tissue consists of a group of cells with similar shapes and functions. In different organs, variable types of tissues can be found. There are four basic types in humans: epithelial, connective, muscular, and nervous tissue.

Epithelial tissue forms the lining of most internal cavities, and it covers the body surface. Secretion, protection, and filtration are the main functions of this tissue. Epithelial tissue has different shapes of cells (thin (stratified), flat (squamous), round (cuboidal) and enlarged (columnar)) [8]. The most abundant and the most widely distributed tissues are connective tissues. These tissues perform different functions, such as support and protection. Ordinary loose connective tissue, fat tissue, dense fibrous tissue, bone, blood, cartilage, and lymph are considered connective tissue in the human body [8]. Muscular tissues are of three types (skeletal, smooth and cardiac). Skeletal muscle is useful in the contraction of parts, and it is a voluntary type. However, smooth muscle is an involuntary type found in the wall of internal organs and blood vessels. Finally, the cardiac muscle is spontaneous, and it is found only in the heart walls.

The function of nerve cells is to receive stimuli and the conduction of impulses to and from all parts of the body, the shape of the nerve cells' neurons are long and string-like [9].

### **1.5.2 BENIGN AND MALIGNANT TUMOUR**

A benign tumour is a mass of cells that cannot invade neighbouring tissue or metastasize to the other parts of the body via the bloodstream or the lymphatic channels and can be removed easily by surgical methods that should result in a cure. The cells are more mature and approximately resemble their tissue of origin [10].

On its own, a benign tumour is not dangerous. However, the location of the tumour is what poses a threat. For instance, a meningioma is a benign, slowly growing tumour arising from the meninges covering the brain. Eventually, it can prove fatal if not removed because it compresses the surrounding healthy brain tissue and interferes with vital brain functions. The following are the most common types of benign tumours:

- Adenomas (epithelial tissue that covers the organs and glands)
- Meningiomas (brain and spinal cord)
- Fibromas or fibroids (connective tissue of any organ – most commonly found in the uterus)
- Papillomas (skin, breast, cervix, and mucous membranes)
- Lipomas (fat cells)
- Nevi (moles)
- Myomas (muscle tissue)
- Hemangiomas (blood vessels and skin)
- Neuromas (nerves)
- Osteochondromas (bones)

Malignant tumours (usually called Cancers), on the other hand, are divided into two broad groups of solid tissue tumours, which are carcinomas and sarcomas [11]. Carcinomas are cancers derived from epithelial cells. This group includes many of the most common cancers. Nearly all cancers developing in the breast, prostate, lung, pancreas, and colon are carcinomas [12]. Whereas sarcomas are cancers from connective tissue (i.e. bone, cartilage, fat, nerve), each develops from cells originating in mesenchymal cells outside the bone marrow [13].

The pathologic examination is used to predict the clinical behaviour of neoplasms. In the benign tumour, the naked eye (macroscopic) is commonly used in an inspection by microscopic examination of the tumour's histologic sections. Electron microscopy, immunohistochemistry can be used to determine the expression of proteins within cells, leading to a whole host of molecular tests evaluating tumour DNA and RNA characteristics[14].

In macroscopic features, benign tumours are sharply demarcated from normal tissue and are often encapsulated (Figure 1-1) by using naked eye examination. The capsule is usually composed of connective tissue. There is expansive growth in benign tumours that compresses the adjacent healthy tissue, which undergoes atrophy and fibrosis [15]. In contrast, malignant tumours lack capsules and are not as clearly separated from healthy tissue as benign.

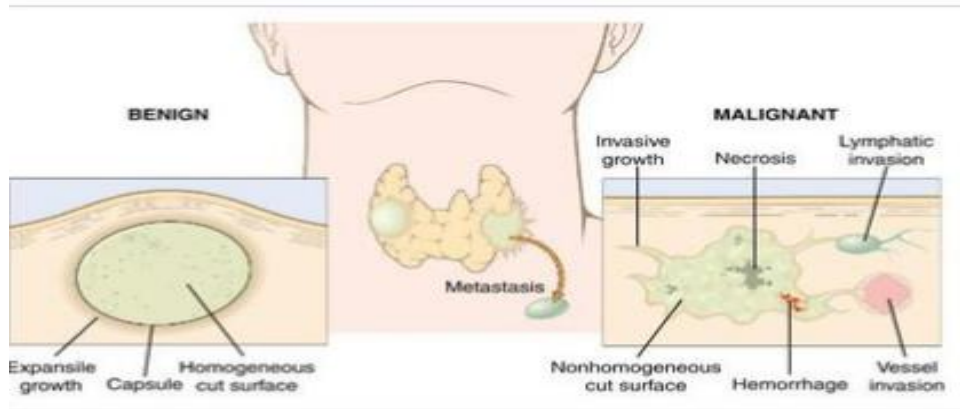


Figure 1-1: Comparison of a benign and a malignant tumour of the thyroid [14].

On histologic examination (Microscopic features), benign tumours consist of cells resembling tissue of origin. They show high degrees of differentiation in shape and colour, as clarified in Figure 1-2. However, the malignant cells demonstrate prominent anaplasia (the exhibition of new features, which are not inherent in the original tissues) [14]. Moreover, malignant tumours may be undifferentiated, as shown in Figure.1-3.

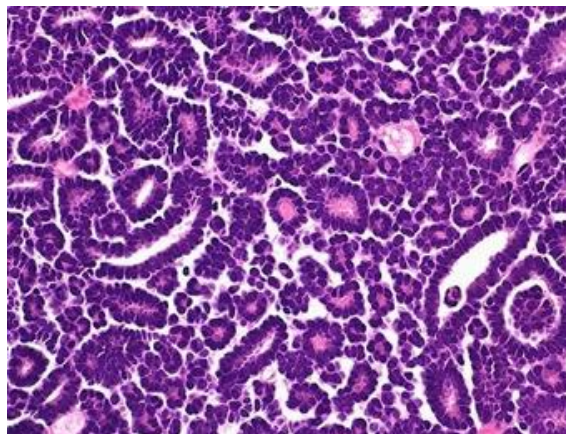


Figure 1-2: Follicular adenoma. The histologic appearance of the thyroid gland's benign tumour cells shows tumour cells that are monomorphic in shape and colour [16].

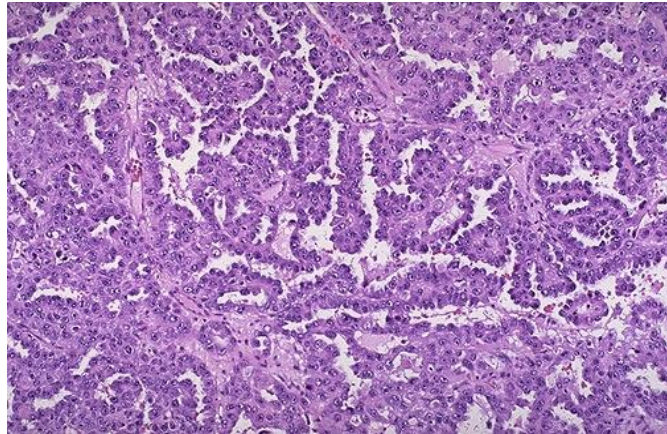


Figure 1-3: Microscopic appearance of a papillary adenocarcinoma of the thyroid. The fronds of tissue have thin fibrovascular cores [17].

Considering the differences between both types of tumours at the cellular features, benign tumours are composed of a uniform cell population. Generally, Benign tumours grow more slowly than malignant tumours, and the tumour cells are usually more differentiated (cells have more normal features)[18]. At the same time, malignant tumours consist of heterogeneous cell populations that often show marked nuclear pleomorphism, which means that there are variations in size, shape and staining properties of tumour cell nuclei [14] (Figure 1-4).

Biologically, benign tumours may retain some of the normal cell's complex functions as the tissue of origin, which is considered well-differentiated. However, there are no signs of differentiation and no specialized function in malignant cells. Table 1-1 demonstrates the most important variations between benign and malignant tumours.

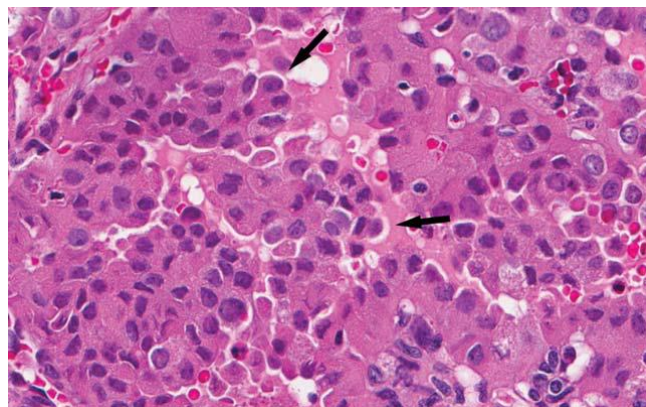


Figure 1-4: Microscopic appearance in a sample of the hobnail variant of papillary thyroid carcinoma, tumour cells have nuclei located toward the middle or apical portion of the cell, producing a surface bulge imparting the so-called "hobnail" appearance (arrows). Occasionally, the cells can appear tall and columnar. Note the ample, eosinophilic, and slightly granular cytoplasm, which is reminiscent of oncocytic cells (H&E stain, original magnification 360) [19].

Table 1-1: Comparison of Benign and Malignant Tumour Produced from [14].

Feature	Benign	Malignant
Growth	Slow	Fast
Metastases (the process that cells move from one part to another part of the body)	No	Yes
Gross Appearance		
External surface	Smooth	Irregular
Capsule	Yes	No
Necrosis	No	Yes
Haemorrhage	No	Yes
Microscopic Appearance		
Architecture	Resemble tissue of origin	Doesn't resemble tissue of origin
Cells	Well-differentiated	Poorly differentiated
Nuclei	Normal size and shape	Pleomorphic
Mitosis (a type of cell division that results in two daughter cells, each having the same number and kind of chromosomes as the parent nucleus, typical of ordinary tissue growth).	Few	Many irregular

## 1.6 THESIS SCOPE

Despite great scientific development, cancer remains a significant health problem. Accurate diagnosis and treatment planning in different cancers have been achieved by using the correct determination of biopsies, an invasive method with the possibility of missing lesions. Continuous development of a more accurate and less invasive approach is urgently needed. Therefore, in this thesis, some non-invasive techniques (optical and resonant techniques) and an initial non or minimally invasive combined technique incorporating a microwave /optical sensor system, have been utilized. This research addressed some problems which can be summarized as non or minimally-invasive, cost-effective, ease of fabrication and simultaneous, real-time measurements.

The optical sensor used in this research can detect the PS of different particle sizes. The resonant coaxial cable and the cavity resonant can detect the normal saline and the PS with different dilutions. The combined sensor Optical/Microwave can detect different particle sizes of PS in simultaneous and real-time measurements. The results showed the probability to utilize in the clinical area as the optical probe showed that each particle size has a different signature and can differentiate various concentrations in simultaneous and real-time measurements for PS dilutions. In our research, the dynamic range of the normal saline is  $5.22E-5$  to  $1.71E+00$  M, It is Lab Prepared Saline Dilutions (more controlled sample preparation) and for PS is 2.5 to 0.098

ppt.

## 1.7 THESIS OVERVIEW

This thesis is split into the following chapters:

**Chapter-2 Diagnostic Techniques** summarises the basic principle of optical techniques, microwave techniques, and other techniques for cancer detection.

**Chapter-3 ELSS Optical Detection** describes the basic principle of detecting ELSS signals and considers some basic designs used in our practical work. Some basic theories and modelling have been presented to indicate general trends.

**Chapter-4 Fabrication and experimental results for the optical probe** describes the fabrication steps necessary to realise two basic probe configurations and shows the results from these probes.

**Chapter-5 Microwave theory, theoretical calculation and simulation work** aims to clarify the basic principle of the mechanism of interaction between the electrical field and materials and the effective permittivity measurements of various PS dilutions. The theoretical description of the coaxial cable (signal transmission and interaction), simulation of our experimental set up for the coaxial probe resonator and different factors affected by the use of the Advance design system software.

**Chapter-6 Microwave cavity technique** describes cavity perturbation theory. Practical work was done using various samples with different concentrations of polystyrene spheres in suspension (PS), normal saline with varying types of preparation and Deionized water (DI-W) as a reference.

**Chapter-7 Resonant coaxial Probe** demonstrates the experimentation of a resonant coaxial probe using various saline concentrations and PS with different particle sizes and the technique for stabilization and corrections.

**Chapter-8 Overcoming challenges and a novel technique for simultaneously detecting microwave and ELSS signals.** This chapter describes some enhancements made to increase the system's sensitivity and Gold (Au) coating of the internal conductor of the coax cable to overcome the corrosion on the probe tip. The final stage for this chapter presents a novel technique: "a combined microwave and optical probe for application in cancer detection".

### 1.7.1 ORIGINAL CONTRIBUTIONS

- The development of the temperature correction of microwave resonant cavity perturbation measurements is summarised in few steps. The first step is removing the frequency effect, which eliminates the room temperature as there is a correlation between the reference and sensing frequency. The second step is removing the impact of the extra temperature effect due to the interconnecting cable—finally, implanting the exponential formula to calculate the sample's asymptotic temperature and overcome the variance between the sample and resonator temperature. This technique can negate a direct measurement for the sample temperature and may have the advantage to apply it in other applications affected by temperature.
- A novel T-Structure and capacitive coupling have been designed to increase the measurements' sensitivity and enable measures at a wide range of discrete frequencies.
- The development of a new approach to temperature correction of a novel T-Structure and capacitive coupling for PS microwave measurements by isolating water experiment results from each set and then a statistical analysis has been done to study the effect of the temperature and the central frequency microwave measurements for all modes.
- The first time use of simultaneously combined microwave / optical system.

## **1.8 PRESENTATIONS**

- Presentation at ENGIN Da Vinci Awards Innovation Pitch 2015-16 on 25<sup>th</sup> Nov.2015.
- Presentations at all Wales Medical Physics and Clinical Engineering in 2016 and 2017. It was a yearly summer meeting. Many experts from all over Wales in the medical area shared their experience with the PhD research at this conference.
- Presentation at Sensors, Signals and Imaging Symposium on 27<sup>th</sup> of June 2017. This symposium was organized by the Sensors, Signals and Imaging Research Group (SSI) at Cardiff School of Engineering by attending experts from various universities in the UK (King's College London, Clifton Medtech Consulting, Bristol, Bristol University and Cardiff University).
- Poster and Presentations at speaking of science Conference in 2016, 2017, 2019 and 2021. This is an annual conference. It allows the students to share the work with other students in Cardiff, Bristol, Bath and Exeter. On 20<sup>th</sup> MAY, 2021, I obtained the best speaker in my session to give an enlightening talk on "A Microwave cavity technique with application in cancer detection".

---

## CHAPTER 2

### DIAGNOSTIC TECHNIQUES

#### 2.1 OPTICAL DIAGNOSTIC TECHNOLOGIES

The established method for characterizing physical and chemical changes in tissues and cells is the optical spectroscopy method. This technique involves the use of light of a specific wavelength range to examine the tissue of interest. In this technique, a particular scattering spectral is a sign to distinguish cancerous from normal tissue by morphological cell and biochemical makeup changes [20]. With this technique, there is a potential for detecting malignant lesions in the first stages before it becomes detectable or viewable (Macroscopically visible) [21]. Various origins have been seen of tumours by using optical spectroscopy technique [22-25].

This technique aims not to distinguish between normal and abnormal tissue, which direct observation methods can achieve, but to differentiate similar clinical characteristics such as dysplasia and carcinoma in situ [26, 27]. The optical spectroscopy method examines pathology areas such as hyperkeratosis, inflammation, dysplasia, carcinoma, and neoplasia in situ. This technique's advantages are that it is non- or minimally invasive and provides real-time diagnostic data for both in-vivo and ex-vivo modalities. Additionally, this technique can reduce healthcare costs by eliminating histology and the need for surgical biopsy in many cases [28]. Furthermore, immediate acquisition of diagnostic information can reduce the emotional trauma to the patient caused during the wait for the result. Several optical techniques are available to the medical community, such as Diffuse Reflectance Spectroscopy (DRS), Fluorescence Spectroscopy (FS), Raman Spectroscopy (RS) and Elastic Light Scattering Spectroscopy (ELSS).

##### 2.1.1 DIFFUSE REFLECTANCE SPECTROSCOPY (DRS)

DRS is an optical technique that measures the properties of intrinsic light absorption and scattering in tissue after broadband of light frequencies interacts with the tissue molecules. The reflected spectrum undergoes many changes due to the combination of scattering and absorption properties at different wavelengths [29]. After illuminating the tissue with the selected broadband light spectrum, the characteristic scattering and absorption are analysed to obtain an optical fingerprint of the tissue. The optical fingerprint represents specific quantities of morphological and biochemical information from the inspected tissue and depends mainly on metabolic rate, vascularity, intravascular Oxygenation and alteration in tissue morphology [30]. The spectra were composed of different samples by using this system. The system comprises a tungsten/halogen broadband light source. Two spectrometers (the two spectrometers resolve the light in the visible wavelength range between 400 nm and 1100 nm and the near-infrared

wavelength range from 800 to 1700 nm, respectively). An optical probe is with three optical fibres. One optical fibre is connected to the light source, and the other two fibres are connected to the spectrometers to collect diffusely scattered light from the tissue (Figure 2-1).

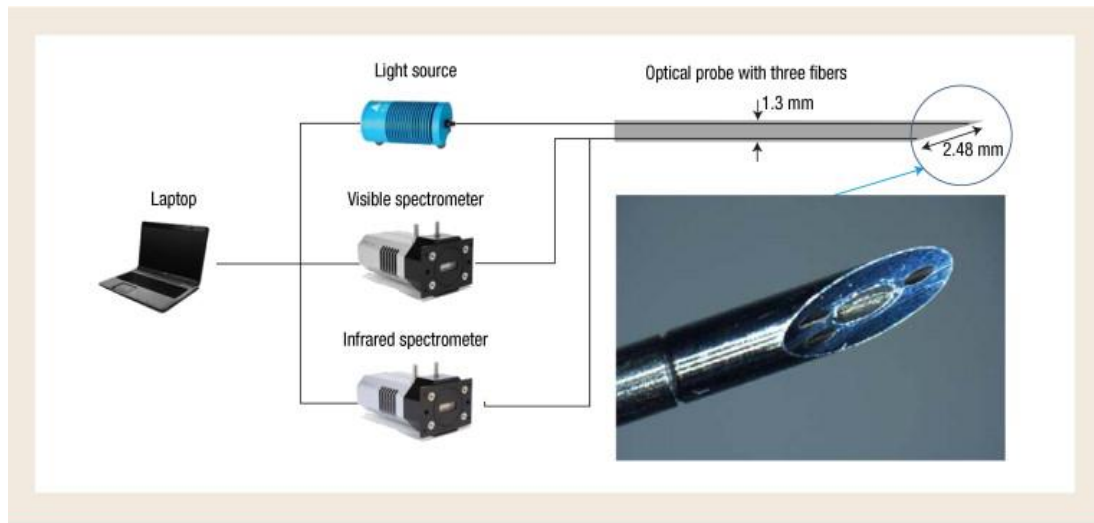


Figure 2-1: Diffuse reflectance spectroscopy set up [31].

DRS can guide surgeons during cancer surgery. Therefore, many authors have used this technique in cancer detection. Over the last twenty years, there has been a gradual increase in the rate of incidence and mortality of primary and secondary liver cancer in all parts of the world [32]. The researchers in the Netherlands Cancer Institute demonstrated the evaluation of scattering amplitude and volume fraction of the bile on healthy and metastatic liver cancer tissues from ex-vivo human liver resections. These values can distinguish between both types of tissue [33]. Another study [30] from the same team has confirmed the ability to use DRS to discriminate metastatic from normal liver tissue with high accuracy and predict the degree of hepatic steatosis. One of the drawbacks of these studies is that there are no in-vivo studies to confirm this technique's clinical applications.

A recent in vivo study investigated 21 patients undergoing lung cancer surgery in routine diagnostic lung biopsy procedures. It found that the DRS technique is a powerful new tool for biopsy guidance after integration into the biopsy needle [34]. Other authors have demonstrated that by using the combination of DRS with conventional imaging techniques, there is an improvement in diagnosis accuracy, with a minimally invasive procedure in the lung [31]. Furthermore, the dual-modality, diffuse reflectance spectroscopy-fluorescence spectroscopy (DRS-FS), has been used for discriminating between healthy and malignant tissue [2, 35-37]. DRS and FS's combination in biopsy devices have significantly enhanced transthoracic biopsies [2]. The advantages of the combination of DRS and FS are for improving the identification of cancerous lesions in different organs [2]. With DRS, the changes in the reflected spectrum translate the variance of tissue interaction. In this way, various chromophores in the tissue such

---

as haemoglobin (oxygenated and deoxygenated),  $\beta$ -carotene, water lipids, and collagen can be quantified and distinguished. Furthermore, the information about the underlying cellular structures can be derived by calculating the scattering coefficient. The FS adds the probability detection of intrinsic fluorophores in the measured tissue, such as Elastin and collagen, which are proteins structure and associated with tissue structure. Also, nicotinamide adenine dinucleotide (NADH) and Flavin-adenine dinucleotide (FAD) indicate the metabolism of cellular energy [37]. Another study has found that the quantitative functional information from dual model DRS-FS plays a vital role in detecting pathologic response. These findings might help observe and predict the efficiency of cancer therapy according to patient response. Hence this technique has high efficiency in monitoring and predicting cancer therapy [36]. Additionally, Zonies et al. approved the DRS's ability to obtain in-vivo information regarding tissue structure and composition. These results have been derived from haemoglobin concentration, oxygen saturation, effective scatter density and effective scatter size. The findings have been collected in vivo from adenomatous polyps on 13 patients undergoing routine colonoscopy [35]. Moreover, optical spectroscopy, DRS and FS, can detect colorectal cancer from surrounding healthy tissue, especially when these small fibres are incorporated into surgical tools, which helps detect the tissue's direct feedback and the real-time response [37]. Prabitha et al. have reported a study on the detection of cervical lesions by multivariate analysis of DRS. They developed an algorithm to discriminate from 48 sites in 34 patients with a sensitivity of 72% and specificity of 87%. Furthermore, this study's findings illustrated that the technique could be used, along with multivariate analytical methods, as a non-invasive method to track cervical disease status in real-time [38].

Breast cancer is the most common cancer in women worldwide; thus, the DRS plays a role in breast cancer diagnosis and improved survival rate. In 2013, Ever et al. studied breast cancer's diagnostic accuracy from 47 female patients' ex-vivo by the DRS technique. This group acquired a sensitivity of 90%, a specificity of 88% and an overall accuracy of 89% to distinguish between the normal and malignant breast tissue and a nearly 100% accuracy in categorizing the results as either benign or malignant [29]. Furthermore, Volynskaya et al. studied breast cancer diagnosis by using a combination of DRS and FS. The findings achieved a sensitivity of 100%, specificity of 96%, the positive predictive value of 69%, and negative predictive value of 100% and overall diagnostic accuracy of 91% respectively; additionally, finding that the combination of DRS and FS yields promising results for distinguishing breast cancer from benign breast lesions [39]. Other studies [40-42] have estimated the concentration of lipids and water in three anaesthetized swine tissues, tissue phantoms, benign tissue, and tumour tissue. These concentrations play a vital role in distinguishing between normal and abnormal tissues in the breast [43] and discriminating benign lesions from cysts in breasts by employing fibre tissue probes [44]. In 2010, researchers found that the confidence in the estimation of water and lipid increased by a factor

of four when used with an optical probe with the detection wavelength extended up to 1600 nm [41], which increases confidence owing to the existence of additional absorption features above 1000 nm. Accurate measurement of water and lipid extinction coefficients can be achieved with a diffuse optical spectroscopy technique (the same principle as DRS) in the same range of wavelengths, giving a reliable estimation of these two chromophores in the mixture by using a phantom study [40]. This study's findings could provide physicians with real-time feedback by measuring the amount of lipid and water in tissues to categorize between malignant, benign and normal samples. A recent study in 2015 [42] confirmed this result, which observed that absorption of lipid and water content in the extended near-infrared wavelength region (1000 to 1600 nm) provides the best recognition between tumour and benign tissue. Also, excellent discrimination between the inside and outside tissue (the border) of the tumour has been obtained by measuring lipids and water ratio.

### 2.1.2 FLUORESCENCE SPECTROSCOPY (FS)

FS analyses the auto-fluorescence, which occurs when the molecules of tissue are excited by narrowband light (obtained via filtering a broadband source or from a narrow laser) as the set up shown in Figure 2-2. All biological tissues have fluorophores such as tryptophan, reiboflavins, NADH, collagen, elastin, and porphyrins. When the light interacts with tissue, these fluorophores absorb the energy and re-emit as fluorescence. The concentration and the characterization of these fluorophores change due to disease (the tissue goes from normal to dysplastic to neoplastic), which varies the characterization of its fluorescent spectrum.

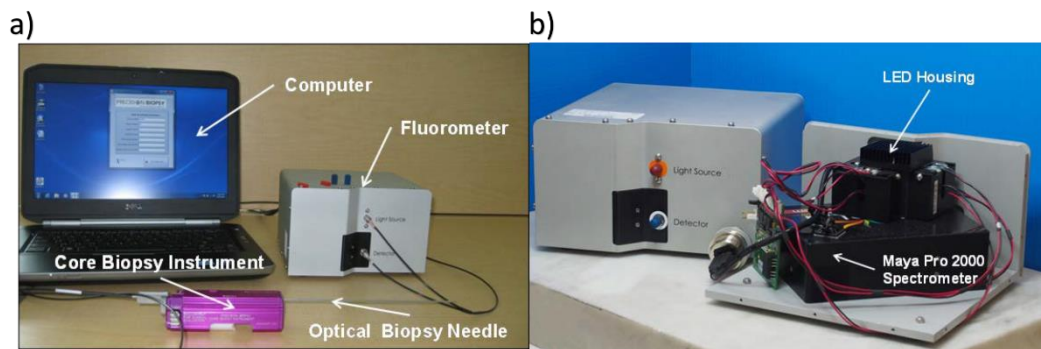


Figure 2-2: Fluorescence spectroscopy setup [45].

This technique has been used in multiple organ systems to identify lesions from normal tissues or abnormal tissues [46]. Thus, researchers have used this technique in cancer diagnosis. In 1998, Gillenwater et al. achieved the ability to distinguish between the fluorescence spectra of the normal and abnormal oral mucosa. Therefore, FS has the potential to improve the diagnosis of oral cavity neoplasia by a non-invasive method. Spectra have been recorded from the oral cavity of 8 healthy volunteers and 15 patients with premalignant or malignant oral cavity lesions at the specific absorption wavelengths (337, 365 and 410 nm) and the emission range of 350 to 700 nm

[47]. Recent publications in 2015 have used the FS technique to differentiate between benign and malignant tissues. Werahera, P.N. et al. studied this technique using two light-emitting diodes at 290 nm and 340 nm to track tryptophan, collagen, and NADH, respectively. The spectra were acquired from 30 patients with prostate cancer, using in-vivo biopsies during radical retro public prostatectomy surgery, the exposed blood flow to the gland intact, and ex-vivo after surgical excision of the prostate. They found a considerable variance between benign and malignant ex-vivo spectra at these two wavelengths compared to in vivo spectra. In vivo spectra were subjected to more background noise due to oxy- and deoxy haemoglobin interference on optical signals. As a result, it affecting the accuracy of in vivo tissue classification [45]. Additionally, Brandao, M.P et al. studied the optical properties of thyroid tissue to distinguish between normal, benign, and malignant lesions. They found a significant difference in the fluorescence lifetimes by analysing variance (Tukey test with an individual confidence level of 98.06% on 17 human thyroid samples) [48].

### **2.1.3 RAMAN SPECTROSCOPY (RS)**

RS is an optical technique that relies on in-elastic light scattering (at different wavelengths to the incident photon) arising from molecular vibrations. RS enables qualitative, sensitive, and specific chemical information regarding significant biological components in tissue milieu and cellular [49]. The effect of RS is based on the interaction of light with the tissue. When photons are directed in the matter, most of these photons pass through unchanged, while others contact molecules. Of those photons that interact, most result in elastic scattering, which causes photons' emission with the same frequency of the incident photon after exciting them to a partial quantum state [50]. A smaller number of these photons scatter through an inelastic mechanism of the electron cloud and bonds of that molecule, creating a difference in energy between the incident photon and the emitted photon due to the energy required to excite the vibration of the molecules - the Raman Effect. In the spontaneous Raman Effect, a type of light scattering, a photon creates an excitation in the molecule from the ground state to a virtual energy state. In the molecule's relaxation time, it emits a photon and changes its direction of vibration state. This new condition causes a shift in the emitted photons frequency away from the excitation frequency [51].

In the RS technique, biological molecules with clear chemical specifications and molecular features such as protein lipids and DNA can be easily detected and quantified without exogenous labels and the pathologic information obtained from the molecular fingerprint variation [51]. Despite the use of RS in cancer diagnosis, significant problems are associated with the Raman application. The signals that are produced by spontaneous Raman spectroscopy are relatively weak. This makes it difficult to detect signals when trying to carry out Raman techniques from optical scattering. Spontaneous RS often requires lasers with high power, which could possibly

cause damage to the biological samples. To overcome the above deficiencies, coherent and surface-enhanced Raman scattering offers improvements. The signal of coherent Raman scattering is up to five orders of value by adding at least one enhancing laser source, enabling real-time vibrational imaging. The use of plasmonic nanoparticles would improve the surface signals and enhance Raman scattering over ten orders of magnitude [51]. The Raman spectroscopy system consists of a diode laser as the excitation source. The instrument has no moveable parts and a spectral resolution as per manufacturer specification. The probe consists of excitation fibre and collection fibre used to couple excitation source and detection system, as shown in Figure 2-3.

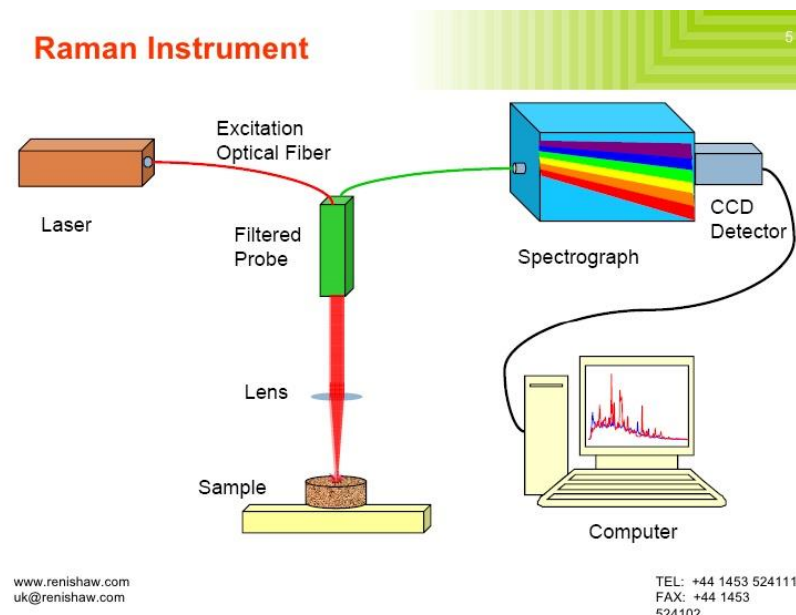


Figure 2-3: Raman Spectroscopy set up

This technique plays a role in oral cancer. Authors have used RS to classify healthy, malignant, and premalignant lesions and identify subtle oral cancer. In 2012, it was suggested that premalignant conditions could be impartially distinguished with both normal and cancerous sites as well as from healthy controls with and without tobacco habits. These results involved 861 spectra from 104 subjects using a fibre optic probe coupled Raman Spectrometer [52]. Besides, Sahu et al. [53] have indicated the possibility of distinguishing between normal and oral cancers. These findings combine contributions of DNA, Proteins, and amino acids.

Furthermore, the higher percentage of nucleic acid phenylalanine and tryptophan and a lower percentage of phospholipids play an essential role to differentiate between control and tumour tissues [54]. In 2015, researchers used the RS technique in distinguishing premalignant and malignant oral lesions from normal mucosa and benign lesions in vivo spectra taken from 18 histologically diagnosed oral disease cases. The findings have been achieved with 100% sensitivity

---

and 77% specificity [55]. Other authors have reported that the Raman technique could differentiate (with sensitivity, specificity) between normal tissue (89%, 86%), carcinoma (69%, 94%) and papilloma (88%, 94%) in the Larynx [56].

### **2.1.4 ELASTIC LIGHT SCATTERING SPECTROSCOPY (ELSS)**

ELSS is an optical technique with the potential to perform a minimally invasive biopsy. ELSS employs optical fibres with specific diameters and geometries to detect human tissue reflectance and light scattering. In ELSS, light enters the tissue and is backscattered without changing the wavelength. Variations in the spectrum of backscattering intensity are due to the difference in the morphological structure. For instance, if there is an increase in the number of mitochondria or the nucleus size, an alteration in the scattering properties will occur. Additionally, the absorption features (the tissue's biochemical function) are easily seen in the ELSS signal [57]. The scattering process occurs due to the differences in density at the cellular and subcellular levels [58].

The scattering event encodes the characteristics of the cellular components, which are called "scattering centres". Pathological scattering determines disorganization in the morphology of epithelial surface texture, thickness, and architecture, changes of epithelial cell orientations, crowding in the cell, increased distance from subepithelial collagen layer, expansion and hyperchromicity of the cell nucleus, a rise in the concentration of the metabolic organelles and irregular protein particles or packages in existence [59].

ELSS system consists of different designs of the probe. A single fibre optical probe, which is used for both delivery and detection of light scattered on interrogated tissue [60-62] or a probe consisting of two fibre optics, one of them is used for emitting light from the light source to the tissue and the second fibre for detecting the light by the spectrometer [28, 63, 64]. A broad wavelength range (300 to 900 nm) is used to measure the subcellular microbiology and cellular composition of tissue by using a pulsed xenon arc lamp as a source of light, a spectrometer is employed to resolve the data, and a computer analyses and records the data (Figure 2-4).

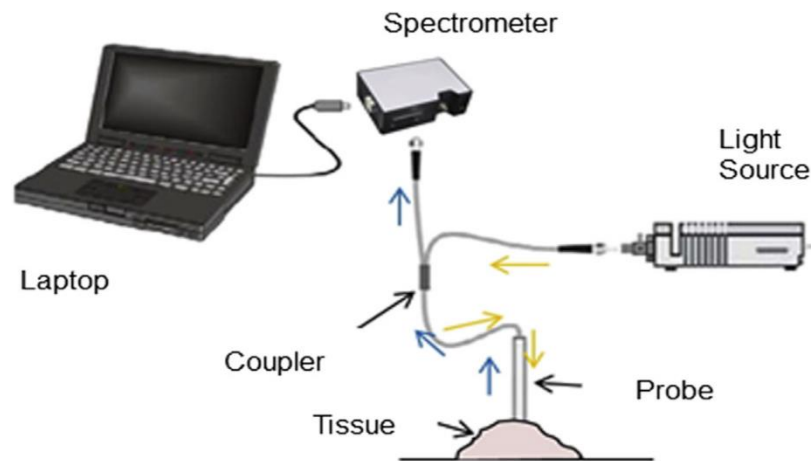


Figure 2-4: ELSS Setup [20].

The system automatically takes a background measurement without firing the lamp, and then the measures of ELSS are taken within 100 ms of the pulsed lamp being triggered. The background spectrum is subtracted from the ELSS spectrum in the next step. For each site measurement, the acquisition of specific data and display time is less than 1 second [59]. To summarise, ELSS is an accurate measurement of the specialized optical geometries sensitive to the sub-cellular architectural changes, such as nuclear grade, nuclear to cytoplasm ratio, mitochondrial size, and the absorption spectra of major chromophores (Oxy/deoxyhemoglobin) [21, 65-67].

According to the World Cancer Research Fund International, prostate cancer is the second most common cancer in men worldwide; two-thirds of prostate cancer cases are diagnosed in more developed world regions. Therefore, many researchers have tried to develop accurate techniques to diagnose prostate cancer. Denkceken et al. confirmed that ELSS is a proper technique to distinguish reactive and metastatic lymph nodes of prostate cancer with Positive Predictive Value (PPV) and Negative Predictive Value (NPV) used to detect metastatic tissues during operation. These findings were achieved by comparing ELSS spectra with histological results from a total of 83 reactive lymph nodes and 12 metastatic lymph nodes sampled from 10 prostatic cancer patients. They reported the distinguishing score by providing a sensitivity of 100% and specificity of 96.4% in discriminating non-metastatic (reactive) from metastatic pelvic lymph nodes with a PPV and NPN of 0.8 and 0.99, respectively [61]. Baykara et al. also confirmed this technique's accuracy to discriminate between benign and malignant surgical margins of prostate tissues with high PPV and NPV. The results compare the histopathological findings with the ELSS spectra data, collected from 31 benign tissue samples and 14 malignant tissue samples from 18 patients. Distinguishing benign from malignant surgical margins of prostate tissues is provided at a sensitivity of 86% and a specificity of 97%, with a PPV of 92%, a NPV of 94% and the area under the receiver operating characteristic curve of 87% [20].

---

Additionally, to reduce the false-negative rate and improve the sensitivity, ultrasound-guided sextant prostate biopsy was used. Amar et al. achieved a sensitivity and specificity of 83% and 87%, respectively, differentiating dysplastic prostatic tissue from benign prostatic tissue. These findings make a comparison between ELSS and histology assessment in 42 ex-vivo prostate glands using guided biopsy and a new fibre-optic probe with an integrated cutting tool, performed in an ELSS portable system [68].

Breast cancer is the most frequent cancer among women. 2.1 million Women have been impacted each year, and breast cancer also causes the most significant number of cancer-related deaths among women. According to the world health organisation, 627,000 women died from breast cancer, approximately 15% of all cancer deaths among women in 2018. Hence, to improve breast cancer outcomes and survival, early detection is critical.

While breast cancer rates are higher among women in more developed regions, rates are increasing in nearly every region globally. In 2018, Zhu et al. have confirmed that an automated Elastic Scattering Spectroscopy scan can be used to recognize non-nodal areas whilst simultaneously diagnosing sentinel node metastases with sensitivity and specificity of 85% and 94%, respectively. To examine if breast cancer has spread to the armpit's lymph glands (the axillary nodes), a biopsy of the Sentinel lymph node is a typical technique for detection in the early stage. Therefore, the surgeons assured the ELSS images could be used as a tool for dependable and prompt intraoperative measures to resolve metastases of sentinel model in breast cancer [28].

Skin cancer is the most common cancer in the world [58]. Each year, there are more new skin cancer cases than the combined incidence of breast, prostate, lung and colon cancers [69, 70]. Therefore, scientists from different universities have applied the ELSS method to the accurate detection of skin cancer. Researchers in the Medical Laser Research Center and Tehran University of Medical Science confirmed that ELSS could classify melanoma and normal spectra with accuracy and sensitivity of 87.5% and 80%, respectively. The data from forty normal and melanoma signals (20 normal and 20 melanoma spectra) have been imported through collaboration with the Biomedical Engineering Department of Boston University. A MATLAB algorithm has been used for differentiation [71].

Researchers at Akdeniz University proved that this technique has the potential to be used as a complementary tool to decrease the number of negative biopsies and diagnose the positive skin margins in real-time. An ELSS spectrum was obtained in vivo from 28 lesions (nine basal cell carcinoma, tumour melanoma, two squamous cell carcinoma) and 13 benign lesions. Moreover, the estimation of intraoperative margin was accomplished on the 28 biopsies. The spectral slopes have been used as a sign to distinguish between malignant and benign lesions (positive for benign and negative for malignant tissues) with a sensitivity of 87% and specificity of 85%. Furthermore,

---

positive surgical margins were detected on 14-excise biopsy samples with sensitivity and specificity of 80% and 90%, respectively [72]. In 2012, a team of researchers found that the ability of ELSS to differentiate between normal, benign, and malignant skin conditions. These findings were obtained by comparing ELSS spectrums with gold standards histopathology in seventy-three patients with clinically suspicious facial skin lesions [58].

The ELSS system has also been used in the detection of oral cancer. Grillone et al. (2017) confirmed that ELSS has the capability to differentiate normal from abnormal tissue in patients undergoing surgical resection for squamous cell cancer of the oral cavity. Between 84% and 100% sensitivity and 7% and 89% specificity have been achieved from their findings. These values have been obtained depending on how the cutoff between normal and abnormal tissue was defined. A considerable difference was reported in the malignancy score between the histologically normal tissue and invasive cancer results and the differentiation between the non-inflamed and inflamed tissue. Thirty-four subjects participated in this study. To conclude, the ELSS technique is the first practical system used to guide mucosal margins in oral cavity cancer. ELSS provides rapid, real-time assessment of tissue without the need for pathological expertise [73].

Jerjes et al. have confirmed that the ELSS technique can detect cervical intranodal metastasis in oral cancer by a sensitivity of 98% and a specificity of 68%. The findings confirmed that the ELSS technique could be used to define nodal involvement as an alternative to histological techniques. One hundred and thirty lymph nodes were examined from 13 patients who underwent neck dissection; the spectrum's intensity was observed at 360, 450, 630 and 690 nm by using a pulsed xenon lamp [5].

To increase the sensitivity and specificity of tumour detection. Muller et al. integrated three optical techniques (FS, DRS, and ELSS) to assess 91 tissue sites from 15 oral carcinoma patients with different degrees of malignancy (normal, dysplastic, and cancerous areas) and eight healthy voluntaries. In the intrinsic fluorescence spectroscopy, the biochemical examination details regarding oral tissue native fluorophores were obtained. These findings were acquired by fitting a linear combination of collagen and nicotinamide adenine dinucleotide (NADH) fluorescence spectra to intrinsic tissue fluorescence spectra excited with 337 nanometers (nm) and 358 nm laser light. Absorption and scattering coefficients of wavelength were measured using a diffuse reflectance spectroscopy technique providing information regarding the absorption of tissue and structure such as haemoglobin concentration and stroma density. From the single scattering of epithelial cell nuclei, the data of light scattering spectroscopes were obtained by subtracting the diffusely reflected component from the measured reflectance. ELSS provides the specific details of nuclei size. They achieved a sensitivity and specificity of tri-model spectroscopy 96% in discriminating normal from abnormal tissue. Also, sensitivity and specificity in distinguishing cancerous from dysplastic tissue were 64% and 90%, respectively [21].

---

Other authors in 2006 have used the ELSS technique to assess oral premalignancy. They achieved a sensitivity and specificity of 72% and 75%, respectively, to distinguish oral dysplasia tissues using linear discriminant analysis. These findings were compared with a histopathology test. A pulsed xenon-arc lamp is used on twenty-five oral sites from 25 patients who suffer from leukoplakia[74]. In 2006, Lovat et al. studied the potential of ELSS to identify high-grade dysplasia or cancer within Barrette's Oesophagus. The ELSS measurements were achieved in-vivo from a 181-match biopsy with a histopathological test from 81 patients; the discrimination of high-grade dysplasia and cancer agrees with the pathologist. The sensitivity and specificity in identifying high-risk sites were 92% and 60%, respectively as well as the sensitivity and specificity in identifying the high-risk area from inflammation with a sensitivity and specificity of 79% [67].

Other researchers studied the ELSS method to differentiate benign from malignant disease in thyroid nodules. Suh et al. collected ELSS data from 36 surgical patients (n=21 benign thyroid nodules, n=15 malignant tumours) from their fresh ex vivo thyroidectomy specimens. The findings indicated that ELSS has an accurate ability to identify benign versus malignant thyroid lesions with a sensitivity of 75% and specificity of 95%, and high PPV and NPV of 92% and 83%, respectively [75]. In 2014, other teams used ELSS to measure the spectral to discriminate between benign and malignant thyroid nodules, supplementing a fine needle aspiration biopsy (FNAB). FNAB evaluated approximately 15-30% of inconspicuous findings, benign or malignant. Thus, the team have used ELSS and achieved a sensitivity and specificity of 74% and 90%, respectively, with 97% of NPV to distinguish the benign from malignant [64]. Some authors focused on using ELSS in detecting breast cancer. Johnson et al. studied the ELSS for intraoperative determination of sentinel lymph node status in the breast. The spectra of ELSS identified from cancerous nodes with 84% sensitivity and 91% specificity (per spectrum analysis) and per-node analysis, sensitivity, and specificity were 75% and 89%, respectively. Spectra were obtained from 139 excised nodes (53 containing cancer) in 68 patients [76].

Laryngeal cancer is one of the most common types of head and neck cancer. In 2018, an estimated 17 million new cases and 9.6 million deaths from cancer regarding the National Cancer Institute [77]. Turhan et al. confirmed that elastic light single-scattering spectroscopy (ELSSS) could discriminate between benign and cancerous Larynx tissue (moderate, severely dysplastic, and malignant) lesions with sensitivity and specificity of 94% and 100%, respectively. This technique proved an ability to classify benign tissue correctly. Moderate, severe dysplastic, and malignant tissues were correctly classified as cancerous. However, this system has a limitation, and mild dysplastic tissue did not classify benign or cancerous. Therefore, nearly half of them were classified as benign and the other half as malignant. The ELSSS system correctly defined 38 out of 41 malignant tissues as cancerous; three were misclassified as benign. The positive slopes were used as a sign for benign and negative for cancerous larynx tissues. Histopathology results were used as a gold standard to define sensitivity and specificity [78]. Table 2-1 shows the overview of

the optical detecting techniques with various tissue types

Table 2-1: Overview of the optical detecting techniques with different tissue types

Authors	Detection method	$\lambda$	Probe geometry	Sensitivity	Specificity	Conclusions
Nachabe' et al. 2011 [33]	DRS	360 to 2500 nm TG	1.3 mm diameter probe. It consists of one fibre for emitting and two fibres for detecting with a core diameter of 200 $\mu$ m.			Differentiation between healthy tissue & metastatic tumour from ex-vivo human liver. In this study, bile, water & lipid are included in addition to oxygenated & haemoglobin for differentiation
Ever et al. 2013 [30]	DRS	360 to 2500 nm TG	1.3 mm diameter probe. It consists of one fibre for emitting and two fibres for detecting with a core diameter of 200 $\mu$ m.	94%	94%	It has the capability for high accuracy in discriminating normal liver tissue for colorectal liver metastases.
Evers et al. 2012 [31]	DRS	360 to 2500 nm TG	1.3 mm diameter probe. It consists of one fibre for emitting and two fibres for detecting. Fibre is located at a distance of 2.48 mm from the side-by-side optical fibres used to collect the diffused light.	89%	79%	Has the capability to discriminate between tumours from lung tissue.
Spliethoff et al. 2016 [34]	DRS	360 to 2500 nm TG	5 g needle contained 3 fibres with a 200 $\mu$ m core diameter. One for emitting and 2 fibres for detecting. The centre-to-centre distance between the emitting & collecting fibres was 1.7 mm.			Water content & scattering amplitude are the primary discriminators for the transition from healthy lung & tumour tissue.
Zones et al. 1999 [35]	DRS	360-685 nm Xenon is a flash lamp	It consists of central optical fibre for delivery and six fibres for light collection arranged in a circle around the central fibre. All fibres with 200 $\mu$ m core diameter with no gap between them. The probe tip was fitted with a quartz shield			It quantifies information about Hb content & information related to the tissue scatters in-vivo & real-time of human adenomatous colon polyps.

			approximately 1.5 mm. in length and diameter.			
Spliethoff et al. 2014 [36]	DSR &FS	360 to 2500 nm TG	22 G adjustable stylet containing four identical fibres with a core diameter of 100 $\mu$ m. Two fibres for the emitting light source (broadband light source & laser), whereas other fibres were connected to spectrometers, two different separates were used ( 1.5 & 0.15) mm.			Dual modality DRS &AFS provides quantitative functional information that corresponds well with the degree of pathologic treatment (monitoring & prediction of cancer therapy) for 36 mice.
Langhout et al. 2015 [37]	DSR &FS	360 to 2500 nm TG	13 G (1.5 mm) optical probe consists of four identical fibre optics with a 200 $\mu$ m core diameter. Two fibres for emitting & two collecting two different source-distance 1.8&0.32 m. 1.8 mm was used for DRS, and 0.32 mm was used to correct absorption and scattering in FS spectra.	95%	88%	Dual modality can identify colorectal cancer from surrounding healthy tissue.
Spliethoff et al. 2013 [2]	DSR &FS	360 to 2500 nm TG	The same above. The separation was 1.9 & 0.32mm.	98% 100% (eliminating inter-patient variation)	86% 100% (eliminating inter-patient variation)	DRS provides an accurate diagnosis of malignant lung lesions how FS enables identifications of necrotic tissue. When both techniques are combined within a biopsy determination, this could significantly enhance the diagnostic performance and the quality of trans thoracic biopsies.
Proabitha et al. 2016 [38]	DRS	360 to 2500 nm TG	The fibre optics consists of an illumination centre, and six surrounding fibres (each has 400 $\mu$ m core diameter) for controlling to	72%	87%	DRS could be used along with Multivariate analytical techniques as a non-invasive technique to monitor cervical

			centre between illumination and collection distance was 500 $\mu\text{m}$ ).			disease status in real-time.
Volynska ya et al. 2008 [39]	DSR &FS	3.08 to 480 nm & 300 to 800 nm	The distal tip consists of single delivery fibre surrounded by six collection fibres with a diameter of 200 $\mu\text{m}$ .			The combination of DRS & FS yields promising results for the discrimination of breast lesions and warrants a prospective clinical study.
Evers et al. 2013 [29]	DRS	360 to 2500 nm TG	The optical probe consists of three fibre optics, one fibre for emitting and 2 for detecting.	90%	88%	The analysis of the optical characteristics of different tissue classes within the breast of a single patient is superior to analysis using cohort data analysis. The integration with a biopsy device, DRS, may potentially improve the diagnostic work flow in breast cancer.
Boer et al. 2015 [42]	DRS	360 to 2500 nm TG	The probe tip incorporating the optical fibres was 1.75 mm in diameter with a distance between the emitting fibre and collecting fibre of 1.5 mm.			The fat/ water provided excellent discrimination between sites clearly inside or outside the tumour and is one test case. By this work, DRS showed the potential to guide the surgeon during breast-conserving surgery.
Nachabe' et al. 2010 [40]	DRS	360 to 2500 nm TG	1.3 mm diameter optical probe. The probe consists of two fibres with an axis of symmetry parallel to the axis of symmetry of the probe 2.48 mm separation at the distal end.			It could provide real-time clinical feedback to physicians on the amount of lipid and water in tissue to classify normal, malignant, and benign samples in the tissue phantom.
Nachabe' et al. 2010 [41]	DRS	360 to 2500 nm TG	The same probe in the above with the end polish by 20°.			The confidence levels of the water and lipid-related parameters increases by a factor for the estimation of

						biological chromophores.
Gillenwater A et al 1998 [47]	FS	350 to 700 nm	The optical probe consists of a central fibre surrounded by six fibres	88%	100%	Consistent differences exist between the fluorescence spectra of the abnormal and normal oral mucosa
Werahera et al 2015 [45]	FS	290 and 340 nm (LED)	The optical probe consists of 8*100 µm source fibres in a circle and a single 200 µm.	72% (in vivo) 75% (ex vivo)	66% (ex vivo) 80% (ex vivo)	It has the potential clinical application of an optical biopsy needle based on fs for prostate cancer diagnosis.
Brandao et al 2015 [48]	FS	200 and 900 nm	The optical probe consists of six fibre bundles of the probe that collected the fluorescence.			FS could become a tool for the surgeon to discriminate between normal and pathological thyroid tissues.
Singh et al. 2012 [52]	RS	The diode laser of 875 nm	The optical probe consists of 105 µm for emitting and 200 µm for collection.			Identification of premalignant lesion in oral, buccal mucosa with both normal and cancerous sites by in vivo RS.
Sahu et al. 2013 [53]	RS	Laser 532 nm	The sample excited by 50x Nikon objective (numerical aperture 0.55).			Find the possibility of distinguishing between normal and oral cancers. These findings combine contributions of DNA, Proteins and amino acids.
Krishnakumar et al. 2013 [54]	RS	Laser 1064 nm	The laser size spot was 200 µm in diameter.			It can investigate the chemopreventive response of naringenin and its nanoparticles in DMBA-induced oral carcinogenesis.
Guze et al. 2015 [55]	RS	0 to 1800 cm <sup>-1</sup>	The probe consists of a single fibre with a diameter of 200 µm for emitting, surrounded by 31 collection fibres.	100%	77%	RS offers the potential to provide a point of care diagnosis of oral disease using non-invasive, convenient, and relatively inexpensive technology.
Lau et al. 2003 [79]	RS	950 to 1650 cm <sup>-1</sup>				It has the ability a spectral differences between normal and cancerous nasopharyngeal.

Denkceken et al. 2015 [61]	ELSSS	200 to 1100 nm (TG)	A single fibre optical probe with 100 µm for both delivery and detection.	100%	96.4%	ELSSS system can accurately distinguish reactive and metastatic pelvic lymph nodes of prostate cancer with high PPV and NPV. It can detect the metastatic tissues during the operation.
A' Amar et al. 2013 [68]	ELSS	330 to 760 nm	Optical probe with two adjacent fibres, one for illumination (400 µm-core diameters) and the other for collection (200 µm-core diameter with separation 350 µm).	83% (for classification) 80% (for distinguishing)	87% (for classification) 87% (for distinguishing)	ELSS can distinguish dysplastic prostatic tissue from benign prostatic tissue.
Baykara et al. 2014 [20]	ELSSS	400 to 850 nm (TG)	A single fibre optical probe with 100 µm for both delivery and detection.	86%	97%	ELSSS can accurately distinguish between benign and malignant margins of prostate tissues with a high PPV and NPV.
Canpolat et al. 2012 [72]	ELSSS	350 to 800 nm (TG)	A single fibre optical probe with 100 µm for both delivery and detection.	87% (Discrimination) 80% (detecting margins)	85% (Discrimination) 90% (detecting margins)	Discrimination between malignant and benign lesions and detecting positive surgical margins of skin
Upile et al. 2011 [58]	ELSS	330 to 900 nm ( Pulsed x-non-arc)	Fibre optics consists of two fibre optics (400 µm for emitting and 200 µm for detecting), centre to centre is 300 µm.	77.8%	80.3%	Discrimination between benign and malignant skin pathologies.
Muller et al. 2003 [21]	FS, DRS and LSS	Xenon flash lamp (350 to 700) nm	Fibre optics consists of single light surrounding by six collection fibres with a core diameter of 200 µm.	96%	96%	Trimodal spectroscopy is a highly sensitive and specific technique to diagnosis oral tissue abnormalities.
Jerjes et al. 2004 [5]	ELSS	330 to 900 nm ( Pulsed x-non-arc)	Fibre optics consists of two fibre optics with 200 µm, centre to centre separation is 350 µm.	98%	68%	Detection of cervical intranodal metastasis in oral cancer.
Sharwani et al. 2006 [74]	ELSS	300 to 900 nm ( Pulsed x-non-arc)	The optical probe consists of fibre optics with 400 µm for emitting	72%	75%	Discrimination malignant lesions from

			and 200 µm for collecting. Centre to centre separation is 300 µm.			normal tissues in the oral cavity.
Grillone et al. 2017 [73]	ELSS		Fibre optics consists of two fibre optics with 200 µm, centre to centre separation is 250 µm.	84% to 100%	71% to 89%	It is the first study to evaluate the effectiveness of ESS in guiding mucosal resection margins in oral cavity cancer. ESS provides fast, real-time assessment of tissue without the need for pathology expertise.
Lovat et al. 2006 [67]	ELSS	320 to 920 nm (Pulsed x-non-arc)	The optical probe consists of fibre optics with 400 µm for emitting and 200 µm for collecting. Centre to centre separation is 300 µm.	92%	60%	Accurately detect high-grade dysplasia and cancer in Barrett's Oesophagus.
Suh et al. 2011 [75]	ELSS	320 to 920 nm (Pulsed x-non-arc)	The optical probe consists of two fibre optics with 200 µm with a fixed separation distance of 250 µm.	75%	95%	The ELSS accurately distinguish benign vs malignant thyroid lesions with high PPV and NPV.
Rosen et al. 2014 [64]	ELSS	320 to 920 nm (Pulsed x-non-arc)	The optical probe consists of two fibre optics with 200 µm with a fixed separation distance of 250 µm.	74%	90%	ELSS has the potential for use in the real-time diagnosis of thyroid nodules as an adjacent to fine-needle aspiration biopsy cytology.
Johnson et al. 2004 [76]	ELSS	320 to 920 nm (Pulsed x-non-arc)	The optical probe consists of fibre optics with 400 µm for emitting and 200 µm for collecting. Centre to centre separation is 350 µm.	84% (per spectrum analysis) 75% (per spectrum analysis)	91% (per spectrum analysis) 89% (per spectrum analysis)	ELSS is a promising technique for the rapid, accurate, and straighter ward detection of metastases in excised sentinel lymph nodes.
Canpolat et al. 2009 [80]	ELSSS	350 to 800 nm (TG)	The single fibre probe was 1*2 fibre optical coupler with a splitting ratio of 50%. The diameter of the distal end of the probe's fibre was 100 µm.	93%	100%	It has the ability for disseminating brain tumours from surrounding normal white matter brain tissue

Zhu et al. 2018 [28]	ELSS	320 to 919 nm ( xenon arc lamp)	Static ESS fibre optic	85%	94%	It can help surgeons for providing a reliable and repaid intraoperative determination of sentinel nodal metastases
----------------------	------	---------------------------------	------------------------	-----	-----	--

ELSS has been selected in our research for many reasons. Firstly, ELSS signals are more intense than FS and RS, giving this method more efficiency and sensitivity. Secondly, the significant optical signal gives elastic scattering the potential to be the fastest and most cost-effective of all-optical detection methods [5]

### 2.1.4.1 TISSUE PHANTOM IN THE ELSS DETECTING

Tissue phantom plays a vital role in testing the sensitivity of the optical probe technique to scattering the light from superficial tissues. Artificial tissues present preliminary results from actual biological samples. The phantom recipe of the ELSS technique has different materials than other optical techniques (DRS, FS and RS). An aqueous suspension of monodisperse polystyrene with varying diameters of microsphere is used as the main material of optical phantom[20, 60, 61, 72, 80-83]. Variations of microsphere diameters may help to predicate the results of actual cancerous tissues characterized by a nucleus size of cells and an enlargement of the nuclei. Table 2-2 shows the overview of the tissue phantom in the ELSS detecting.

Table 2-2: Overview of the tissue phantom in the ELSS detecting

Authors	Suspension polystyrene microspheres Size	Concentration	$\lambda$ (nm)	Probe design	Advantages
Canpolat, and Mourant, 2001 [81]	0.194, 0.329, 0.426, 0.451, 0.505, 0.672, 0.852, 0.890, 0.990, 1.530 and 2.202 $\mu\text{m}$ .	2% by the manufacturer	350-2500 (TG)	Two 100 $\mu\text{m}$ fibres were butted up against the 200 $\mu\text{m}$ fibre optics.	The maximum and minimum of the oscillations can determine scatterer size for monodisperse distributions of spheres. Additionally, the effect of the

					absorption, broad distribution of scatterers and depth probed.
Amelink et al., 2003 [82]	One or two layers of suspensions of monodisperse $4.5 \pm 0.2 \mu\text{m}$ and $9.4 \pm 0.6 \mu\text{m}$ .	One or two layers of $4.5$ and $9.4 \mu\text{m}$ and a bulk layer of intralipid-20% and a top layer of $4.5\% \mu\text{m}$ polystyrene spheres.	350-2500 (TG)	Single fibre optics for collecting and delivery with core diameter $400 \mu\text{m}$ .	Tested the sensitivity to light scattering from superficial layers of tissue, which can detect superficial precancerous epithelial lesions.
Canpolat et al. 2009, 2011 and Denkceken et al,2013 [60, 72, 80]	$2 \pm 0.5 \mu\text{m}$	10%	350-2500 (TG)	The single fibre optical probe was $1 \times 2$ fibre optical coupler with a splitting ratio of 50% with $100 \mu\text{m}$ of the optical fibre at the distal end.	Tested the performance of the single fibre optical probe.
Baykara et al. 2014 and Denkceken et al. 2015 [20, 61]	$1.5 \pm 0.02 \mu\text{m}$	10%	350-2500 (TG)	Same [ above	Same the above

Kucuksayan et al. 2015 [83]	5 $\mu\text{m}$	1.25%	350-2500 (TG)	Same above	Same the above
--------------------------------	-----------------	-------	------------------	------------	----------------

In our research, three particle sizes have been chosen 0.413, 0.8 and 2  $\mu\text{m}$  with various concentrations that will explain this in section 4.2.1. The selection for these three particle sizes is due to the outcome Jacques [84]. His work proved that the scattering of smaller size spheres is strongly dependent on the wavelength (it becomes increasingly wavelength-independent) compared to the large size spheres. Moreover, Jacques confirmed the scattering of the smaller size would become less at longer wavelengths, whilst the size of the large sphere scatters less at all wavelengths.

## 2.2 MICROWAVE TECHNIQUES

To understand the material behaviour (electrical or magnetic characteristics of the materials), measurements of dielectric properties play an essential role in characterising the physical and chemical properties related to storage and energy loss in multiple kinds of materials [85]. The permittivity values show an external field's interaction with the electric dipole moment of the material [86]. It can be used for non-destructive monitoring of specific properties of materials undergoing physical or chemical changes.

To understand the mechanism of the dielectric properties of biological tissues. Joines et al [87].clarified that the frequency dependence of dielectric properties of biological tissues is related to the polarization of molecules and structural interfaces in response to the applied electric field. Also, the relaxation time in malignant tissues is more extensive than that in normal tissue, which indicates a considerable rise in the motional freedom of water.

Regarding the sodium concentration and water content in the malignant and normal tissue, the per cent of sodium concentration is higher in the malignant cells compared to the normal cells [88]. The increase in sodium concentration affects the cell membrane potentials [87, 89, 90] and causes the malignant tissue to retain more fluid. As a result, the increase in the sodium concentration alone would increase the conductivity and permittivity values in the malignant tissue compared to the normal tissue. Additionally, the fluid retains in bound water with larger conductivity and permittivity values than free water [88, 89, 91] confirmed a significant increase in the water content in the malignant compared to the normal tissue. Also, the relationship between relative permittivity and water content is strikingly similar to the relationship between conductivity and water content. That result can summarise that the same mechanism is responsible for the change in both dielectric properties. Therefore, to measure the dielectric properties (permittivity), two techniques are used resonant and non-resonant methods.

## 2.2.1 RESONANT TECHNIQUES

The resonance technique is widely used for measurements of microwave dielectric properties [92]. With this method, the ability to accurately measure the dielectric resonance is the main advantage. However, there are several disadvantages. Usually, for each sample, only a single frequency point can be measured, and the calculation of the dielectric properties is generally very complicated. The third disadvantage is the requirement for a specific sample dimension; high sensitivity measurements are only achieved with small sample volumes.

### 2.2.1.1 CAVITY PERTURBATION TECHNIQUE

One technique for measuring the dielectric properties of various materials is the cavity perturbation technique. This technique's essential principle is based on a shift in resonant frequency and a decrease in the cavity's quality factor, which is attributable to the presence of a dielectric sample in the resonant cavity technique [93]. The change in the resonant frequency measures the dielectric constant, and the difference in the quality factor estimates the dielectric loss [86]. The Vector Network Analyzer (VNA) automatically displays changes in the frequency and bandwidth for ease of measurement. Some factors affect the efficiency of the measures, such as the geometry and the sample position. To obtain accurate measurements with this technique, there are some requirements for the sample. Firstly, the sample should occupy the resonator's entire central volume [94]. Figure 2-5 demonstrates the maximal axial field in the centre of the  $TM_{010}$  cavity. Secondly, keeping the same orientation each time is required for accurate measurements. Also, a small volume sample is required to ensure small perturbation occurs at the maximum intensity of the cavity mode, achieving a maximum change in resonant frequency [95]. Additionally, the sample tube's shape (such as a long thin tube), increases the accuracy of the measurements as there is a correlation between the sample shape and the depolarization.

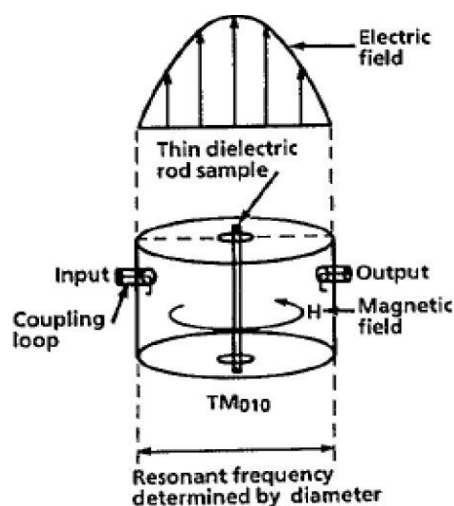


Figure 2-5:  $TM_{010}$  Cavity is commonly used for perturbation measurements of up to 10 GHz [96].

Despite the advantages of the cavity perturbation technique, there are some limitations. The

---

resonant cavity systems restrict the measurements to single-frequency [94]. It provides dielectric data at a single frequency. This technique presents a big challenge for biological tissue measurements due to complicated sample preparation [95]. In addition, there are other reasons which can affect the measured properties, such as loss of fluid from the tissue and an increase in density from pushing the tissue into the cavity and the presence of air pockets within the sample. Finally, settling particles in the case of a particle suspension has been found to impact measurements.

## **2.2.2 NON-RESONANT METHODS**

In these techniques, the material properties are fundamentally deduced from their impedance and wave velocities therein. There is a change in these characteristics when an electromagnetic wave propagates from one element to another. A partial reflection of the wave is a result of the interface between two materials. Permittivity and permeability can be provided from the reflection from such an interface and the transmission through it. Reflection and reflection/transmission methods mainly occur in non-resonant methods. Thus, non-resonant methods require a means of directing the electromagnetic energy toward the material and then collecting the reflected and transmitted signals [97].

### **2.2.2.1 OPEN-ENDED TRANSMISSION LINE TECHNIQUES**

It is a convenient, non-invasive, fast broadband response and requires no sample preparation for measuring lossy materials' complex permittivity at RF and microwave frequencies. It requires a small sample suitable for characterizing the biological samples from surgery [98]. The open-ended probe basically modifies the transmission line method, which forms a flat plane boundary with the sample. The measurements are made by immersing the probe into a liquid or touching it to a solid (or powder) material's flat face. This structure creates capacitive fields that fringe into the material beyond the conductors. The dielectric properties can be calculated from the phase and the amplitude of the reflection signal at the end of an open-ended coaxial line which are obtained by insertion of the probe into the sample.  $S_{11}$  (the reflected signal) can be measured and related to sample permittivity [99]. The sample's reflection coefficient is calculated by a VNA and a computer software algorithm (such as LabVIEW), converting the measured data to dielectric constant versus frequencies (Figure 2-6 a). This technique is ideal for permittivity measurements of liquid and semisolid materials of relatively high loss, including biological materials. It operates with a range of frequencies 200 MHz to 50 GHz. In liquids, the air bubbles need to be eliminated from the coaxial probe's face and the sample. An air gap between the probe and sample can be a significant source of error unless the sample face is machined to be at least as flat as the probe face. It is the source for shifting in the measurements. To keep the proper calibration and guarantee control and repeatability, all parts of the instruments (including the probe) should be fixed mechanically to avoid changes in instruments' configuration or cable shape. Calibration at

the tip of the probe needs to be performed before measuring. A coaxial cable's standard calibration is achieved using an open-end, a short circuit and matched load ( $50 \Omega$  resistance for standard calibration). Despite the many advantages of this technique, some limitations, such as the thickness of the sample. The ideal thickness needs to appear "infinite" to the probe, i.e. the evanescent fields at the open end of the coaxial cable should decay almost completely within the sample. It occurs within a distance of the order of a few times the inner diameter of the probe [100]. Figure 2-6 b presents the measurements on liquids, gels, and solid materials to allow perfect contact with the sensor's face without any air gaps.

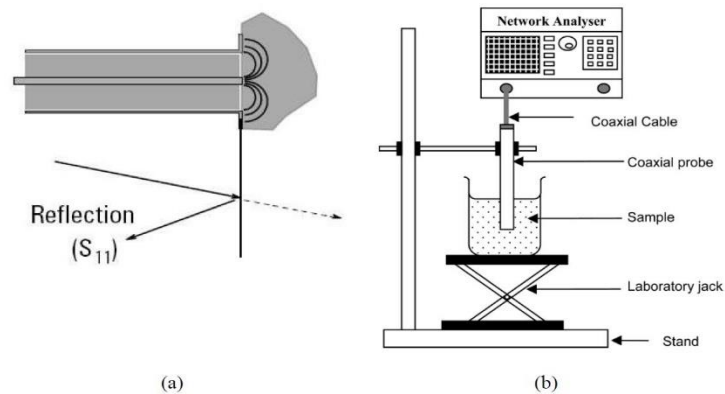


Figure 2-6: (a) the reflection scheme of the signal; (b) Illustration of the apparatus used for microwave probe liquid measurements [101].

### 2.2.2.2 WAVEGUIDE AND COAXIAL TRANSMISSION LINE TECHNIQUES

The two-port transmission line technique is a useful technique for a material that can be precisely machined. It is perhaps less widely used for liquid, powder, and gases; however, a specially developed cuvette must be used to contain the substance. There is a change in impedance and propagation characteristics in the loaded section of the line when the sample is placed in the transmission line segment [100]. This transmission line method covers a broad range of frequencies, but there is difficulty manufacturing a toroidal-shaped sample. Furthermore, despite this technique's accuracy, there is a limitation in resolution from low loss materials, depending on sample length. For a liquid and any other material, the required length depends on the loss tangent [100]. The approximate thickness of the sample is one-quarter of the wavelength of the energy that has penetrated the sample. As the shift in the wavelength is related to the dielectric constant, a guess must be made as to the magnitude of the constant. For instance, at 2450 MHz ranges, the typical is 5 mm for woods to 19 mm for fats and oils [102] (Figure 2-7).

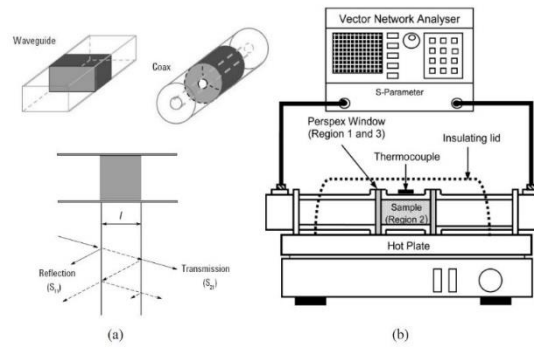


Figure 2-7: (a) Transmission line method; waveguide and coaxial line case; (b) A practical example of the transmission line ( waveguide) setup for microwave measurements under temperature control [103, 104].

### 2.2.2.3 FREE SPACE TRANSMISSION TECHNIQUES

The free-space method is a contactless and non-destructive measuring technique. It consists of a VNA; two antennas facing each other with a sample holder between them. The sample is placed between two transmitting and receiving antennae, attached to software and hardware to translate the data (Figure 2-8).

The antennae plays a vital role in focusing the microwave energy at or through a slab of material without the need for a test fixture. In this technique, they do not require special sample preparation and one is practically suitable for measuring materials at high temperature and for homogenous dielectrics. The attenuation phase shifts are measured. The measurement in this technique can be achieved over a wide range of frequencies. Also, it is employed at higher frequencies (above 10 GHz). Special attention must be paid to the choice of the radiating elements, holder sample design, geometry sample and the location between radiating samples [97].

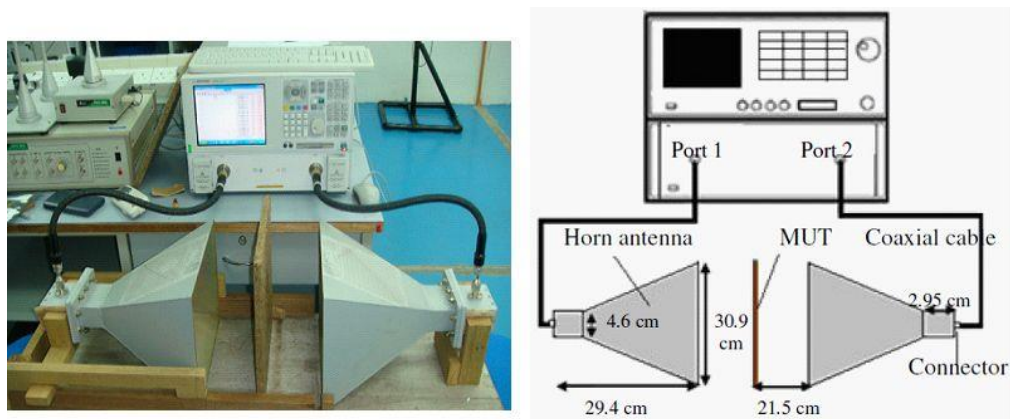


Figure 2-8: Free space setup [105]

#### 2.2.2.4 SURVEY THE MICROWAVE TECHNIQUES FOR CANCER DIAGNOSTICS.

Owing to the capabilities of using the electromagnetic energy in the microwave frequency range to find the balance in competing requirements for resolution and penetration depth, researchers have begun to investigate the possibility of microwave techniques for cancer diagnosis. In 1988, Surowiec et al. utilised the radio frequency range of 20 kHz to 100 MHz to detect breast carcinoma and the surrounding tissues. The diagnostic was done at 37 °C by using a VNA and an end-of-line capacitive sensor at this frequency range. The Cole-Cole dielectric parameters were determined by curve fitting. In this study, three main categories have been detected (the central part, surrounding and peripheral tissue). Seven patients participated in this study. The large spread of the dielectric data for different specimens suggests the structure and cellular inhomogeneities of the tumour tissue vary within each category. The results illustrated that this study shows a remarkable difference in dielectric properties between samples taken from different locations.[106].

A researcher group from Duke University presented an initial review to discriminate the dielectric properties of normal and malignant breast tissues in the range of 10 kHz to 20 GHz. Moreover, this study showed that the range of 100 MHz to 3 GHz is useful as a diagnostic for breast tissue dielectric properties [107].

Confocal microwave imaging has been used to illuminate a small sample of 6 mm breast tumours with an ultra-wideband pulse from many antenna locations. The sample detection occurred in 3D with a numerical model of two system configurations involving synthetic cylindrical and planar antenna arrays. Image reconstruction algorithms showed that both systems are rapid and straightforward to interrogate the breast for the tumour in 3D [108].

In vitro studies of female human breast tissue found a rectangular resonant cavity perturbation technique to distinguish between benign and malignant breast tumour by characterising the variation of the dielectric properties and bound water content between benign and malignant

---

breast tissue concerning the dielectric parameters of the normal tissue. This study was done with six patients' samples collected from the surgery department at Lourde Hospital [109].

A non-invasive method for detecting the bladder tumour at 465 MHz has been utilised for bladder cancer detection. Cystoscopy is the gold standard for this research. At this frequency (465 MHz TRIM probe™), the amplitude reduction of 80-90% is observed in a space region enclosed in a cone of angle  $\theta_c$  around the straight-line joining transmitting point of the TRIM probe™ and the patient's bladder. This study showed an overall accuracy of 89.5%, a PPV of 83.3% and a NPV of 93.1%. One hundred and fourteen patients participated, and cystoscopy was used as a gold standard [110].

An open-ended coaxial probe between 0.5 to 20 GHz was utilised to discriminate between normal (adipose, glandular and fibro connective), malignant (invasive and non-invasive ductal and lobular carcinomas) and benign (fibroadenomas and cysts) tissues. 319 measurements were taken on freshly excised breast tissue specimens from 169 patients undergoing lumpectomies, mastectomies, and biopsies at the University of Wisconsin and University of Calgary hospitals. This study fits one pole-Cole-Cole model to the complex permittivity data set of each characterised sample. This study concluded that there is a possibility as large as 10:1 of distinguishing between malignant and normal adipose—the dominant tissue in the breast, while the contrast in the microwave-frequency dielectric properties between malignant and normal glandular/ fibroconnective tissues in the breast is no more than about 10% [111]. In 2010, Kuhn et al.[112] used open-ended coaxial probe measurements for breast cancer detection. For more robust measures, four material calibration methods were used across the frequency range of 3 to 17 GHz. In this research, a coaxial probe technique distinguished between the normal (healthy) and cancerous breast tissue. A software High-Frequency Structure Simulator (HFSS) was used for simulation to show the potential of the microwave diagnosis of breast cancer. Regarding the experimental work, human and snake tissues have been used as a sample to highlight the nature of biological tissues and the dependence of complex permittivity on tissue temperature. A neural network has been used to differentiate between the normal and cancerous breast tissue in the frequency range.

Researchers in UAE have utilised an open-ended coaxial cable (200 MHz to 13.6 GHz) to characterise normal, and breast cancer cell lines cultured in-vitro. This technique showed the ability to distinguish between healthy non-tumorigenic, MCF-10A and breast cancer, MDA-MB-231, Hs578T, T47D and MCF-7 cell lines by determining the dielectric constant, dielectric loss and conductivity. They found a variation between the dielectric properties of breast and colon cancer cells, they suggest that each cancer type has a unique microwave signature [113].

In our research, open-ended at frequency range 0.1 to 3 GHz and circular cavity as a reference have been selected for a non-resonant and resonant technique, respectively.

## **2.3 OTHER TECHNIQUE FOR CANCER DIAGNOSIS**

X-ray, Computed tomography, Ultrasound, and Endoscopy are different techniques used for cancer investigation. Currently, histopathology is the gold standard technique for assessing pathological changes in tissue. Histopathology is a diagnosis method for diseased tissue. It inspects tissue or cells under the microscope [114]. In this technique, despite the ability to obtain a large qualitative result in nature, there are many drawbacks. Firstly, it is a painful and invasive method [115].

Additionally, it is also time-consuming and expensive due to tissue sample preparation (tissue fixation, sectioning, and staining [35]. Biopsy site selection is critical to ensure that a lesion's nature is captured [55, 73]. Finally, an expert pathologist needs to interpret the results [55].

## **2.4 CHAPTER SUMMARY**

The survey of the earlier publications showed the capability of several optical techniques ( DRS, FS, RS, and ELSS) for detecting various organs in the body. Then, the result of this survey is an optical ELSS method selecting in our system as the first step, and the results will be found in section 4.6. Then, choosing the suspension polystyrene sizes was an output of the survey, which were the samples used as artificial tissue in our system for detecting. Finally, the survey for various microwave techniques showed the ability for detection with different organs. Therefore, the microwave techniques have been selected to use in the detection in our system, Non-resonance as the first instance for detecting in section 5.6, cavity as a reference in ch 6 and T- Structure and capacitive coupling as a novel of our study which the results will find in chapter 7.

## CHAPTER 3

### ELSS OPTICAL DETECTION

#### 3.1 TRANSPORTATION OF LIGHT IN TISSUE

When light rays interact with tissue, part of these is reflected, transmitted, absorbed, refracted or scattered, depending on the optical properties of that material. Refraction occurs if there is a variance in the refractive index at a boundary. Optical tissue is a dielectric medium in which the refractive index is higher (1.35 to 1.55) [116] than that of air (1.0003). Thus, a change in the direction of a light ray occurs, which defines reflection, while the rest penetrates the tissue (transmission). The absorption can be defined as the transference of light energy, usually to the internal energy of the absorber. Additionally, tissues are not only absorbing but also can scatter. The biological tissues are optically inhomogeneous with different levels of organization which includes cell organelles, cells, inclusions, and various fibre and tubular structures. Scattering occurs due to the gradient in the optical index of refraction because of the different intensities that may occur at a cellular and subcellular level (Figure 3-1).

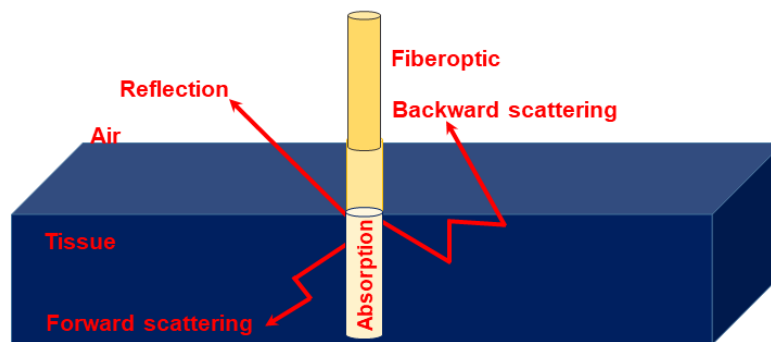


Figure 3-1: Interaction of light incident with the tissue.

##### 3.1.1 OPTICAL PROPERTIES OF BIOLOGICAL TISSUES

The determination of diverse biological tissue's optical properties plays a vital role in improving optical techniques in a different era in modern medicine [117]. The escape of light can assess the diagnostic application after penetrating and interrogating the tissue components [118, 119]. However, the therapeutic applications determine the ability to penetrate and deposit energy via the tissue [120, 121]. The optical properties of tissue are described in terms of the absorption coefficient ( $\mu_a$ ), the scattering coefficient ( $\mu_s$ ), reduced scattering coefficient ( $\mu'_s$ ), the scattering function  $P(\theta, \phi)$  ( $\text{sr}^{-1}$ ) and the real refractive index of the tissue  $n$ .

When molecules and atoms absorb an incident photon, the absorbed light can be converted to heat, radiation in the form of fluorescence or the consumption in photochemical reactions. The absorption coefficient gives information about the probability that the medium per unit length will absorb a photon. The Beer-Lambert Law describes the loss in intensity due to absorption as the light moves through the medium:

$$I = I_0 e^{-\mu_a x} \quad (3-1)$$

Where  $I_0$  is the intensity of the incident light,  $\mu_a$  is the absorption coefficient,  $x$  is the thickness of tissue. The scattering coefficient  $\mu_s$  ( $\lambda$ ) ( $\text{cm}^{-1}$ ) is a description for a medium with many scattering particles and different concentrations described as a volume density ( $\rho_s$ )  $\text{cm}^3$ . The size of the particle (cross-sectional area) plays a role in the efficiency of the scattering. The scattering coefficient is defined by:

$$\mu_s = \rho_s \cdot \sigma_s \quad (3-2)$$

Here,  $\rho_s$  is the density of scattering particles per unit volume ( $\text{cm}^{-3}$ ) and  $\sigma_s$  is the scattering cross-section. The density of the scattering sites is given by:

$$\rho_s = \frac{f_v}{V} \quad (3-3)$$

Where,  $f_v$  is the concentration, and  $V$  is the volume of the particle. The scattering cross-section ( $\sigma_s$ ) Equation is:

$$\sigma_s = Q_s \cdot A_s \quad (3-4)$$

Here,  $A_s$  is the actual cross-section of the particle and  $Q_s$  is the fractional scattering efficiency.

The reduced scattering coefficient ( $\mu'_s$ ) which is used to describe the diffusion of photons in a random walk of step size of  $1/\mu'_s$  gives rise to the reduced scattering coefficient:

$$\mu'_s = \mu_s (1 - g) \quad (3-5)$$

Where  $g$  is the anisotropy and can be measured from the cosine theta of the scattering angle. In terms of the scattering phase function, it is defined as the probability of scattering  $g$  with different angles  $\theta$  and  $\psi$  which are the scattering angles in the scattering planes and in-plane perpendicular to scattering plane, respectively [122](Figure 3-2). The scattering anisotropy factor  $g$  is considered a dependable parameter for measuring  $P(\theta)$ . It is defined as the parameter for measuring the amount of forwarding propagation retained after a single scattering event.

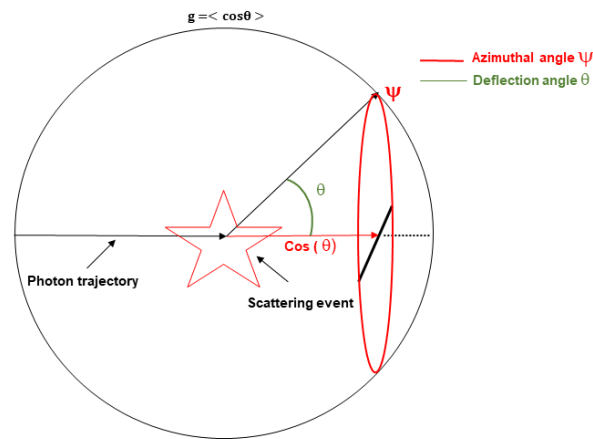
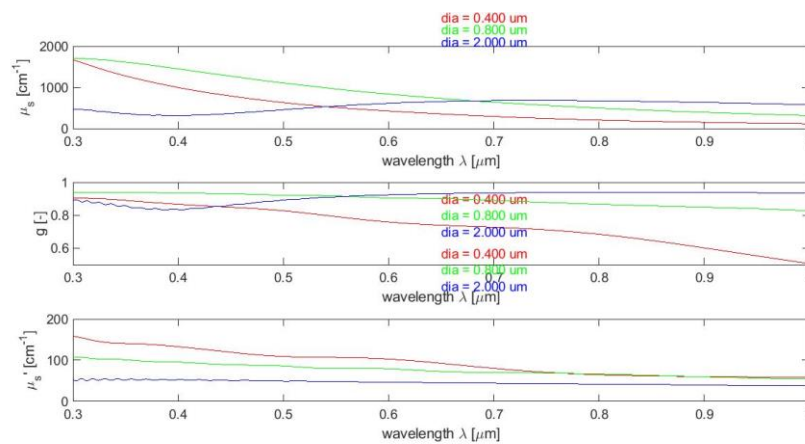


Figure 3-2: Anisotropy in scattering.

In our research, three aqueous suspensions of monodisperse polystyrene were used in our experiments, as mentioned in section 2.1.4.1. Figure 3-3 illustrated the optical properties ( $\mu_s$ ,  $g$  and  $\mu'_s$ ) of three sizes of polystyrene suspension. In this figure, there is a considerable variance of  $\mu_s$  values between three particle sizes in between 0.3 to 0.55  $\mu\text{m}$ . An overlap shown in between 0.55 to 0.65  $\mu\text{m}$ . At 0.7 to 1  $\mu\text{m}$ , a slight difference can be shown for the three particle sizes. Regarding  $g$  value, an overlap was shown for the low wavelength 0.3 to 0.5  $\mu\text{m}$ . On the other hand, a significant difference between 0.5 and 1  $\mu\text{m}$ . In terms of  $\mu'_s$ , a noticeable variance has been found in between 0.3 to 0.75  $\mu\text{m}$ . In contrast to the overlapping shown in between 0.75 to 1  $\mu\text{m}$  for 0.4 and 0.8  $\mu\text{m}$ . Straight pattern at 2  $\mu\text{m}$ .

Figure 3-3: Optical properties ( $\mu_s$ ,  $g$  and  $\mu'_s$ ) of three particle sizes of PS, 2, 0.8 and 0.4  $\mu\text{m}$ .

## 3.2 SCATTERING

Scattering is a physical process when energy waves of some incident radiation are caused to diverge from a straight trajectory due to non-uniformities in the medium.

In biological tissue, the difference in the index of refraction between subcellular or organelles and the surrounding cytoplasm is the source of the scattering. Thus, some incident light is scattered with a range of angles relative to the scattering particles [122].

Scattering processes play a vital role in diagnosis as well as in therapeutic applications. In diagnosis, the diversity in diseased tissue components such as lipid membranes, nuclei, and collagen fibres cause an effect on the scattering signals. Additionally, these variations can be used to determine optical light dosimetry and provide useful feedback during therapy. Many parameters play an essential role in propagating light in tissues, such as the shape, size, and density of these structures, their refractive index relative to the tissue ground substance, and the polarization states of the incident light in tissues.

In 1908 [123], Mie applied rigorous solutions to address the scattering light from an isotropic spherical particle. Mie theory is thus an exact mathematical solution to any value of diameter particle size, any scatter (weak or very efficient scatter which depends on the wavelength), or the refractive index (the sphere's dielectric properties and the surrounding medium).

A comparison between the particle size and wavelength of light being scattered is an essential feature of scattering. Accordingly, when the particle size is less than one-tenth of the photon's wavelength, Rayleigh scattering occurs. In this type of scattering, the number of backscatters from the incident light (the amount of extinguishing due to the absorption is approximately the same as the amount of the light continuing forward). As the particle becomes more than one-tenth of the wavelength and less than the photon's wavelength, Mie scattering occurs. With this type of scattering, more scattering is forward going than backscattering. Finally, when the particle size reaches the wavelength or more, Mie scattering occurs as an optical scattering, which means uniform scattering forward with the same direction as backscattering (Figure 3-4).

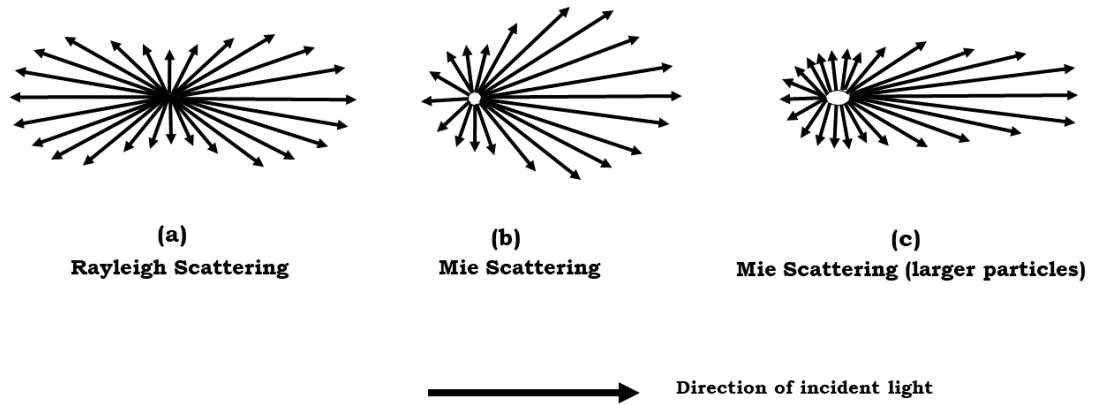


Figure 3-4: Effect of the particle size on the scattering types.

Our study used three different sizes of particle 413 nm, 800 nm, and 2000 nm due to the reason mentioned in section 2.1.4.1 with the incident light in the range 450 to 1000 nm. The above information clarifies that our study's scattering occurs at the Mie scattering section. To characterize the system, a size parameter  $X$  and the ratio of refractive index ( $m$ ) are mainly used. The ratio between the radius of the particle sphere and the wavelength (size of the photon)  $\lambda = \lambda_0/n_m$  represents the size parameter which can be expressed as:

$$X = \frac{2\pi a n_m}{\lambda_0} \quad (3-6)$$

Where  $a$  is the radius of the particle,  $\lambda_0$  is the wavelength (632.8 nm) and  $n_m$  is the refractive index of the medium. The ratio of the refractive index of the sphere ( $n_s$ ) and the surrounding medium ( $n_m$ ) defined as  $m$ :

$$m = \frac{n_s}{n_m} \quad (3-7)$$

Our study used 1.58 as the refractive index for the polystyrene suspension [83] and 1.333 for water.

For a randomly polarized light source, the total intensity of scattering light ( $S_{11}$ ) corresponds to scattering phase function  $P(\cos \theta)$ , which is shown in Equation 3-8 [124].

$$p(\cos \theta) = S_{11}(\theta) = \frac{|S_1(\theta)|^2 + |S_2(\theta)|^2}{2} \quad (3-8)$$

Where  $P(\cos \theta)$  is the scattering phase function,  $S_1(\theta)$  and  $S_2(\theta)$  the angular scattering function.

Therefore, to calculate  $S_{11}$  which equals  $p(\cos \theta)$  the angular function,  $S_1$  and  $S_2$  are required.

Consequently, the scattered components of a plane wave at an angle  $\theta$  are found by Mie [125]. This amplitude is written in terms of spherical functions.

$$S_1(\theta) = \sum_{n=1}^{\infty} \frac{2n+1}{n(n+1)} (a_n \pi_n(\cos\theta) + b_n \tau_n(\cos(\theta))) \quad (3-9)$$

$$S_2(\theta) = \sum_{n=1}^{\infty} \frac{2n+1}{n(n+1)} (a_n \tau_n(\cos(\theta)) + b_n \pi_n(\cos(\theta))) \quad (3-10)$$

$\pi_n$  and  $\tau_n$  are represent by Legendre Polynomials  $P_n$

$$\pi_n(\cos(\theta)) = \frac{1}{\sin\theta} P_n(\cos(\theta)) \quad (3-11)$$

$$\tau_n(\cos(\theta)) = \frac{d}{d\theta} P_n(\cos(\theta)) \quad (3-12)$$

$a_n$  and  $b_n$  are the Mie coefficients which are the key parameters for Mie calculation.  $a_n$  and  $b_n$  are computed the amplitudes of the scattered field.

$$a_n = \frac{\Psi'_n(y)\Psi_n(x) - m\Psi_n(y)\Psi'_n(x)}{\Psi'_n(y)\xi_n(x) - m\Psi_n(y)\xi'_n(x)} \quad (3-13)$$

$$b_n = \frac{m\Psi'_n(y)\Psi_n(x) - \Psi_n(y)\Psi'_n(x)}{m\Psi'_n(y)\xi_n(x) - \Psi_n(y)\xi'_n(x)} \quad (3-14)$$

Where  $\Psi_n$  and  $\xi_n$  are the Riccati -Bessel functions.

### 3.3 ELASTIC LIGHT SCATTERING SPECTROSCOPY (ELSS)

#### PRINCIPLE

Various optical spectroscopy techniques have been used, as mentioned in the review chapter:

Diffuse reflectance spectroscopy (DRS), Fluorescence spectroscopy (FS), Raman Spectroscopy (RS), and Elastic Light Scattering Spectroscopy (ELSS). ELSS has been selected from the optical techniques for the reasons mentioned in section 2.1.4. ELSS is an optical technique with the potential to perform a minimally invasive biopsy. ELSS employs optical fibres with specific diameters and geometries to detect human tissue reflectance and light scattering. In ELSS, light enters the tissue and is backscattered without changing the wavelength. Variations in the spectrum of backscattering are due to the difference in the morphological structure of cells. For instance, an alteration in the scattering properties will occur if there is an increase in the number of mitochondria or the nucleus size (Figure 3-5).

Additionally, the absorption features (the tissue's biochemical function) are easily seen in the ELSS signal [57]. The scattering process occurs due to the differences in density at the cellular and subcellular level [58]. The scattering event encodes the characteristics of the cellular components, which are called “scattering centres”. Pathological scattering determines disorganization in the morphology of epithelial surface texture, thickness, and architecture, changes of epithelial cell orientations, crowding in the cell, raised distance from subepithelial collagen layer, enlargement, and hyper-chromicity of the cell nucleus, increased concentration of metabolic organelles and presence of abnormal protein particles or packages [59].

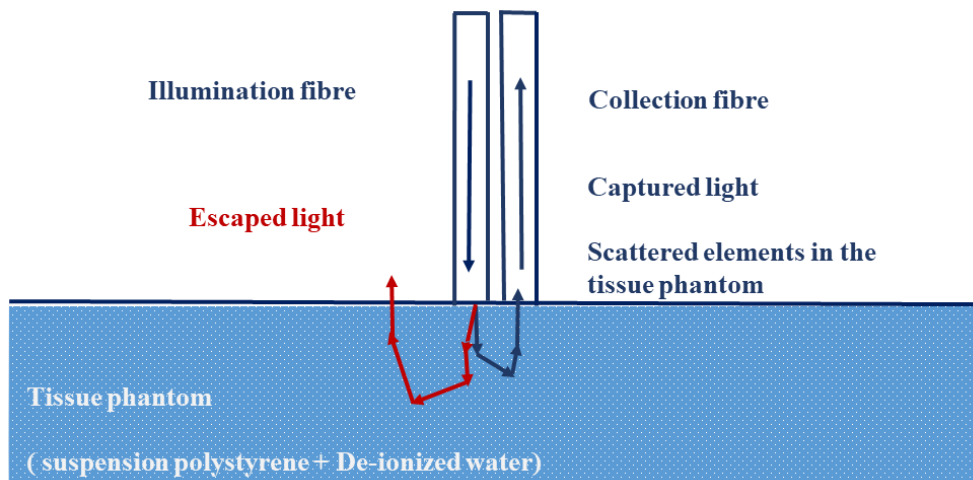


Figure 3-5: Schematic set up of the ELSS

## 3.4 MATHEMATICAL MODEL

### 3.4.1 DEFINITION AND OBJECTIVE

A simple mathematical model has been built to represent the probe utilising two identical fibre optic cables. The fibre diameter, the separation between them and the scattering angle derive the scattered intensity as light from one fibre is collected by the adjacent fibre.

### 3.4.2 EQUATIONS OF THE MATHEMATICAL MODEL

The basic Equations used to describe our initial mathematical model are the Beer-Lambert law and the standard Gaussian distribution function.

In Optics, Laser (light) beams often occur in the form of Gaussian beams. Here we use the Gaussian function as the intensity profile of light emerging from the fibre and the collection of light in the receiving fibre.

The full width at half maximum (FWHM) of the intensity correlates with the diameter of the Gaussian beam.

$$f(X, \sigma, \mu) = \frac{1}{(2\pi\sigma^2)^{1/2}} e^{\frac{-(x-\mu)^2}{2\sigma^2}} \quad (3-15)$$

Where  $\sigma$  is the FWHM,  $\mu$  is the position of the centre of the fibre, and  $x$  is the position variable.

In our research, other Equations are used that are specific to the design. Equation 3-16 is used to model the FWHM of the emerging beam as it propagates into the medium (the  $z$ -axis, which is perpendicular to the face of the fibre aperture). The further the beam propagates, the wider the FWHM. If this is also applied to the receiving fibre, then the two beams will begin to overlap at a certain distance from the fibre face. This overlapping region is the sensing or interaction volume, and as such, if the light is backscattered in this region, it has the potential to be captured by the receiving fibre, see Figure 3-6.

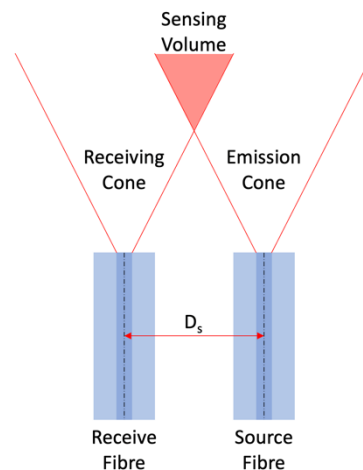


Figure 3-6: Schematic diagram illustrating the overlap between the emission cones of both fibres giving rise to the sensing volume and the fibre separation  $D_s$ .

As the source of the cancer is in the epithelium (the top layer), the typical thickness is 100 to 300  $\mu\text{m}$ . Also, the separation between the source fibre and the detector fibre plays an essential role in

detecting the top layer. Thus, if the area between the two fibres is overlapping, the sensitivity will be further restricted to the epithelium [122].

A three-dimensional spatial intensity distribution model was coded into MATLAB (Appendix A-1) that took the sum of the product of the Gaussian intensity distribution for each fibre at discrete locations forward of the fibre faces. This provided a simple measure of the coupling intensity (efficiency) for different fibre diameters, separations, and refractive index of the medium in front of the fibres for fibre core diameters defined by  $D_{core}$ . The FWHM, or  $\sigma$ , is calculated at each  $z$  position away from the fibre faces. See Figure below and Equation (3-16).

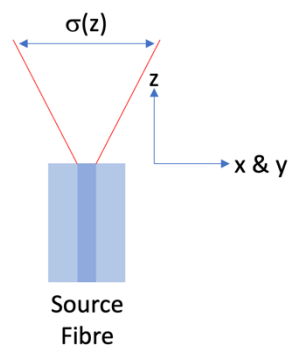


Figure 3-7: Schematic diagram illustrating the position-dependent FWHM,  $\sigma$  as a function of distance from the fibre face.

$$\sigma = (D_{core} + 2 * Y_{values(i)} * \tan(\theta_a)) / n_{\sigma} \quad (3-16)$$

The acceptable tangent angle, which depends on the numerical aperture (NA) and the medium's refractive index, is illustrated in Figure 3-8.

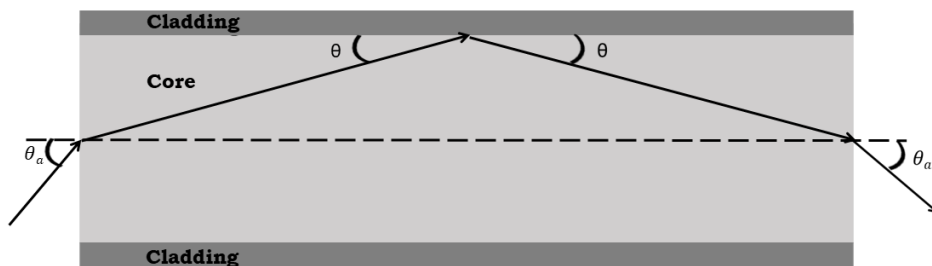


Figure 3-8: The effect of core diameter and the acceptance angle  $\theta_a$  and  $\theta$  is the critical angle for the total internal reflection.

Equation (3-17) is used to measure the three-dimensional scattering intensity.

$$I(x, y, z) = e^{-(\gamma+z)} * \left( \frac{1}{\sqrt{2 * \pi * \sigma^2}} \right) * \left[ e^{-\frac{(y-\mu)^2}{2\sigma^2}} * \left( e^{-\frac{(x-(\mu-D_s/2))^2}{2\sigma^2}} + e^{-\frac{(x+(\mu-D_s/2))^2}{2\sigma^2}} \right) \right] \quad (3-17)$$

The variables in the above two Equations are as follows.  $D_{core}$  is the diameter of the optical fibre core.  $\theta_a$  is the acceptance angle.  $n_\sigma$  is a truncation parameter that governs the FWHM.  $\mu$  is an arbitrary location between the centre of each fibre core in space (x,y).  $D_s$  is the fibre separation. Finally,  $\gamma$  is the attenuation coefficient from the Beer-Lambert law and represents scattering.

### 3.4.3 EFFECT OF SOME PARAMETERS ON THE MATHEMATICAL MODEL

The finite width of optical fibre implies that the extent of the Gaussian intensity function must be truncated.  $n_\sigma$  is used simply to vary this truncation, as illustrated in Figure 3-9 below. In this figure, at  $n_\sigma=2$  showed that the light does not go to zero, or is cut off abruptly. However, at  $n_\sigma=6$  illustrated that the light diminishing almost to zero at the periphery. Therefore, this parameter is used to determine the FWHM of the emerging beam and to provide variance relevant to the real fibres.

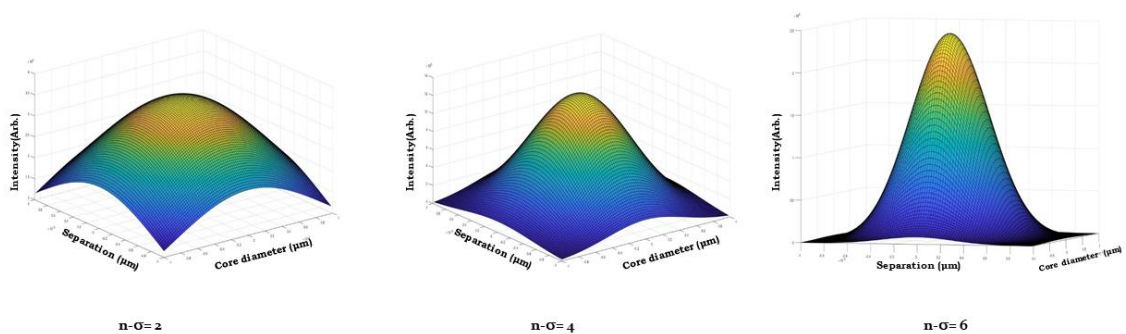


Figure 3-9: The intensity profile for the different number of sigma ( $n_\sigma$ ).

The acceptance angle ( $\theta_a$ ) plays an essential role in collecting incident light in optical fibres. It is defined as the maximum angle of a light ray that can enter the fibre. If the incident angle is at or below  $\theta$ , the beam will be propagated as shown in Figure 3-10.

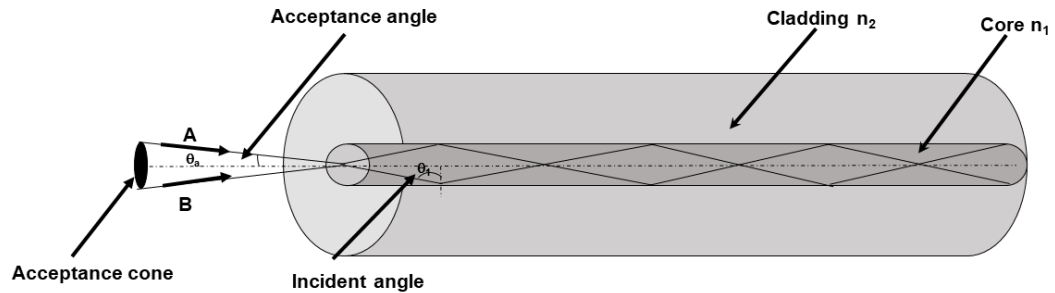


Figure 3-10: The acceptance angle and the incident ray

When the value of  $\theta_i$  decreases, this means the entire ray must be found within the acceptance cone to ensure total internal reflection occurs inside the fibre. The acceptance angle is typically reported in terms of numerical aperture ( $NA$ ).

$$NA = n_0 \sin\theta_a \quad (3-18)$$

Where  $n_0$  is the ambient refractive index and  $\theta_a$  is the acceptance angle.

From the Equation,  $NA$  is expressed a correlation between the ambient refractive index and the acceptance angle.  $NA$  plays an essential role in defining how light is collected from the source and retained light inside the fibre [126]. In our research,  $n_0$  which is the refractive index of water equals 1.333. The  $NA$  of our optical fibre is 0.22 therefore  $\theta_a$  is  $9.5^\circ$ .

### 3.4.3.1 RESULTS OF PARAMETERS AFFECTING THE MATHEMATICAL MODEL

Figure 3-11 illustrates the effect of the acceptance angle ( $\theta_a$  water is  $9.5^\circ$  and  $\theta_a$  air is  $12.7^\circ$ ) on the scattering intensity with different separation. Overall, the acceptance angle of water showed a significant increase in the scattering intensity compared to the acceptance angle of air. The general outcome is that the lower the differences in refractive index, the more light is coupled from source fibre to sense fibre.

Or the higher the refractive index, the slower the light travels, which causes a corresponding increased change in the direction of the light within the material.

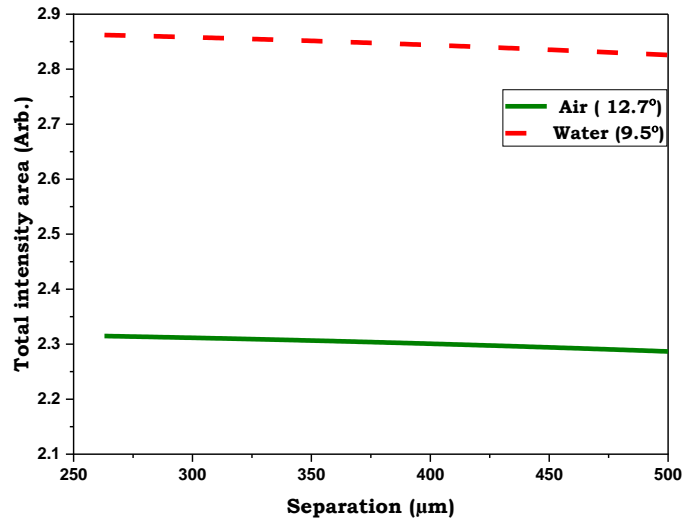


Figure 3-11: The effect of acceptance angle on the scattering intensity

In our research, the sphere and medium's refractive index and particle size are independent variables that change with the dependent variable  $\gamma$  (the scattering coefficient). In theory, the scattering coefficient depends on the density of scattering particles per volume and cross-section of the particle. Therefore, we studied the effect of scattering on our geometrical model.

Figure 3-12 demonstrates the scattering (scattering coefficient) efficiency of scattering intensity over the separation range 263 to 500 nm. Overall, the scattering intensity increases when the scattering coefficient decreases over the whole range of the separation. Figure 3-12 demonstrated that there is a considerable increase in reducing the number of scattering events, which can be explained as it is the interaction of a photon with a particle that results from in elastic scattering.

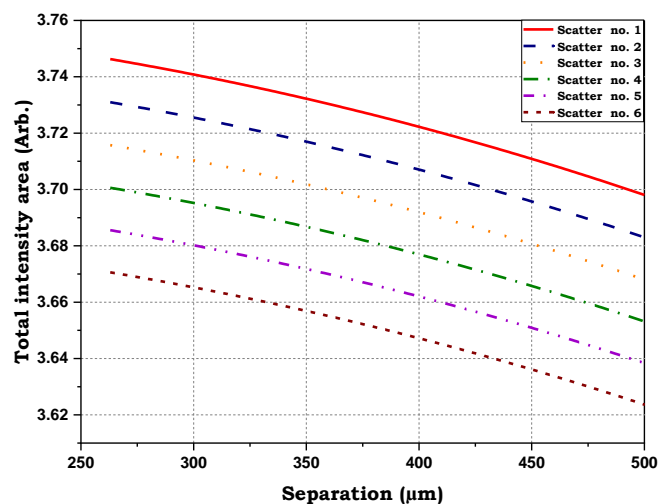


Figure 3-12: The effect of the scatter on the scattering intensity

The separation of the fibre centres plays a vital role in tumour detection for many reasons. The

separation of the source and detector is one controlling factor for sampling the top layer (epithelium) where most cancer arises. As the source and detector are moved closer together, a more superficial region is probed. Moreover, the sensitivity will be further restricted to the epithelium if the incident and detection fibres are overlapped. The most prominent issue for our probe design is that the fibres are not co-located and have to be physically separated. The smallest separation between the illumination and light collection of the geometrical probe increases the likelihood of detecting high scatter angle events. To clarify this, if a photon travels forward and does not scatter, the scattering angle is zero. If it is scattered directly backwards, the angle is high (180 degrees). Since our detection fibre is adjacent to the source, to be detected, the scattering angle must be high, around 180 degrees. As a result, changing the source-detector separation will change the elastic scatter signal. Hence, we have studied the effect of centre separation to assess potential cancer detection sensitivity.

The graph below illustrates the scattering intensity as a function of fibre centre separation. Overall, there was a decrease in scattering with increasing separation. Furthermore, the design with small separation (263) is more efficient in scattering intensity than the significant separation (400) (Figure 3-13).

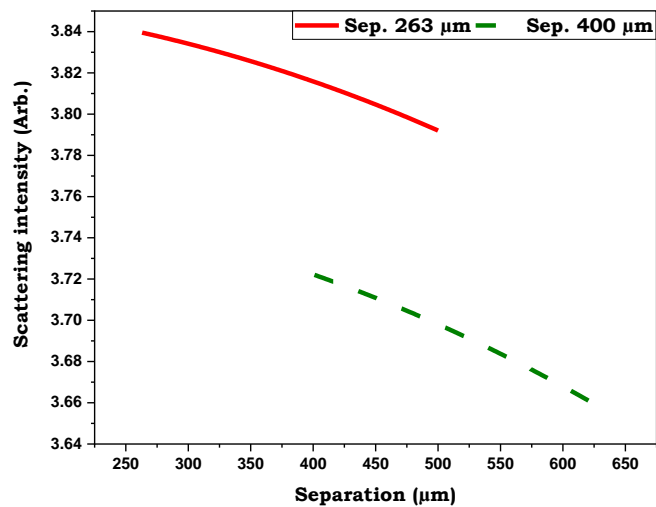


Figure 3-13: The effect of the separation on the scattering intensity

The graph below shows the effect of core diameter on scattering intensity over the range of separation (120 to 500). There was a significant increase in the scattering intensity at a core diameter of 100 μm in comparison to 200 μm over the whole range of separation (Figure 3-14). These two diameters have been selected as they are used in our probe's fabrication.

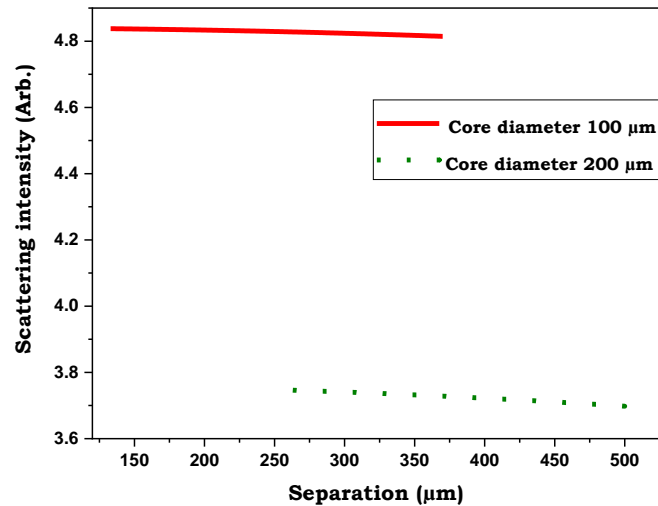


Figure 3-14: The effect of the diameter on the scattering intensity

The smaller fibre produces more coupling and may be counter-intuitive since the more significant fibre's emission and collection areas are larger. However, the fact that these can be brought closer suggests that the separation is dominating, and the smaller fibres produce a more concentrated interaction volume.

A slightly different approach to the modelling of the fibre system was taken that made the computation more efficient and exploited the assumption that the fibre is a so-called 'Lambertian' emitter. For simplicity, the emitters, in this case, are point sources and can be separated by different amounts. Figure 3-15 shows a sequence of the 3-D intensity distribution for 8 different  $z$  values (distance from fibre faces into the sample) resulting from MATLAB Code (Appendix A-2).

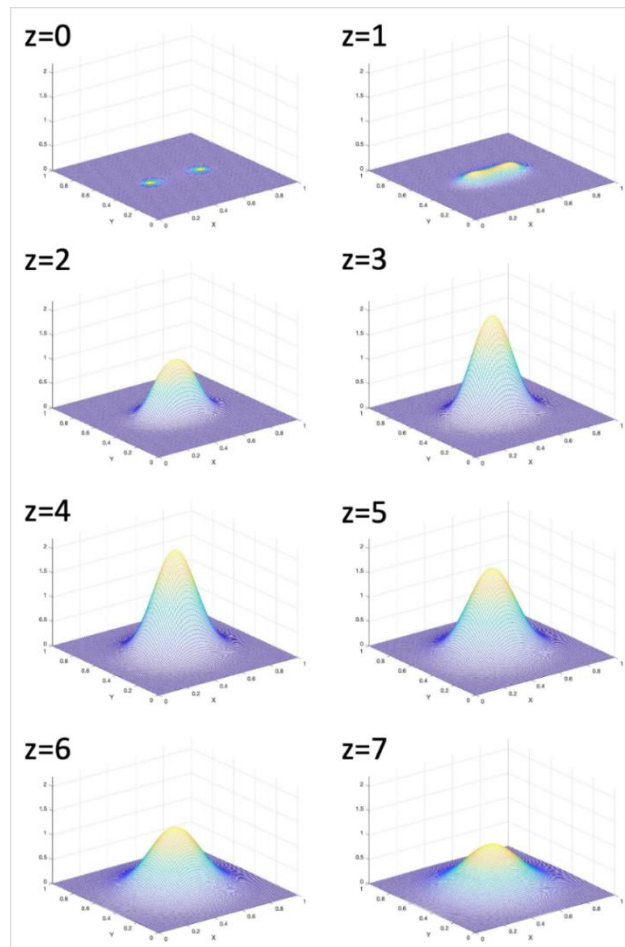


Figure 3-15: 3-D intensity profiles for different distances from the fibre faces. (Lambertian emitter model.),  $Z$  is a position away from the tip of the fibre aperture (it is the assumption number without the unit in the figure).

As can be seen here, the two competing effects of increasing overlap vs increasing attenuation are at play. There is clearly an optimum coupling efficiency at a specific distance from the fibre faces representing the 'sensing volume'.

Figure 3-16 shows how the coupling intensity generally varies as a function of the distance between the fibres for two different acceptance angles (15 and 25 degrees). Clearly, the wider acceptance angle has a greater coupling efficiency, as expected. The intensity here was obtained from taking the volume under the surface from the above graphs.

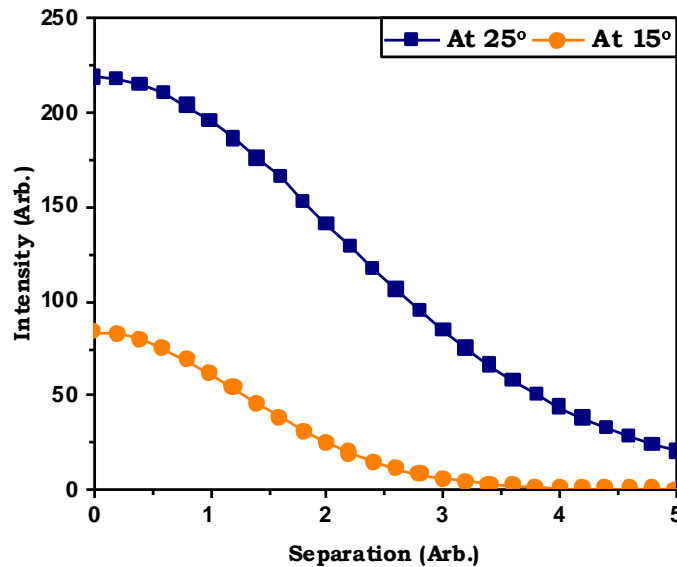


Figure 3-16: Coupling intensity as a function of the distance between the fibres for two different acceptance angles (15 and 25 degrees). (Lambertian emitter model.).

The above analysis serves only as a means of assessing the general trends. Since the geometry of the fibre probe is largely restricted due to practical considerations, further analysis of this type would be best suited to more advanced commercial optical design software.

### 3.5 CHAPTER SUMMARY

The basic principle for the transmission of light in tissue, the optical properties of biological tissue and the scattering phenomena as the basic principle for the selected method in our system (ELSS) have been clarified. A mathematical model has been designed using the Beer-Lambert law and the standard Gaussian distribution function to characterize the specific parameters on the geometrical design. Then, the effect of some parameters on the geometrical design has been studied, such as  $n$ -sigma, acceptance angle, scattering, centre to centre separation and diameter of the optical probe. The outcome of the mathematical model showed, six is the ideal number of sigmas to obtain a typical Gaussian intensity function. The general outcome of the acceptance angle effect is that the lower the difference in the refractive index, the more light is coupled from source fibre to sense fibre. A considerable increase in the intensity in reducing the number of scattering events. Regarding the separation centre to centre and the core diameter effect. The design with a small separation of 263  $\mu\text{m}$  is more efficient in scattering intensity than the separation of 400  $\mu\text{m}$ . A probe with 100  $\mu\text{m}$  shown a substantial increase in the scattering intensity in comparison to 200  $\mu\text{m}$ , which are the actual core diameters of the experiment work over the whole range of separation 225 to 675  $\mu\text{m}$ . Finally, to increase computation efficiency, a slightly different approach to modelling the fibre system was designed using a 'Lambertian'

emitter. This model showed that by increase the z-axis, which is perpendicular to the face of the fibre aperture. The further the beam propagates, the wider the FWHM. Also, the wider acceptance angle (by reducing the centre-to-centre separation between the emitting and receiving fibres) has a greater coupling efficiency of the intensity.

---

# CHAPTER 4

## FABRICATION AND EXPERIMENTAL RESULTS FOR THE OPTICAL PROBE

### 4.1 GEOMETRICAL DESIGN AND FABRICATION

The fabrication steps have been done by following the below steps. Firstly, selecting the suitable fibre optics, fabrication steps in the Lab., preparation tissue phantom samples polystyrene spheres in suspension (PS) and finally, experimental results using our optical probe fabricated by using different PS dilutions 2.5%, 1.25% and 0.625% for three particle sizes 2, 0.8 and 0.413  $\mu\text{m}$ .

#### 4.1.1 SELECTING THE OPTICAL FIBRE

There are two categories in fibre optics, namely single-mode and multi-mode. The single-mode describes a fibre that supports one transmission mode, a small core diameter ( $<10 \mu\text{m}$ ) and a low numerical aperture. The multi-mode describes a fibre that can help more than one transmission mode, have bigger core diameters ( $> 50 \mu\text{m}$ ) and a corresponding larger numerical aperture (0.2 to 0.4) for silica core fibres. Multi-mode fibres are commonly employed in biomedical applications and have two basic configurations: step-index and gradient index. Step - multimode index fibres have a core diameter of  $>100 \mu\text{m}$ . The name refers to the sharp change in refractive index in the fibre material at the core-cladding boundary. By contrast, gradient index fibres with smaller core diameters (50 to 90)  $\mu\text{m}$  have a refractive index that reduces gradually from the centre of the core to the cladding. The numerical aperture (NA) collects the light from a source and preserves the fibre's light. Fibres with a high NA allow an extensive range of incident (optic) axis of the fibre, which causes the rays to travel in longer path lengths (high order modes). Fibres with low NA allow the incoming radiation to enter at smaller angles, and as a result, rays pass through in shorter path lengths (low order modes). The wavelength range choice plays an essential role in selecting appropriate core and cladding materials that allow for suitable light transmission. Conventional glass and plastic core fibres are highly transparent to wavelengths in the visible spectrum and lose  $\leq 0.1$  absorption per metre. High-grade fused silica cores are more suitable for optical transmission in the ultraviolet (UV) or infrared (IR) wavelength ranges. In these wavelength ranges, hydroxyl (OH) radicals in the silica core have the most robust characteristics of transmission and absorption of the fibre. Major extrinsic loss mechanism is caused by absorption due to water (as the hydroxyl or OH<sup>-</sup> ions) introduced in the glass fibre during fibre pulling by means of oxyhydrogen flame. In the UV region ( $200 \text{ nm} < \lambda < 360 \text{ nm}$ ), high OH are preferred, however in the near-infrared (NIR), and up to 2400 nm, low OH concentration

fibres provide the most favourable transmission [126]. Thus, in our optical fibre, the multi-mode is selected because it can be applied for tumour detection in cases with a core diameter of 200  $\mu\text{m}$  and 100  $\mu\text{m}$  as well as in cases with step-index categories due to detect fibre optics with core diameter  $>100 \mu\text{m}$ . In conclusion, the optical fibres chosen have the following characteristics. Core diameter  $200 \pm 4 \mu\text{m}$ , Cladding diameter  $220 \pm 4.4 \mu\text{m}$ , outer diameter  $245 \pm 5 \mu\text{m}$ , 0.22 NA for VIS/NIR (300 to 2400  $\mu\text{m}$ ), Fused silica (substrate) [127]. And Core diameter  $100 \pm 2 \mu\text{m}$ , Cladding diameter  $110 \pm 2.2 \mu\text{m}$ , Outer diameter  $130 \pm 5 \mu\text{m}$  and 0.22 NA for VIS/NIR (300 to 2400  $\mu\text{m}$ ), Fused silica (substrate) [128].

### 4.1.2 FABRICATION AND GEOMETRICAL DESIGN

Two ELSS optical probes, probe 1 and probe 2, consist of two silica-silica identical adjacent fibres. One for the illumination, the other for detection with a numerical aperture of 0.22 in the air. Probe 1 uses fibres of 200  $\mu\text{m}$  diameter, and for probe 2, 100  $\mu\text{m}$  core diameter. The centre-centre separation is 263 and 132  $\mu\text{m}$  for probes 1 and 2, respectively. The distal end is housed in a rigid stainless steel needle casing for easy handling. The diameters of the whole assembly are 0.8 and 0.5 mm, respectively. Figure 4-1 and 4-2 demonstrate the steps of our fabrication. Figure 4-1 demonstrates the fabrication steps which started by adjacent two identical fibre optics in a rigid stainless steel needle using the specific glue for fibre optics (F120 - Epoxy for Fiber Optic Connectors, Fast Room Temperature Cure, Thorlabs Company, US). Then the drier has been used to fix all. Finally, the separation for two fibres has been done using a fabricated plastic part, one as a source and the second as a receiver fibre. Figure 4-2 shows the polishing steps for the SMA905 fibre connectors which one was used as a source and the second one as a detector fibre optics. The steps started by hanging the connector in a safe spot after inserting fibre into epoxied connector. Then to make it ready for polishing, a Protrude fibre has been done. Ultimately, a polishing fibre has been done using specific fibre polishing film/ Lapping Film for use with stainless steel Ferrules with different sizes 5  $\mu\text{m}$ , 3  $\mu\text{m}$ , 1  $\mu\text{m}$  and 0.3  $\mu\text{m}$  and connectorised fibre polishing pucks to hold the fibre connector securely and to maintain the proper angle. Figure 4-3 and 4-4 illustrate the design and physical embodiment of the optical probe.



Figure 4-1: Fabrication steps 1-Gluing two fibre optics after adjacent both of them.2- Glue and house the adjacent fibres in a rigid stainless steel needle.3- drying all gluing parts.4- Fix and separate two fibres, one as a source and the second as a receiver.

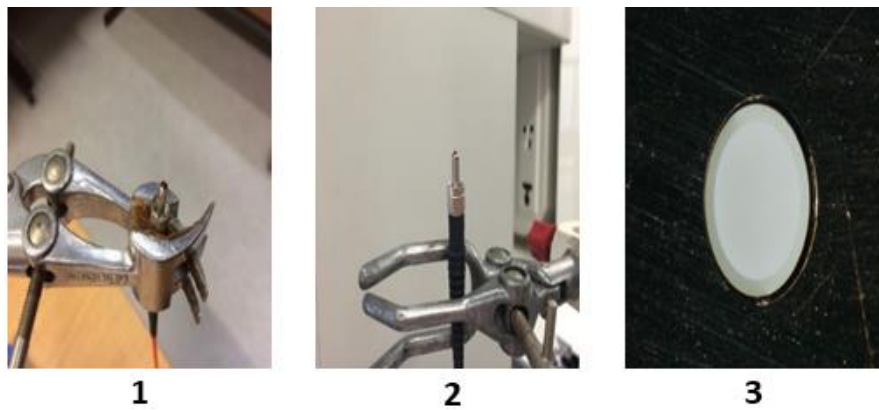


Figure 4-2: Polishing steps for the SMA905 Fibre connectors.1-Hang the connector in a safe spot after inserting fibre into epoxied connector.2- Protrude fibre to make ready for polishing. 3- Fibre after polishing.

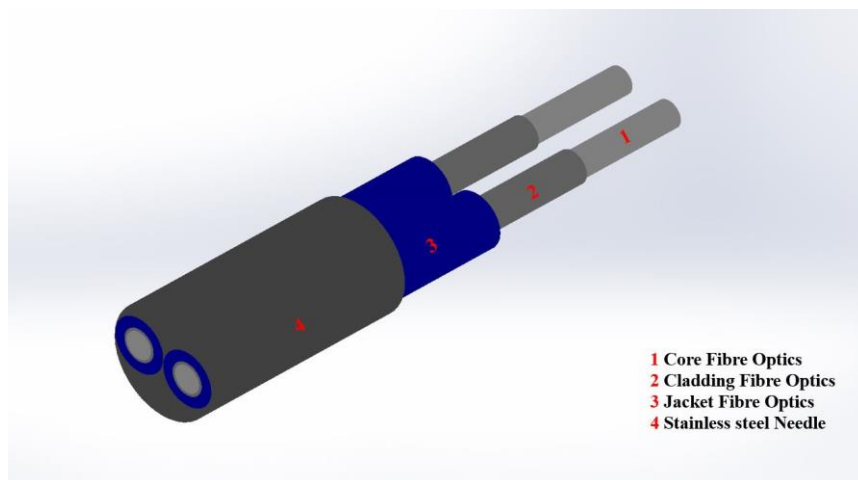


Figure 4-3: The design of the Optical Probe



Figure 4-4: The physical optical probe

## 4.2 TISSUE PHANTOM PREPARATION

### 4.2.1 OPTICAL TISSUE PHANTOM

Three aqueous suspensions of monodisperse polystyrene microsphere (Corpuscular Inc, Marvel of Nanoscience, and the USA) [129] are used in the experiments. Diameters of the microsphere were 0.413, 0.8 and 2  $\mu\text{m}$ , as demonstrated in section 2.1.4.1. The samples consisted of 250 microliters ( $\mu\text{l}$ ) of stock (2.5%) (The original concentration from the manufacturer), 250  $\mu\text{l}$  of the stock added to 250  $\mu\text{l}$  of deionized water (DI-W), and half of this mixture is used as the first concentration (1.25%). The other half is added to 250  $\mu\text{l}$  of DI-W, and half of this mixture is used as a second concentration (0.625%) (Figure 4-5). The last concentration ranges from reduced scattering coefficient 12.972-27.89  $\text{cm}^{-1}$  (within various tissue types). The reduced scattering coefficient of different tissue types varies between 1.2 to 40  $\text{cm}^{-1}$  [83]. All particle size measurements were performed on suspensions with reduced scattering coefficients in the range 6.489 to 111.584  $\text{cm}^{-1}$ . Mie theory has been used to calculate the reduced scattering coefficient using a value of 1.58 and 1.333 for the particle and DI-W refractive index, respectively at 632.8 nm. The Scott Prahl calculator is used to calculate the Mie scattering [130].

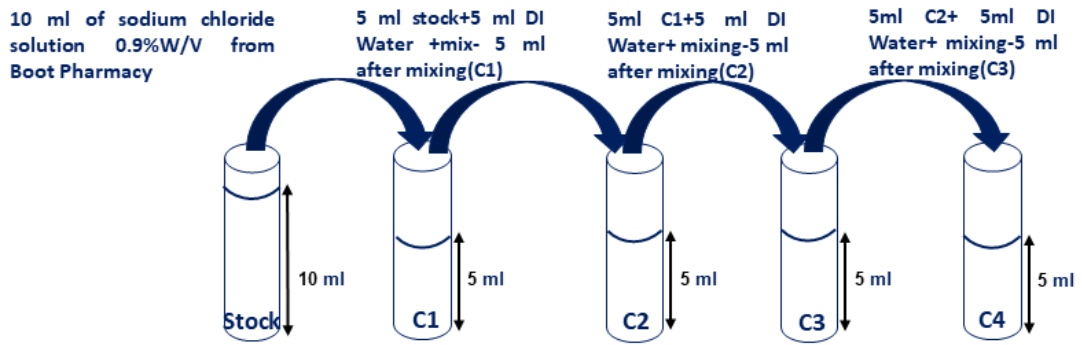


Figure 4-5: Polystyrene preparation

### 4.3 ANALYSING DATA

The measured spectra were corrected for the wavelength dependence of system components and specular reflection. The spectrum is corrected by using the Equation below [80].

$$R(\lambda) = \frac{R(\lambda)_s - R(\lambda)_{bg}}{R(\lambda)_c - R(\lambda)_{bg}} \quad (4-1)$$

Where,  $R(\lambda)_s$  is the measured spectrum from a suspension of monodisperse polystyrene microspheres by inserting the probe inside the sample by 5 mm,  $R(\lambda)_{bg}$  is the background spectrum, which was measured from pure water by inserting the tip of the optical probe in the black container of the DI-W to define the back reflection  $R(\lambda)_c$  is a spectrum of spectralon (Labsphere, Inc., Ocean Optics). The probe was nearly placed 1 mm above the spectralon to calibrate the spectral response of the system by recording a reference spectrum from a spectrally flat diffuse reflector (Spectralon).

### 4.4 INSTRUMENTS

The ELSS system instrumentation consists of an 'Ocean Optics' Maya Pro USB Spectrometer, Original Equipment Manufacturer (OEM) ocean view software (Maya2000 Pro, Ocean Optics Company, US). The optical resolution for this system is 0.47 nm, and a stabilized tungsten-halogen Light Source has been used (VIS-IR) (Thorlabs Company, US). The computer is used to control the various components and record the spectra. An automatic motor was used to fix the sample. Mobile scanning stage in X-Y raster pattern was used to insert the probe into the sample to the same position repeatably. The step size of the stage is less than 1  $\mu\text{m}$  (Figure 4-6).

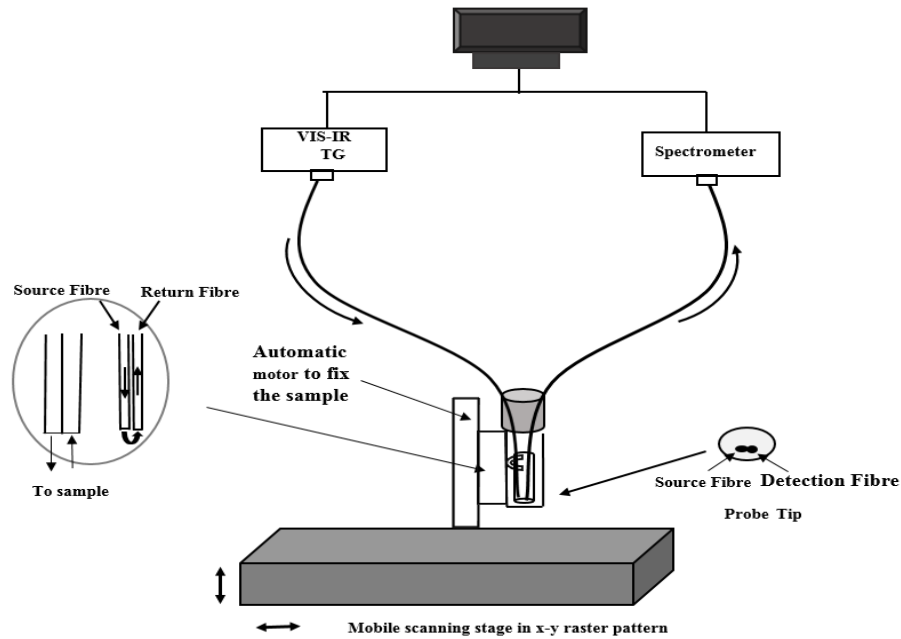


Figure 4-6: Set up of the experiment

## 4.5 CONFIGURATION TYPES

A first configuration was fabricated using two identical optical fibres glued together into a 3d printed plastic housing. These two attached fibres are threaded into a stainless-steel needle for insertion into the sample. The other ends of the probe, the source and receive fibre were fitted with SMA connectors. See Figure 4-7 below. In this first configuration, two probes with different diameters have been fabricated, as mentioned in section 4.1.2. The comparison of these two probes will follow.

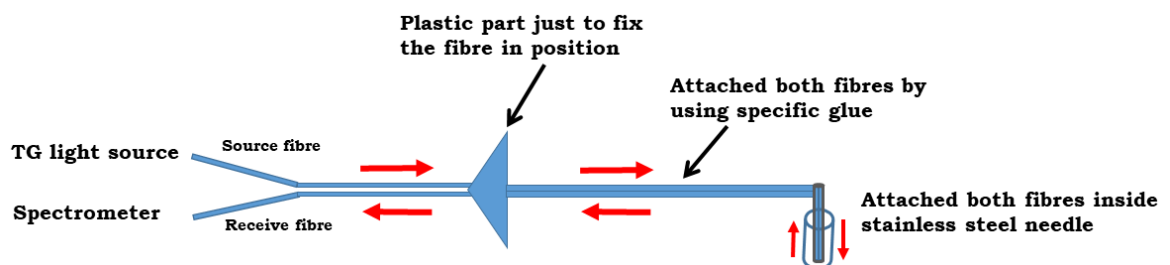


Figure 4-7: Schematic diagram of the first set-up.

The goal here was to efficiently detect single backscatter events. It was not possible to manufacture a probe with a single fibre optics because of a lack of access to a fibre fusion splicer.

Therefore, a second configuration was tried to ensure single backscattering could be detected. A probe consisting of a single fibre with a core diameter of 400  $\mu\text{m}$  has been fabricated in this setup. With this probe, the two ends were fitted into separate stainless-steel needles. One end for sensing, the other to be butt connected to two smaller diameter fibres (probe 1 in section 4.1.2 which consists of two identical fibres with core diameters 200  $\mu\text{m}$ ), partially overlapping and glued together with index matching gel. In this configuration, the illumination fibre partially couples to the larger sensing fibre. Light travelling back from the sensing fibre is partially coupled into the spectrometer fibre, as illustrated in (Figure 4-8).

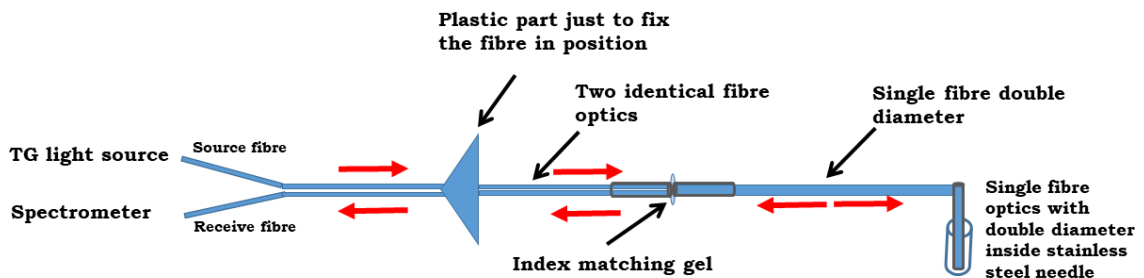


Figure 4-8: The diagram of the second set-up

## 4.6 EXPERIMENTAL RESULTS

### 4.6.1 EFFECT OF THE PARTICLE SIZE (TISSUE PHANTOM POLYSTYRENE SPHERES IN DI-W)

Figure 4-9 shows the spectra for three tissue phantoms of polystyrene suspension with particle diameters 2, 0.8 and 0.413  $\mu\text{m}$  and a concentration of 0.625%. The reduced scattering coefficient for this is in the range of 12.972 to 27.89  $\text{cm}^{-1}$  within the range of different tissue types. Figure 4-11 shows the number of peaks increases with increasing particle size over the whole range of wavelengths (450 to 1000) nm. Figure 4-10 demonstrates the spectra's derivative (gradient). The frequency of oscillations in the derivative spectra increases with a particle size as expected but without the background offset. The spectrum in Figures 4-9 and 4-10 represent the characteristic signature for each particle size.

The number of the maxima and minima in the derivative spectra provided information regarding the particles' diameter (Figure 4-11). With particle diameters of 0.413, 0.8 and 2  $\mu\text{m}$ , there is an approximately linear relationship between the total number of maxima (or minima) and particle size. The size of the cells plays an essential role in differentiating between normal and cancer cells. Canpolat and Mourant confirmed this as they used the number of the maxima and minima

of the derivative spectra to determine the scatterer size [81]. In this case, the scattering medium consists of a monodisperse distribution of spheres with the known refractive index (1.58) at a wavelength range of 450 to 800 nm [81]. This technique can distinguish various scatterer sizes (0.1 to 2)  $\mu\text{m}$  [81]. Therefore, our project's probe can identify the different size of particles (0.413, 0.8 and 2)  $\mu\text{m}$  as there is a significant difference between the particle size and the number of the maxima and minima (Figure 4-11), which is related to the correlation between the particle size and the wavelength clarified in section 3.2.

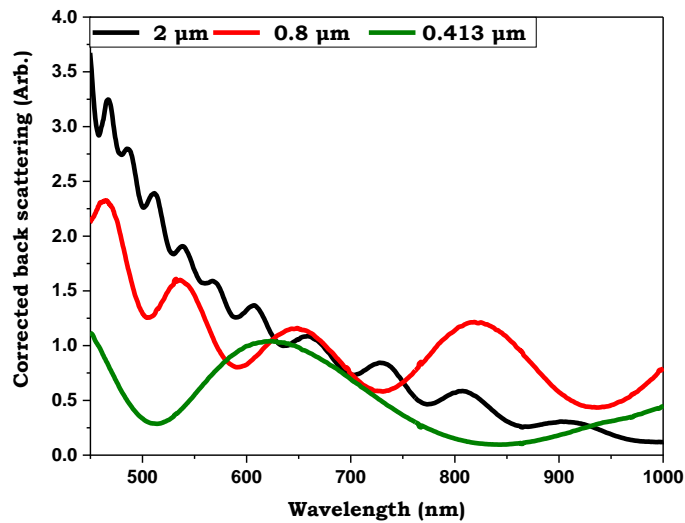


Figure 4-9: Comparison between three particle sizes at 0.625 % PS concentration by using an optical probe with 100  $\mu\text{m}$ , each particle size with a different signature.

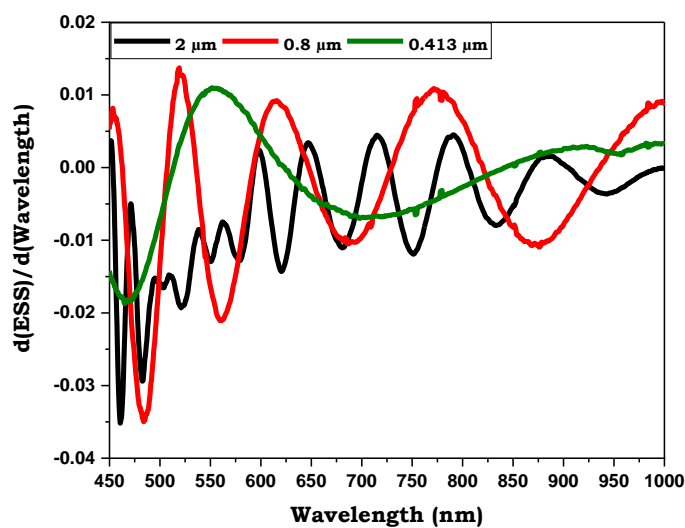


Figure 4-10: Derivatives of the spectra in figure 4.9

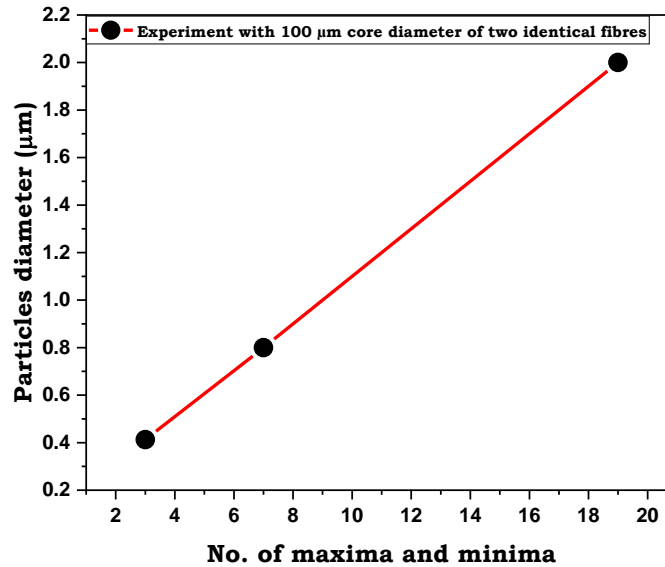


Figure 4-11: Particle diameter as a function of the total number of maxima and minima of the elastic scatter spectrum derivatives between 450 and 800 nm.

#### 4.6.2 EFFECT OF THE DIMENSION OF THE CORE DIAMETER AND THE SEPARATION BETWEEN FIBRE OPTICS ON THE MEASUREMENTS OF NON-ABSORBING TISSUE PHANTOMS. POLYSTYRENE IN DI-W

Figure 4-12 shows the spectra for the three tissue phantoms with particle diameters 2, 0.8 and 0.413  $\mu\text{m}$  with a concentration of 2.5% (the original concentration). For each particles size in this Figure, it is evident that the signal strength is superior for the 100  $\mu\text{m}$  core diameter as opposed to the fibre of 200  $\mu\text{m}$ . Here, the fibre separations are 132  $\mu\text{m}$  centre and 263  $\mu\text{m}$ , respectively. This corresponds with the modelling in chapter 3. The spectra in Figure 4-13 were acquired from all particles with different concentrations (different reduced scattering coefficient) using a fibre core diameter of 100  $\mu\text{m}$ . In this Figure, all particles' spectra are clear for all concentrations and, in particular, at 0.625% (Figure 4-13 C), which this concentration within the same range of reduced scattering coefficient for various tissue types as mentioned in section 4.2.1. In addition, the corrected backscattering showed a decrease with reduced concentration at 2  $\mu\text{m}$ . However, at 0.8 and 0.413  $\mu\text{m}$  particle size, it did not show this, which may be attributed to setting particles. The output of these results showed a similar signature for particles 2, 0.8 and 0.413  $\mu\text{m}$  with results of Canpolat and Mourant [81] as they used the polystyrene particles diameter were 0.329, 0.451, 0.890 and 2.020  $\mu\text{m}$ .

Therefore, two factors of the design will affect the quality of scattering detection. The first factor

is the centre-to-centre separation. The small source-detector separation can provide the most significant enhancement and is a controlling factor for sampling the top layer. This sensitivity will be restricted to the epithelium, where most adult cancer arises; this skin layer is typically 100 to 300  $\mu\text{m}$  thick [122]. Also, the small separation of illumination and collection fibre enables the collected light to undergo only a small number of scattering events. The lower number of scattering events, the more significant the influence of details such as size, shape, or refractive index of the tissue's scattering centres [57]. The second factor which affects the quality of scattering is the diameter of the optical fibre. Optical fibres with smaller diameters can be used to detect single scatter events. These photons provide information regarding the dimensions of the scattering [20]. Additionally, probing a small volume allows for more localised particle size measurement [81].

Moreover, regarding the first design, some limitations are due to the absorbance that may occur due to the separation formed from the glue between two fibre optics. This issue may affect the scattering efficiency. The ELSS signals decrease due to the absorption in the medium, which depends on the collected photons' path length. The longer the path length, the more light is absorbed, again, as demonstrated in the simple models of chapter 3. However, a shorter path length is attainable when a single fibre geometry is used. The Figures below show the scattering data from the type one fibre probes containing two adjacent fibres with different fibre core diameters.

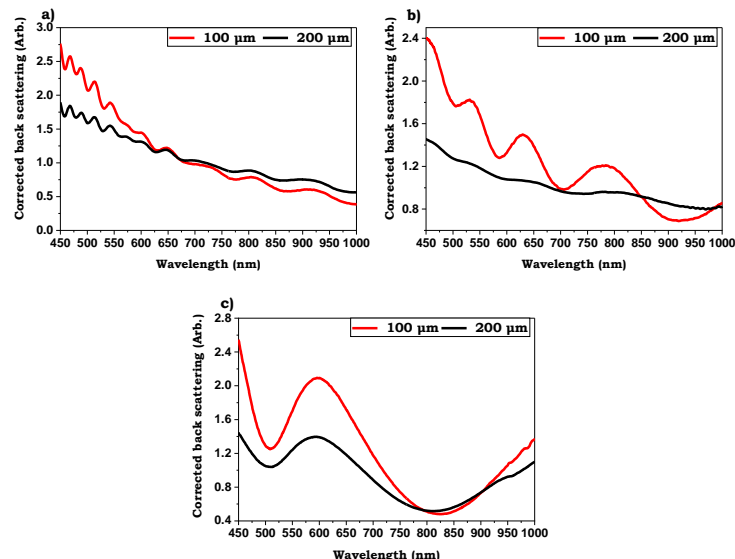


Figure 4-12: Comparing the core diameter 100 and 200  $\mu\text{m}$  for three particles 2, 0.8 and 0.413(a, b and c) micron with concentration (2.5%) stock PS concentration.

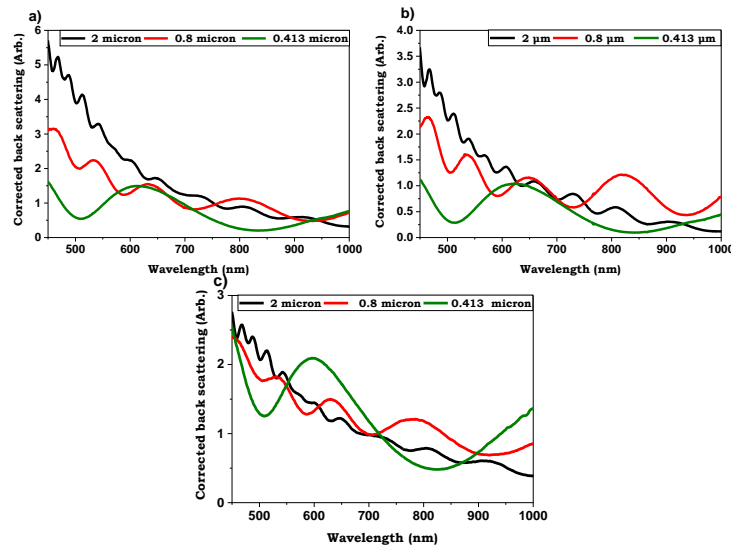


Figure 4-13: The spectrum for three particles 2, 0.8 and 0.413  $\mu\text{m}$  (a, b and c) with various concentrations 2.5%, 1.25% and 0.625% PS concentration, respectively, by using the probe of 100  $\mu\text{m}$  core diameter

### 4.6.3 CONCLUSION FOR OF THE PARTICLE SIZE (TISSUE PHANTOM POLYSTYRENE SPHERES IN DI-W) OF THE FIRST CONF

The outcome showed that the fabricated optical probe with 200 and 100 core diameters mentioned in section 4.1.2 can distinguish with different particle sizes of PS used in our experiments (2, 0.8 and 0.413)  $\mu\text{m}$  with various dilutions 2.5% to 0.625% (S to C<sub>2</sub>). Each size has a different signature and the number of maxima and minima, which is the result of the derivative spectrum increases with increasing the size particle. Also, the results showed that the fabricated optical probe with 100  $\mu\text{m}$  core diameter is more effective than 200  $\mu\text{m}$

## 4.7 LIGHT SOURCE, LIGHT-EMITTING DIODE (LED)

A white light-emitting diode was tested in place of the tungsten-halogen Light Source (TG). If a simple, low-cost diagnostic system is to be employed, a LED source would be preferable as it is physically smaller, low cost and power efficient. However, the type of LED is of great importance since modern 'white light' phosphors generally produce strong but narrow emission peaks in the red, green and blue parts of the spectrum as opposed to a broad (black body type) spectrum. These discrete colour LEDs would not be suitable in this application. The corrected ELSS spectra from the TG and LED light source for all particles size 2, 0.8 and 0.413  $\mu\text{m}$ , respectively, are shown in Figure 4-14. Figure 4-14 B and C, TG, and LED's spectra are quite clear and similar over the range of wavelength 450 to 750 nm for 0.8 and 0.413  $\mu\text{m}$ , respectively. The TG spectra is

approximately close to that of the LED with particle size  $2\ \mu\text{m}$  in the same range of the wavelength (Figure 4-14 A). Regarding the difference between the correcting backscattering for the same concentration in TG and LED are just the residual background reflection and ambient light levels. Hence, this is the reason to use a black container as mentioned in section 4.3. This suggests that an LED light source is viable; however, the TG light source will be used in all subsequent experiments due to convenience.

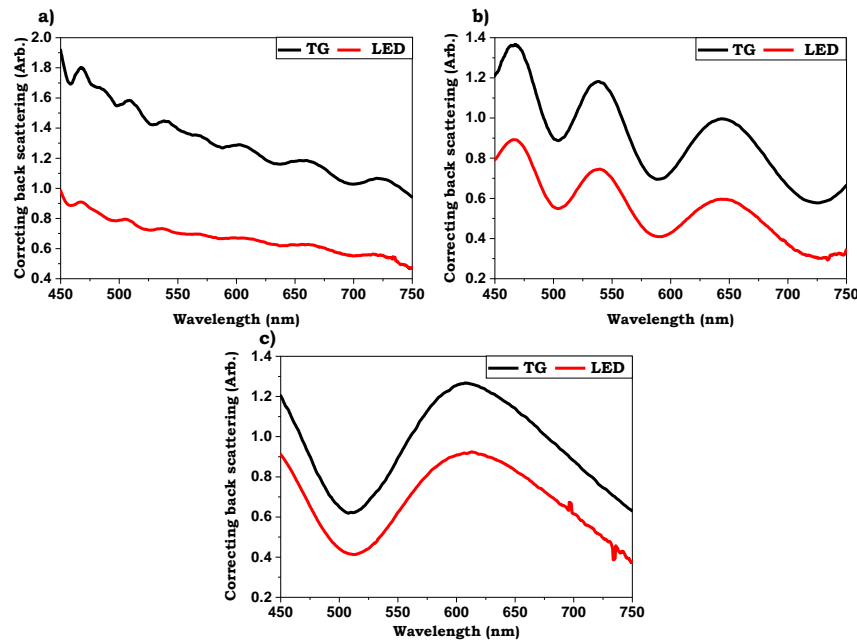


Figure 4-14: Comparing TG and LED three particles' sizes  $2$ ,  $0.8$  and  $0.413\ \mu\text{m}$  (a, b and c) at  $2.5\ \%$  PS concentration with  $200\ \mu\text{m}$  core diameter.

## 4.8 SPliced FIBRE CONFIGURATION

Given that the first configuration is not ideal, a second configuration, described in section 4.5, was fabricated to attempt to obtain a more efficient scattering (single scattering) detection. Figure 4-15 to 4-17 compares the signals between the first probe structure (probe 1: side by side) and the second setup (fibre splice). The experiment uses the manufacturer's initial concentration of PS  $2.5\%$  and dilutions of  $1.25\%$  and  $0.625\%$ . The probe is placed in a black Eppendorf container with an aqueous suspension of polystyrene  $2$ ,  $0.8$  and  $0.413\ \mu\text{m}$ . As can be seen in Figures as the maxima and minima are not that prominent in the second setup compared to that of the first. Since we were attempting to re-create the configuration described in [81], some obvious issues are present. The reduced fidelity in the signals obtained from the fibre splice configuration is

largely due to poor coupling at the splice interface. The overlap of the fibres is not perfect, and there is a great opportunity for direct reflection of the source light back to the spectrometer at the junction.

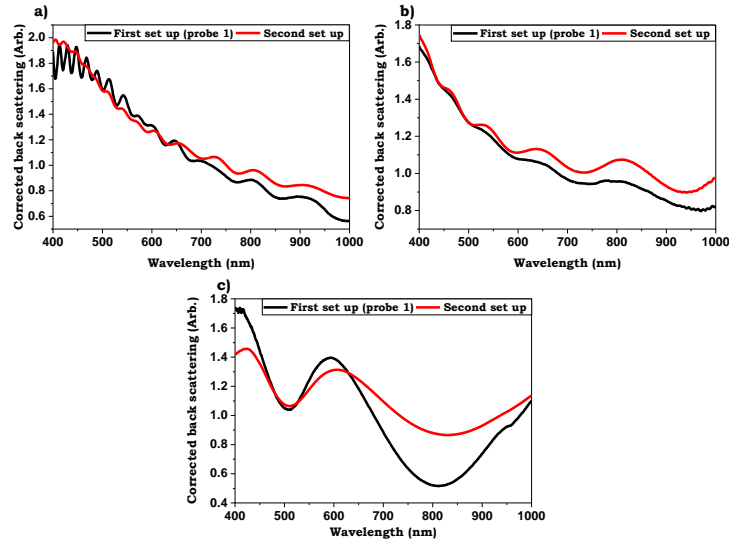


Figure 4-15: Comparison between the first (Probe 1 with 200 for the two identical core diameter) and a second configuration set up for three particles sizes 2, 0.8 and 0.413  $\mu\text{m}$  (a, b and c) at 2.5 % PS concentration.

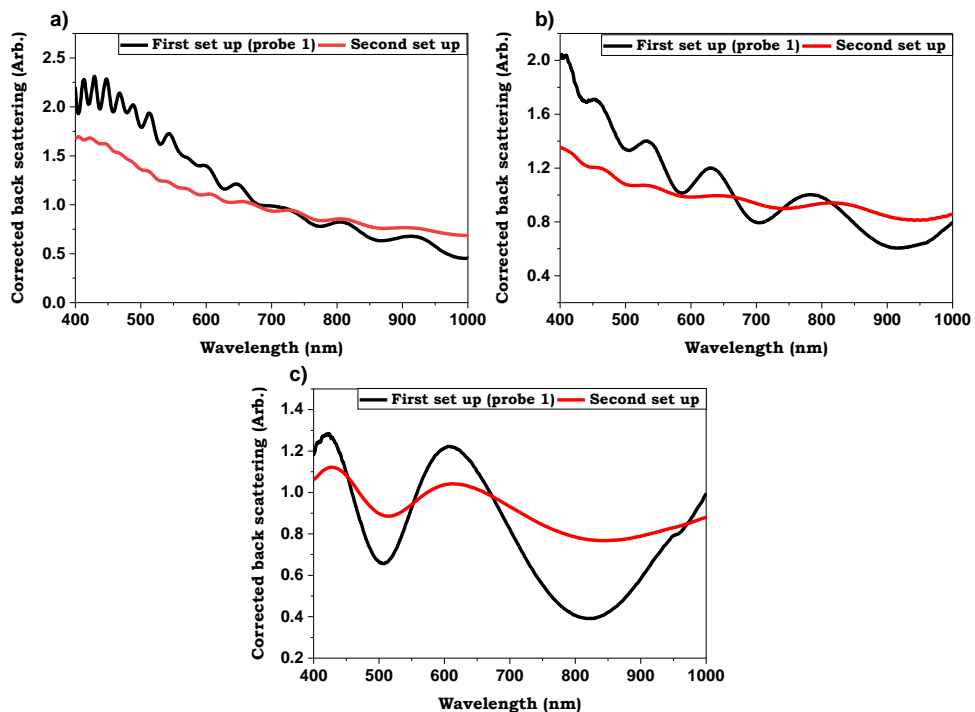


Figure 4-16: Comparison between the first (Probe 1 with 200 for the two identical core diameter) and a second configuration set up for three particles sizes 2, 0.8 and 0.413  $\mu\text{m}$  (a, b and c) at 1.25 % PS concentration.

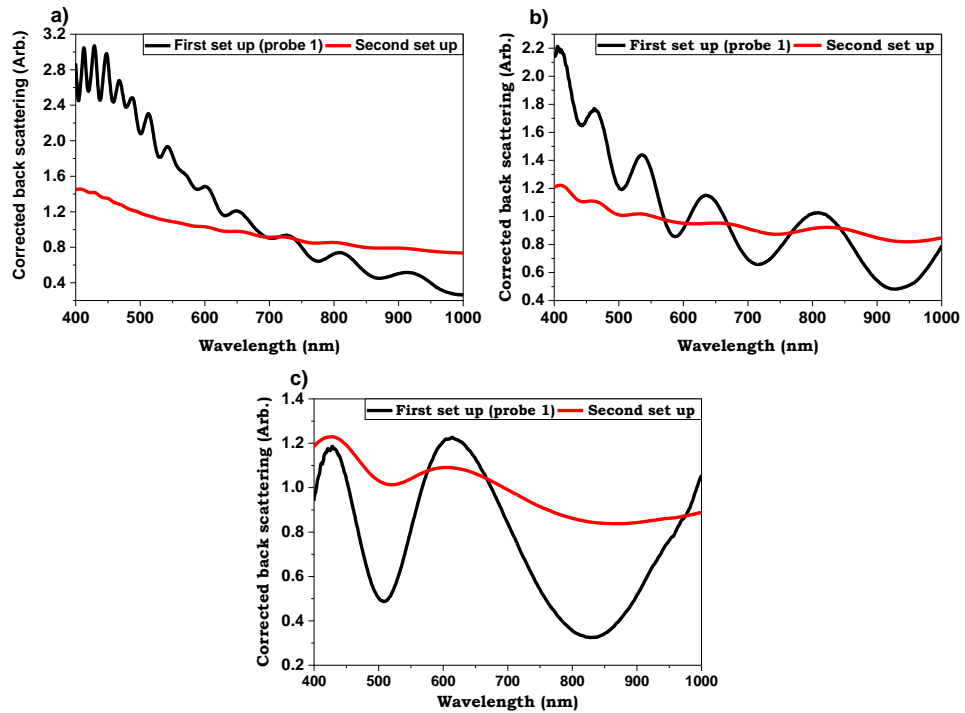


Figure 4-17: Comparison between the first (Probe 1 with 200 for the two identical core diameter) and a second configuration set up for three particles sizes 2, 0.8 and 0.413  $\mu\text{m}$  (a, b and c) at 0.625 % PS concentration.

The probe design plays a vital role in determining the number of maxima and minima. As shown in Figure 4-18, the number of maxima and minima depends on the particle size. Generally, the number of the maxima and minima of the spectra's derivatives increases significantly with increasing the particle size as seen with all different probe designs. Furthermore, the number of the maxima and minima is varied with various designs and different core diameters.

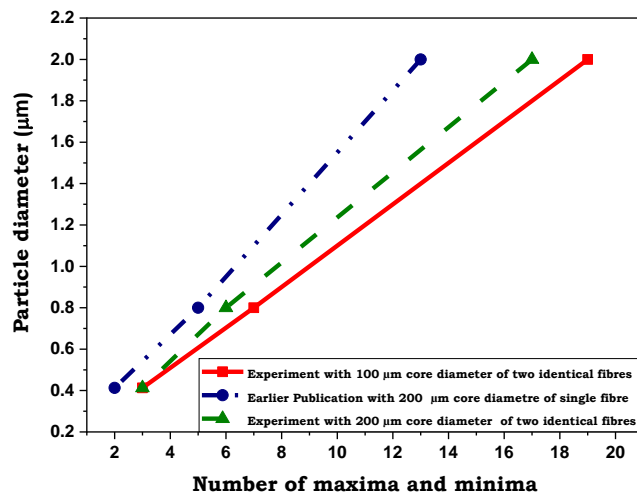


Figure 4-18: A number of maxima and minima among three different designs.

---

### 4.8.1 CONCLUSION FOR SPLICED FIBRE CONFIGURATION

In summary, the second type of configuration was an attempt to obtain single scattering events but was limited by reflection at the fibre junction compared to the two identical adjacent optical probes.

The single fibre configuration was used in the paper [81]. While measurements with a single fibre are more sensitive to backscattering, this thesis aims to design an integrated optical microwave probe structure. Therefore, the twin fibre configuration was chosen for the integrated design as it was more robust and produced stronger maxima and minima.

## 4.9 CHAPTER SUMMARY

Two optical probes have been fabricated in our Lab. with various core diameters and separation centre to centre. Probe 1 uses fibres of 200  $\mu\text{m}$  and probe 2, 100  $\mu\text{m}$  core diameter for the emitting and receiving fibre. The centre-centre separation is 263 and 132  $\mu\text{m}$  for probes 1 and 2, respectively. The diameters of the whole assembly probe 1 and 2 are 0.8 and 0.5 mm, respectively. Three particles' sizes of suspension polystyrene 2, 0.8 and 0.413  $\mu\text{m}$  with different dilutions (2.5% to 0.625% (S to C<sub>2</sub>)) have been utilized as an artificial tissue phantom for sample detection in the range of wavelength 400 to 1000 nm. A fabricated optical probe with 100  $\mu\text{m}$  showed the efficient distinction among three different PS particles. It was confirmed by finding that the number of the maxima and minima of the spectra' derivatives increased with increasing the particle size.

Regarding the geometrical effect, Probe 1 with a core diameter of 100  $\mu\text{m}$  showed is more efficient than 200  $\mu\text{m}$  for three particle sizes (2, 0.8 and 0.413  $\mu\text{m}$ ). The efficient optical probe (100  $\mu\text{m}$ , core diameters) showed more precise results at 0.625%, which the reduced scattering efficiency of this dilution within the range of the human tissue. Also, the low-cost LED light source revealed good detecting at 0.8 and 0.413  $\mu\text{m}$ . A second configuration has been tried as an attempt to obtain a more efficient scattering (single scattering) detection, which formed by attaching probe 1 with another probe consisting of double core diameter. Unoptimistic results showed as the maxima and minima are not that prominent in the second setup compared to that of the first.

# CHAPTER 5

## MICROWAVE THEORY, THEORETICAL CALCULATION AND SIMULATION WORK

### 5.1 INTRODUCTION

There are many examples of microwave techniques employed in cancer research and other applications, with numerous examples here at Cardiff. In 2017, Ehtaiba found a novel application of microwave open-ended coaxial probes for characterising the electrical properties of normal and cancer tissues for cancer therapy applications [131]. Also, microwaves are used in a broad range of materials analysis, etc. Partridge investigated the real-time and long term electrical properties of semiconductivity pigments when exposed to light and other environmental stimuli [132]. Hefford developed the microwave heating and sintering of powder compacts using a cavity resonator. The work considered microwave sintering to reduce the microwave absorption of metal powder compacts and studied a technique for measuring the surface resistance [133]. Two techniques stand out, namely open-ended coaxial probe and microwave cavity techniques. Both have received extensive research attention at Cardiff with a broad range of tools and expertise in house.

In the context of the previous chapter on optical techniques, the general form and arrangement of the sensing system are more aligned with the method of open-ended coax probing of samples since its geometry is comparable with that of the optical probe. Therefore, open-ended coaxial microwave probes will be the main focus of study in these subsequent chapters. For the suitability of coaxial probes to be determined, the use of microwave cavity resonators will be highlighted later in the next chapter to serve as a reference, as it is a well-established technique for measuring the dielectric properties of materials. To lay down the foundations of these microwave techniques, the first sections of the first part of the chapter is dedicated to defining some of the key concepts required for building an understanding of these techniques (Interaction between different materials and an alternating electric field, the Debye Model for water and effective permittivity) the second part is the theoretical measurements of the effective permittivity. Then, the experiment works for the non-resonant method. The final part is the resonant coaxial probe which consists of the theory of coaxial cable, electromagnetic resonators and simulation of the coaxial probe resonator and Novel 'tee' coupling.

## 5.2 INTERACTION BETWEEN DIFFERENT MATERIALS AND AN ALTERNATING ELECTRIC FIELD

Microwaves behave in a similar manner to that of light when energy is directed toward a material interface. Part of that energy is reflected, part is transmitted through the material, and a part is absorbed by the material itself.

The dielectric properties define the proportions of these three categories and are characterised by the complex permittivity  $\bar{\epsilon}_r$ . This is the fundamental material property in a dielectric material [134]. For the purposes of this thesis, the magnetic field interactions are ignored since none of the materials studied has magnetic permeability, i.e.,  $\bar{\mu}_r = 0$ . In order to facilitate the understanding of permittivity, Figure 5-1 demonstrates two charged plates that are separated with equal and opposite charges on both sides and an electric field is directed from the positive to negative charges. If a dielectric material is placed in between the two plates, such as water, the molecular dipole of the water molecule will align in the opposite direction to the electric field. In the absence of an electric field, the molecules have a random orientation (Figure 5-2). However, with the electric field's presence, the molecules are aligned (polarised) by their dipole moment opposing the direction of the external electric field. Overall, these results in a reduction of the electric field due to the presence of this material (Figure 5-3).

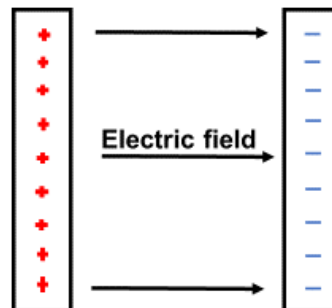


Figure 5-1: Electric field between oppositely charged plates.

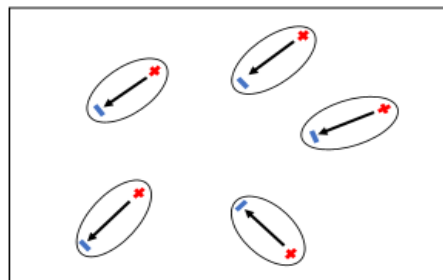


Figure 5-2: Water molecule dipoles randomly orientated in the absence of an applied electric field.

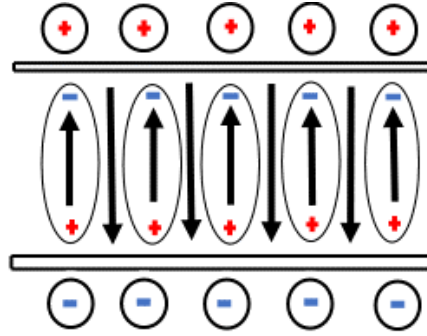


Figure 5-3: Polarised (aligned) water dipoles opposing the applied electric field.

The polarisation augments the total displacement of charge in the system and gives rise to a displacement current or flux  $\bar{D}$  due to the electric dipole moment, which can be expressed as:

$$\bar{D} = \epsilon_0 \bar{E} + \bar{P}_e \quad (5-1)$$

Where  $\epsilon_0$  is the permittivity of free space and  $\bar{E}$  is the applied electric field and  $\bar{P}_e$  is the additional polarisation vector. There is a linear relationship between the electric polarisation and the applied electric field in a linearly polarisable medium, which can be expressed as:

$$\bar{P}_e = \epsilon_0 \chi_e \bar{E} \quad (5-2)$$

Here  $\chi_e$  is an electric susceptibility, which is a dimensionless constant that determines the magnitude of the polarisation produced by a material in the presence of an applied field. The displacement flux can be defined as:

$$\bar{D} = \epsilon_0 (1 + \chi_e) \bar{E} = \epsilon \bar{E} \quad (5-3)$$

Between the polarisation and the electric field within the material, there is a phase lag at high frequencies. This is because the water molecules have inertia and will take a short time to respond to the external influence. The 'in phase' part of this quantifies the stored electric field energy called polarisation, whereas the 'out of phase' part determines the electric field-driven energy dissipated due to damping of the dipole moments. Because of this, relative permittivity can be considered a complex quantity, which is expressed below.

$$\epsilon = \epsilon' - j\epsilon'' \quad (5-4)$$

Where,  $\epsilon'$  is the real part commonly referred to as permittivity in static field scenarios, and which gives a measure of how much external electrical field energy is stored in the material.  $\epsilon''$  is the imaginary part of the permittivity, which provides a measure of the amount of energy loss occurring in the material in the presence of an alternating external electric field. And  $j = \sqrt{-1}$ , this value must be negative since energy can only be dissipated in a dielectric and not generated [135]. Often, dielectric materials have electrical conductivity denoted by the parameter,

$\sigma$  [ohm<sup>-1</sup>] or [siemens]. Conductivity will give rise to a conduction current density in the presence of an electric field and is defined as:

$$\bar{j} = \sigma \bar{E} \quad (5-5)$$

By considering Maxwell's Equation for Ampere's law, where the curl of  $\bar{H}$  is defined in terms of the dielectric displacement current and the conduction current density:

$$\nabla \times \bar{H} = j\omega \bar{D} + \bar{j} \quad (5-6)$$

$$= j\omega \epsilon \bar{E} + \sigma \bar{E} \quad (5-7)$$

$$= j\omega \left( \epsilon - j \frac{\sigma}{\omega} \right) \bar{E} \quad (5-8)$$

$$= j\omega \left( \epsilon' - j \left( \epsilon'' + \frac{\sigma}{\omega} \right) \right) \bar{E} \quad (5-9)$$

We arrive at Equation 5-9, which shows the presence of three distinct terms governing the properties of a conductive dielectric. The stored energy remains the same; however, the loss mechanism is now split into two components. Observing the loss in an experimental context presents an issue in differentiating between the two mechanisms for loss, i.e. if it is due to conductivity or dielectric damping. A modified form of the Equation for relative permittivity is arrived at when a conductive dielectric is considered:

$$\epsilon = \frac{1}{\epsilon_0} \left( \epsilon' - j \left( \epsilon'' + \frac{\sigma}{\omega} \right) \right) \quad (5-10)$$

Polarisation in a dielectric material can be attributed to three different aspects [136]. Electronic polarisation can be defined as the movement of the bound electron clouds around the ions in the material. Secondly, molecular polarisation is caused due to a stretching process of the bonds between the atoms of a molecule. This stretching results from transferring or sharing electrons between different parts of the molecule due to the bonding processes, which results in changes in the positive or negative charge densities. Finally, orientational polarisation, which is the rotation of whole molecules that have a permanent or induced dipole moment. In conductive or semiconductor materials, there is a possibility for the electron to move beyond the bounds of the atom. However, there is also a restriction on overall boundaries in a material due to small particles or solid domain boundaries. Dielectric relaxation is the momentary delay in the dielectric constant of a material. This is usually caused by the delay in molecular polarisation concerning a changing electric field in a dielectric medium. The Debye relaxation Equation is used to describe the mechanism of conductivity and polarisation [137].

$$\epsilon(\omega) = \epsilon(\infty) + \frac{\epsilon(0) - \epsilon(\infty)}{1 + i\omega\tau} \quad (5-11)$$

Here,  $\varepsilon(0)$  is the low-frequency permittivity,  $\varepsilon(\infty)$  is the extrapolated high-frequency permittivity,  $\omega$  is the frequency at which the permittivity transitions between these extremes and  $\tau$  is the relaxation time.

The ‘Cole - Cole’ model is the other improvement to the Debye model, which describes dielectric relaxation in polymers and the ‘Cole - Davidson’ formulae that raises different denominator parts to power. In the case that the mechanism has a restoring force, alternatively a Lorentz resonator model can be used [138].

$$\varepsilon_{r,Lorentz}(\omega) = \varepsilon'(\infty) + \varepsilon'(0) \frac{\omega_p^2}{\omega_r^2 - \omega^2 + j\gamma\omega_r\omega} \quad (5-12)$$

### 5.3 THE DEBYE MODEL FOR WATER

In our research, pure Deionised water (DI-W) has been used as a reference liquid for many reasons: the most obvious, of course, is that all biological tissue is water-based, and so DI-W is the most suited reference liquid in terms of calibration and test measurements. Furthermore, its abundance in ecological, industrial, and medical scenarios means it is likely the most studied material in existence. Of most relevance is the work of Kaatze [137].

A simple Debye model of DI-W has been put together to calculate its real and imaginary permittivity that is pertinent for this study. The low-frequency permittivity  $\varepsilon(0)$ , extrapolated high-frequency  $\varepsilon(\infty)$  and a relaxation time ( $\tau$ ) were used in the calculation and modelled from the published data available. A simple method has been used for calculating these parameters in steps. Firstly, a linear and polynomial fitting procedure have been applied to the discrete data over the temperature range (15 to 35) °C for DI-W. The well-known paper by Kaatze [137] has been used for obtaining data of the parameters of pure water in this range of temperatures. Secondly, the fitting values (intercept and slope values) have been used for calculating these parameters at different temperatures (Figure 5-4 to 5-6). Thirdly, the real and imaginary permittivity calculated using the Debye equation is relative to the parameters mentioned at different frequencies and temperatures (Figure 5-7). Figure 5-7 demonstrates the Debye model at different frequencies and temperatures. In this Figure, the red arrow shows that the permittivity (real and imaginary) decreases with increasing temperature over the range (15 to 35)°C. An obvious decrease in the real permittivity is observed between 100 MHz to approximately 8 GHz with increasing temperature. This trend inverts for the mid-frequency range between 8 GHz to 100 GHz. In terms of the imaginary permittivity, a decrease is observed with increasing temperature as illustrated between 1 GHz and 20 GHz in contrast to the range 20 GHz to 200 GHz.

An Excel-based calculator has been developed for providing the real and imaginary permittivity

as a function of frequency and temperature and utilises the parameters ( $\epsilon(0)$ ,  $\epsilon(\infty)$  and  $\tau$ ) (Figure 5-8).

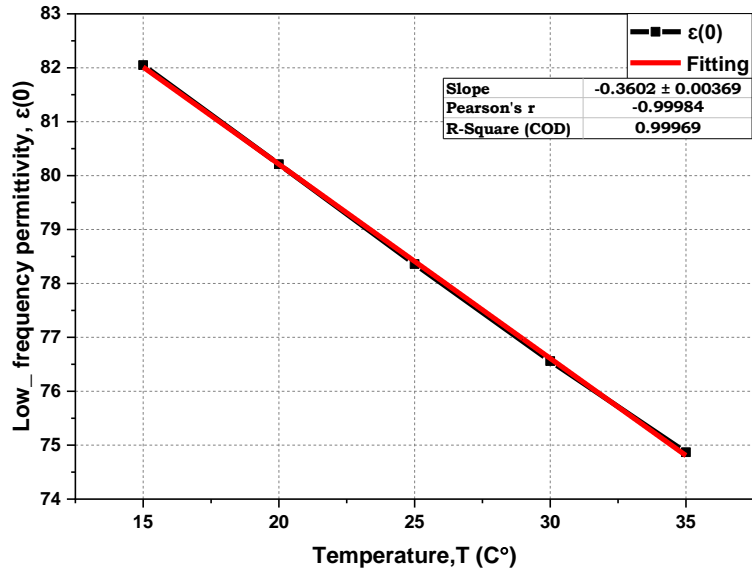


Figure 5-4: Corrected Low frequency permittivity  $\epsilon(0)$  with the range of the temperature (15 to 35) C°.

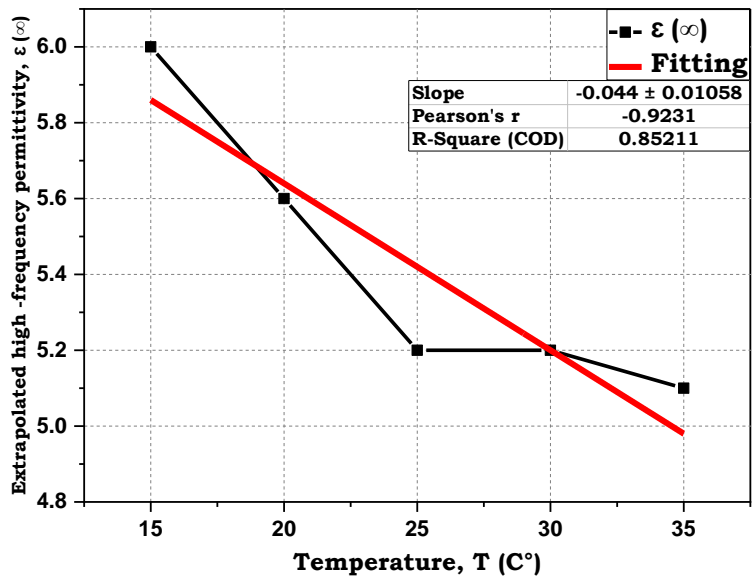


Figure 5-5: Corrected extrapolated high-frequency permittivity  $\epsilon(\infty)$  with the range of the temperature (15 to 35) C°.

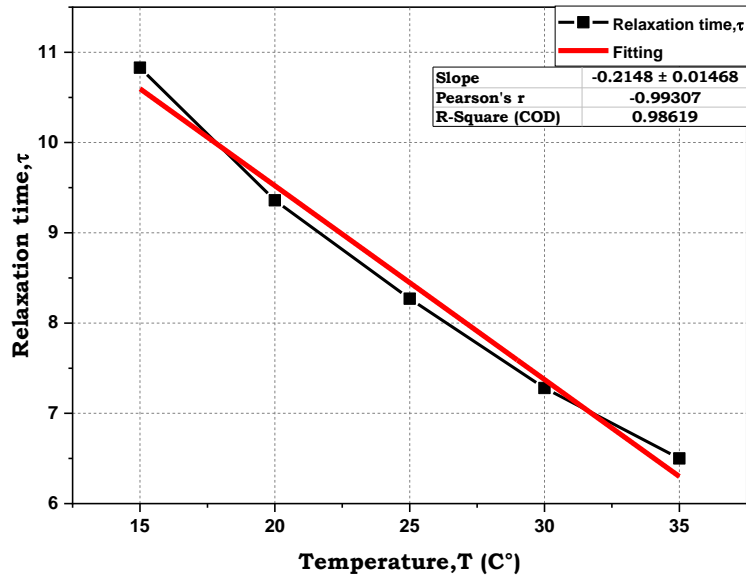


Figure 5-6: Corrected relaxation time  $\tau$  with the range of the temperature (15 to 35) C°.

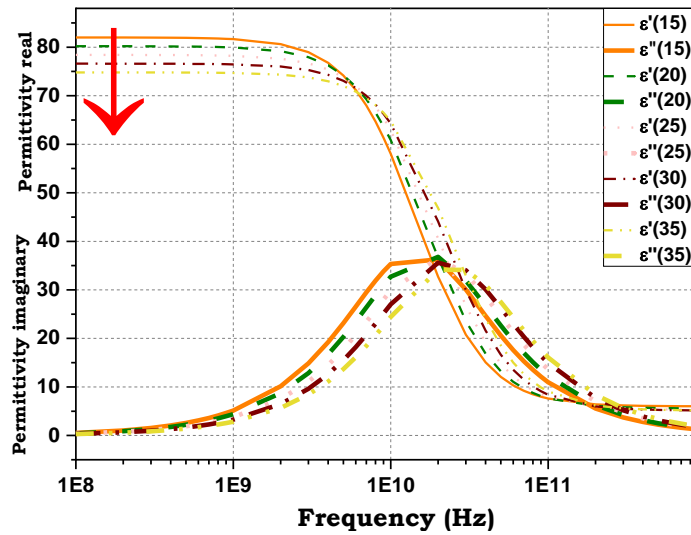


Figure 5-7: Mathematical Debye model from our work, permittivity real and imaginary with the range of frequency (1E8-1E12) Hz at range temperature (15 to 35) C°.

Permittivity Calculator				
Enter Temp				
	24 C°	$\tau$	$\epsilon(\infty)$	$\epsilon(0)$
		8.45668	5.32562	78.77
Enter Freq		$\epsilon'$	$\epsilon''$	
	2488012497 Hz	77.5086635	9.5426174	

Figure 5-8: Our calculator laboratory for measuring the real and imaginary permittivity for specific frequency and temperature.

## 5.4 EFFECTIVE PERMITTIVITY ( $\epsilon_{eff}$ )

The most common method used for calculating the bulk dielectric properties of inhomogeneous materials is the Maxwell-Garnett or MG approximation, also known as the Clausius-Mossotti estimate. This method is useful when one of the components can be considered as a host in which inclusions of the other elements are embedded. This method involves an exact calculation of the field induced in the uniform host by a single spherical or ellipsoidal inclusion and a treatment of its distortion by the electrostatic interaction between the different compositions. The charged dipoles cause this distortion, and higher multipoles may be induced in the other inclusions. The induced dipole moments cause the longest-range distortions, and their average effect is included in the MG approximation, which results in a uniform field inside all of the inclusions [139]. To derive the Maxwell-Garnett mixing formula, the Lorentz local field concept with an array of polarisable particles is used to obtain the Clausius-Mossotti relation (The Clausius-Mossotti relation expresses the dielectric constant (relative permittivity,  $\epsilon_r$ ) of a material. This is given in terms of the atomic polarizability,  $\alpha$ , of the material's constituent atoms and/or molecules, or a homogeneous mixture thereof. It is named after Ottaviano-Fabrizio Mossotti and Rudolf Clausius. It is equivalent to the Lorentz-Lorenz equation. It may be expressed as [140]:

$$\frac{\epsilon - 1}{\epsilon + 2} = \frac{4\pi}{3} \sum N_j \alpha_j \quad (5-13)$$

Here  $N_j$  is the number of particles per unit volume.  $\alpha_j$  is the polarizability:

$$\alpha = \left( \frac{\epsilon_i - 1}{\epsilon_i + 2} \right) a^3 \quad (5-14)$$

Where  $\epsilon_i$  is the dielectric constant and  $a$  is the radius of the particle. The effective permittivity is obtained by combining Equation (5-13) and (5-14):

$$\left( \frac{\epsilon_{eff} - 1}{\epsilon_{eff} + 2} \right) = f_i \left( \frac{\epsilon_i - 1}{\epsilon_i + 2} \right) \quad (5-15)$$

Here  $\epsilon_{eff}$  is the effective dielectric constant of the medium,  $\epsilon_i$  is one of the inclusions, and  $f_i$  is eq. As with the model of Maxwell Garnett, it is a composition of a matrix medium with inclusions, and we enhance the Equation:

$$f_i = \frac{4\pi a^3 N_j}{3} \quad (5-16)$$

Where  $N_j$  is the number of particles per unit volume

Consequently, the microporous morphology modifies the effective permittivity.

---

## 5.5 THEORETICAL MEASUREMENTS OF THE EFFECTIVE PERMITTIVITY OF POLYSTYRENE SPHERES IN A WATER HOST

In our research, the effective permittivity of polystyrene spheres in a water host has been calculated in steps. The first step is calculating the real and imaginary permittivity for the water and the polystyrene. In terms of water, the real and imaginary permittivity's have been calculated using our calculator mentioned above (Figure 5-8) at  $T = 25\text{ }^{\circ}\text{C}$  as within a range of room temperature and the whole range for the frequency 0.1 to 3 GHz in the first instance. The real and imaginary values of permittivity for polystyrene were obtained from Ahmad [141] for the same range of frequencies. Moreover, the volume fraction of the original volume concentrations from the manufacturer and the fractional concentrations used in the experimental work have been applied as 2.5%, 2.25%, 2%, 1.75%, 1.5%, and 1.25% with a total volume of 250  $\mu\text{l}$  (representing dilutions by reducing 25  $\mu\text{l}$  of particles and an increase of DI-W with volume to obtain 250  $\mu\text{l}$  for each concentration. Finally, the magnitude of the complex permittivity has been found by calculating the root mean square for the real and imaginary permittivity, shown in Figures 5-9 and 5-10. In these two Figures, the results present the variation in the magnitude of complex permittivity and loss tangent ( $\tan\delta$ ) with frequency at different concentrations between pure water, stock polystyrene suspension at 2.5% and 5 subsequent half dilutions down to 1.25%.  $\tan\delta$  is used to express the losses in a dielectric material. It is expressed as the ratio between the imaginary and the real part of the permittivity. This parameter refers to a phasor in the complex plane whose real and imaginary parts are the resistive (lossy) components of an electromagnetic field, and it's a reactive (lossless) counterpart, respectively.

Figure 5-9 shows a considerable difference between the magnitude of the complex permittivity for water and the rest of the concentrations for the whole range of frequencies. Additionally, the complex permittivity increases consistently with decreasing concentrations for the entire range of frequencies for concentrations 2.5% to 1.25%, which serves as a good indicator for this technique's viability in detecting cancer. However, Figure 5-10, showed that the loss tangent between water and all concentrations is not significantly different across the whole frequency range.

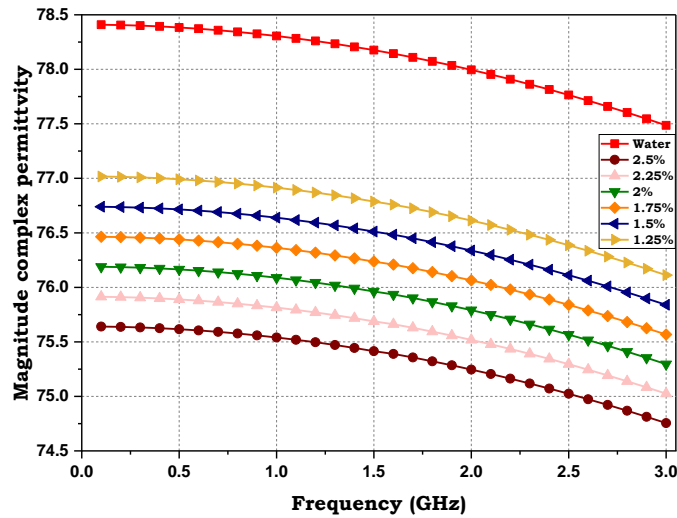


Figure 5-9: Magnitude complex effective permittivity for DI-W and different concentration of suspension polystyrene (2.5%, 2.25%, 2%, 1.75%, 1.5% and 1.25%) at frequency range (0.1 to 3) GHz.

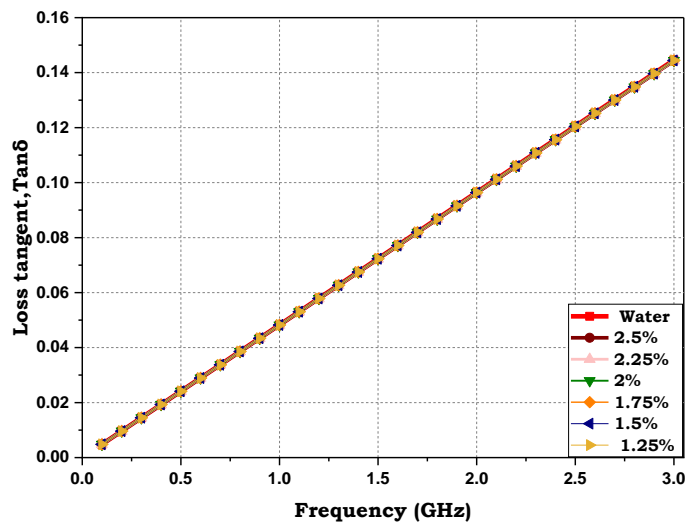


Figure 5-10: Tangent  $\delta$  for DI-W and different concentration of suspension polystyrene (2.5%, 2.25%, 2%, 1.75%, 1.5% and 1.25%) at frequency range (0.1 to 3) GHz.

Figures 5-11 and 5-12 show the real and imaginary effective permittivity versus the same range of frequency mentioned above and the same range of the volume concentrations.

In Figure 5-11, the results have again shown a significant difference between water and the rest of the concentrations. Additionally, there is a consistent reduction in the real complex value with increasing concentrations of the sample. In contrast, there is no considerable variance in loss tangent or effective imaginary permittivity between water and the rest of the concentrations 2.5%

to 1.25% as presented in Figure 5-12.

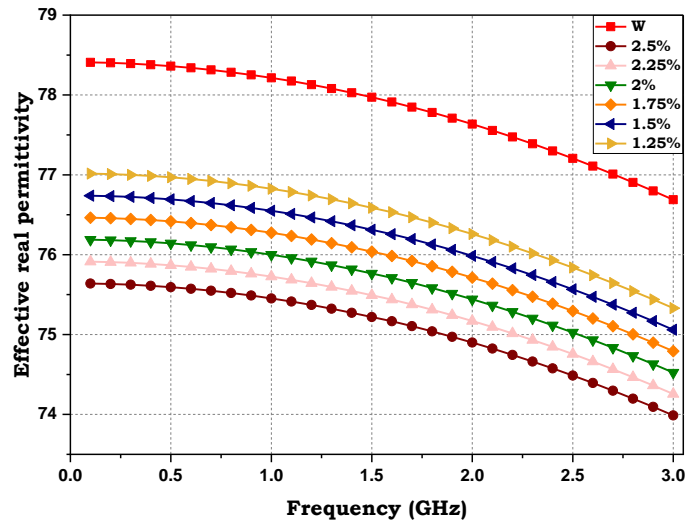


Figure 5-11: Effective real permittivity for DI-W and different concentration of suspension polystyrene (2.5%, 2.25%, 2%, 1.75%, 1.5% and 1.25%) at frequency range (0.1 to 3) GHz.

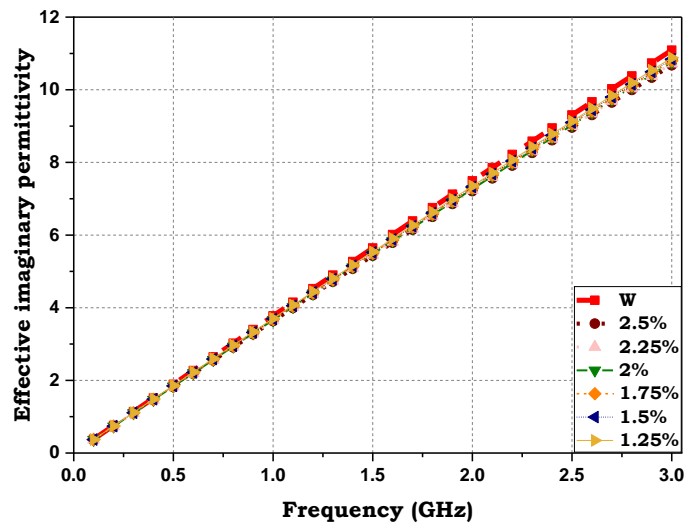


Figure 5-12: Effective imaginary permittivity for DI-W and different concentration of suspension polystyrene (2.5%, 2.25%, 2%, 1.75%, 1.5% and 1.25%) at frequency range (0.1 to 3) GHz.

## 5.6 EXPERIMENTAL WORKS FOR NON-RESONANT METHOD

A non-resonant method utilising an open-ended coax probe utilising a  $50 \Omega$ , small diameter semi-rigid coaxial cable was used for detecting the reflection ( $S_{11}$ ) at a frequency range between 0.1 to 3 GHz with respect to the three different particle sizes 0.413, 0.8, and 2  $\mu\text{m}$  for different concentrations (DI-W and 2.5%-1.25%) as mentioned in section 5.5.

Figure 5-13 presents the reflection  $S_{11}$  as a function of frequency over the range of 0.1 to 3 GHz for the 0.413  $\mu\text{m}$  particles. In this Figure, generally, there is no significant difference in the reflection  $S_{11}$  for the whole range of frequencies between water and the different concentrations (DI-W and 2.5% to 1.25%). On expanding the frequency axis, comparing the reflection  $S_{11}$  in three parts of the frequency range (i.e., 0.1 to 1, 1 to 2 and 2 to 3) GHz, the results showed that there is a slight difference between 0.1 to 1 GHz; also the  $S_{11}$  increased gradually with decreasing the concentrations. Conversely, at the range between 1 and 2 GHz, there is no difference between different concentrations. At 2 to 3 GHz, the results demonstrated a slight variation within an irregular decrease of the reflection  $S_{11}$  with decreasing concentrations. This issue could be caused by a lack of precision in the calibration, measurement errors, or probe tip corrosion. (This issue will be extensively covered in later sections as it was not discovered until much later in the project.) Or they were related to sampling errors such as the settling of the suspension polystyrene particles or bubbles between the tip of the probe and sample. Additionally, errors related to the tissue sample, i.e. probe sample contact and pressure, temperature, the procedure of sample handling, tissue properties and heterogeneity [95]. The same trend has been found for the particle size of 0.8  $\mu\text{m}$  and 2  $\mu\text{m}$ .

By focusing on the frequency range between 0.1 to 0.2 GHz, a substantial variance is shown for the three particle sizes (0.413, 0.8 and 2)  $\mu\text{m}$  at Figure 5-14 to 5-16, respectively. The reflection  $S_{11}$  decreased systematically with increasing sample concentrations.

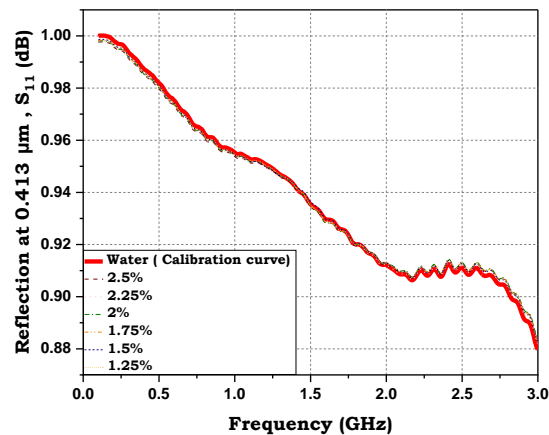


Figure 5-13: The reflection  $S_{11}$  as a function to the range of the frequency (0.1 to 3) GHz for the DI-W (calibration curve) and the concentrations range (2.5% to 1.25%) at 0.413  $\mu\text{m}$  particle size.

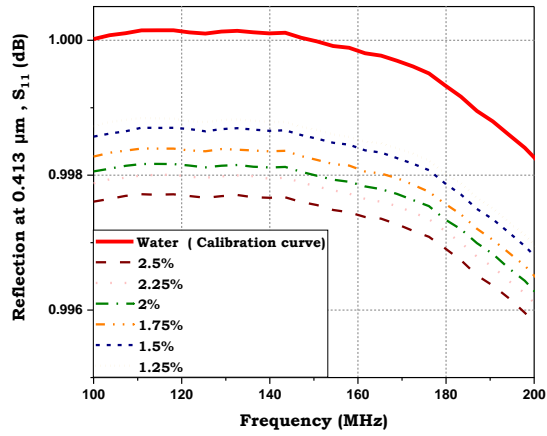


Figure 5-14: The reflection  $S_{11}$  as a function to the range of the frequency (100 to 200) MHz for the DI-W (calibration curve) and the concentrations range (2.5% to 1.25%) at 0.413  $\mu\text{m}$  particle size.

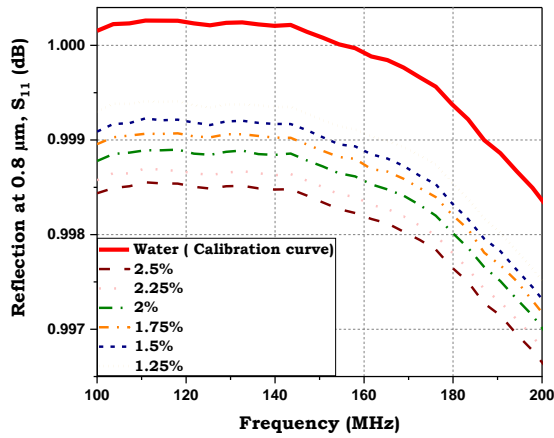


Figure 5-15: The reflection  $S_{11}$  as a function to the range of the frequency (100 to 200) MHz for the DI-W (calibration curve) and the concentrations range (2.5% to 1.25%) at 0.8  $\mu\text{m}$  particle size.

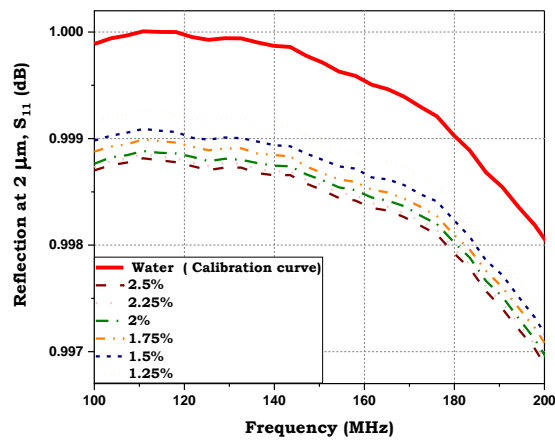


Figure 5-16: The reflection  $S_{11}$  as a function to the range of the frequency (100 to 200) MHz for the DI-W (calibration curve) and the concentrations range (2.5% to 1.25%) at 2  $\mu\text{m}$  particle size.

## 5.7 COMPARISON BETWEEN THEORETICAL AND EXPERIMENTAL WORK

Figure 5-17 compares the experimental results for the non-resonant technique and the theoretical calculations over a frequency range of 100 to 200 MHz for different concentrations of PS. Of particular note is the frequency dependence of the experimental data compared to the constant theoretical results. The relative variation in values for different concentrations are, however, comparable.

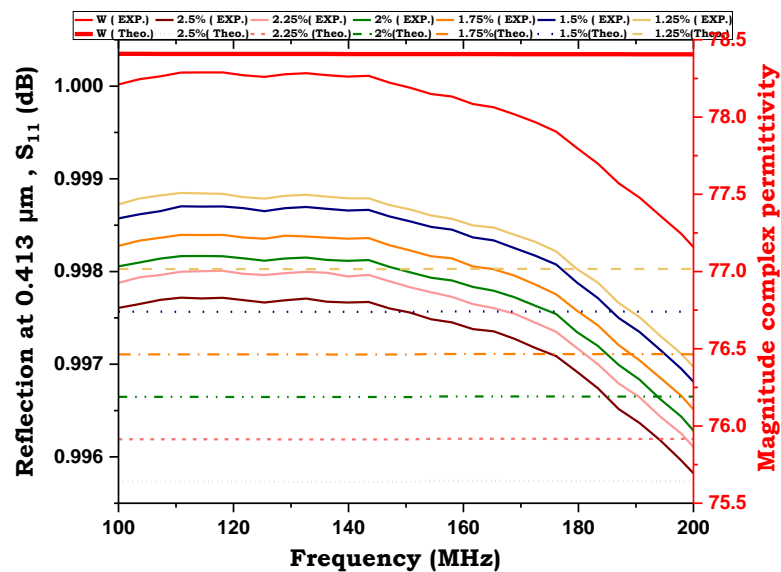


Figure 5-17: The comparison between the theoretical calculation and the experimental results for non-resonant method at frequency range 100 to 200 MHz for the DI-W and the concentrations range 2.5% to 1.25%.

## 5.8 METHOD SELECTION IN OUR MEASUREMENTS

Amongst all the microwave techniques that have been described in Chapter 2, two methods have been selected for our measurements. The first method is the resonant cavity which was used to obtain baseline data which will be clarified in chapter 6, and the second method is the open-ended coaxial probe. Exploratory non-resonant measurements have been mentioned above in this chapter, and a more robust and *novel* resonant method will be presented later in chapter 7. Regarding the open-ended coaxial probe, it is non-destructive, simple, low cost, and easy to use. It has the capability to measure the voltage reflection coefficient  $S_{11}$  for a broadband measurement for in-vivo and ex-vivo. This reflection is the result of an impedance mismatch between the coaxial cable and the sample under test. However, there are many challenges associated with our experiments that may arise. For example, the presence of air bubbles, settling of the particles during the measurements and the overall capability of the measurement device,

in this case, a Hewlett Packard VNA. The stability of the probe and the holder of the sample are also areas of concern. Therefore, in our experiments, the resonant coaxial probe has been chosen for many reasons: Firstly, the resonant technique offers improved accuracy and uncertainty compared to the broadband method [142]. Secondly, its overall geometry lends itself to the application being discussed and is compatible with the optical probe. Finally, it can operate at multiple frequencies [143]. To increase the measurements' sensitivity, a *novel* T-Structure and capacitive coupling have been designed to enable measures at a wide range of discrete frequencies. Therefore, the basic principle of the coaxial cable theory and the simulation to emulate the experimental work will explain in the sections below, and the experimental work will be explained in chapter 7.

## **5.9 RESONANT COAXIAL PROBE**

### **5.9.1 INTRODUCTION**

A resonant coaxial cable has been selected for many reasons mentioned in section 5.8. Additionally, a *novel* T-Structure and capacitive coupling have been designed to enable measurements at a wide range of discrete frequencies, as mentioned above. Therefore, the sections below will demonstrate the basic principle of the coaxial cable theory in detail and the simulation work of this structure.

### **5.9.2 THEORY OF COAXIAL CABLE**

#### **5.9.2.1 SIGNAL PROPAGATION CHARACTERISTICS ALONG WITH THE TRANSMISSION ELECTROMAGNETIC WAVE (TEM) TRANSMISSION LINE STRUCTURE**

There are many different topologies that can be used for a Transmission Electromagnetic Wave (TEM) transmission line design of specific impedance, such as Coaxial cable, Microstrip, Stripline and Coplanar. From all of them, coaxial cable has been selected in our research as it is the best option to support pure TEM waves. There are some factors that will cause loss or attenuation of the signal, in spite of the quality of the coaxial cable for transmission. This is of significance when considering a resonating structure as it will affect the Quality factor (Q factor). The sections below will highlight this in some detail.

#### **5.9.2.2 ANALYSIS OF THE LOSSLESS TRANSMISSION LINE (TL)**

The circuit shown in Figure 5-18 below represents a model of a distributed transmission line where the physical length of the section below is much smaller than the wavelength of the

radiation that is propagating along the line. In this circuit, the voltage  $v$  and the current  $i$  satisfy wave Equations, e.g. for  $v$  as expressed below:

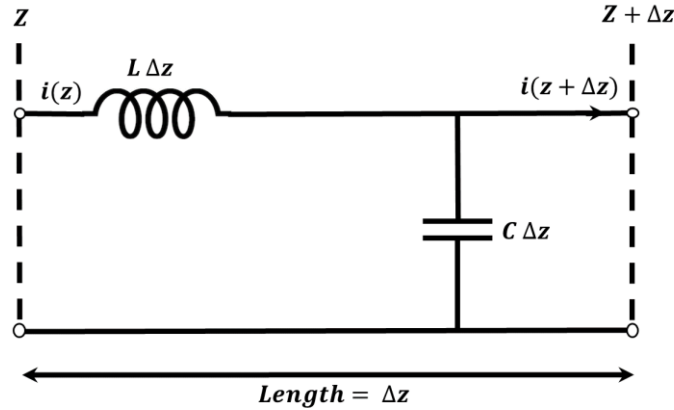


Figure 5-18: Line transmission model.

$$\frac{\partial^2 v}{\partial z^2} = -\omega^2 LCv \equiv -\beta^2 v \tag{5-17}$$

Here  $v^\mp(z, t) = V_0^\mp e^{j(\omega t \mp \beta z)}$ , the sign is related to the direction of the propagating energy wave, such as  $V_0^+$  which is the peak amplitude of the forward travelling wave.  $\beta = \omega\sqrt{LC} = \frac{\omega}{v_p}$  represents the corresponding wavenumber (inverse of wavelength) of the propagating energy and is independent of frequency.

### 5.9.2.3 PROPAGATION OF SIGNAL ALONG A LOSS TL

The resistance  $R$  of the conductors (inductance) and the conductance  $G$  of the dielectric (capacitance) are the reason for the TL losses, as shown in the circuit below (Figure 5-19):

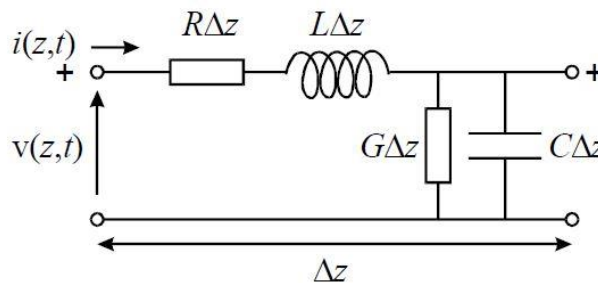


Figure 5-19: Loss transmission model.

In this circuit,  $L$  is the inductance,  $C$  is the capacitance,  $R$  is the resistance, and  $G$  is the conductance, all per unit  $\Delta z$ . Therefore, including these losses to the lossless TL, we see that  $j\omega L$  will become  $R + j\omega L$  and  $j\omega C$  will become  $G + j\omega C$ . The wave equation for voltage then  $v$  becomes:

$$\frac{\partial^2 v}{\partial z^2} = (R + j\omega L)(G + j\omega C)v \equiv \gamma^2 v \quad (5-18)$$

$$\gamma = \sqrt{(R + j\omega L)(G + j\omega C)} \equiv \alpha + j\beta \quad (5-19)$$

Here,  $\gamma$  is the propagation constant of the TL.

#### 5.9.2.4 ATTENUATION OF A SIGNAL ALONG WITH A LOSSY TL

As we mentioned the forward propagating solution to the lossy wave equation is expressed as:

$$v^+ = V_o^+ e^{j\omega t} e^{-\gamma z} \quad (5-20)$$

Where

$$\gamma = \alpha + j\beta \quad (5-21)$$

Therefore,

$$v^+ = V_o^+ e^{-\alpha z} e^{j(\omega t - \beta z)} \quad (5-22)$$

The term  $e^{j(\omega t - \beta z)}$  is referred to as a phasor associated with a travelling wave. On the other hand,  $e^{-\alpha z}$  is expressed as an exponential decay of the amplitude of the travelling wave, which  $\alpha$  is the real part of  $\gamma$  and is called the amplitude attenuation constant.

To fully understand the loss, some extreme boundary cases are considered.

Firstly, for a lossless TL,  $\alpha = \text{zero}$ , so,  $\gamma = j\beta$  and the amplitude is zero. Furthermore, for a lossy TL (normal propagation),  $\alpha$  must be related to the TL losses (i.e., to  $R$  and  $G$ ). The amplitudes reduce gradually with a distance of wave transmission, as illustrated in Figure 5-20 for the two cases.

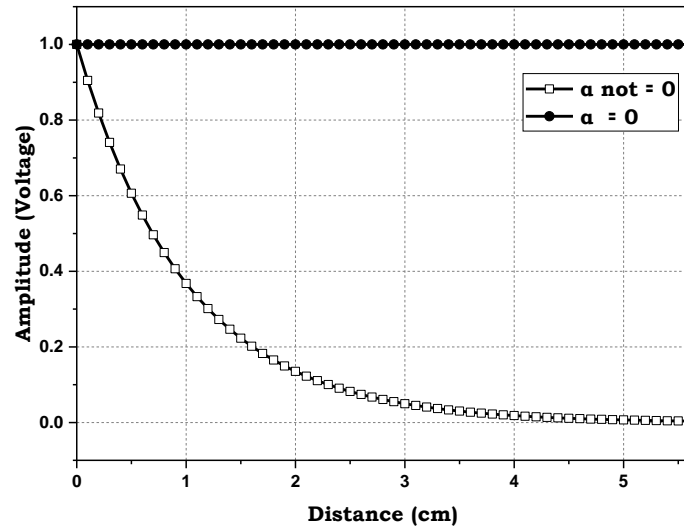


Figure 5-20: Losing features.

For the case where losses are small,  $R \ll \omega L$  and  $G \ll \omega C$ , therefore:

$$\begin{aligned}
 \gamma &= \sqrt{(R + j\omega L)(G + j\omega C)} & (5-23) \\
 &= \sqrt{RG - \omega^2 LC + j\omega(LG + CR)} \\
 &\approx \sqrt{-\omega^2 LC \left(1 - j \left(\frac{G}{\omega C} + \frac{R}{\omega L}\right)\right)} \\
 &\approx \mp j\omega\sqrt{LC} \cdot \left(1 - \frac{1}{2}j \left(\frac{G}{\omega C} + \frac{R}{\omega L}\right)\right)
 \end{aligned}$$

Here, there is an assumption that  $x$  is small,  $\sqrt{1 - jx} \approx 1 - \frac{1}{2}jx$  (we neglect the very small, second-order terms of  $RG$ ).

For the lossless case:

The wavenumber is:

$$v^+ = V_o^+ e^{-\alpha z} e^{j(\omega t - \beta z)} \quad (5-24)$$

The amplitude attenuation constant is  $\alpha = \text{Re}(\gamma) \approx \frac{R}{2Z_o} + \frac{1}{2}GZ_o$ ,  $\alpha$  is the summation of two terms  $\alpha_c$  associated with conductor loss and  $\alpha_d$  related to the dielectric loss, both are expressed as:

$$\alpha_c = \frac{R}{2Z_o}, \quad \alpha_d = \frac{GZ_o}{2} \quad (5-25)$$

### 5.9.2.4.1 EXPLANATION OF THE AMPLITUDE ATTENUATION OF THE CONDUCTOR AND THE DIELECTRIC LOSS ( $\alpha_c$ AND $\alpha_d$ RESPECTIVELY).

A resonator is a device that oscillates with greater amplitude at specific resonant frequencies, which are called resonant frequencies. Resonators are used to create waves at specific frequencies or for selecting specific frequencies from the signal.

To understand the basic principle of the resonator, this section summarises this information. At the resonant frequency, a series or parallel lumped equivalent circuit can be used for modelling the microwave resonator.

#### Series Resonant Circuit Model

Figure 5-21 demonstrates the series RLC resonator. In this Figure, there are two parts, the resistance R which is the loss in the system whereas L and C are correlated to storage energy. The series impedance can be represented as

$$Z = R + j\omega L - j\frac{1}{\omega C} \quad (5-26)$$

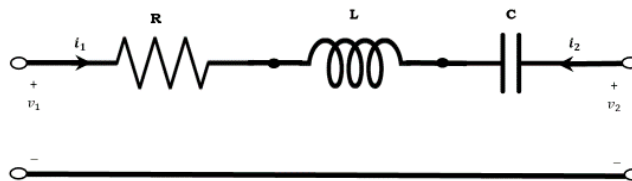


Figure 5-21: Series RLC resonator circuit.

The resonant frequency ( $\omega_0$ ) is where the reactive component of Equation 5-26 cancels, leaving a purely resistive impedance.

$$\omega_0 = \frac{1}{\sqrt{LC}} \quad (5-27)$$

Moreover, the second important parameter is the Q factor which measures the loss of a resonant circuit (inversely correlated) at resonance disregarding external loading effects. For the unloaded case, it is expressed as:

$$Q_0 = \frac{\omega_0 L}{R} = \frac{1}{\omega_0 RC} \quad (5-28)$$

Equation 5-26 illustrates the off-resonance impedance and will tend to an open circuit (low frequency (LF) behaviour of C and high frequency (HF) behaviour of L). Figure 5-22 demonstrates the response of the RLC series resonator [135]. In this Figure, the half-power width is defined when the impedance magnitude becomes  $\frac{R}{0.707}$ .

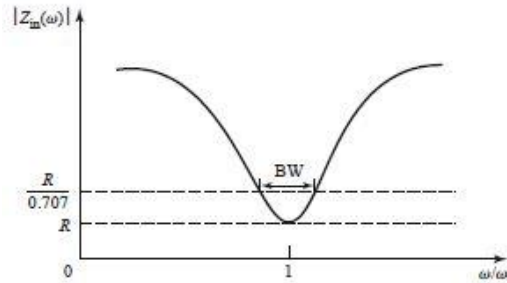


Figure 5-22: Input impedance versus frequency of the series resonant.

Reflection  $S_{11}$  and scattering parameters for transmission ( $S_{21}$ ) are obtained, firstly by using the ABCD identity in series.

$$\begin{bmatrix} A & \cdots & B \\ \vdots & \ddots & \vdots \\ C & \cdots & D \end{bmatrix} = \begin{bmatrix} 1 & \cdots & Z \\ \vdots & \ddots & \vdots \\ 0 & \cdots & 1 \end{bmatrix} \quad (5-29)$$

The Equation of  $S_{11}$  and  $S_{21}$  are found by substituting the ABCD matrix into well-known conversions [135].

$$S_{11} = \frac{Z}{2Z_0 + Z} \quad (5-30)$$

$$S_{21} = \frac{2}{Z/Z_0 + 2} \quad (5-31)$$

#### Parallel Resonant Circuit Model

Figure 5-23 illustrates the parallel RLC resonant circuit. In this Figure, there are two ports, R represents the real ohm losses of the system, whereas L and C represented the storage energy. The input impedance is represented as:

$$Z = \left( \frac{1}{R} + \frac{1}{j\omega L} + j\omega C \right)^{-1} \quad (5-32)$$

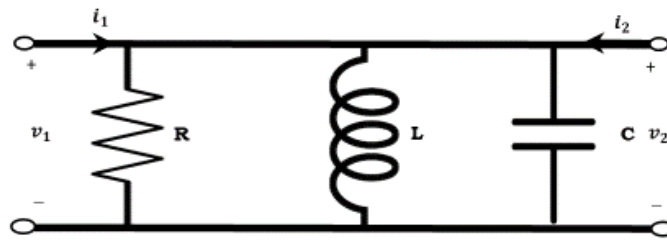


Figure 5-23: Parallel RLC resonator circuit.

The resonance occurs when the electric and magnetic stored energies are equal to series resonance. The pure resistance impedance  $\omega_0$  is the same as series resonance.

$$\omega_0 = \frac{1}{\sqrt{LC}} \quad (5-33)$$

Furthermore, the Q factor in the parallel resonant circuit is defined by:

$$Q_0 = \frac{R}{\omega_0 L} = \omega_0 RC \quad (5-34)$$

In this Equation the  $Q_0$  is proportional to resistance.

Figure 5-24 shows the behaviour of the magnitude of the input impedance versus frequency.[135].

The half-power bandwidth edges occur at frequencies ( $\frac{\Delta\omega}{\omega_0} = BW/2$ ).

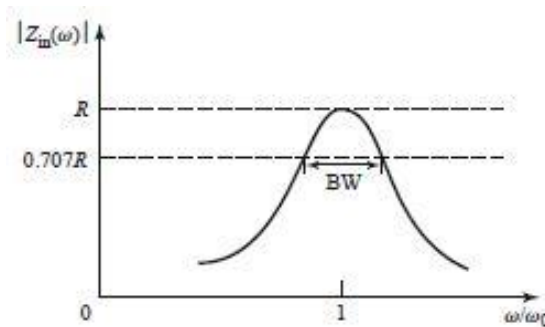


Figure 5-24: Input impedance versus frequency of the parallel resonant.

For a section of cable to be resonant, the length of the cable must be an integer number of half wavelengths, satisfied by the condition:

$$l = \frac{1}{2}n\lambda = \frac{nc}{2f} \quad (5-35)$$

Also:

$$\beta = \frac{n\pi}{l} = \frac{2n\pi f}{c} \quad (5-36)$$

The Q factor at resonance is expressed by:

$$Q = \frac{\beta}{2 * \alpha} \quad (5-37)$$

Here  $\beta$  is dependent on the geometry of the cable (the length),  $\alpha$  is dependent on the size of the loss. Therefore, the losses are defined as:

$$\alpha = \frac{1}{2} \frac{R}{Z_0} + \frac{1}{2} GZ_0 \quad (5-38)$$

$$\alpha = \alpha_c + \alpha_d$$

Here  $\alpha_c = \frac{1}{2} \frac{R}{Z_0}$  and  $\alpha_d = \frac{1}{2} GZ_0$

The Q factor of a resonator made from a length of cable is defined as:

$$Q_c = \frac{\beta}{2 \alpha_c} \quad (5-39)$$

$$Q_d = \frac{\beta}{2 \alpha_d} = \frac{n\pi}{2 \alpha_d l} \quad (5-40)$$

To fully understand the origin of  $\alpha_c$ , each coaxial cable has a support material between the inner and outer conductors, as shown in Figure 5-25. The thickness of this material is called the skin depth  $\delta$  which depends on the frequency. There is an inverse correlation between  $\delta$  and the frequency (due to the resistivity at higher frequencies). (The electrical thickness is different to the physical thickness).

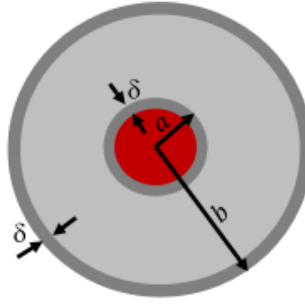


Figure 5-25: Regions for carrying current.

$$\delta = \sqrt{\frac{2\rho}{\omega\mu_0}} \quad (5-41)$$

Where  $\mu_0$  is the magnetic permeability of air,  $\rho$  is the resistivity.

To find the resistance of the wire

$$R = \frac{\rho * l}{2\pi a \delta} \quad \text{Since } R_s = \frac{\rho}{\delta} \quad (5-42)$$

Therefore,

$$R = \frac{R_s l}{2\pi a} \quad (5-43)$$

Here,  $R_s$  is the surface resistance and  $a$  is the radius of the wire.

As a coaxial cable has an inner core conductor and an outer conductor (Figure 5-25), these conductors represent two series resistances since the current flow opposite each conductor.

$$R \approx \frac{\rho l}{2\pi a \delta} + \frac{\rho l}{2\pi b \delta} \equiv \frac{R_s}{2\pi} \left( \frac{1}{a} + \frac{1}{b} \right) \text{ per unit length} \quad (5-44)$$

Therefore, the attenuation due to the conductors of a coaxial cable is given by:

$$\alpha_c \approx \frac{R}{2Z_0} \approx \frac{R_s \sqrt{\epsilon_r}}{2\eta_0 \ln(b/a)} \left( \frac{1}{a} + \frac{1}{b} \right) \quad (5-45)$$

This Equation proves that the loss of the conductors is dependent on the geometry, the properties of the material and the square root of the frequency.

With regard to  $\alpha_d$ , associated with a lossy capacitor, there are two parallel plates with an area and

a separation  $d$ . If the region between the two plates is filled with a dielectric material, the relative permittivity of that dielectric material  $\epsilon_r$ , serves to increase the capacitance. This increase will result in an increase in the voltage for a given charge. Therefore, in this case:

$$\sigma = \frac{1}{\rho} \quad (5-46)$$

Here,  $\sigma$  is the conductivity.

$$R = \frac{\rho * d}{A} \quad (5-47)$$

Where  $R$  is the resistive,  $d$  is the separation between two plates.

The conductance  $G$  is defined as:

$$G = \frac{1}{R} = \frac{A}{\rho * d} = \frac{\sigma * A}{d} \quad (5-48)$$

And the capacitance can be expressed as:

$$C = \frac{\epsilon_r \epsilon_0 A}{d} \quad (5-49)$$

Therefore, the ratio between  $G$  and  $C$

$$\frac{G}{C} = \frac{\sigma * A}{d} * \frac{d}{\epsilon_r \epsilon_0 A} = \frac{\sigma}{\epsilon_r \epsilon_0} \quad (5-50)$$

For the coaxial cable,

$$C = \frac{\epsilon_r \epsilon_0}{2\pi \ln \frac{b}{a}} \quad (5-51)$$

And

$$G = \frac{\sigma}{2\pi \ln \frac{b}{a}} \quad (5-52)$$

Therefore, the ratio between  $G$  and  $C$  in the coaxial cable is the same as the universal definition of a lossy capacitor as shown below:

$$\frac{G}{C} = \frac{\sigma}{\epsilon_r \epsilon_0} \quad (5-53)$$

For an ideal capacitor  $\sigma = 0$ ,  $G \ll \omega C$ ,  $\frac{G}{\omega C} \ll 1$

At low loss  $\frac{1}{\omega} \frac{\sigma}{\epsilon_r \epsilon_0} \ll 1$ , which depends on the conductivity and frequency.

For a full understanding of the impedance of the capacitor:

$$Z = \frac{1}{j\omega C}, \text{ so loss } R = \frac{1}{G} \quad y = \frac{1}{Z} = j\omega C \quad (5-54)$$

$$y = G + j\omega C = j\omega C'$$

$$j\omega C' = G + j\omega C$$

Here  $C'$  is the loss effect on the transmission line (the effective capacitance).

$$C' = \frac{G}{j\omega} + C = C - j \frac{G}{\omega} \quad (5-55)$$

$$C' = C \left( 1 - j \frac{G}{\omega C} \right)$$

As we mentioned at Equation 5-44, therefore the general capacitor

$$C' = C_0 \epsilon_r \left( 1 - j \frac{\sigma}{\omega \epsilon_r \epsilon_0} \right) \quad (5-56)$$

$$C' = C_0 \left( \epsilon_r - j \frac{\sigma}{\omega \epsilon_0} \right) = C_0 \cdot \epsilon$$

$$\epsilon = \epsilon_r - j \frac{\sigma}{\omega \epsilon_0}$$

$$= \epsilon_1 - j \epsilon_2$$

$$= \epsilon_1 \left( 1 - j \frac{\epsilon_2}{\epsilon_1} \right)$$

Since  $\frac{\epsilon_2}{\epsilon_1}$  equals  $\tan \delta$

Therefore,

$$= \epsilon_1 (1 - j \tan \delta) \quad (5-57)$$

$$C' = C \left( 1 - j \frac{G}{\omega C} \right)$$

So

$$\tan \delta = \frac{G}{\omega C}, \frac{G}{C} = \omega \tan \delta = \omega \frac{\epsilon_2}{\epsilon_1} \quad (5-58)$$

To understand the loss in the dielectric and its associated Q factor at resonance,  $Q_d$

$$\alpha_d = \frac{1}{2} G Z_0 \quad (5-59)$$

$$Q_d = \frac{\beta}{2 \alpha_d} = \frac{\beta}{G Z_0} \quad (5-60)$$

As

$$\beta = \frac{2\pi}{\lambda}, f = \frac{v}{\lambda} \text{ then } \beta = \frac{2\pi f}{v} \quad (5-61)$$

$$Q_d = \frac{\beta}{G Z_0} = \frac{2\pi f}{v} \cdot \frac{1}{G Z_0}$$

$$v \cdot Z_0 = \frac{1}{\sqrt{LC}} \cdot \sqrt{\frac{L}{C}} = \frac{1}{C}$$

$$Q_d = \frac{\omega C}{G} = \frac{1}{\tan \delta}$$

This means that the  $Q_d$  depends on the frequency and the properties of the sample material.

### 5.9.3 ELECTROMAGNETIC RESONATORS

At low frequencies (up to a few MHz), a simple resonant circuit is made which consists of parallel LC circuit components. However, at high frequency (above 1 GHz), circuits become distributed (size > wavelength) and instead, the TL sections replace the lumped LC components.

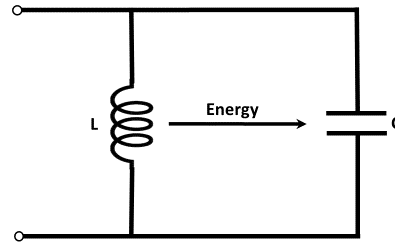


Figure 5-26: Losing features.

In an LC parallel circuit (Figure 6-26), the resonant frequency equals  $\omega_0 = \frac{1}{\sqrt{LC}}$  which suggests that at resonance, the stored energy oscillates between the electric field of C and the magnetic field of L. Furthermore, the Q factor of a resonator quantifies the selective frequency, which can be defined as:

$$Q = \omega_0 * \frac{\text{time - averaged stored energy}}{\text{time - average power dissipated}} = \frac{\omega_0 \langle U \rangle}{\langle P \rangle} \quad (5-62)$$

The half-power bandwidth of the resonator is given by:

$$\omega_B = \omega_0 / Q \quad (5-63)$$

EM field and resonant frequencies of a TEM TL resonator

A low loss TEM TL line supports backwards and forward propagating waves with  $\gamma \approx \mp j\beta$ .

Standing waves (i.e., resonances) in v use the Equations as mentioned before and I (and E and H) are set up when its length L satisfies

$$l = n \cdot \frac{\lambda}{2}, \text{ since } \beta = \frac{2\pi}{\lambda} \equiv \frac{n\pi}{l} \quad (n = 1, 2, 3, \text{ etc.}) \quad (5-64)$$

Also:

$$f_0 = \omega_0 / 2\pi \quad (5-65)$$

### 5.9.3.1 UNLOADED Q FACTOR $Q_0$ OF A TL RESONATOR

The conventional method to express  $Q_0$  is:

$$\frac{1}{Q_0} = \frac{1}{Q_c} + \frac{1}{Q_d} \quad (5-66)$$

Here,  $Q_0$  is the unloaded Q factor,  $Q_c$  is the conductor Q factor and  $Q_d$  is the dielectric Q factor,

which can be express as:

$$Q_c \equiv n\pi/2\alpha_c l \propto n/R_s, \quad (5-67)$$

$$Q_d \equiv n\pi/2 \alpha_d l \approx (\tan \delta)^{-1}$$

### 5.9.3.2 UNLOADED ( $Q_0$ ) AND LOADED Q FACTOR ( $Q_L$ )

Q factor is a dimensionless parameter. It describes the loss of energy within a resonant element. It indicates the correlation between the loss and stored energy within the system. Therefore, for higher Q factors, the rate of energy loss decreases and gives stability to the circuit. At constant stored energy within a specific frequency, hence the mathematical formula can be expressed as

$$Q = \frac{E_{stored}}{E_{lost \text{ per cycle}}} \quad (5-68)$$

At resonance, the Q factor is expressed as:

$$Q = \frac{f_0}{f_{3dB}} \quad (5-69)$$

Here  $f_0$  is the central frequency,  $f_{3dB}$  is defines as the -3 dB bandwidth (Figure 5-27).

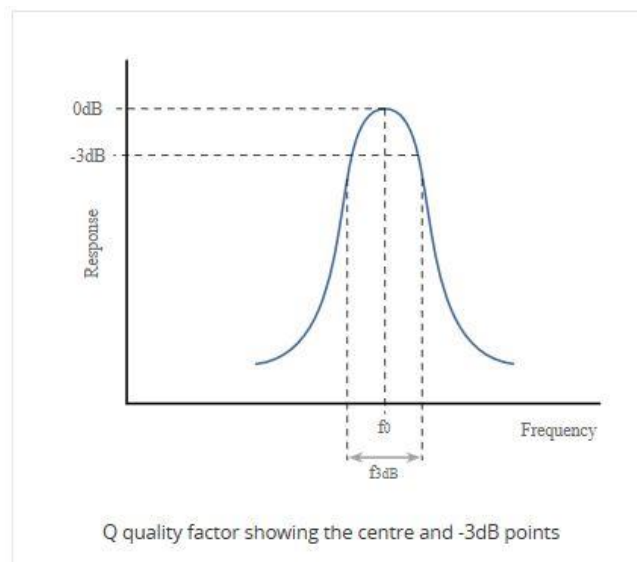


Figure 5-27: Calculation of the Q factor.

The general definition of the Q factor of a resonator is the ratio of the resonant frequencies and the full bandwidth at half power of its power spectrum. In terms of the unloaded Q factor  $Q_0$

$$Q_0 = \frac{\beta_0}{2 \alpha} = \frac{n\pi}{2 \alpha l} \quad (5-70)$$

It is clear from this Equation that  $Q_0$  is affected by the material and the physical dimensions of the resonator, not by the coupling structure. On the other hand, the loaded Q factor ( $Q_L$ ) (including the effects of coupling), decreases the Q factor compared to  $Q_0$ . The  $Q_L$  the factor can be expressed as:

$$Q_L = Q_0 \div (1 + g) \quad (5-71)$$

This Equation shows that finite coupling; whilst ensuring power transfer to the resonator, will come at the expense of increased bandwidth.

### 5.9.3.3 INSERTION LOSS ( $S_{21}$ )

Another important microwave factor is Insertion loss ( $S_{21}$ ). It can be defined as a loss of power that occurs as a signal move through a component or system. This loss is called the Insertion loss which is defined as:

$$Insertion\ loss = 10 * \log \left( \frac{P_o}{P_i} \right) \quad (5-72)$$

Here,  $P_o$  is the power out and  $P_i$  is the power in.

There are many reasons for Insertion loss: Firstly, Reflected losses. In addition, the dielectric losses are due to the dissipated power in the dielectric materials and finally the copper losses owing to dissipated power to the conducting surfaces of the connector.

## 5.10 SIMULATION OF *NOVEL* 'TEE' STRUCTURE AND CAPACITIVE COUPLING.

The coaxial probe resonator, together with its coupling arrangement” Novel ‘tee’ Structure and Capacitive Coupling”, has been simulated using Keysight’s Advance Design System software (ADS) (Figure 5-28), the values will change depends on the experiments in section 5.11. As the same experimental setup is shown in Figure 5-29.

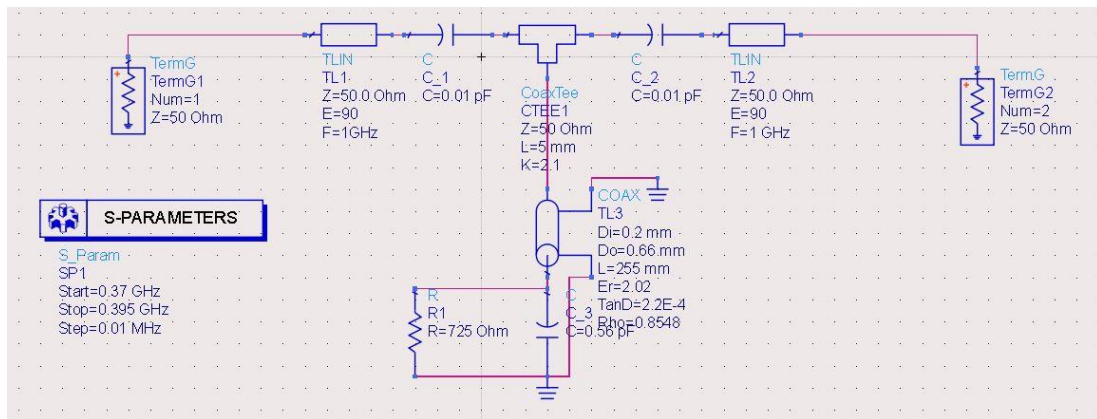


Figure 5-28: The schematic of the coaxial probe simulation.

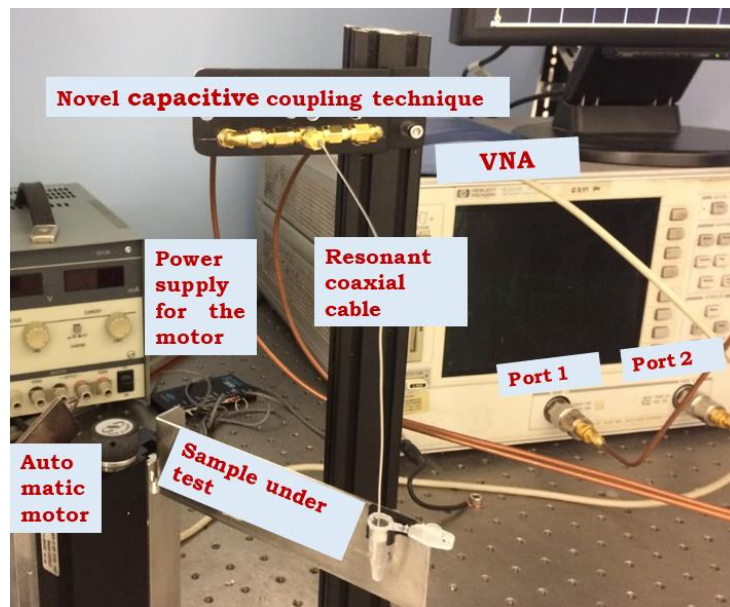


Figure 5-29: Experimental physical set-up.

The circuit consists of a central stem that represents the coaxial resonator structure. The SMA RF Tee connector at the top enables coupling to the resonator; TL<sub>3</sub>, the coax section is the resonator body; the length of this will determine the resonant frequency. Coupling capacitors C<sub>1</sub> and C<sub>2</sub> are formed using the female-female SMA converters which provide a convenient variable capacitive coupling mechanism. These are subsequently connected to the VNA launch cables (RG-405) to ports 1 and 2 respectively.

The resonator section utilises a 50  $\Omega$  Semi-rigid Coaxial Cable (.034AG-W-P-50) (Jyebao

Company) [144]. This cable consists of the central conductor diameter ( $0.20 \pm 0.0127$ ) mm, dielectric diameter ( $0.66 \pm 0.0254$ ) mm, outer conductor diameter ( $0.86 \pm 0.0508$ ) mm. Regarding material specifications, the outer conductor is Silver Plated Copper, the dielectric is polytetrafluoroethylene (PTFE), and the centre conductor is reported to be a silver-plated copper wire (SPCW) from the datasheet, however, following the use of the cable, it was determined that the core of the central conductor was in fact steel. It is silver-plated copper-clad steel after checking with the supplier. In the simulation,  $L$  refers to the length of the cable. Different cable lengths have been studied to establish the effect on the  $Q$  factor and the insertion loss. A cable of any length can in principle carry any number of modes up to the cut off frequency of the cable. What we are interested in though is the number of modes within the frequency range of the VNA 100 MHz to 6 GHz. A longer cable can support more modes in this frequency range than a short cable.  $\epsilon_r$  is the dielectric constant of dielectric between the inner and outer conductor ( $\epsilon_r=2.02$  for the PTFE).  $\tan \delta$  is the dielectric loss tangent which equals 0.00022 for PTFE [145].  $\rho$  is defined as the conductor resistivity as a ratio of the value of copper. For silver, a value of 0.8548 has been used. A capacitor ( $C_3$ ) and resistance ( $R_1$ ) are connected at the tip of the coaxial cable to emulate the behaviour of the sample material with different conductor values. Finally, S-Parameters (small-signal AC-simulation) are used to define the signal wave response of an  $n$  port electrical element at a given frequency. It controls the start, stop and step of frequency. S-parameters describe the input-output relationship between ports (or terminals) in an electrical system. In our set-up,  $S_{21}$  represents the power transferred from Port 1 to Port 2.  $S_{21}$  is a much bigger signal and high signal to noise ratio compared to  $S_{11}$ . Therefore,  $S_{21}$  has been used to represent the power transmission in the simulation and the experiment work.

### 5.10.1 DESIGN SETUP

To emulate the same experimental behaviours, an ADS simulation has been established with the same experimental parameters as follows; firstly, by fixing  $R_1$  at 1000 ohm (the resonance case),  $C_3$  has been set to obtain the same resonant frequencies of air obtained from the experimental work (0.56 pF). Furthermore,  $R_1$  is set to achieve the same experimental bandwidth of the first mode (9.025 K $\Omega$ ). Finally, the coupling capacitors,  $C_{-1}$  and  $C_{-2}$  are set to obtain the same  $S_{21}$  value for the first mode of the experimental work on air (0.0075 pF).

## 5.11 THE EFFECT OF CIRCUIT PARAMETERS ON THE BANDWIDTH (BW), Q FACTOR AND $S_{21}$

### 5.11.1 EFFECT OF SYMMETRY IN THE COUPLING CAPACITANCES.

The effect of varying the coupling capacitor values (0.0075, 0.01, 0.05, 0.075 and 0.1) pF on BW,  $CF$ , Q factor and  $S_{21}$  were studied at the number of modes within the frequency range of the VNA 100 MHz to 6 GHz at a resonator length of 255 mm (Figure 5-30 to 5-33).

In Figure 5-30, there is a consistent BW increase with increasing mode number and hence  $CF$  for all coupling capacitors values. Additionally, there is no significant BW difference at low frequency in between (0.379 to 1.904) GHz with different values of the capacitors. However, the difference started to become significant at higher frequencies (2.3 to 5.4) GHz for all capacitor values. Whilst it appears that the BW increases with increasing coupling capacitor; given that there is no real additional mechanism for a loss here, the apparent increase in BW is likely down to the increasing skew of the resonance peaks and the inherent difficulty associated with obtaining the -3dB bandwidth.

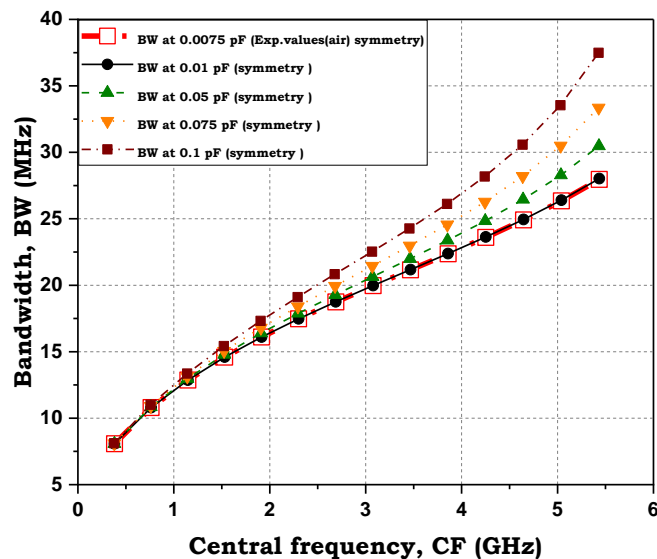


Figure 5-30: The measured BW for all modes in the range of the frequency (0.1 to 6) GHz with symmetric values of the capacitors (0.0075, 0.01, 0.05, 0.075 and 0.1) GHz.

As expected, the central frequency of each resonance showed no dependence on the coupling capacitor, with increasing the number of modes, see Figure (5-31).

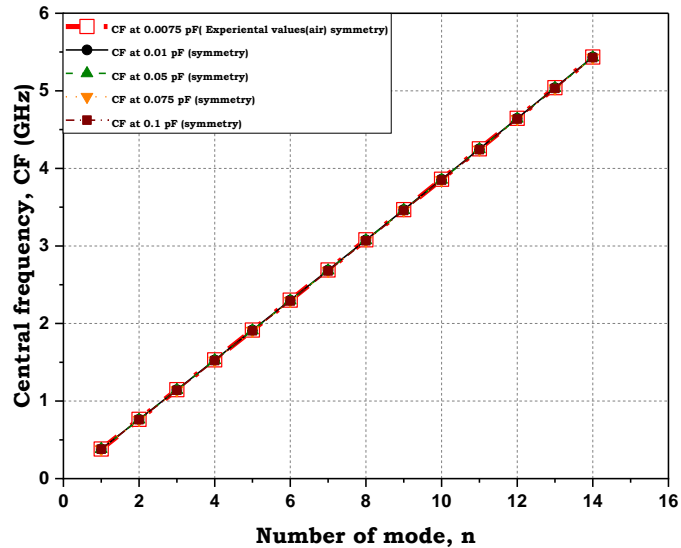


Figure 5-31: Central frequency measurements for the range of the frequency (0.1 to 6) GHz with symmetric values of the capacitors (0.0075, 0.01, 0.05, 0.075 and 0.1) pF.

In Figure 5-32, there appears to be a regular increase in the Q factor for all modes within the range of frequencies and for all coupling capacitors values. For the higher values of the coupling capacitor, the Q factor is seen to reduce from an overall peak at a higher frequency. Again, since there is no real mechanism for additional loss relating to the coupling capacitors, the apparent decrease in the Q factor is likely attributed to the emerging skew of the higher-order resonances.

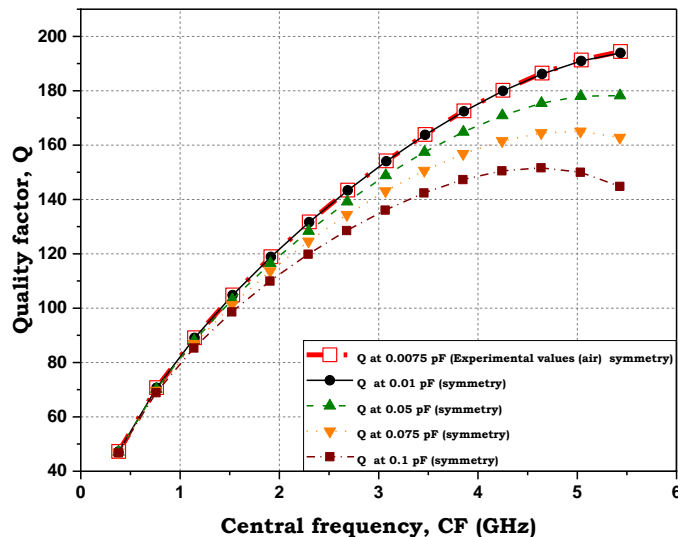


Figure 5-32: The measured Q factor for the range of the frequency (0.1 to 6) GHz with symmetric values of the capacitors (0.0075, 0.01, 0.05, 0.075 and 0.1) pF.

Further evidence for the role of the skew in distorting the obtained values of BW and Q factor may be seen in Figure 5-33 below. The general shape of the insertion loss curve as a function of mode number (or frequency) is identical for each value of the coupling capacitor. The variation in insertion loss generally increases as frequency increases since the structure's associated losses

are frequency dependent. The DC shift upwards is simply a result of increased coupling due to increased coupling capacitance. The bigger the capacitance at the top of the tee means more energy is directly coupled from port 1 to port 2. i.e the  $S_{21}$  signal is bigger as the capacitance increases. More capacitance means more power passing through the tee means more power available to the resonator means more signal.

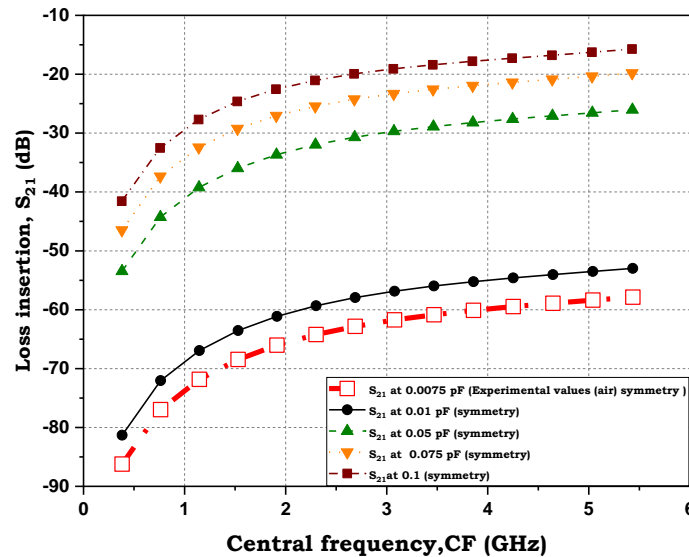


Figure 5-33:  $S_{21}$  measurements for the range of the frequency (0.1 to 6) GHz with symmetric values of the capacitors (0.0075, 0.01, 0.05, 0.075 and 0.1) pF.

### 5.11.2 EFFECT OF ASYMMETRY IN THE COUPLING CAPACITANCES

The effect of asymmetrical coupling capacitor values ( $C_1$  0.1 and  $C_2$  0.05 and vice versa) on BW, CF, Q factor and  $S_{21}$  were studied for a coaxial probe length of 255 mm.

Figure 5-34 shows an almost identical trend for BW as for the symmetrical case (0.05, 0.1 and 0.075) pF and asymmetrical capacitor set up  $C_1$  (0.05) pF and  $C_2$  (0.1) pF and vice versa for the range of frequency (0.37 to 5.4) GHz. The trend for the values of the asymmetrical capacitors for 0.05 and 0.1 pF and vice versa (0.1 and 0.05) pF appears to be positioned between those for the symmetrical case. The average value of the two asymmetric capacitances is 0.075 pF. It appears that the asymmetrical result is approximately identical to the case where both capacitors are 0.075 pF.

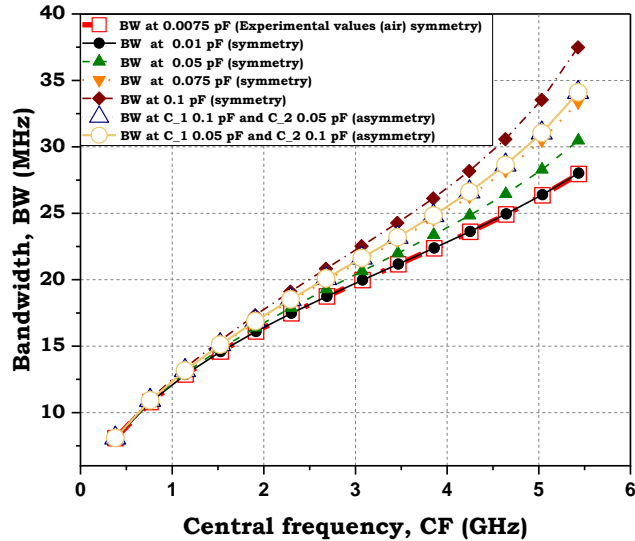


Figure 5-34: Comparison between BW measured of asymmetric capacitors (0.1 and 0.05) pF and the opposite, symmetric capacitors (0.05, 0.1 and 0.075 (the ave. value of the asymmetrical capacitors) pF for the range of the frequency (0.1 to 6) GHz.

As expected, no variation in the central frequency of each mode for these difference coupling scenarios (Figure 5-35).

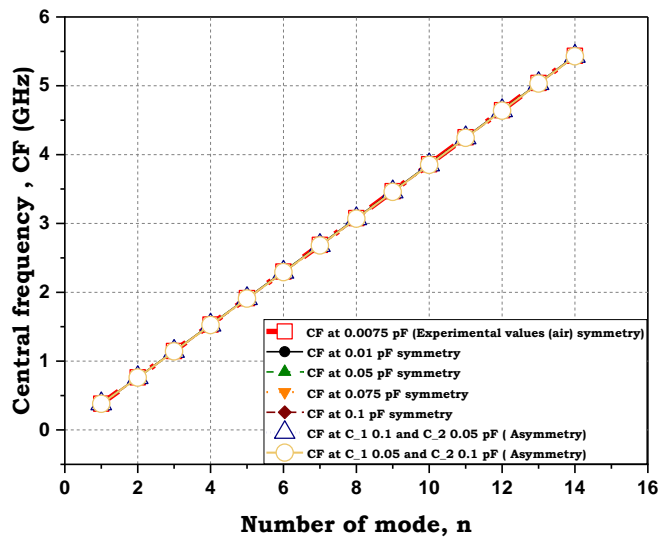


Figure 5-35: Comparison between CF measured of asymmetric capacitors (0.1 and 0.05) pF and the opposite, symmetric capacitors (0.05, 0.1 and 0.075 (the ave. value of the asymmetrical capacitors) pF for the range of the frequency (0.1 to 6) GHz.

Regarding the Q factor, the orientation of the coupling asymmetry gives identical results. The variation in Q for the asymmetric cases is placed in between the values for the symmetrical coupling case (0.05, and 0.1) pF. Again, the asymmetrical coupling follows the trend associated with the average capacitor value, 0.075 pF (Figure 5-36).

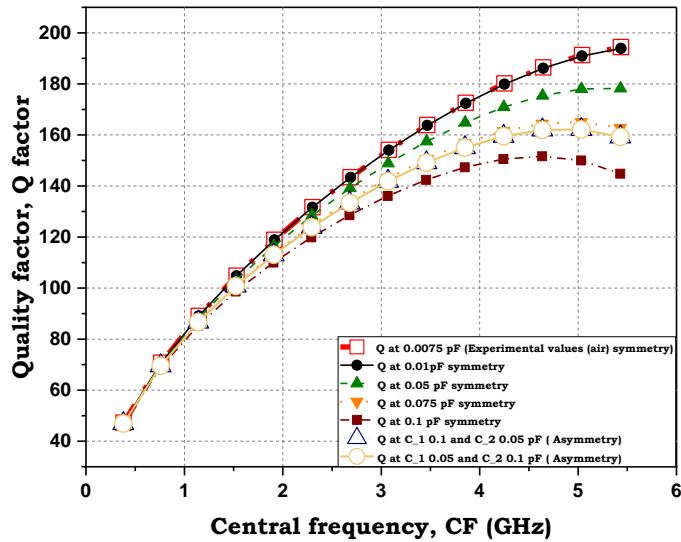


Figure 5-36: Comparison between Q factor measured of asymmetric capacitors (0.1 and 0.05) pF and the opposite, symmetric capacitors (0.05, 0.1 and 0.075 (the ave. value of the asymmetrical capacitors) pF for the range of the frequency (0.1 to 6) GHz.

For the insertion loss, there does appear to be a difference between the asymmetrical cases and that of the average symmetrical coupling at 0.075 pF. The very slight difference observed above for the BW was attributed to the error in obtaining the BW from the skewed resonances. However, here, the respective insertion losses are obviously different and will be further investigated in the below Figure (Figure 5-37).

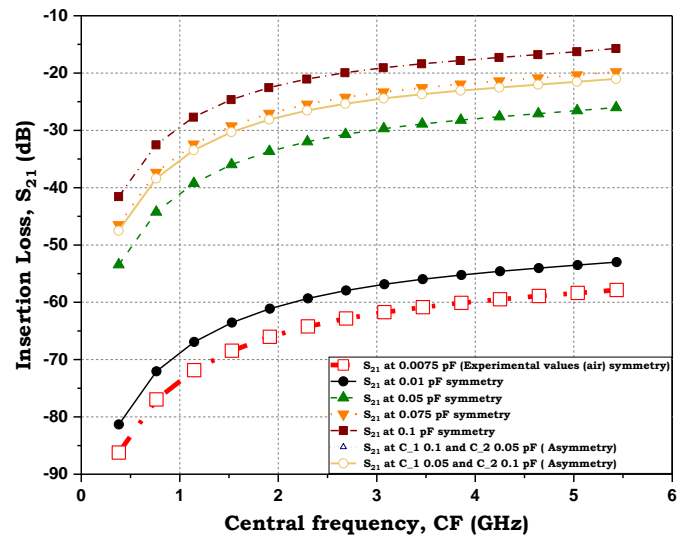


Figure 5-37: Comparison between  $S_{21}$  measured of asymmetric capacitors (0.1 and 0.05) pF and the opposite, symmetric capacitors (0.05, 0.1 and 0.075 (the ave. value of the asymmetrical capacitors) pF for the range of the frequency (0.1 to 6) GHz.

Figures 5-38 and 5-39 below show the changes in the resonance of the first and the last mode of

the resonator for asymmetric coupling capacitors for two options 0.05 and 0.1 pF, 0.06 and 0.09 pF, 0.07 and 0.08 pF and the symmetrical 0.075 pF case. Since symmetric coupling is preferred from a data analysis point of view, this result suggests that the symmetric scenario has a less overall loss that similar a-symmetric capacitance values in both modes. Therefore, the adjustment of the physical capacitors in the resonator to the asymmetric case should be straightforward. Setting one capacitor and then adjusting the other to find a maximum in the peak will set the coupling to symmetric. Additionally, we found a significant effect of the skew on the last mode (Figure 5-39) trend with high frequency (non-identical) in comparison to the identical trend for the first mode. The effect of resonance skew will study in the next section.

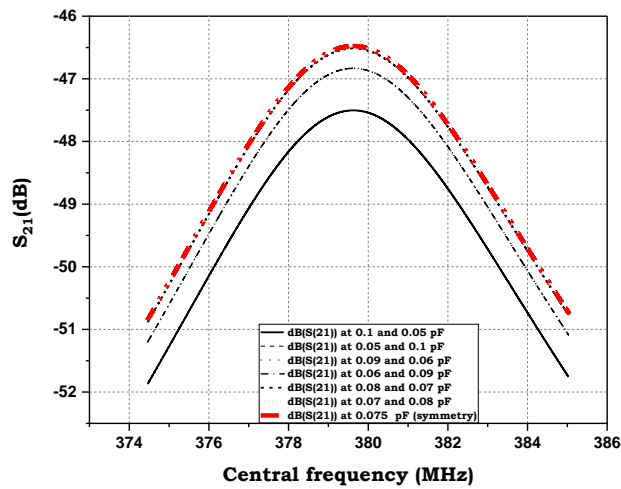


Figure 5-38: Comparison between different asymmetrical (0.05 & 0.1 pF, 0.06 & 0.09 pF, 0.07 & 0.08, and vice versa) pF and the symmetrical 0.075 pF case for the actual first mode (lower frequency).

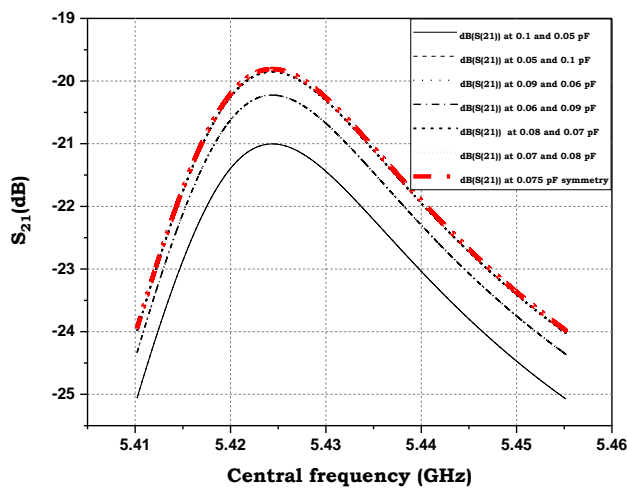


Figure 5-39: Comparison between  $S_{21}$  measured of asymmetric capacitors (0.1 and 0.05) pF and the opposite, symmetric capacitors (0.05, 0.1 and 0.075 (the ave. value of the asymmetrical capacitors) pF for the range of the frequency (0.1 to 6) GHz.

### 5.11.3 EFFECT OF COAXIAL CABLE LENGTH ON THE BANDWIDTH, CENTRAL FREQUENCY, QUALITY FACTOR, AND INSERTION LOSS

The effect of the coaxial length (105, 180 and 255) mm on the microwave parameters (BW, CF, Q factor and  $S_{21}$ ) were studied for symmetric coupling capacitors 0.0075 pF (air EXP.) in Figure 5-40 to 5-43 respectively.

A slight difference is shown in the BW between 0.1 to 3 GHz, and 4 to 6 GHz, whilst, we have found overlapping between 3 to 4 GHz when we compare the results of various coaxial lengths (105, 180 and 255) mm. Additionally, we found there is a considerable BW increase with decreasing the coaxial length for the first range of the frequency and vice versa in the range 4 to 6 GHz (Figure 5-40). On the other hand, the number of the mode (the no of the resonant frequencies) increased with increasing the length of the coaxial cable Figure 5-41.

In terms of the Q factor, a marginal variance on the Q factor of 0.1 to 3 GHz and 4 to 6 GHz was seen. While an overlap is shown between 3 to 4 GHz on comparing the three coaxial lengths. Moreover, a considerable increase has been shown in the Q factor with reducing the coaxial cable length in the range of 0.1 to 3 GHz and vice versa between 4 to 6 GHz (Figure 5-42). However, a substantial reduction in the loss is shown with the increasing coaxial length for the whole range Figure 5-43.

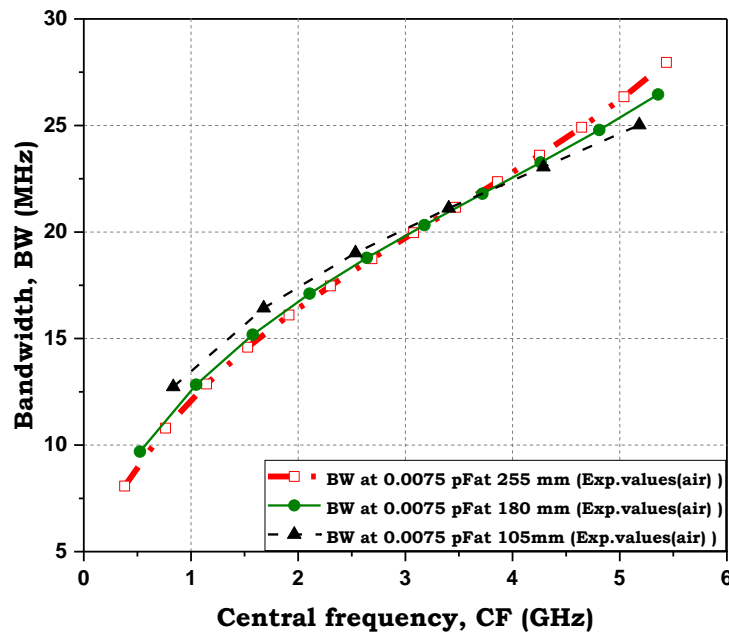


Figure 5-40: Comparison between BW measurements at symmetric capacitors 0.0075 pF with different coaxial lengths (255, 180 and 105) mm.

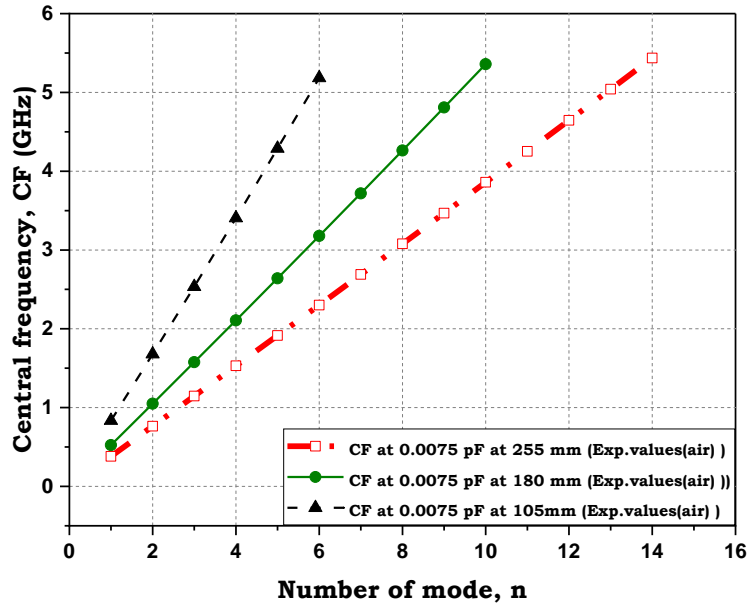


Figure 5-41: Comparison between resonant frequency measurements at symmetric capacitors 0.0075 pF with different coaxial lengths (255, 180 and 105) mm.

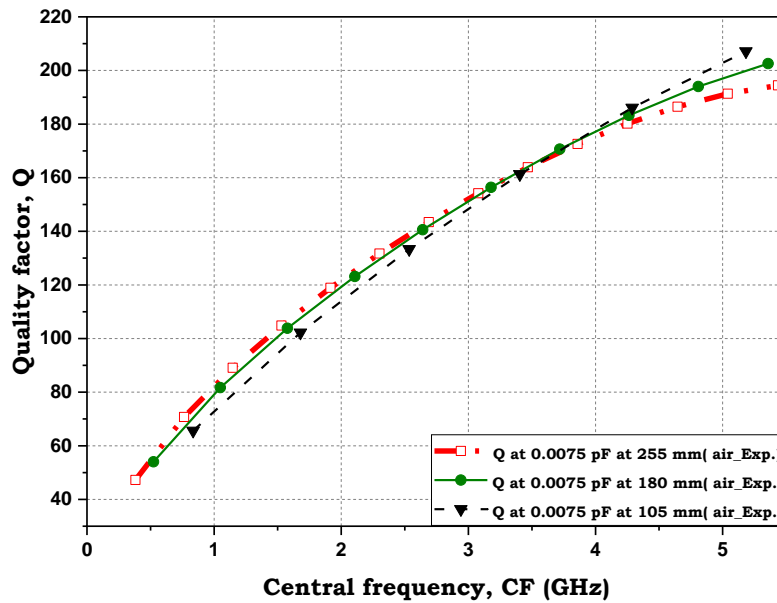


Figure 5-42: Comparison between Q factor measurements at symmetric capacitors 0.0075 pF with different coaxial lengths (255, 180 and 105) mm.

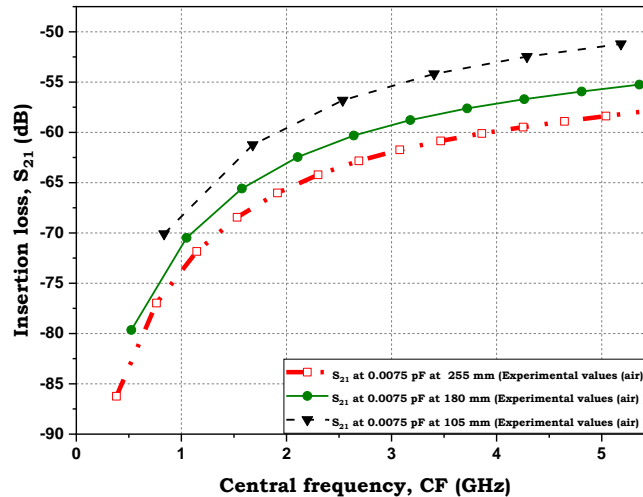


Figure 5-43: Comparison between  $S_{21}$  measurements at symmetric capacitors 0.0075 pF with different coaxial lengths (255, 180 and 105) mm.

## 5.11.4 SAMPLE EFFECT

To emulate experiment samples, air, water and various concentrations stock ( $S=0.154$  M), first concentration ( $C_1=0.077$  M) and second concentration ( $C_2=0.039$  M).have been measured.

### 5.11.4.1 EFFECT OF AIR AND WATER SAMPLES

#### 5.11.4.1.1 DESIGN SETUP FOR AIR AND WATER SAMPLES

The ADS simulation was run with the same experimental parameters in some of the examples above to emulate the same experimental behaviours of air and water. Firstly, by fixing  $R_1$  at 1000 ohm (the resonance case),  $C_3$  was set to obtain the same resonant frequencies of the air experimental work (0.56 pF) and (0.74 pF) for water. Furthermore,  $R_1$  was set to achieve the same experimental bandwidth of the first mode 9.025 and 7.519 K $\Omega$  for air and water, respectively. Finally, the coupling capacitors,  $C_1$  and  $C_2$  were set to obtain the same  $S_{21}$  value for the first mode of air experimental work 0.0075 pF and 0.0073 pF for water.

#### 5.11.4.1.2 RESULTS OF ADS FOR AIR AND WATER SAMPLES

The below Figures (5-44 to 5-46) illustrated the comparison between the experimental data for air and water samples for the whole range of the VNA frequency (0.1 to 6) GHz and at a specific

frequency the first mode (0.382 GHz) and the last mode (5.433 GHz). In the whole range of the frequencies (0.1 to 6) GHz, a slight drift in  $S_{21}$  for water compared to air is shown in Figure 5-44. For more clarification, it is obvious there is a substantial variance between two different samples of air and water for the first and the last frequency (0.382 GHz and 5.433 GHz respectively) (Figures 5-45 and 5-46).

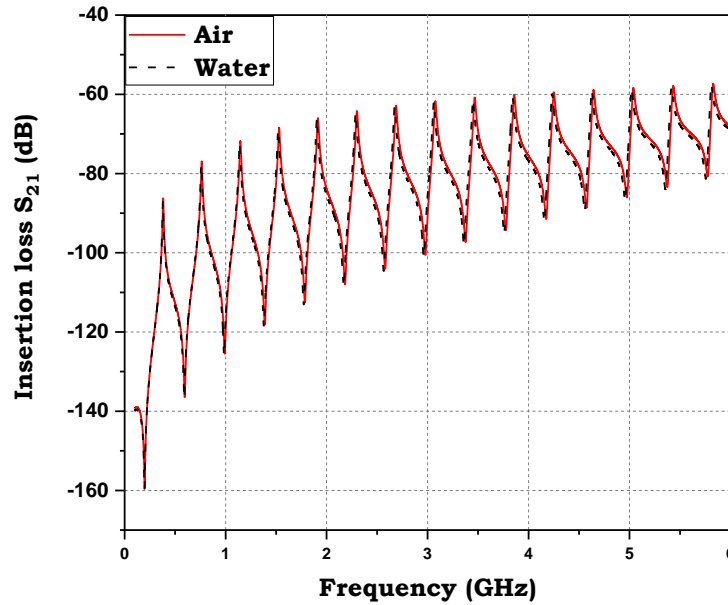


Figure 5-44: Comparison between  $S_{21}$  measured for different samples (air and DI-W) at step size 0.1GHz, symmetric capacitors (0.0075) pF and (0.0073) pF for air and water, respectively for the whole range of frequency (0.1 to 6) GHz.

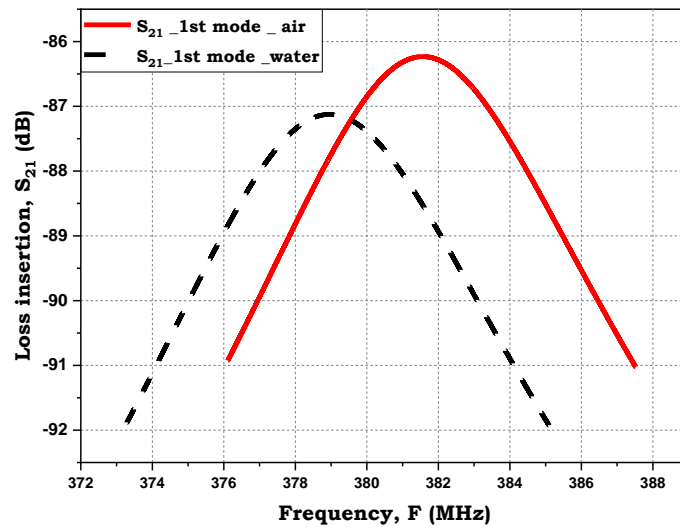


Figure 5-45: Comparison between  $S_{21}$  measured for different sample (air and DI-W) at symmetric capacitors (0.0075) pF and (0.0073) pF for air and water respectively at the first mode at resonant frequency 0.382 GHz.

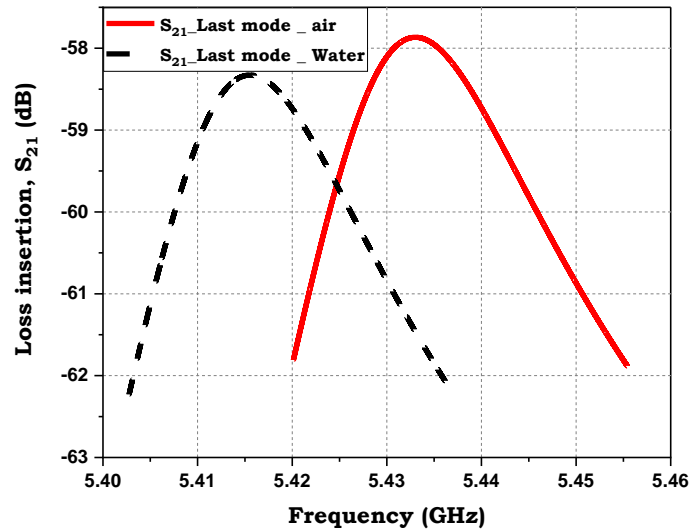


Figure 5-46: Comparison between  $S_{21}$  measured for different sample (air and DI-W) at symmetric capacitors (0.0075) pF and (0.0073) pF for air and water respectively at the last mode at resonant frequency 5.433 GHz.

### 5.11.4.1.3 CONCLUSION OF ADS FOR AIR AND WATER SAMPLES

To summarise, water sample measurements showed a drift in  $S_{21}$  compared to the air sample.

### 5.11.4.2 EFFECT OF DIFFERENT CONCENTRATIONS OF THE STOCK (S), FIRST CONCENTRATION (C1) AND SECOND CONCENTRATION (C2).

#### 5.11.4.2.1 DESIGN SETUP FOR OBTAINING VALUES FOR DIFFERENT NORMAL SALINE CONCENTRATIONS (S, C1 AND C2)

The same steps in section 5.11.4.1 have been followed for obtaining the saline values of  $R_1$ ,  $C_3$  and the coupling capacitor ( $C_{-1}$  and  $C_{-2}$ ) for stock ( $S=0.154$  M), first concentration ( $C_1=0.077$  M) and second concentration ( $C_2=0.039$  M). Thus,  $R_1$  is 1.242, 1.912 and 2.712  $K\Omega$ , respectively.  $C_{-3}$  is 0.798, 0.789 and 0.785 pF for the same arrangement mentioned above.  $C_{-1}$  and  $C_{-2}$  are 0.0043, 0.0048 and 0.0052 pF.

#### 5.11.4.2.2 RESULTS OF ADS FOR DIFFERENT CONCENTRATIONS

Figure 5-47 shows a substantial variance in  $S_{21}$  measured at variance concentrations of normal

saline, the commercial saline (BOOT'S pharmacy) 0.154 M (S) and the two concentrations 0.077 M (C<sub>1</sub>) and 0.039 M (C<sub>2</sub>), respectively at the first resonant frequency (0.76 GHz).

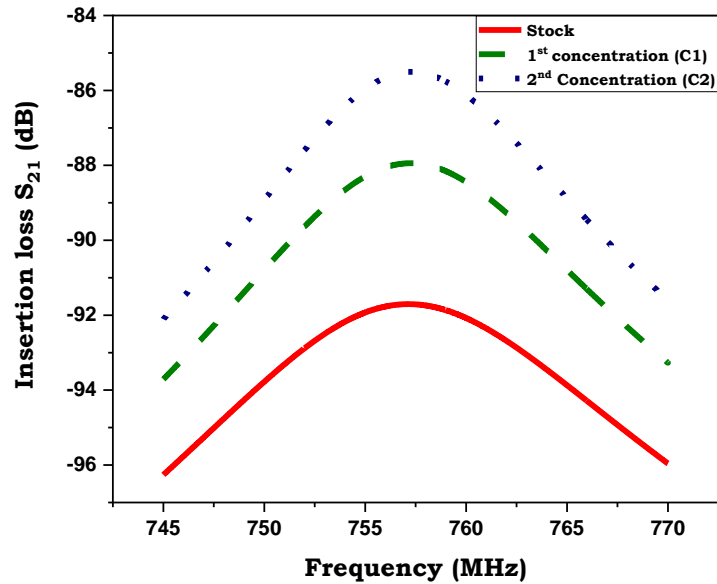


Figure 5-47: Comparison between  $S_{21}$  measured for different of normal saline sample concentrations (stock= 0.154 M, first concentrations (C<sub>1</sub>=0.077M) and second concentrations (C<sub>2</sub>=0.039 M)) at the first resonant frequency (0.76 GHz).

### 5.11.4.2.3 CONCLUSION OF ADS FOR DIFFERENT CONCENTRATIONS

In summary, a significant variation in  $S_{21}$  was observed at the first resonant frequency (0.76 GHz) and variance concentrations of normal saline, commercial saline (BOOT'S pharmacy) 0.154 M (S), and the two concentrations 0.077 M (C<sub>1</sub>) and 0.039 M (C<sub>2</sub>), respectively.

## 5.12 RESONANCE SKEW

Following the observation that BW appears to increase as coupling capacitors increase, the work of Jerome Cuenca and Sam Partridge shed some light on the process behind this. The Figure below (Figure 5-48) [132, 146] showed various types of skew responses due to the capacitive and inductive cross-coupling and nearby modes. The resonance curve changes as the degree of direct cross-coupling increases. In some cases, if multiple modes are close enough the quality factor shows an increase in comparison to the theoretical maxima. Moreover, if the measurement is not within the -3db bandwidth or the fitting of Lorentzian curve fitting is limited to the window of the back. Therefore, the skew phenomenon has been shown which is the measurement of the symmetry of a distribution.

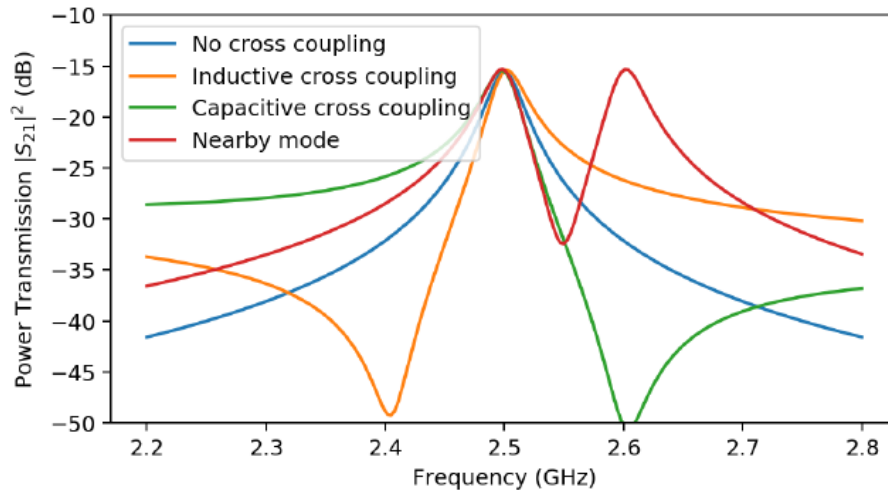


Figure 5-48: Skew examples owing to inductive, capacitive cross-coupling and nearby modes

In our circuit, the two series capacitors  $C_1$  and  $C_2$  provide a direct coupling path from port 1 to port 2. It is this direct coupling that gives rise to the skew. The impedance of our resonant probe can be simply described in terms of  $R$ ,  $L$  and  $C$ , as shown below in Figure 5-49.

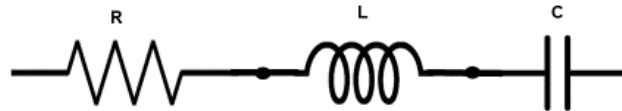


Figure 5-49: Resistive capacitive and inductive elements that represent a lossy resonant circuit.

The operation of the microwave resonant occurs by exchanging the energy between the electric and magnetic fields, which can be represented as a series resonant circuit RLC. In this circuit, the loss represents by the resistance whilst the stored energy within the electric and magnetic fields represent by the inductance and the capacitance. The impedance can be expressed by the following Equation:

$$Z(\omega) = R + j\omega L + \frac{1}{j\omega C} \approx R \left[ 1 + j2Q_0 \left( \frac{\omega - \omega_0}{\omega_0} \right) \right] \quad (5-73)$$

The impedance becomes absolutely real in the resonant case. The Equation for complex resonant frequency can be derived from the reactance roots

$$\omega \approx \omega_0 + j \frac{\omega_0}{2Q_0} \quad (5-74)$$

In our system, to overcome the resonant coaxial cable issues, a resonator coupling is used as it is useful to be coupled to an external system. This section will clarify the theoretical part of the coupling.

There are two coupling types in the microwave resonator: the first type is capacitive coupling by using an open circuit transmission that couples to the resonator electric field. The second type is the inductive coupling using a short circuit line, and it combines the magnetic field. Figure 5-50 demonstrated the equivalent circuit of an inductively coupled resonator.

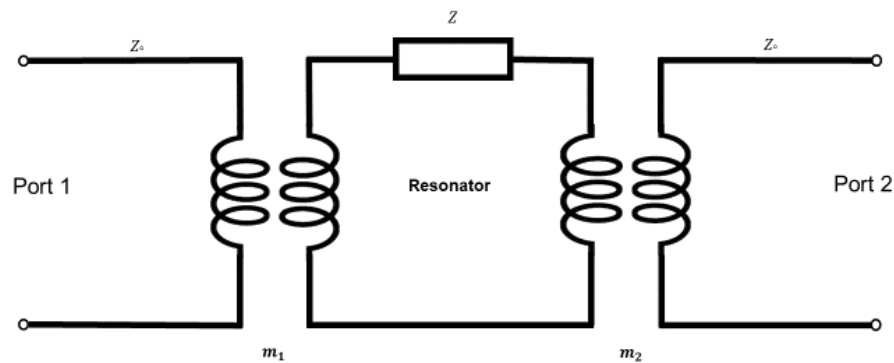


Figure 5-50: The equivalent circuit of a two-port, loop-coupled resonator. The resonator is modelled as a series LRC circuit of impedance  $Z$ .

The coupling loops are terminated in the input and output lines which creates a pair of mutual inductances  $m_1$  and  $m_2$  at port 1 and 2 respectively of the resonator. The geometry plays a depended role such as the orientation and position relative to the resonator in the loop area. The symmetric coupling with a single mutual inductance  $m = m_1 = m_2$  can show identical loops. The resonator is modelled as a series LRC circuit which the impedance  $Z(\omega)$  defined in Equation 5-65. The resonant frequency  $\omega_0$  and the unloaded Q factor  $Q_0$  can express in the following Equations.

$$\omega_0 = \frac{1}{\sqrt{LC}} \quad (5-75)$$

$$Q_0 = \frac{\omega_0 L}{R} \quad (5-76)$$

The forward voltage transmission coefficient  $S_{21}$  and the power transmission coefficient  $P(f)$  in the frequency domain  $f = \frac{\omega}{2\pi}$  are the resonant for analysing the loop couple resonator in Figure

5-49 in the limited of high  $Q_0$ .

$$S_{21}(f) = \frac{2\sqrt{g_1 g_2}}{1 + g_1 + g_2 + 2jQ_0 \frac{f - f_0}{f_0}} \quad (5-77)$$

$$P(f) = |S_{21}|^2 = \frac{4g_1 g_2}{(1 + g_1 + g_2)^2 + 4Q_0^2 \left(\frac{f - f_0}{f_0}\right)^2} \quad (5-78)$$

Here  $g_1$  and  $g_2$  the coupling coefficient can be express as

$$g_1 = \frac{\omega_0^2 m_1^2}{Z_0 R} = \frac{\omega_0 m_1^2 Q_0}{L} \quad (5-79)$$

$$g_2 = \frac{\omega_0^2 m_2^2}{Z_0 R} = \frac{\omega_0 m_2^2 Q_0}{L} \quad (5-80)$$

Here,  $Z_0$  is the characteristic impedance of the input/output line (usually  $50\Omega$ ). As there is a correlation between  $g$  and  $m^2 Q_0$ . Therefore, stronger coupling, there is a higher power transmission at resonance obtaining by increasing  $m$ ,  $Q_0$  or by increasing both.

Then, at performance measurements, we will obtain the loaded quality which affecting the coupling coefficients to expand the 3dB bandwidth. Here, the loaded Q factor reduces the measures by the factor of  $1+g_1+g_2$ . Moreover, the peak transmitted power  $P_0$  is measured at the resonant frequency. At  $\omega = \omega_0$ ,  $|S_{21}|^2$  can be derived as

$$|S_{21}|^2 = \frac{P_0}{1 + 4Q_L^2 \left(\frac{\omega - \omega_0}{\omega}\right)^2} \quad (5-81)$$

Where

$$P_0 = \left(\frac{2g}{1 + 2g}\right)^2 \quad (5-82)$$

And

$$Q_L = Q_0(1 - \sqrt{P_0}) \quad (5-83)$$

Where,  $P_0$  is the peak power at resonance,  $Q_L$  is the loaded Q factor which is smaller than  $Q_0$  due to the loading effects of the coupling

At symmetric coupling ( $g_1 = g_2$ , identical coupling), the standard Lorentzian function  $\frac{1}{1+x^2}$  with appropriate translation and scaling. The  $|S_{21}|^2$  the measurement from the network analyser can then either be a non-linear curve fit to the above Equation or can be directly extracted the measurement of  $P_0$  and  $Q_L$ . In general, a non-linear curve fit is preferred as it is less liable to noise, practically at low power levels.

Symmetric coupling is traditionally achieved by ensuring  $S_{11}$  and  $S_{22}$  have troughs of the same amplitude. Alternatively, the method described above can also be used.

In our research, transmission measurements have been made, which require two ports. Furthermore, the coupling technique has used capacitive coupling, which exploits electric rather than magnetic field interactions.

### 5.12.1 RESONANCE SKEW AND CORRECTION

For a mode with a high Q factor and no nearby interfering modes, Equation 5-78 is accurate. Conversely, if there are other modes nearby or cross-coupling between the coupling antennas, the curve shows a considerable skewed and Equation 5-78 is not a good fit. Figure 5-51 illustrates an arbitrary number of modes and cross-couplings in the resonator model.

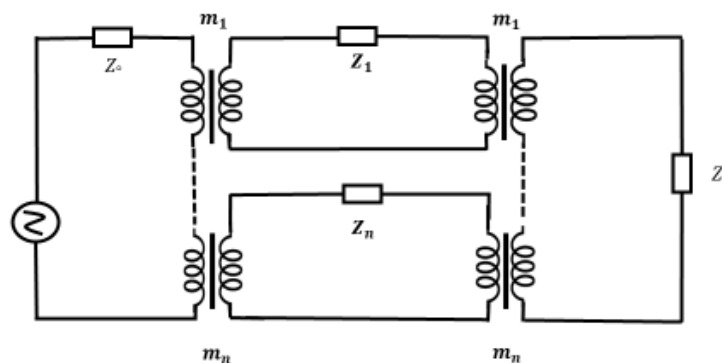


Figure 5-51: Microwave resonator model with an arbitrary number for resonance or crosstalk terms.

At N terms,  $S_{21}$  response can be derived as

$$S_{21,N} = \frac{2 \sum_{n=1}^N \frac{g_n}{G_n(\omega)}}{1 + 2 \sum_{n=1}^N \frac{g_n}{G_n(\omega)}} \quad (5-84)$$

Here  $G_n = \frac{Z_n}{R}$ . In resonant case,  $Z_n$  equals to Equation 5-73

$$Z(\omega) = R + j\omega L + \frac{1}{j\omega C} \approx R \left[ 1 + j2Q_0 \left( \frac{\omega - \omega_0}{\omega_0} \right) \right] \quad (5-85)$$

Then the result of the

$$G_n = 1 + j2Q_0 \left( \frac{\omega - \omega_0}{\omega_0} \right) \quad (5-86)$$

$$G_n^{ind} = \frac{j\omega L_{skew}}{R} \quad (5-87)$$

Depending on the nature of the coupling (capacitive in our case), the power transmission response can be defined as follows.

$$|S_{21}|^2 = \frac{2g \left( 1 + \frac{G_{res}(\omega)}{G_{skew}(\omega)} \right)}{G_{res}(\omega) + 2g \left( 1 + \frac{G_{res}(\omega)}{G_{skew}(\omega)} \right)} \quad (5-88)$$

To minimise cross-coupling, ideally, the skew impedance should be a lot larger than the resonator impedance to eliminate the skew term in the dominator. A correction small amount skew Equation has been obtained by reorganising and substitutions [132]

$$|S_{21}|^2 = \frac{P_0 + 2P_0 \frac{G_{res}}{G_{skew}} + P_0 \left( \frac{G_{res}}{G_{skew}} \right)^2}{1 + 4Q_L^2 \left( \frac{\omega - \omega_0}{\omega_0} \right)^2} \quad (5-89)$$

Using the above Equation, a representative comparison between resonator and skew capacitance can be made. The following Figure (Figure 5-52) shows the normalised resonance as the amount of skew capacitance increases.

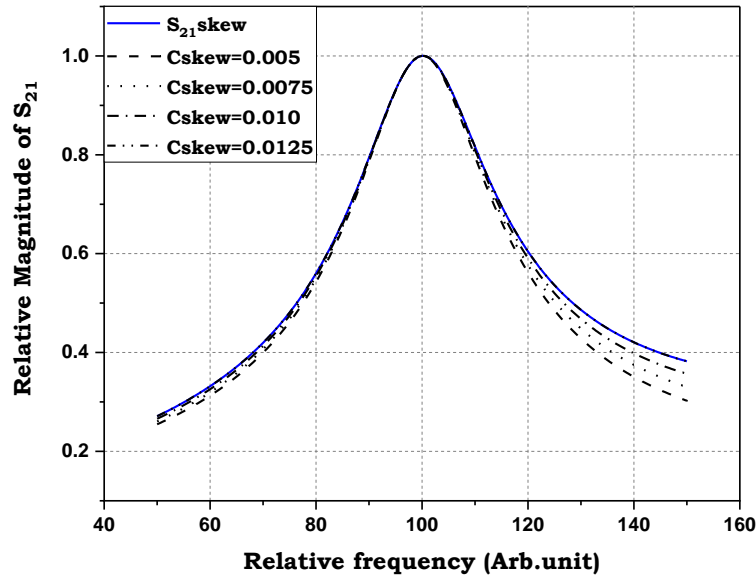


Figure 5-52:  $|S_{21}|$  shown the no skew case ( $S_{21}$ -line) and for increasing skew ratio.

As can be seen from this, the apparent BW is increasing as the skew capacitance increases. The BW changes are highlighted below in Figure 5-53.

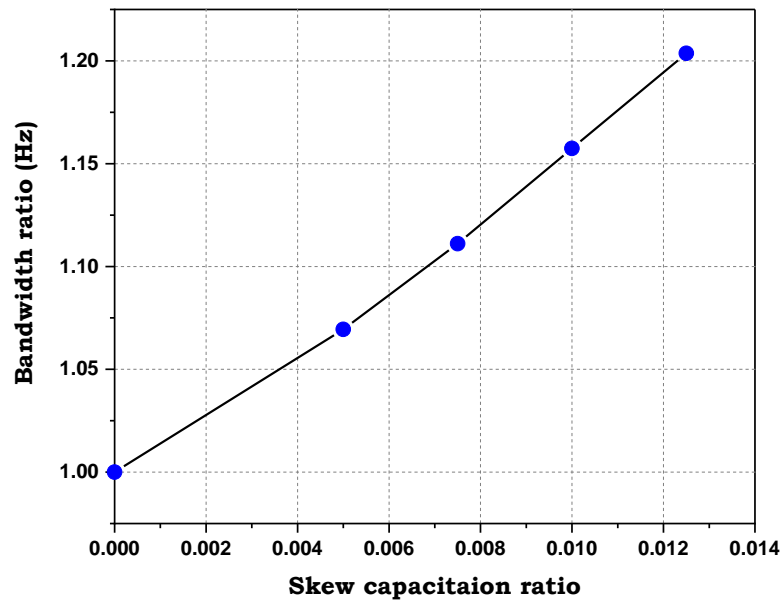


Figure 5-53:  $|S_{21}|$  shown the no skew case ( $S_{21}$ -blue) and for increasing skew ratio.

### 5.13 EXPERIMENT OF DE-SKEW

The de-skewing process of the resonance curves obtained from the coaxial probe utilises a combination of Excel and MATLAB and is described as follows. One of the harmonics, centred

at 4.315 GHz was chosen to demonstrate the process. The skewed resonance peak is shown below in Figure 5-54.

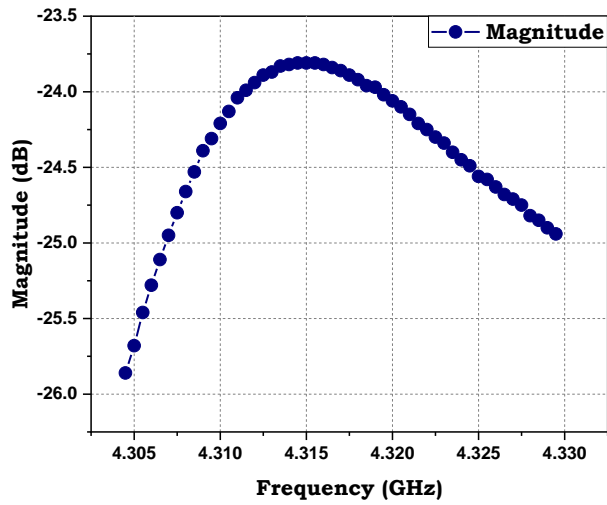


Figure 5-54: Example of a typical skewed resonance curve.

The first stage is to use the phase and magnitude information to plot the resonance on a polar chart as shown in Figure 5-55. The MATLAB circle fit routine( Appendix B-1) [147] was utilised to find the centre of the circle and the corresponding radius of the best fit circle. The location of the peak of the resonance is highlighted in red and the cross represents the circle centre.

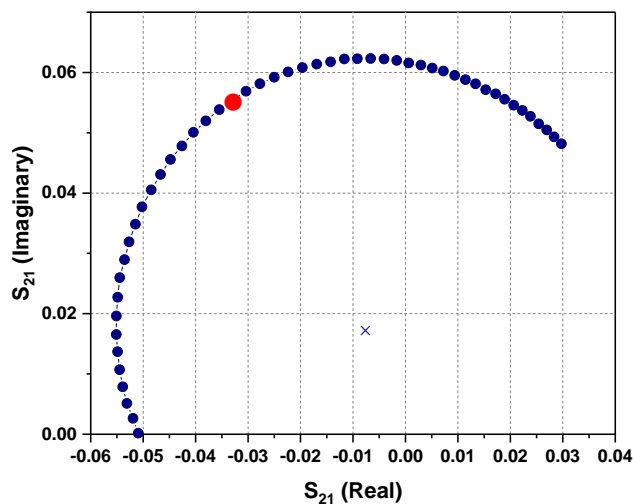


Figure 5-55: The polar plot of the resonance above, the position of the peak is highlighted with the red dot and the centre of the circle is denoted with the cross.

Since the peak of the resonance is meant to be on the real axis, the de-skewing process requires that the circle is rotated and displaced such that the peak is positioned on the real axis.

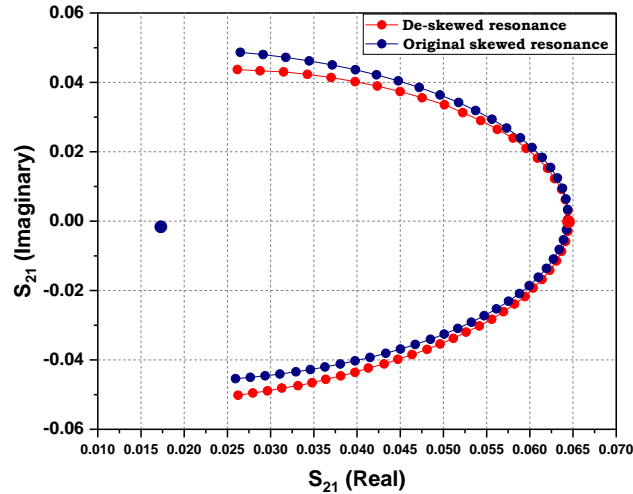


Figure 5-56: De-skewed resonance (red) and original skewed resonance (blue).

Figure 5-56 above shows the original resonance trace, still skewed, but in the correct position on the polar chart (i.e., the centre and peak on the real axis). The MATLAB circle fit (Appendix B-2) then performs a weighted fit to the raw data and generates the best fit circle as shown in red. (The weighted fitting gives priority to the data points near the centre of the resonance peak.) The fitted data points are then converted back to  $S_{21}$  vs frequency and the resultant, de-skewed resonance is shown in Figure 5-57.

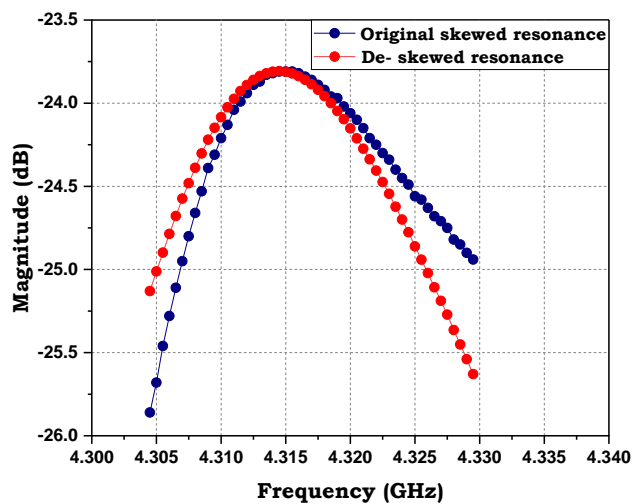


Figure 5-57: De-skewed resonance (red) and original skewed resonance (blue).

At this stage in the research, the process of de-skewing these resonances is timely and requires a manual transfer of data between Excel and MATLAB. Ideally, this process can be streamlined and incorporated into the LabVIEW programme that manages the data acquisition.

## 5.14 CHAPTER SUMMARY

This chapter introduced several parts of the theoretical part of microwave detection. The first step presented the concept of microwave measurements, including the interaction between different materials and, alternatively electric fields. This explains the simple explanation to understand the permittivity and the reduction of the electric field due to the presence of this material (polarized). As the pure DI- W used in our research as a reference liquid. A simple Debye mode of DI-W has been built using the Debye relaxation equation to calculate the real and imaginary permittivity pertinent to this study. Additionally, an Excel-based calculator has been developed for providing the real and imaginary permittivity as a function of frequency and temperature and utilizes the parameters ( $\epsilon(\omega)$ ,  $\epsilon(\infty)$  and ( $\tau$ )).

Then, the basic principle for deriving the equation of the effective permittivity demonstrated to use in the theoretical calculation for three particle sizes 2, 0.8 and 0.413  $\mu\text{m}$  in between the stock from the manufacture (2.5%) and various dilutions (2.25% to 1.25%) for the frequency range 100 MHz to 3GHz as the first instance. The experimental method for the non-resonant method has been done for the same particles, dilutions, and the same range of frequency. A significant separation has been found for the whole range at magnitude complex permittivity and the real effective permittivity when comparing water, stock, and various dilutions. The reflection  $S_{11}$  showed good separation between water and dilutions between 100 to 200 MHz at all particles in experiment work (open-ended technique).

The final part presented the theory of the resonant coaxial probe. This part includes how the characteristic of the signal propagates and loss along with transmission. It introduces the resonator principles and the interaction on the tip of the coaxial cable. The ADS simulation of its novel T- Structure and capacitive coupling arrangement has been done at a frequency range of 0.1 to 6 GHz to emulate the same experimental behaviours. This simulation compares just symmetry and symmetry, and asymmetry coupling capacitor has done for BW, CF, Q factor and  $S_{21}$  for different coupling capacitor values. On comparing the symmetry coupling capacitor, the differences in the BW started to become significant at higher frequencies 2.3 to 5.4 GHz for all capacitor values. However, the Q factor reduces at a higher frequency. The apparent increase in the BW and decrease in the Q factor is likely related to the skew of a high order. The variation in insertion loss  $S_{21}$  generally increases as frequency increases as the associated losses in the structure are frequency dependent.

Regarding the comparison between the symmetry and asymmetry coupling values, asymmetrical values appear to be positioned in between that of the symmetry case for BW, Q factor and  $S_{21}$ . The effect of the coaxial cable length was studied. Importunately here, the number of resonant frequencies showed an increase with increasing the length of the coaxial cable. Furthermore, a substantial reduction in the loss has increased the coaxial length for the whole frequency range.

A slight shift has been seen when comparing the experimental data set up of air and water samples for the whole range of frequency 0.1 to 6 GHz to emulate the experiment work behaviours. Moreover, a remarkable difference showed for the first and the last mode (0.38 and 5.43 GHz), respectively and a significant difference on comparing the stock (0.154 M) and two dilutions ( $C_1=0.077$  M and  $C_2=0.039$  M). A combination of Excel and MATLAB has been utilised for the de-skewing process of the resonance curves.

---

# CHAPTER 6

## MICROWAVE CAVITY TECHNIQUE

### 6.1 INTRODUCTION

As a means of reference, the complex permittivity of test solutions of NaCl and Polystyrene suspensions are measured using the cavity perturbation technique utilising the cylindrical cavity resonators (CCRs) used by researchers at the Centre for High-Frequency Engineering at Cardiff (CHFE). To re-cap, the insertion loss, resonant frequency, and resonance bandwidth are used to obtain the complex permittivity of the material under test (MUT). Together with relative measurements, this can provide a measure of the concentration of NaCl in solution and polystyrene spheres in suspension (PS). The NaCl concentration and water content of cells can differentiate between normal and cancerous cells [107]. The role of PS as a cancer phantom has been explained in section 2.1.4.1. This chapter will cover the theoretical part (basic principle of the cavity, cavity perturbation theory), practical part (experimental measurements using cavity and Eppendorf tube for two sample preparations commercially obtained saline and Lab prepared saline and polystyrene spheres in suspension (PS) concentrations and other experiments by using Eppendorf long thin tube for Lab prepared saline and PS dilutions) and converting microwave measurements to permittivity and finally enhanced exponential correction calculation.

### 6.2 BASIC PRINCIPLE OF THE CAVITY RESONATOR

To determine the complex permittivity of a MUT using non-destructive methods, the application of perturbation theory for a microwave cavity can be used.

The basic principle of this method is to measure the resonant characteristic of a hollow metal space with and without the sample inside, as shown in Figure 6-1. This hollow geometry can be rectangular, cylindrical or spherical, and the resonant frequency of the cavity is determined by the geometry. In this hollow region, the sample (MUT) can perturb the electromagnetic standing waves within the boundaries of this space, containing both nodes and anti-nodes in the E and H-field depending upon the wavelength. For a rectangular space, the standing waves are dependent upon sinusoids, whereas curved spaces are dependent upon Bessel functions [135].

As a result, changes in the resonant frequency, bandwidth, and insertion loss occur and are related to the material's electric or magnetic properties. These properties can be measured independently depending on whether the perturbation occurs in a region of a high electric or high magnetic field, respectively.

So-called transverse modes occur because of boundary conditions imposed on the wave by the waveguide (cavity). For instance, in a hollow metal waveguide, the wave must have zero tangential electric field at waveguide walls. The pattern of the electric field is then restricted to that which can fit between the walls (quantization). The waveguide modes can be classified as Transverse electromagnetic (TEM) modes; here, there is neither an electric nor magnetic field component in the direction of propagation. Transverse electric (TE) modes, where there is no electric field component in the direction of propagation. Transverse magnetic (TM) modes have no magnetic field component in the direction of propagation. Finally, there are hybrid modes, non-zero electric and magnetic fields in the direction of propagation.

The cavity measurements can be highly sensitive owing to the potentially high Q factors, which are due to the high density of electromagnetic energy stored in the space due to the high reflectivity of the metal walls and minimal surface current losses [148, 149]. Also, the highest sensitivity occurs when the sample is placed parallel to the field.

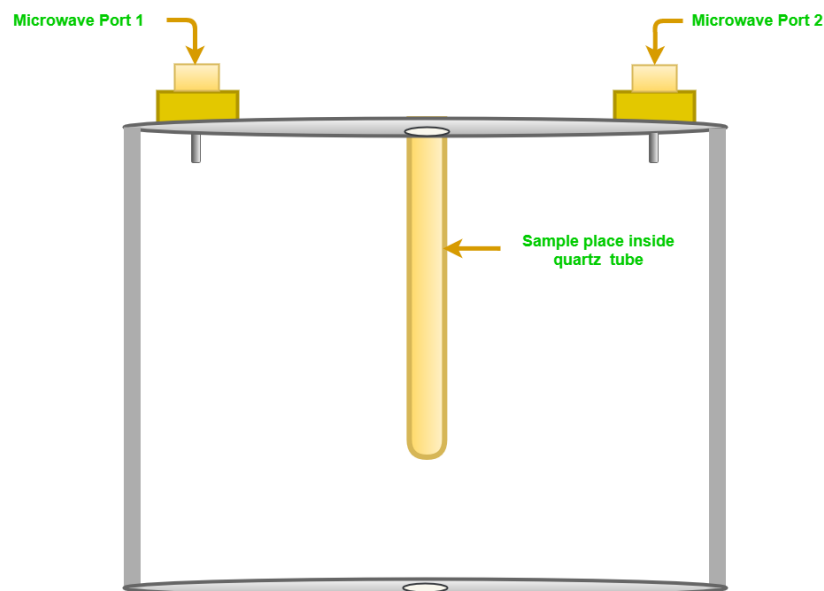


Figure 6-1: The physical cavity principle.

### 6.3 CAVITY PERTURBATION THEORY

Cavity perturbation can be described as a technique for measuring the variation in the electric and magnetic fields caused when inserting a sample into the resonator. In our research, the magnetic field interactions are ignored since none of the materials studied here have magnetic permeability. Therefore, this section will focus on the dielectric field theory. The simplest way to understand this is through the derivation of Equations for obtaining the complex permittivity, starting with:

$$\Delta u = \frac{1}{2} p E_0 \quad (6-1)$$

Here  $\Delta u$  is a change in the energy of the resonator,  $p$  is the polarization of the material inside the resonator and  $E_0$  is the externally applied energy. The change is with respect to a resonator cavity with no material inside, the so-called un-loaded cavity.

The real part ( $Re(pE_0)$ ) represents the shift in the resonant frequency ( $\frac{\Delta f}{f_1}$ ) and which corresponds to the stored energy in the resonator. The imaginary part ( $Im(pE_0)$ ) represents the phase lag of the material as its polarization tries to maintain alignment with the externally applied field. This is defined as a shift in the reciprocal Q factor of the resonator  $\Delta\left(\frac{1}{Q}\right)$  and corresponds to the power dissipated.

When an externally applied electric field  $E_0$ , passes through a dielectric material, the field inside the material can be expressed as:

$$E_{in} = \frac{E_0}{1 + N(\varepsilon - 1)} \quad (6-2)$$

Where N is a depolarisation factor that depends on the geometry of the material and  $\varepsilon$  is the complex permittivity. In terms of polarisation, this can be expressed as:

$$p = \varepsilon_0(\varepsilon - 1)E_{in}V_s \quad (6-3)$$

Where  $V_s$  and  $\varepsilon_0$  are the volume sample and permittivity of free space, respectively.

Substituting Equation 6-2 gives:

$$p = \frac{\varepsilon_0(\varepsilon - 1)}{1 + N(\varepsilon - 1)} E_0 V_s \quad (6-4)$$

We may now utilise this to define the stored energy parameter:

$$\frac{\Delta f}{f_1} = \frac{-Re(p E_0)}{4 u} \quad (6-5)$$

Where,

$$u = \frac{1}{2} \varepsilon_0 \int_V E^2 dV \quad (6-6)$$

$$\text{Then,} \quad \frac{\Delta f}{f_1} = \frac{-Re(p E_0)}{2\varepsilon_0 \int_V E^2 dV} \quad (6-7)$$

$$\text{Giving,} \quad = \frac{\varepsilon_0(\varepsilon - 1)|E_0|^2}{2\varepsilon_0(1 + N(\varepsilon - 1)) \int_V E^2 dV} \quad (6-8)$$

Here  $\frac{|E_0|^2}{\int_V E^2 dV}$  represents the sample volume  $V_s$ , however  $\frac{\int_V E^2}{|E_0|^2}$  represents effective volume  $V_{eff}$

$$\frac{\Delta f}{f_1} \cong -Re \left[ \frac{\varepsilon - 1}{1 + N(\varepsilon - 1)} \right] \frac{V_s}{2V_{eff}} \quad (6-9)$$

Where  $V_s$  is the sample volume and  $V_{eff}$  is the effective volume.  $\varepsilon$  Equals  $\varepsilon' - j\varepsilon''$ .

For long thin samples, we can assume that  $N=0$ . With this simplification, energy storage mechanisms are measured through the real part  $\varepsilon'$  (frequency) and any energy loss mechanisms are measured through the imaginary part  $\varepsilon''$  (quality factor) as expressed in the Equations below:

$$\frac{\Delta f}{f_1} = -(\varepsilon' - 1) \frac{V_s}{2V_{eff}} \quad (6-10)$$

$$\Delta \frac{1}{Q} = \frac{1}{Q_L} - \frac{1}{Q_0} = \varepsilon'' \frac{V_s}{V_{eff}} \quad (6-11)$$

Where  $Q_L$  is the loaded quality factor and  $Q_0$  is the unloaded quality factor.

## 6.4 EXPERIMENTAL MEASUREMENTS USING CYLINDRICAL CAVITY RESONATORS

### 6.4.1 INTRODUCTION

Whilst the use of CCRs is well established in distinguishing various concentrations of the normal saline and the suspension polystyrene, they are often extremely sensitive to external factors such as temperature, movement, and sample changes. The descriptions that follow would not be

complete without a section highlighting the inherent difficulties associated with performing these experiments.

## 6.5 SAMPLE PREPARATION, CORRECTION SOLUTIONS AND MEASUREMENTS

This section will cover the measurements on commercially obtained saline, detection limits and sample classification and measurements of lab prepared saline dilutions.

### 6.5.1 MEASUREMENTS ON COMMERCIALY OBTAINED SALINE

The normal saline (sodium concentration) play an essential role in detecting cancer as Damadian found that tumour cells have more sodium concentration in comparison to the normal cells [88]. Thus, the first impression is to test the performance of our system for detecting with the commercial stock of normal saline. This section will consist of the preparation dilution steps, correction steps and results for commercial obtained saline.

#### 6.5.1.1 PREPARATION DILUTION STEPS FROM COMMERCIAL OBTAINED SALINE

A range of saline dilutions ( $0.45$  to  $5.49E-05$ ) % w/v or ( $0.077$  to  $9.400E-06$ ) Molarity were prepared from the original stock  $0.9\%$  w/v ( $0.154$  M) and purchased from Boot's Pharmacy. The half dilution technique has been applied for the preparation of almost all samples mentioned in this thesis. Figure 6-2 illustrates the dilution steps. For precise preparations, an electronic balance was used for checking the weight at each step. Small saline concentrations have been prepared in an attempt to provide a means for identifying detection limits and will lead to developing a sensor to potentially detect cancer in vivo.

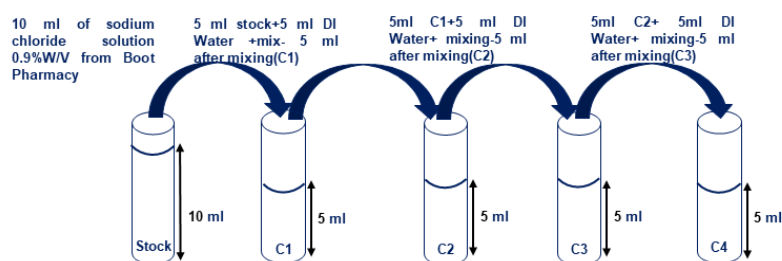


Figure 6-2: The preparation dilution steps from Commercially Obtained Saline.

### 6.5.1.2 CORRECTION STEPS FOR COMMERCIAL OBTAINED SALINE

The measurement of the microwave cavity perturbation technique affecting by factors due to a temperature change such as environmental changes or exothermic/ endothermic chemical reactions within the sample [150-153]. The change in the temperature affecting the cavity geometry which is the function of measuring the resonant frequency and the bandwidth of the cavity. Therefore, the temperature of the cavity and the environment are routinely recorded during all the measurements made in this study, and where possible, the effect of temperature has been compensated for. However, there are a number of situations that make measuring temperature quite difficult. In the first instance, the sample's temperature can often be different from that of the resonator. Simply because the samples need to be handled, means that the sample temperature is often elevated before the sample is placed into the cavity. Unfortunately, directly measuring this accurately is not possible. However, a warm sample once placed into the cavity displays a very distinctive exponential cooling which, often, can easily be compensated for. Details of this particular aspect of data correction will be presented later in section o. Another aspect of data correction was discovered following the observation of many repeated experiments and is highlighted below. Finally, by virtue of the fact that the CCR is multi-mode, there are resonant modes that can interact with the sample volume (the sensing modes) and those that don't interact with the sample volume (reference modes). There are two distinct modes that this particular cavity resonates at. One interacts strongly with the sample: the  $TM_{010}$  E-field mode at 2.492 GHz and another, the reference mode: the  $TM_{210}$  E-field mode at 5.33 GHz, which does not interact. Figure 6-3 shows the electric field distribution for these resonant modes generated using COMSOL and is reproduced from Clark [154].

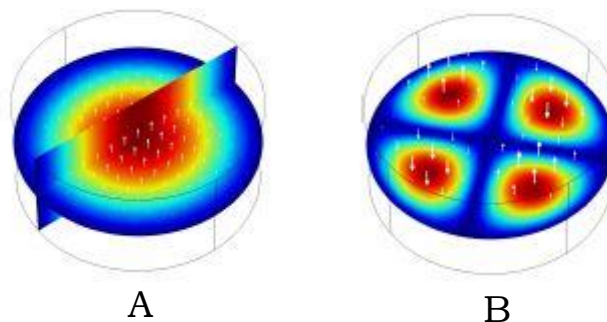


Figure 6-3: COMSOL simulations of E-field distributions for two cavity modes. A:  $TM_{010}$  E-Field at 2.45 GHz, B:  $TM_{210}$  E-Field at 5.33 GHz

The regions of a high electric field are indicated by the red regions, and it can be clearly seen that

the centre of the cavity, where the sample is placed, overlaps with the electric field strongly for A (the sensing mode) and very little for B (the reference mode).

Figure 6-4 shows a typical  $S_{21}$  spectrum obtained from the VNA over the range 2.1 GHz to 6 GHz. The sensing and reference modes are highlighted.

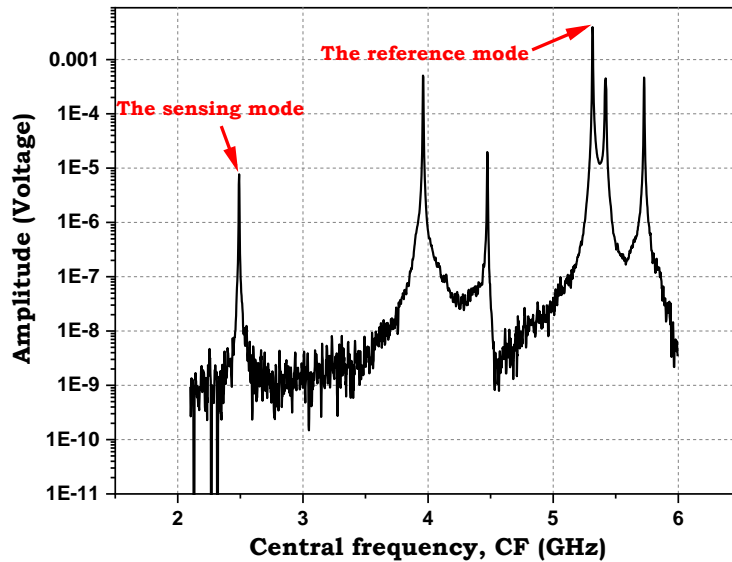


Figure 6-4:  $|S_{21}|$  for the CCR used with sensing and reference modes highlighted.

There is a strong correlation between these two modes, and the change in their centre frequency, as a function of the temperature of the CCR, is fundamentally linked. Figure 6-5 shows this correlation and provides a robust method for tracking the global changes that may affect the resonator, such as temperature and enabling a correction to the experimental data to be made.

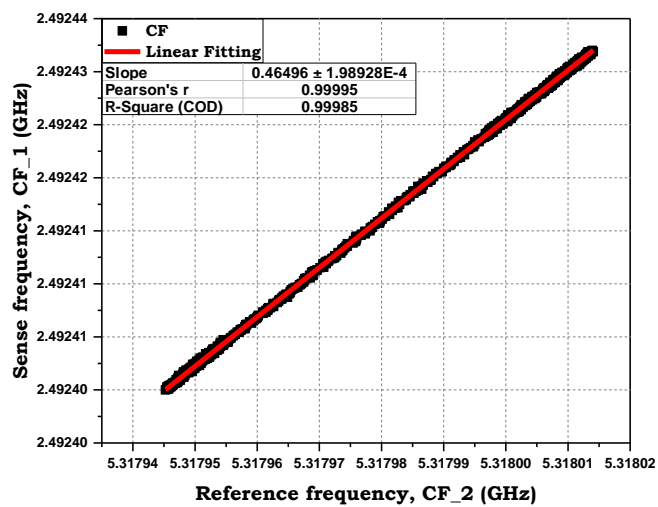


Figure 6-5: Relationship between the signal mode (vertical axis) and the reference mode (horizontal axis) measured over a period of time where the temperature of the cavity was allowed to change. Correlation coefficient 0.999.

### 6.5.1.2.1 REFERENCE MODE FREQUENCY CORRECTION

To minimise the variation in the samples, a single DI-W Eppendorf was placed into the CCR, and its Q factor was measured over a period of time (typically 30 minutes to allow for some environmental temperature change). This particular example of obtaining a correction reference is shown below in Figure 6-6. The Q factor ( $Q_{(SENSE)}$ ) is measured along with the central frequency (CF) of the reference resonance. Since the reference resonance is insensitive to the sample, any drift in the CF of the reference ( $CF_{(REF)}$ ) will equally affect the CF of the sensing resonance  $CF_{(SENSE)}$ . Despite the measurement of  $Q_{(SENSE)}$  being quite noisy, there is a distinct correlation between  $Q_{(SENSE)}$  and  $CF_{(REF)}$ . A linear fit to this data is obtained and can be used to correct the measurement of saline samples subsequently

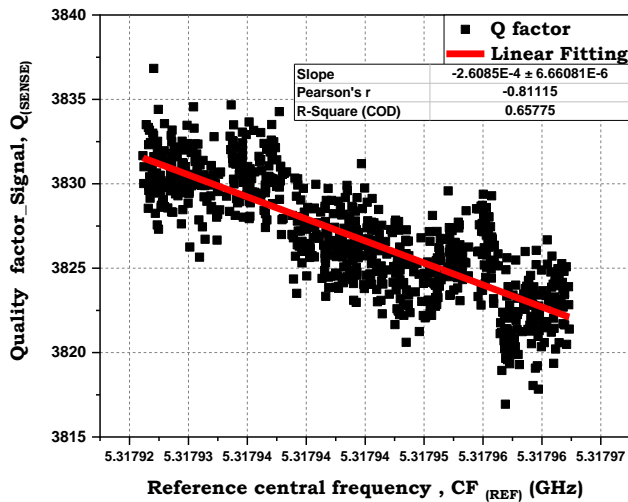


Figure 6-6: Fitting correlation between the  $Q_{SENSE}$  and  $CF_{REF}$  for DI-W.

Since the Q factor is derived from  $CF_{(SENSE)}$ , the correction may be applied directly to  $Q_{SENSE}$  or  $CF_{(SENSE)}$ , requiring the Q factor to be re-calculated from this and the BW data  $BW_{(SENSE)}$ . A simple illustration of the correction process is shown (Figure 6-7).

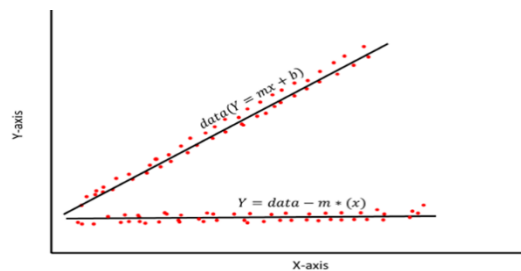


Figure 6-7: Correction linear equation.

---

This method of tracking a reference mode provides a robust and reliable means of correcting for environmental changes that affect the CCR.

With the data now corrected for  $CF_{(REF)}$ , essentially environmental temperature corrected, a further correlation has been observed between each of  $Q_{(SENSE)}$ ,  $BW_{(SENSE)}$ ,  $|S_{21}(SENSE)|$  and  $CF_{(SENSE)}$ . This correlation may not at first seem intuitive. However, it is based on extensive observations and is largely down to very subtle changes in sample orientation, meniscus and possibly bubbles. This was first observed when the same sample was repeatedly removed and re-inserted into the resonator. One would expect the parameters  $Q_{(SENSE)}$ ,  $BW_{(SENSE)}$ ,  $|S_{21}(SENSE)|$  to remain the same. In fact, the orientation of the sample placement was different in each case and found to produce measurable shifts in these parameters and also correlated with changes in  $CF_{(SENSE)}$ . It appears that small changes in  $CF_{(SENSE)}$  provide an insight into small changes in sample volume/mode volume overlap. Since the machining of the cavity is not perfect, the sample holder is likely not square with the cavity axis. This hypothesis is largely confirmed by observing the change in these parameters as a single sample is rotated in its holder. Fluctuations in the measured parameters as the sample was rotated in its holder at the top of the cavity were found to repeat following each complete revolution. Following this observation, a mechanical marker was placed on the cavity to ensure that the samples were inserted at the same orientation each time measurement was carried out. When multiple DI-W samples were used, noting that the orientation was identical in each case, again, subtle variations in  $Q$ ,  $BW$  and  $|S_{21}|$  were observed and were found to correlate with  $CF_{(SENSE)}$ . These variations were much smaller than that observed with sample orientation and are speculated to be indicative of differences in the way the meniscus is formed in each sample. It was not possible to characterise the meniscus, suffice to say, there were observable differences between some samples. These observations were further reinforced in later measurements when PS samples were used. Shaking these samples, in order to disperse the PS spheres, led to bubble formation and was always made evident by a curious shift in the measured parameters. Whilst the evidence for this is largely circumstantial, there is nevertheless a significant correlation between  $Q_{(SENSE)}$ ,  $BW_{(SENSE)}$ ,  $|S_{21}(SENSE)|$  and  $CF_{(SENSE)}$ , and subsequent correction for this does deliver improvement in the spread of measured values. One such example of a correlation between  $Q_{(SENSE)}$  and  $CF_{(SENSE)}$  is shown in Figure 6-8 below for the experiment done to study the effect of the frequency on the microwave measurements by using the DI-W.

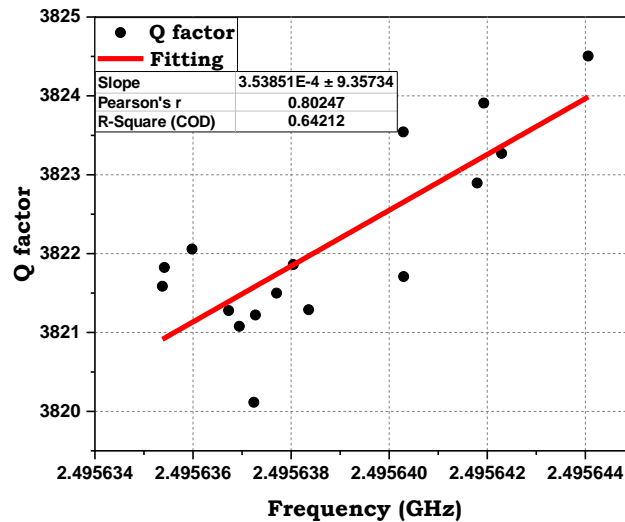


Figure 6-8: Affection cavity frequency correction of Q factor.

### 6.5.1.2.2 TEMPERATURE CORRECTION

Whilst the effects of temperature on the CCR have been removed, there are still additional components in the system that are affected by temperature. These are mainly the interconnecting cables that link the VNA to the CCR. To clarify this, the cable effects are all part of the noise. In our experiment, despite the big and high SNR of the  $S_{21}$  signal, the noise from the cable effect on the  $S_{21}$  is negligible but not completely gone. Therefore, a check has been done to remove it perfectly. Since the room temperature is also recorded with the other parameters, it is easy to relate any given measurement to the room temperature at that time. Following some data averaging, the graph below (Figure 6-9) highlights the strength of the correlation between temperature and Q factor for example.

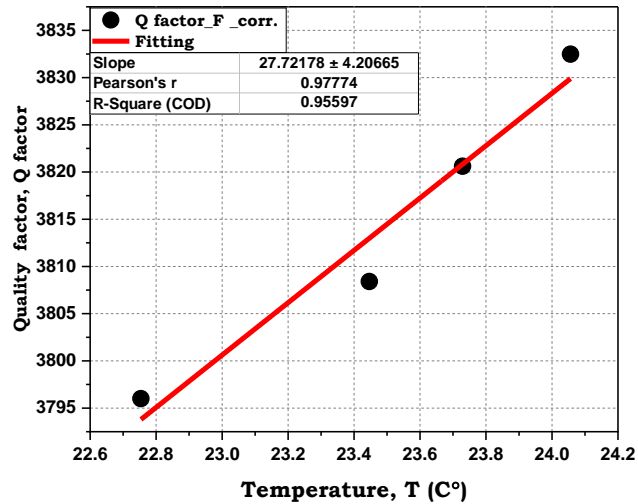


Figure 6-9: Effect of cavity temperature correction for Q factor after frequency correction (Q factor\_F\_corr.).

### 6.5.1.2.3 EXPONENTIAL CORRECTION

As mentioned earlier, each time a sample is inserted into the resonator, the temperature falls exponentially. This is because of the temperature difference between the ambient and the cavity resonator. In many cases, the sample was also warmed up by hand to exaggerate this effect. Once the sample is placed inside the resonator, the heat is drawn from the sample by thermal conduction into the metallic resonator body. It is possible to characterise this heat loss as a means to predict the temperature of the sample during the measurement window. If the temperature at any given time can be calculated, then the sample temperature dependence of the measured Q factor of the resonance  $|S_{21}|$ , and bandwidth can be corrected. The basic Equation describing the exponential change in temperature of a body is given by:

$$T(t) = T_c + (T_0 - T_c)e^{-kt} \quad (6-12)$$

In this case, the parameter  $T_c$  is the temperature of the resonator and represents the asymptote. Assuming the heat is lost to the resonator body, this is a reasonable estimate. Since the measurement system makes multiple measurements at fixed intervals over a period of time, the following formula can be used to determine the asymptotic temperature of the sample. Thus, negating the need to measure the sample temperature directly. This is a *novel* idea that may have merit in other applications.

$$T_c = T_1 - \frac{(T_1 - T_2)}{T_1 - 2T_2 - T_3} \quad (6-13)$$

$T_1$ ,  $T_2$  and  $T_3$ , they are three temperatures from the exponential curve of the temperature with

the same time interval (Figure 6-10). Therefore, Equation 6-13 has applied for the Q factor,  $|S_{21}|$  and BW data measurements after frequency and temperature correction.

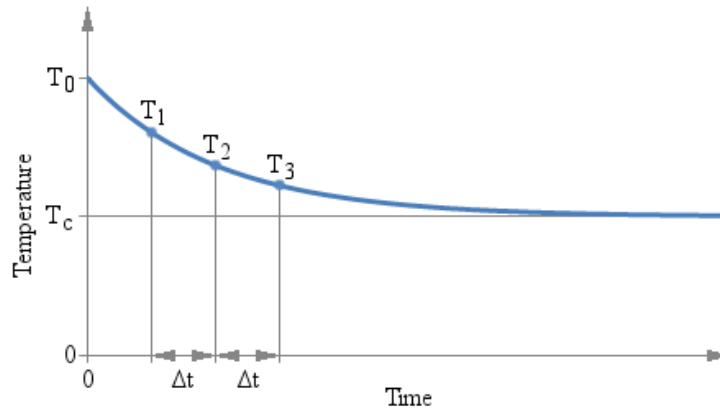


Figure 6-10: Exponential change of the temperature.

The exponential correction technique is an extremely useful method of removing the effect of sample temperature. The above simplification, however, is not robust enough, especially for data that is noisy. The above formula can be easily implemented in Excel. Later, a more robust pre-processing of the raw data will be introduced that utilises a more sophisticated MATLAB curve fitting algorithm to determine the asymptotic value of the relevant parameter as recorded by the system. Clearly this is an added overhead in the process of data preparation and correction.

### 6.5.1.3 RESULTS FOR COMMERCIAL OBTAINED SALINE

The results obtained from a number of experiments are collated and corrected in the section below. The LabVIEW code written to coordinate the data acquisition polls the VNA for  $|S_{21}|$  data at a pre-defined centre frequency and span. Two different requests to the VNA are made, representing the signal mode and reference mode. The BW, CF,  $|S_{21}|$  and calculated Q factor are outputted to a data file along with various temperature measurements. Each data point is time stamped with a millisecond count. A total of 150 records of these variables are made for each sample inserted into the resonator. This represents a period of up to about 10 minutes. Clearly, many environmental factors can change at this time. This is why it is important to apply an appropriate correction to the recorded data. A total of 17 different samples are placed into the resonator, equating to many hours of experimental effort. For the graphs shown below, a sequence of 14 half dilutions was tested, along with the stock solution and two DI-W samples at the start and end of each block. Differences in the two DI-W measurements can assist with identifying any inherent drift in the data over that timeframe. This block was then repeated twice

more to check for system measurement stability, consistency, and reproducibility.

The first two Figures serve to highlight the volume of data obtained from each experiment and the additional processing required to gather the processed results. Figures 6-11, 6-12 and 6-13 show the Q factor,  $|S_{21}|$  and BW respectively. Each graph shows the raw data (black), the  $CF_{(REF)}$  correction (yellow), subsequent temperature correction (green) and exponential correction in red. Whilst this is not an ideal way to present the data, it does serve to highlight all the necessary preparation required to generate the results shown in subsequent sections. It is obvious; however, that the different saline concentrations follow a distinct trend. One of these will be studied in more detail. The concentrations labels represent the following dilutions.

Table 6-1: Dilutions prepared from commercially obtained saline (BOOT's pharmacy)

Concentration	Abbreviation	Weigh in % w/v	Molarity(M)
Stock	S	9.00E-01	1.54E-01
Half stock	C1	4.50E-01	7.70E-02
Half 1st concentration	C2	2.25E-01	3.85E-02
Half 2nd concentration	C3	1.13E-01	1.93E-02
Half 3rd concentration	C4	5.63E-02	9.63E-03
Half 4th concentration	C5	2.81E-02	4.81E-03
Half 5th concentration	C6	1.41E-02	2.41E-03
Half 6th concentration	C7	7.03E-03	1.20E-03
Half 7th concentration	C8	3.52E-03	6.02E-04
Half 8th concentration	C9	1.76E-03	3.01E-04
Half 9th concentration	C10	8.79E-04	1.50E-04
Half 10th concentration	C11	4.39E-04	7.52E-05
Half 11th concentration	C12	2.20E-04	3.76E-05
Half 12th concentration	C13	1.10E-04	1.88E-05
Half 13th concentration	C14	5.49E-05	9.40E-06

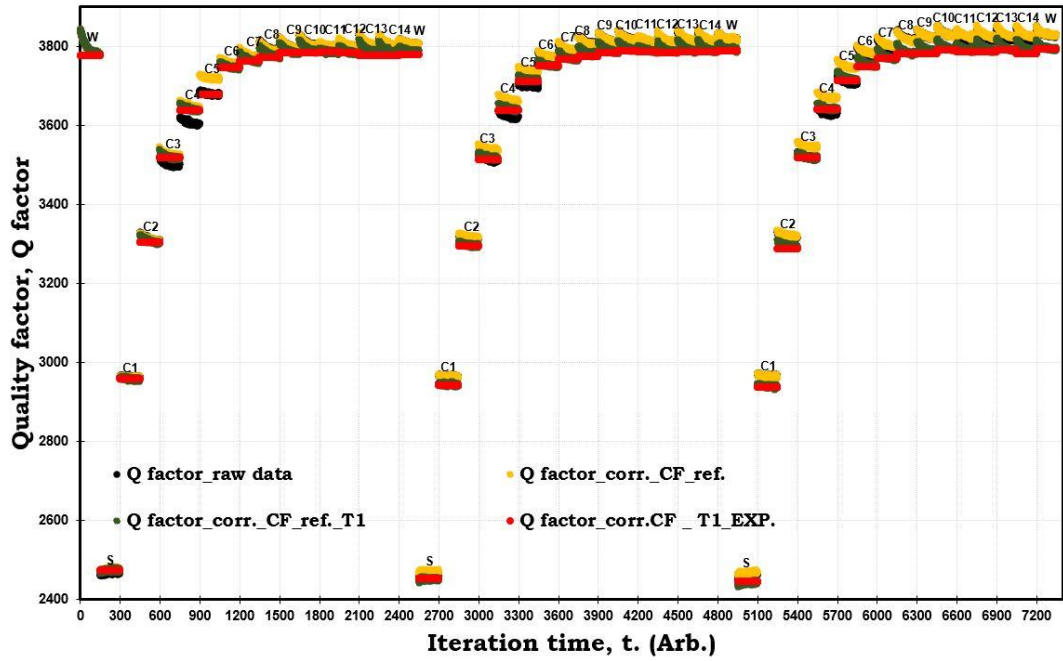


Figure 6-11: Raw data, Frequency, Temperature and Exponential corrections for Q factor measurements for different concentrations of the normal saline (0.154 to 9.400E-06) Molarity (Commercial obtained saline) of TM010 Cavity (Eppendorf sample tube).

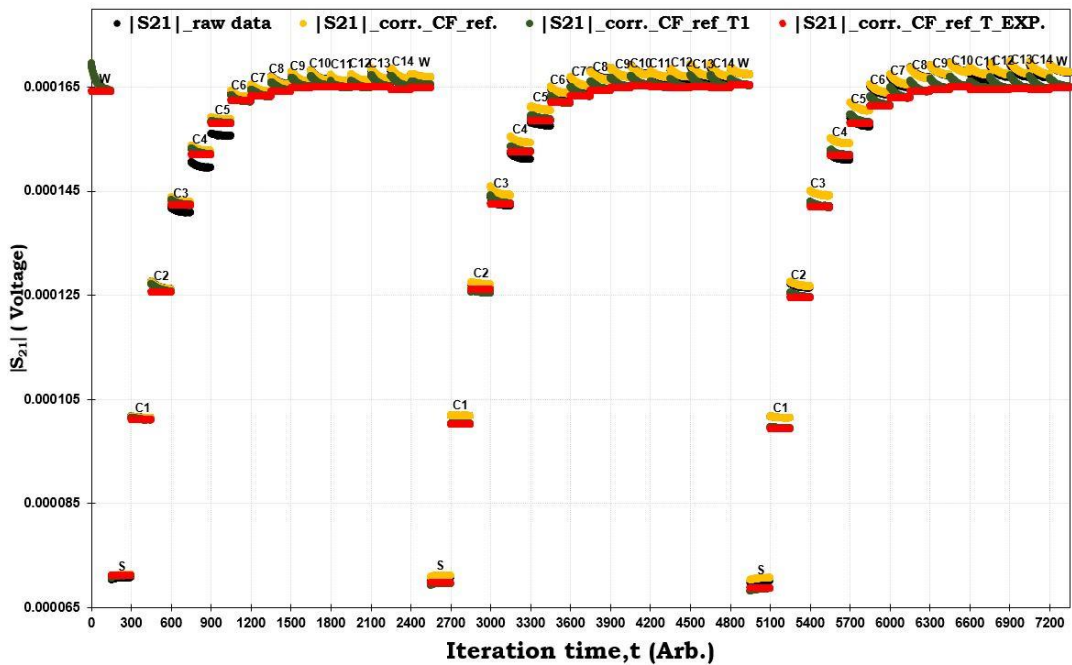


Figure 6-12: Raw data, Frequency, Temperature and Exponential corrections for  $|S_{21}|$  measurements for different concentrations of the normal saline (0.154 to 9.400E-06) Molarity (Commercial obtained saline) of TM010 Cavity (Eppendorf sample tube).

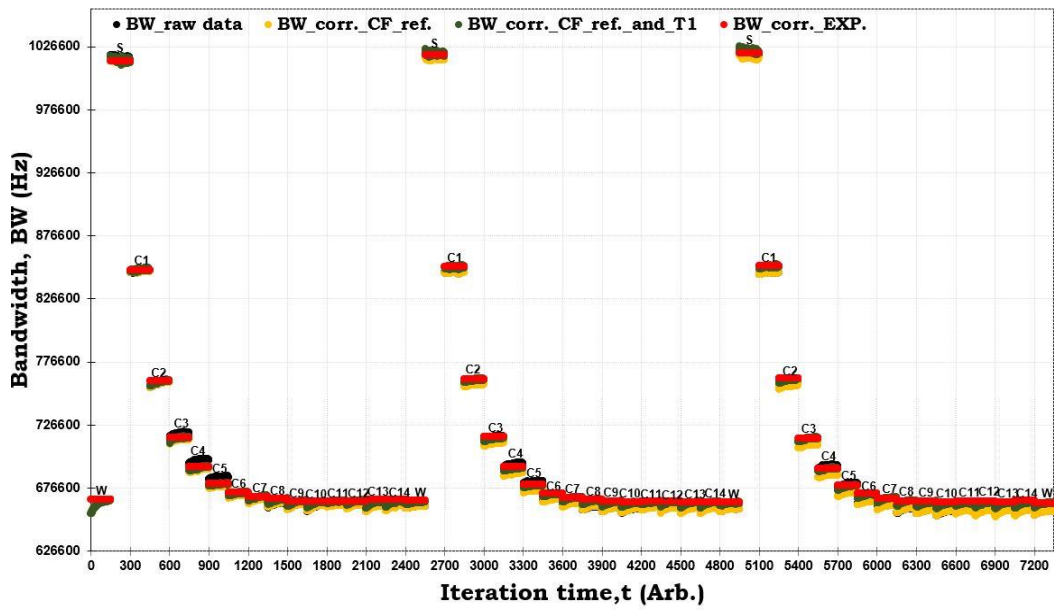


Figure 6-13: Raw data, Frequency, Temperature and Exponential corrections for BW measurements for different concentrations of the normal saline (0.154 to 9.400E-06) Molarity (Commercial obtained saline) of M010 Cavity (Eppendorf sample tube).

Figures 6-14, 6-15 and 6-16 show a simpler result where the average of the corrected data is displayed over the recording time interval. The Q factor,  $|S_{21}|$  and BW are shown, respectively. A clear trend is observed as the dilutions increase and tend towards the value for DI-W as would be expected. A key question here is what is the detection limit of the system? This will be addressed in section 6.5.2.

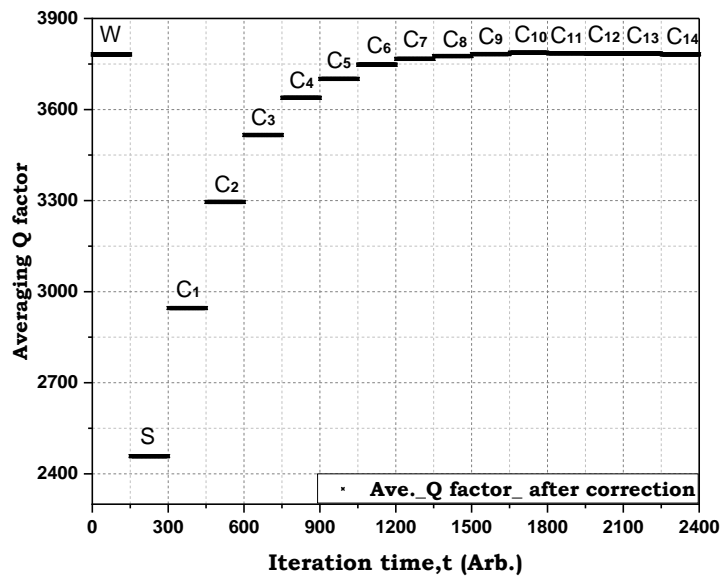


Figure 6-14: Ave. of Q factor over the three sets after applying all the corrections of the normal saline (0.154 to 9.400E-06) Molarity.

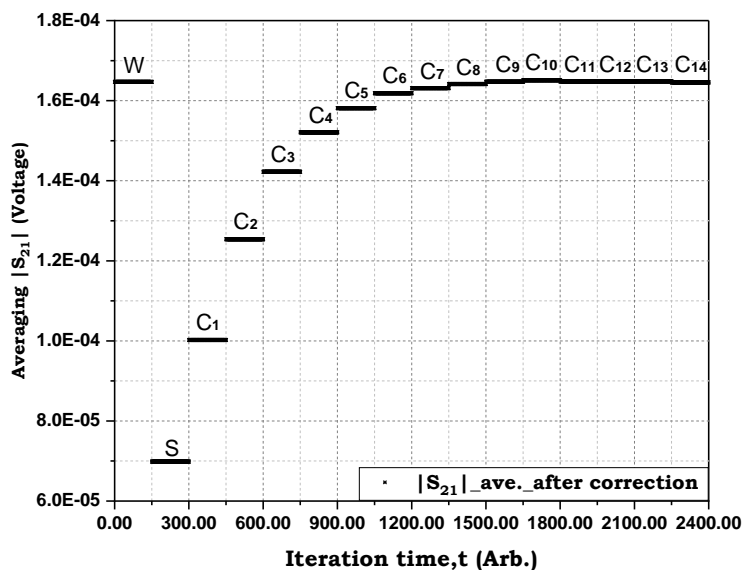


Figure 6-15: Averaging  $|S_{21}|$  over the three sets after applying all the corrections of the normal saline (0.154 to  $9.400E-06$ ) Molarity.

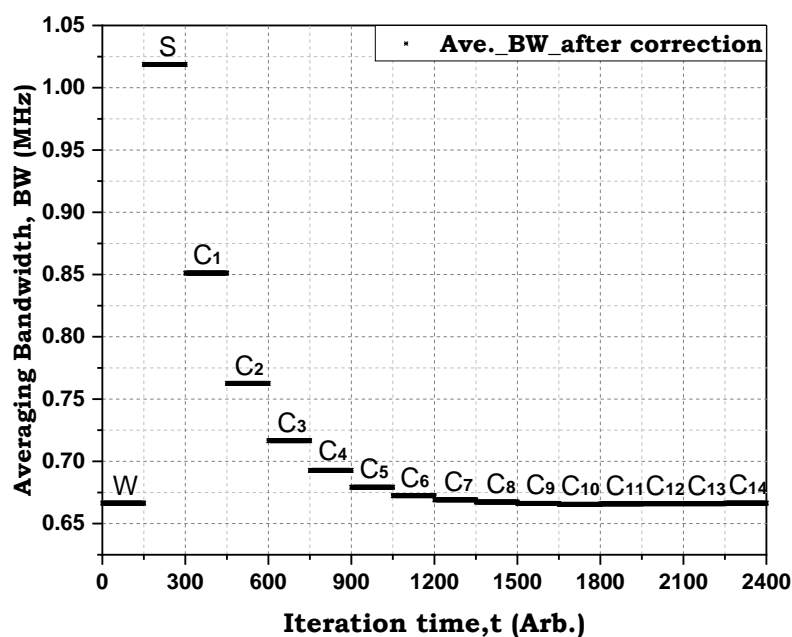


Figure 6-16: Averaging BW over the three sets after applying all the corrections of the normal saline (0.154 to  $9.400E-06$ ) Molarity.

## 6.5.2 DETECTION LIMITS AND SAMPLE CLASSIFICATION

Since the concentration of the samples is known in these experiments, it is pertinent to ask, “if a sample of unknown concentration was measured, what degree of confidence would there be to classify its concentration and what is the lowest concentration that could confidently be measured?”

In probability theory, a probability density function (PDF), is used to describe the probability of a continuous random 'sample' falling within a distinct range of values. This function demonstrates the probability density function and how the mean and the deviation play an essential role. It can be used to infer the difference between two samples.

The Normal (or Gaussian) distribution is the most common probability density function (PDF). Figure 6-17 clarifies that the number of observations falls within the correlation range of the mean, and this number rises with increasing standard deviation. The Figure shows approximately 68% of observations should fall within one standard deviation of the mean, and about 95% of observations should fall within two standard deviations of the mean.

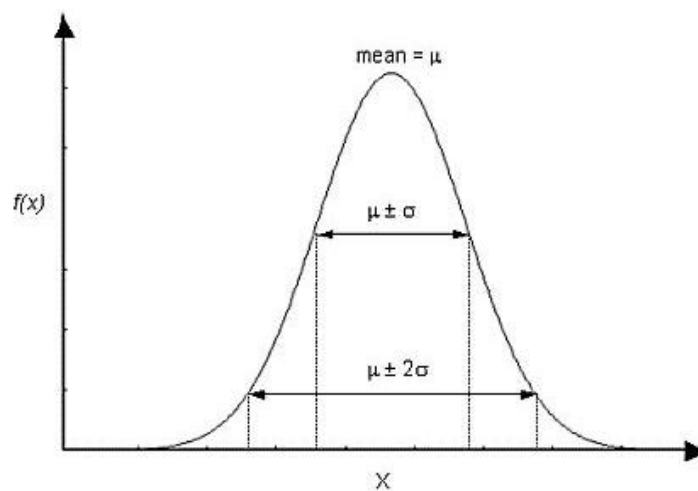


Figure 6-17: Ranges of STDEV in the Normal probability density function.

In our research, this concept is applied to indicate the detection limits between the DI-W and other concentrations, in particular, the limitations found for the low concentrations

The Figures below (Figure 6-18, 6-19 and 6-20) show this simple statistical approach and highlight the detection boundary between DI-W and the lower saline concentrations. These Figures show the limit of detection is  $2.41\text{E-}03$  M (C6) for corrected Q factor,  $|S_{21}|$  and BW, respectively.

In the following graphs, the  $\pm 2\sigma$  and  $\pm 3\sigma$  bands are generated from the average and standard deviation of all the independent water measurements and are used as a global representation of uncertainty in all measurements.

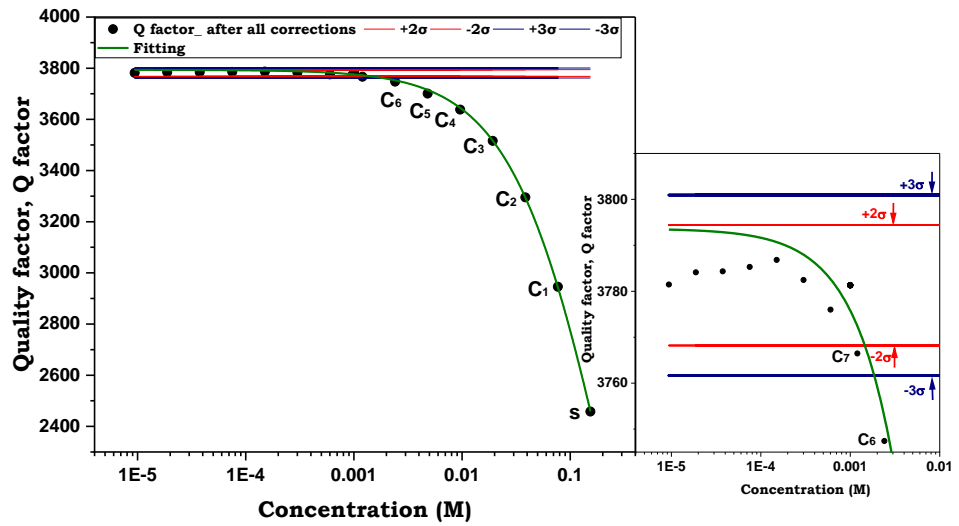


Figure 6-18: The correlation between the corrected Q factor data with different concentrations and statistical detection  $\pm(2\sigma(\text{red})$  and  $3\sigma(\text{blue}))$ .

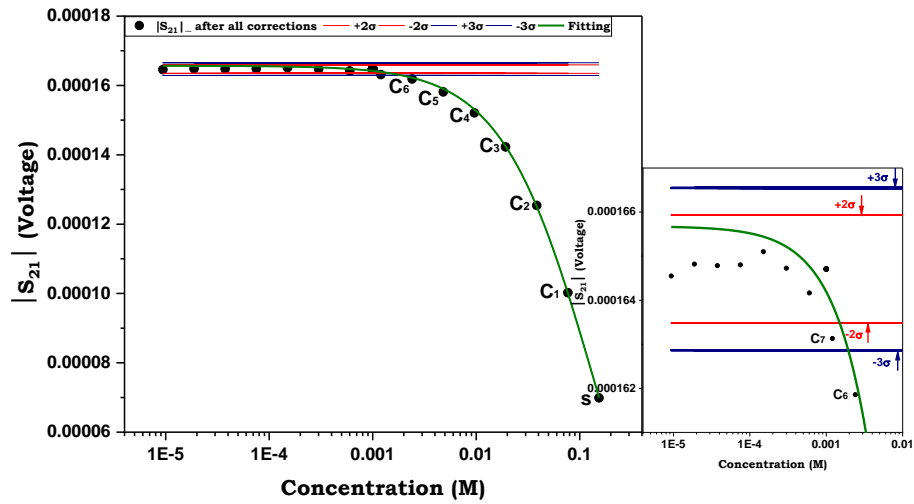


Figure 6-19: The correlation between the corrected  $|S_{21}|$  data with different concentrations and statistical detection  $\pm(2\sigma(\text{red})$  and  $3\sigma(\text{blue}))$ .

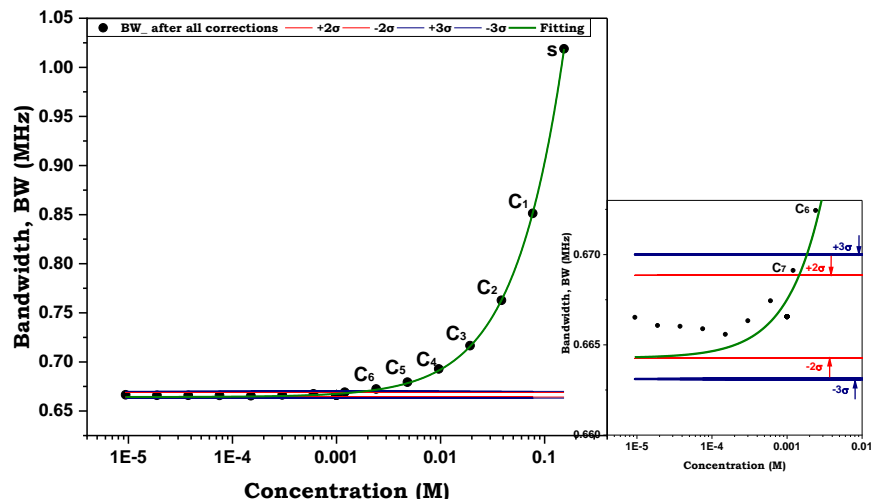


Figure 6-20: The correlation between the corrected BW data with different concentrations and statistical detection  $\pm(2\sigma)$  (red) and  $3\sigma$  (blue).

Figure 6-21 to 6-24 indicates the averaged variance data obtained for the concentrations measured after repeating three times. The Q factor,  $|S_{21}|$ , BW and CF are plotted, respectively. With regards to the CF (Figure 6-24), there is a fluctuation in this parameter that does not seem to correlate with concentration. It is likely that this may be attributed to sample position, bubbles or meniscus. The standard error in the CF data is high for all concentrations.

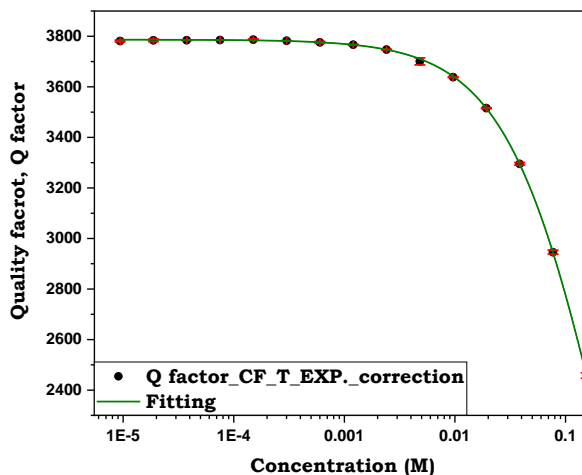


Figure 6-21: Averaging of Q factor corrections after repeating three times at a concentration between (0.154 to 9.400E-06) Molarity.

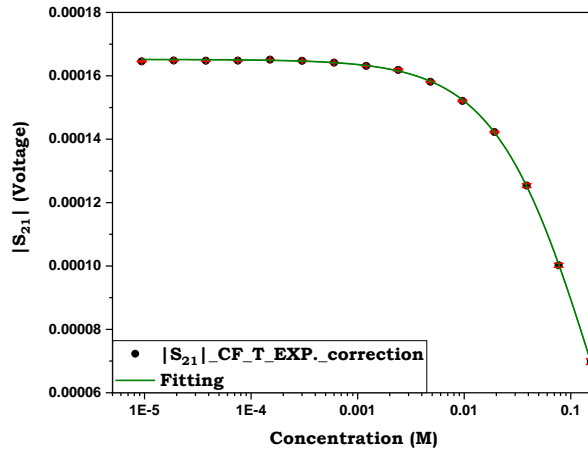


Figure 6-22: Averaging of  $|S_{21}|$  corrections after repeating three times at a concentration between (0.154 to 9.400E-06) Molarity.

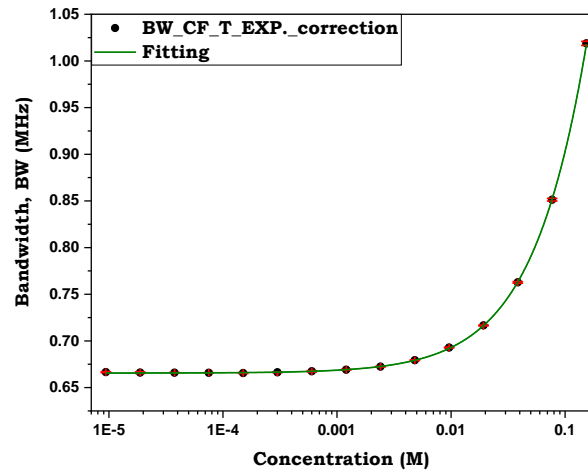


Figure 6-23: Averaging of BW corrections after repeating three times at a concentration between (0.154 to 9.400E-06) Molarity.

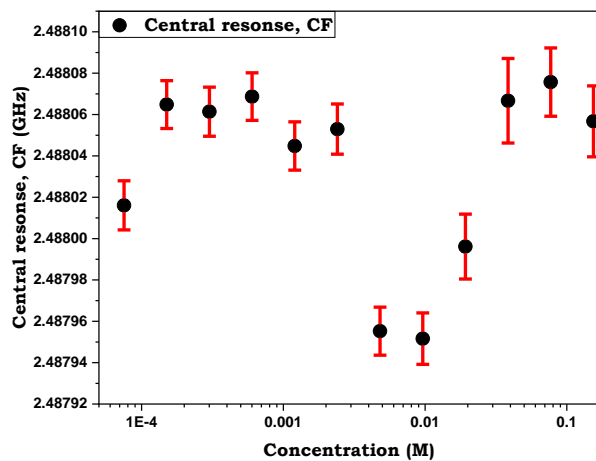


Figure 6-24: Average resonant frequency  $CF_{SENSE}$  after repeating three times at a concentration between (0.154 to 9.400E-06) Molarity.

### 6.5.2.1 CONCLUSION FOR COMMERCIALLY OBTAINED SALINE

A range of commercial obtained saline ( $0.154$  to  $9.400\text{E-}9$ ) M was used as samples detection at resonant cavity  $\text{TM}_{010}$ . At these measurements, the correction steps have been done for the frequency by using the reference and sense frequency as it found a strong correlation between them. Then the temperature correction has been done as a second step to remove the effect of interconnecting cable. Finally, the exponential correction has been utilized to remove the effect of temperature falling exponentially due to the temperature variation between the ambient and the cavity resonator. The outcome of the correction steps showed a systematic increase in  $Q$  and  $|S_{21}|$  and a decrease in  $\text{BW}$  by reducing the concentration with some limitations for the low concentrations. The probability density function is used to address this issue. Therefore,  $2.41\text{E-}03$  M (C6) has been shown the limit of detection for corrected  $Q$  factor,  $|S_{21}|$  and  $\text{BW}$ .

### 6.5.3 MEASUREMENTS OF LAB PREPARED SALINE DILUTIONS

This section will cover the preparation dilution steps, correction steps and results for Lab Prepared Saline Dilutions.

#### 6.5.3.1 PREPARATIONS OF LAB PREPARED SALINE DILUTIONS

For the samples of saline that were acquired from Boots, the dilutions that were made for these experiments used a source of water that was probably different from that used by the manufacturer. For more controlled sample preparation, 100ml DI-W extra pure, deionized (Organic) from Fisher scientific company [155] mix with 100 g of Sodium chloride (NaCl) from (Sigma-Aldrich) [156] are used as the stock solutions. The dilutions are completed by using the same DI-W to prepare the stock. The method for preparation of the stock and the dilutions steps are illustrated in Figure 6-25. Table 6-2 shows the concentration labels for this set of dilutions.

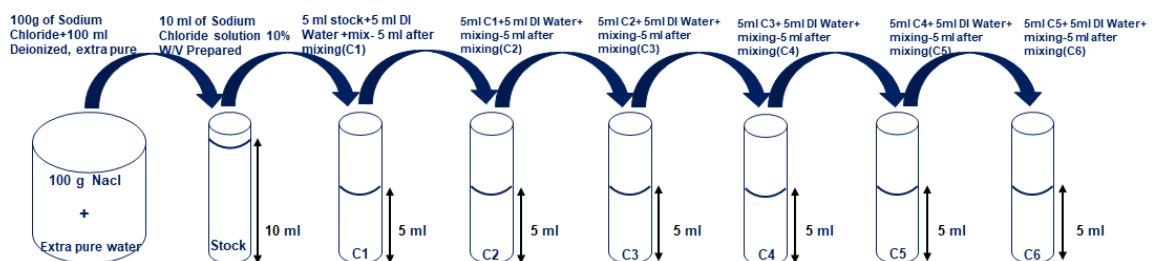


Figure 6-25: Preparation steps of Lab Prepared Saline Dilutions.

Table 6-2: Sample labels and respective concentrations.

Concentration	Abbreviation	Weigh in % w/v	Molarity(M)
Stock	S	1.00E+01	1.71E+00
Half stock	C1	5.00E+00	8.56E-01
Half 1st concentration	C2	2.50E+00	4.28E-01
Half 2nd concentration	C3	1.25E+00	2.14E-01
Half 3rd concentration	C4	6.25E-01	1.07E-01
Half 4th concentration	C5	3.13E-01	5.35E-02
Half 5th concentration	C6	1.56E-01	2.67E-02
Half 6th concentration	C7	7.81E-02	1.34E-02
Half 7th concentration	C8	3.91E-02	6.68E-03
Half 8th concentration	C9	1.95E-02	3.34E-03
Half 9th concentration	C10	9.77E-03	1.67E-03
Half 10th concentration	C11	4.88E-03	8.36E-04
Half 11th concentration	C12	2.44E-03	4.18E-04
Half 12th concentration	C13	1.22E-03	2.09E-04
Half 13th concentration	C14	6.10E-04	1.04E-04
Half 14th concentration	C15	3.05E-04	5.22E-05

### 6.5.3.2 CORRECTION METHOD OF LAB PREPARED SALINE DILUTIONS

As described above, a similar process was carried out to obtain correlation and apply a correction to the raw data obtained from the measurements on this new saline dilution. The frequency data is pre corrected by the LabVIEW data acquisition programme based on simultaneous measurement of  $CF_{SENSE}$  and  $CF_{REF}$ . The reference to raw data below should be interpreted as  $CF_{REF}$  corrected raw data.

#### 6.5.3.2.1 TEMPERATURE AND EXPONENTIAL CORRECTION

Figures 6-26 to 6-28 show a strong correlation between the cavity temperatures ( $T_1$ ) and the Q factor,  $|S_{21}|$  and BW measurements. The gradient factor can be found from these charts and used to apply the temperature correction factor.

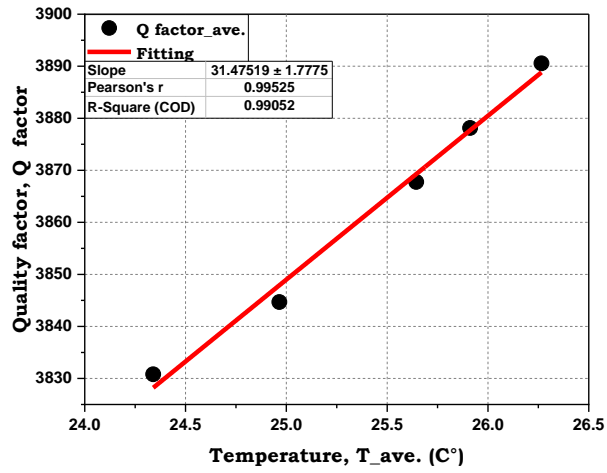


Figure 6-26: Fitting temperature correction for Q factor.

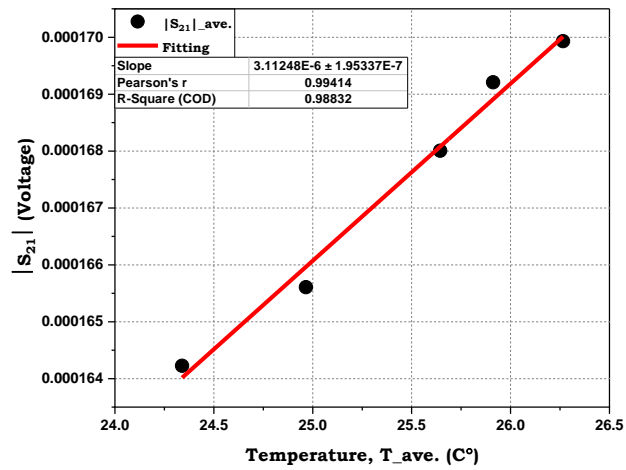


Figure 6-27: Fitting temperature correction for |S<sub>21</sub>|.

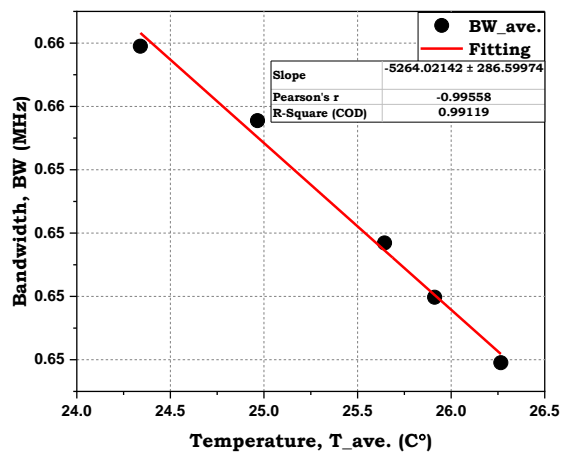


Figure 6-28: Fitting temperature correction for BW measurements.

### 6.5.3.3 RESULTS FOR LAB PREPARED SALINE DILUTIONS

Figures 6-29 to 6-31 show the Q factor,  $|S_{21}|$  and BW measurements respectively for concentrations over the range concentrations ( $5.22E-05$  to  $1.71$ ) M. For each graph, temperature correction has been applied for the raw data and subsequent exponential correction has been implemented. As before, the data has been presented in this way to convey the output of the whole experiment and the correction processes that have been applied.

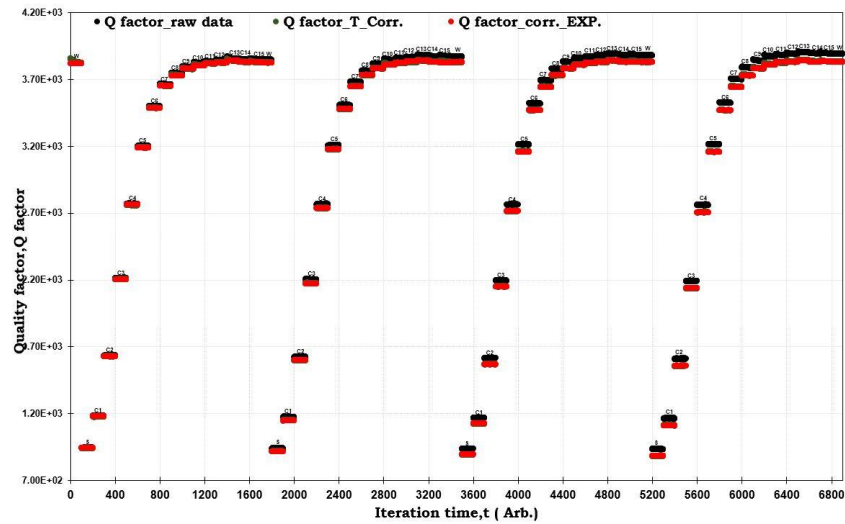


Figure 6-29: Raw data black, temperature green and Exponential in red Corrections for Q factor measurements for variance concentrations ( $5.22E-05$  to  $1.71$ ) M (Lab Prepared Saline Dilutions) of M010 Cavity (Eppendorf sample tube).

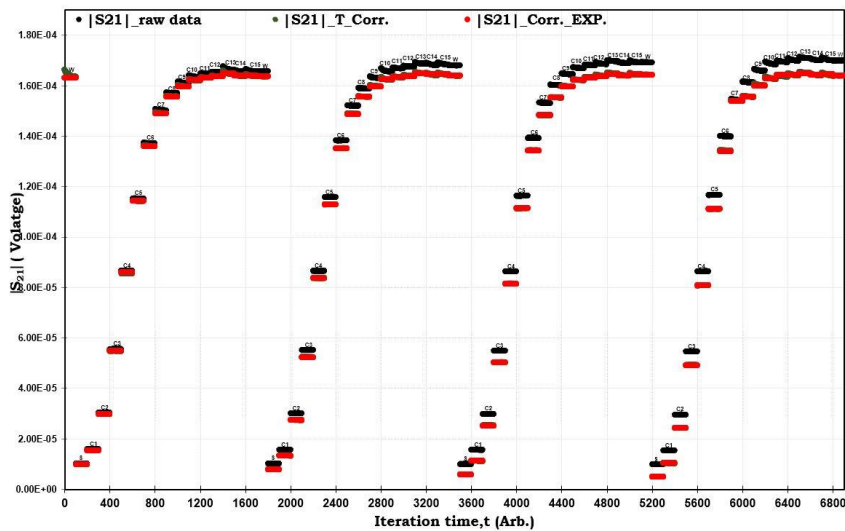


Figure 6-30: Raw data black, temperature green and Exponential in red Corrections for  $|S_{21}|$  measurements for variance concentrations ( $5.22E-05$  to  $1.71$ ) M (Lab Prepared Saline Dilutions) of M010 Cavity (Eppendorf sample tube).

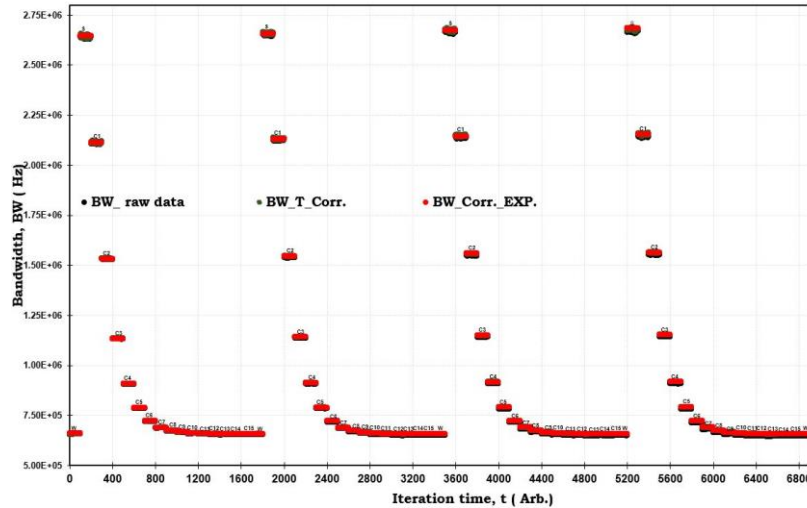


Figure 6-31: Raw data black, temperature green and Exponential in red Corrections for BW measurements for variance concentrations (5.22E-05 to 1.71) M (Lab Prepared Saline Dilutions) of M010 Cavity (Eppendorf sample tube).

Now, turning to the details of Figures 6-29, 6-30 and 6-31 show Q factor,  $|S_{21}|$  and BW, respectively. Generally, a systematic change is shown in the four sets for parameters (Q factor,  $|S_{21}|$ , and BW, respectively). Since the stock concentration here is higher than the Boots sample, the trends highlighted in these graphs are similar for the low concentrations but differ at the high concentrations. As before, the measurements tend towards that of DI-W as the concentration decreases.

Figures 6-32, 6-33 and 6-34 show Q,  $|S_{21}|$  and BW averaged over the four sets after applying all the corrections. Good separation between the samples to around  $3.34E-03$  M (C9) or  $1.67E-03$  M (C10) can be observed.

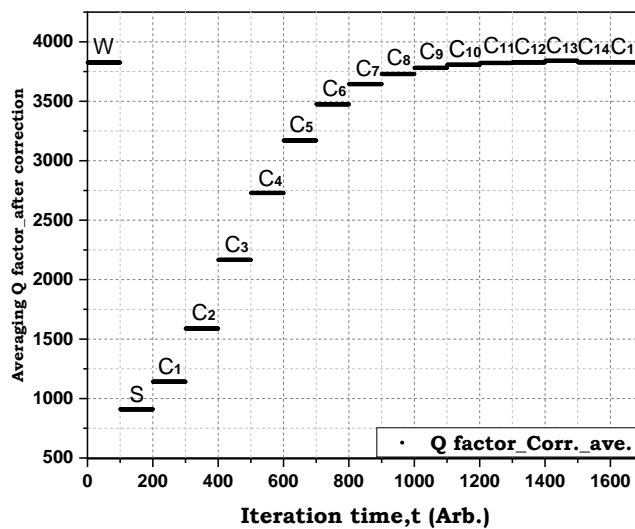


Figure 6-32: Ave. of Q factor over the four sets after applying all the corrections for variance concentrations (5.22E-05 to 1.71) M.

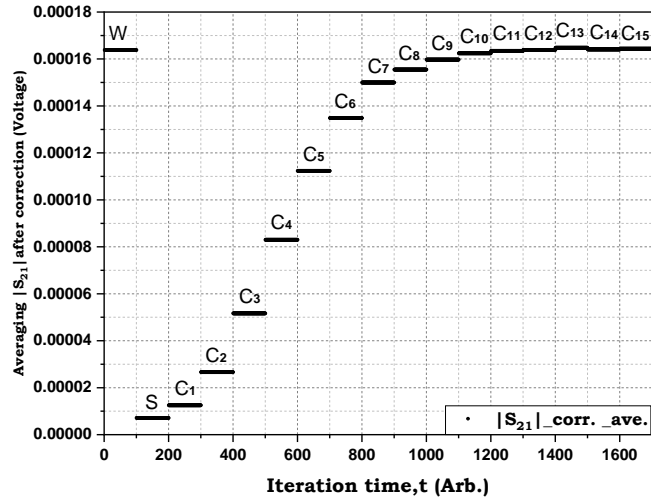


Figure 6-33: Ave. of  $|S_{21}|$  over the four sets after applying all the corrections for variance concentrations (5.22E-05 to 1.71) M.

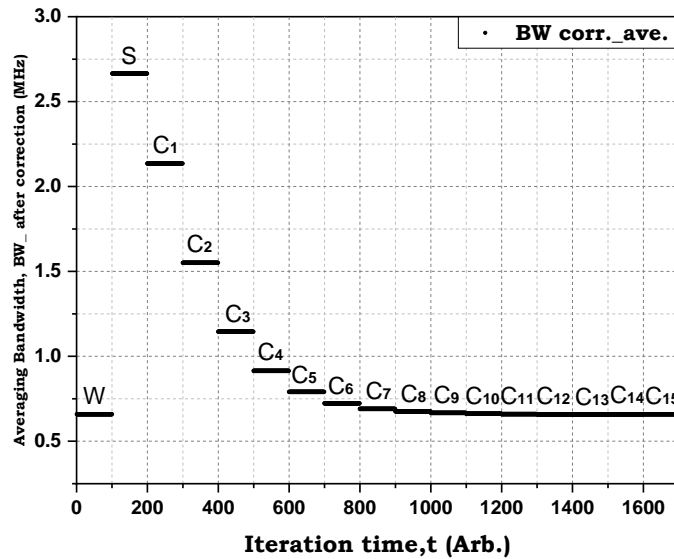


Figure 6-34: Ave. of BW over the four sets after applying all the corrections for variance concentrations (5.22E-05 to 1.71) M.

Figures 6-35, 6-36 and 6-37 show a distinct improvement in the detection limit for the low concentrations. With this preparation type, the Figures show good separation until 1.67E-03 M (C10) with Q factor,  $|S_{21}|$  and BW measurements. Again, the  $\pm 2\sigma$  and  $\pm 3\sigma$  bands are generated from the corresponding DI-water measurements.

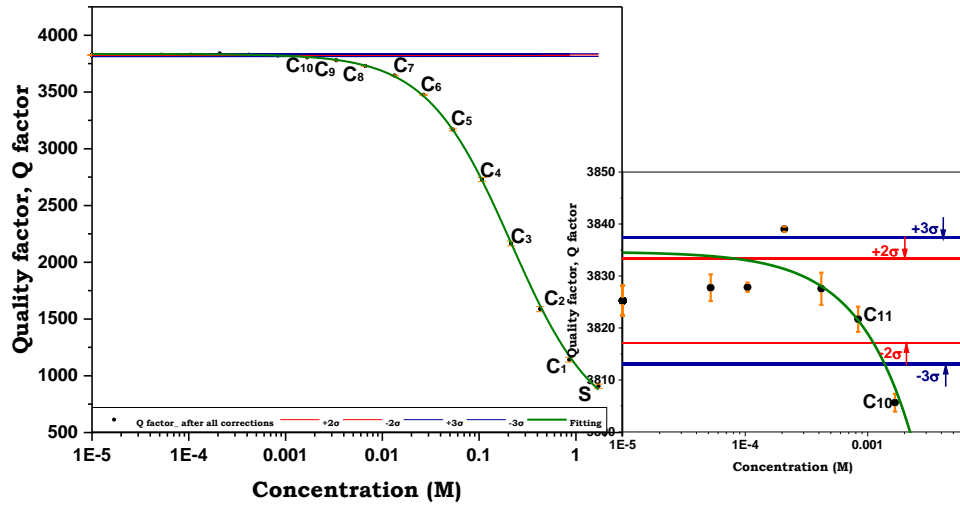


Figure 6-35: The correlation between the corrected Q factor data with different concentrations and statistical detection  $\pm(2\sigma$ (red) and  $3\sigma$ (blue)).

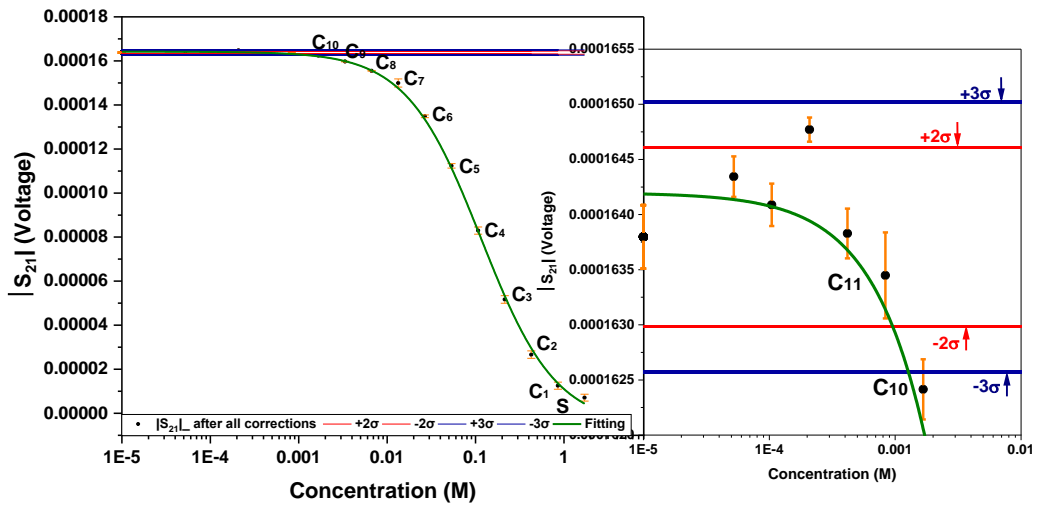


Figure 6-36: The correlation between the corrected  $|S_{21}|$  data with different concentrations and statistical detection  $\pm(2\sigma$ (red) and  $3\sigma$ (blue)).

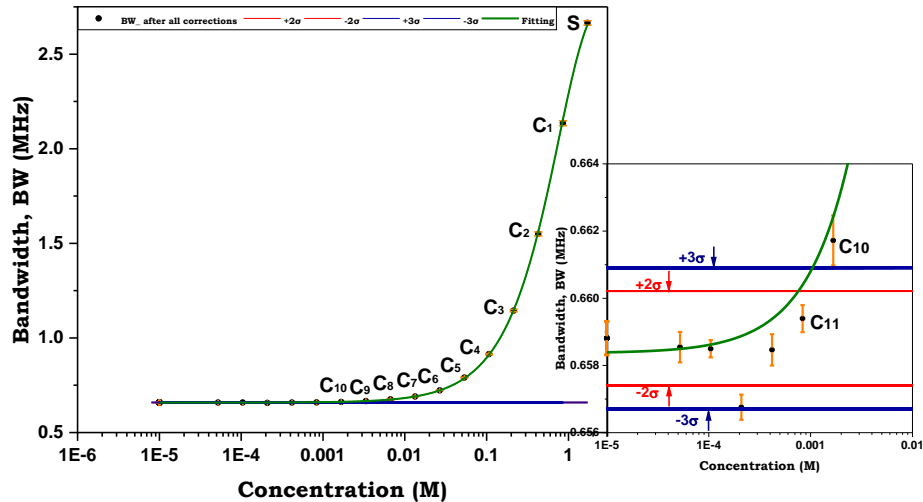


Figure 6-37: The correlation between the corrected BW data with different concentrations and statistical detection  $\pm(2\sigma(\text{red})$  and  $3\sigma(\text{blue})$ ).

#### 6.5.3.4 CONCLUSION FOR LAB PREPARED SALINE DILUTIONS

For more controlled sample preparation, LAB prepared saline dilutions  $5.22\text{E-}05$  to  $1.71\text{E+}00$  M have been utilized for samples detecting of resonant cavity  $\text{TM}_{010}$ . Raw data has been corrected by applying just temperature and exponential corrected as the same steps done in the commercial preparation and the frequency correction implanted in LABVIEW code. At this type of preparation, a considerable improvement at microwave measurements (Q factor,  $|S_{21}|$  and BW) to  $1.67\text{E-}03$  M (C10) compared to  $2.41\text{E-}03$  M (C6) of commercial obtained saline

### 6.6 COMPARISON BETWEEN PREPARATION TYPES

Figures 6-38 to 6-41 show how the parameters, Q,  $|S_{21}|$ , BW and CF vary with concentration for the two types of solution preparation. At first glance, there appears to be a slight difference in Q between the two preparation methods. Generally, the subsequent Figures show that there is little difference between the samples except for CF. Since it is not possible to ascertain the precise composition of the Boots saline, it is not possible to attribute any tangible reason for this difference. If one were to speculate however, it could be a possibility that the wetting characteristics of the two samples may differ. This could lead to a subtle change in the meniscus angle which may have an observable impact on CF. See Figure 6-41.

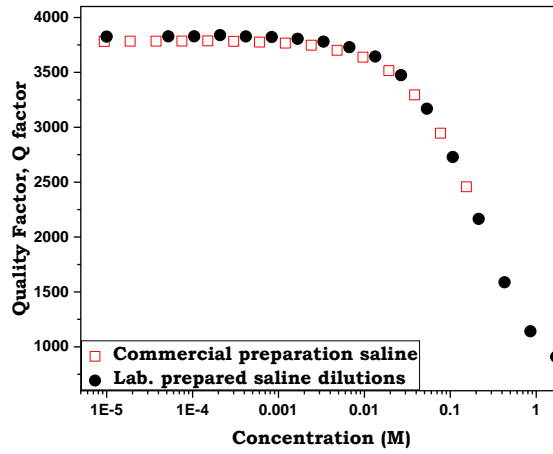


Figure 6-38: Comparison between commercially obtained saline and Lab prepared saline dilutions for Q factor measurements.

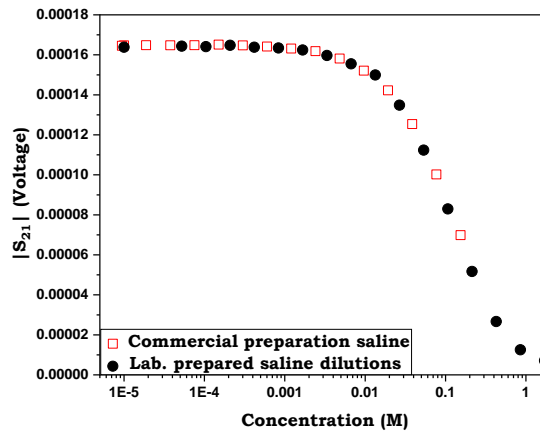


Figure 6-39: Comparison between commercially obtained saline and Lab prepared saline dilutions for |S<sub>21</sub>| measurements.

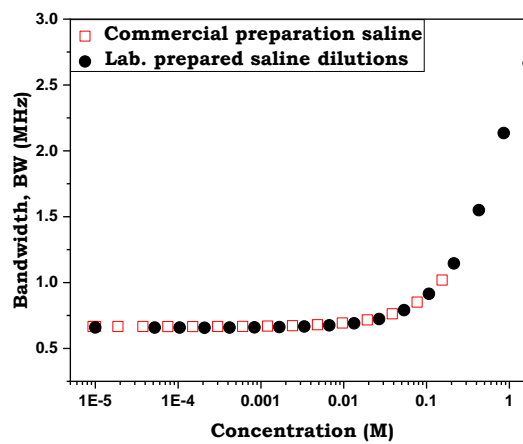


Figure 6-40: Comparison between commercially obtained saline and Lab prepared saline dilutions for BW measurements.

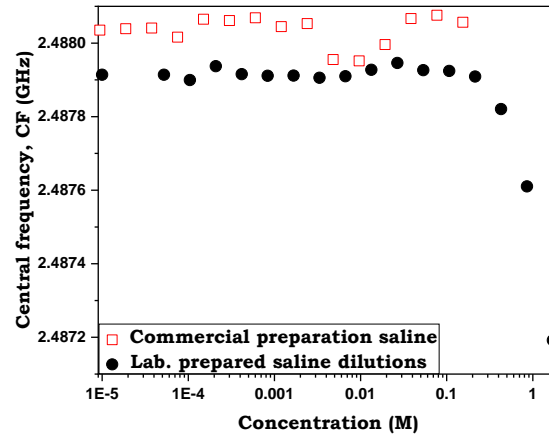


Figure 6-41: Comparison between commercially obtained saline and Lab prepared saline dilutions for CF measurements.

## 6.7 CONVERTING THE MICROWAVE PARAMETERS TO THE PERMITTIVITY

### 6.7.1 INTRODUCTION

As the dielectric properties play a vital role in defining the physical and chemical properties of the detecting sample [85], a few steps have been applied to our experimental microwave data to find the constants of permittivity. To convert the microwave parameters, Equations 6-14 and 6-15 are used. The constant values  $k_1$  and  $k_2$  are important for calculating the real and imaginary part of the permittivity, respectively. Thus, an experiment has been carried out to find the central frequency and the quality factor of a loaded (with sample) and unload cavity (without sample) which help to find these values.

$$\frac{\Delta f}{f_1} = k_1(\epsilon_w - \epsilon_{air}) \quad (6-14)$$

Here  $\frac{\Delta f}{f_1}$  is the ratio between the variation of the CF of the unloaded and loaded cavity and  $f_1$  is the central frequency for the loaded cavity, which is calculated from the average values of the experimental work.  $k_1$  is a constant and  $\epsilon_w$  is the real permittivity of water which has been obtained from our calculator (Figure 5-8) with specific values relating to our experimental conditions such as the cavity temperature and the frequency of the cavity.  $\epsilon_{air}$  is the real permittivity of the air (which is equal to 1.0006). Equation 6-15 is used initially to find the value of  $k_2$  and then subsequently for the different concentrations.

$$\Delta\left(\frac{1}{Q}\right) = k_2(\varepsilon_w - \varepsilon_{air}) \quad (6-15)$$

$\Delta Q$  is the difference in the quality factor between the loaded and unloaded cavity. By fixing the temperature and the central frequency,  $\varepsilon_{air}$  is the imaginary permittivity of the air (equal to zero). In response to the shift in the resonance frequency, the difference in  $Q$  and constants  $k_1$  and  $k_2$ , the real permittivity  $\varepsilon'$  and the imaginary permittivity  $\varepsilon''$  values can be found by applying the following Equations.

$$\varepsilon' - 1 = \frac{2}{k_1} \frac{f_0 - f_1}{f_1} \quad (6-16)$$

$$\varepsilon'' = \frac{1}{k_2} \left( \frac{1}{Q_1} - \frac{1}{Q_0} \right) \quad (6-17)$$

Here,  $f_0$  is the resonant frequency for DI-W,  $f_1$  is the resonant frequency for saline,  $Q_0$  is the quality factor for DI-W and  $Q_1$  is the quality factor for the saline.

## 6.7.2 METHODOLOGY

In our experiment, two sources of DI-W have been used for the two sets of series dilutions (9.00E+00 to 5.49E-04) ppt (parts per thousand). The first source was from an in-house DI-W filtration system. The second was purchased from Sigma Aldrich. The second set had dilutions in the range (1.00E+02 to 3.05E-03) ppt. The data obtained from [157] provides permittivity information for concentrations: 2.733E+02, 1.640E+02, 5.467E+01, 1.093E+01 and 2.733 ppt. Finally, permittivity data from Chaplin [158] for the range 35-0 ppt in steps of 5 ppt.

## 6.7.3 RESULTS

Figures 6-42 and 6-43 compare our results for the two different preparations with published data for the real and imaginary permittivity of saline. There is good agreement between the values of permittivity, with the exception of the real permittivity for the Boots saline preparation. The large standard error in this data set and the deviation from the published data at the lower concentrations (<1 ppt) are mainly attributed to the CF measurement issue as described above.

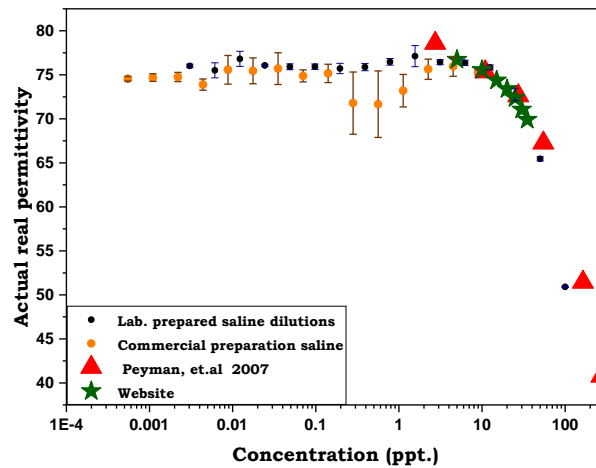


Figure 6-42: The comparison among the real permittivity among the Lab prepared saline dilutions at ( $1.00E+02$ ,  $5.00E+01$ - $7.81E-01$ ) ppt, Commercial obtained saline at ( $9.00E+00$ - $5.49E-04$ ) ppt., Penman's results at ( $2.73E+02$ ,  $1.64E+02$ ,  $5.47E+01$ ,  $2.73E+01$ ,  $1.09E+01$  and  $2.73E+00$ ) ppt and Website at (35 to 0) ppt.

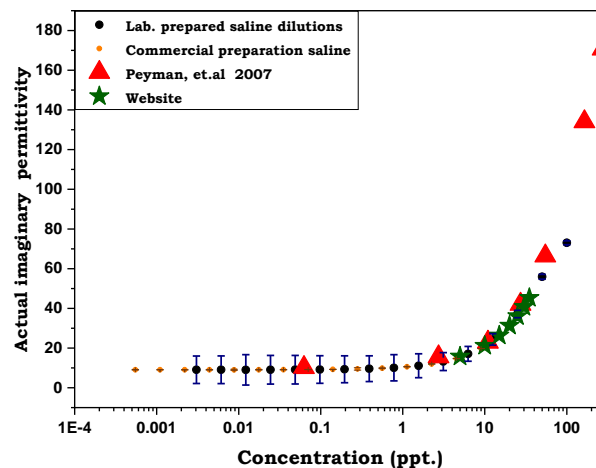


Figure 6-43: The comparison among the imaginary permittivity among the Lab prepared saline dilutions at ( $1.00E+02$ ,  $5.00E+01$ - $7.81E-01$ ) ppt, Commercial obtained saline at ( $9.00E+00$ - $5.49E-04$ ) ppt., Peyman's results at ( $2.73E+02$ ,  $1.64E+02$ ,  $5.47E+01$ ,  $2.73E+01$ ,  $1.09E+01$  and  $2.73E+00$ ) ppt and Website at (35 to 0) ppt.

## 6.8 ENHANCED EXPONENTIAL CORRECTION

The simple three-point exponential decay extrapolation technique described above, in many cases, failed to detect the asymptotic value of the relevant parameter. This is mainly due to the shot to shot noise in the raw data. To overcome this, an algorithm was written in MATLAB to plot each block of 100 data points and fit to an exponential function using the least-squares minimum search function (Appendix C-1). The raw data and best fit were plotted to allow the user to accept the fit or to re-run the search function. This was sometimes necessary as the function used random numbers to initiate the search.

The results obtained from the curve fit are compared with the simpler asymptote detection used

by Excel. Whilst the differences are less than a few percent, the curve fit provides a much better estimate of the asymptote, see Figures 6-44 and 6-45 below.

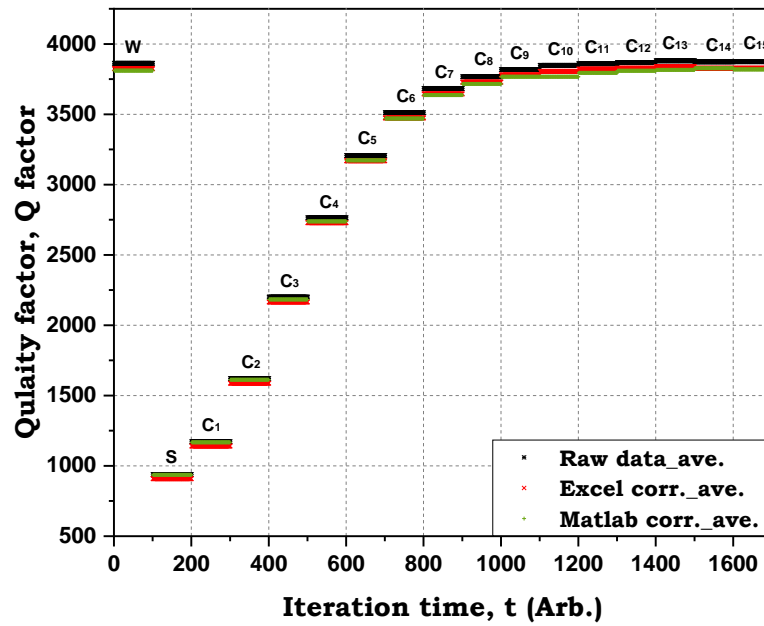


Figure 6-44: The comparison between the EXCEL and MATLAB Corrections.

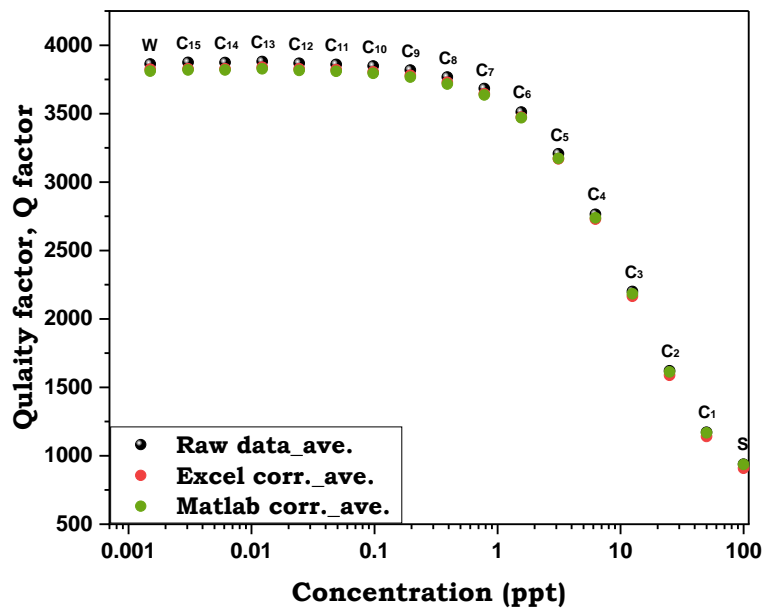


Figure 6-45: Demonstrated the comparison between the average for raw data and the corrections of EXCEL and MATLAB.

Figure 6-46 showed the variation between the Excel correction method (a) and MATLAB fitting data (b) in different sets and the averages. It shows that the variation is limited to a few percent

between the two methods at concentrations less than 1 ppt.

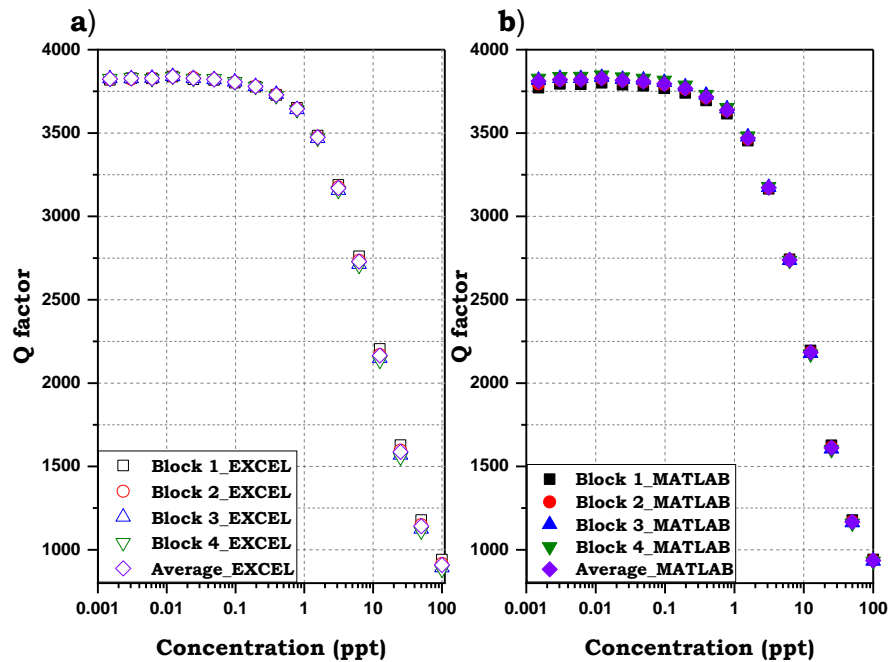


Figure 6-46: Comparison between the EXCEL corrections (a) and MATLAB for different sets (b), averaging.

## 6.9 POLYSTYRENE RESULTS BY USING THE EPPENDORF TUBE SAMPLE

For the multitude of reasons already mentioned, the problem of measurement stability is somewhat more of a problem with the PS samples with various concentrations of 2  $\mu\text{m}$  with half technique preparation followed in almost thesis in between 12.5 to 0.195 ppt ( $C_1$  to  $C_7$ ), since they need to be frequently shaken as the particles would settle over a period of about 10-15 minutes. Ensuring that the sample is properly mixed during the measurement is challenging. The variation in CF for different concentrations is shown in Figure 6-47. Taking this raw data on face value suggests that there is very little consistency in the measurements. However, as has been shown, there are opportunities for data correction here that can yield reasonable detection limits.

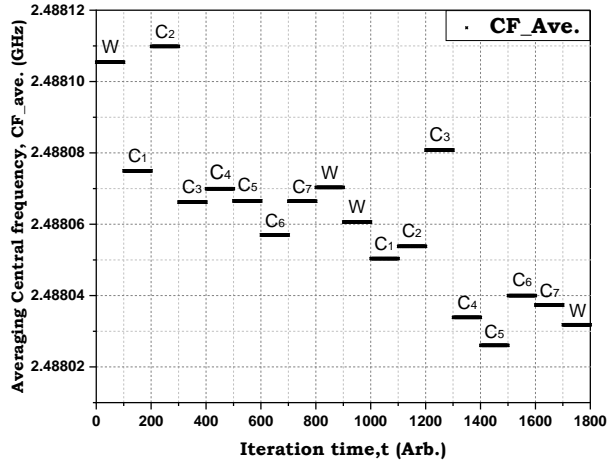


Figure 6-47: Averaging central frequency for suspension polystyrene (2 μm) with different concentrations (12.5 to 0.195) ppt.

Figures 6-48, 6-49 and 6-50 show the output from a typical experiment on PS for Q,  $|S_{21}|$  and BW respectively. Again, the raw data, and subsequent corrections are included in order to convey the task of data processing that takes place. The raw data in this set is dominated by the exponential decay curves originating from the elevated sample temperatures. Elevating the sample temperature was deliberate by using body heat from hand holding the samples for a specific time since it provided a good curve for the fitting algorithm. The red lines show the overall average value for that sample; the full range of concentrations was repeated twice in this case. The expected trend is observed with the measurements for each sample tending to that of water as the concentrations decrease. The repeatability of the data set was however poor and likely attributed to the settling of the PS particles and any bubbles from the prior mixing.

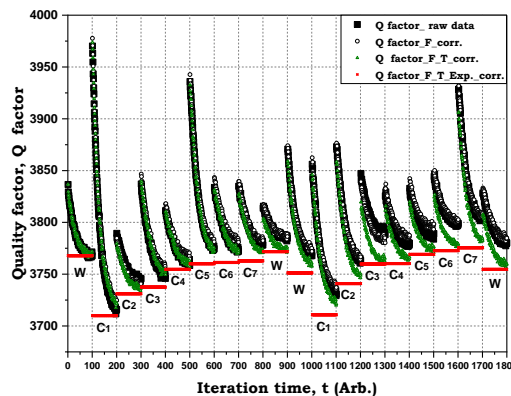


Figure 6-48: Raw data, Frequency, Temperature and Exponential Corrections for Q factor Measurements of dilutions prepared from suspension polystyrene (2μm) with different concentrations (12.5 to 0.195) ppt by using Eppendorf tube sample (cavity TM010).

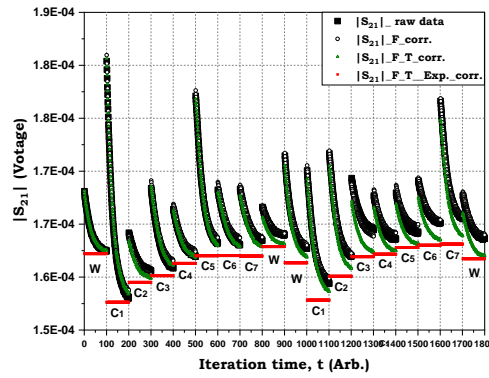


Figure 6-49: Raw data, Frequency, Temperature and Exponential Corrections for  $|S_{21}|$  Measurements of dilutions prepared from suspension polystyrene ( $2\mu\text{m}$ ) with different concentrations (12.5 to 0.195) ppt by using Eppendorf tube sample (cavity TM010).

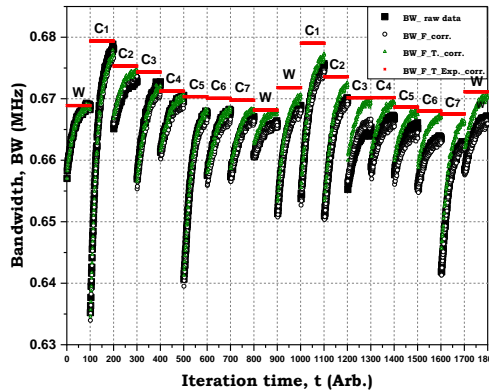


Figure 6-50: Raw data, Frequency, Temperature and Exponential Corrections for Bandwidth Measurements of dilutions prepared from suspension polystyrene ( $2\mu\text{m}$ ) with different concentrations (12.5 to 0.195) ppt by using Eppendorf tube sample (cavity TM010).

The averaging of all of the data for each concentration yielded the results below; again, for  $Q$ ,  $|S_{21}|$  and BW respectively (Figures 6-51 to 6-53).

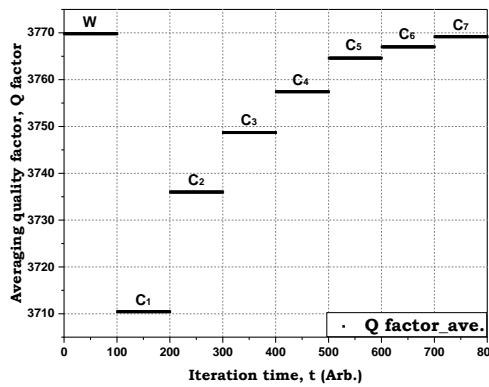


Figure 6-51: Averaging of Q factor over the two sets after applying all the corrections for suspension polystyrene ( $2\mu\text{m}$ ) with different concentrations (12.5 to 0.195) ppt by using Eppendorf tube sample (cavity M010).

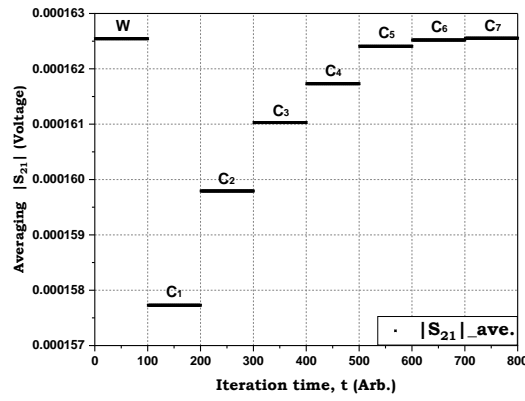


Figure 6-52: Averaging  $|S_{21}|$  over the two sets after applying all the corrections for suspension polystyrene (2  $\mu\text{m}$ ) with different concentrations (12.5 to 0.195) ppt by using Eppendorf tube sample (cavity M010).

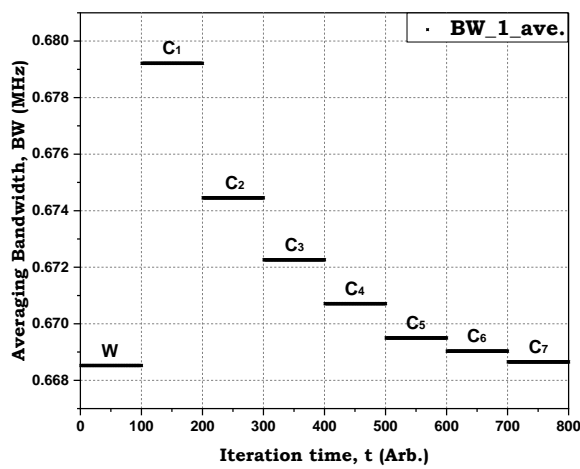


Figure 6-53: Averaging Bandwidth over the two sets after applying all the corrections for suspension polystyrene (2  $\mu\text{m}$ ) with different concentrations (12.5 to 0.195) ppt by using Eppendorf tube sample (cavity M010).

By considering the spread in the values obtained for water, the  $\pm 2\sigma$  and  $\pm 3\sigma$  ranges are highlighted below and suggest a detection limit of down to 1.56 ppt ( $C_4$ ) in Q factor and BW measurements and 3.13 ppt ( $C_3$ ) in  $|S_{21}|$  for this cavity measurement.

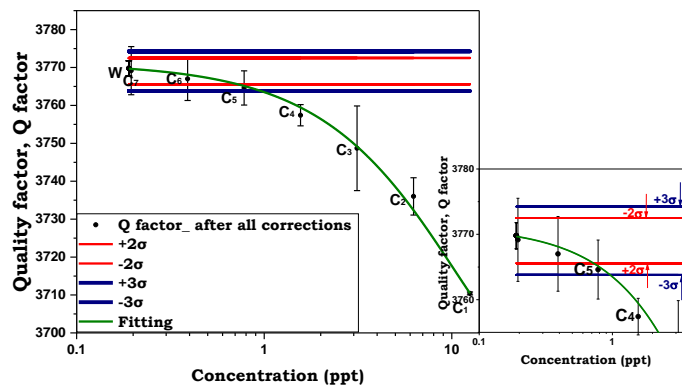


Figure 6-54: The correlation between the corrected Q factor, corrected data with different concentrations for suspension polystyrene of 2  $\mu\text{m}$  (12.5 to 0.195) ppt and statistical detection  $\pm 2\sigma$  (red) and  $3\sigma$  (blue)).

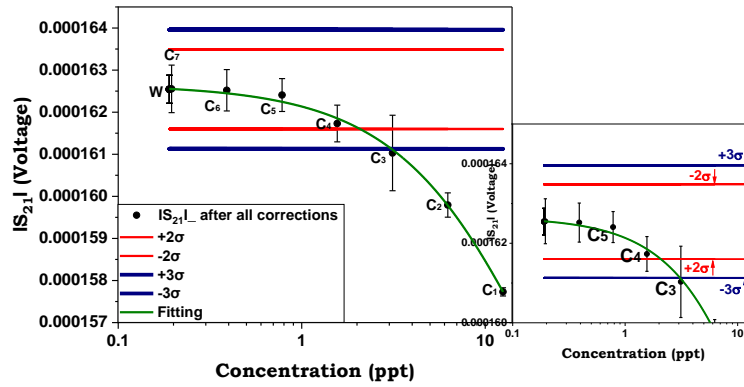


Figure 6-55: The correlation between the corrected  $|S_{21}|$  corrected data with different concentrations for suspension polystyrene of  $\mu\text{m}$  (12.5 to 0.195) ppt and statistical detection  $\pm(2\sigma(\text{red})$  and  $3\sigma(\text{blue})$ ).

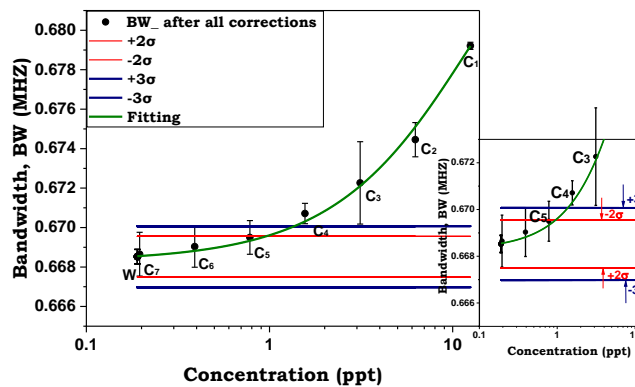


Figure 6-56: The correlation between the corrected BW corrected data with different concentrations for suspension polystyrene of 2  $\mu\text{m}$  (12.5 to 0.195) ppt and statistical detection  $\pm(2\sigma(\text{red})$  and  $3\sigma(\text{blue})$ ).

In Figures 6-57 and 6-58, the trends in  $Q$  and  $|S_{21}|$  are as expected and tend to that of water as the concentration decreases. The standard error (SE) increased with reducing the concentrations in both measurements, which may be attributed to the use of different fresh samples and the associated problems with mixing. In terms of BW measurements (Figure 6-59), there was a gradual decrease with decreasing the concentration. The SE was considerably increased with decreasing the concentrations, which may be due to the same reason. Regarding the resonant frequency, there is no discernible trend with a high standard error for all concentrations which may be due to settling or the position of the sample (Figure 6-60).

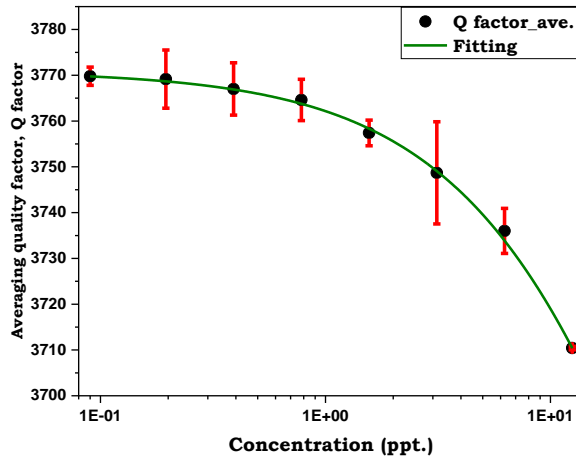


Figure 6-57: Averaging Quality factor for suspension polystyrene (2  $\mu\text{m}$ ) with concentration range 12.5 to 0.195 ppt by using Eppendorf tube sample (cavity TM010).

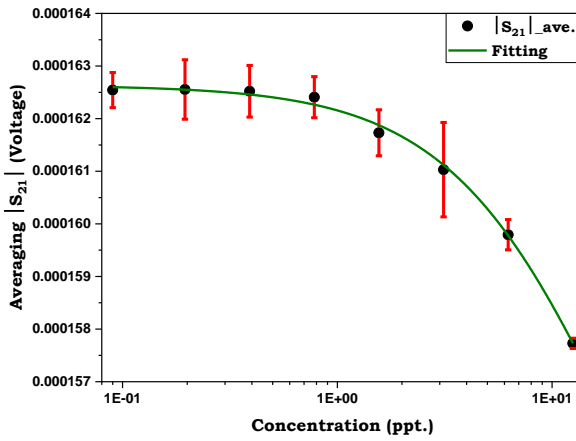


Figure 6-58:  $|S_{21}|$  measurements for suspension polystyrene (2  $\mu\text{m}$ ) with concentration range 12.5 to 0.195 ppt by using Eppendorf tube sample (cavity TM010).

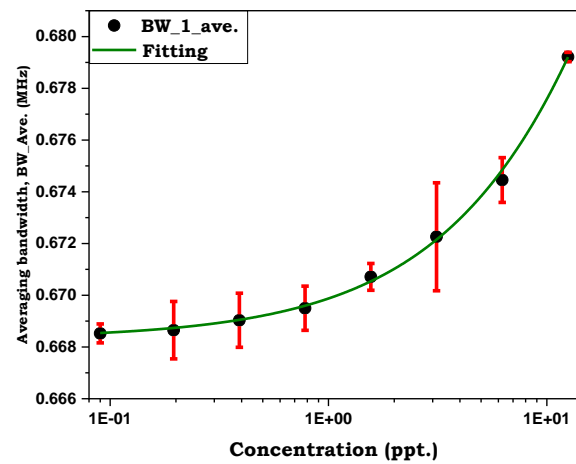


Figure 6-59: Averaging Bandwidth measurements for suspension polystyrene (2  $\mu\text{m}$ ) with concentration range 12.5 to 0.195 ppt by using Eppendorf tube sample (TM010).

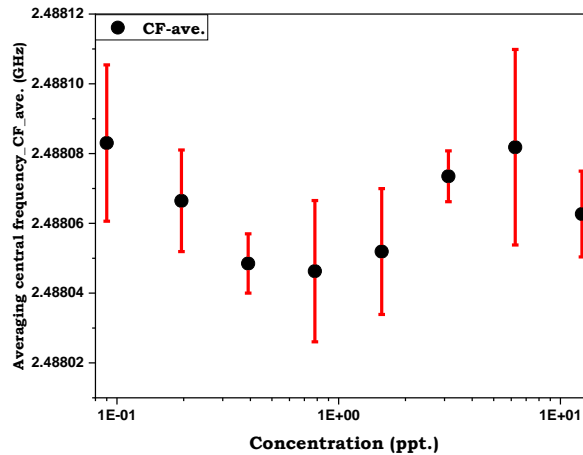


Figure 6-60: Averaging central frequency measurements for suspension polystyrene (2 $\mu$ m) with concentration range 12.5 to 0.195 ppt by using Eppendorf tube sample (TM010).

### 6.9.1 CONCLUSION FOR POLYSTYRENE RESULTS BY USING THE EPPENDORF TUBE SAMPLE

12.5 to 0.195 ppt of polystyrene in the suspension of 2  $\mu$ m particle size and pure water as a reference for detecting using Eppendorf tube sample in the cavity resonance. The same correction steps mentioned in 6.5.3.4 has been applied for all microwave measurements. Despite the difficulties of settling particles, presence of bubbles due to shake samples, the detection limit showed to 1.56 (C<sub>4</sub>) for Q factor and BW and 3.13 (C<sub>3</sub>) for |S<sub>21</sub>|.

### 6.10 RESULTS BY USING THIN AND LONG EPPENDORF TUBE SAMPLE.

In this part, a long thin Eppendorf sample tube was chosen specifically to decrease the depolarization effect due to the sample shape. Two samples have been used in the detection, normal saline 1.71 E<sub>00</sub> to 5.22E-05 M (normal saline lab preparation mentioned in section 6.5.3.1) and PS with 12.5 to 0.195 ppt of 2  $\mu$ m suspension polystyrene. The same LabVIEW data acquisition was used in section 6.5.3.2.

#### 6.10.1 RESULTS FOR SALINE SAMPLES

Figures 6-61 to 6-63 highlight the raw data and corrected data using a long thin Eppendorf sample tube chosen specifically to decrease the depolarisation effect due to the sample shape as clarified in Equations 6-9 and 6-10. Saline was used in this experiment to ascertain whether the thinner sample tubes showed any improvement. A total of 100 records of these variables are made for

each saline sample inserted into the resonator. The trends are as to be expected and are shown in Figures 6-61 to 6-63.

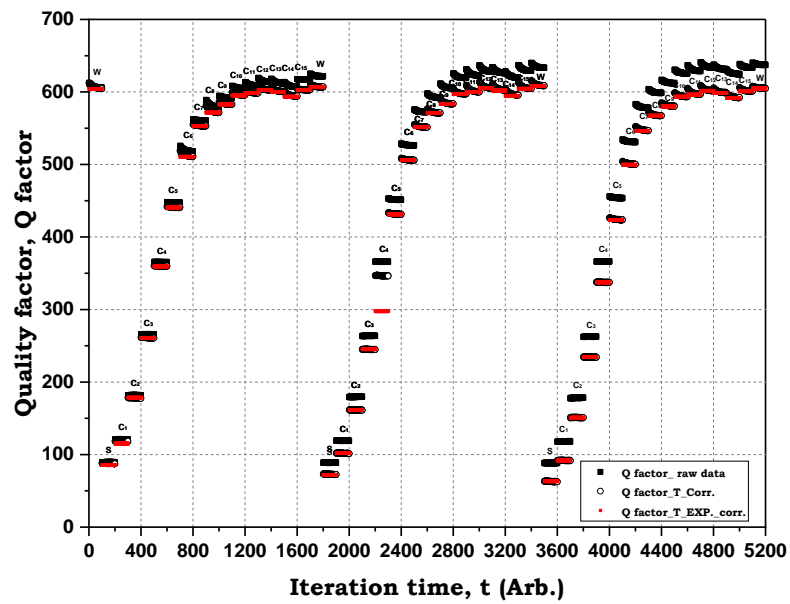


Figure 6-61: Raw data, Temperature and Exponential Corrections for Q factor Measurements of Lab prepared saline dilutions for variance concentrations (5.22E-05 to 1.71E+00) M by using a long thin Eppendorf tube sample.

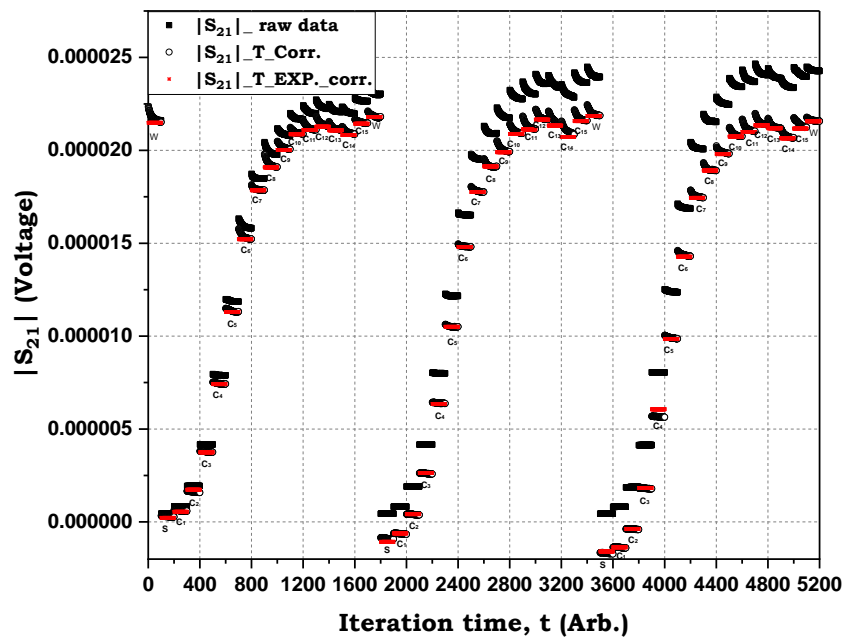


Figure 6-62: Raw data, Temperature and Exponential Corrections for  $|S_{21}|$  Measurements of Lab prepared saline dilutions for variance concentrations (5.22E-05 to 1.71E+00) M by using a long thin Eppendorf tube sample.

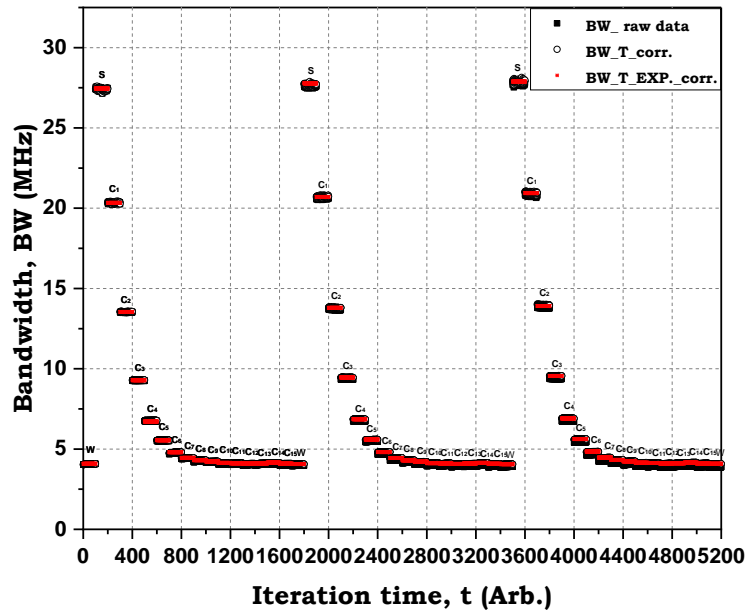


Figure 6-63: Raw data, Temperature and Exponential corrections for BW Measurements of Lab prepared saline dilutions for variance concentrations (5.22E-05 to 1.71E+00) M by using a long thin Eppendorf tube sample.

As before, the spread in water measurements was used to define the  $\pm 2\sigma$  and  $\pm 3\sigma$  bands to indicate the detection limit. Here the  $8.36E-04$  M ( $C_{11}$ ) concentration could be regarded as the lowest concentration that can be confidently differentiated from that of water (Figures 6-64 to 6-66). A slight improvement in detecting the lowest concentration has been shown in comparing between this cavity ( $C_{11}$ ) and  $TM_{010}$   $1.67E-03$  M ( $C_{10}$ ). The data point relating to  $1.04E-04$  M ( $C_{14}$ ) seems anomalous and should be disregarded. This occasionally (and consistently) happens and may be related to a fixed bubble or a deformity in the long thin Eppendorf tube.

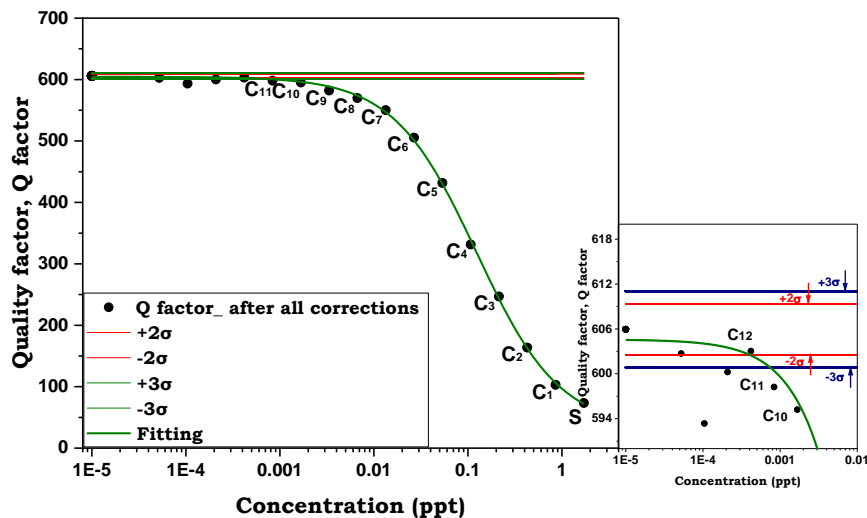


Figure 6-64: The correlation between the corrected Q factor data with different concentration for variance saline concentration (5.22E-05 to 1.71) M and statistical detection  $\pm(2\sigma(\text{red})$  and  $3\sigma(\text{blue}))$  by using a long thin Eppendorf tube sample.

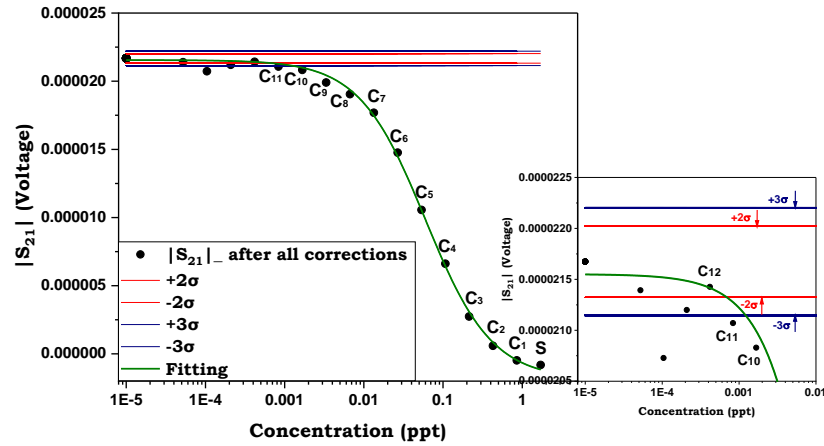


Figure 6-65: The correlation between the corrected  $|S_{21}|$  data with different concentration for variance saline concentration (5.22E-05 to 1.71) M and statistical detection  $\pm(2\sigma(\text{red})$  and  $3\sigma(\text{blue})$ ) by using a long thin Eppendorf tube sample.

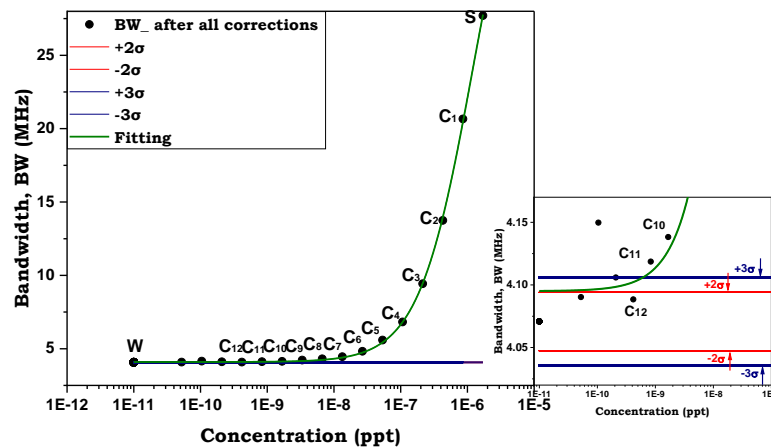


Figure 6-66: The correlation between the corrected BW data with different concentration for variance saline concentration (5.22E-05 to 1.71) M and statistical detection  $\pm(2\sigma(\text{red})$  and  $3\sigma(\text{blue})$ ) by using a long thin Eppendorf tube sample.

### 6.10.2 COMPARISON BETWEEN OUR EXPERIMENTAL WORK AND EARLIER PUBLICATIONS FOR THE SALINE

The results obtained from the long thin Eppendorf tubes have been converted to real and imaginary permittivity. This has been plotted against the published data and the earlier work using the wider tubes. Figures 6-67 and 6-68 show good agreement between this work and the published data.

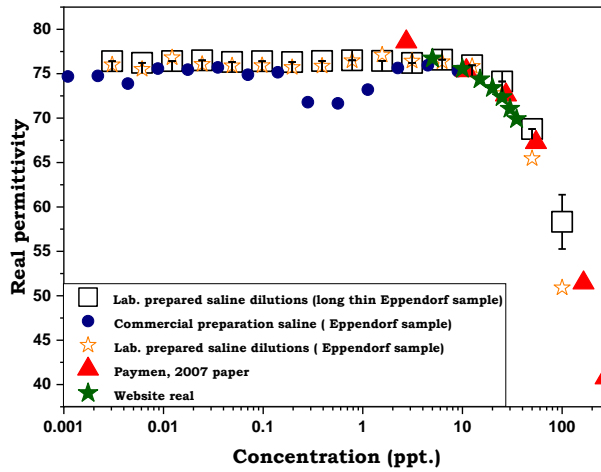


Figure 6-67: Real permittivity comparison among Lab prepared saline dilutions by using Eppendorf and long thin Eppendorf tube sample and commercially obtained saline, previous authors work.

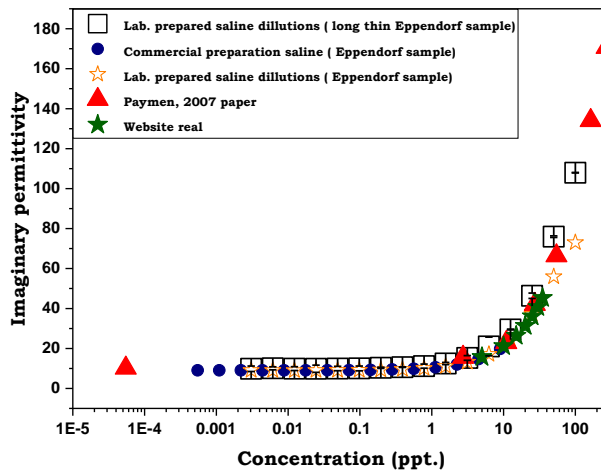


Figure 6-68: Imaginary permittivity comparison among Lab prepared saline dilutions by using Eppendorf and long thin Eppendorf tube sample and commercially obtained saline and previous authors work.

### 6.10.3 POLYSTYRENE RESULTS USING THIN AND LONG EPPENDORF TUBE SAMPLE

The raw and corrected data for  $Q$ ,  $|S_{21}|$ , and BW, using the long thin tube Eppendorf samples were studied and the results are shown in Figures 6-69 to 6-71.

In Figure 6-69 and 6-70, generally, the  $Q$  factor and the  $|S_{21}|$  increases gradually with decreasing concentration of the PS from 12.5 to 0.195 ppt. The BW data gradually reduces with decreasing concentration for the same range of concentrations (Figure 6-71).

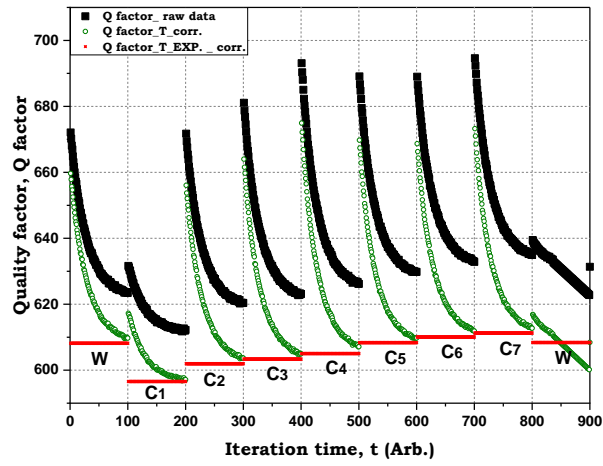


Figure 6-69: The averaging corrected quality factor of the suspension polystyrene 2  $\mu\text{m}$  with various concentrations 12.5 to 0.195 ppt and DI-W for a long thin Eppendorf tube.

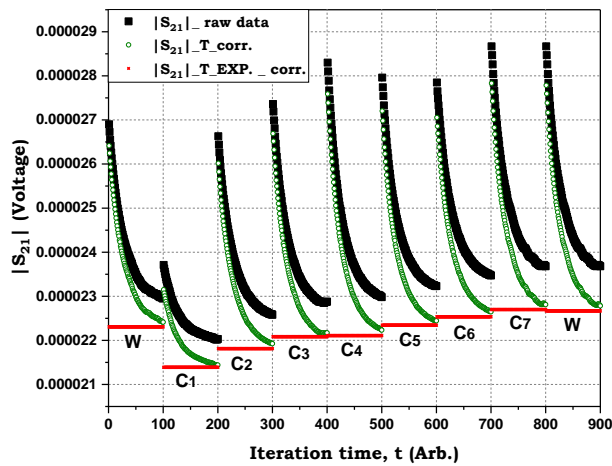


Figure 6-70: The averaging corrected  $|S_{21}|$  of the suspension polystyrene 2  $\mu\text{m}$  with various concentrations 12.5 to 0.195 ppt and DI-W for a long thin Eppendorf tube.

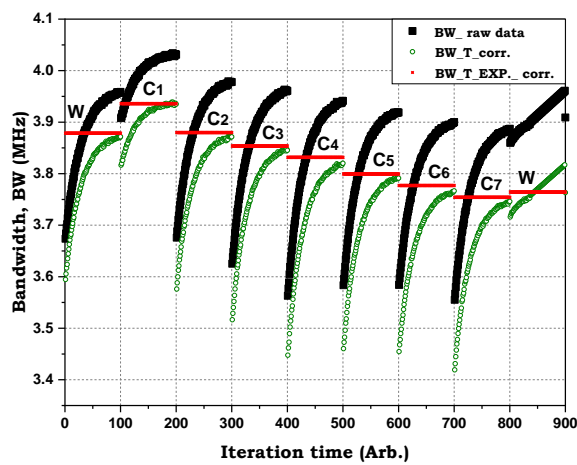


Figure 6-71: The averaging corrected BW of the suspension polystyrene 2  $\mu\text{m}$  with various concentrations 12.5 to 0.195 ppt and DI-W for a long thin Eppendorf tube.

The results below were obtained by averaging the corrected data. Sample concentrations over the range 12.5 to 0.195 ppt were prepared for the measurement of  $Q$ ,  $|S_{21}|$ , BW and CF, respectively (Figures 6-72 to 6-75). In Figures 6-72 to 6-74, we have found no evidence that the measurements are converging to that of water in all cases. It is worth pointing out that it was very difficult to maintain a suitably well-mixed sample with these tubes, in comparison to the wider body tubes. In order to displace the settled PS at the bottom of the tubes, it was necessary to displace the air bubble, normally at the top of the tube, to the bottom. This had the effect of returning the settled particles back into suspension. With the thin long tubes, it was almost impossible to displace the air bubble at the top of the tube and consequently, the re-mixing proved extremely challenging. Therefore, it was difficult to repeat the measurement due to the reason mentioned above.

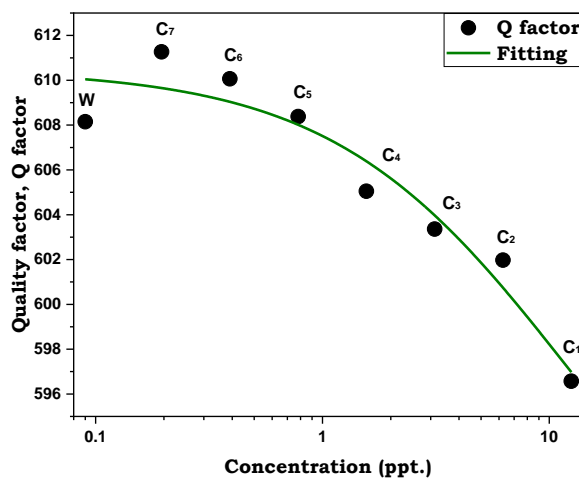


Figure 6-72: The corrected quality factor and the concentration of the suspension polystyrene 12.5 to 0.195 ppt and DI-W for a long thin Eppendorf tube.

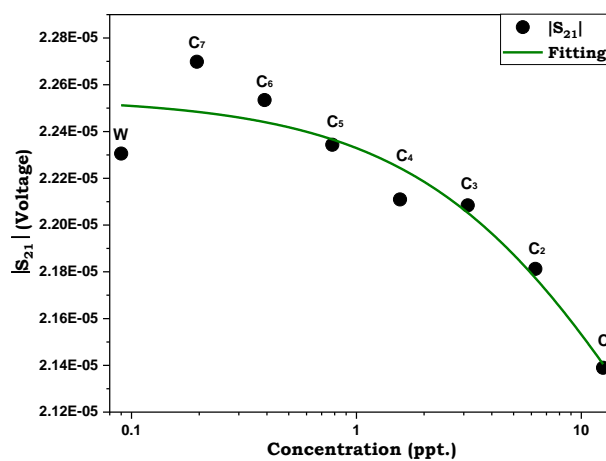


Figure 6-73: The corrected  $|S_{21}|$  and the concentration of the suspension polystyrene 12.5 to 0.195 ppt and DI-W for a long thin Eppendorf tube

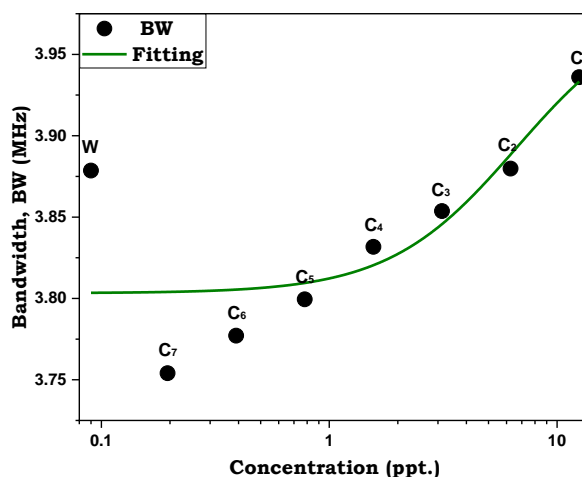


Figure 6-74: The corrected BW and the concentration of the suspension polystyrene 12.5 to 0.195 ppt and DI-W for a long thin Eppendorf tube

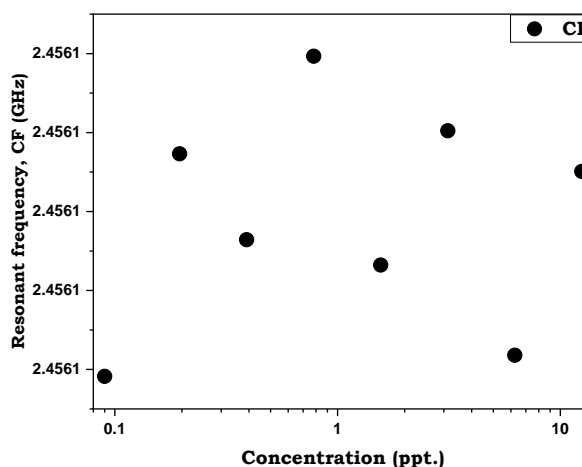


Figure 6-75: The resonant frequency and the concentration of the suspension polystyrene 12.5 to 0.195 ppt and DI-W for a long thin Eppendorf tube

#### 6.10.4 CONCLUSION FOR SALINE AND POLYSTYRENE RESULTS USING THIN AND LONG EPPENDORF TUBE SAMPLE

To summarise this part of this chapter, a long thin Eppendorf was used to reduce the depolarisation effect compared to the sample shape of Eppendorf utilized in section 6.5.3 for normal saline detecting  $5.22 \times 10^{-5}$  to  $1.71 \times 10^{+00}$  M. The results of the long thin Eppendorf showed a slight improvement in detection limit to  $8.36 \times 10^{-04}$  M (C<sub>11</sub>) compared to  $1.67 \times 10^{-03}$  M (C<sub>10</sub>), the result in section 6.5.3. Regarding the PS samples of the long thin Eppendorf, it was a big challenge to do the microwave measurements with this type of Eppendorf. Therefore, just one experiment set has been done.

### 6.10.5 COMPARISON BETWEEN THE PERMITTIVITY OF THE EXPERIMENTAL AND THE THEORETICAL (THE EFFECTIVE PERMITTIVITY) WORK FOR THE POLYSTYRENE

The comparison between the values of real and imaginary permittivity for the PS suspension are presented next and shown in Figures 6-76 and 6-77.

Unfortunately, it was found that there was a very poor agreement with the theoretical values of permittivity obtained from the effective medium calculation (section 5.4) and that obtained experimentally. For the real permittivity, virtually no comparable trend is observed. Interestingly, however, the imaginary permittivity showed almost the opposite trend to the calculated values. The predicted decrease in imaginary permittivity for increasing concentration relies on the idea that field enhancement is taking place around each particle. However, the observed measurements are opposite to this. One possible explanation here is that as the sample is shaken, microbubbles are created in the process that may cling to the PS particles or sit in the spaces between the particles. Any assumptions made about field enhancement here would have to factor in the presence of bubbles. Unfortunately, since the particles settle, the requirement to constantly shake the samples and return the settled particles into suspension makes it impossible to measure a truly representative suspension.

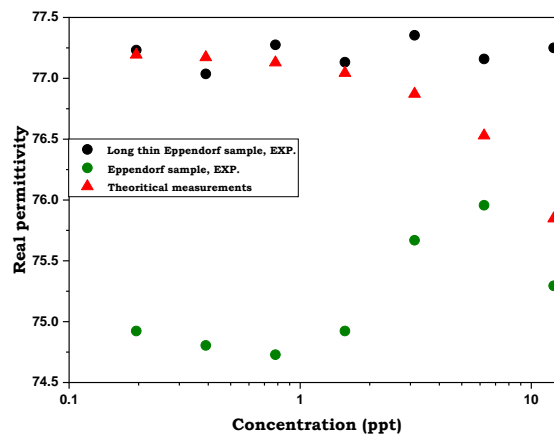


Figure 6-76: Real permittivity comparison between the Experimental and the Theoretical at the concentration of the suspension polystyrene 12.5 to 0.195 ppt.

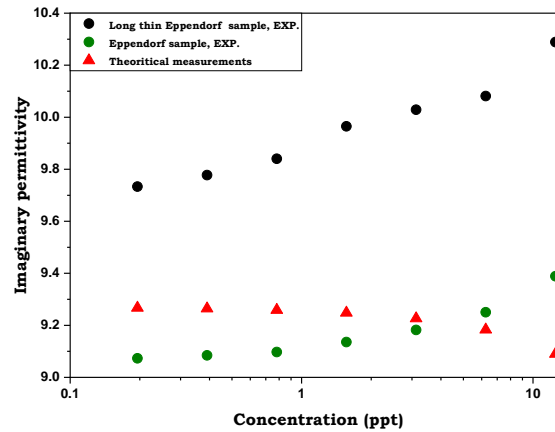


Figure 6-77: Imaginary permittivity comparison between the Experimental and the Theoretical at the concentration of the suspension polystyrene 12.5 to 0.195 ppt.

## 6.1 CHAPTER SUMMARY

Ch.6 investigates the reference value of detecting different dilutions of normal saline and PS using the previously circular resonant cavities. Two types of saline preparation have been used for detecting. Preparation of commercial obtained saline and lab preparation saline dilutions. Frequency, temperature, and exponential correction have been applied. The frequency correction has been done by a reference frequency as we found this frequency do not interact with sample volume. At experimental work, a strong correlation between sensing and reference mode has been found. Therefore, a robust and reliable correction from the environment that affects CCR has been applied at commercial obtained saline data. However, pre corrected frequency data has been applied for Lab preparation saline dilutions data by the LabVIEW data acquisition programme. Temperature correction has been done to remove the additional components in the system that are affected by the temperature such as the interconnect cables that link the VNA to the CCR. The exponential correction has been applied owing to the temperature difference between the ambient and the cavity resonator.

Even an exponential method is an extremely useful method for removing the effect of temperature, a curve fitting of MATLAB algorithm applied to determine the asymptotic value of the relevant parameter as recorded by the system.

A discrete improvement in the detection limit for low concentration has been found for lab preparation saline dilutions. A good separation down to  $1.67 \times 10^{-3}$  M (C10) with Q factor,  $|S_{21}|$  and BW measurements for lab preparation saline dilutions in comparison to  $2.41 \times 10^{-3}$  M (C6) for commercial obtained saline with the same measurements.

Regarding the detecting between the two previously circular resonant cavities, one by using the Eppendorf tube sample and Eppendorf long thin tube sample. A slight improvement in limit detecting for low concentration to  $8.36 \times 10^{-4}$  M (C11) for Eppendorf long thin tube sample in

---

comparison to  $1.67 \times 10^{-3}$  M ( $C_{10}$ ) for Eppendorf tube sample using saline samples. However, the comparison for SP could not find as the second set by using the long thin tube sample was difficult to find.

On comparing among two types of preparation the saline dilutions by using the Eppendorf tube sample, Lab. preparation saline dilutions by using Eppendorf long thin tube and previous authors' publications, a good agreement was found between the values of real and imaginary permittivity, with the exception of the real permittivity for the commercial's saline preparation.

In terms of the PS, a very poor agreement for the real permittivity with the theoretical values of permittivity obtained from the effective medium calculation. However, the imaginary permittivity showed almost the opposite trend to the calculated values.

# CHAPTER 7

## RESONANT COAXIAL PROBE

### 7.1 INTRODUCTION

Despite the advantages of the non-resonant coaxial cable probe that was mentioned in section 2.2.2.1; there are some limitations with this technique, such as the probe design, the accuracy of probe fabrication, calibration procedure, the capabilities of the VNA (VNA drift over time), and cable movement that detracts from the reliability. In the case of a liquid sample, air bubbles may be present which can be avoided by gentle insertion of the probe. To overcome many of the issues faced with the non-resonant probe, a *novel* T- Structure and capacitive coupling has been designed to increase the measurements' sensitivity and enable measures at a wide range of discrete frequencies (Figure 7-1 and 7-2).

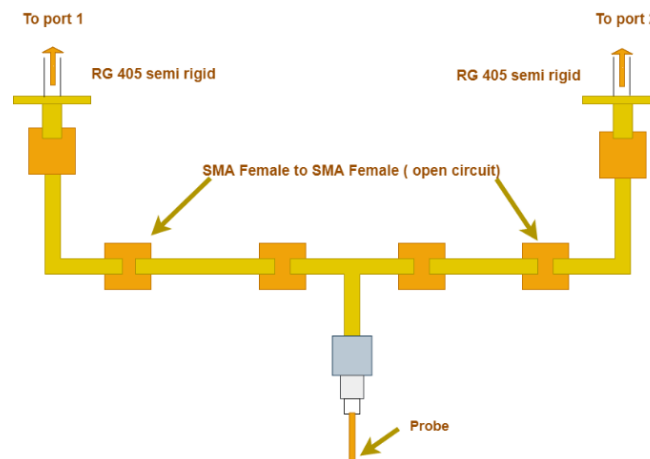


Figure 7-1: Schematic design of a *novel* T- Structure and capacitive coupling.

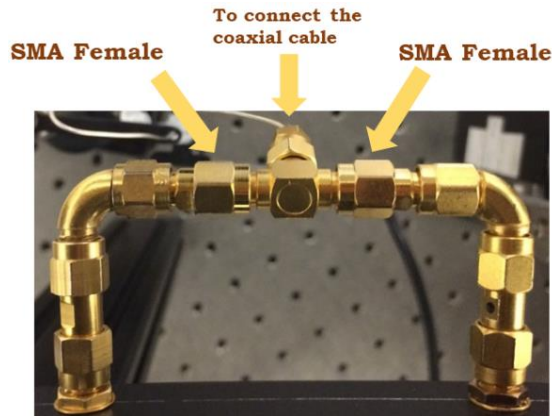


Figure 7-2: Physical design of a *novel* T- Structure and capacitive coupling.

## 7.2 METHODOLOGY

The semi-rigid coaxial cable with 255 cm has been used for fabrication in our design as it is cheap and easily available (The characterisation of this coax cable is mentioned in section 5.10). The VNA was used to measure the reflection of the broadband frequency and the transmission coefficient of the assembled device. The LabVIEW code has been used to extract the data as in Chapter 6. A Lorentzian curve was fitted to each resonance to measure the resonant frequency and bandwidth in real-time.

### 7.2.1 RESULTS OF COAXIAL RESONATOR (FIRST SET OF FREQUENCIES)

Four frequencies (0.757, 1.52, 2.3 and 3) GHz have been selected for the coaxial resonator's initial experiments. The same normal saline solution was prepared with a range of concentrations (0.154 to 9.40E-06) Molarity, as clarified in Table 6-26-1 Figures 7-3, 7-4 and 7-5 show raw measurements (black) and averaging (red) for the Q factor,  $|S_{21}|$  and BW, respectively for four frequencies 0.757, 1.52, 2.3 and 3 GHz. The averaging has been done without correction as the results the experiment was left to run overnight using the water sample. did not show a correlation between the microwave measurements and the temperature from

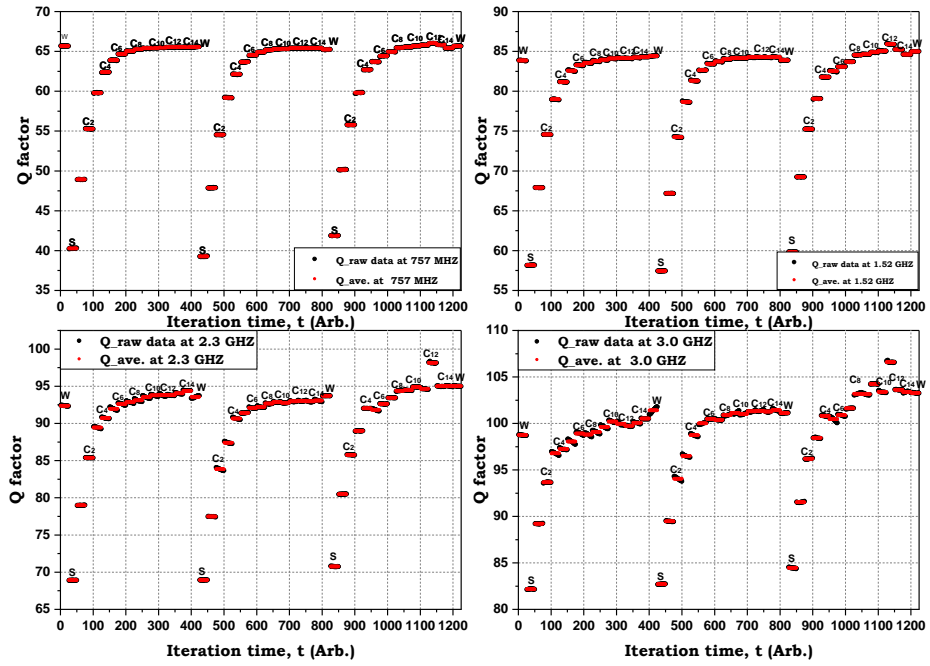


Figure 7-3: Raw and averaging data for Q factor measurements of commercial obtained saline for variance concentrations (0.154 to 9.400E-06) M.

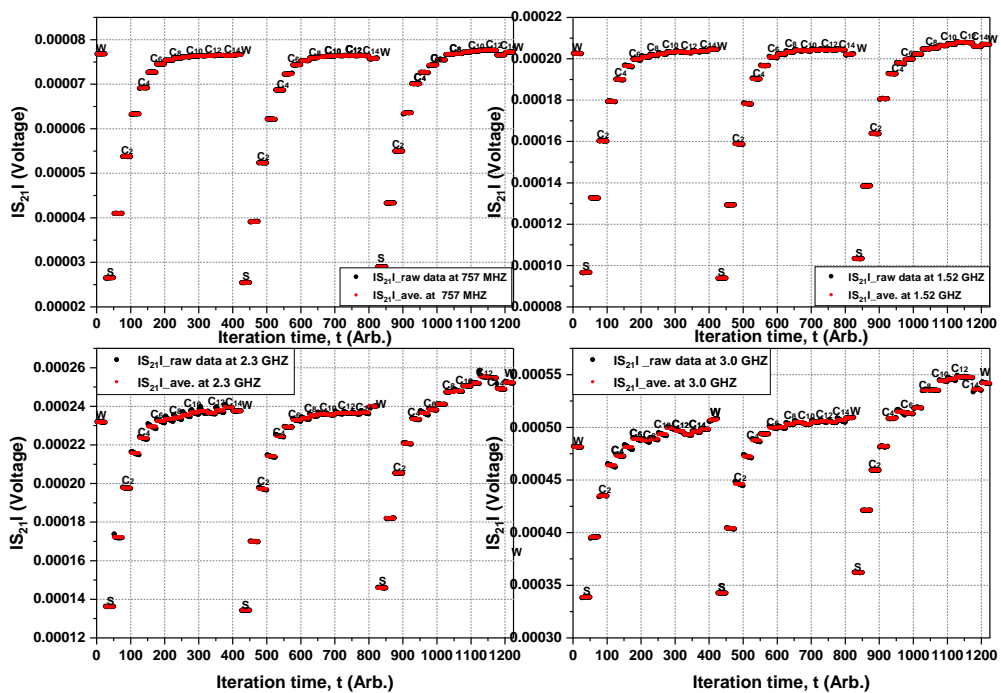


Figure 7-4: Raw and averaging data for  $|S_{21}|$  of commercial obtained saline for variance concentrations (0.154 to 9.400E-06) M.

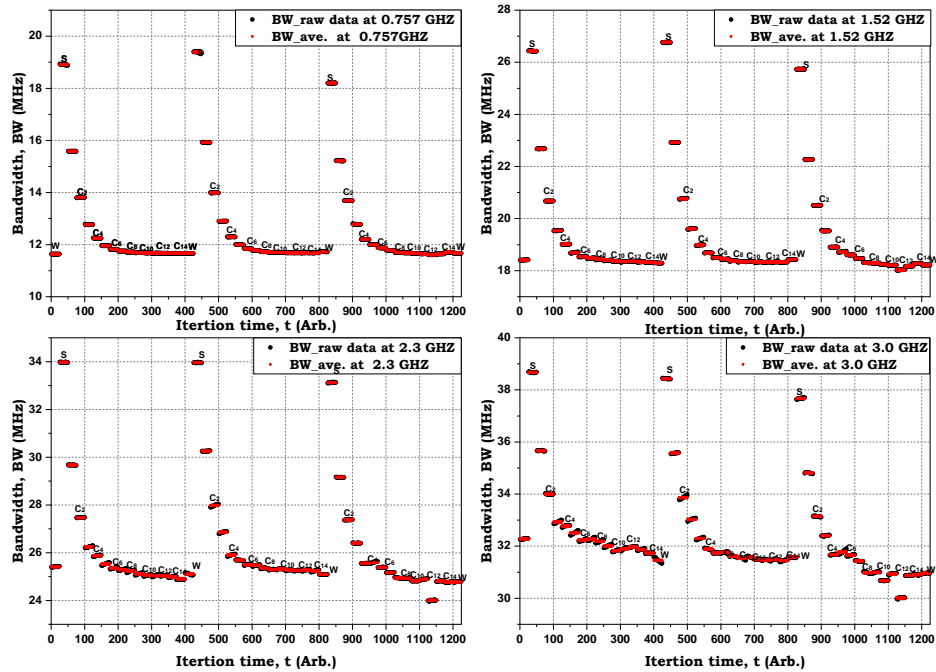


Figure 7-5: Raw and averaging data for BW measurements of commercial obtained saline for variance concentrations (0.154 to 9.400E-06) M.

Generally, it can be seen that there is a systematic change in the three sets of parameters consistent with the difference in the concentration of saline. In each graph above, the experiment was repeated three times. These trends are stable at the lower frequencies but become more erratic at higher frequencies. Maintaining consistency in the repeat experiments was also challenging, and deviations from the expected trends may be due to bubbles present. In each case, the measurements tend towards that of DI-W as the concentration decreases.

Appendix D-1, D-2 and D-3 represented the averaged values of  $Q$ ,  $|S_{21}|$  and BW over the three sets. For each of the frequencies, there is a clear separation between the  $4.81\text{E-}03$  M (C5) and  $2.41\text{E-}03$  M (C6) concentrations, beyond that, the ability to differentiate between the lower concentrations becomes difficult.

To show the detection boundary between DI-W and the lower concentrations of saline in the BW, the same statistical method mentioned in section 6.5 has been applied. Figures 7-6 to 7-8 indicates the  $3\sigma$  detection limit for each frequency together with the modelled trend. The graphs would suggest a detection limit down to  $2.41\text{E-}03$  M (C6),  $4.81\text{E-}03$  M (C5) and  $9.63\text{E-}03$  M (C4) for the first, second, and third modes, respectively. Regarding the fourth mode, the raw data variability suggests that no dilutions can be detected beyond the stock solution.

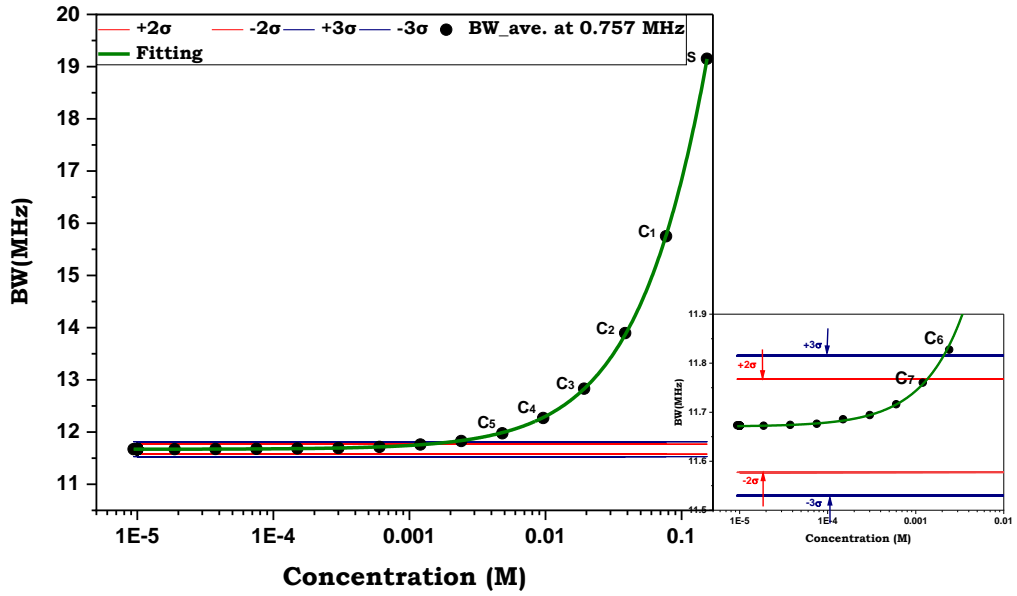


Figure 7-6: Detection limits at BW in the first mode 0.757 GHz over a range of dilutions (0.154 to 9.400E-06) M.

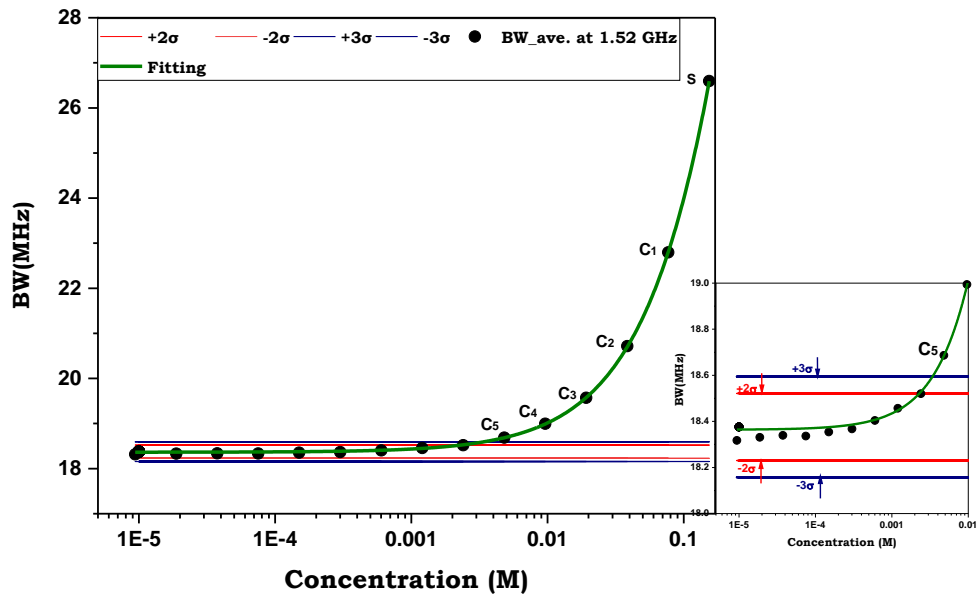


Figure 7-7: Detection limits at BW in the second mode 1.52 GHz over a range of dilutions (0.154 to 9.400E-06) M.

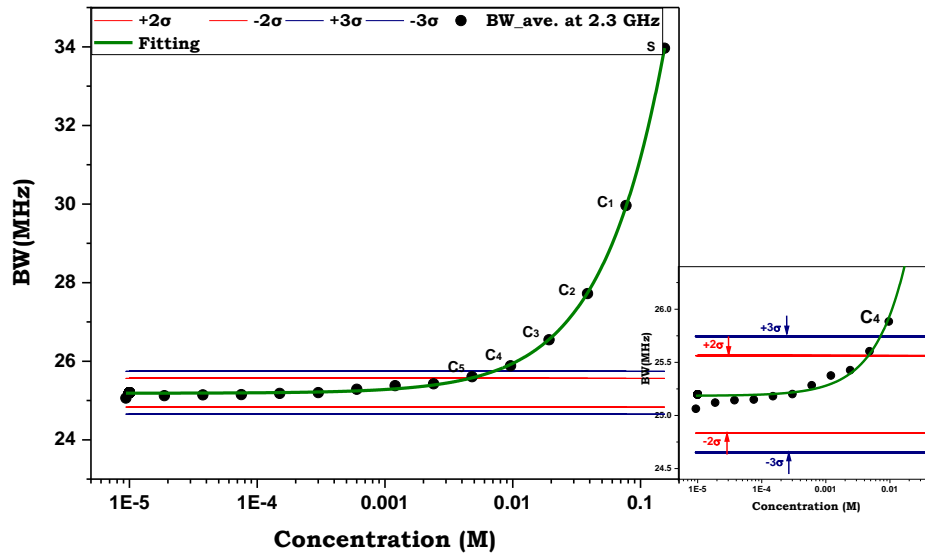


Figure 7-8: Detection limits at BW in the third mode 2.3 GHz over a range of dilutions (0.154 to 9.400E-06) M.

Figures 7-9 to 7-12 show the difference between Q factor,  $|S_{21}|$ , BW and CF measurements, respectively, and variance in concentrations of the normal saline (0.154 to 9.400E-06) Molarity. It is clear that the SE increases at higher frequencies and in particular at the fourth mode (3 GHz) for Q factor,  $|S_{21}|$ , and BW. This increase is related to the corrosion found in the centre conductor steel core in the resonant coax cable that was explored at the end of normal saline experiments and will explain in detail in section 7.2.2.5.

Regarding the CF, there is a fluctuation in the four modes, which might be due to the presence of bubbles or to the rust found out later on the tip of the probe. The smaller penetration depth for the high frequencies suggests it is more sensitive to tip surface morphology. The CF measurements' standard error is high for all modes overall concentrations (Figure 7-12).

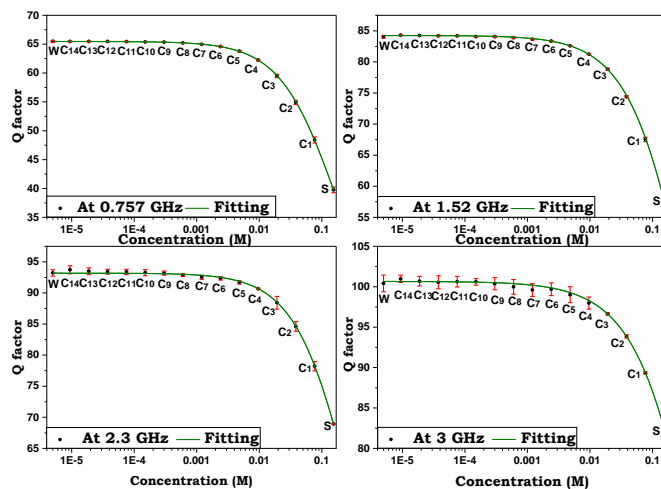


Figure 7-9: Comparison between Q factor of different frequencies (0.757, 1.52, 2.3 and 3) GHz for variance concentrations (0.154 to 9.400E-06) M.

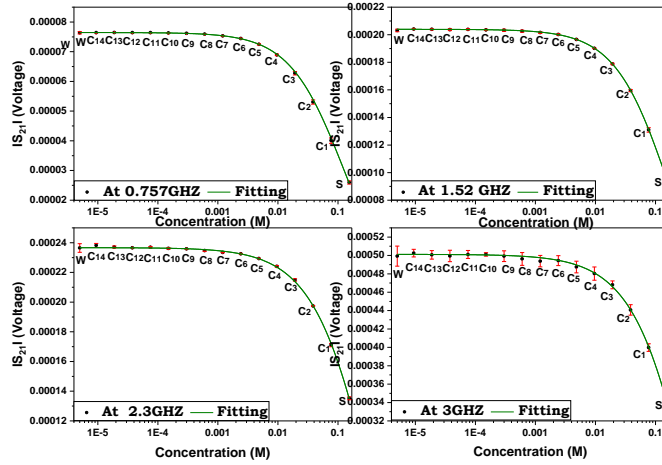


Figure 7-10: Comparison between  $|S_{21}|$  of different frequencies (0.757, 1.52, 2.3 and 3) GHz for variance concentrations (0.154 to 9.400E-06) M.

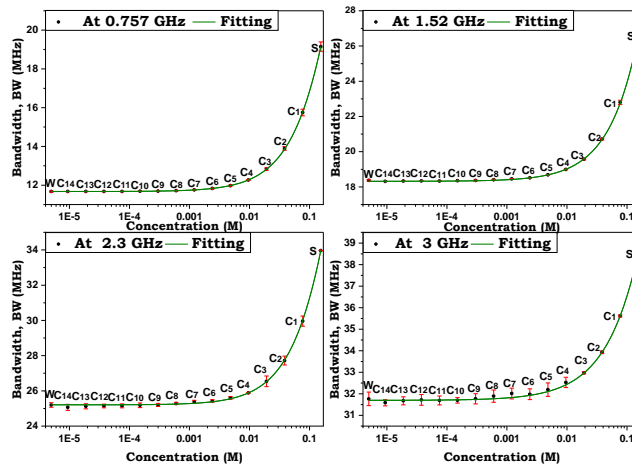


Figure 7-11: Comparison between BW of different frequencies (0.757, 1.52, 2.3 and 3) GHz for variance concentrations (0.154 to 9.400E-06) M.

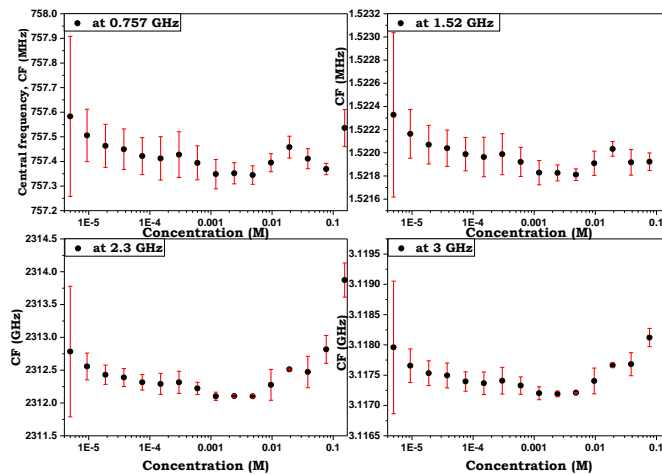


Figure 7-12: Comparison between CF of different frequencies (0.757, 1.52, 2.3 and 3) GHz for variance concentrations (0.154 to 9.400E-06) M.

---

### 7.2.1.1 CONCLUSION OF THE FIRST SET OF FREQUENCY

The outcome of using four frequencies for detection showed that the high frequencies (2.3 and 3) GHz are not effective in detecting compared to the lower frequencies (0.757 and 1.52) GHz.  $9.63\text{E-}03$  M (C4) and no dilutions can be detected beyond the stock solution are the detection limit for 2.3 and 3 GHz, respectively. However,  $2.41\text{E-}03$  M (C6) and  $4.81\text{E-}03$  M (C5) are the detection limit for 0.757 and 1.52 GHz, respectively.

### 7.2.2 A SECOND SET FREQUENCIES DETECTION

From the previous work results, it was obvious that the high frequency (2.3 and 3) GHz are not efficient in detecting the solution concentrations, particularly for the small concentrations. Therefore, another set of frequencies (0.378, 0.757, 1.14 and 1.52) GHz by using coax cable with length 255 mm was selected for detection (the same coax cable used in section 7.2.1). This step has been done before recognising the corrosion in the probe. For this set of frequencies (0.378, 0.757, 1.14 and 1.52) GHz, the samples used were from the preparation mentioned in section 6.5.3.1 (Lab Prepared Saline Dilutions) with a range of concentrations ( $5.22\text{E-}05$  to 1.71) M clarified in Table 6-2.

#### 7.2.2.1 STEPS FOR IMPROVING THE RAW DATA

To correct the raw data from the temperature, Pico temperature ( $T_0$ ), sample temperature ( $T_1$ ) and ambient temperature ( $T_2$ ), which were controlled using the thermocouple in Pico technology, an experiment was left to run overnight using the water sample. This experiment shows that there is no evidence of a correlation between the Q factor and each of the temperatures  $T_0$ ,  $T_1$  and  $T_2$  for any of the resonator modes. Figures 7-13 and 7-14 show the results for just the first frequency, which exhibits the same trend as the other frequencies. Despite this, the temperature will become a feature of later data analysis once corrosion is resolved. The lack of correlation suggests that changes occur at the probe tip, which is not currently accounted for.

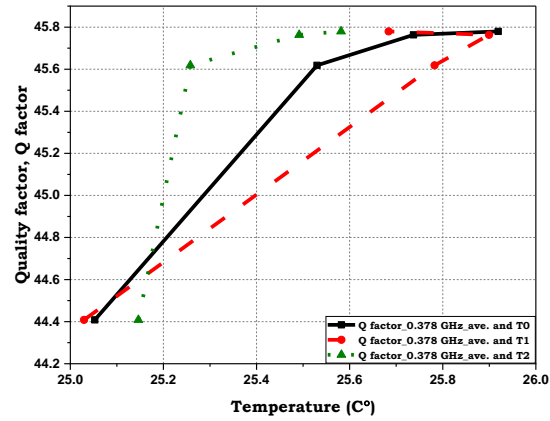


Figure 7-13: Variation in the quality factor at 0.378 GHz with the Pico temperature (T0), which is a simple term interface between thermocouple and the PC, sample temperature (T1) and ambient temperature (T2).

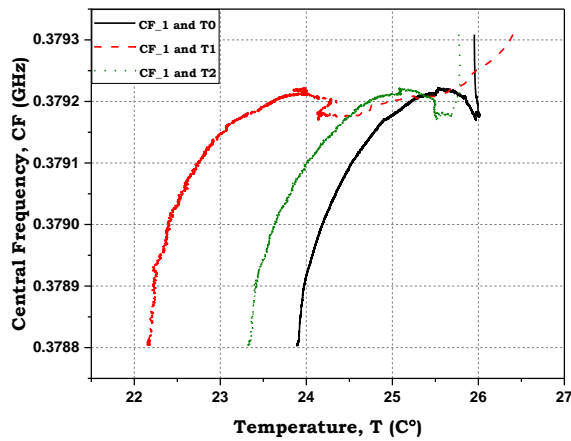


Figure 7-14: Correlation of the central frequency (CF\_1) 0.378 GHz with the Pico temperature (T0), sample temperature (T1) and ambient temperature (T2).

### 7.2.2.2 RESULTS FOR THE SECOND SET FREQUENCIES DETECTION

Figures 7-15 to 7-17 present information about the Q factor,  $|S_{21}|$  and BW measurements respectively for 0.378, 0.757, 1.14 and 1.52 GHz for saline over the range of concentrations ( $5.22 \times 10^{-5}$  to 1.71) M. These Figures show the average values for three repeat data sets in the appendix (Appendix D-4 to D-6). Good separation has been found up to  $6.68 \times 10^{-3}$  M (C8) for all modes.

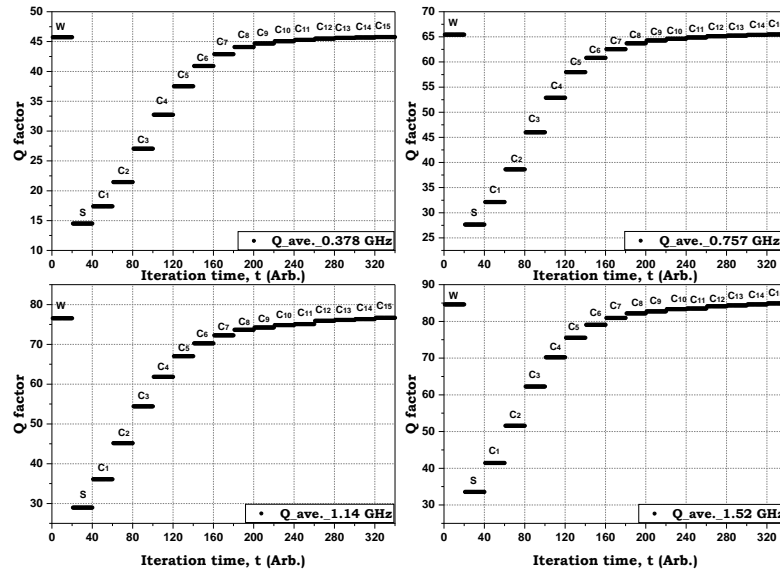


Figure 7-15: The average Q factor measurements of Lab. prepared saline for variance concentrations (5.22 e-05 to 1.71) M.

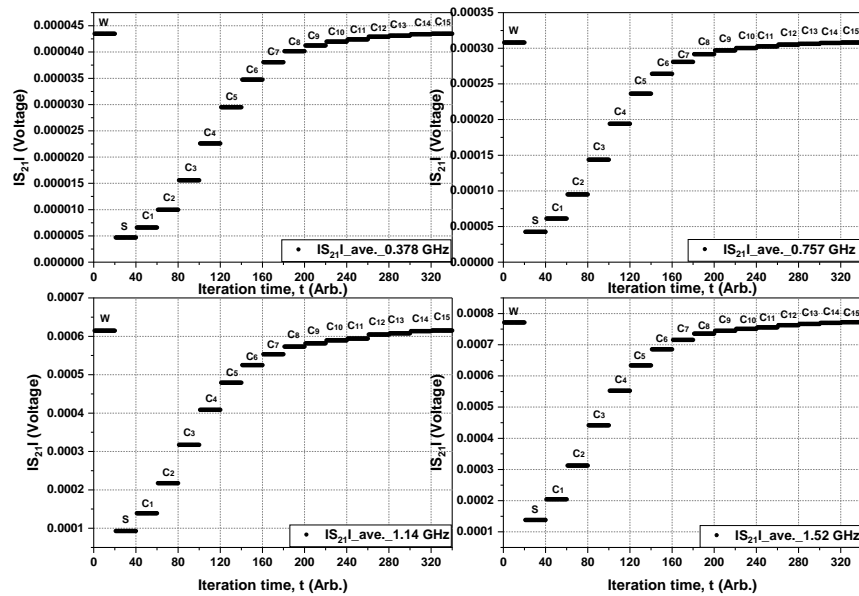


Figure 7-16: The average  $|S_{21}|$  measurements of Lab. prepared saline for variance concentrations (5.22e-05 to 1.7) M.

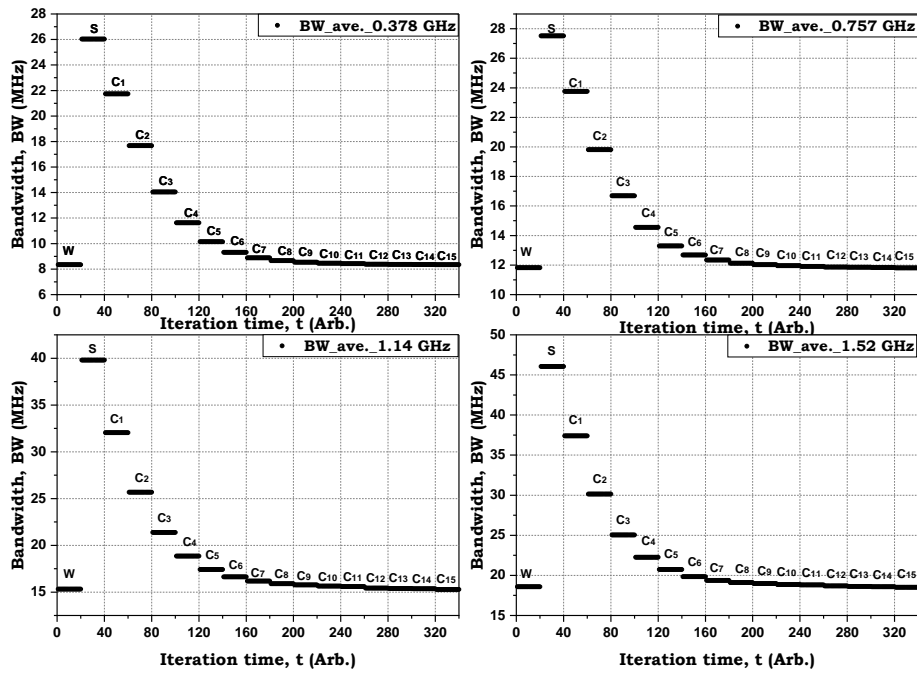


Figure 7-17: The average BW measurements of Lab. prepared saline for variance concentrations (5.22E-05 to 1.71) M.

This type of preparation (Lab Prepared Saline Dilutions), Figures 7-18 to 7-21 show a slight improvement in the lower frequencies and a considerable improvement from higher frequencies in terms of the detection limit with the low concentration. The Figures showed good separation down to  $1.34 \times 10^{-2}$  M (C7),  $3.34 \times 10^{-3}$  M (C9), and  $2.67 \times 10^{-2}$  M (C6) for the first, second, third and fourth mode, respectively.

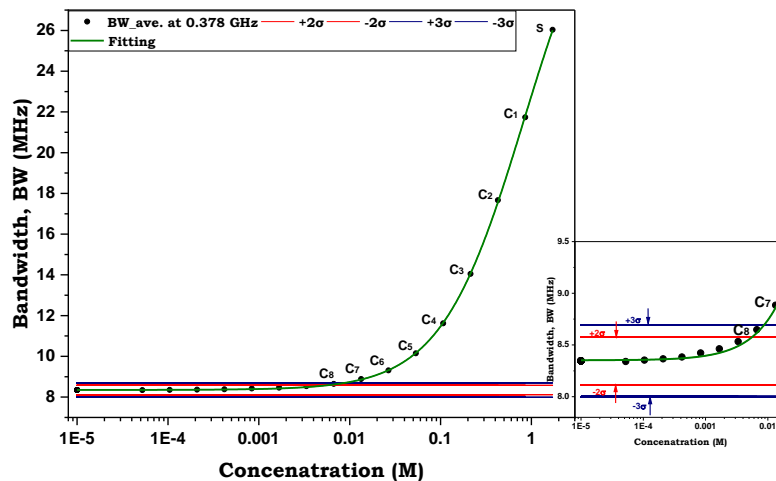


Figure 7-18: Detection limits at BW in the first mode 0.378 GHz over a range of dilutions (5.22E-05 to 1.71) M.

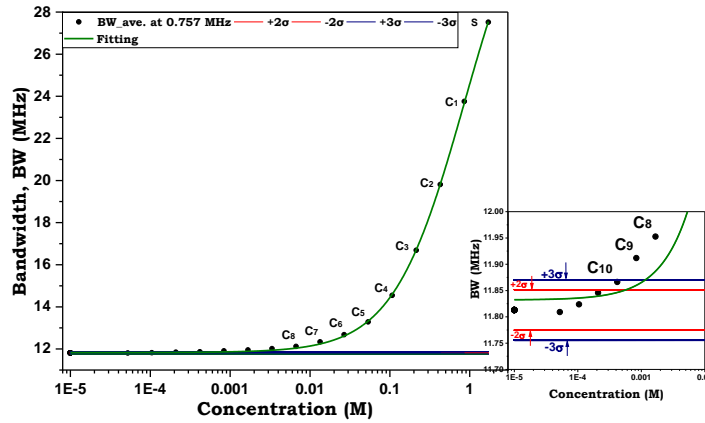


Figure 7-19: Detection limits at BW in the second mode 0.757 GHz over a range of dilutions (5.22E-05 to 1.71) M.

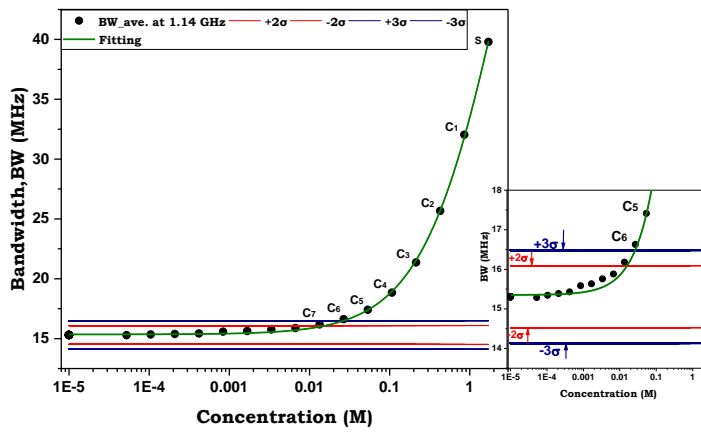


Figure 7-20: Detection limits at BW in the third mode 1.14 GHz over a range of dilutions (5.22E-05 to 1.71) M.

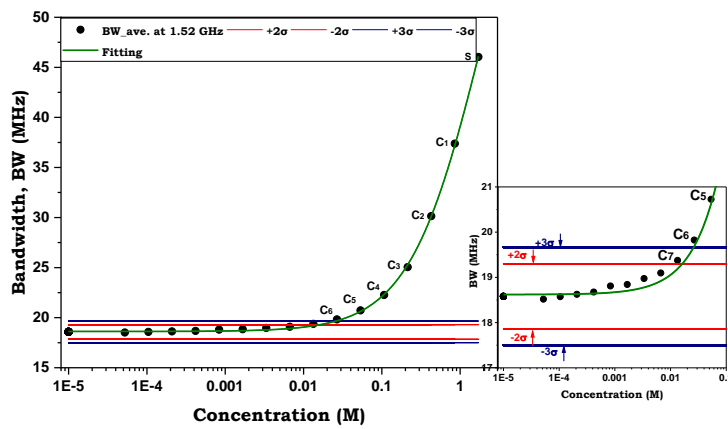


Figure 7-21: Detection limits at BW in the fourth mode 1.52 GHz over a range of dilutions (5.22E-05 to 1.71) M.

---

### 7.2.2.3 EFFECT OF VARIOUS CONCENTRATIONS ON MICROWAVE MEASUREMENTS AT 0.378, 0.758, 1.14 AND 1.52 GHz

Figures 7-22 to 7-25 show the variance in the data obtained for Q factor,  $|S_{21}|$ , BW and CF for the same set of the frequencies with the range of concentration  $5.22E-05$  to  $1.71$  M.

The trend in the Q factor and  $|S_{21}|$  increase with reducing the concentrations and vice versa with BW. To understand the correlation between the Q factor,  $S_{21}$  and BW with the concentration, the following paragraphs serve as an explanation.

The Q factor of a resonator measures the strength of the damping of its oscillations or for the relative linewidth. As this increases, the relative amount of damping decreases. Damping refers to the reduction in oscillation magnitude because of the dissipation of energy. So to take it one step further, damping affects the gradual fading of oscillation amplitude and affects the natural frequency of the oscillator. An increase in solute concentration would increase the damping of the resonator due to the additional conduction losses due to the presence of the mobile ions,  $Na^+$  and  $Cl^-$ . Since there is an inverse correlation between the Q factor and BW (Q factor is defined in terms of BW and CF), the BW increases with decreasing the Q factor. Regarding the insertion loss  $S_{21}$ , at high concentration, the attenuation increases at a higher frequency (high Q factor) in comparison to the low frequency.

In terms of the CF in Figure 7-25, it is clear that the trend at low frequencies (375 and 757) MHz is different than that at high frequencies (1.14 and 1.52) GHz. The trend gradually increases with decreasing concentrations at low frequencies. However, at high frequencies, the feature started to decrease then increase with decreasing concentrations. This may be related to the presence of bubbles. The standard error in the CF data is higher at higher frequencies more than at low frequencies. Based on observations, bubbles may be related to the probe tip 'capturing' some air as it is inserted into the solution. The presence of the bubble in the liquid can be considered as a representative example from nonlinear dynamical systems theory with its resonances. It is difficult to fully describe owing to infinite complexity. Furthermore, the possible presence of rust on the tip surface may absorb air in its inclusions, which dissipate or dissolve over time. Whilst this is conjecture, it may explain the reduction of the SE as time goes by.

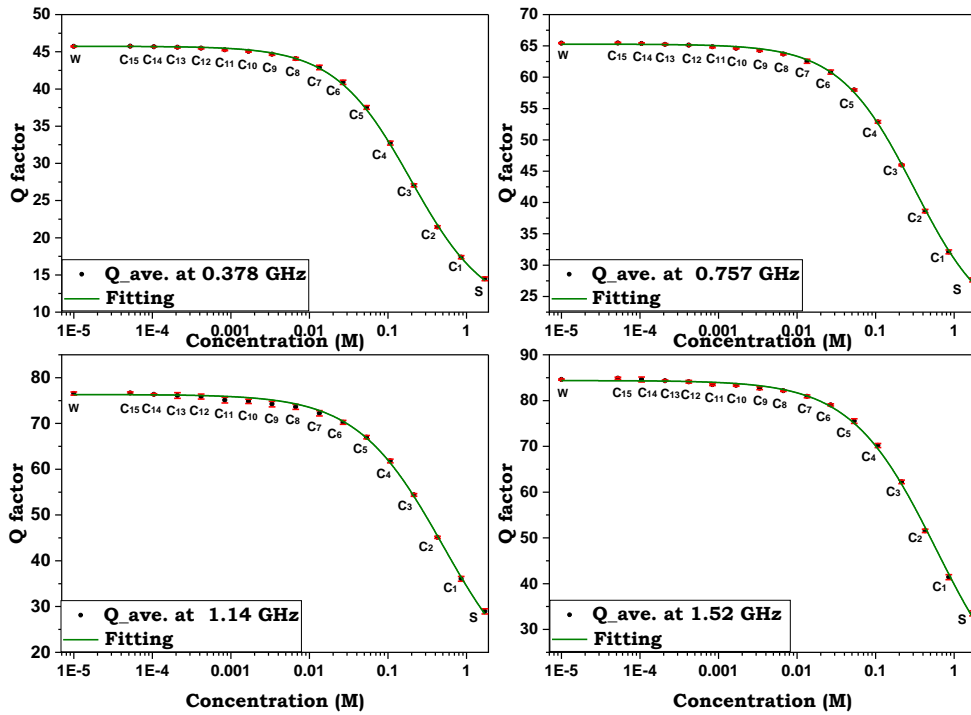


Figure 7-22: Comparison between Q factor of different frequencies (0.378, 0.757, 1.14 and 1.52) GHz for variance concentrations (5.22e-05 to 1.71) M.

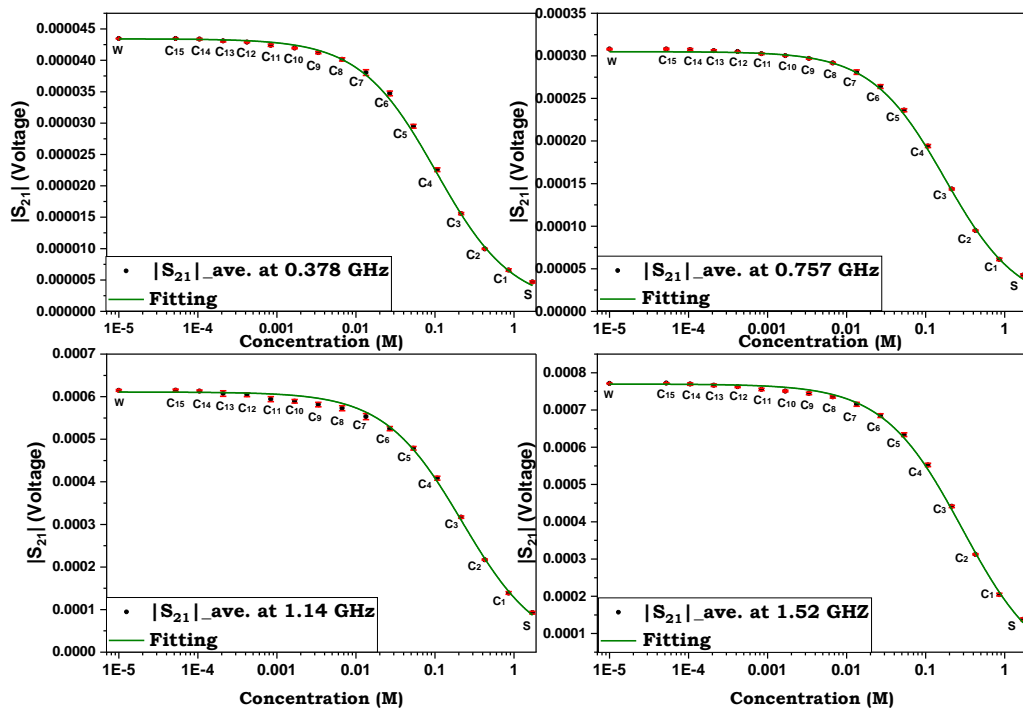


Figure 7-23: Comparison between |S<sub>21</sub>| of different frequencies (0.378, 0.757, 1.14 and 1.52) GHz for variance concentrations (5.22e-05 to 1.71) M.

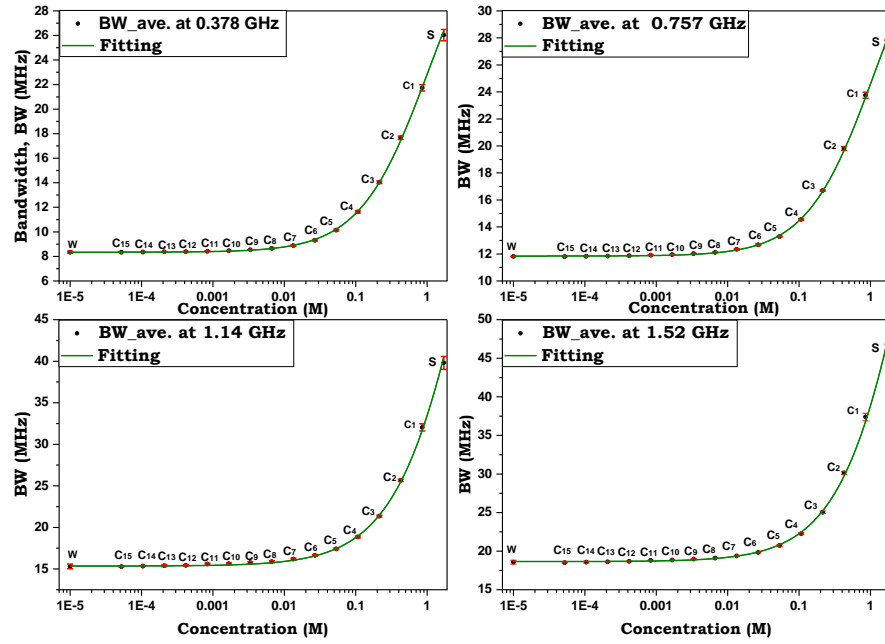


Figure 7-24: Comparison between BW of different frequencies (0.378, 0.757, 1.14 and 1.52) GHz for variance concentrations (5.22e-05 to 1.71) M.

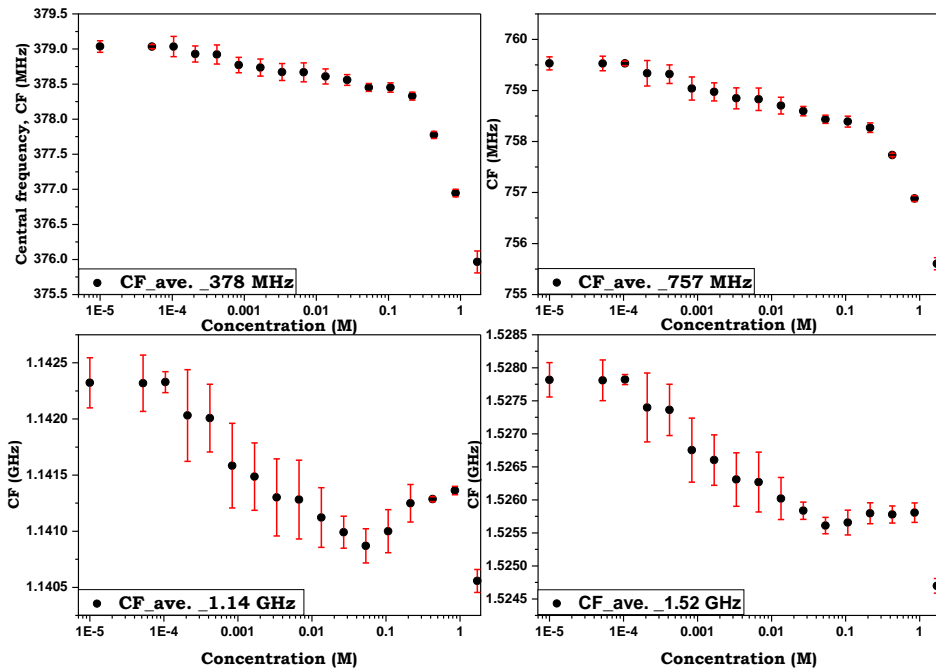


Figure 7-25: Comparison between CF of different frequencies (0.378, 0.757, 1.14 and 1.52) GHz for variance concentrations (5.22e-05 to 1.71) M.

### 7.2.2.4 CONCLUSION FOR THE SECOND SET FREQUENCIES DETECTION

In the Lab Prepared Saline Dilutions, the detection limit with low concentrations showed a minor improvement at lower frequencies (0.378 and 0.757) GHz and a significant improvement at higher frequencies (1.14 and 1.52) GHz. On comparing between the two preparations methods (commercial saline obtained and Lab saline prepared) at 0.757 and 1.52 GHz. An improvement in detection found in the Lab saline prepared compared to the commercial saline obtained. Lab saline prepared can be detected to  $3.34 \times 10^{-3}$  M (C<sub>9</sub>), and  $2.67 \times 10^{-2}$  M (C<sub>6</sub>) for 0.757 and 1.52 GHz compared to  $2.41 \times 10^{-3}$  M (C<sub>6</sub>) and  $4.81 \times 10^{-3}$  M (C<sub>5</sub>) for the commercial obtained saline at the same frequencies.

### 7.2.2.5 COMPARISON BETWEEN TWO TYPES OF SALINE PREPARATION.

Figures 7-26 to 7-28 present the variation in Q factor,  $|S_{21}|$ , BW with different concentrations for two types of saline solution, prepared from various source materials. And the CF comparison is shown in appendix D-7 and D-8.

For the Q factor, the small difference in the two saline preparations' trends could be down to the exact nature of the water used in the commercially obtained saline from Boots. It is known that the source of water used to make the solution and that used in the dilutions are different. For this reason, pure NaCl and DI-W were procured to prepare the 'in-house' saline stock. This ensured that the dilution water was from the same source.

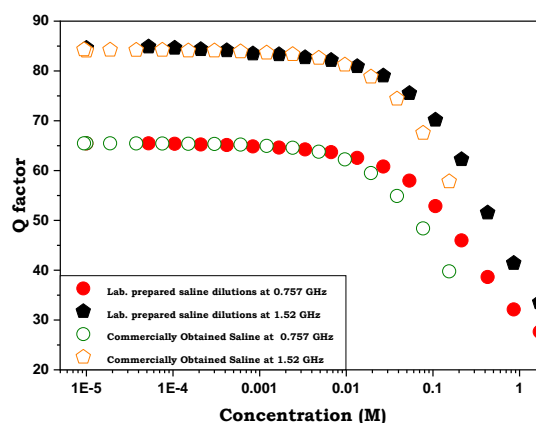


Figure 7-26: Comparing between the Q factor measurements of different frequencies for variance concentrations of commercially obtained saline (0.154 to  $9.4 \times 10^{-6}$ ) M and Lab. prepared saline dilutions ( $5.22 \times 10^{-5}$  to 1.71) M.

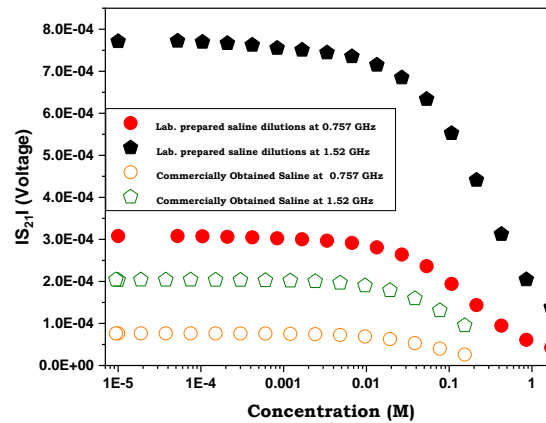


Figure 7-27: Comparing between the  $|S_{21}|$  measurements of different frequencies for variance concentrations of commercially obtained saline (0.154 to  $9.4\text{E-}06$  M) and Lab. prepared saline dilutions ( $5.22\text{e-}05$  to 1.71) M.

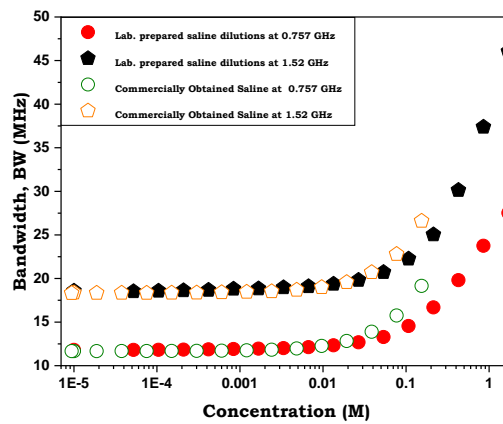


Figure 7-28: Comparing between BW measurements of different frequencies for variance concentrations of commercially obtained saline (0.154 to  $9.4\text{E-}06$  M) and Lab. prepared saline dilutions ( $5.22\text{e-}05$  to 1.71) M.

A microscope inspection was done for the single resonator probe to explore the potential for probe tip corrosion. The photos clarify the corrosion of the centre conductor's steel core in the single resonator (Figure 7-29). As there is an inverse correlation between the frequency and the penetration depth, the presence of the rust layer on the tip of the probe as a result of the saline solution and water are likely to affect the results of the higher frequencies more than the lower frequencies. To fully understand, the skin depth for 0.378 and 1.52 GHz are 3.26 and 1.63  $\mu\text{m}$  in our research which was determined by using the calculator in [159]. Therefore, the resistance of the wire increases with decreasing the skin depth at high frequency as shown in Equation 5-42. As result, the smaller penetration depth for the high frequencies suggests it is more sensitive to tip surface morphology.

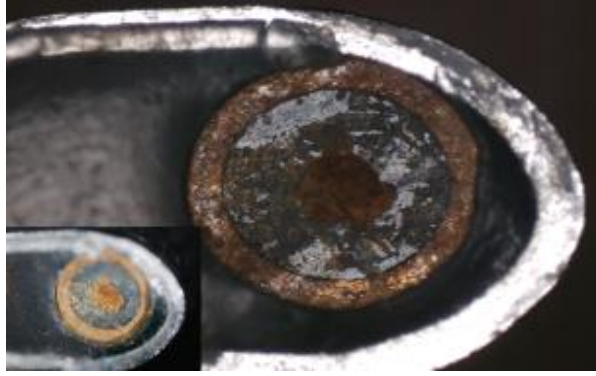


Figure 7-29: Corrosion of the steel centre conductor

### 7.2.2.6 CONVERTING THE MICROWAVE MEASUREMENTS TO REAL AND IMAGINARY PERMITTIVITY

The same steps highlighted in section 6.5.3.4 have been applied to all frequencies for converting the microwave measurements into real and imaginary permittivity, as shown in Figures 7-30 and 7-31, respectively. In Figure 7-30, the first two modes vary as expected. However, the higher two modes show that the trends switch gradient at around 3 ppt which may be attributed to the variance of the central frequency with decreasing the concentration at high frequencies as shown in Figure 7-25. Conversely, the imaginary permittivity decreases gradually for all frequency sets with reducing concentration, as shown in Figure 7-31. There is a similar trend for all modes.

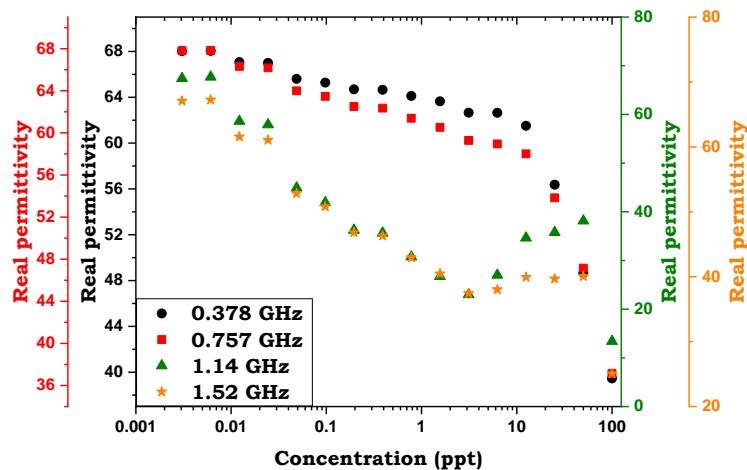


Figure 7-30: Comparing between Real permittivity of different frequencies 0.378, 0.757, 1.14 and 1.52 GHz of Lab. prepared saline dilutions (5.22e-05 to 1.71) M.

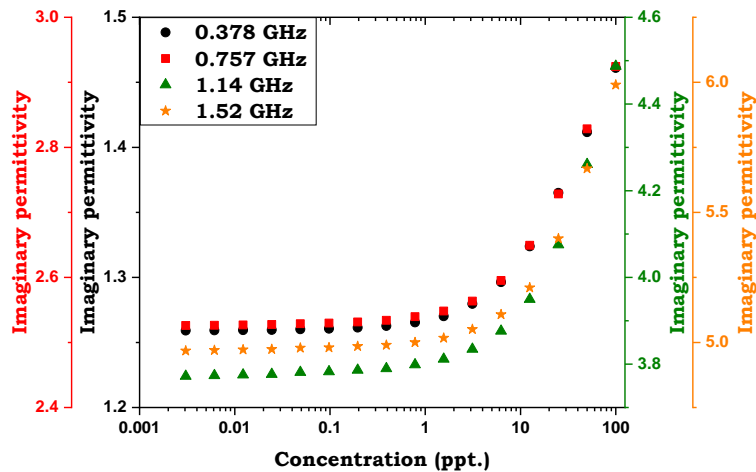


Figure 7-31: Comparing between imaginary permittivity of different frequencies 0.378, 0.757, 1.14 and 1.52 GHz of Lab. prepared saline dilutions ( $5.22 \times 10^{-5}$  to 1.71) M.

## 7.3 COAXIAL CABLE AND POLYSTYRENE EXPERIMENTS

Despite the corrosion of the steel centre conductor, the same cable has been utilised after polishing.

In these experiments, three particle sizes 2, 0.8 and 0.413  $\mu\text{m}$  with different concentrations were used to measure BW, Q factor,  $|S_{21}|$  and CF. Four modes are selected for these measurements at 0.378, 0.757, 1.14 and 1.52 GHz, with three different polystyrene spheres in suspension (PS). Five different concentrations were prepared: stock (S with 25 ppt from the manufacturer), the gradual half concentrations (the same preparation method in section 4.2.1). 25 to 1.56 ppt (S, C<sub>1</sub>, C<sub>2</sub>, C<sub>3</sub>, and C<sub>4</sub>) and pure DI-W as a reference for 2 and 0.8  $\mu\text{m}$  and 25 and 12.5 to 3.13 ppt (S and C<sub>1</sub> to C<sub>3</sub>) at 0.413.  $\mu\text{m}$ . The following sections will discuss all the microwave measurements separately for each particle and the necessary data correction steps.

### 7.3.1 MICROWAVE MEASUREMENTS AT 2 $\mu\text{m}$ POLYSTYRENE SPHERES IN SUSPENSION

Figures 7-32, 7-33 and 7-34 show the raw data for BW, Q factor and  $|S_{21}|$  measurements. The first impression suggests that the scatter of points for each measurement are clustered for the first two modes but show a correlation with some, as yet unknown quantity, for the higher modes. These measurements were with different concentrations of PS 25 ppt and 12.5 to 1.56 ppt. (S and C<sub>1</sub> to C<sub>4</sub>), and pure water as a reference in our measurements.

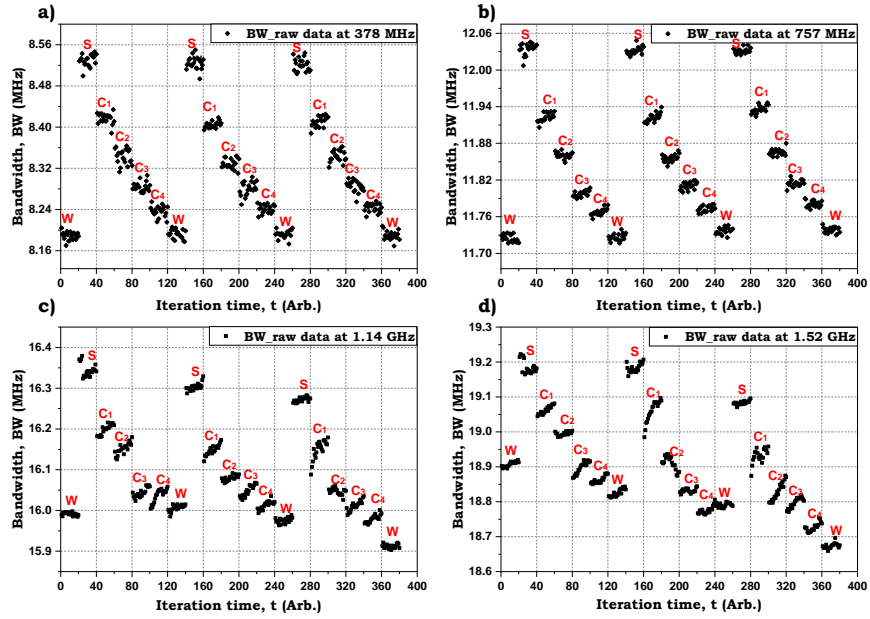


Figure 7-32: Raw data for BW measurements of polystyrene with 2 μm of four modes for variance concentrations (25 to 1.56) ppt.

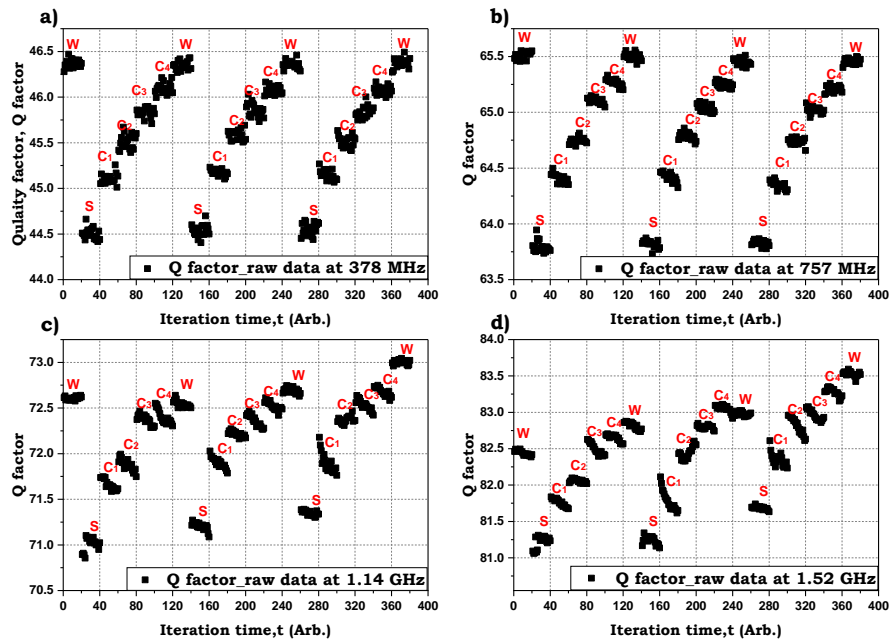


Figure 7-33: Raw data for Q factor of polystyrene with 2 μm of four modes for variance concentrations (25 to 1.56) ppt.

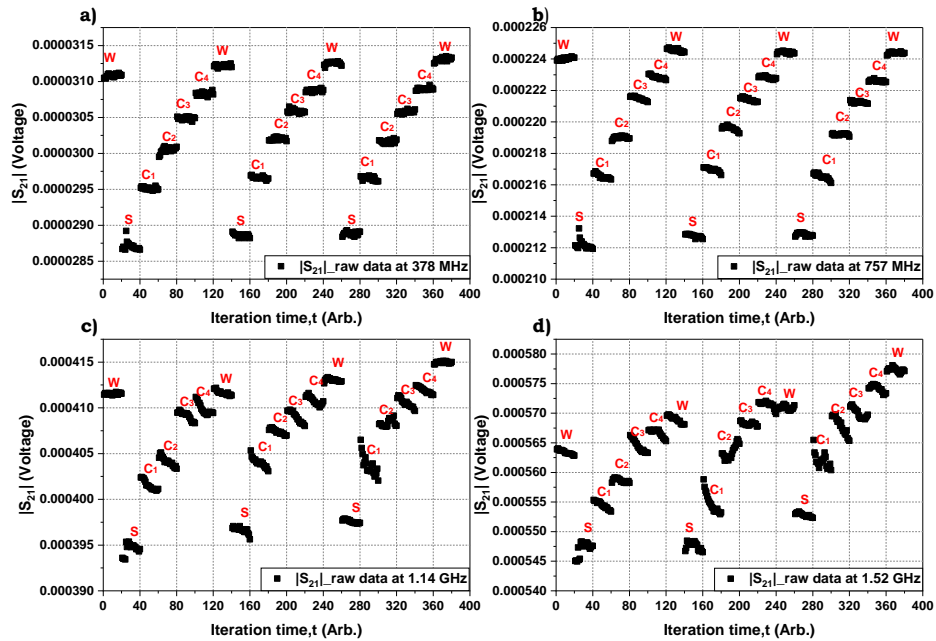


Figure 7-34: Raw data for  $|S_{21}|$  of polystyrene with  $2 \mu\text{m}$  of four modes for variance concentrations (25 to 1.56) ppt.

To overcome the spread in the clusters and the apparent drift, another correction procedure has been applied by isolating water raw data from each set (water experiments have been repeated four times as shown in Figures 7-32 to 7-34), to provide a stable reference measurement. Some statistical analysis has been studied on the effect of temperature and CF on microwave measurements for all modes, relating to the data points' spread over time. Note each sample (x-axis in the above graphs) represents about 15 seconds (20 measurements); this is the time taken for the LabVIEW programme to complete the data acquisition. Note that we focus on the BW correction steps only for clarity as there is also a correlation between Q factor, BW and CF and even the data for  $|S_{21}|$  follows similar trends. The same steps are followed for the Q factor and  $|S_{21}|$  measurements. CF data is not shown but is used in the data correction process. There is no apparent correlation between either temperature or frequency and the raw data in the first mode. This may be due to the same reason clarified in section 7.2.2.5 that the high penetration depth is less sensitive to the tip surface morphology. Therefore, just averaging has been applied (Figure 7-35).

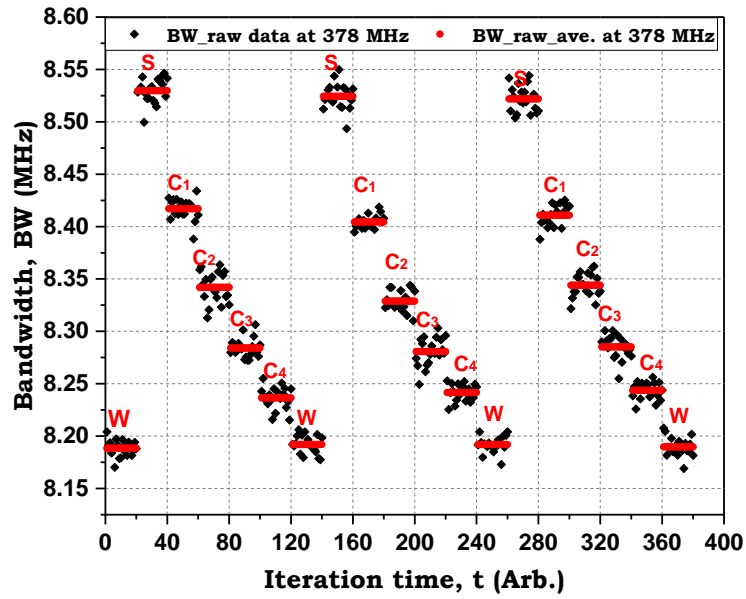


Figure 7-35: Raw data-black and corrected data in red of polystyrene with 2  $\mu\text{m}$  at the first mode (378 MHz) for variance concentrations (25 to 1.56) ppt.

Regarding the second mode (757 MHz), a correlation factor of 0.977 was found just between the average of the BW and the average temperature for each block of 20 samples for water tested for correlation and is shown in the Figure.7-36

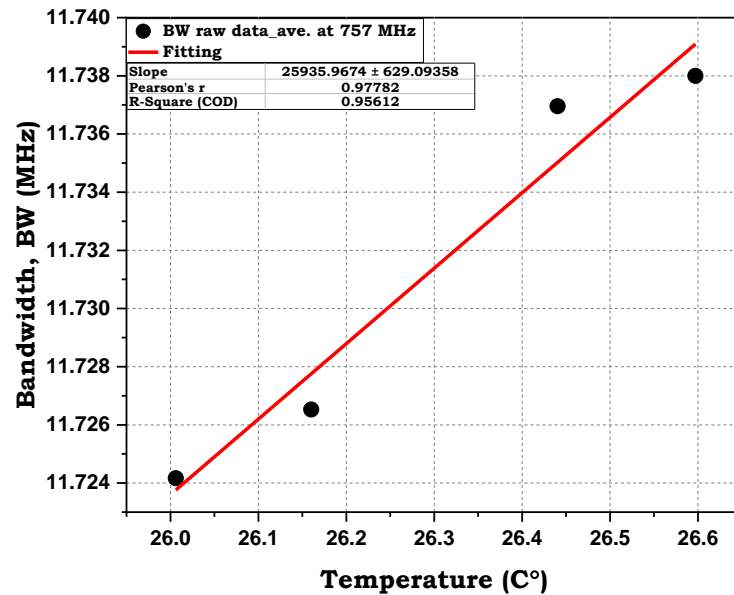


Figure 7-36: Fitting averaging raw data and Temperature (T) in the second mode (757 MHz).

Figure 7-37 shows the scattering of BW after applying temperature correction for mode 2.

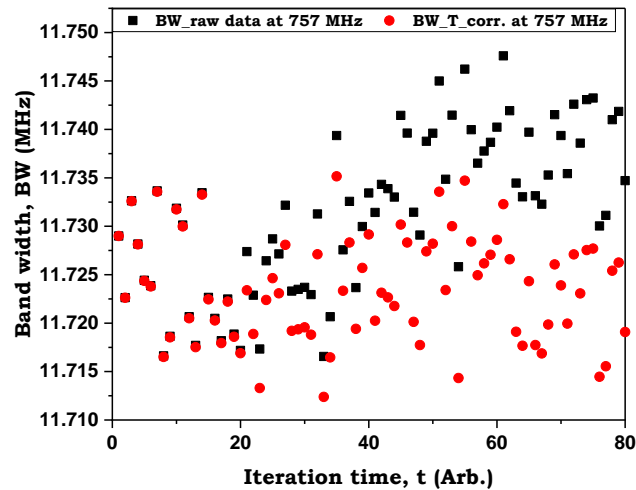


Figure 7-37: Scatter in the BW for water for mode 2 (Raw data- Black and Corrected data-Red).

Figure 7-38 shows the result after applying the correction and the averaging after corrections to the whole data set of PS samples with varying concentrations 25 ppt and 12.5 to 1.56 ppt (S and C<sub>1</sub> to C<sub>4</sub>) of the second mode (757 MHz).

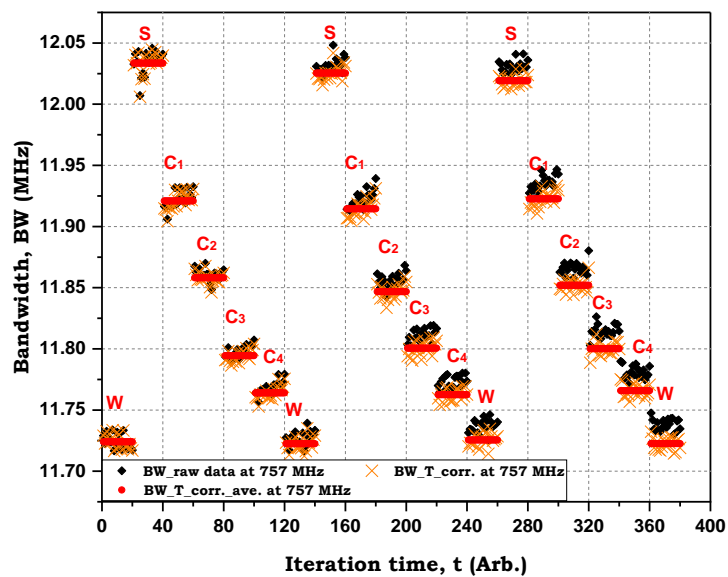


Figure 7-38: Scatter and averaging after correction in the BW for three sets for mode 2 (Raw data - Black, Corrected data-Orange and averaging after corrections - Red).

In terms of the third resonance at 1.14 GHz, a similar correction process was followed. It is obvious in the Figure 7-39; there was a strong correlation between the average BW for water and the average CF (correlation coefficient -0.964).

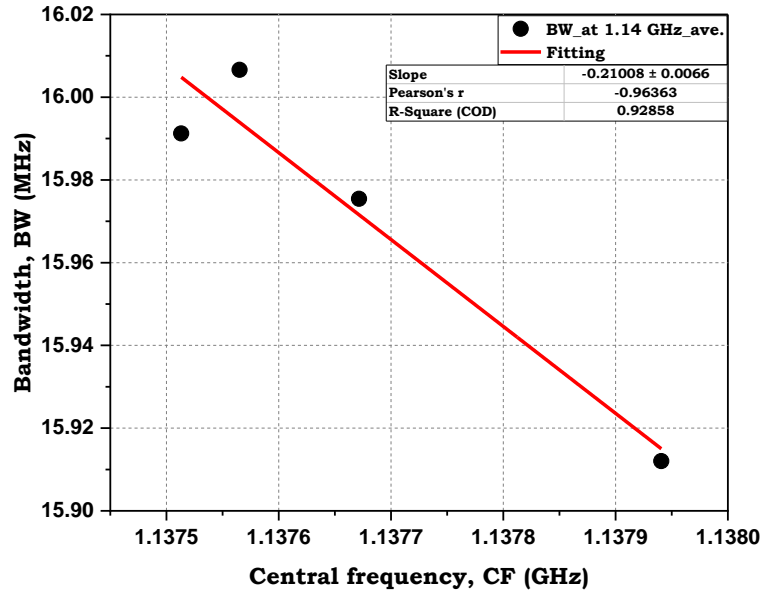


Figure 7-39: Fitting averaging raw data and CF in the third mode (1.14 GHz).

Figure 7-40 shown the corresponding adjustment in the water data.

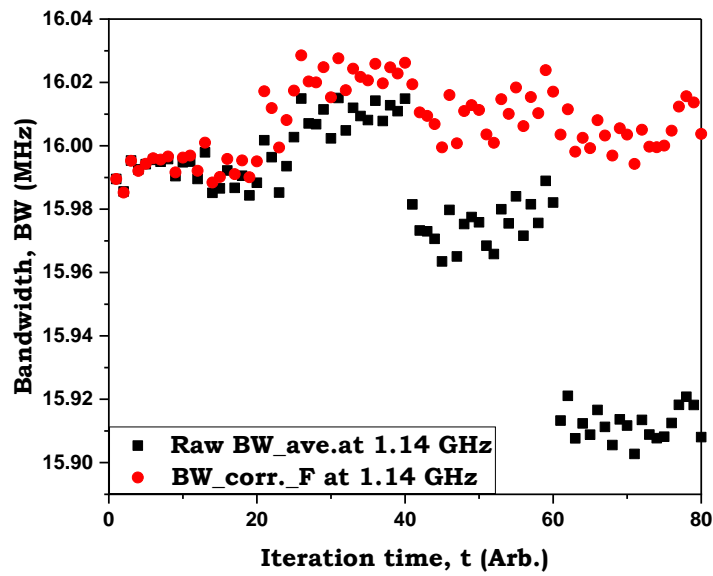


Figure 7-40: Scatter in the BW for water for mode 3 (Raw data-Black and Corrected data-Red).

A further temperature correction was applied after applying the CF correction, as shown in Figure.7-41.

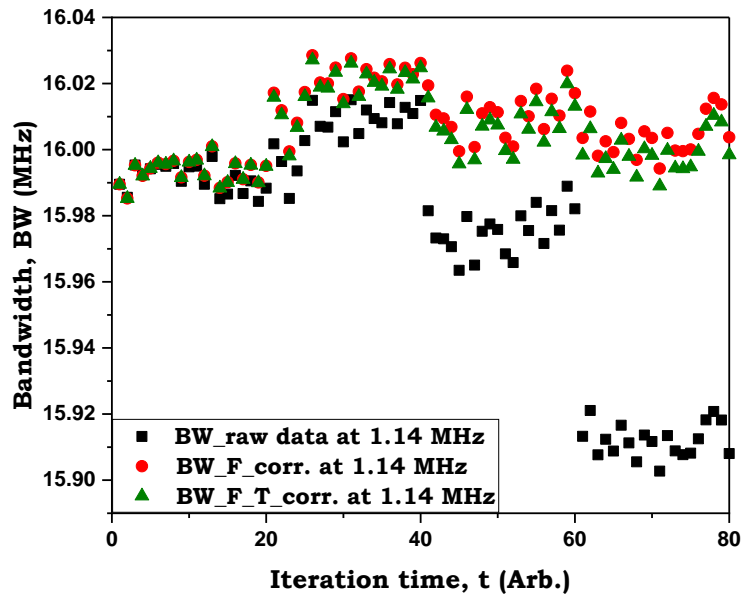


Figure 7-41: Scatter in the BW for water for mode 3 (Raw data – Black, CF corrected data Red – and temperature corrected in green).

Figure 7-42 shows the average after applying both of these corrections on raw data with different concentrations. It is clear to find that there is a significant improvement in the BW measurements after all corrections for all concentrations at all experiment repeats. In addition, there is a regular reduction in the BW measurements with decreasing the concentrations. However, there is a non-regularity in the first experiment. This may be relative to the presence of bubbles or settling particles.

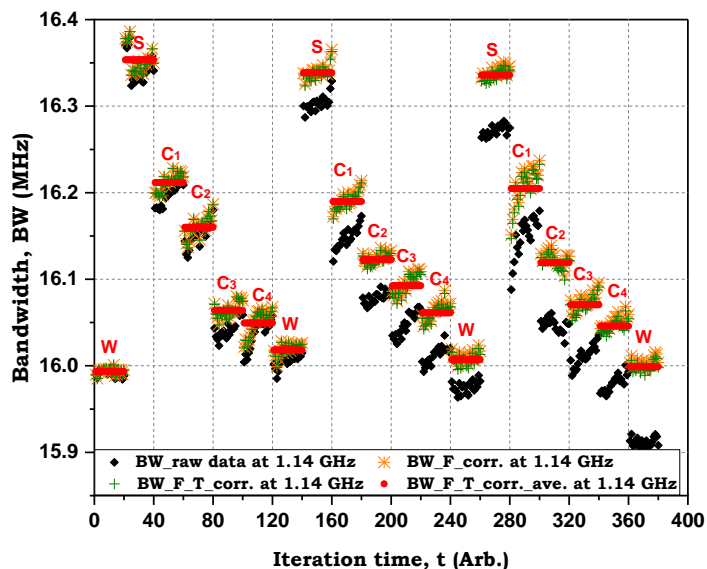


Figure 7-42: Corrected and averaged the BW for all samples for mode 3 (Raw data– Black, CF corrected data- Orange, Temperature corrected data- Green and averaging after corrections in Red).

Regarding the fourth resonance at 1.52 GHz, similar correction steps have been applied for mode

four. In this mode, CF correction was used first as it was found that there was a strong correlation between BW\_ave. and CF\_ave. (-0.986) and demonstrated in Figure 7-43. Then, the temperature correction has been applied as there is a correlation (0.4) after removing the CF's effect for water.

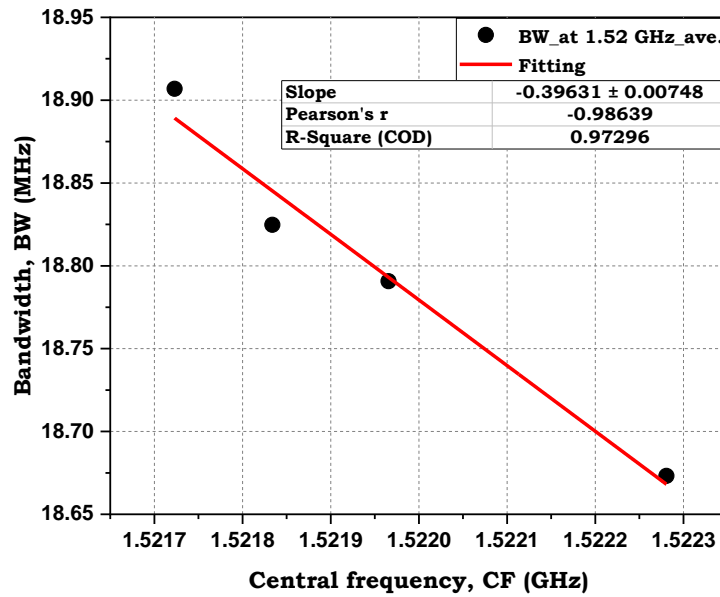


Figure 7-43: Fitting averaging BW- raw data and CF of the fourth mode (1.52 GHz).

Figure 7-44 showed the distribution of the corrected raw data for water after removing the frequency and temperature effect.

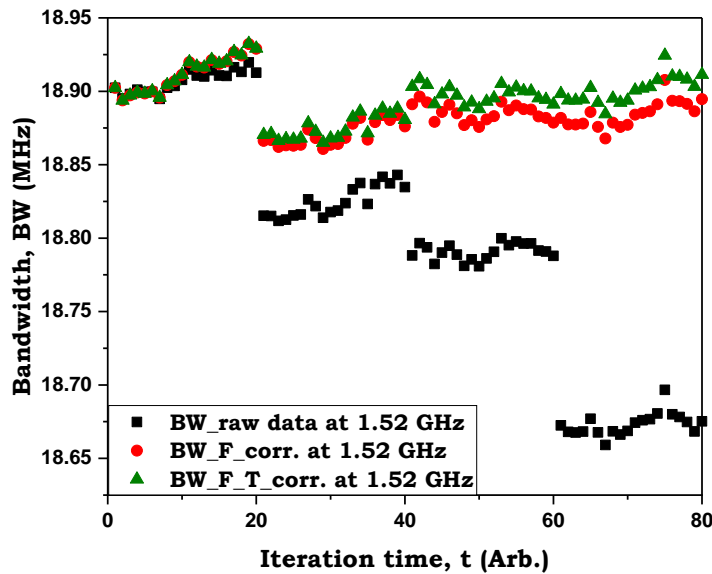


Figure 7-44: Scatter in the BW for water for mode 4 (1.52 GHz) (Raw data - Black, CF corrected data – Red and Temperature corrected data in Green).

Figure 7-45 shows the application of both corrections and the averaged data after corrections for the stock (25 ppt) different concentrations 12.5 to 1.56 ppt (C1 to C4) at a frequency of 1.52 GHz.

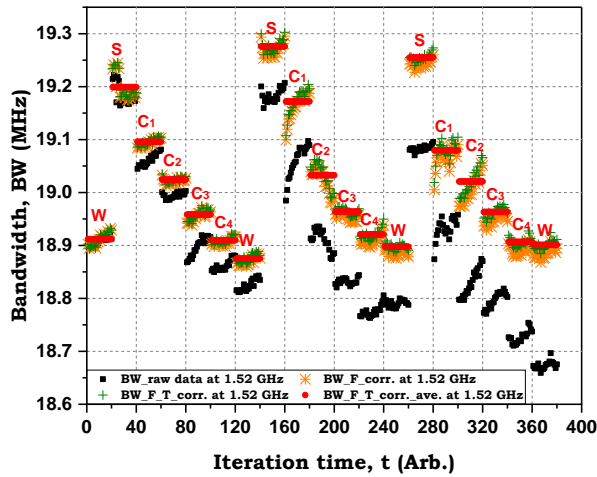


Figure 7-45: Corrected and averaged the BW for all samples for mode 4 (Raw data- Black, CF corrected data- Orange, Temperature corrected data- Green and averaging after corrections in Red).

The same corrections steps described in detail above for BW have been followed for Q factor and  $|S_{21}|$ . Figures 7-46 and 7-47 show the corrections and averaging after correction for all modes. In these Figures, it is clear to find there is a systematic change in three sets for parameters (Q factor and  $|S_{21}|$ ) at mode 1 and 2 (378 and 757) MHz. Importantly here, it is clear to see there is a significant improvement after removing the effect of the CF and the temperature at mode 3 and 4 (1.14 and 1.52) GHz.

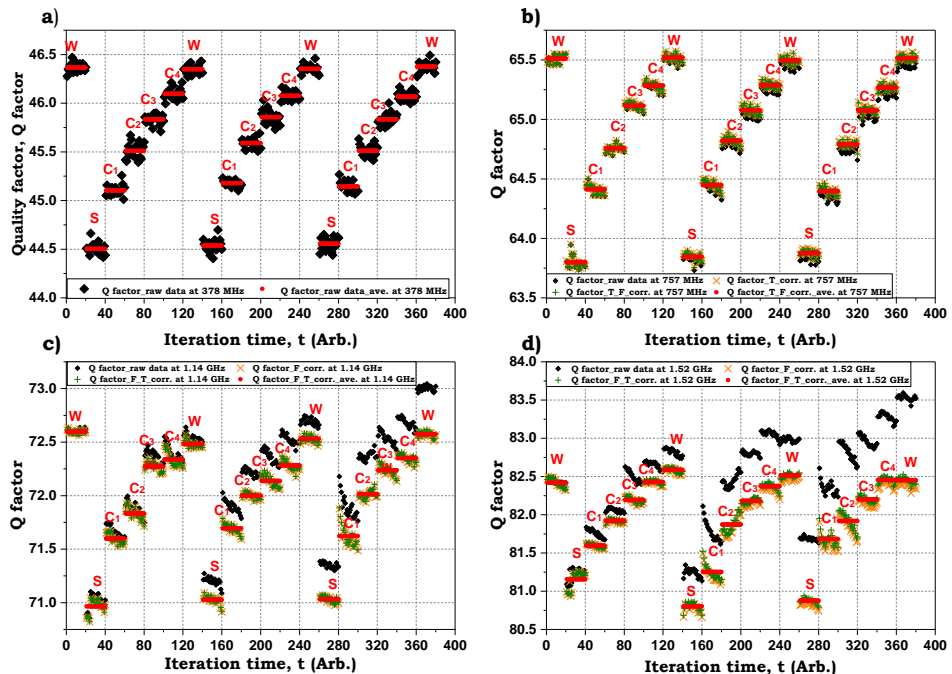


Figure 7-46: Raw data, corrections and averaging of Q factor Measurements for all modes at variance concentrations (25 to 1.56) ppt of 2  $\mu\text{m}$  (Raw data - Black, corrected data - orange and green and averaging in Red).

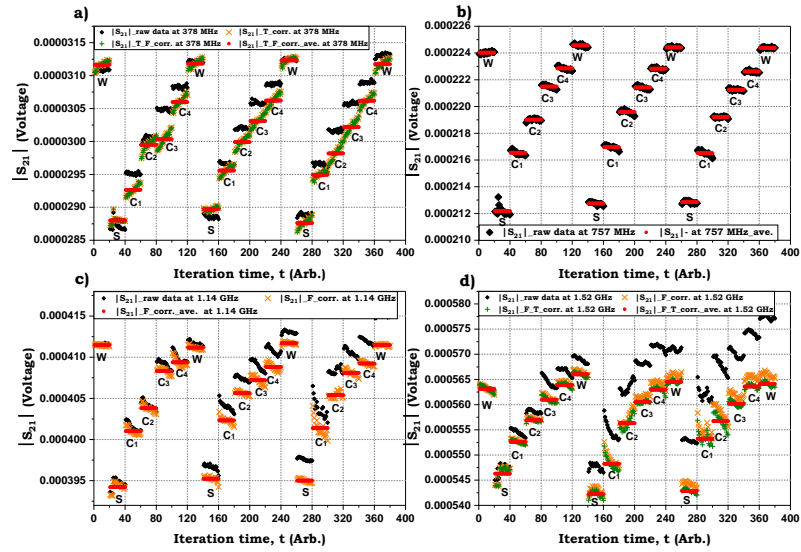


Figure 7-47: Raw data, corrections and averaging of  $|S_{21}|$  Measurements for all modes at variance concentrations (25 to 1.56) ppt of  $2 \mu\text{m}$  (Raw data - Black, corrected data-orange and green and averaging in Red).

Figures 7-48, 7-49 and 7-50 show BW, Q factor, and  $|S_{21}|$  averaged over the three sets after applying the correction. It is obvious that there is a good separation between the different concentrations of samples.

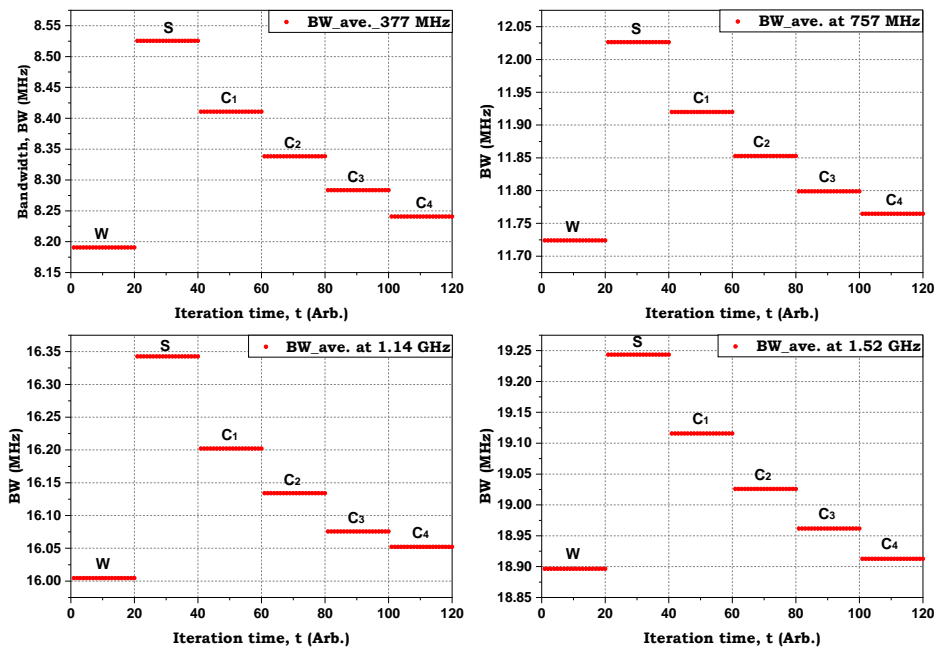


Figure 7-48: Ave. of BW over the three sets after applying all the corrections for variance concentrations (25 to 1.56) ppt at  $2 \mu\text{m}$ .

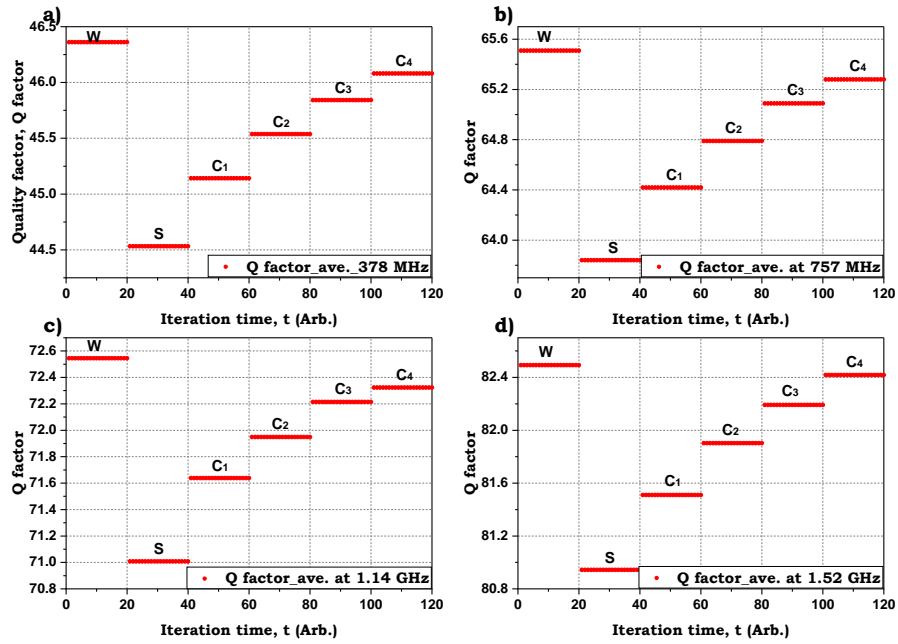


Figure 7-49: Ave. of Q factor over the three sets after applying all the corrections for variance concentrations (25 to 1.56) ppt at 2  $\mu\text{m}$ .

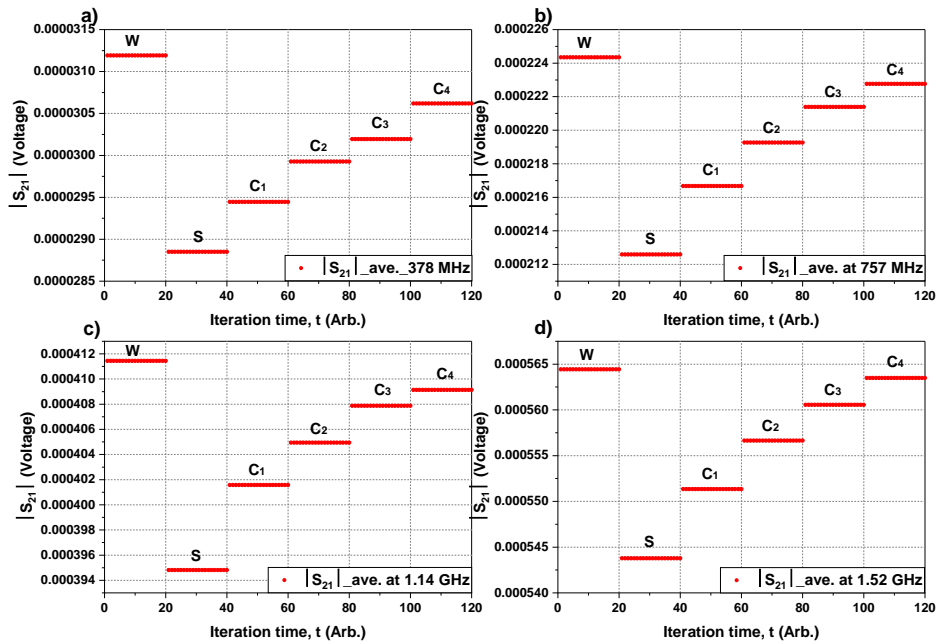


Figure 7-50: Ave. of  $|S_{21}|$  over the three sets after applying all the corrections for variance concentrations (25 to 1.56) ppt at 2  $\mu\text{m}$ .

Figure 7-51 shows the BW detection limit for all concentrations for all modes. In this Figure, a good separation has been found for all concentrations at all modes except 1.56 ppt (C4) at mode four 1.52 GHz.

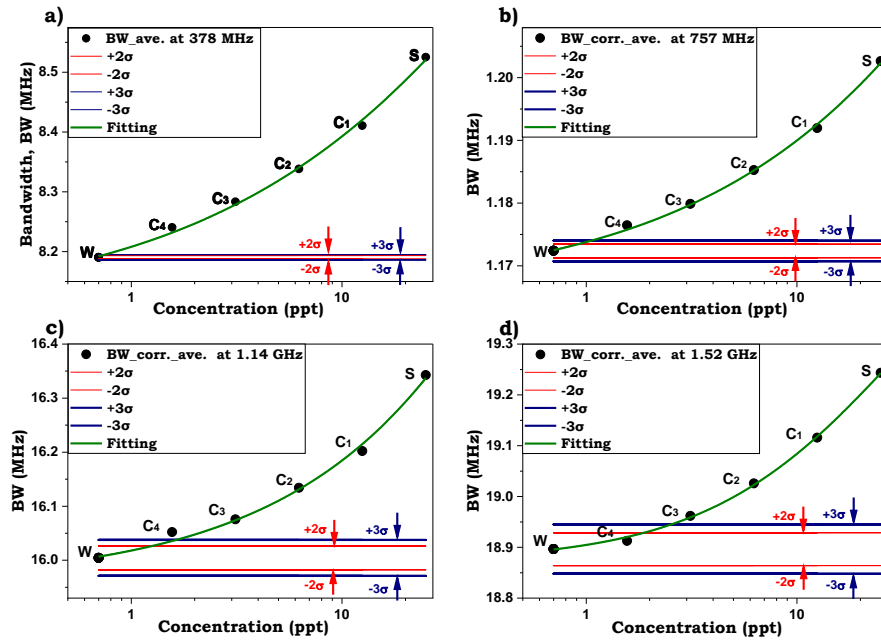


Figure 7-51: The correlation between the Bandwidth corrected data with different concentrations and statistical detection ( $2\sigma$  and  $3\sigma$ ) at  $2\ \mu\text{m}$ .

In Figure 7-52, the trend of BW in the above sections tends to decrease gradually with decreasing the concentration as expected. The SE showed an increase at 25 ppt (S) and 12.5 ppt ( $C_1$ ) at mode four (1.52) GHz. In terms of the Q factor and  $|S_{21}|$  measurements (Figures 7-53 and 7-54), the trend of both of them showed that measurements reduce as the concentration decreases. The SE increased at 25 and 12.5 ppt (S and  $C_1$ ) at mode four (1.52) GHz. Regarding the resonant frequency, there is no noticeable trend with a high standard error of all concentrations at all modes. This may be attributed to either bubble or settling particles (Figure 7-55).

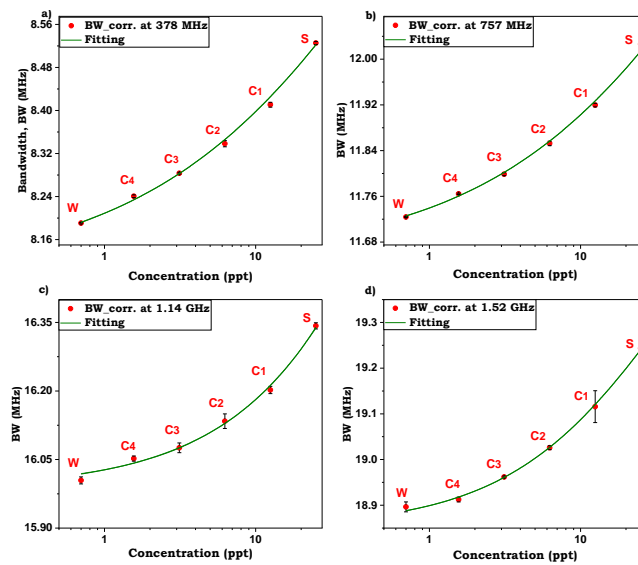


Figure 7-52: The average BW measurements after corrections for suspension polystyrene ( $2\ \mu\text{m}$ ) with a concentration range of 25 to 1.56 ppt.

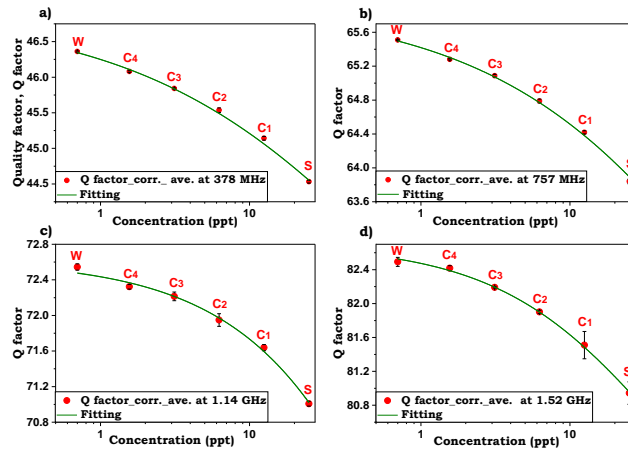


Figure 7-53: The average Q factor measurements after corrections for suspension polystyrene (2 μm) with a concentration range of 25 to 1.56 ppt.

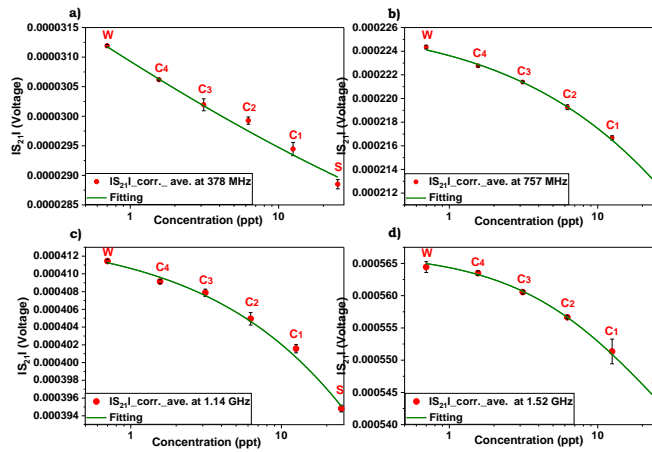


Figure 7-54: The average  $|S_{21}|$  measurements after corrections for suspension polystyrene (2 μm) with a concentration range of 25 to 1.56 ppt.

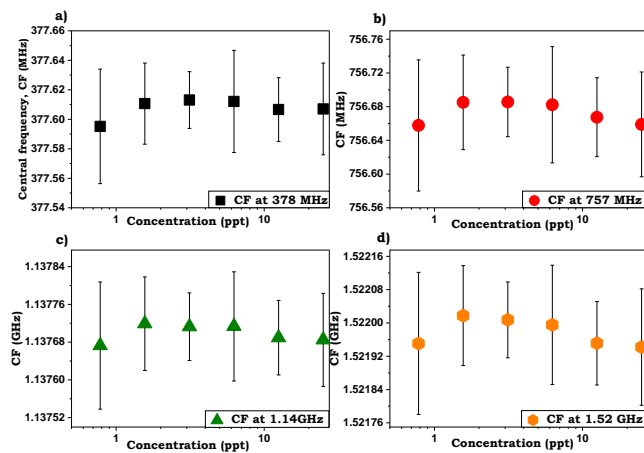


Figure 7-55: The average CF measurements for suspension polystyrene (2 μm) with a concentration range of 25 to 1.56 ppt.

### 7.3.1.1 CONVERTING THE MICROWAVE MEASUREMENTS TO REAL AND IMAGINARY PERMITTIVITY

The microwave measurements are converted to the real and imaginary permittivity by following the same steps described in section 6.6 for each frequency separately, as shown in Figure 7-56 and 7-57, respectively. Figure 7-56 demonstrated the real permittivity of the experimental work for each mode. In this Figure, there is a good agreement between the experimental work at all modes (757 MHz and 1.14 and 1.52 GHz) except mode 1 (378 MHz) (no discernible trend) which may be related to the CF effect in addition to other factors that are affecting the central frequency.

Regarding the imaginary permittivity shown in Figure 7-57, there is good agreement between the trends for all modes and all concentrations.

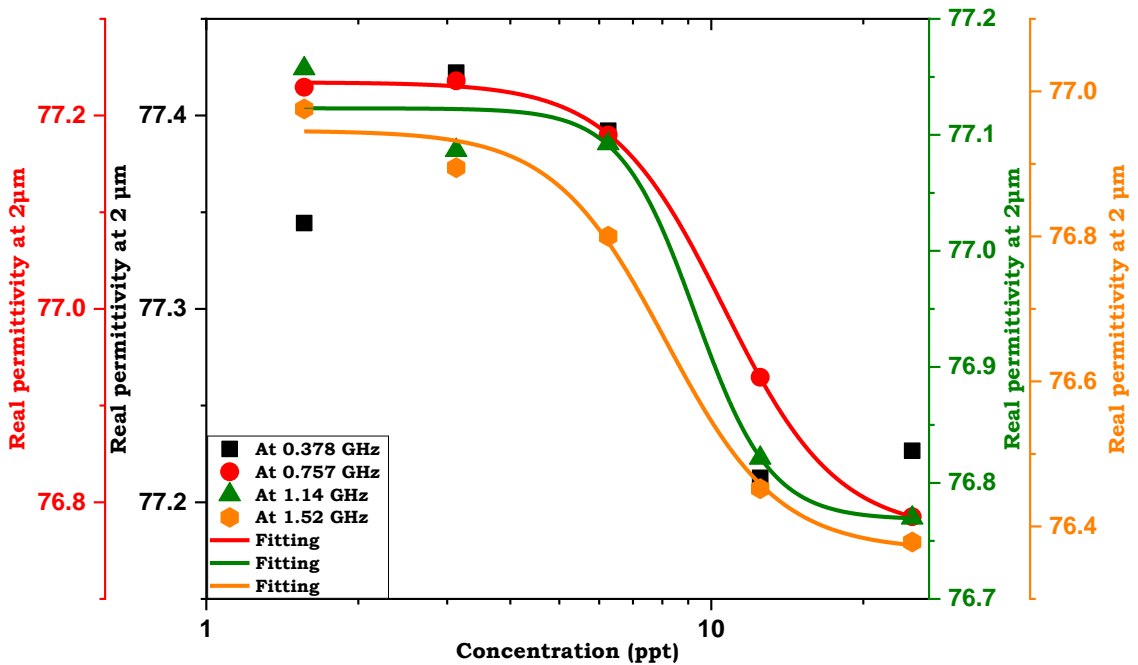


Figure 7-56: Real permittivity of the experimental work for different mode (0.377, 0.757, 1.14 and 1.52) GHz at variance concentrations of the 2  $\mu\text{m}$  for suspension polystyrene (25 to 1.56) ppt.

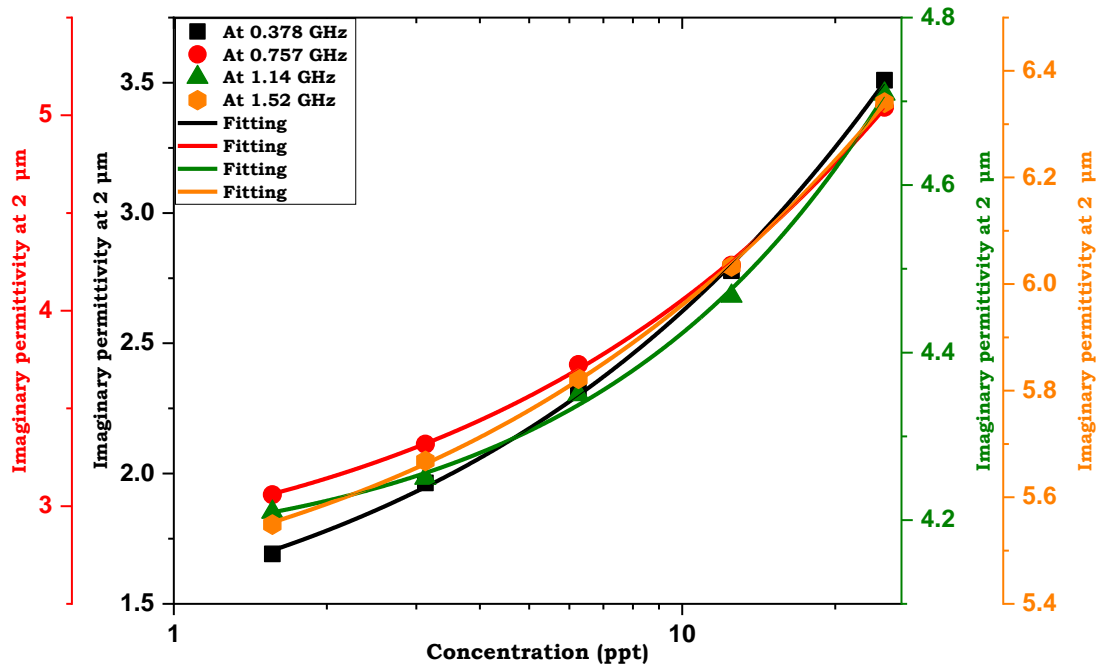


Figure 7-57: Imaginary permittivity of the experimental work for different modes (0.377, 0.757, 1.14 and 1.52) GHz at variance concentrations of the 2  $\mu\text{m}$  for suspension polystyrene (25 to 1.56) ppt.

### 7.3.2 MICROWAVE MEASUREMENTS AT 0.8 $\mu\text{m}$ POLYSTYRENE SPHERES IN SUSPENSION

For the 0.8  $\mu\text{m}$  PS spheres, the same concentrations were used as for the 2  $\mu\text{m}$ . Figures 7-58 to 7-60 show the BW, Q factor and  $|S_{21}|$  measurements respectively in the three sets for concentrations over the range of concentrations (25 to 1.56) ppt. For each graph, similar correction steps have used for the BW at 2  $\mu\text{m}$  (section 7.3.1) to study the effect of CF and temperature on the raw data. Subsequently, an average has been implemented after corrections. Importantly here, it is obvious to find there is a considerable improvement in particular, at mode three and four (1.14 and 1.52) GHz after applying correction steps and it can be seen that there is a systematic change for all measurements. Additionally, the trends highlighted a difference with all concentrations, and the measures tend towards that of DI-W as the concentration decreases.

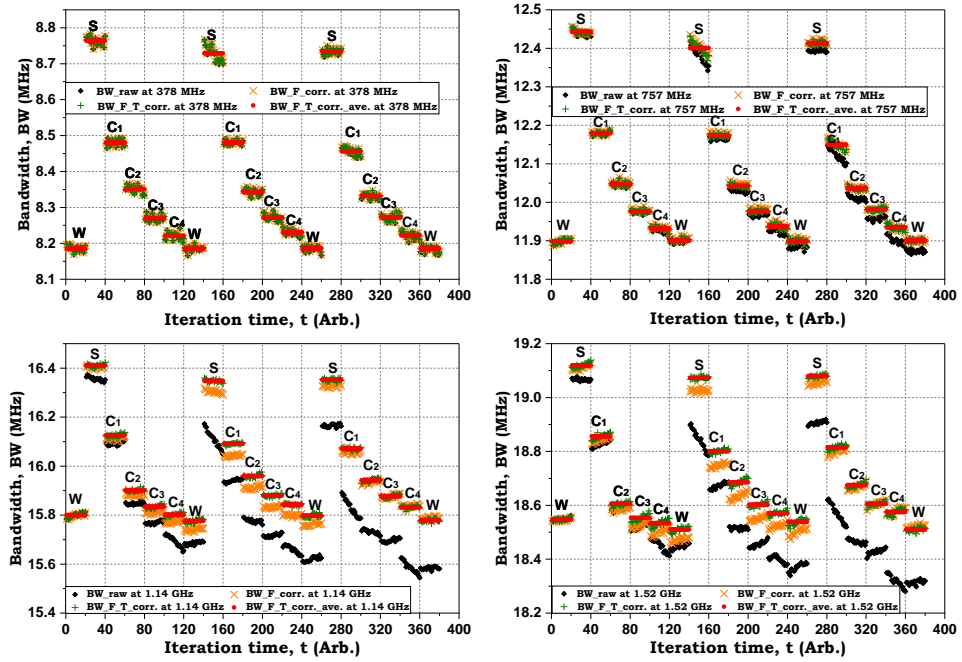


Figure 7-58: Raw data, corrections and averaging of BW Measurements for all modes at variance concentrations (25 to 1.56) ppt of 0.8  $\mu\text{m}$  (Raw data - Black, corrected data - orange and green and averaging in Red).

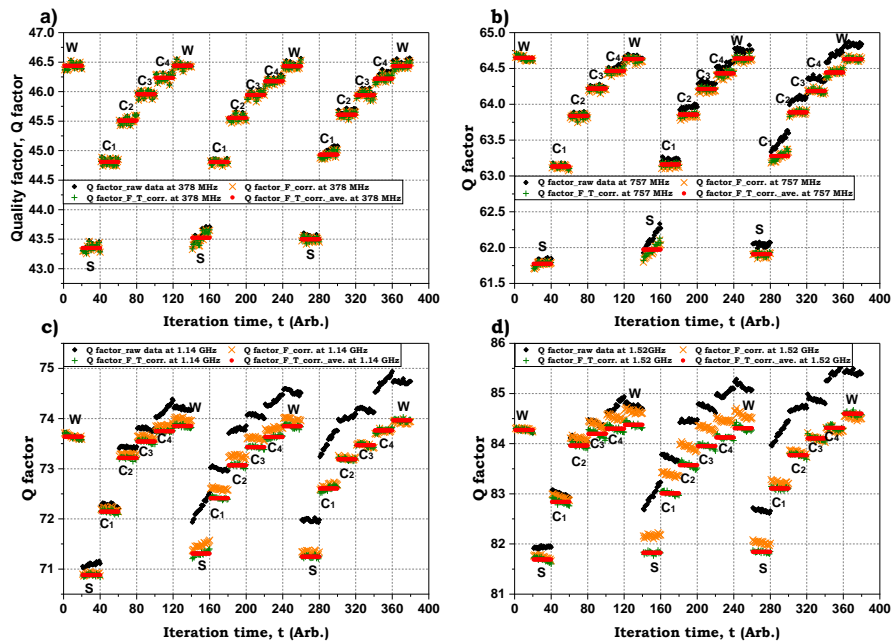


Figure 7-59: Raw data, corrections and averaging of Q factor Measurements for all modes at variance concentrations (25 to 1.56) ppt of 0.8  $\mu\text{m}$  (Raw data - Black, corrected data - orange and green and averaging in Red).

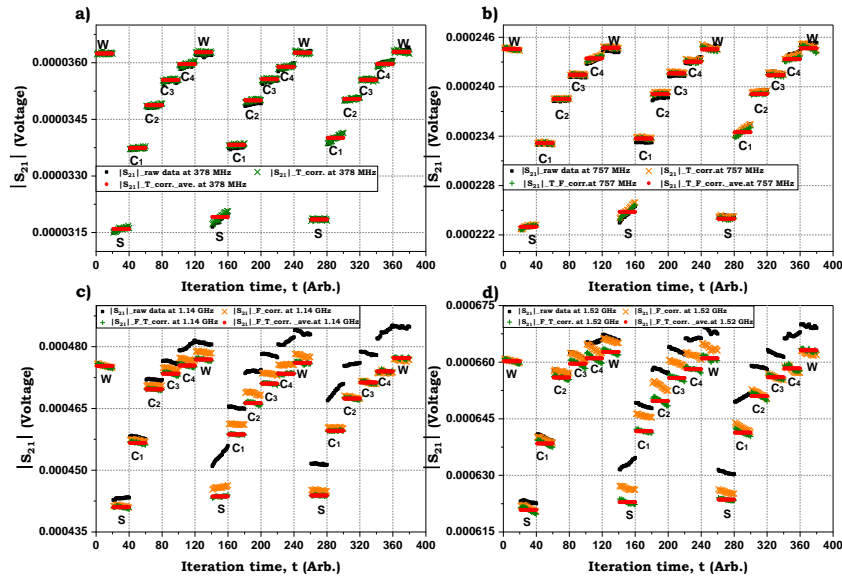


Figure 7-60: Raw data, corrections and averaging of  $|S_{21}|$  Measurements for all modes at variance concentrations (25 to 1.56) ppt of  $0.8 \mu\text{m}$  (Raw data - Black, corrected data - orange and green and averaging in Red).

The averaging over three sets of all modes after applying all the corrections for BW, Q factor and  $|S_{21}|$  in Appendix D-9 to D-11, respectively.

Figure 7-61 demonstrated the detection limit for BW for all concentrations and all modes. This Figure shows a good separation for all concentrations at all modes except 1.56 ppt ( $C_4$ ) at mode three and 3.13 ppt ( $C_3$ ) at mode four.

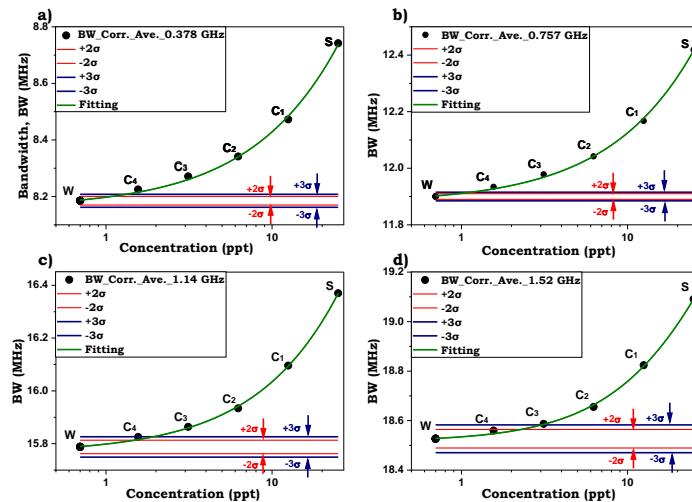


Figure 7-61: The correlation between the corrected BW data with different concentrations and statistical detection  $\pm(2\sigma(\text{red})$  and  $3\sigma(\text{blue}))$  at  $0.8 \mu\text{m}$  for all modes.

For the BW measurements (Figure 7-62), a gradual decrease is shown with decreasing

concentration at all modes. The SE shows a marginal increase at high concentration 25 ppt, 12.5 to 6.25 ppt (S, C1 to C2) at modes 3 and 4. In terms of Q factor and  $|S_{21}|$  (Figures 7-63 and 7-64), the trend tends to be that of water with reduced concentration. It is noticeable that the SE slightly increases with Q factor at all concentrations at mode 4 (1.52 GHz) and at 25 ppt (stock) and 12.5 ppt (C1) at mode 3. However, an insignificant increase in between 12.5 to 3.13 ppt (C1 to C3) of mode 4 at  $|S_{21}|$ . With regard to the CF (Figure 7-65), there is no discernible trend over the whole range of concentrations. The standard error is high for all concentrations at mode 4 which may be related to that the smaller penetration depth for the high frequencies suggests it is more sensitive to tip surface morphology as clarified in section 7.2.2.5.

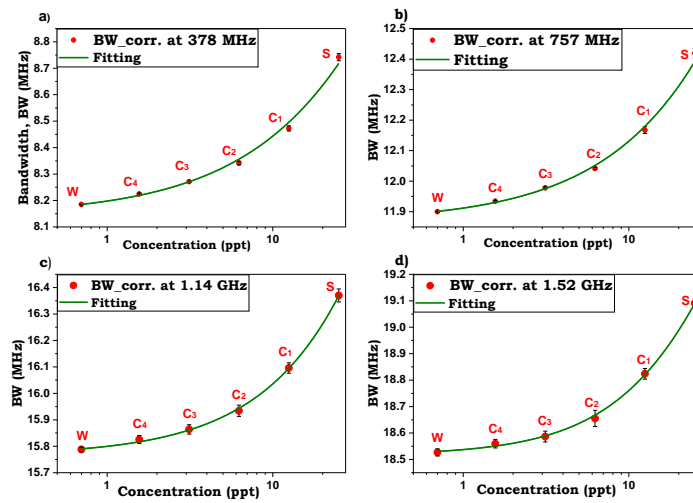


Figure 7-62: Ave. BW measurements after corrections for suspension polystyrene (0.8  $\mu\text{m}$ ) with concentration range 25 to 1.56 ppt of all modes.

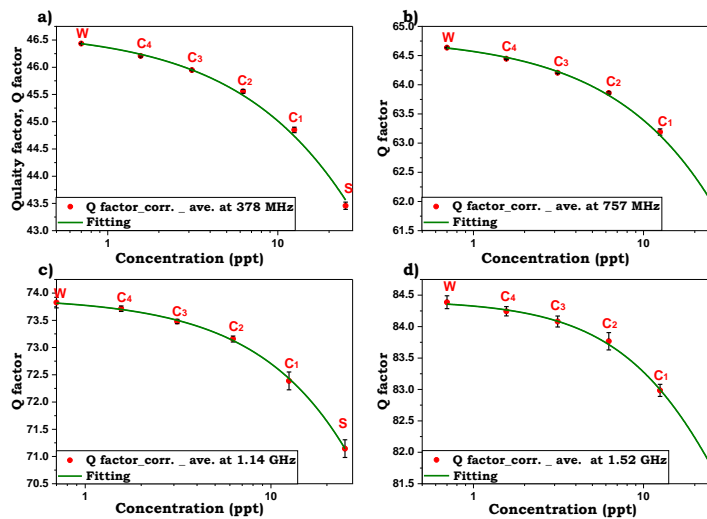


Figure 7-63: Ave. Q factor measurements after corrections for suspension polystyrene (0.8  $\mu\text{m}$ ) with concentration range 25 to 1.56 ppt of all modes.

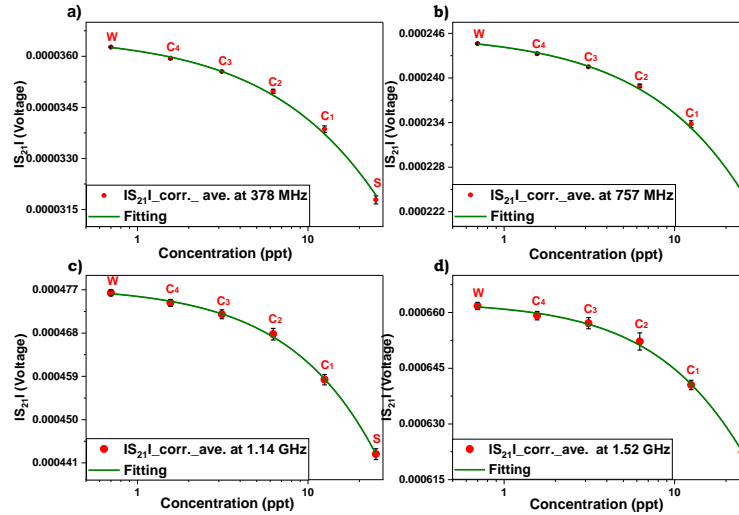


Figure 7-64: Ave.  $|S_{21}|$  measurements after corrections for suspension polystyrene ( $0.8 \mu\text{m}$ ) with concentration range 25 to 1.56 ppt of all modes.

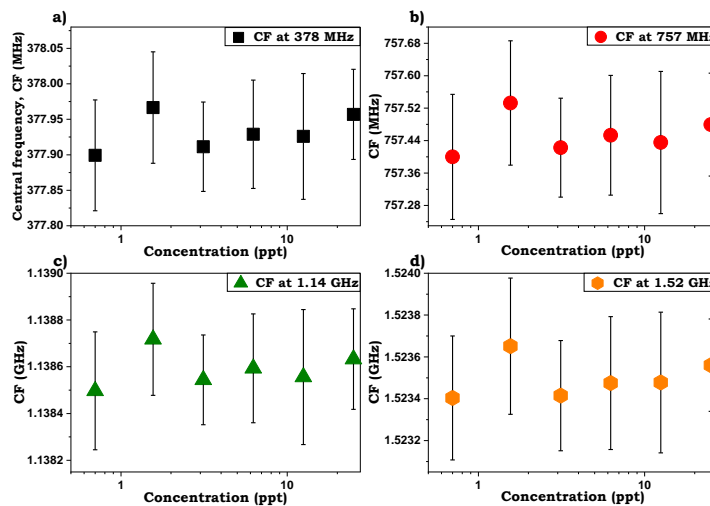


Figure 7-65: Ave. CF measurements for suspension polystyrene ( $0.8 \mu\text{m}$ ) with concentration range 25 to 1.56 ppt.

### 7.3.2.1 CONVERTING THE MICROWAVE MEASUREMENTS TO REAL AND IMAGINARY PERMITTIVITY

The microwave measurements are converted to the real and imaginary permittivity in the same way as for the  $2 \mu\text{m}$  PS by following the same steps described in section 6.6 for each frequency separately as shown in Figures 7-66 and 7-67. Figure 7-66 illustrates the real permittivity of the experimental works for each mode. In this Figure, there is no discernible trend for the whole range of concentrations. This is likely related to fluctuations in CF for all concentrations as shown in Figure 7-65. However, the imaginary permittivity shows the expected trends for all modes of

all concentrations (Figure 7-67).

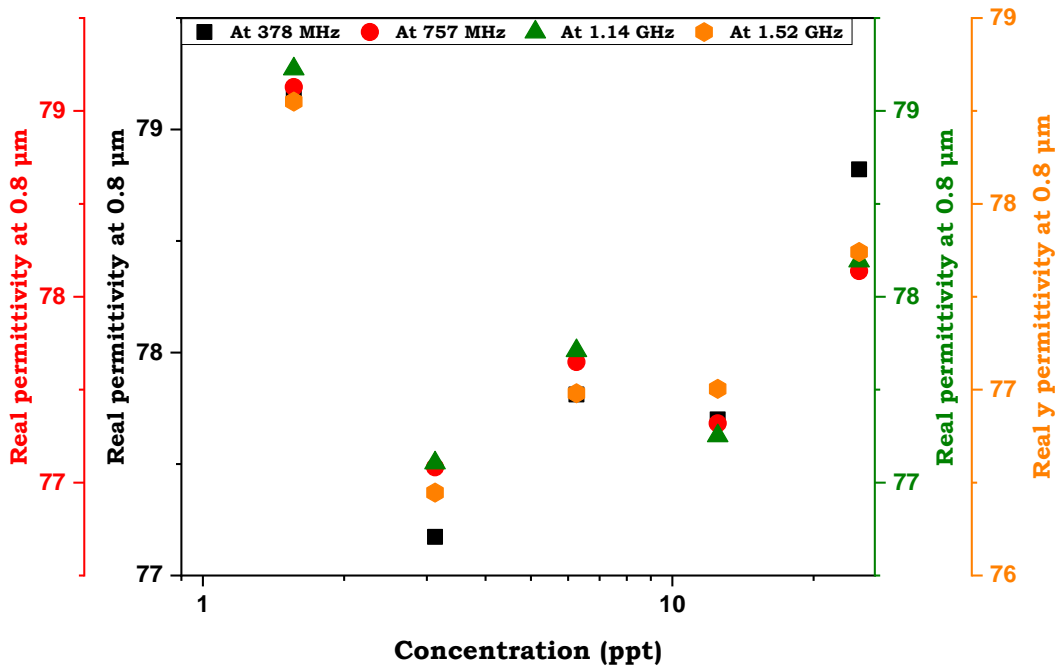


Figure 7-66: Real permittivity of the experimental work for different mode (0.378, 0.757, 1.14 and 1.52) GHz at variance concentrations of 0.8 μm for suspension polystyrene (25 to 1.56) ppt.

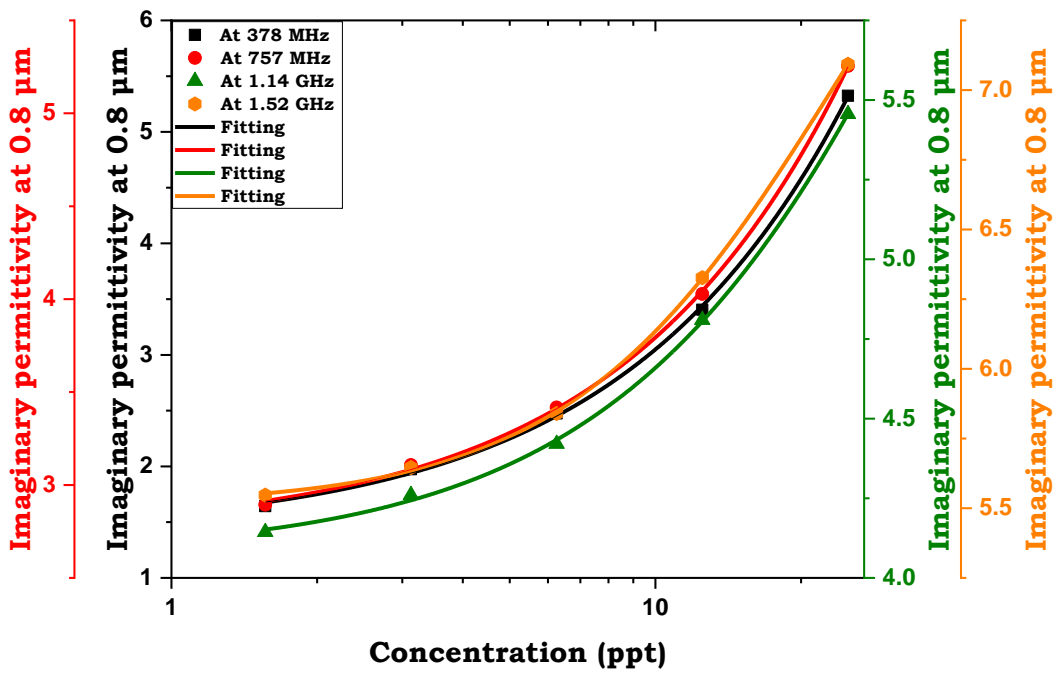


Figure 7-67: Imaginary permittivity of the experimental work for different modes (0.378, 0.757, 1.14 and 1.52) GHz at variance concentrations of 0.8 μm for suspension polystyrene (25 to 1.56) ppt.

---

### 7.3.3 MICROWAVE MEASUREMENTS AT 0.413 $\mu\text{M}$ OF POLYSTYRENE SPHERES IN SUSPENSION

The third particle size studied was 0.413  $\mu\text{m}$ . At this particle size, three various concentrations have been utilised 12.5 to 3.13 ppt ( $C_1$  to  $C_3$ ) in addition to stock at 25 ppt and the resultant microwave measurements (BW, Q factor and  $|S_{21}|$ ) are shown in appendix D-12 to Figure D-14. From these figures, it is obvious to find significant noise and drift at mode 3 and 4 as 2 and 0.8  $\mu\text{m}$ . Therefore, the same successful procedure used to correct the data has been implemented. It can be seen that there is a systematic change at all modes and in particular at modes 3 and 4.

For consistency, the same averaging steps were followed as for the 2 and 0.8  $\mu\text{m}$ . An average of over three sets is shown after applying all the correction steps for all measurements (Appendix D-15 to D-17).

The detection limits for BW over the concentrations of 0.413  $\mu\text{m}$  for all modes showed no improvement in detection (Appendix D-18) compared to particle sizes 2 and 0.8  $\mu\text{m}$ .

Appendix D-19 to D-22 showed how the parameters BW, Q factor,  $|S_{21}|$  and CF vary with concentrations. The trend followed that of the other particles. BW decreased with reducing concentration and vice versa for Q factor and  $|S_{21}|$ . The BW SE increased for  $C_1$  at modes 2, 3 and 4 and almost at mode 3 and 4 for Q factor and  $|S_{21}|$ .

Appendix D-23 and D-24 present the real and imaginary permittivity of the experimental work for each mode. The real permittivity shows no discernible trend for the whole range of concentrations, attributed to fluctuations in CF, as shown in appendix D-22 for all concentrations. However, the imaginary permittivity shows similar trends for all modes of all concentration's appendix D-24.

### 7.3.4 DISCUSSION OF POLYSTYRENE SPHERES IN SUSPENSION

An artificial tissue of suspension polystyrene with various sizes of particles has been used in detection. It is the same sample used in optical detection to study the combination of Microwave/optical systems in the application of cancer detection. For this reason, the same detecting sample has been used in microwave measurements. Importantly, here It is clear to find that there is a significant improvement in the output after implanting all corrections (removing the effect of temperature and central frequency) for all microwave measurements (Q factor,  $|S_{21}|$ , and BW) at all modes ( 0.378, 0.757, 1.14 and 1.52) GHz and in particular to the higher frequency at 1.14 and 1.52 GHz. Hence, a result this showed an improvement in the detection.

Regarding the effectiveness of frequency detection, 378 MHz showed an efficient detection frequency compared to three particle sizes at all modes. This may be because the larger penetration depth for the low frequencies suggests it is less sensitive to tip surface issues. Therefore, this frequency may not affect the coax cable's tip, such as the bubbles or other issues.

Figures 7-68 and 7-69 showed comparing the real and imaginary permittivity among three various sizes of suspension polystyrene 2, 0.8 and 0.413  $\mu\text{m}$  with different concentrations 25 to 1.56 ppt ( $C_1$  to  $C_4$ ) for 2 and 0.8  $\mu\text{m}$  and 25 to 3.12 ppt ( $C_1$  to  $C_3$ ) for 0.413  $\mu\text{m}$ . Figure 7-68 demonstrated the real permittivity of the experiment works for each mode with various PS sizes. In this Figure, there is no discernible trend for the whole range of concentrations on different PS sizes. This is likely related to fluctuations in CF for all concentrations at all suspension polystyrene sizes, as shown in Figures 7-55, 7-65 and D-22. The imaginary permittivity in Figure 7-69 showed a considerable separation at 2 and 0.413  $\mu\text{m}$  for all modes. However, it found overlapping with 0.8  $\mu\text{m}$  at 12.5 ppt ( $C_1$ ) and 6.25 ppt ( $C_2$ ) at mode 1 (378 MHz), mode 3 (1.14 GHz) and mode 4 (1.52 GHz) in addition to 3.13 ppt ( $C_3$ ) for this mode which would be possible to the presence of bubbles or settling particles. There is a regular reduction in the imaginary permittivity with decreasing the concentrations for particle sizes at all modes in this Figure. At this point, this system (resonant coaxial probe with T-Structure and capacitive coupling) showed the ability to detect various concentrations. Therefore, this technique could be used to diagnose cancer tissue as a good sign in detecting water content in the tissue. Authors groups [88, 91] found that the water content significantly increased in malignant than the normal tissue. This results in agreement with the theoretical result in section 5.5 that showed a remarkable variance between the magnitude of the complex permittivity for water and the rest of the concentrations for the whole range of frequencies (0.1 to 3) GHz.

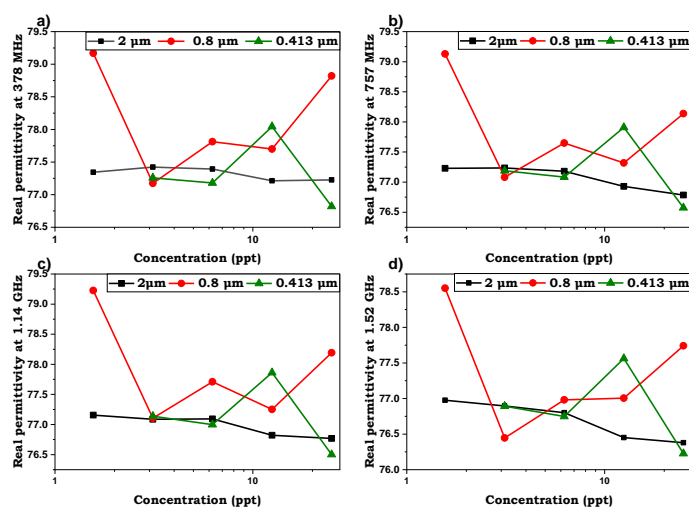


Figure 7-68: Comparison between the real permittivity at different modes (0.378, 0.757, 1.14 and 1.52) GHz at variance concentrations for three particle sizes (2, 0.8 and 0.413)  $\mu\text{m}$  (25 to 1.56 ppt for 2 and 0.8  $\mu\text{m}$  and (25 to 3.12) ppt for 0.413  $\mu\text{m}$ ).

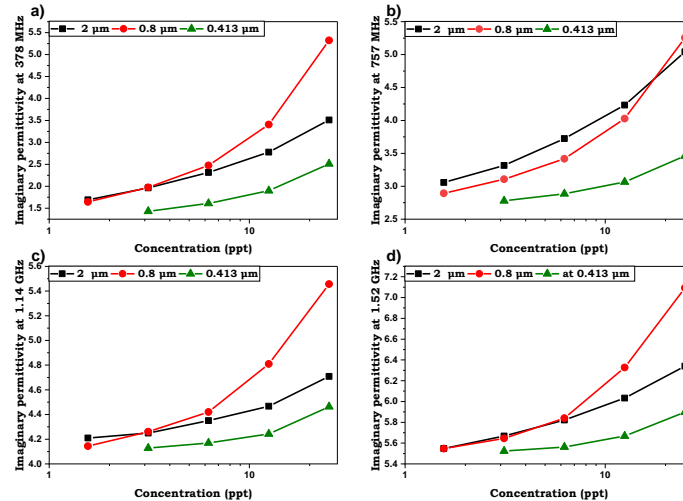


Figure 7-69: Comparison between the imaginary permittivity at different modes (0.378, 0.757, 1.14 and 1.52) GHz at variance concentrations for three particle sizes (2, 0.8 and 0.413)  $\mu\text{m}$  (25 to 1.56) ppt for 2 and 0.8  $\mu\text{m}$  and (25 to 3.12) ppt for 0.413  $\mu\text{m}$ .

## 7.4 CHAPTER SUMMARY

This chapter has shown the capability of a novel T- Structure and capacitive coupling arrangement to measure  $S_{21}$ . It is a new design to overcome the non-resonant probe issues, which result in increased sensitivity of the measurements and the opportunity to measure at a wide range of discrete frequencies. Two frequency sets have been selected to find out the best frequencies for detection. The first set was 757 MHz, 1.52 GHz, 2.3 GHz and 3 GHz and the second set was 378 MHz, 757 MHz, 1.14 GHz and 1.52 GHz. Normal saline with various concentrations has been utilised for detection, as the same preparation samples used in ch.6 preparation of commercial obtained saline and lab preparation saline dilutions. Here, no correction steps have been applied. The results did not correlate between the microwave measurements and either temperature or central frequency due to corrosion found at the end of normal saline's experiments. Therefore, just an averaging has been done for both preparations. The outcome showed a significant improvement in detection at low frequency (757 MHz) to  $3.34\text{E-}3$  M (C9) on comparing to  $2.41\text{E-}3$  M (C6) of the commercial preparation, whilst a marginal improvement was found at high frequency (1.52 GHz) to  $2.67\text{E-}2$  M Lab preparation (C6) in contrast to  $4.81\text{E-}3$  M (C5) of the commercial preparation. The second sample type was PS with different sizes (2, 0.8 and 0.413)  $\mu\text{m}$  and various dilutions over the range of concentrations 25 to 1.56 ppt (S to C4) for 2 and 0.8  $\mu\text{m}$  and 25 to 3.13 ppt (S to C3) for 0.413  $\mu\text{m}$  with the same second set of frequency. In this experiment, another correction method has been applied than in Ch. 6. In this correction method, an isolating of water set to provide stability in the measurements and then a statistical study for the effect of the CF and temperature have been applied for correction of the raw data.

---

A significant improvement has been shown for all modes, particularly at high frequencies (1.14 and 1.52 GHz) after using all correction steps. At 2  $\mu\text{m}$ , the detection was limited to 1.56 ppt (C<sub>4</sub>) for low frequencies (378 and 757 MHz) and high frequency at 1.14 GHz and 3.13 ppt (C<sub>3</sub>). Also, 1.56 ppt (C<sub>4</sub>) at low frequencies and 3.13 (C<sub>3</sub>) at mode 3 (1.14 GHz) and 6.25 ppt (C<sub>2</sub>) at mode 4(1.52 GHz) at 0.8  $\mu\text{m}$ . In contrast, there is no improvement in detection for all modes at 0.413  $\mu\text{m}$ . 378 MHz showed the efficient detection frequency on comparing for three particles sizes at all modes. LabVIEW programme has been applied to complete the data acquisition for both samples (normal saline and PS).

## CHAPTER 8

# OVERCOMING CHALLENGES AND A NOVEL TECHNIQUE FOR SIMULTANEOUSLY DETECTING MICROWAVE AND ELSS SIGNALS

### 8.1 INTRODUCTION

To overcome the corrosion in the silver-plated copper-clad steel (SPCW) in the core of the central conductor probe explored in CH.7, three techniques (the 'Crimp Cut' Protruding Probe, Gold (Au) Coating of the Internal Conductor (flat shape) and Silver Plated Copper (SPC) of Centre conductor Coax cable) will present in this chapter. The microwave measurements have been done using 0.8  $\mu\text{m}$  polystyrene spheres in suspension (PS) with 25 to 0.098 ppt (S to C8) and pure DI-W as a reference. Additionally, a *novel* system for detecting both optical and microwave properties will be presented in this chapter. Both measurements have been done using Coaxial Cable with SPCW and all particle sizes (2, 0.8 and 0.413  $\mu\text{m}$ ) with various concentrations 25 to 0.098 ppt (S to C8) and pure DI-W as a reference.

### 8.2 OVERCOMING THE CORROSION OF THE PROBE

Three alternative probe configurations have been studied due to the complications associated with the corrosion of the steel centre conductor. The most obvious one is to use a coax cable that does not have steel as a centre conductor. Incidentally, this was the most difficult to implement as there are very few instances of small diameter wire available that do not have a steel core. These are generally referred to as Silver Plated Copper (SPC) as opposed to the more prolific Silver-Plated Copper Clad Steel (SPCW). Fortunately, in the final stages of writing this thesis, an SPC sample was obtained from Castle Microwave Ltd (Jyebao Company). The results of using this as a resonating probe are discussed later in section 8.2.3. The other methods adopted were a simple crimp cut of a protruding centre conductor and the selective gold plating of the centre conductor.

#### 8.2.1 THE 'CRIMP CUT' PROTRUDING PROBE

A probe resonator was prepared that had a protruding Centre conductor that was 'cut back' using

a pair of Lindstrom wire cutters. This had the effect of not only cutting the wire but deforming the conductor, more or less preserving the silver plate over the majority of the chamfered cut surface. This achieved two things, an increased surface area, likely to increase the probe's sensitivity and to minimise the ratio of plated to steel area. Whilst crude, this proved most effective, and a picture of the cut probe tip is shown below (Figure 8-1).



Figure 8-1: Protruding probe 'cut back'

### 8.2.1.1 RESULTS OF THE PROTRUDING PROBE FOR 0.8 $\mu\text{M}$ PS

On implementing the 'cut back' protruding probe, 0.8  $\mu\text{m}$  PS with 25 to 0.098 ppt (S to C8) and pure DI-W as a reference used in detection. The first four modes (0.432, 0.868, 1.32 and 1.76 GHz), of the probe resonator with a length of 180 cm were selected for detection.

First impressions of the data obtained suggest that the process has delivered increased sensitivity and stability when measuring different concentrations of PS (Figure 8-2). Again, we focus on the BW measurements only for clarity. CF data is not shown but is used in the data correction process. As before, this measure is erratic but indicative of very subtle changes that correlate well with BW.

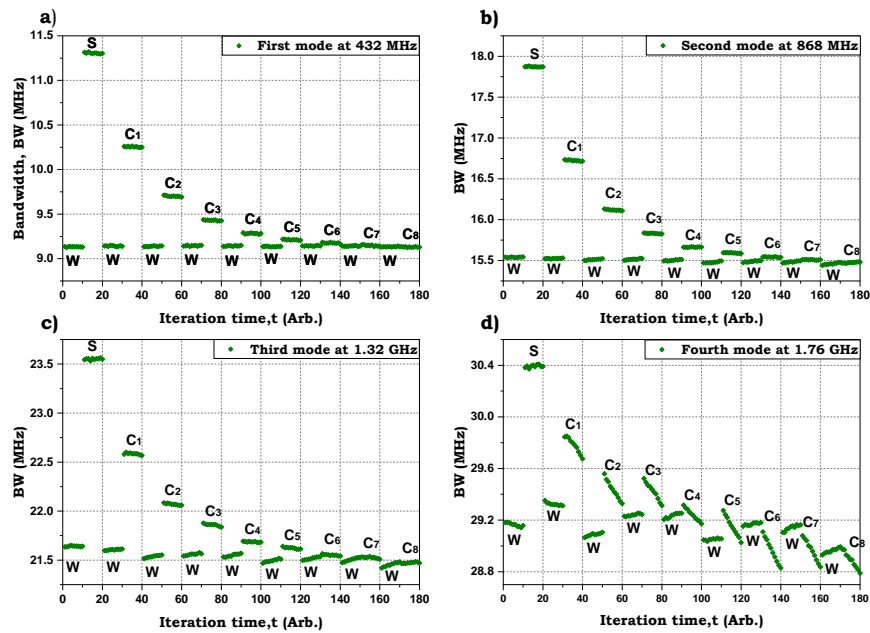


Figure 8-2: Bandwidth measured for different concentrations of  $0.8 \mu\text{m}$  PS spheres at the first 4 modes of the probe resonator.

To check the measurement's stability, water was measured before each dilution of PS and to obtain any trends, in addition as an extra step that might improve data correction procedure in section 7.3.1. Clearly, the ability to differentiate between  $0.78 \text{ ppt}$  ( $C_5$ ) and  $0.39 \text{ ppt}$  ( $C_6$ ), even with raw data for at least the first two modes represents a significant improvement over any of the previous incarnations of the probe resonator structure. To provide a measure of the stability in the measurements described in section 7.3.1, we have isolated the data for water only for each mode and provided some statistical analysis of the spread of the data points over time. Note each sample here (x-axis in the above graphs) represents about 6 to 7 seconds; this is the time taken for the LabVIEW programme to complete the data acquisition. Most noticeable is the way in which the PS samples seem to drift downwards in the data for mode 4, whilst the rest of the PS data is reasonably flat over each of the 10 measurements (corresponding to about 70 seconds).

For mode 1 at 432 MHz, the average value for the raw BW water measurement is 9.13 MHz with a standard deviation of 5.52 kHz, corresponding to 0.0604% of the average. Table 8-1 showed the comparison with other modes.

Table 8-1: Mean, standard deviation and percentage error for four modes of the BW.

Mode No.	Frequency	Mean	Standard deviation	Percentage
<b>1</b>	<b>432 MHz</b>	<b>9139773</b>	<b>5521</b>	<b>0.0604</b>
<b>2</b>	<b>868 MHz</b>	<b>15500648</b>	<b>24754</b>	<b>0.1597</b>
<b>3</b>	<b>1.31 GHz</b>	<b>21539912</b>	<b>55981</b>	<b>0.2599</b>
<b>4</b>	<b>1.76 GHz</b>	<b>29152701</b>	<b>104443</b>	<b>0.3583</b>

Recall that this is the raw data as recorded without any correction.

A number of techniques are described below that seek to find a correlation between the bandwidth and other recorded parameters and to ultimately reduce the standard deviation of the water data over the whole range. This will lead to an improved dilution detection limit. Previous work has suggested that there is a correlation between the values of BW and centre frequency. This observation has been made over many hours of conducting experiments. If one considers the water data alone, any drift or variation in the measured BW should be due to external influence. While the overall changes in centre frequency are relatively small, they seem to relate to things like the presence of microbubbles near and on the probe surface. They are similar to the issues relating to microbubbles, and fluid meniscus with the CCR mentioned in 6.5.2. The previous section (section 7.2.2.1), details the extreme difficulty in getting reliable data due to the simple matter of the coaxial probe tip corroding in water over a period of time. Since the surface area of the polished coaxial probe was dominated by the steel core of the inner conductor, any build-up of corrosion over time caused a significant drift in the measurements. With the current embodiment, the protruding probe has less dependence on the area of the inner core. But more importantly, the crimping effect of cutting the inner conductor with wire cutters has served to minimise the amount of steel core that is exposed to the sample.

First to be considered is the relationship between BW and centre frequency of mode 1. The average of the BW, CF, and T for each block of 10 samples for water was tested for correlation. A correlation factor of -0.7609 was found between the BW and CF for the first mode and is shown in Figure (8-3), together with the linear best fit.

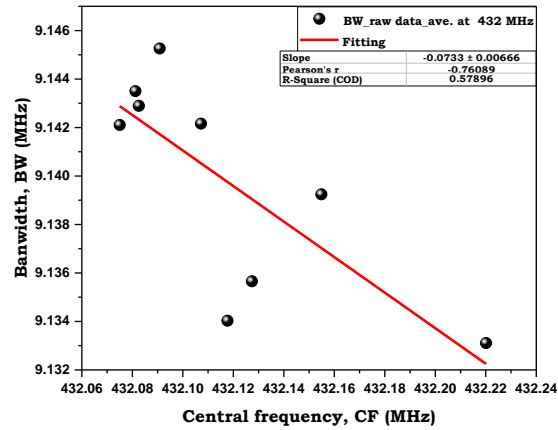


Figure 8-3: Fitting averaging raw data and central frequency (CF) in the first mode (432 MHz).

By using this dependence on CF, the water data was corrected to remove the effect of these small changes. The results are a narrower scatter of the water data and a reduced standard deviation, as highlighted in Table 8-2.

Table 8-2: Mean, standard deviation and percentage error for row and corrected first mode data (432 MHz).

Mode No.	Frequency	Mean	Standard deviation	Percentage	SE
Raw	432 MHz	9139773	5521	0.0604	3904
Corrected	432 MHz	9132670	4515	0.0494	3193

The resultant compression of the data scatter is shown in Figure 8-4 for water only.

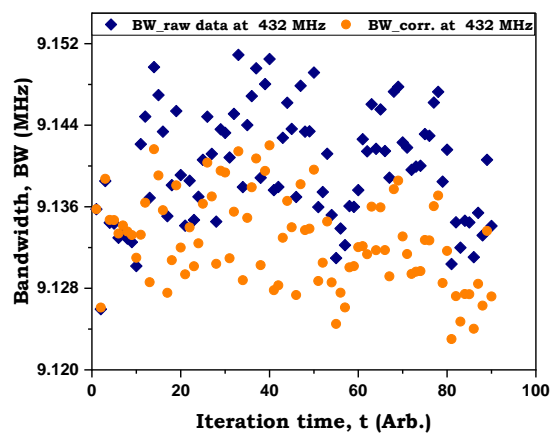


Figure 8-4: Scatter in the BW for water for mode 1 (Raw data \_ Blue and Corrected data \_ Orange).

When applying this correction to the whole data set, including the PS samples, the following graph (Figure 8-5) is obtained. Note that the vertical axis has been re-scaled to draw attention to the lower concentration PS measurements.

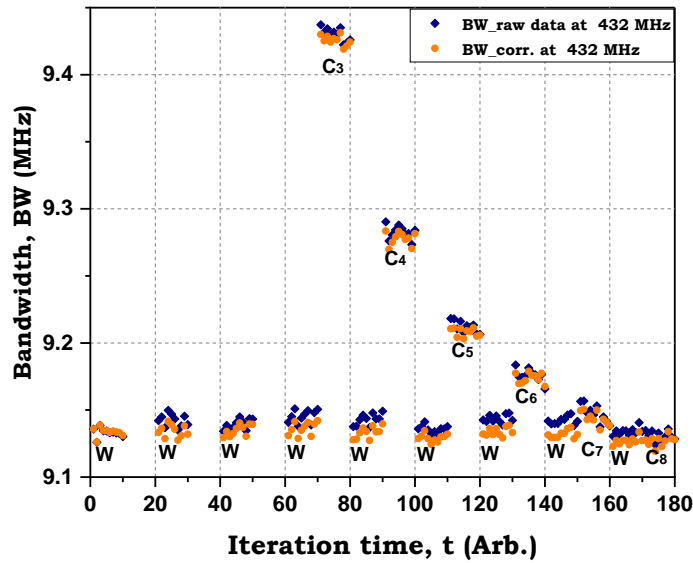


Figure 8-5: Scatter in the BW for all samples for mode 1 (Raw data \_ Blue and Corrected data \_ Orange).

While this may not appear to be a significant improvement, it has linearised the water measurements and enhanced the differentiation between water and 0.39 ppt (C6), possibly 0.195 ppt (C7). 0.098 ppt (C8) remains indistinguishable. Below, is the same data but averaged over each block of 10 data points (Figure 8-6).

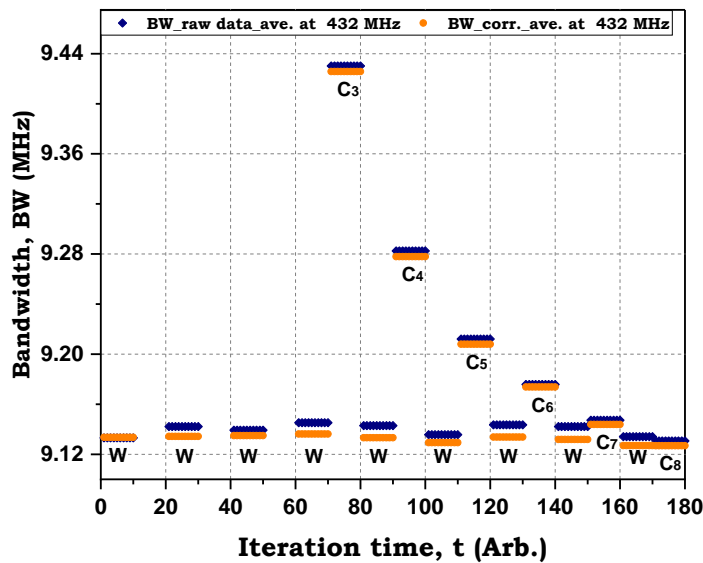


Figure 8-6: Average of the BW for all samples for mode 1 (Raw data \_ Blue and Corrected data \_ Orange).

The salient point to be raised here is if sample 0.195 ppt (C7) is measured, what level of confidence is there that it is not water? One simple way of determining this is to consider the average value of BW for water and specifically the range of values within plus and minus two standard deviations as utilised in sections above. In this case, the  $\pm 2\sigma$  range is between 9141700 Hz and 9123640 Hz. The mean value for the 0.195 ppt (C7) concentration is just outside this range, but

the 0.098 ppt (C8) concentration is not. This suggests that the 0.195 ppt (C7) concentration of PS spheres in water is at the limit of detection. In going to the  $\pm 3\sigma$  range, the 0.195 (C7) concentration is no longer distinguishable. See Figure 8-7 for an illustration.

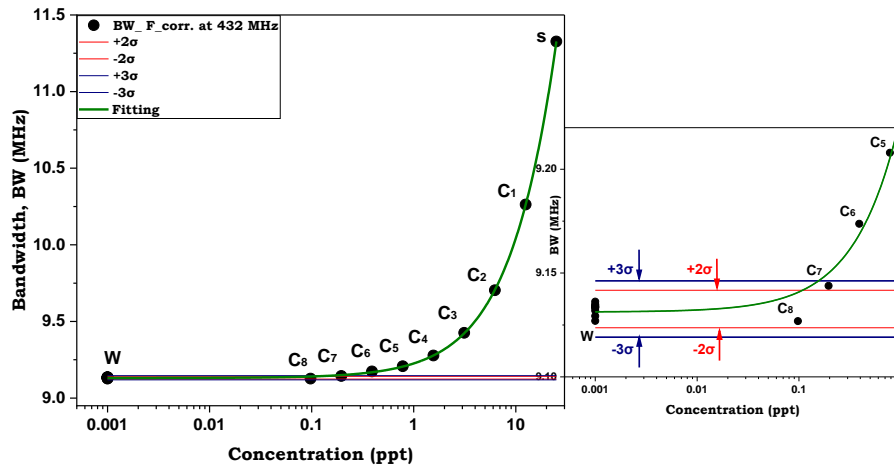


Figure 8-7: The correlation between the corrected data with different concentrations and statistical detection ( $2\sigma$  and  $3\sigma$ ) of mode1 (432) MHz

In terms of the second resonance at 868 MHz, a similar correction process was followed. Importantly here, there was a strong correlation with the average BW for water and the average temperature of the environment as shown in Figure (8-8) (correlation coefficient-0.907).

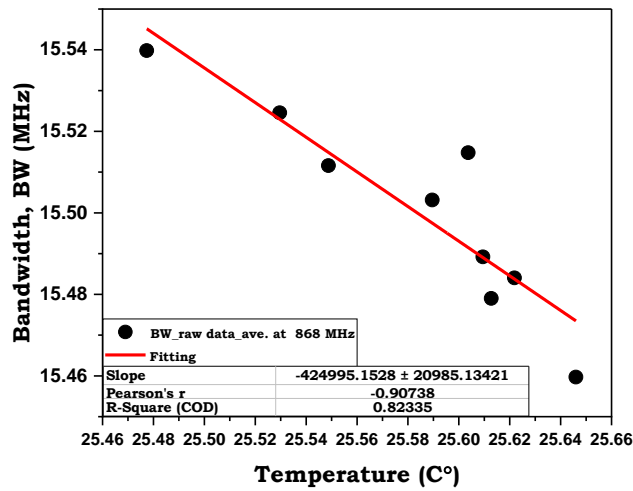


Figure 8-8: Fitting averaging raw data and temperature of the environment in the second mode (868 MHz).

The corresponding adjustment in the water data is shown in Figure 8-9.

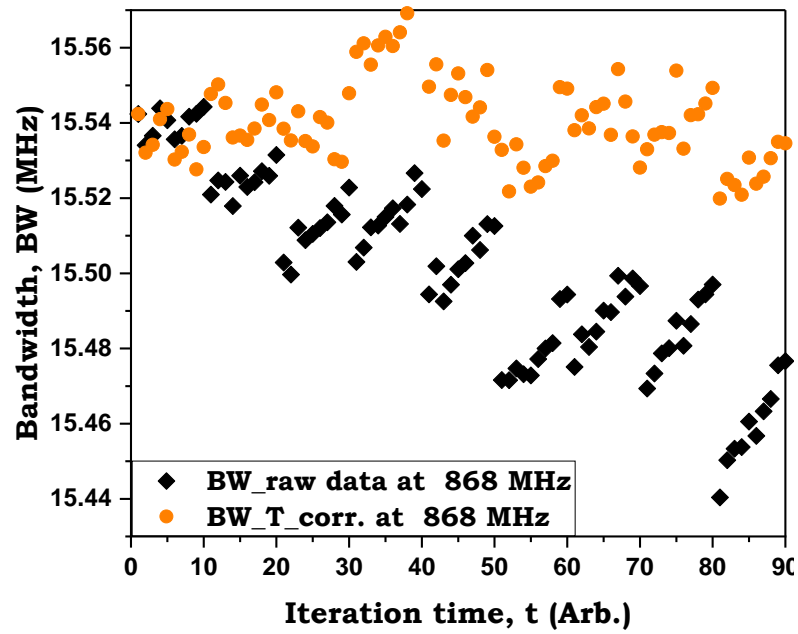


Figure 8-9: Scatter in the BW for water for mode 2 (Raw data – Blue and Corrected data – Orange).

Following the temperature correction, a further CF correction was applied (correlation coefficient -0.5792). See Figure 8-10.

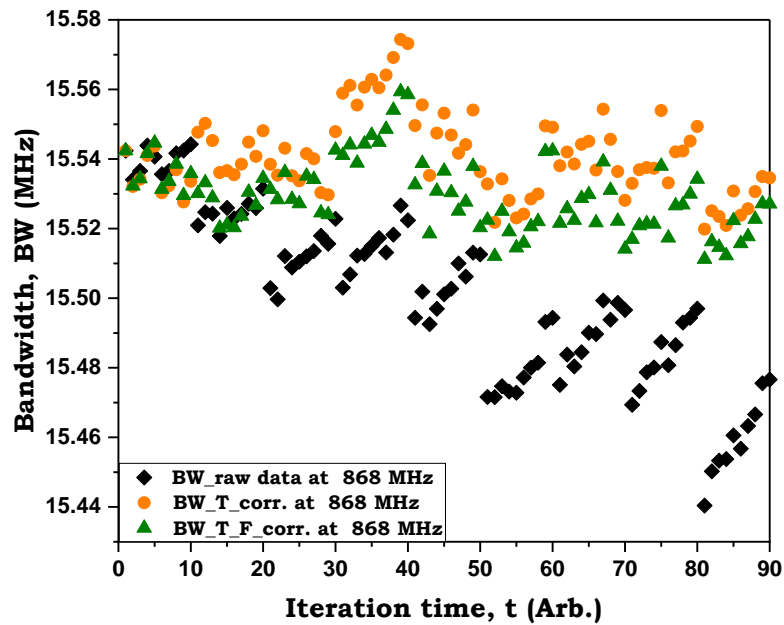


Figure 8-10: Scatter in the BW for water for mode 2 (Raw data – Blue, temperature corrected data – Orange and CF corrected in green).

Applying both these corrections provide the following averaged data (Figure 8-11).

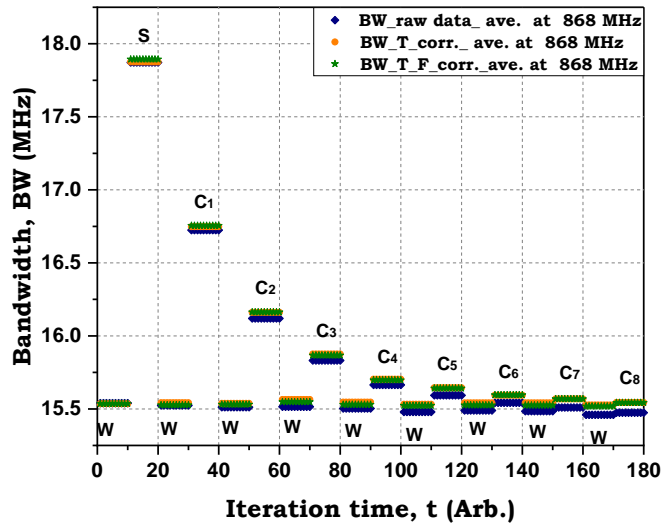


Figure 8-11: Average of the BW for all samples for mode 2 (Raw data – Blue, temperature corrected data – Orange and CF corrected in green).

The corresponding changes in the mean, standard deviation and standard error are shown in Table 8-3.

Table 8-3: Mean, standard deviation and percentage error for raw and corrected data of second mode (686 MHz).

Mode No.	Frequency	Mean	Standard deviation	Percentage	SE
Raw	686 MHz	15500648	24754	0.1597	17503
T Corrected	686 MHz	15540761	11830	0.0761	8365
F Corrected	686 MHz	15529531	10457	0.0673	7394

In terms of detection limits, the second mode suggests that the 0.195 ppt ( $C_7$ ) concentration is outside even the  $3\sigma$  range for water, an improvement on the first mode (Figure 8-12).

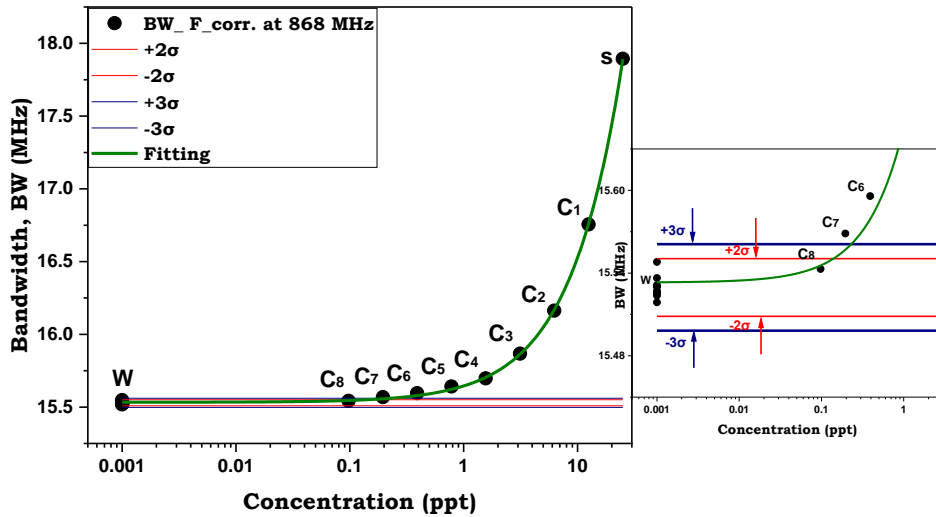


Figure 8-12: The correlation between the corrected data with different concentrations and statistical detection ( $2\sigma$  and  $3\sigma$ ) for mode 2.

Regarding the third resonance at 1.31 GHz, similar correction steps for the second mode have been applied. In this mode, temperature correction was the first step, as with mode 2, as there is a strong correlation between  $BW_{ave.}$  and average ambient temperature ( $-0.92$ ) as clearly shown in Figure 8-13. Then, the frequency correction was applied as the correlation coefficient was  $-0.74$  between the average BW after removing the effect of the ambient temperature for water and the central frequency.

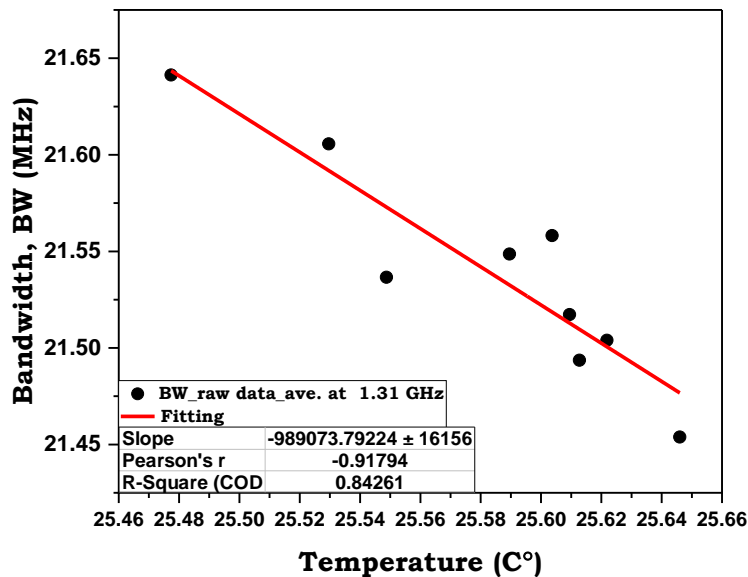


Figure 8-13: Fitting averaged raw data and temperature of the environment in BW of the third mode (1.31 GHz).

Figure 8-14 shows the correction of the averaged raw data and the ambient temperature with correlation coefficient  $-0.9179$ . And Figure 8-15 presents the averaging of the BW after corrections

of all samples.

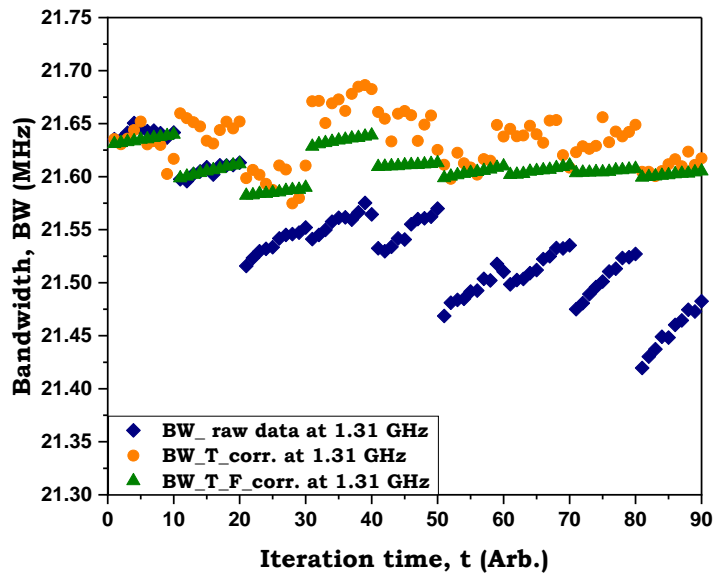


Figure 8-14: Scatter in the BW for water for mode 3 (Raw data – Blue, temperature corrected data – Orange and CF corrected in green).

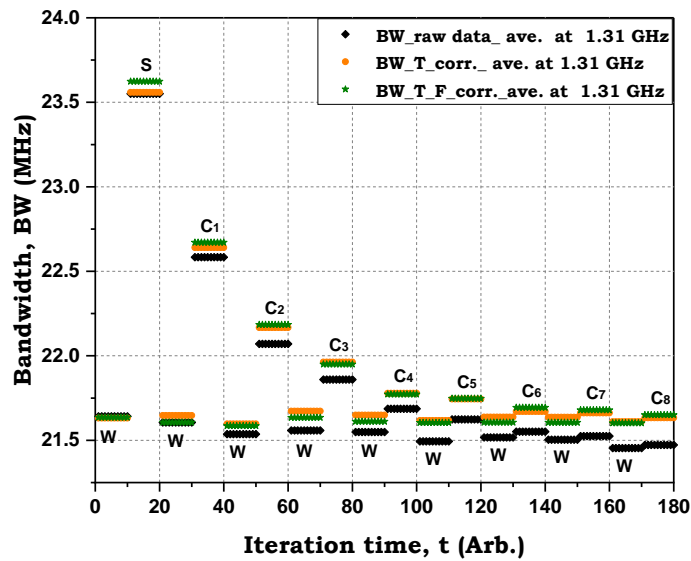


Figure 8-15: The Average of the BW for all samples for mode 3 (Raw data – Blue, temperature corrected data – Orange and CF corrected in green).

Table 8-4 shows the variation in the mean, standard deviation, and standard error for corrected data.

Table 8-4: Mean, standard deviation and percentage error for mode three of the BW.

Mode No.	Frequency	Mean	Standard deviation	Percentage	SE
Raw	1.31 GHz	21539912	55981	0.2599	39584
T Corrected	1.31 GHz	21633266	24534	0.1134	17348
F Corrected	1.31 GHz	21609910	15195	0.0703	10744

In this mode, it is clear that the 0.195 ppt (C7) concentration is outside both the 2σ and 3σ bands. However, 0.098 ppt (C8) is within the area of +3σ (Figure 8-16).

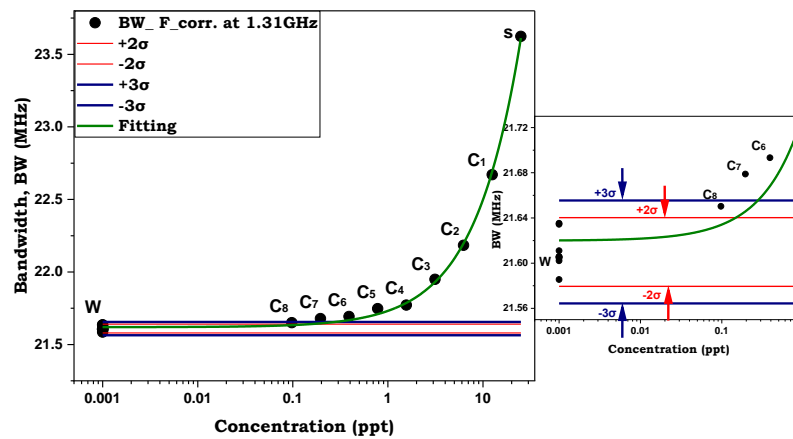


Figure 8-16: The correlation between the corrected data with different concentrations and statistical detection (2σ and 3σ).

Regarding mode 4 (1.76 GHz), the frequency correction was the first step, as there was a stronger correlation between the average BW and the CF in mode 4 (-0.6002) than with the environment temperature (-0.5376) as demonstrated in Figure 8-17. Then, the temperature correction has been applied and in doing so, the correlation coefficient increased to -0.876 after removing the effect of the ambient temperature for water.

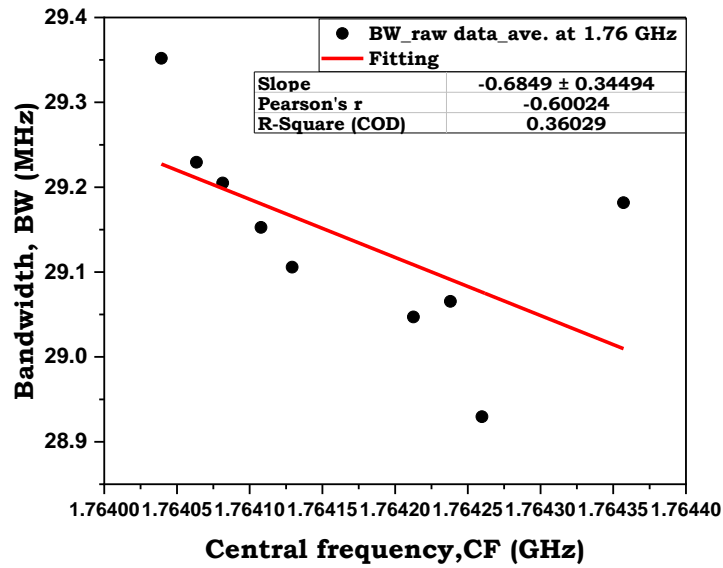


Figure 8-17: Fitting averaging row data and temperature of the environment in BW of the fourth mode (1.76 GHz).

Figure 8-18 shows the distribution of the raw data corrected after removing the frequency effect. And Figure 8-19 presents the distribution of raw data and after all correction steps (removing the effect of temperature and frequency).

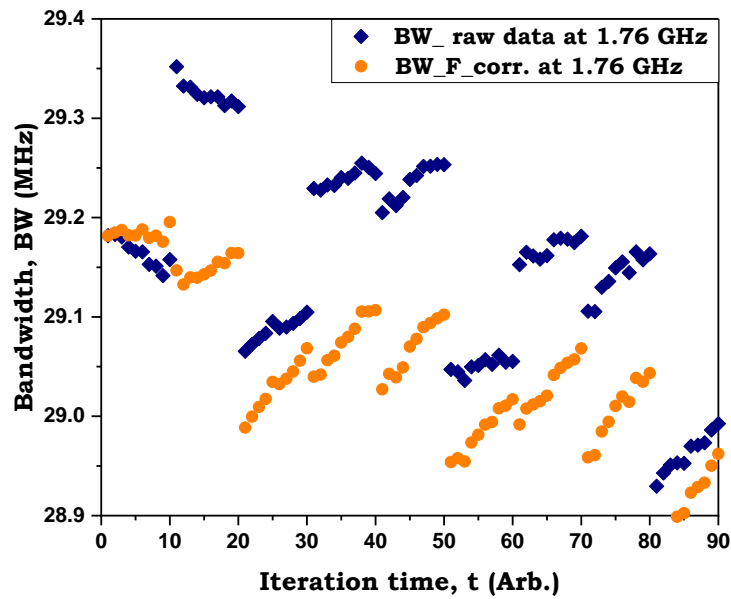


Figure 8-18: Illustrated the raw data, corrected of CF, and ambient temperature with correlation coefficient (-0.8764).

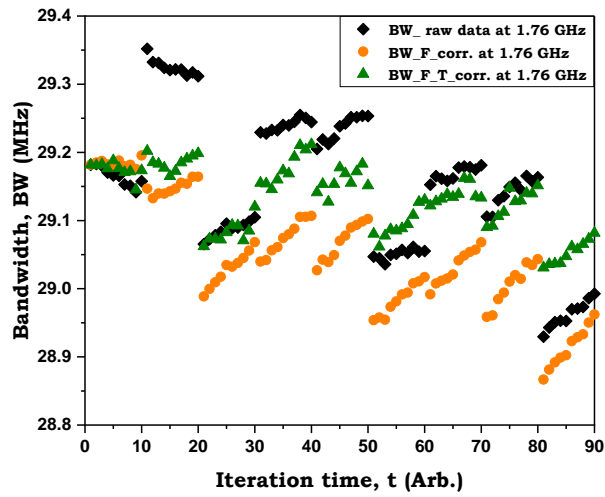


Figure 8-19: Scatter in the BW for water for mode 4 (Raw data – Blue, temperature corrected data – Orange and CF corrected in grey).

Applying both these corrections provides the following averaged data as demonstrated in Figure 8-20.

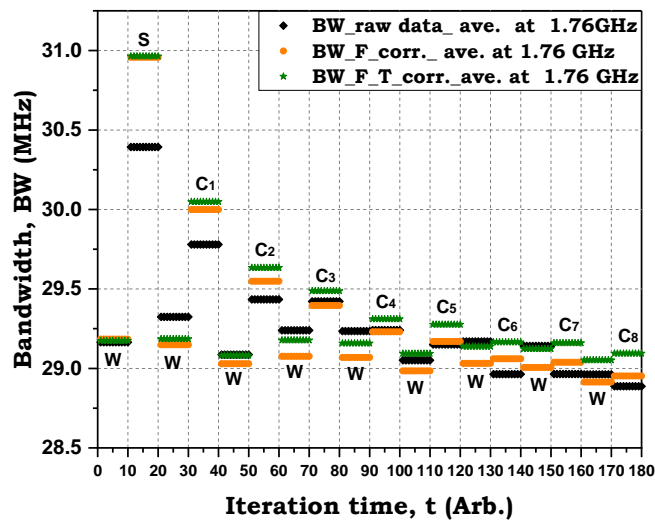


Figure 8-20: Average of the BW for all samples for mode 4 (Raw data – Blue, Corrected data from frequency – Orange and Corrected frequency data from temperature - green).

The corresponding changes in the mean, standard deviation and standard error are shown in Table 8-5.

Table 8-5: Mean, standard deviation and percentage error for mode 4 of the BW.

Mode No.	Frequency	Mean	Standard deviation	Percentage	SE
Raw	1.76 GHz	29152701	104443	0.3583	73852
F Corrected	1.76 GHz	29049125	81425	0.2803	57576
T Corrected	1.76 GHz	29131966	47856	0.1643	33839

In terms of detection limits, it is clear that the mean value of 0.39, 0.195 and 0.098 ppt (C6, C7 and C8) are within the range of  $\pm 2\sigma$  (29227678 Hz and 29036253 Hz) which creates a limitation to the usefulness of this mode for detection (Figure 8-21).

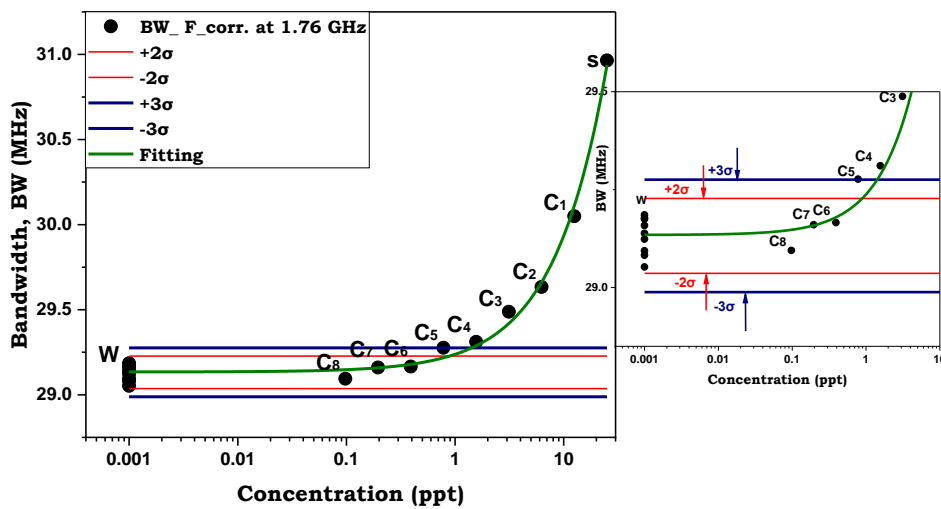


Figure 8-21: The correlation between the corrected data with different concentrations and statistical detection ( $2\sigma$  and  $3\sigma$ ).

Overall, the CF correction has proved extremely beneficial and, in some cases, totally transformed the raw data.

The trends observed for modes 2 to 4 (e.g. Figures 8-14 and 8-19) show a linear drift in the raw measurements over the 10 data samples, which is not present in the data for the first mode. It is accepted that the higher-order modes seem to be more sensitive to ‘other’ phenomena. It is quite possible that wetting, corrosion and sample temperature changes are behind this drift. Note that ‘wetting’ is implying that the water may be creeping in between the gaps, crevices and cuts that are present on the probe tip. It is also possible that the water may be creeping in between the centre conductor and the insulation material.

## 8.2.2 GOLD (Au) COATING OF THE INTERNAL CONDUCTOR (FLAT SHAPE)

Gold was plated onto the inner conductor to reduce the effect of corrosion. This is shown in Figure 8-22. The gold plating was performed by a third party (it is mentioned in the acknowledgement.) and little detail is available on the process other than to note that a gold plating solution was used and a small bench power supply. The process took around 10 minutes without any sophisticated electro polishing beforehand. Here, Stock and eight polystyrene spheres in suspension (PS) concentrations 25 to 0.098 ppt (S to C8) with size 0.8  $\mu\text{m}$  were used in detecting. The first four modes 0.46, 0.92, 1.4 and 1.9 GHz of the probe resonator with a length of 185 cm have been selected for detection.



Figure 8-22: Coated flat coaxial cable with Au.

### 8.2.2.1 RESULTS OF THE Au COATING MATERIAL

Despite Au coating, the raw data showed that this process is sensitive and stable for high concentrations 25 to 1.56 ppt (S to C4) but not for the lower concentrations, 0.78 to 0.098 ppt (C5 to C8) for all modes when measuring with different concentrations of polystyrene spheres 25 to 0.098 ppt (S to C8).

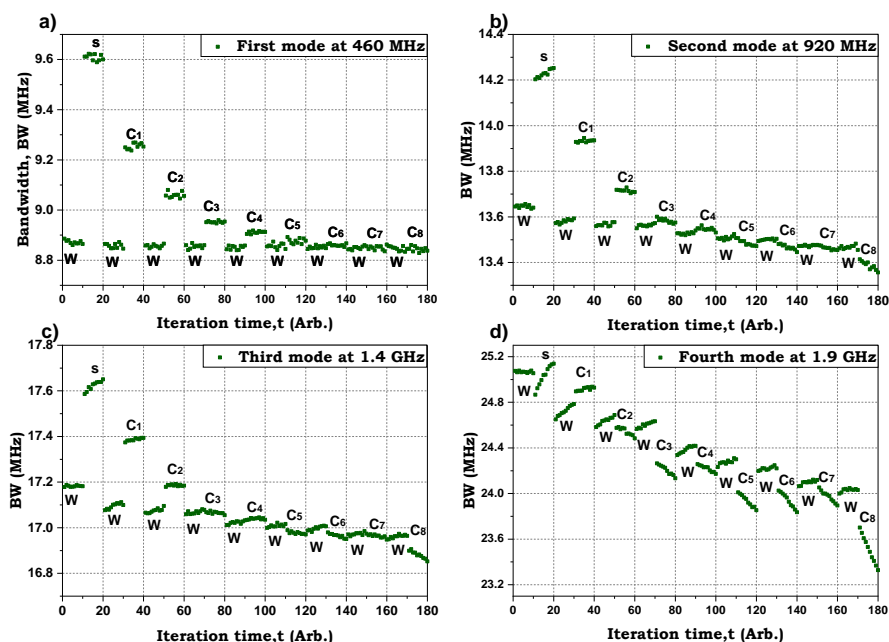


Figure 8-23: Bandwidth measured for different concentrations of  $0.8 \mu\text{m}$  PS spheres at the first 4 modes of the probe resonator after coating with Au.

For consistency, the same measurement process and subsequent correction as described above in section 8.2.1.1 have been followed. Clearly, the raw data is quite noisy despite the Au coating which does not appear to be working well. The raw data in Figure 8-23 suggests that only concentrations down to 1.56 ppt ( $C_4$ ) might be outside the detection limit. Moreover, there is again a noticeable drift downward in the raw data for mode 4 for each block. Table 8-6 showed the mean, standard deviation and percentage error in BW for the four modes. The spread in the raw data increases with increasing frequency.

Table 8-6: Mean, standard deviation and percentage error in the BW for the four modes.

Mode No.	Frequency	Mean	Standard deviation	Percentage
1	460 MHz	8854954	10269	0.12
2	920 MHz	13536981	55001	0.41
3	1.4 GHz	17042730	66643	0.39
4	1.9 GHz	24448328	319411	1.31

A correlation factor of  $-0.870$  was found between the BW and CF at the first mode. Subsequent linear fitting was applied and the resultant changes in scattering are summarised in the table 8-7.

Table 8-7: Mean, standard deviation and percentage error for first mode of the BW.

Mode No.	Frequency	Mean	Standard deviation	Percentage	SE
Raw	460 MHz	8854954	10269	0.12	7261
F Corrected	460 MHz	8861858	8585	0.10	6071

The same process that was used in section 8.2.1.1 for determining the detection limits is applied here. Figure 8-24 showed that 0.39 to 0.098 ppt (C6 to C8) are within the  $\pm 2\sigma$  for the average value of BW for water. Regarding 0.78 ppt (C5), it is within the range of  $\pm 3\sigma$ , which means that there is a limitation in detection for these concentrations, see the Figure below (Figure 8-24).

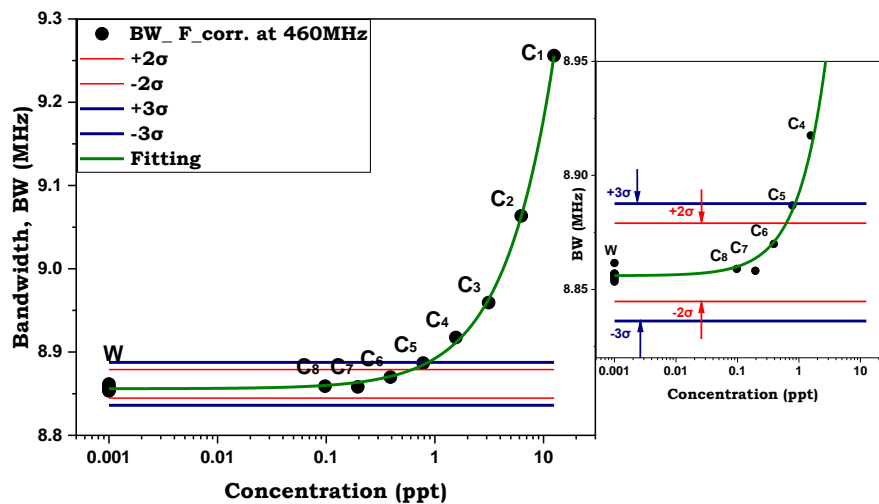


Figure 8-24: The correlation between the corrected data with different concentrations and statistical detection ( $2\sigma$  and  $3\sigma$ ) at the first mode.

Regarding the second resonance at 920 MHz, a correlation of  $-0.995$  between the BW and CF resulted in the following correction as shown in Table 8-8.

Table 8-8: Mean, standard deviation and percentage error for second mode of the BW.

Mode No.	Frequency	BW Mean	BW STDev	Percentage	Standard Error
Raw	920MHz	13536981	55001	0.41	38892
F Corrected	920MHz	13634535	7625	0.06	5392

Only concentrations down to 3.13 ppt (C<sub>3</sub>) are distinguishable from water in this case (Figure 8-25).

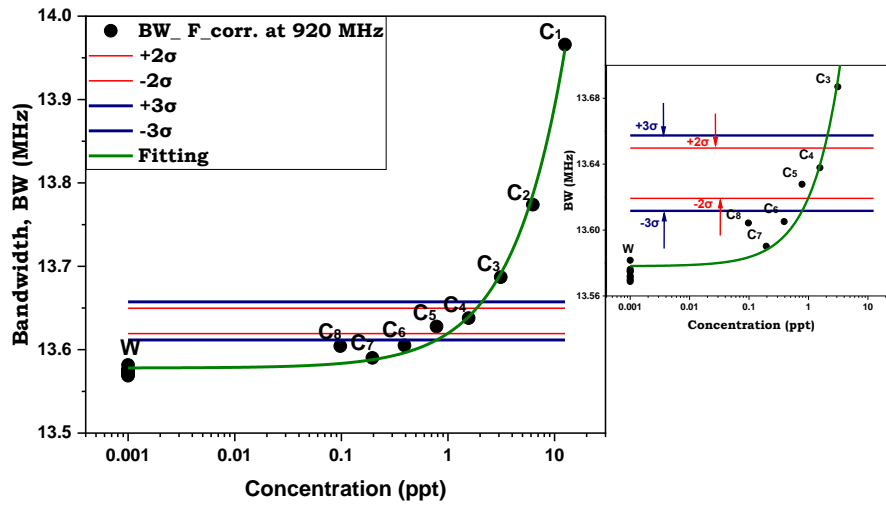


Figure 8-25: The correlation between the corrected data with different concentrations and statistical detection ( $2\sigma$  and  $3\sigma$ ) at the second mode.

For the third mode, the following was obtained with only those down to 6.25 ppt (C<sub>2</sub>) being distinguishable (Table 8-9).

Table 8-9: Mean, standard deviation and percentage error for third mode of the BW.

Mode No.	Frequency	Mean	Standard deviation	Percentage	SE
Raw	1.4 GHz	17042730	66643	0.391	47124
F Corrected	1.4 GHz	17160102	12633	0.074	8933
T Corrected	1.4 GHz	17156817	12317	0.072	8710

In this mode, there is a limitation in detection for the low concentrations and high concentration as well 3.13 ppt, 1.56 ppt and 0.78 ppt (C<sub>3</sub>, C<sub>4</sub> and C<sub>5</sub>). 1.56 ppt C<sub>4</sub> and 0.78 ppt C<sub>5</sub> within the range of  $\pm 2\sigma$ . However, 3.13 ppt (C<sub>3</sub>) is with the range of  $\pm 3\sigma$  (Figure 8-26).

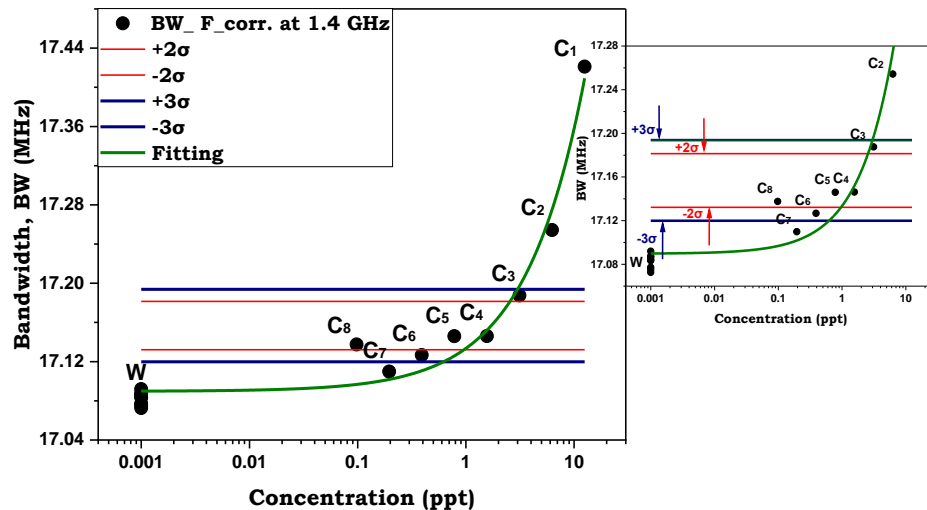


Figure 8-26: The correlation between the corrected data with different concentrations and statistical detection ( $2\sigma$  and  $3\sigma$ ) at the third mode.

Mode 4 showed virtually no improvement and is not shown.

### 8.2.3 SILVER PLATED COPPER (SPC) OF CENTRE CONDUCTOR COAX CABLE

The limitations found in detection at high frequencies that may be attributed to corrosion occurred due to the steel centre conductor and were confirmed in our experimental work. A new coaxial cable 50Ω Semi-rigid (.031CU-C-L-50) (Jyebao Company) with approximately similar dimensions for the coaxial cable utilised in the sections above (8.2.1 and 8.2.2) and different material. This cable consists of the central conductor diameter ( $0.203 \pm 0.013$ ) mm, dielectric diameter ( $0.615 \pm 0.038$ ) mm, outer conductor diameter ( $0.787 - 0.025/+0.051$ ) mm. In terms of the material specifications, the outer conductor is Bare Copper, the dielectric is expanded PTFE, and the centre conductor is silver-plated copper (SPC). Stock and eight polystyrene spheres in suspension (PS) concentrations 25 to 0.098 ppt (S to C8) with size  $0.8 \mu\text{m}$  used in detection. The first four modes 0.44, 0.887, 1.31 and 1.75 GHz of the probe resonator with a length of 179 cm have been selected for detection.

In this type, the first impression of the raw data showed good stability with limitation in detection when measuring various concentrations of PS  $0.8 \mu\text{m}$  (Figure 8-27) at all modes.

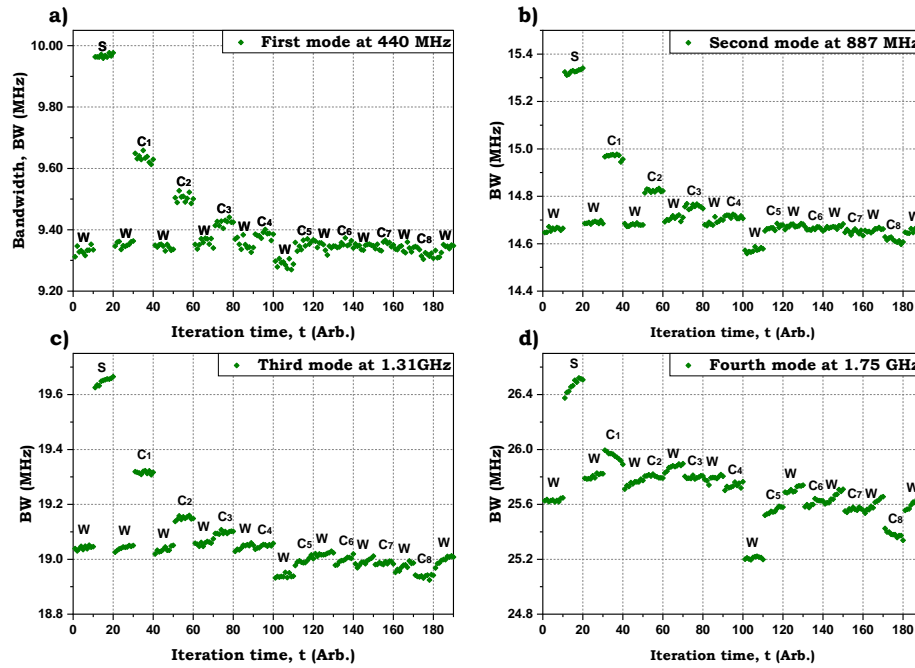


Figure 8-27: Bandwidth measured for different concentrations of 0.8 μm PS spheres at the first 4 modes of the SPC probe resonator.

The same measurement process and consequent correction as clarified in the above section (section 8.2.1.1) has been followed. Obviously, despite the approximate stability found in this type of cable when measuring the different concentrations of polystyrene spheres, a limitation in detection can be seen at all modes (up to 0.78 ppt (C5) at the first and second mode, up to 1.56 ppt (C4) at mode 3 and up to 6.25 ppt (C2) at mode 4). Table 8-10 showed the mean, standard deviation and percentage error in BW for the four modes.

Table 8-10: Mean, standard deviation and percentage error in the BW at the four modes.

Mode No.	Frequency	Mean	Standard deviation	Percentage
1	440 MHz	9339418	21948	0.2350
2	887 MHz	14665779	35676	0.2433
3	1.31 GHz	19014278	37612	0.1978
4	1.75 GHz	25662847	177203	0.6905

As a strong correlation factor between the average of BW and CF (-0.99) at the first mode, a fitting was applied, and the results are shown in Table 8-11.

Table 8-11: Mean, standard deviation and percentage error in the BW at the first mode.

Mode No.	Frequency	Mean	Standard deviation	Percentage	Standard Error
Raw	440 MHz	9339418	21948	0.2350	15519
Corrected	440 MHz	9326951	12349	0.1324	8732

The detection limit has been found by the same process used in section 8.2.1.1. Figure 8-28 illustrated that just 0.098 ppt (C8) is within the plus and minus two and three standard deviations of the average value of BW for water. As a result, there is a limitation in detection only for 0.39 ppt (C6). 0.195 ppt (C7) looks to be anomalous and has therefore been discounted.

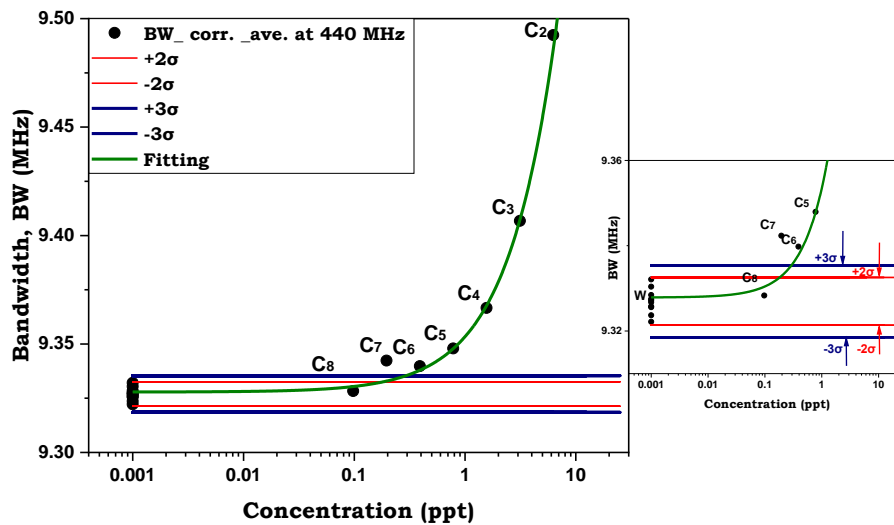


Figure 8-28: The correlation between the corrected data with different concentrations and statistical detection ( $2\sigma$  and  $3\sigma$ ) of  $0.8 \mu\text{m}$  PS spheres at the first mode of the SPC probe resonator.

In terms of the second resonance at 887 MHz, Table 8-12 shows the corresponding correction (correlation -0.96).

Table 8-12: Mean, standard deviation and percentage error in the BW at the second mode.

Mode No.	Frequency	Mean	Standard deviation	Percentage	Standard Error
Raw	887 MHz	14665779	35676	0.2433	25227
Corrected	887 MHz	14637665	12414	0.0848	8778

The concentrations down to 1.56 ppt (C4) can be discriminated from water at the second mode (887 MHz) (Figure 8-29).

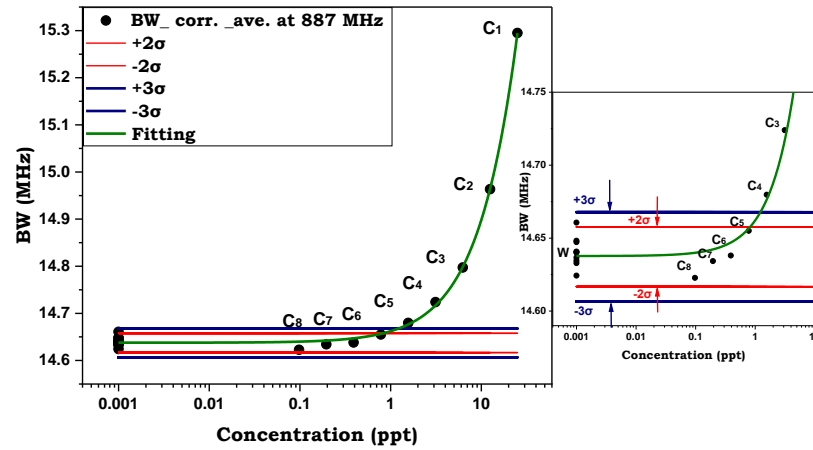


Figure 8-29: The correlation between the corrected data with different concentrations and statistical detection ( $2\sigma$  and  $3\sigma$ ) of  $0.8 \mu\text{m}$  PS spheres at the second mode of the SPC probe resonator.

In mode three, the Table 8-13 shows the raw data and the resultant values after correction.

Table 8-13: Mean, standard deviation and percentage error in the BW at the third mode.

Mode No.	Frequency	Mean	Standard deviation	Percentage	Standard Error
Raw	1.31 GHz	19014278	37612	0.1978	26595
F Corrected	1.31 GHz	18995053	27070	0.1425	19142

At this mode (mode 3), it is obvious to see a limitation in detection in between 3.13 to 0.098 ppt ( $C_3$  to  $C_8$ ). The concentration from 1.56 to 0.098 ppt ( $C_4$  to  $C_8$ ) is within the range of  $\pm 2\sigma$ , whereas 3.13 ppt ( $C_3$ ) is within the range of  $\pm 3\sigma$  (Figure 8-30).

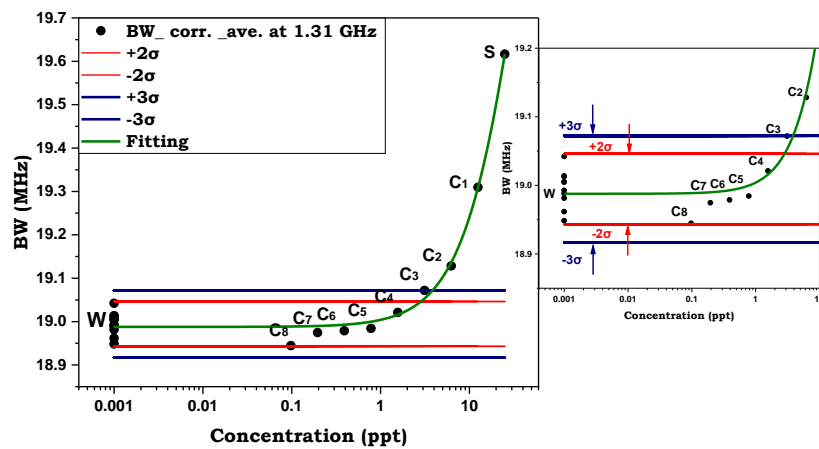


Figure 8-30: The correlation between the corrected data with different concentrations and statistical detection ( $2\sigma$  and  $3\sigma$ ) of  $0.8 \mu\text{m}$  PS spheres at the third mode of the SPC probe resonator.

Regarding mode 4, no improvement has been found in this mode even after applying the correction steps.

### **8.2.4 DISCUSSION FOR THE OVERCOMING THE CORROSION OF THE PROBE**

Three alternate probe configurations (Crimp Cut Protruding Probe, Gold (Au) Coating of the Internal Conductor, and SPC Centre conductor Coax cable) were studied due to corrosion of the steel core of the centre conductor in the probe resonator. In these measurements, before each dilution of PS, water was sampled to ensure that the measurements were stable and to gather trends. Isolating water sets and evaluating the effect of CF and temperature are the same as the correction processes outlined in chapter 7. The protruding centre conductor probe showed an improvement in the lowest detection limits for all modes (0.39 ppt (C6) at first mode, 0.195 ppt (C7) at second and third mode and 1.56 ppt (C4) at mode four) compared to the measurements of the flat tip gold coating and SPC centre conductor coax cable. This improvement in detection may be related to increasing the surface area of detection and minimising the ratio of the plated area (steel) for the tip of the cut protruding probe.

Regarding the gold plating flat tip, the gold plating seemed to present its own problems and did not appear to improve the sensitivity. It is very likely that the plating process's chemicals were not effectively cleaned and that there was a possibility of contamination of the samples. Also, the quality of the plating process could not be assessed, and as such, the surface quality may have been poor. Incomplete plating, holes, inclusions, crevices, gold adhesion etc. could all have played a part in either capturing and holding water or PS from a previous measurement. If done well, there is no reason why the gold plating would not prove extremely useful in preventing the corrosion of such wires.

In terms of the new coax cable with the silver-coated copper (SPC), unfortunately, SPC internal conductor showed no improvement in detection sensitivity. This may be related to the flat shape of the probe's tip, which in result the small surface area of silver for detection and the thicker layer of dielectric and copper may reduce the efficiency for detecting. Finally, it should be noted that these experiments were conducted extremely late in the project and access to the laboratory was limited due to COVID restrictions.

## 8.3 A COMBINED MICROWAVE / OPTICAL SPECTROSCOPY SYSTEM

A combined Microwave / Optical system has been demonstrated for the first time, as shown in Figure 8-31 and Figure 8-32 for the schematic and physical set-up respectively. This system consists of a Microwave resonator section. Using a 50  $\Omega$  Semi-rigid Coaxial Cable with SPCW of the central conductor after polishing (the same probe used in chapter 7), VNA has been used to analyse microwave data. An optical probe with a 100  $\mu\text{m}$  core diameter for illumination and detection fibre optics has been fabricated as described in section 4.1.2. This optical probe has been selected owing to obtaining a good result in chapter 4. A USB spectrometer with Ocean view operation software (Maya 2000 Pro, Ocean Optics Company, US) and a stabilised tungsten-halogen light source have been used. A LabVIEW data acquisition programme was developed to simultaneously measure both the microwave and optical signals. Figure 8-33 demonstrates the schematic of the combined system tip.

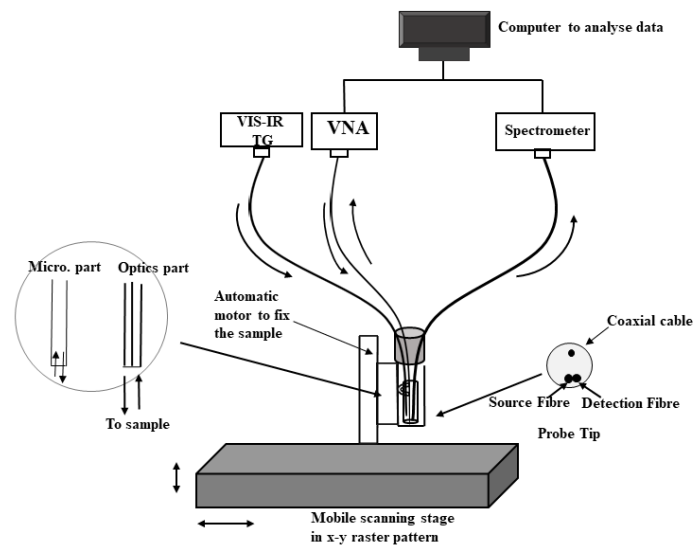


Figure 8-31: Schematic of a combined system.

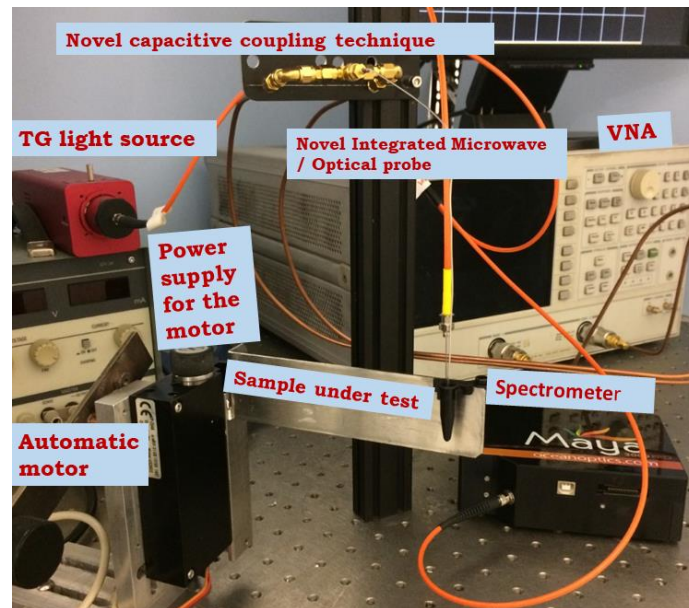


Figure 8-32: Experimental physical set-up of a combined system.

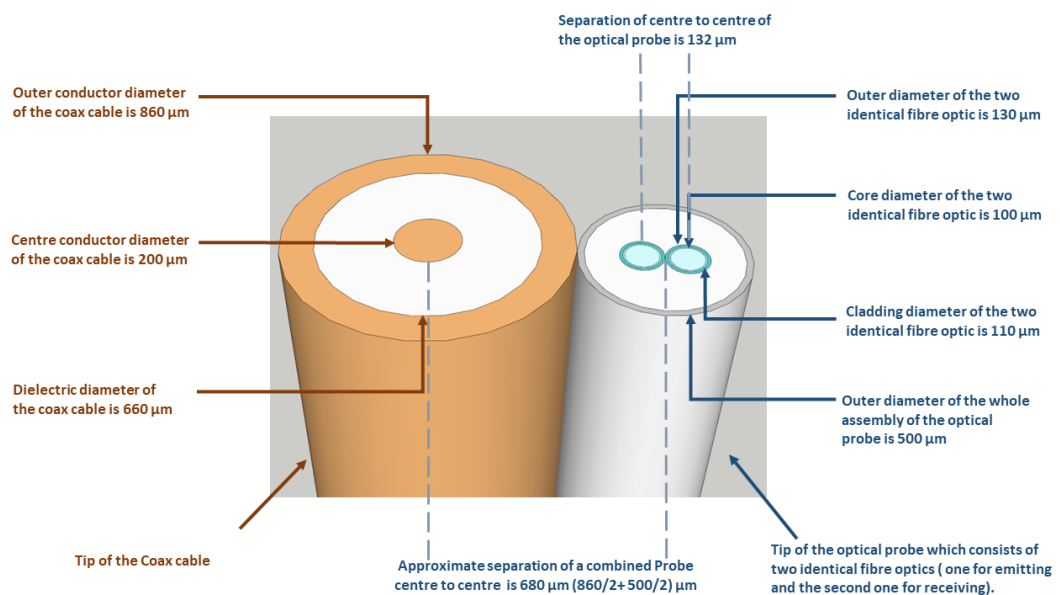


Figure 8-33: Schematic for combined Microwave/ optical system tip

In this system, the same three particle sizes 2, 0.8 and 0.413  $\mu\text{m}$  with different concentrations were used for the combined measurements. The same four modes (0.378, 0.757, 1.14 and 1.52) GHz in section 7.2.2 are selected in these measurements for detecting with various particle sizes. Six different concentrations stock (S with 25 ppt from the manufacture), the gradual half concentrations as prepared in section 4.2.1. 12.5 to 0.78 ppt (C<sub>1</sub> to C<sub>5</sub>) and pure extra DI-W as a reference sample are studied. Wavelengths in the range of 400 to 1000 nm have been used for

optical detection. Three experimental sets have been done for each concentration.

### 8.3.1 A COMBINED BW MICROWAVE/ OPTICAL RESULTS AT 2 $\mu$ M OF PS

As before, the raw BW measurements of all four modes are shown in Table 8-14.

Table 8-14: Mean, standard deviation and percentage error in the BW for the four modes.

Mode No.	Frequency	Mean	Standard deviation	Percentage
1	378 MHz	8201121	14749	0.18
2	757 MHz	11736135	16471	0.14
3	1.14 GHz	15606045	71609	0.46
4	1.52 GHz	18595875	44404	0.24

The same correction process, as described in the above section (7.3.1), has been applied for all modes. At the first mode (378 MHz), as a strong correlation factor -0.97 was found between the BW and CF, a linear fitting was applied, and resultant changes for CF and T are shown in Table.8-15.

Table 8-15: Mean, standard deviation, percentage error and SE for first mode of the BW.

Mode No.	Frequency	Mean	Standard deviation	Percentage	SE
Raw	378 MHz	8201121	14749	0.180	10429
F Corrected	378 MHz	8187261	10685	0.131	7555
T Corrected	378 MHz	8186821	10681	0.130	7552

In terms of the second mode at 757 MHz, a significant correlation of -0.92 between the BW and CF and the results after correction for CF and T are shown in Table.8-16.

Table 8-16: Mean, standard deviation, percentage error and SE for second mode of the BW.

Mode No.	Frequency	Mean	Standard deviation	Percentage	SE
Raw	757 MHz	11736135	16471	0.140	11647
F Corrected	757 MHz	11716082	7867	0.0671	5563
T Corrected	757 MHz	11715302	7848	0.0670	5550

Regarding modes 3 and 4 (1.14 and 1.52) GHz, the correlation between CF and BW at modes 3 and 4 was -0.99 and -0.94, respectively. The results after CF and T correction are demonstrated in Tables 8-17 and 8-18.

Table 8-17: Mean, standard deviation, percentage error and SE for third mode of the BW.

Mode No.	Frequency	Mean	Standard deviation	Percentage	SE
Raw	1.14 GHz	15606045	71609	0.459	50635
F Corrected	1.14 GHz	15508956	13950	0.0899	9864
T Corrected	1.14 GHz	15507665	13919	0.0898	9842

Table 8-18: Mean, standard deviation, percentage error and SE for fourth mode of the BW.

Mode No.	Frequency	Mean	Standard deviation	Percentage	SE
Raw	1.52 GHz	18595875	45120	0.243	31905
F Corrected	1.52 GHz	18538145	18016	0.09719	12740
T Corrected	1.52 GHz	18538857	18015	0.09717	12738

Averaging after correction using Equation.4-1 has been done over three sets of samples for the optical detection. Figure 8-34 demonstrates the combined detection showing the averaged optical and BW microwave signals, after corrections over three sets of 2 μm PS for all modes.

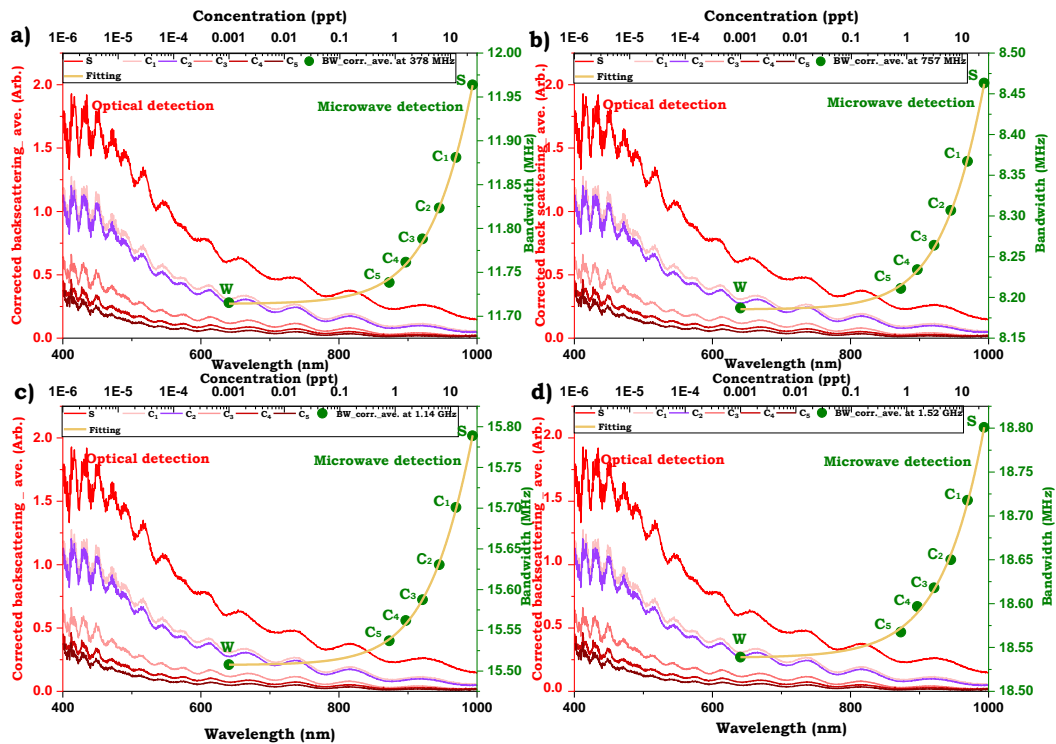


Figure 8-34: The Presentation of a combined Microwave/ Optical corrected data for PS (2 μm) with Stock from the manufacturer (25 ppt) and different concentrations (12.5 to 0.78) ppt of four modes (0.378, 0.757, 1.14 and 1.52) GHz of BW measurements and over the wavelength range (400 to 1000) nm for optical detection.

Figure 8-35 showed the BW microwave measurements of all modes after correction. The

corrected backscattering varies as expected with concentration.

At first glance, a similar trend appears for the combined detection method after correction. Generally, the Figure showed a slight difference between the two detection methods for all modes. This may be attributed to either settling particles or the presence of bubbles. Also, the detection volume is very different for both techniques.

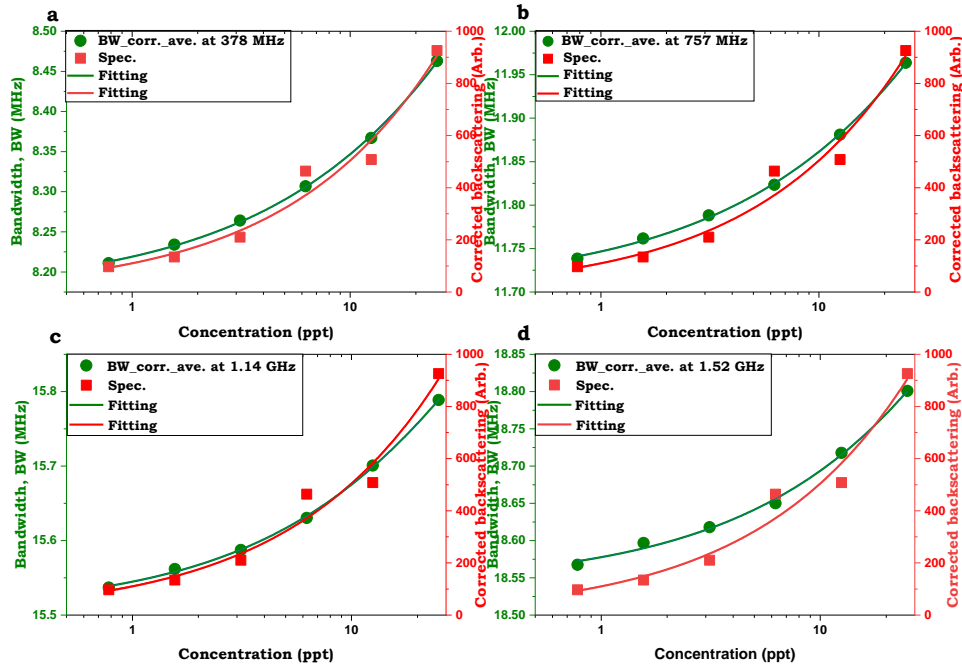


Figure 8-35: The average corrected of a combined Microwave (BW)/ Optical detection and the concentration of the PS (12.5 to 0.78) ppt and stock from the manufacturer (25) ppt at 2  $\mu\text{m}$  for all modes separately.

By comparing the optical and BW Microwave measurements for all modes together in Figure 8-36, good agreement has been found with a little difference. This agreement proves that the original hypothesis and the motivation for this research, a combined Optical detecting by elastic light scattering Spectroscopy fabricated probe and Microwave detecting by developing a novel T-Structure and capacitive coupling technique has been justified.

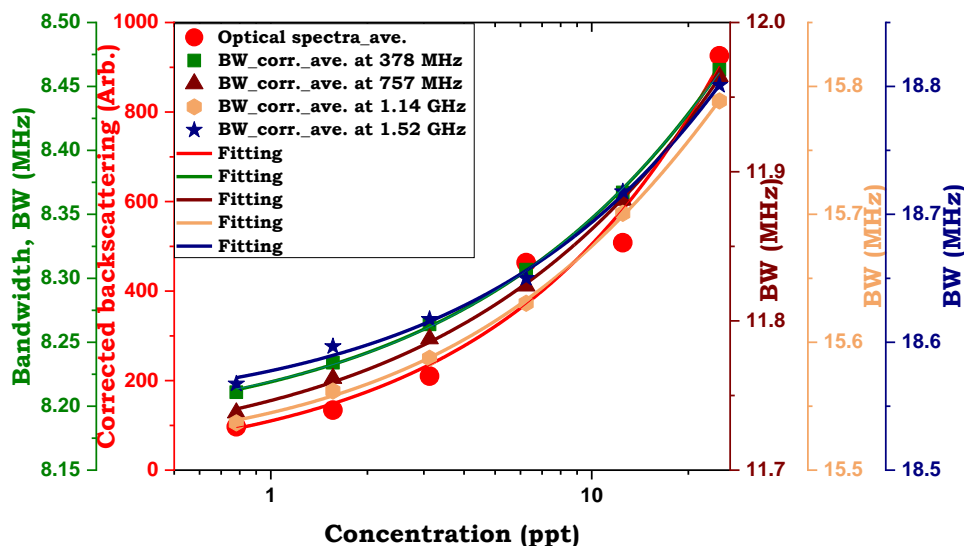


Figure 8-36: The average corrected of a combined Microwave (BW)/ Optical detection and the concentration of the PS (12.5 to 0.78) ppt and stock from the manufacturer (25) ppt at 2  $\mu$ m for all modes together.

### 8.3.1.1 THE AREA UNDER THE CURVE (AUC)

To quantify the sample concentration from the optical data, the area under the recorded spectrum has been measured. Since the detail in the optical spectra provides a measure of the particle size [81], it does not provide concentration information directly.

Figure 8-37 shows the AUC of the optical together with the BW measurements for all modes. It is clear the trend of BW for all modes is as expected. On comparing the BW and the optical signal, it is obvious that the optical data for 6.25 ppt ( $C_2$ ) does not agree well with the BW, which may be attributed to either settling particles or the presence of bubbles.

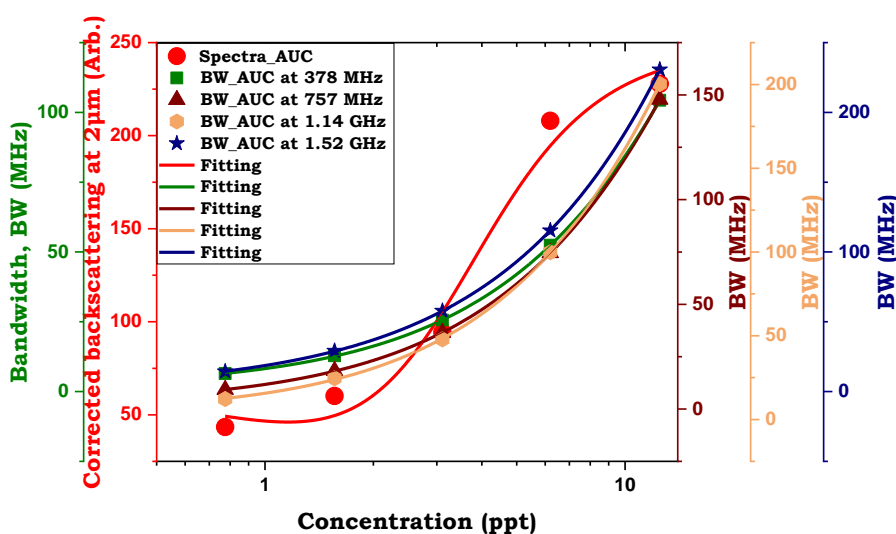


Figure 8-37: Area under curve (AUC) of a combined Microwave (BW)/ Optical detection and the concentration of the PS (12.5 to 0.78) ppt at 2  $\mu$ m for all modes together.

### 8.3.2 A COMBINED BW MICROWAVE/ OPTICAL RESULTS AT 0.8 $\mu\text{m}$ OF PS

At 0.8  $\mu\text{m}$ , the BW and optical data have been corrected with the same correction steps used for the 2  $\mu\text{m}$  PS. Figure 8-38 shows the averaged optical and BW microwave signals, after corrections over three sets of PS for all modes at simultaneous measurements for both techniques. This figure demonstrated that the optical spectrum at this particle size (0.8  $\mu\text{m}$ ) showed a different signature than 2  $\mu\text{m}$  as mentioned in ch.4 and the capability to detect various concentrations by using the microwave technique on simultaneous and real-time measurements.

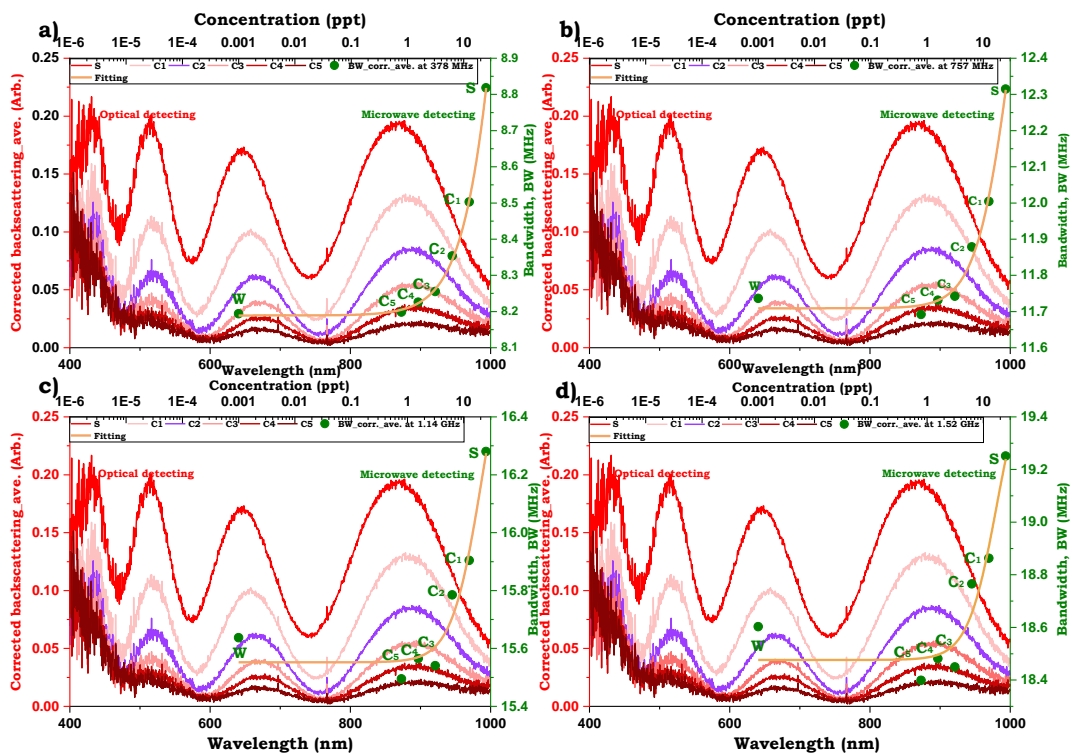


Figure 8-38: The Presentation of a combined Microwave/ Optical corrected data for PS (0.8  $\mu\text{m}$ ) with Stock from the manufacturer (25 ppt) and different concentrations (12.5 to 0.78 ppt) of four modes (0.378, 0.757, 1.14 and 1.52) GHz of BW measurements and over the wavelength range (400 to 1000) nm for optical detection.

Figure 8-39 shows how the data from combined techniques and its variation with concentration. It is clear that there is excellent agreement between the optical and BW measurements for all modes. These results showed the capability of using this system to distinguish the cell size and sample concentration at the same time.

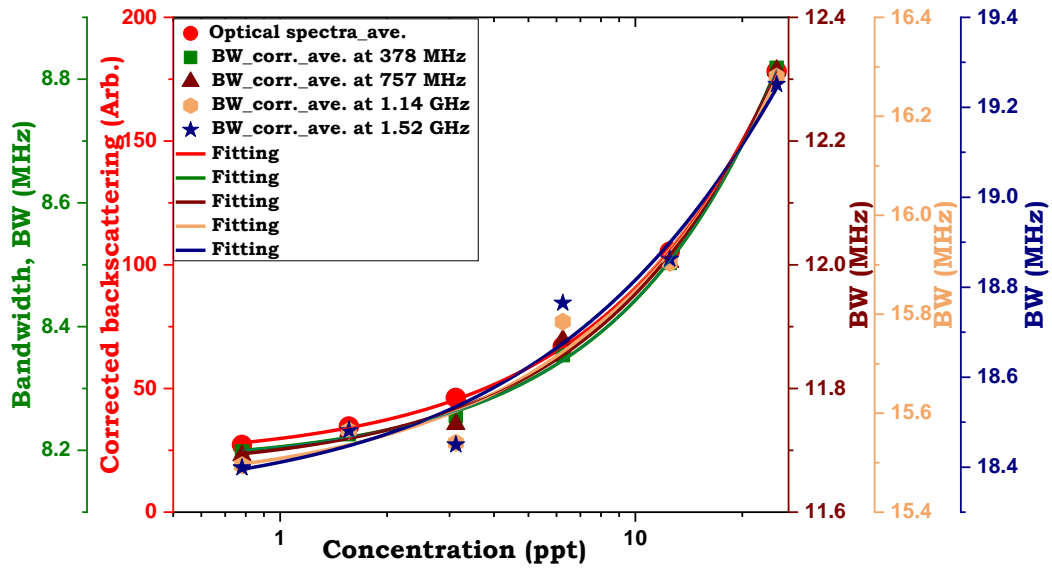


Figure 8-39: The average corrected of a combined Microwave (BW)/ Optical detection and the concentration of the PS (12.5 to 0.78) ppt and stock from the manufacturer (25) ppt at 0.8  $\mu\text{m}$  for all modes together.

Figure 8-40 shows the AUC of the optical together with the BW measurements for all modes at 0.8  $\mu\text{m}$ . The trend of BW for all modes is as expected. The BW and optical signal show good agreement.

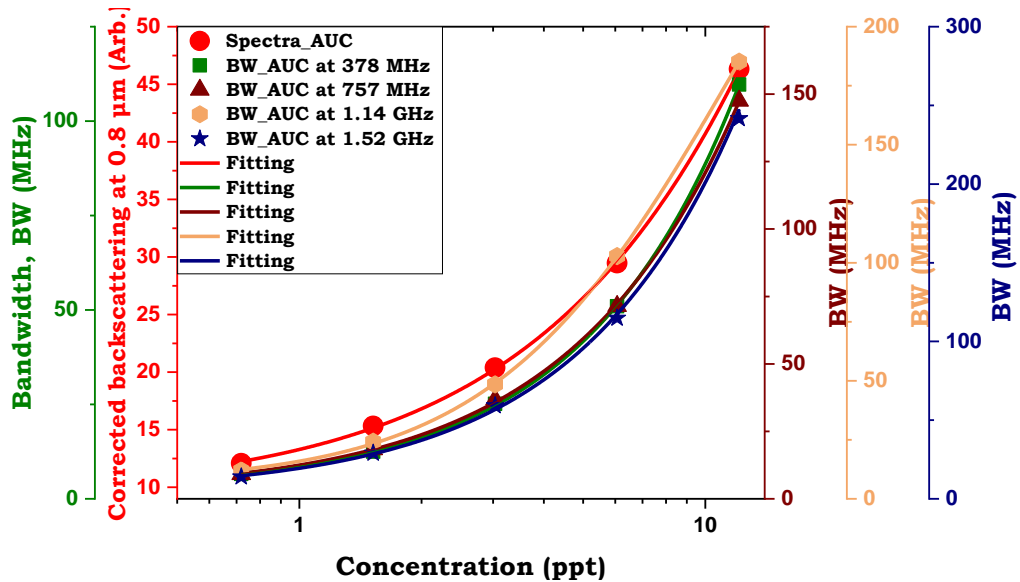


Figure 8-40: Area under curve (AUC) of a combined Microwave (BW)/ Optical detection and the concentration of the PS (12.5 to 0.78) ppt at 0.8  $\mu\text{m}$  for all modes together.

### 8.3.3 A COMBINED BW MICROWAVE/ OPTICAL RESULTS AT 0.413 μM OF PS

At 0.413 μm, the BW and optical data have been corrected with the same correction steps used for the 2 μm PS.

Figure 8-41 shows the averaged optical and BW microwave signals, after corrections over three sets of PS for all modes.

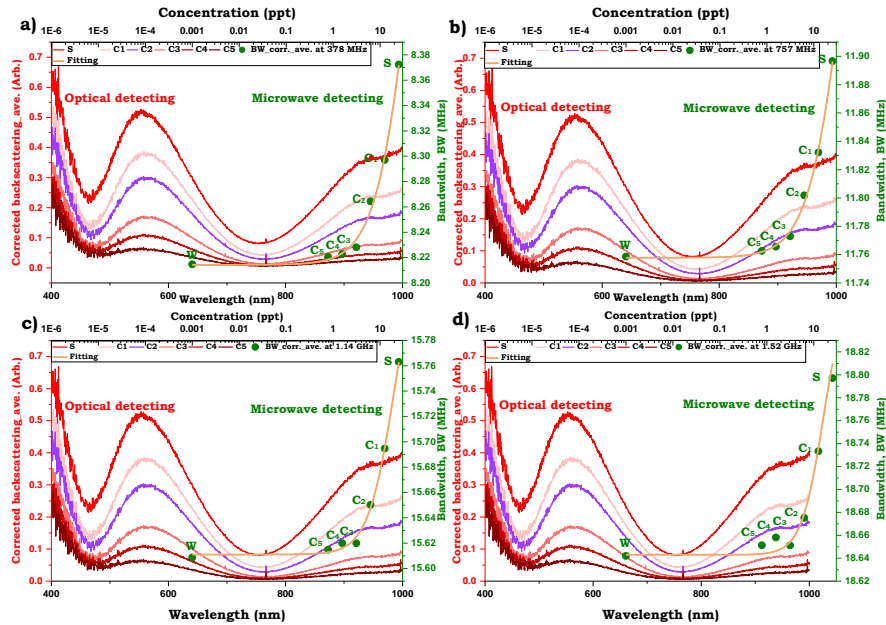


Figure 8-41: The Presentation of a combined Microwave/ Optical corrected data for PS (0.413 μm) with Stock from the manufacturer and different concentrations (12.5 to 0.78) ppt of four modes (0.378, 0.757, 1.14 and 1.52) GHz of BW measurements and over the wavelength range (400 to 1000) nm for optical detection.

Figure 8-42 shows the data from the combined technique and its variation with concentration.

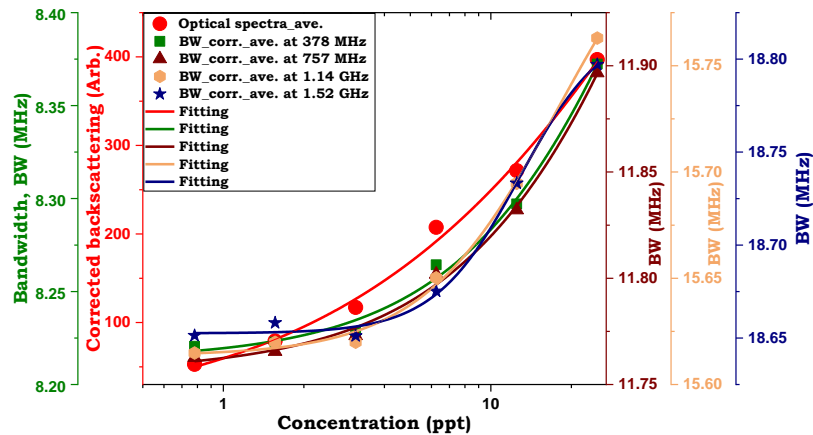


Figure 8-42: The averaging corrected of a combined Microwave (BW)/Optical detection and the concentration of the PS (12.5 to 0.78) ppt and stock from the manufacturer (25) ppt at 0.413 μm for all modes together.

At 0.413  $\mu\text{m}$ , the AUC of the optical together with the BW measurements for all modes is shown in Figure 8-43.

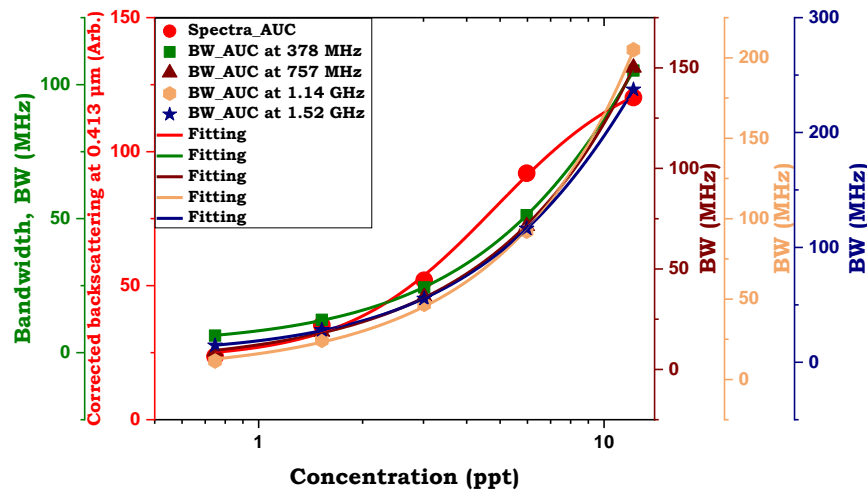


Figure 8-43: Area under curve (AUC) of a combined Microwave (BW)/ Optical detection and the concentration of the PS (12.5 to 0.78) ppt at 0.413  $\mu\text{m}$  for all modes together.

### 8.3.4 DISCUSSION FOR THE COMBINED SYSTEM

The combination of Microwave detection and optical detection by elastic light scattering has been used for the first time in the context of cancer detection. In this study, the same PS size (2, 0.8 and, 0.413)  $\mu\text{m}$  were used in all research studies. The range of the concentration was 25 to 0.78 ppt ( $C_1$  to  $C_5$ ) for all particle sizes. Simultaneous measurements have been done for both techniques by using the LabVIEW data acquisition programme. In this system, relative measurements were done without calibration for microwave measurements, while the optical measurements were calibrated by recording a reference spectrum from a spectrally flat diffuse reflector (Spectralon).

Even though the challenges found during the measurements, such as settling particles, bubbles, and centre to centre separation for both two probes, an agreement with a little difference has been found in comparing the optical and BW Microwave measurements all modes together and different concentrations for all particle size. At 0.8  $\mu\text{m}$ , an excellent agreement has been found except for 6.25 and 3.13 ppt ( $C_2$  and  $C_3$ ) at high frequencies (1.14 and 1.52 GHz) compared to 2 and 0.413  $\mu\text{m}$ . At 2  $\mu\text{m}$  and 0.413  $\mu\text{m}$ , the output showed an agreement with little difference at 6.25, 3.13, 1.56 and 0.78 ppt ( $C_2$ ,  $C_3$ ,  $C_4$  and  $C_5$ ) at low frequencies (378 and 757) MHz and high frequency (1.52 GHz) with 2  $\mu\text{m}$ . At 0.413  $\mu\text{m}$ , an agreement was found for all concentrations except at 6.25 and 3.13 ppt ( $C_2$  and  $C_3$ ) at all microwave modes. This difference in agreement regarding the size particle may be because the concentration of the 0.8  $\mu\text{m}$  particles is more

homogeneous than the rest particles during the time of the measurement. Particle settling during the measurements remains challenging.

Whilst the optical system has the capability of measuring particle sizes, as shown in Figures 8-34, 8-38 and 8-41, a simple measure of AUC was used to quantify the sample concentration from the optical data. Figure 8-44 confirmed that the area under the curve of each spectrum is proportional to particle concentration. This is of relevance for detecting cancer when there is a change in cell size. To find the agreement for two techniques in detection, the output of AUC for both methods (Microwave and optical) showed good agreement in general for all particle sizes.

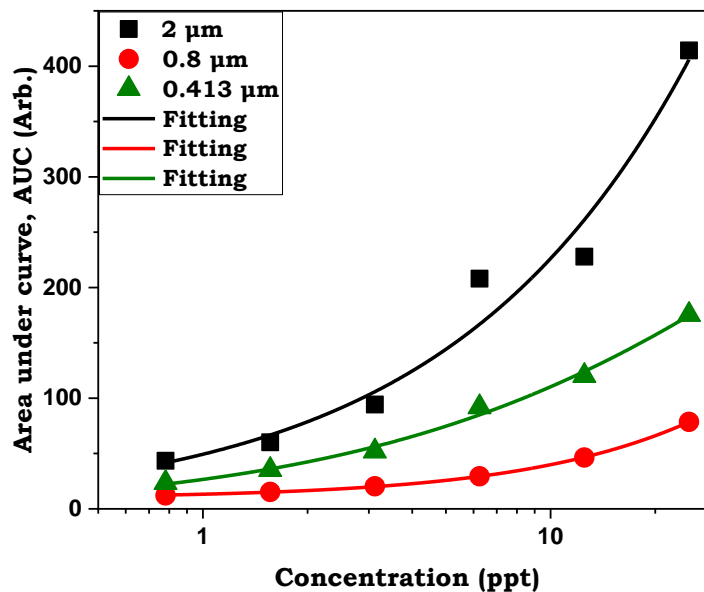


Figure 8-44: Area under curve (AUC) comparison for all particles (2, 0.8 and 0.413)  $\mu\text{m}$  at wavelength detecting range (400 to 1000) nm over various dilutions (25 to 0.78) ppt.

Regarding frequency detection, four modes have been selected (0.378, 0.757, 1.14 and 1.52) GHz for all particle sizes. Figures 8-45 to 8-47 showed the detection limit for these frequencies' detection with various particle sizes. In these figures, the output showed that the low frequency 0.378 GHz is the most sensitive and showed the lowest detection limit 1.56 ppt (C<sub>4</sub>) for three particle sizes. This may be due to that 0.378 GHz is less sensitive to factors affecting the tip of the coax cable for either the bubbles or the corrosion found at the end of normal saline experiments. Finally, since the centre-to-centre separation between the optical probe and coaxial cable is approximately 680  $\mu\text{m}$ , this combined system will be more suited to the detection of bulk tissue samples rather than single cells.

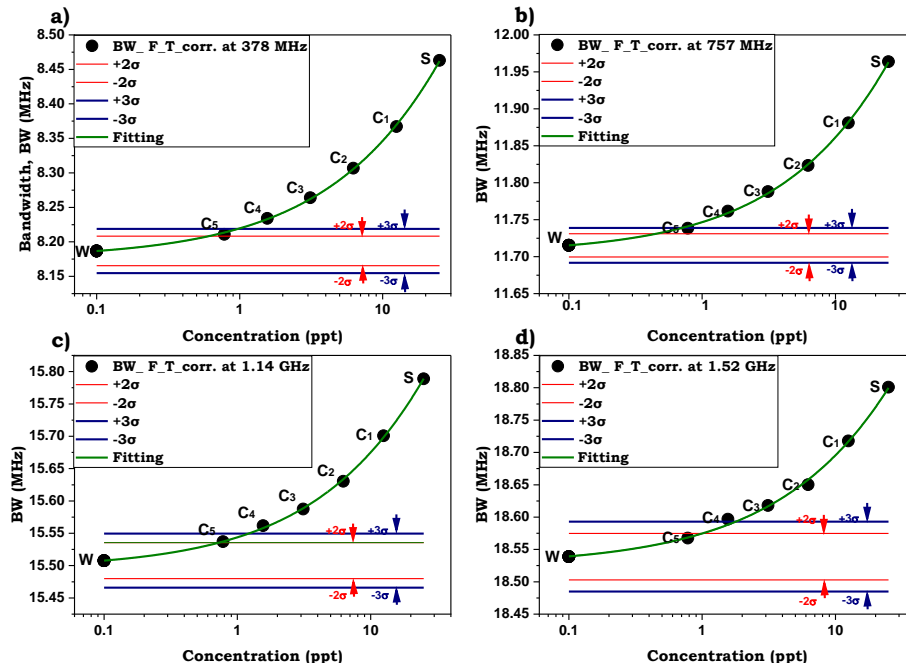


Figure 8-45: The correlation between the corrected BW data of 2 μm with different concentrations (25 to 0.78) ppt and statistical detection  $\pm(2\sigma(\text{red})$  and  $3\sigma(\text{blue}))$ .

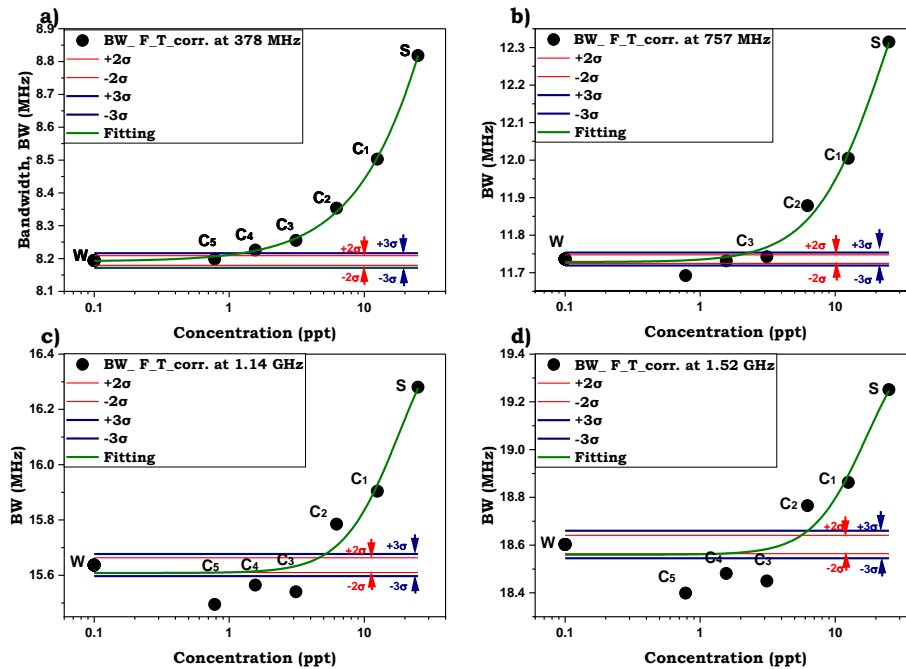


Figure 8-46: The correlation between the corrected BW data of 0.8 μm with different concentrations (25 to 0.78) ppt and statistical detection  $\pm(2\sigma(\text{red})$  and  $3\sigma(\text{blue}))$ .

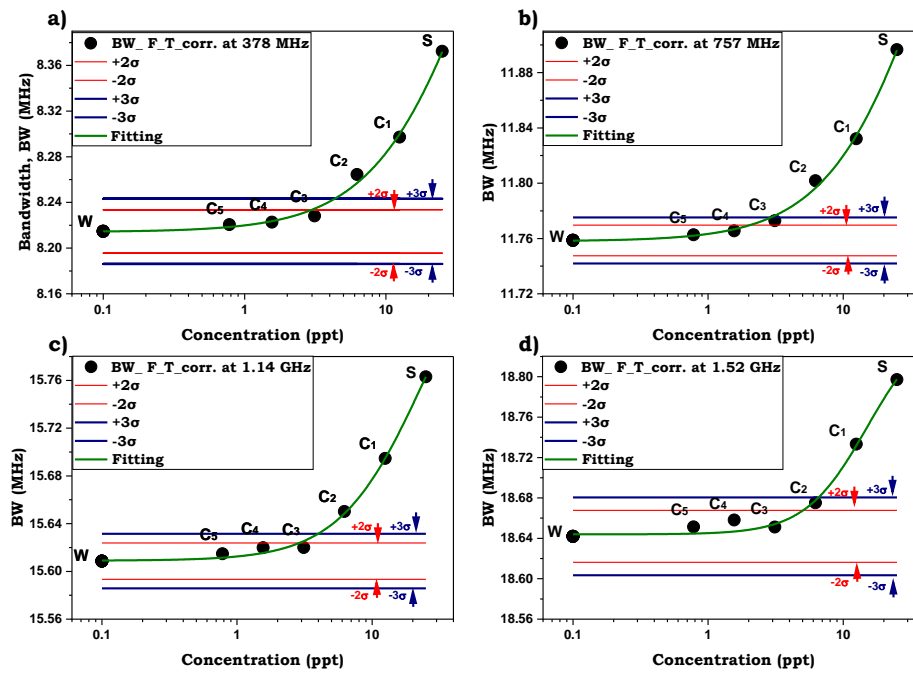


Figure 8-47: The correlation between the corrected BW data of  $0.413 \mu\text{m}$  with different concentrations (25 to 0.78) ppt and statistical detection  $\pm(2\sigma(\text{red})$  and  $3\sigma(\text{blue}))$ .

## 8.4 CHAPTER SUMMARY

To summarise the first part of this chapter, due to the corrosion of the steel core of the centre conductor in the single resonator has explored by microscope inspection, three alternative probe configurations have been utilised for detecting different dilutions of the PS (Crimp Cut' Protruding Probe, Gold (Au) Coating of the Internal Conductor and SPC of Centre conductor Coax cable). In these measurements, water was measured before each dilution of PS and to check the stability of the measurement and to obtain any trends. Then the same correction steps have been mentioned above by isolating the water set to study the effect of the CF and temperature. The output from all these measurements after correction, an improvement in detection has been found in the protruding centre conductor probe by increasing the surface area and minimise the ratio of the plated area (steel) is the best for improving detection limits for low concentrations of PS spheres.

Regarding the second part of this chapter, the results from the combined Microwave/ Optical probe showed an excellent agreement at  $0.8 \mu\text{m}$  and good agreement at 2 and  $0.413 \mu\text{m}$  for both techniques. This new technique clarified that the optical data could facilitate distinction between different particle sizes, which is proved in Figures 8-34, 8-38 and 8-41. The outcome for these graphs showed that each particle size has a different periodic signature. Moreover, Figure 8-44

confirmed that the area under the curve of each spectrum is proportional to particle concentration. This is of relevance for detecting cancer when there is a change in cell size. Additionally, the microwave technique demonstrated the ability to distinguish various concentrations, as shown in Figures 8-45 to 8-47. By applying a combined system for the first time, this work has the capability to distinguishing various cancer cells and sample concentrations simultaneously and in real-time. 0.378 GHz showed the capability for efficient detection of low concentrations for all modes at all particle sizes. Finally, this combined system has the capability for detecting tissue samples more than a single cell.

---

## CHAPTER 9:

### CONCLUSIONS AND FUTURE WORK

#### 9.1 CHAPTER CONCLUSIONS

The objectives of this thesis have been successfully achieved. It showed the capability of a fabricated optical probe with the optical selection technique in detecting different particle sizes 2, 0.8 and 0.413  $\mu\text{m}$  with various polystyrene spheres in suspension (PS) concentrations. Another aspect of this study is to highlight the ability of the microwave with multiple methods in detecting the normal saline and PS with various dilutions. The non-resonant method (open-ended coaxial cable) uses the frequency range 0.1 to 3 GHz to detect using the PS with different dilutions. A more efficient, resonant method showed the ability of the cavity and Novel T-Structure and capacitive coupling technique in detecting various concentrations of the normal saline and the PS. Finally, the integration of Microwave /Optical system in PS detection. This conclusion will highlight the essential points in each chapter.

Chapter 2 presented the diagnostic techniques for both detection methods optical, microwave and other cancer detection techniques. In terms of optical detection, several methods (DRS, FS, RS and ELSS) have been discussed. ELSS method has been selected for our fabrication. Regarding microwave detection, resonant and non-resonant procedures have been highlighted. Open-ended at frequency range 0.1 to 3 GHz used for a non-resonant, and circular cavity as a reference selected for resonant method. 2, 0.8 and 0.413  $\mu\text{m}$  have been chosen for detection as a phantom tissue sample due to the review of the earlier publications.

Chapter 3 introduced the basic principle for the transmission of light in tissue and the optical properties. It presented the scattering theory as it is the basic principle for the selected technique in our research (ELSS). A mathematical model based on Beer-Lambert law and the standard Gaussian distribution function has been done to characterize the specification parameters of our design. Some parameters affecting the mathematical model are studied: N-sigma, acceptance angle, scattering, centre to centre separation, and diameter of the optical probe. In terms of N-sigma. Six is the ideal number to obtain a typical Gaussian intensity function.

Regarding the acceptance angle, the general outcome is that the lower the differences in refractive index, the more light is coupled from source fibre to sense fibre. The intensity showed a

---

remarkable increase with a decrease in the number of scattering events. For more efficiency in computation, a slightly different approach to modelling the fibre system was designed using a 'Lambertian' emitter. In this model, the increase in the z-axis, which is perpendicular to the face of the fibre aperture. The further the beam propagates, the wider the FWHM. Finally, by reducing the centre-to-centre separation between the emitting and receiving fibres (wider acceptance angle), a greater coupling efficiency of the intensity has been obtained.

Chapter 4 presented the fabrication steps for our optical probe using the ELSS technique. In our research, two probe types have been fabricated with different core diameters of 100 and 200  $\mu\text{m}$  (the core diameter was identical for emitting and receiving fibres for both optical probes). Centre to the centre separation of both types was 132 and 263  $\mu\text{m}$ ; respectively These factors play a vital role in detecting three particle sizes of polystyrene suspension 2, 0.8 and 0.413  $\mu\text{m}$  with different dilutions 2.5% to 0.625% (S to C2). Each particle has a different spectral signature in the range 400 to 1000 nm. The number of the maxima and minima of the spectra' derivatives increased with increasing the particle size.

This chapter concludes that the 100  $\mu\text{m}$  fibre core diameter and separation distance 132  $\mu\text{m}$  is more efficient for detecting than the probe 200  $\mu\text{m}$  fibre at 263  $\mu\text{m}$  separation distance for the same range of the wavelength., An LED has been used as a cheap and available light source. Good results were obtained for 0.8 and 0.413  $\mu\text{m}$  to compare the two light sources used. An attempt has been made to obtain a more efficient scattering (single scattering) detection by attaching a 200  $\mu\text{m}$  core diameter probe for emitting and receiving fibres with another probe consisting of single fibre with double core diameter. Unoptimistic results showed as the maxima and minima are not that prominent in the second setup compared to that of the first.

Chapter 5 introduced several aspects of the theory underpinning microwave detection. The first section presented the concept of microwave measurements. This included the interaction between different materials and alternating electric fields. This gives rise to a simple explanation of permittivity and reducing the electric field due to this material's presence (polarization). Pure DI-W was used in our research as a reference liquid. A simple Debye model of DI-W has been built using the Debye relaxation Equation to calculate the real and imaginary permittivity pertinent for this study. Additionally, an Excel-based calculator has been developed for providing the real and imaginary permittivity as a function of frequency and temperature and utilizes the parameters ( $\epsilon(0)$ ,  $\epsilon(\infty)$  and  $(\tau)$ ).

Next, the basic principle for deriving the Equation of the effective permittivity was demonstrated and used in the theoretical calculation for three particle sizes 2, 0.8 and 0.413  $\mu\text{m}$ , for

---

concentrations between the stock from the manufacture (2.5%) and various dilutions (2.25% to 1.25%) over the frequency range 100 MHz to 3 GHz. A significant separation between the dilutions was found for the whole frequency range regarding the magnitude of complex permittivity and the real effective permittivity when comparing water, stock, and various dilutions for the theoretical calculation. Regarding the practical part, the initial experiment utilised non-resonant methods and has been done for the same particles, dilutions, and frequency range. The reflection  $S_{11}$  showed good separation between water and subsequent dilutions between 100 to 200 MHz for all particles sizes.

The final part presented the theory of the resonant coaxial probe. This includes how the signal propagates and along lossy and lossless transmission lines. It introduces the resonator principle and the interaction on the tip of the coaxial cable. The ADS simulation of the *novel* T- Structure and capacitive coupling arrangement has been done over the frequency range of 0.1 to 6 GHz to emulate the same experimental conditions. In this simulation, the comparison between symmetrical and asymmetrical coupling has been done for BW, CF, Q factor and  $S_{21}$  for different coupling capacitor values. The BW differences became significant at higher frequencies (2.3 to 5.4) GHz for all capacitor values when comparing the symmetrical coupling. However, the Q factor reduces at a higher frequency. The apparent increase in the BW and decrease in the Q factor are related to a high order skew. The variation in insertion loss  $S_{21}$  generally increases as frequency increases as the structure's associated losses are frequency dependent. A combination of Excel and MATLAB calculation was utilised for the resonance curves' de-skewing process at the end of the chapter.

Regarding the comparison between the symmetrical and asymmetrical coupling values, asymmetrical values appeared to be positioned between the symmetrical case for BW, Q factor and  $S_{21}$ . The effect of the coaxial cable length was also studied. It found that the number of resonant frequencies rose with increasing the length of the coaxial cable and a remarkable decrease in the loss with an increase in the length of coaxial cable at a whole frequency range detected to emulate the experiment work behaviours, the effect of the concentration has been studied. Here, a marginal shift has been shown in comparing the experimental data set up of air and water at the whole range of frequency (0.1 to 6 GHz). However, at the first and the last mode (0.38 and 5.43 GHz), a significant variation was shown in comparing the stock (0.154 M) and two dilutions ( $C_1=0.077$  M and  $C_2=0.039$  M). For the de-skewing of the resonance curves, a combination of Excel and MATLAB was used.

Chapter 6 investigated the detection of saline and PS dilutions using circular resonant cavities. This chapter started by describing the basic principle of cavity resonance and the theory of cavity perturbation. Two types of saline preparation were used for detecting a preparation of

---

commercially obtained saline and lab prepared saline dilutions. Frequency and temperature corrections have been applied to the raw data. The frequency correction was done by utilising a resonant reference mode that did not interact with sample volume. Since there is a strong correlation between sensing and reference modes of the resonator, a robust and reliable method of correcting the data for environmental changes was made. Temperature correction has been done to remove the additional components in the system affected by the temperature, such as the interconnect cables that link the VNA to the CCR. The exponential correction has been applied due to the sample's temperature difference under test and the cavity resonator. The exponential method was extremely useful for removing the effect of sample temperature, and a curve fitting MATLAB algorithm was applied to determine the asymptotic value of the relevant parameter as recorded by the system.

A discrete improvement in the detection limit for low concentrations has been found for lab prepared saline dilutions. A good separation between the sample dilutions down to  $1.67\text{E-}03$  (C10) was visible with Q factor  $|S_{21}|$  and BW for the lab prepared saline dilutions compared to  $2.41\text{E-}03$  (C6) for commercial obtained saline with the exact measurement. Good agreement was found between the values of real and imaginary permittivity of the lab prepared saline, commercial preparation saline and previous authors' publications, with the exception of the real permittivity for the commercial saline preparation.

A margin improvement has been found in detection to  $8.36\text{E-}04$  (C11) for the long thin Eppendorf sample compared to  $1.67\text{E-}03$  (C10) for the Eppendorf tube sample with lab saline prepared. A good agreement was found between the values of real and imaginary permittivity, with the exception of the real permittivity for the commercial's saline preparation, on comparing among two types of preparation the saline dilutions by using the Eppendorf tube sample, Lab. preparation saline dilutions by using long thin tube and previous authors' publications

Regarding the PS, a very poor agreement for the real permittivity with the theoretical values of permittivity obtained from the effective medium calculation. However, the imaginary permittivity showed almost the opposite trend to the calculated values. This is generally due to the problems associated with particle settling by using Eppendorf.

Chapter 7 investigated the use of a *novel* T- Structure and capacitive coupling arrangement that enables an  $S_{21}$  measurement. It is a new design to overcome the issues associated with normal  $S_{11}$  measurements, increasing the sensitivity, and obtaining the opportunity to measure at a wide range of discrete frequencies. The same two saline preparations described in chapter 6 were used with the coax probe. Lab. preparation saline dilutions showed a significant improvement in detection at low frequency (757 MHz) to  $3.34\text{E-}3$  M (C9) on comparing to  $2.41\text{E-}3$  M (C6) of the

---

commercial preparation, whilst a marginal improvement was found at high frequency (1.52 GHz) to  $2.67 \times 10^{-2}$  M Lab preparation (C6) in contrast to  $4.81 \times 10^{-3}$  M (C5) of the commercial preparation. This new design was used to measure PS of different sizes (2, 0.8 and 0.413)  $\mu\text{m}$  with various dilutions. With PS detection, an improvement has been found in the data, particularly with the high frequencies after applying a simple technique for correction. Repeated water measurements throughout the experiments enabled the correction of the raw data. At 2  $\mu\text{m}$ , the detection was limited to 1.56 ppt (C4) for low frequencies (378 and 757 MHz) and high frequency at 1.14 GHz and 3.13 ppt (C3). Also, 1.56 ppt (C4) at low frequencies and 3.13 ppt (C3) at mode 3 (1.14 GHz) and 6.25 ppt (C2) at mode 4 (1.52 GHz) at 0.8  $\mu\text{m}$ . In contrast, there was no improvement in detection for all modes at 0.413  $\mu\text{m}$ . 378 MHz proved to be the most efficient detection frequency on comparing for three particles sizes at all modes.

In chapter 8, because the steel core of the probe resonator's centre conductor was corroding, three alternative probe configurations (Crimp Cut Protruding Probe, Gold (Au) Coating of the Internal Conductor, and SPC Centre Conductor Coax Cable) were studied. Before each dilution of PS, water was measured to check that the measurements were stable and to obtain trends. The same correction steps have been applied (it mentioned in Ch. 7) by isolating the water sets and studying the effect of the CF and temperature. The protruding centre conductor probe has been shown an improve in detection as a result of these measurements. Therefore, by increasing the surface area and minimising the ratio of the plated area (steel), an improvement has been shown in the detection limits for PS spheres at low concentrations. Furthermore, a significant improvement in detection was shown with the protruding centre conductor probe compared to a flat tip probe of Au plated probe and SPC probe at PS 0.8  $\mu\text{m}$ .

Another novelty of the system has been explored in this chapter. It is a combined Microwave / Optical spectroscopy system. In this system, two methods have been used in detecting samples simultaneously in real-time. A LABVIEW data acquisition programme was devised to make simultaneous measurements of both the microwave and optical signals. There is excellent agreement at 0.8  $\mu\text{m}$  and good agreement at 2 and 0.413  $\mu\text{m}$  for both techniques. 378 MHz showed the ability to the lowest detection limit of all particle sizes. This new technique showed the optical detection's ability, significantly in terms of distinguishing between different sizes of the PS and different concentrations of samples, in agreement with the microwave signals. And this system will be more effective to detect tissue samples than a single cell in the clinical relevance for a cancer diagnostic.

## 9.2 FUTURE WORK

The integrated Microwave / Optical spectroscopy system described in this thesis consists of two simultaneous, real-time techniques with the potential to facilitate rapid cancer screening. This is of particular importance in the post-COVID-19 era where the NHS in the UK is facing a major backlog of cancer treatment and diagnosis. To further this research, collaboration with clinicians must be established to test the system's effectiveness with real cancer tissue.

Given the enhancements seen in chapter 8 with the modification to the probe tip geometry, a comprehensive COMSOL based study should be carried out to optimise the microwave probe tip, together with a more serious attempt at gold plating. Further enhancements in terms of data processing should be investigated, particularly in the incorporation of the de-skew correction in the data acquisition software. In terms of optical detection, this would benefit from the use of commercial optical modelling software such as Zemax, to enhance and improve the sensitivity and robustness of the measurements.

A lab-based VNA has already been proved to be overkill in this application and therefore more effort should be devoted to the miniaturisation and simplification of the microwave hardware. The motivation for this is to reduce the cost of the system and to make it easy to use by trained technicians.

## APPENDICES

### APPENDIX (A) MATHEMATICAL MODEL FOR GEOMETRICAL PROBE CHARACTERISATION

Appendix A-1: MATLAB code to find the Intensity shown below.

```
water_theta = 9.5;
air_theta = 12.7;
%Choose a water or air calculation below.
theta = air_theta;
%theta = water_theta;

min_sep = 262;
max_sep = 500;

dif_sep = max_sep-min_sep;

I_tot = zeros(dif_sep,1);
separation = zeros(dif_sep,1);

for q=1:dif_sep

    mu = 0;
    n_sigmas = 5;
    d_core = (200e-6);
    d_separation = (262e-6)+(q*1e-6);
    separation(q) = min_sep+q;

    scatter = 1;

    x_min = -1000e-6;
    x_max = 1000e-6;
    x_size = 100;

    x = x_min;
    dx = (x_max-x_min)/x_size;

    X_values = zeros(x_size,1);

    for i = 1:x_size

        X_values(i) = x;
        x = x + dx;

    end

    y_min = -1000e-6;
    y_max = 1000e-6;
```

```

y_size = 100;

y = y_min;
dy = (y_max-y_min)/y_size;

Y_values = zeros(y_size,1);

for j = 1:y_size

    Y_values(j) = y;
    y = y + dy;

end

z_min = 0;
z_max = 10000e-6;
z_size = 100;

z = z_min;
dz = (z_max-z_min)/z_size;

Z_values = zeros(z_size,1);

Sigma = zeros(z_size,1);
I = zeros(x_size,y_size,z_size);
Scat_plot = zeros(x_size);

for k = 1:z_size

    Z_values(k) = z;
    Sigma = (d_core + 2*Z_values(k)*tand(theta))/n_sigmas;
    z = z + dz;

    for j = 1:y_size

        for i = 1:x_size

            I(i,j,k) = exp(-(scatter*Z_values(k)));
            I(i,j,k) = I(i,j,k)*(1/sqrt(2*pi*Sigma^2))*(exp(-(
(Y_values(j)-mu)^2/(2*Sigma^2))));
            I(i,j,k) = I(i,j,k)*(1/sqrt(2*pi*Sigma^2))*((exp(-
(X_values(i)-(mu-d_separation/2))^2/(2*Sigma^2)))+(exp(-
(X_values(i)-(mu+d_separation/2))^2/(2*Sigma^2))));
            I_tot(q) = I_tot(q) + I(i,j,k);

        end

    end

end

end

I_plot = zeros(x_size,y_size);

```

```

for i=1:x_size
    for j=1:y_size

        I_plot(i,j) = I(i,j,50);

    end
end

figure
surf(X_values, Y_values, I_plot);

figure
plot(I_tot, 'r*')

```

Appendix A-2: MATLAB code to find the Lambertian emitter model. shown below.

```

I0=0.7;
I0_total=I0;
alpha = 0.5;
theta=25;

m=-log10(2)/log10(cosd(theta));

X_Position = [0.3 0.7];
Y_Position = [0.5 0.5];

lx=1; ly=1; lz=1;

dx = 0.01;
dy = 0.01;

x=0:dx:lx;
y=0:dy:ly;

[XRec,YRec]=meshgrid(x,y);

E_PPF_1 = zeros(length(y),length(x));
E_PPF_2 = zeros(length(y),length(x));

height = 0.08;
frames = 8;

for r = 1:frames

    h = height * r;

    D = sqrt((XRec-X_Position(1)).^2 + (YRec-Y_Position(1)).^2 +
h^2);
    cos_phi = h./D;
    E_PPF_1 = (I0_total*cos_phi.^m)./(D.^2);

```

```

    D = sqrt((XRec-X_Position(2)).^2 + (YRec-Y_Position(2)).^2 +
h^2);
    cos_phi = h./D;
    E_PPF_2 = (I0_total*cos_phi.^m)./(D.^2);

    unit_area = dx*dy;

    E_lux = (E_PPF_1 .* E_PPF_2) * exp(-alpha*h);

    E_tot = sum(E_lux, 'all');

    figure(1)
    meshc(x,y, (E_lux));
    %contourf(x,y,E_lux);
    zlim([0,2.2]);
    xlabel('X');
    ylabel('Y');
    F(r) = getframe(gcf);
    drawnow

end

```

## APPENDIX (B) DE-SKEWED RESONANCE

Appendix B-1: MATLAB code Standard Circle Fit Function by I. Butcher shown below

```
function [xc,yc,R,a] = circfit(x,y)
%
% [xc yc R] = circfit(x,y)
%
% fits a circle in x,y plane in a more accurate
% (less prone to ill condition )
% procedure than circfit2 but using more memory
% x,y are column vector where (x(i),y(i)) is a measured point
%
% result is centre point (yc,xc) and radius R
% an optional output is the vector of coefficient a
% describing the circle's equation
%
%  $x^2+y^2+a(1)*x+a(2)*y+a(3)=0$ 
%
% By: lzhak bucher 25/oct /1991,
    x=x(:); y=y(:);
    a=[x y ones(size(x))]\(-(x.^2+y.^2));
    xc = -.5*a(1);
    yc = -.5*a(2);
    R = sqrt((a(1)^2+a(2)^2)/4-a(3));
```

Appendix B-2: MATLAB code Weighted Circle Fit Routine shown below

```
format long;

x0(1) = 0.0026;
x0(2) = 0.0028;
x0(3) = 0.00543;

th = linspace(0,2*pi,51)';

fun = @(x) sseval_circle(x,x_data,y_data,weights);

bestx = fminsearch(fun,x0)

a = bestx(1);
```

```

b = bestx(2);
r= bestx(3);

xe = r*cos(th)+a; ye = r*sin(th)+b;

figure(3)

plot(x_data,y_data, '*')
hold on
plot(xe,ye, 'o')
grid on

xlabel('t')
ylabel('Q1')
hold off
axis equal

function sse = sseval_circle(x,xdata,ydata,weights)

a = x(1);
b = x(2);
r = x(3);

sse = sum(weights.*((r - sqrt((xdata - a).^2 + (ydata -
b).^2)).^2));

```

## APPENDIX (C) ENHANCED EXPONENTIAL CORRECTION

Appendix C-1: MATLAB code fitting data shown below.

```
format long;

M = csvread('saline_null.txt');

period = 100;

sets = length(M)/period;
%sets = 2;

X = zeros(sets,4);
t = zeros(period,1);

for j = 1:period
    t(j)=j;
end

i = 1;

while i <(sets+1)

    elmnt_strt = ((i-1)*period)+1;
    elmnt_stop = ((i-1)*period)+period;

    x0 = rand(3,1) %#ok<NOPTS>
    x0(1) = 3766;
    x0(3) = 3766;

    fun = @(x)sseval_exp(x,t,M(elmnt_strt:elmnt_stop));

    bestx = fminsearch(fun,x0) %#ok<NOPTS>

    mean(M(elmnt_strt:elmnt_stop))

    A = bestx(1);
    lambda = bestx(2);
    T_env = bestx(3);

    yfit = (T_env + (A-T_env)*exp(-lambda*t));

    figure(1)
```

```

plot(t,M(elmnt_strt:elmnt_stop), '*')
hold on
plot(t,yfit, '*')

xlabel('T1')
ylabel('Q1')
hold off

i %#ok<NOPTS>

str = input('OK (Y/N) :','s') %#ok<NOPTS>
if str=='n'
    break
end

if str == "y"

    X(i,1) = i;
    X(i,2) = A;
    X(i,3) = lambda;
    X(i,4) = T_env;

    i=i+1;

end

end

figure(2)
plot(X(:,1),X(:,4), '*')

sseval_exp.m

function sse = sseval_exp(x, tdata, ydata)
A = x(1);
lambda = x(2);
T_env = x(3);
sse = sum((ydata - (T_env + (A-T_env)*exp(-lambda*tdata))).^2);

```

# APPENDIX (D) RESONANT COAXIAL PROBE RESULTS

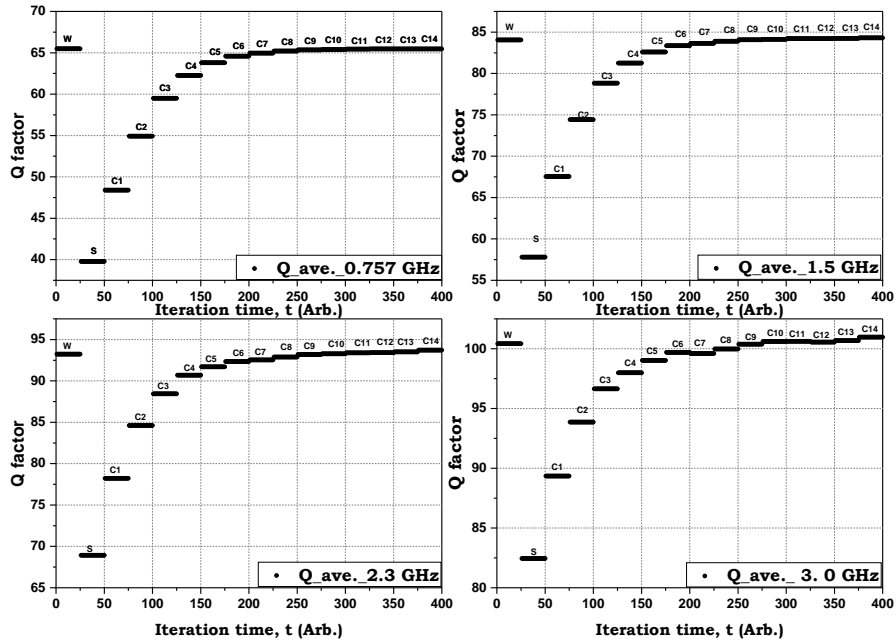


Figure D-1: The Average Q factor over the three sets for variance concentrations (0.154 to 9.400E-06) M

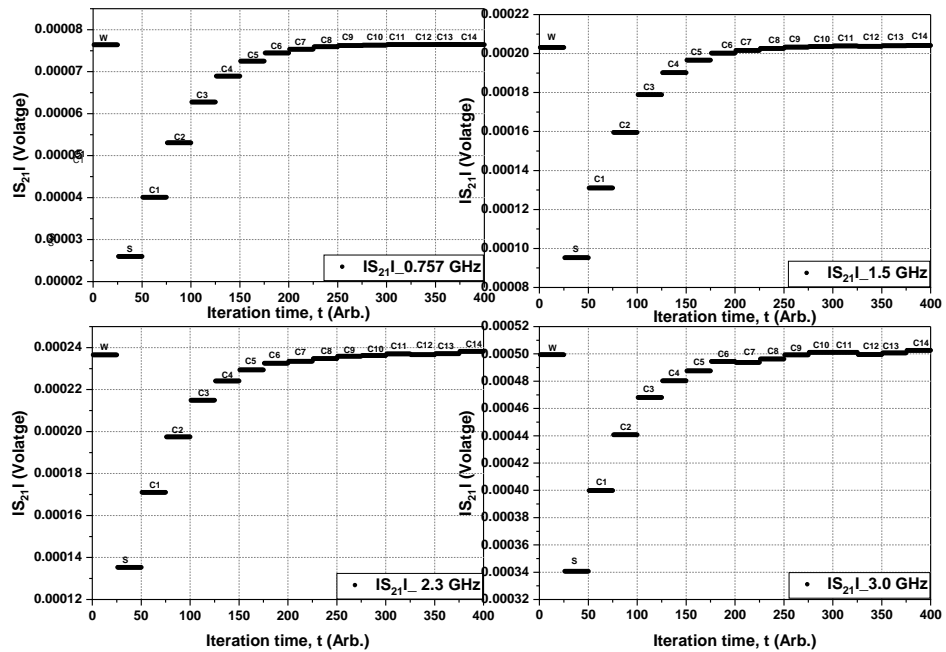


Figure D-2: The Average  $|S_{21}|$  over the three sets for variance concentrations (0.154 to 9.400E-06) M.

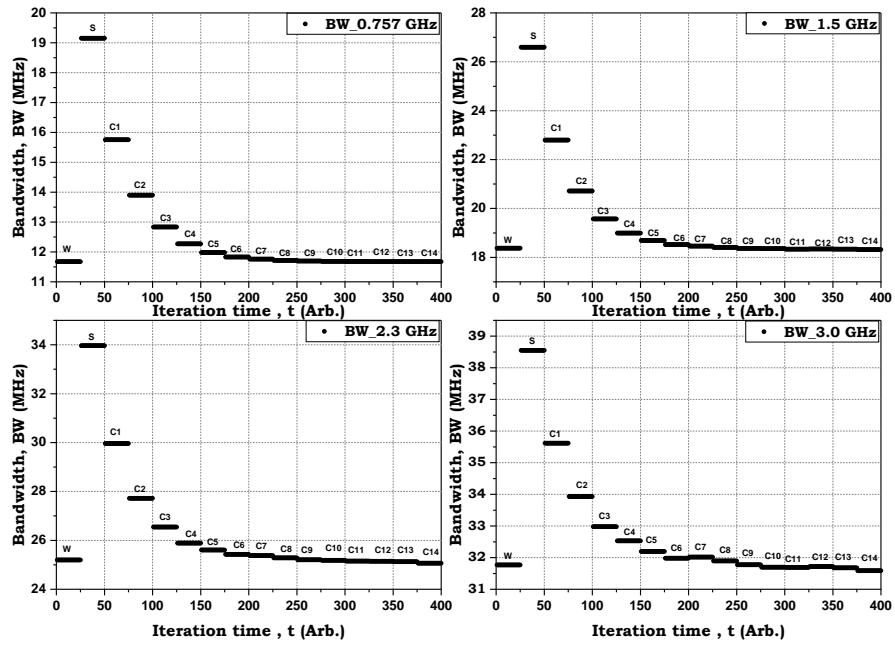


Figure D-3: The Average BW over the three sets for variance concentrations (0.154 to 9.400E-06) M.

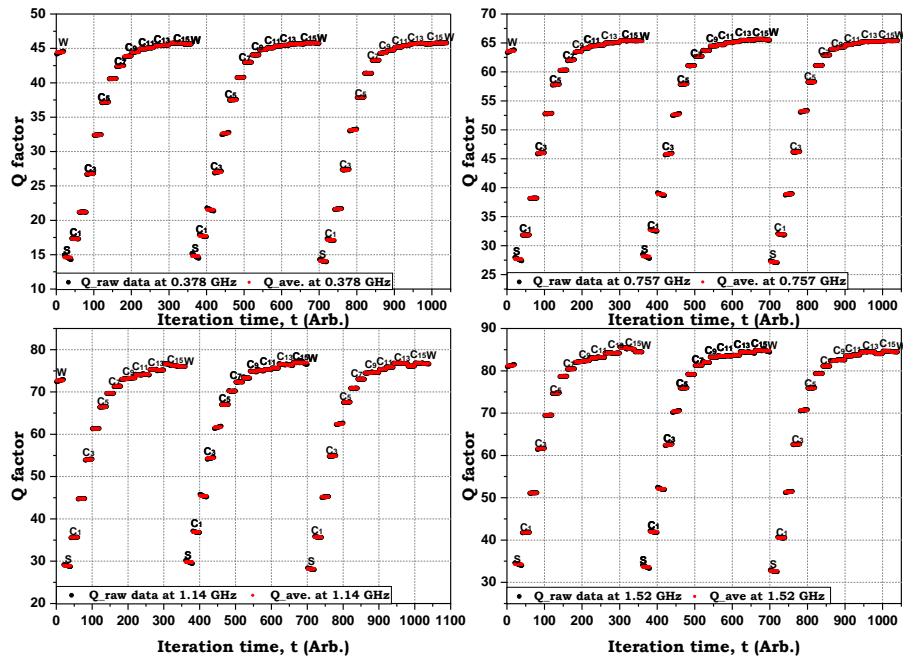


Figure D-4: Raw (black) and averaged data (Red) for Q measurements of Lab. prepared saline for variance concentrations (5.22e-05 to 1.71) M.

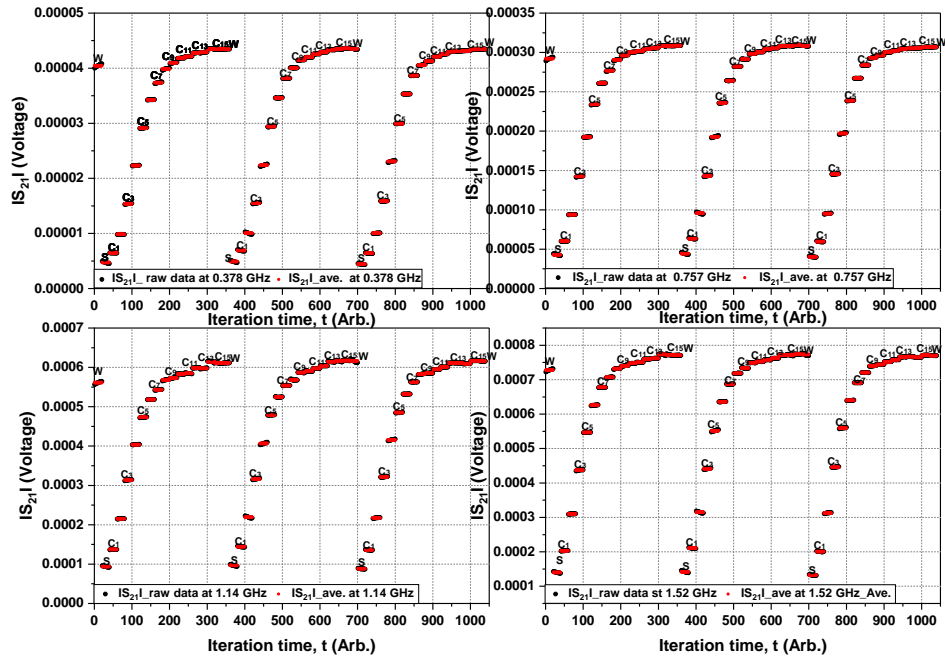


Figure D-5: Raw (black) and averaged data (Red) for  $|S_{21}|$  measurements of Lab. prepared saline for variance concentrations (5.22e-05 to 1.71) M.

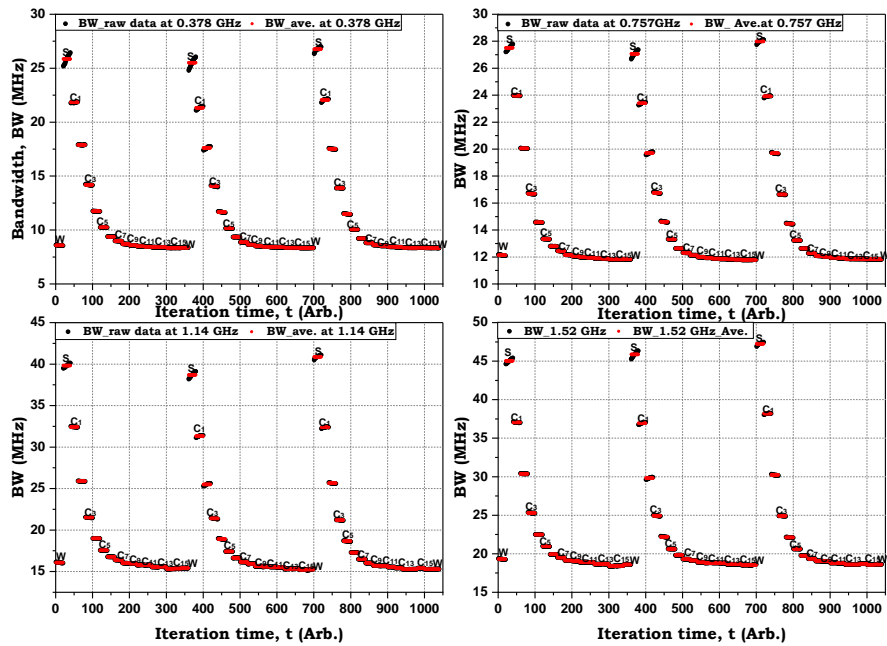


Figure D-6: Raw (black) and averaged data (Red) for BW measurements of Lab. prepared saline for variance concentrations (5.22e-05 to 1.71) M.

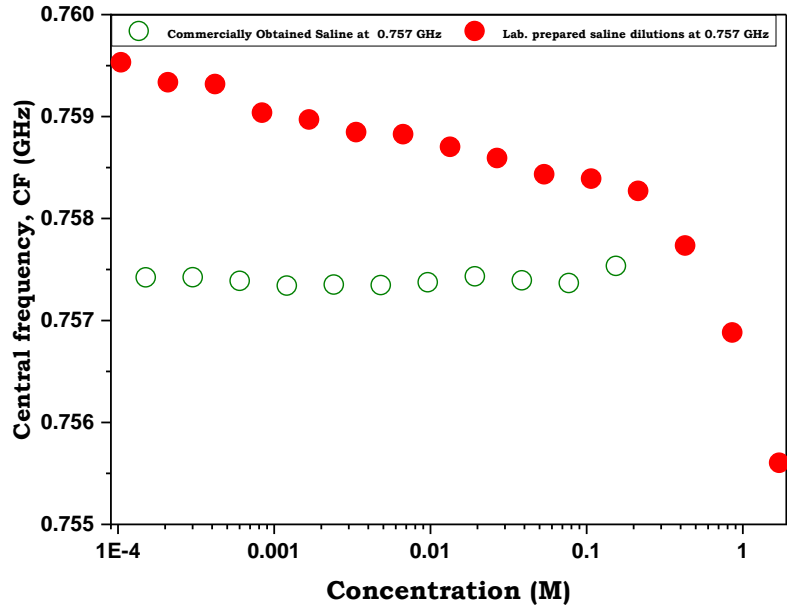


Figure D-7: Comparing CF measurements of different frequencies for variance concentrations of commercially obtained saline (0.154 to 9.4E-06) M and Lab. prepared saline dilutions (5.22e-05 to 1.71) M.

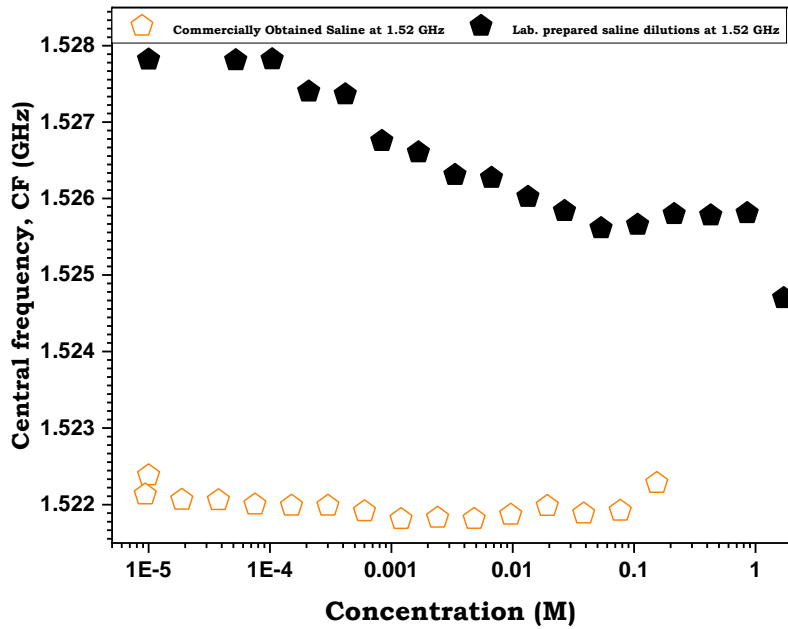


Figure D-8: Comparing CF measurements of different frequencies for variance concentrations of commercially obtained saline (0.154 to 9.4E-06) M and Lab. prepared saline dilutions (5.22e-05 to 1.71) M.

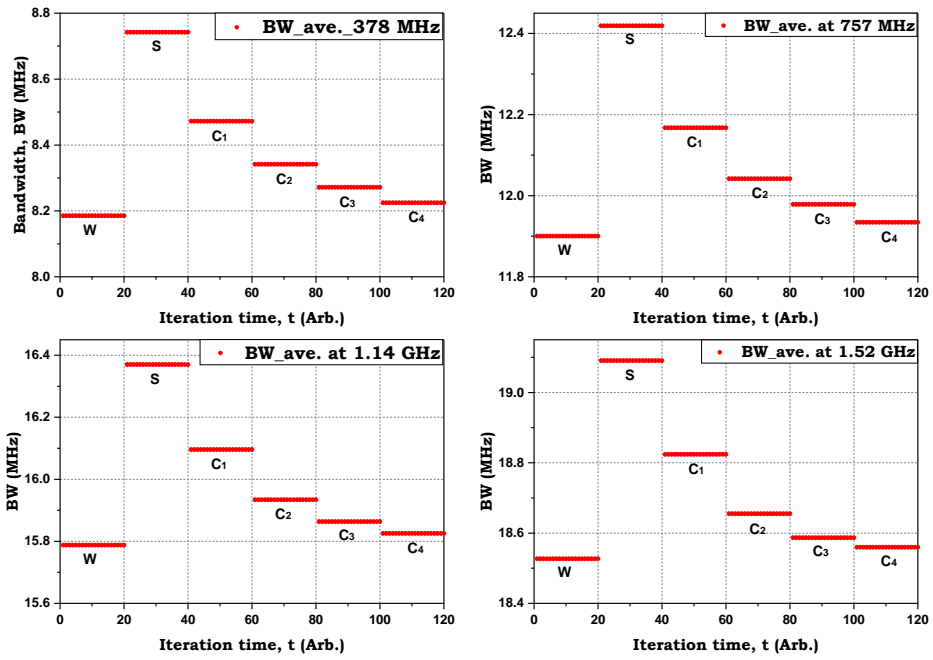


Figure D-9: Ave. of BW over the three sets after applying all the corrections for variance concentrations (25 to 1.56) ppt at 0.8  $\mu\text{m}$ .

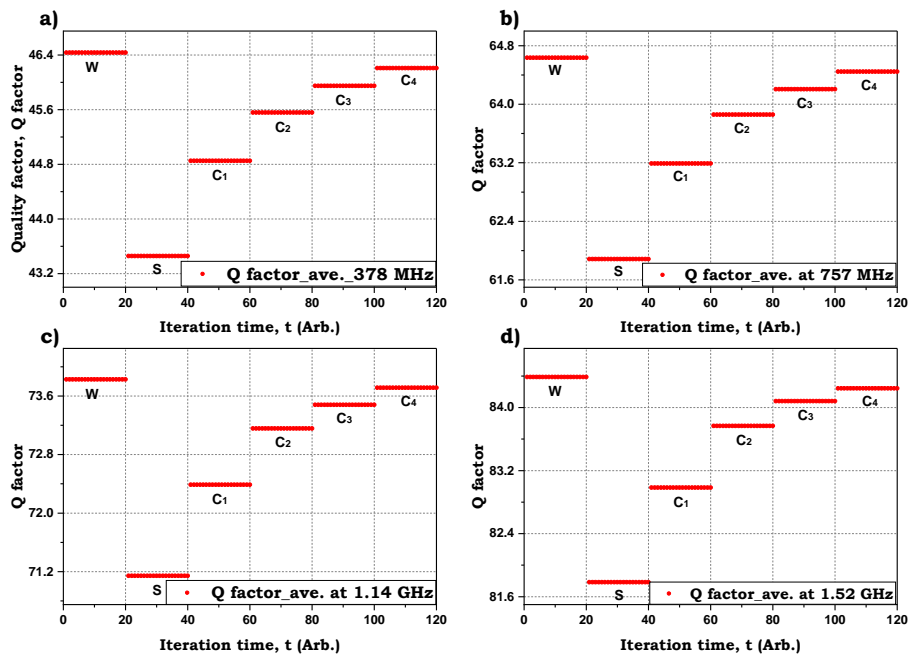


Figure D-10: Ave. of Q factor over the three sets after applying all the corrections for variance concentrations (25 to 1.56) ppt at 0.8  $\mu\text{m}$ .

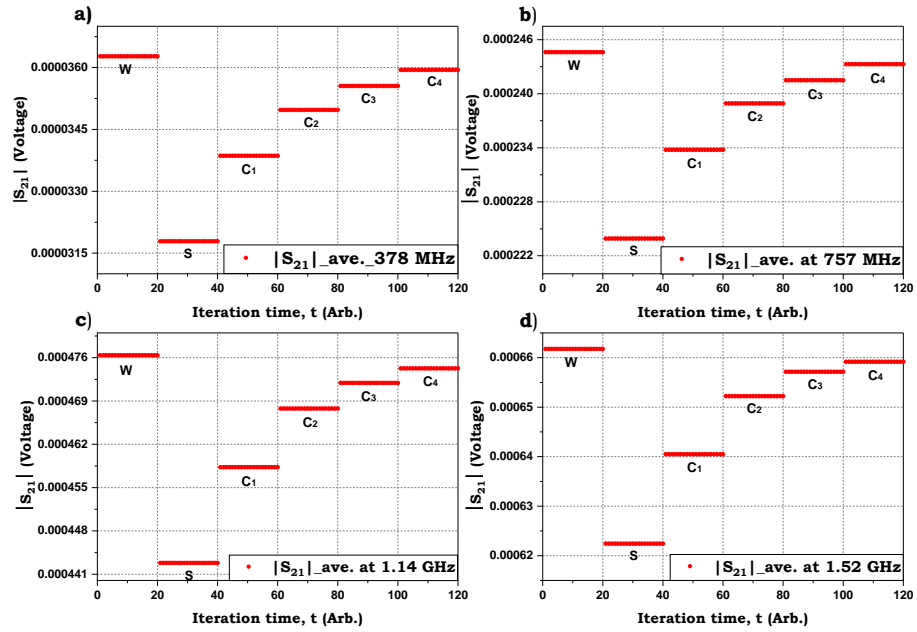


Figure D-11: Ave. of  $|S_{21}|$  over the three sets after applying all the corrections for variance concentrations (25 to 1.56) ppt at  $0.8 \mu\text{m}$ .

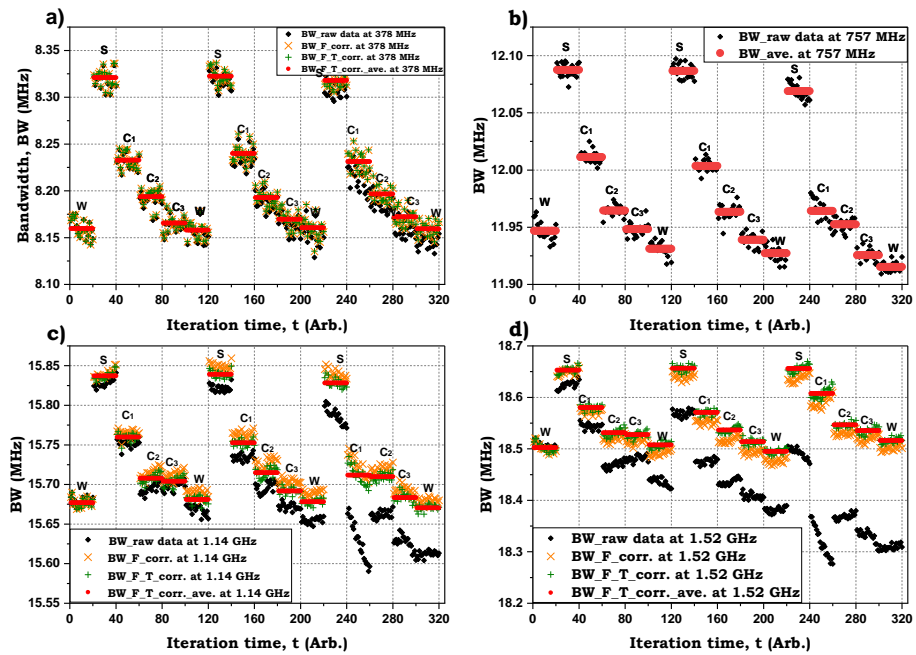


Figure D-12: Raw data, corrections and averaging of BW Measurements for all modes at variance concentrations (25 to 3.13) ppt of  $0.4 \mu\text{m}$  (Raw data-Black, corrected data - orange and green and averaging in Red).

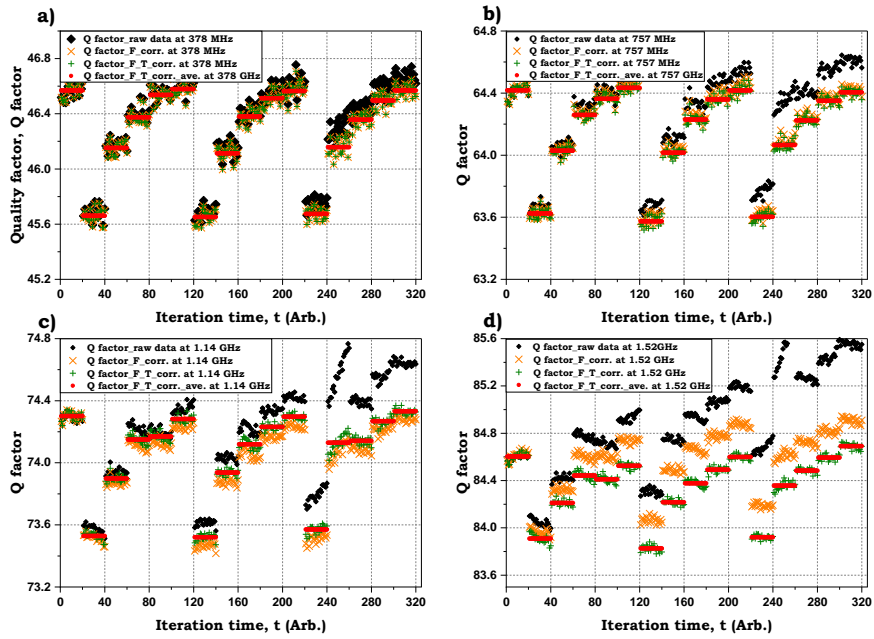


Figure D-13: Raw data, corrections and averaging of Q factor Measurements for all modes at variance concentrations (25 to 3.13) ppt of  $0.413 \mu\text{m}$  (Raw data - Black, corrected data - orange and green and averaging in Red).

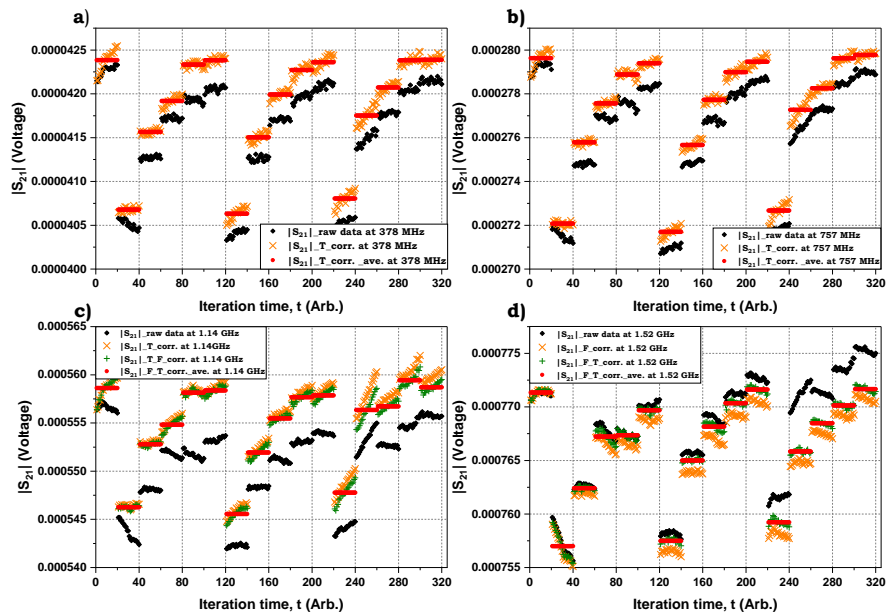


Figure D-14: Raw data, corrections and averaging of  $|S_{21}|$  Measurements for all modes at variance concentrations (25 to 3.13) ppt of  $0.8 \mu\text{m}$  (Raw data - Black, corrected data - orange and green and averaging in Red).

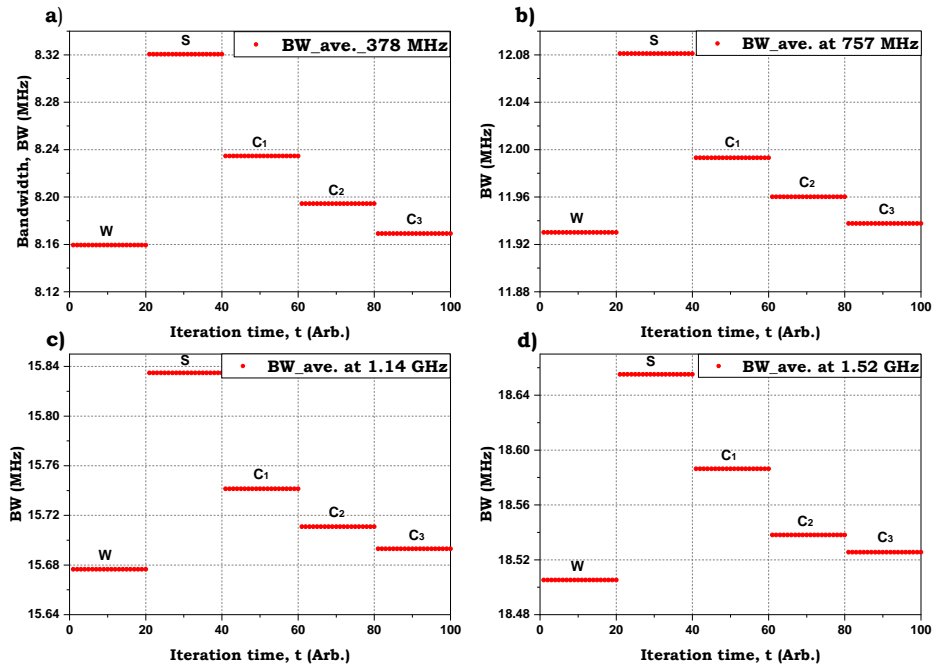


Figure D-15: Ave. of BW over the three sets after applying all the corrections for variance concentrations (25 to 3.13) ppt at 0.413  $\mu\text{m}$ .

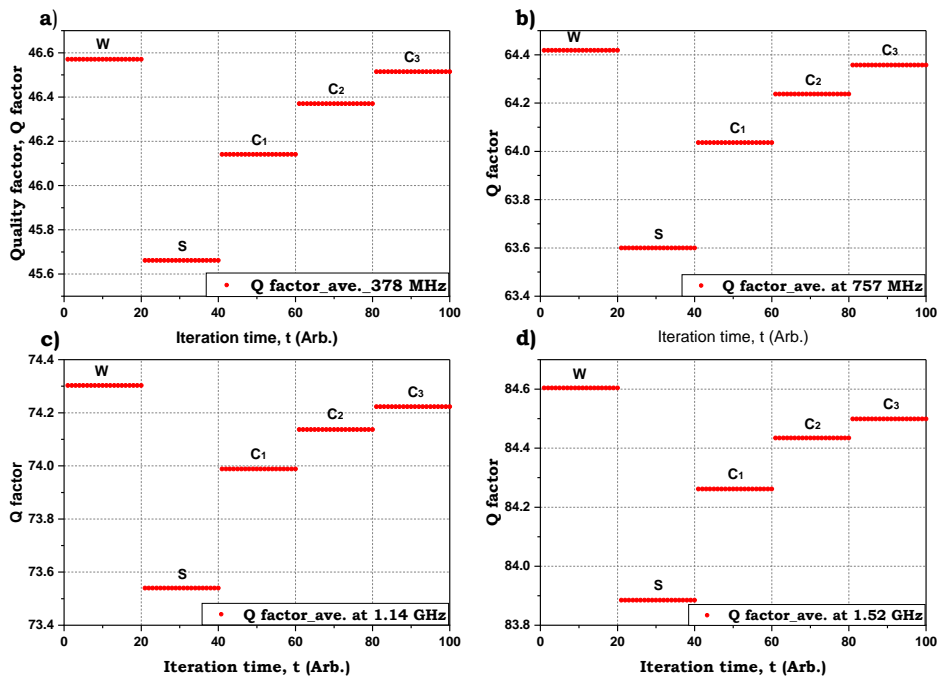


Figure D-16: Ave. of Q factor over the three sets after applying all the corrections for variance concentrations (25 to 3.13) ppt at 0.413  $\mu\text{m}$ .

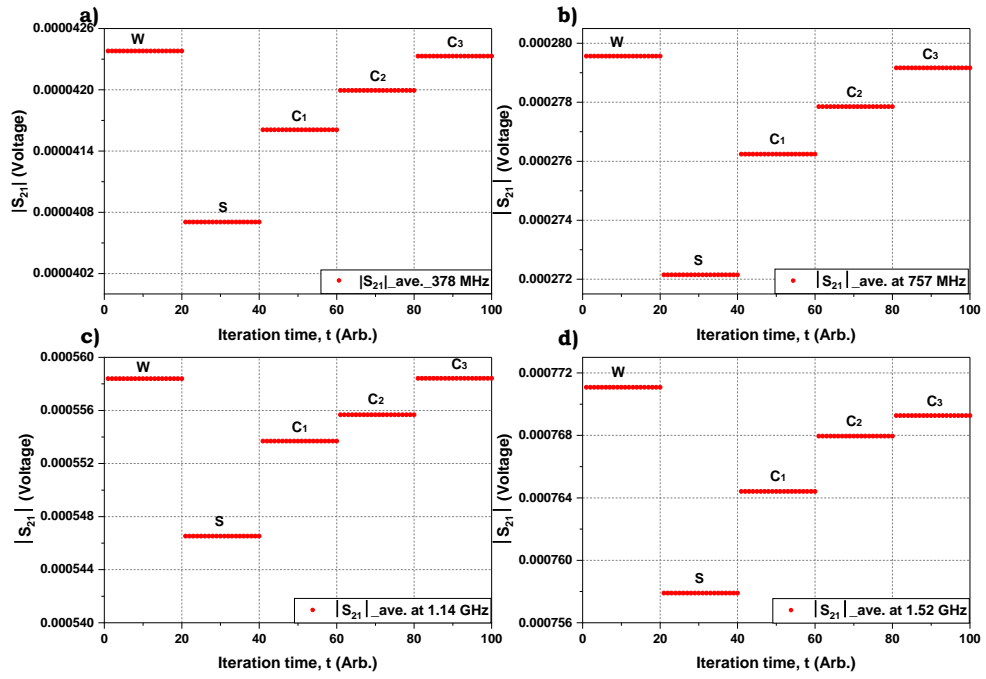


Figure D-17: Ave. of  $|S_{21}|$  over the three sets after applying all the corrections for variance concentrations (25 to 3.13) ppt at  $0.413 \mu\text{m}$ .

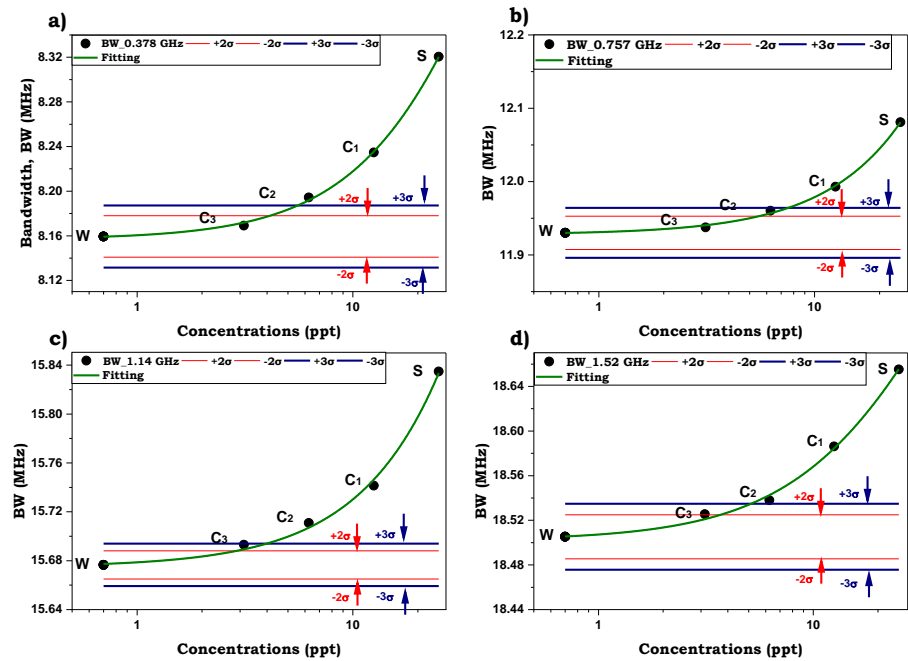


Figure D-18: The correlation between the corrected BW data with different concentrations and statistical detection  $\pm 2\sigma$  (red) and  $\pm 3\sigma$  (blue) at  $0.413 \mu\text{m}$  for all modes.

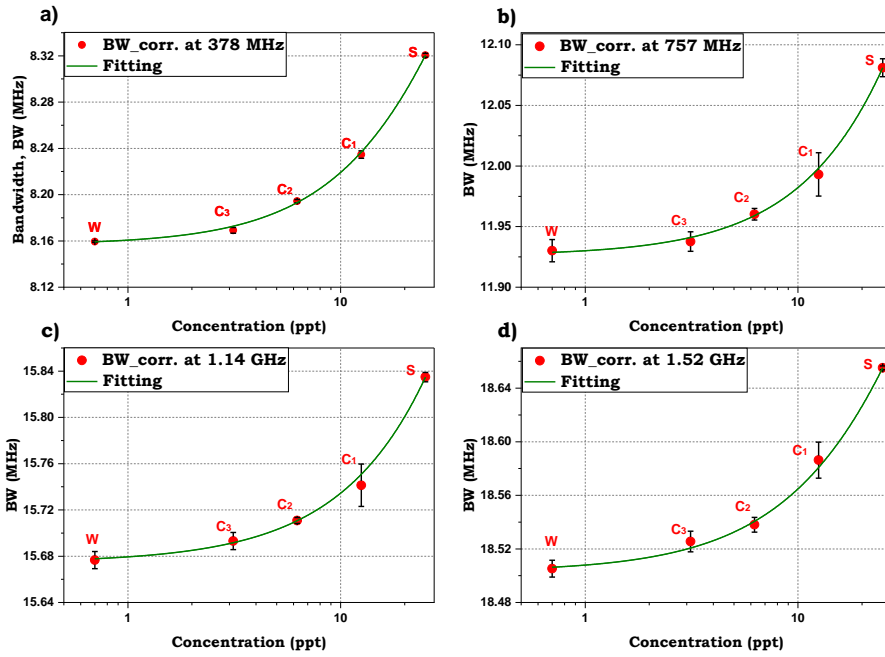


Figure D-19: BW measurements after corrections for suspension polystyrene (0.413  $\mu\text{m}$ ) with a concentration range of 25 to 3.13 ppt of all modes.

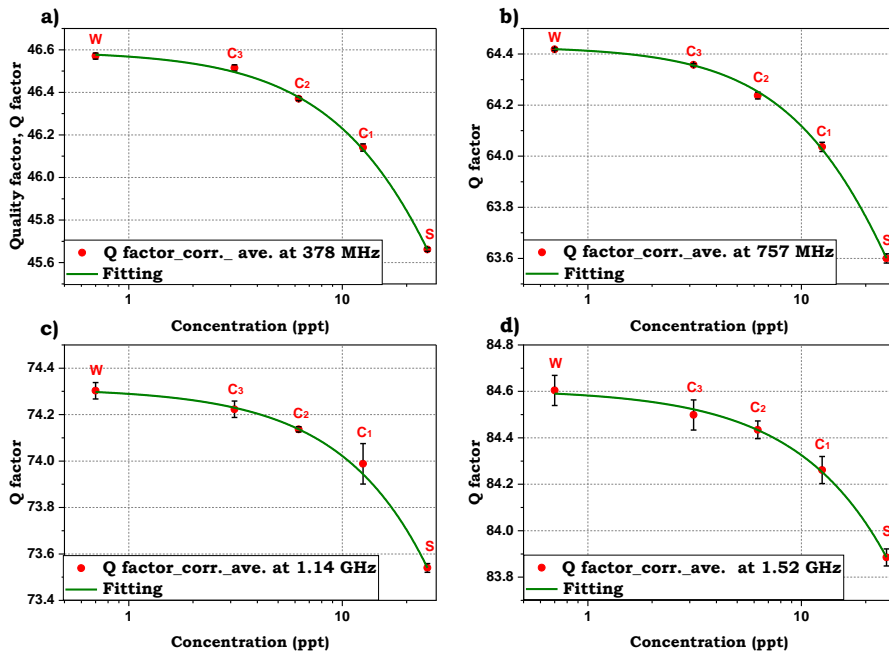


Figure D-20: Q factor measurements after corrections for suspension polystyrene (0.413  $\mu\text{m}$ ) with a concentration range of 25 to 3.13 ppt of all modes.

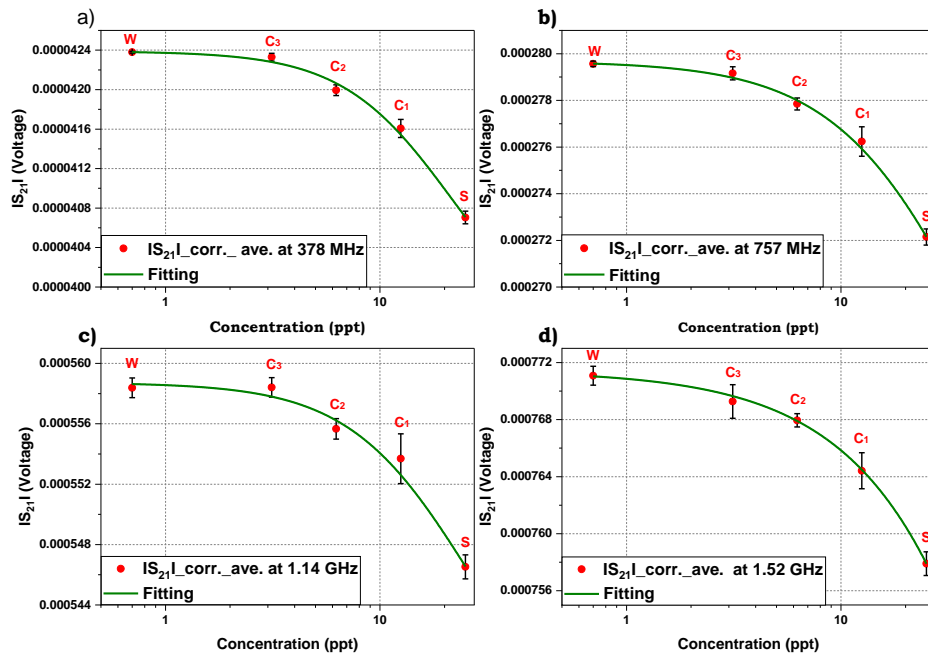


Figure D-21:  $|S_{21}|$  measurements after corrections for suspension polystyrene (0.413  $\mu\text{m}$ ) with concentration range 25 to 3.13 ppt of all modes.

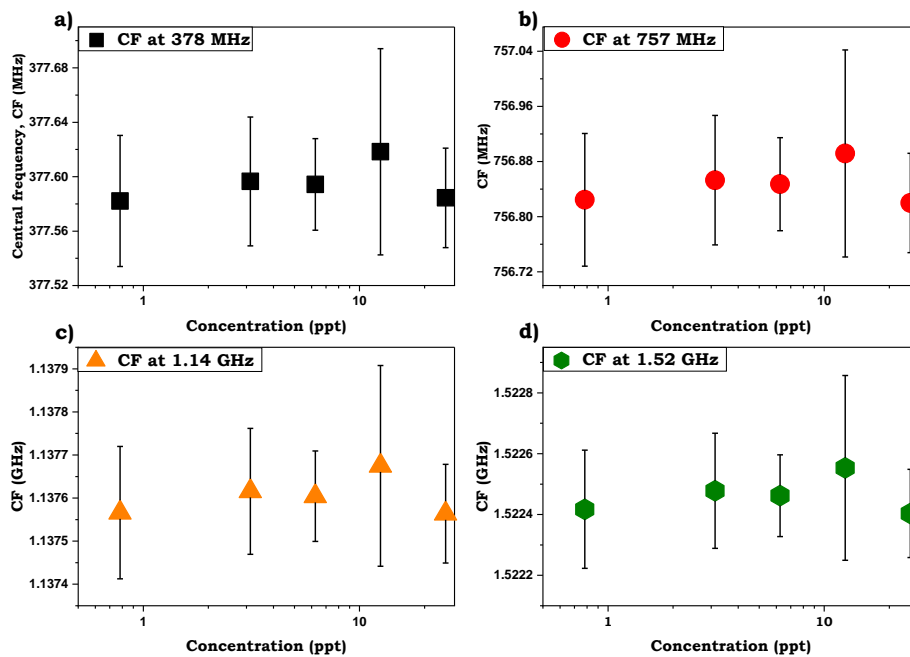


Figure D-22: CF measurements after corrections for suspension polystyrene (0.413  $\mu\text{m}$ ) with a concentration range of 25 to 3.13 ppt of all modes.

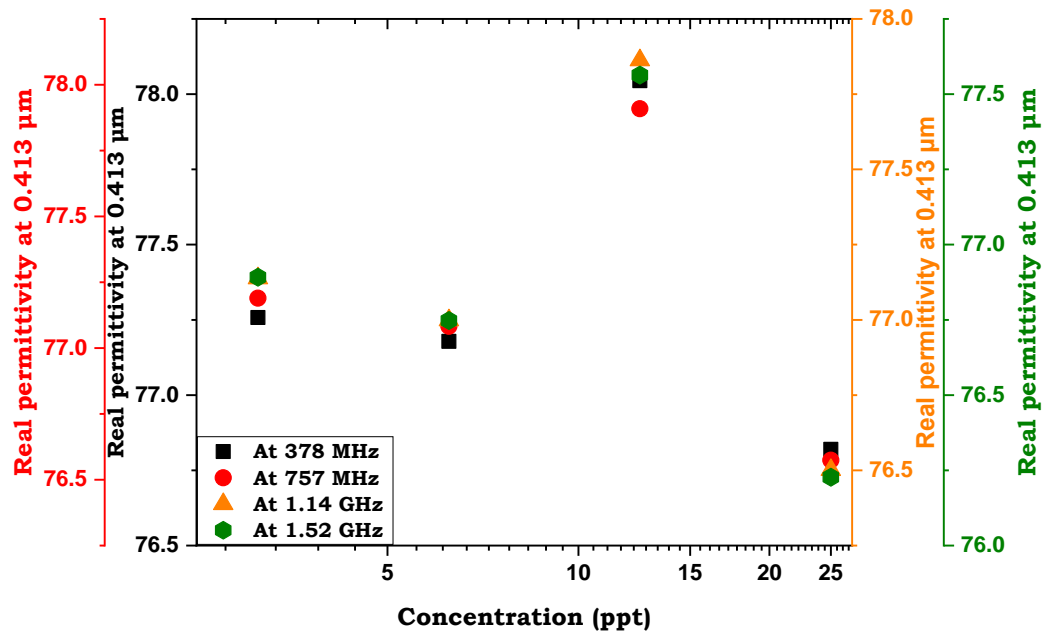


Figure D-23: Real permittivity of the experimental work for different modes (0.378, 0.757, 1.14 and 1.52) GHz at variance concentrations of the 0.413 μm for suspension polystyrene (25 to 3.13) ppt.

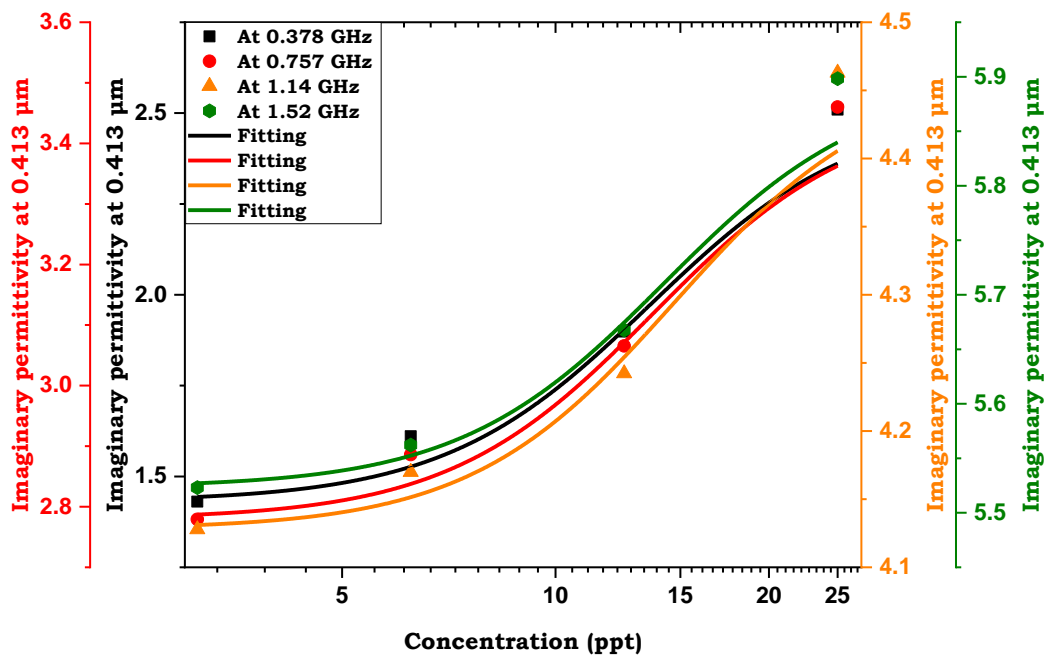


Figure D-24: Imaginary permittivity of the experimental work for different modes (0.378, 0.757, 1.14 and 1.52) GHz at variance concentrations of the 0.413 μm for suspension polystyrene (25 to 3.13) ppt.



## REFERENCES

1. Spliethoff, J.W., et al., *Real-time in vivo tissue characterization with diffuse reflectance spectroscopy during transthoracic lung biopsy: a clinical feasibility study*. Clin Cancer Res, 2015.
2. Spliethoff, J.W., et al., *Improved identification of peripheral lung tumors by using diffuse reflectance and fluorescence spectroscopy*. Lung Cancer, 2013. **80**(2): p. 165-71.
3. Nachabe, R., et al., *Diagnosis of breast cancer using diffuse optical spectroscopy from 500 to 1600 nm: comparison of classification methods*. J Biomed Opt, 2011. **16**(8): p. 087010.
4. Halter, R.J., et al., *Electrical impedance spectroscopy of benign and malignant prostatic tissues*. J Urol, 2008. **179**(4): p. 1580-6.
5. Jerjes, W., et al., *Detection of cervical intranodal metastasis in oral cancer using elastic scattering spectroscopy*. Oral Oncol, 2004. **40**(7): p. 673-8.
6. Foster, K.R. and H.P. Schwan, *Dielectric properties of tissues*. CRC handbook of biological effects of electromagnetic fields, 1986: p. 27-96.
7. Grant, J., et al., *In vivo dielectric properties of human skin from 50 MHz to 2.0 GHz*. Physics in Medicine & Biology, 1988. **33**(5): p. 607.
8. Kuehnel, W., *Color Atlas of Cytology, Histology and Microscopic Anatomy*. 4 th edition ed. 2003, Germany.
9. Mescher, A.L., *Junqueira's basic histology: text and atlas*. 2013: Mcgraw-hill.
10. Two, B., *Cancer Characteristics and Selection of Cases*. ; 1992. Book Three: Tumor Registrar Vocabulary: The Composition of Medical Terms, 1993.
11. Stephens, F.O. and K.R. Aigner, *Basics of oncology*. 2009, Springer Dordrecht Heidelberg London New York.
12. Cao, H., et al., *Epithelial-mesenchymal transition in colorectal cancer metastasis: A system review*. Pathol Res Pract, 2015. **211**(8): p. 557-69.
13. Lin, P.P. and S. Patel, *Bone sarcoma*. 2013: Springer Science & Business Media.
14. Damjanov, I., *Pathology for the health professions* 4 th edition ed. 2012, US.
15. Chinyama, C., *Benign Breast Disease Rdilogy- Pathology -Risk Assessment* 2 nd ed. 2014, UK.
16. Kumar, V., K. Abbas Abdul, and N.R. Fausto, *Cotran pathological basis of disease 7th edition*. 2005, Saunders.

17. Younes, S. *Thyroid gland, Benign neoplasms, Follicular adenoma*. 2016, July 7 [cited 2020 Oct, 22 ]; Available from: <https://cutt.ly/EgcNEpA>.
18. Herbert, M., *World Development Institute 39 Main Street, Flushing, Queens, New York 11354, USA, ma708090@ gmail. com*. *growth*. **22**(23): p. 24.
19. Lastra, R.R., V.A. LiVolsi, and Z.W. Baloch, *Aggressive variants of follicular cell-derived thyroid carcinomas: a cytopathologist's perspective*. *Cancer Cytopathol*, 2014. **122**(7): p. 484-503.
20. Baykara, M., et al., *Detecting positive surgical margins using single optical fiber probe during radical prostatectomy: a pilot study*. *Urology*, 2014. **83**(6): p. 1438-42.
21. Muller, M.G., et al., *Spectroscopic detection and evaluation of morphologic and biochemical changes in early human oral carcinoma*. *Cancer*, 2003. **97**(7): p. 1681-92.
22. Bard, M.P., et al., *Optical spectroscopy for the classification of malignant lesions of the bronchial tree*. *Chest*, 2006. **129**(4): p. 995-1001.
23. Zhou, C., et al., *Diffuse optical monitoring of blood flow and oxygenation in human breast cancer during early stages of neoadjuvant chemotherapy*. *Journal of biomedical optics*, 2007. **12**(5): p. 051903.
24. Brown, J.Q., et al., *Optical assessment of tumor resection margins in the breast*. *IEEE Journal of selected topics in Quantum Electronics*, 2009. **16**(3): p. 530-544.
25. Wang, H.-W., et al., *Diffuse reflectance spectroscopy detects increased hemoglobin concentration and decreased oxygenation during colon carcinogenesis from normal to malignant tumors*. *Optics express*, 2009. **17**(4): p. 2805-2817.
26. Swinson, B., et al., *Optical techniques in diagnosis of head and neck malignancy*. *Oral Oncol*, 2006. **42**(3): p. 221-8.
27. Upile, T., et al., *Optical diagnostic techniques in the head and neck*. *Dent Update*, 2007. **34**(7): p. 410-2, 415-6, 419-20 passim.
28. Zhu, Y., et al., *Elastic scattering spectroscopy for early detection of breast cancer: partially supervised Bayesian image classification of scanned sentinel lymph nodes*. *J Biomed Opt*, 2018. **23**(8): p. 1-9.
29. Evers, D.J., et al., *Diffuse reflectance spectroscopy: towards clinical application in breast cancer*. *Breast Cancer Res Treat*, 2013. **137**(1): p. 155-65.
30. Evers, D.J., et al., *Optical sensing for tumor detection in the liver*. *Eur J Surg Oncol*, 2013. **39**(1): p. 68-75.

31. Evers, D.J., et al., *Diffuse reflectance spectroscopy: a new guidance tool for improvement of biopsy procedures in lung malignancies*. Clin Lung Cancer, 2012. **13**(6): p. 424-31.
32. Mohammadian, M., et al., *Liver cancer in the world: epidemiology, incidence, mortality and risk factors*. World cancer research journal, 2018. **5**(2).
33. Nachabe, R., et al., *Effect of bile absorption coefficients on the estimation of liver tissue optical properties and related implications in discriminating healthy and tumorous samples*. Biomed Opt Express, 2011. **2**(3): p. 600-14.
34. Spliethoff, J.W., et al., *Real-time In Vivo Tissue Characterization with Diffuse Reflectance Spectroscopy during Transthoracic Lung Biopsy: A Clinical Feasibility Study*. Clin Cancer Res, 2016. **22**(2): p. 357-65.
35. Zonios, G., et al., *Diffuse reflectance spectroscopy of human adenomatous colon polyps in vivo*. Appl Opt, 1999. **38**(31): p. 6628-37.
36. Spliethoff, J.W., et al., *Monitoring of tumor response to Cisplatin using optical spectroscopy*. Transl Oncol, 2014. **7**(2): p. 230-9.
37. Langhout, G.C., et al., *Differentiation of healthy and malignant tissue in colon cancer patients using optical spectroscopy: A tool for image-guided surgery*. Lasers Surg Med, 2015.
38. Prabitha, V.G., et al., *Detection of cervical lesions by multivariate analysis of diffuse reflectance spectra: a clinical study*. Lasers Med Sci, 2016. **31**(1): p. 67-75.
39. Volynskaya, Z., et al., *Diagnosing breast cancer using diffuse reflectance spectroscopy and intrinsic fluorescence spectroscopy*. J Biomed Opt, 2008. **13**(2): p. 024012.
40. Nachabe, R., et al., *Estimation of lipid and water concentrations in scattering media with diffuse optical spectroscopy from 900 to 1,600 nm*. J Biomed Opt, 2010. **15**(3): p. 037015.
41. Nachabe, R., et al., *Estimation of biological chromophores using diffuse optical spectroscopy: benefit of extending the UV-VIS wavelength range to include 1000 to 1600 nm*. Biomed Opt Express, 2010. **1**(5): p. 1432-1442.
42. de Boer, L.L., et al., *Fat/water ratios measured with diffuse reflectance spectroscopy to detect breast tumor boundaries*. Breast Cancer Res Treat, 2015. **152**(3): p. 509-18.
43. Cerussi, A., et al., *In vivo absorption, scattering, and physiologic properties of 58 malignant breast tumors determined by broadband diffuse optical spectroscopy*. J Biomed Opt, 2006. **11**(4): p. 044005.

44. Pifferi, A., et al., *Four-wavelength time-resolved optical mammography in the 680-980-nm range*. Opt Lett, 2003. **28**(13): p. 1138-40.
45. Werahera, P.N., et al., *Human feasibility study of fluorescence spectroscopy guided optical biopsy needle for prostate cancer diagnosis*. Conf Proc IEEE Eng Med Biol Soc, 2015. **2015**: p. 7358-61.
46. Brandao, M.P., FREITAS, L.C. F.and Bachmann, L., *Optical Diagnosis for Thyroid and Parathyroid Tissues - A Review Applied Spectroscopy Reviews*, 2015. **50**: p. 670-677.
47. Gillenwater, A., et al., *Noninvasive diagnosis of oral neoplasia based on fluorescence spectroscopy and native tissue autofluorescence*. Arch Otolaryngol Head Neck Surg, 1998. **124**(11): p. 1251-8.
48. Brandao, M.P., et al., *Optical characterization of normal, benign, and malignant thyroid tissue: a pilot study*. J Fluoresc, 2015. **25**(2): p. 465-71.
49. Kong, K., et al., *Raman spectroscopy for medical diagnostics--From in-vitro biofluid assays to in-vivo cancer detection*. Adv Drug Deliv Rev, 2015. **89**: p. 121-34.
50. Swain, R.J. and M.M. Stevens, *Raman microspectroscopy for non-invasive biochemical analysis of single cells*. Biochem Soc Trans, 2007. **35**(Pt 3): p. 544-9.
51. Austin, L.A., S. Osseiran, and C. Evans, L., *Raman technologies in cancer diagnostics (critical review)* Analyst, 2016. **141**: p. 476-503.
52. Singh, S.P., et al., *In vivo Raman spectroscopic identification of premalignant lesions in oral buccal mucosa*. J Biomed Opt, 2012. **17**(10): p. 105002.
53. Sahu, A., et al., *Raman spectroscopy of serum: an exploratory study for detection of oral cancers*. Analyst, 2013. **138**(14): p. 4161-74.
54. Krishnakumar, N., et al., *Raman spectroscopic investigation of the chemopreventive response of naringenin and its nanoparticles in DMBA-induced oral carcinogenesis*. Spectrochim Acta A Mol Biomol Spectrosc, 2013. **115**: p. 648-53.
55. Guze, K., et al., *Pilot study: Raman spectroscopy in differentiating premalignant and malignant oral lesions from normal mucosa and benign lesions in humans*. Head Neck, 2015. **37**(4): p. 511-7.
56. Lau, D.P., et al., *Raman spectroscopy for optical diagnosis in the larynx: preliminary findings*. Lasers Surg Med, 2005. **37**(3): p. 192-200.

57. Hielscher, A.H., Mourant, J.R. AND Bigio, J. I. , *Biomedical Diagnostics with Elastic Light Scattering in Cell Suspensions and Tissues* 19th International Conference 1997.
58. Upile, T., et al., *Elastic scattering spectroscopy in assessing skin lesions: an "in vivo" study*. Photodiagnosis Photodyn Ther, 2012. **9**(2): p. 132-41.
59. Omar, E., *Current concepts and future of noninvasive procedures for diagnosing oral squamous cell carcinoma--a systematic review*. Head Face Med, 2015. **11**: p. 6.
60. Denkceken, T., et al., *Elastic light single-scattering spectroscopy for the detection of cervical precancerous ex vivo*. IEEE Trans Biomed Eng, 2013. **60**(1): p. 123-7.
61. Denkceken, T., et al., *Diagnosis of pelvic lymph node metastasis in prostate cancer using single optical fiber probe*. Int J Biol Macromol, 2015.
62. Morgan, M.S., et al., *Light reflectance spectroscopy to detect positive surgical margins on prostate cancer specimens*. The Journal of urology, 2016. **195**(2): p. 479-484.
63. Bigio, I.J., et al., *Diagnosis of breast cancer using elastic-scattering spectroscopy: preliminary clinical results*. J Biomed Opt, 2000. **5**(2): p. 221-8.
64. Rosen, J.E., et al., *Preoperative discrimination of benign from malignant disease in thyroid nodules with indeterminate cytology using elastic light-scattering spectroscopy*. IEEE Trans Biomed Eng, 2014. **61**(8): p. 2336-40.
65. Mourant, J.R., et al., *Evidence of intrinsic differences in the light scattering properties of tumorigenic and nontumorigenic cells*. Cancer, 1998. **84**(6): p. 366-74.
66. Mourant, J.R., et al., *Light scattering from cells: the contribution of the nucleus and the effects of proliferative status*. J Biomed Opt, 2000. **5**(2): p. 131-7.
67. Lovat, L.B., et al., *Elastic scattering spectroscopy accurately detects high grade dysplasia and cancer in Barrett's oesophagus*. Gut, 2006. **55**(8): p. 1078-83.
68. A'Amar, O.M., et al., *Comparison of elastic scattering spectroscopy with histology in ex vivo prostate glands: potential application for optically guided biopsy and directed treatment*. Lasers Med Sci, 2013. **28**(5): p. 1323-9.
69. *Cancer Facts & Figures*. <http://www.cancer.org/acs/groups/content/@research/documents/document/acspsc-047079.pdf>. [cited March 17, 2016.; annual report ].

70. Society, A.C., *Cancer facts & figures 2014*. 2014: American Cancer Society.
71. Shirkavand, A., et al., *Detection of Melanoma Skin Cancer by Elastic Scattering Spectra: A Proposed Classification Method*. Iranian Journal of Medical Physics, 2017. **14**(3): p. 162-166.
72. Canpolat, M., et al., *Diagnosis and demarcation of skin malignancy using elastic light single-scattering spectroscopy: a pilot study*. Dermatol Surg, 2012. **38**(2): p. 215-23.
73. Grillone, G.A., et al., *The color of cancer: Margin guidance for oral cancer resection using elastic scattering spectroscopy*. Laryngoscope, 2017. **127 Suppl 4**: p. S1-s9.
74. Sharwani, A., et al., *Assessment of oral premalignancy using elastic scattering spectroscopy*. Oral Oncol, 2006. **42**(4): p. 343-9.
75. Suh, H., et al., *Elastic light-scattering spectroscopy for discrimination of benign from malignant disease in thyroid nodules*. Ann Surg Oncol, 2011. **18**(5): p. 1300-5.
76. Johnson, K.S., et al., *Elastic scattering spectroscopy for intraoperative determination of sentinel lymph node status in the breast*. J Biomed Opt, 2004. **9**(6): p. 1122-8.
77. Cancer Research UK. *Worldwide cancer statistics*. 2020,Oct.25 2020,Oct.25]; Available from: <https://www.cancerresearchuk.org/health-professional/cancer-statistics/worldwide-cancer>.
78. Turhan, M., et al., *Intraoperative assessment of laryngeal malignancy using elastic light single-scattering spectroscopy: A pilot study*. Laryngoscope, 2017. **127**(3): p. 611-615.
79. Lau, D.P., et al., *Raman spectroscopy for optical diagnosis in normal and cancerous tissue of the nasopharynx—preliminary findings*. Lasers in surgery and medicine, 2003. **32**(3): p. 210-214.
80. Canpolat, M., et al., *Intra-operative brain tumor detection using elastic light single scattering spectroscopy: a feasibility study*. Journal of biomedical optics 2009. **14**(5): p. 054021-1- 054021-7.
81. Canpolat, M. and J.R. Mourant, *Particle size analysis of turbid media with a single optical fiber in contact with the medium to deliver and detect white light*. Appl Opt, 2001. **40**(22): p. 3792-9.
82. Amelink, A., et al., *Single-scattering spectroscopy for the endoscopic analysis of particle size in superficial layers of turbid media*. Appl Opt, 2003. **42**(19): p. 4095-101.
83. Sircan-Kucuksayan, A., T. Denkceken, and M. Canpolat, *Differentiating cancerous tissues from noncancerous tissues using single-fiber reflectance spectroscopy with different fiber diameters*. J Biomed Opt, 2015. **20**(11): p. 115007.

84. Jacques, S.L., *Origins of tissue optical properties in the UVA, visible, and NIR regions*. Advances in Optical Imaging and Photon Migration 1996: p. P.364-371.
85. Wee, F., et al. *Free space measurement technique on dielectric properties of agricultural residues at microwave frequencies*. in 2009 SBMO/IEEE MTT-S International Microwave and Optoelectronics Conference (IMOC). 2009. IEEE.
86. Venkatesh, M. and G. Raghavan, *An overview of dielectric properties measuring techniques*. Canadian biosystems engineering, 2005. **47**(7): p. 15-30.
87. Joines, W.T., et al., *Microwave power absorption differences between normal and malignant tissue*. International Journal of Radiation Oncology\* Biology\* Physics, 1980. **6**(6): p. 681-687.
88. Damadian, R. and F.W. Cope, *NMR in cancer. V. Electronic diagnosis of cancer by potassium (39K) nuclear magnetic resonance: spin signatures and T1 beat patterns*. Physiological chemistry and physics, 1974. **6**(4): p. 309-322.
89. Joines, W.T., *Frequency-dependent absorption of electromagnetic energy in biological tissue*. IEEE transactions on biomedical engineering, 1984(1): p. 17-20.
90. Tanabe, E. and W.T. Joines, *A nondestructive method for measuring the complex permittivity of dielectric materials at microwave frequencies using an open transmission line resonator*. IEEE Transactions on Instrumentation and Measurement, 1976(3): p. 222-226.
91. Foster, K. and J. Schepps, *Dielectric properties of tumor and normal tissues at radio through microwave frequencies*. Journal of Microwave Power, 1981. **16**(2): p. 107-119.
92. Petersan, P.J. and S.M. Anlage, *Measurement of resonant frequency and quality factor of microwave resonators: Comparison of methods*. Journal of applied physics, 1998. **84**(6): p. 3392-3402.
93. Sheen, J., *Study of microwave dielectric properties measurements by various resonance techniques*. Measurement, 2005. **37**(2): p. 123-130.
94. Jha, S.N., et al., *Measurement techniques and application of electrical properties for nondestructive quality evaluation of foods—a review*. Journal of food science and technology, 2011. **48**(4): p. 387-411.
95. La Gioia, A., et al., *Open-ended coaxial probe technique for dielectric measurement of biological tissues: Challenges and common practices*. Diagnostics, 2018. **8**(2): p. 40.

96. Afsar, M.N., et al., *The measurement of the properties of materials*. Proceedings of the IEEE, 1986. **74**(1): p. 183-199.
97. Saeed, K., et al., *Planar microwave sensors for complex permittivity characterization of materials and their applications*. Applied Measurement Systems, 2012: p. 319-350.
98. Martellosio, A., et al., *0.5–50 GHz dielectric characterisation of breast cancer tissues*. Electronics Letters, 2015. **51**(13): p. 974-975.
99. Blackham, D.V. and R.D. Pollard, *An improved technique for permittivity measurements using a coaxial probe*. IEEE Transactions on Instrumentation and Measurement, 1997. **46**(5): p. 1093-1099.
100. Shaforost, O.N., *Microwave whispering-gallery resonators for nanolitre liquid sensing*. 2009.
101. Note, A.A., *Agilent basics of measuring the dielectric properties of materials*. Agilent literature number, 2006.
102. Torgovnikov, G.I., *Dielectric properties of wood-based materials*, in *Dielectric properties of wood and wood-based materials*. 1993, Springer. p. 135-159.
103. Gibson, A.A., et al., *An overview of microwave techniques for the efficient measurement of food materials*. Food Manufacturing Efficiency, 2008. **2**(1): p. 35.
104. Note, A., *Basics of measuring the dielectric properties of materials*. Agilent Technologies, 2006: p. 1e31.
105. Hoon, W.F., et al., *Alternatives for PCB Laminates: Dielectric Properties' Measurements at Microwave Frequencies*. Dielectric Material, 2012.
106. Surowiec, A.J., et al., *Dielectric properties of breast carcinoma and the surrounding tissues*. IEEE Transactions on Biomedical Engineering, 1988. **35**(4): p. 257-263.
107. Sha, L., E.R. Ward, and B. Stroy. *A review of dielectric properties of normal and malignant breast tissue*. in *Proceedings IEEE SoutheastCon 2002 (Cat. No. 02CH37283)*. 2002. IEEE.
108. Fear, E.C., et al., *Confocal microwave imaging for breast cancer detection: Localization of tumors in three dimensions*. IEEE Transactions on biomedical engineering, 2002. **49**(8): p. 812-822.
109. Bindu, G., et al. *Microwave characterization of female human breast tissues*. in *2006 European Conference on Wireless Technology*. 2006. IEEE.
110. Gervino, G., et al., *Diagnosis of bladder cancer at 465 MHz*. Electromagnetic biology and medicine, 2007. **26**(2): p. 119-134.
111. Lazebnik, M., et al., *A large-scale study of the ultrawideband microwave dielectric properties of normal, benign and malignant*

- breast tissues obtained from cancer surgeries. Physics in medicine & biology, 2007. 52(20): p. 6093.*
112. Kuhn, M.J., et al. *Open-ended coaxial probe measurements for breast cancer detection. in 2010 IEEE Radio and Wireless Symposium (RWS). 2010. IEEE.*
  113. Hussein, M., et al., *Breast cancer cells exhibits specific dielectric signature in vitro using the open-ended coaxial probe technique from 200 MHz to 13.6 GHz. Scientific reports, 2019. 9(1): p. 1-8.*
  114. Ross, M.H. and W. Pawlina, *Histology. 2006: Lippincott Williams & Wilkins.*
  115. Colton, D. and P. Monk, *A new approach to detecting leukemia: Using computational electromagnetics. IEEE Computational Science and Engineering, 1995. 2(4): p. 46-52.*
  116. Bolin, F.P., et al., *Refractive index of some mammalian tissues using a fiber optic cladding method. Applied optics, 1989. 28(12): p. 2297-2303.*
  117. Wei, H.-J., et al., *Determination of optical properties of normal and adenomatous human colon tissues in vitro using integrating sphere techniques. World Journal of Gastroenterology: WJG, 2005. 11(16): p. 2413.*
  118. Dremin, V., et al. *Imaging of early stage breast cancer with circularly polarized light. in Tissue Optics and Photonics. 2020. International Society for Optics and Photonics.*
  119. Aboughaleb, I.H., M.H. Aref, and Y.H. El-Sharkawy, *Hyperspectral imaging for diagnosis and detection of ex-vivo breast cancer. Photodiagnosis and Photodynamic Therapy, 2020. 31: p. 101922.*
  120. Robijns, J., et al., *The use of low-level light therapy in supportive care for patients with breast cancer: review of the literature. Lasers in medical science, 2017. 32(1): p. 229-242.*
  121. Xu, X., H. Lu, and R. Lee, *Near infrared light triggered photo/immuno-therapy toward cancers. Frontiers in Bioengineering and Biotechnology, 2020. 8.*
  122. Vo-Dinh, T., *Biomedical Photonics Handbook. 2003, USA.*
  123. Mie, G., *Beiträge zur Optik trüber Medien, speziell kolloidaler Metallösungen. Annalen der physik, 1908. 330(3): p. 377-445.*
  124. Bohren, D., *Huffman. Absorption and scattering of light by small particles”, John Willey & Sons, New York, 1983.*
  125. Henyey, L.G. and J.L. Greenstein, *Diffuse radiation in the galaxy. The Astrophysical Journal, 1941. 93: p. 70-83.*
  126. Chin, L.C., W.M. Whelan, and I.A. Vitkin, *Optical fiber sensors for biomedical applications, in Optical-thermal response of laser-irradiated tissue. 2010, Springer. p. 661-712.*

127. Edmund Optics /Worldwild. *200 $\mu$ m 0.22 NA VIS/NIR Fiber, 10m Length* February 13, 2021]; Available from: <https://www.edmundoptics.co.uk/p/200mum-022-na-visnir-fiber-10m-length/14079/>.
128. Edmund Optics /Worldwild. *100 $\mu$ m 0.22 NA VIS/NIR Fiber, 10m Length.* February 13, 2021]; Available from: <https://www.edmundoptics.co.uk/p/100mum-022-na-visnir-fiber-10m-length/14077/>.
129. Microspheres-Nanospheres. *Plain polystyrene nanospheres and microspheres.* 2003-2011 2021, March 11]; Available from: <https://www.microspheres-nanospheres.com/Microspheres/Organic/Polystyrene/PS%20Plain.htm>.
130. Scott Prahl. *Mie scattering calculations.* 2018 2021, March 11]; Available from: [https://omlc.org/calc/mie\\_calc.html](https://omlc.org/calc/mie_calc.html).
131. Ehtaiba, M.H., *Use of microwave techniques in medical diagnostics and therapy.* 2017, Cardiff University.
132. Partridge, S., *Electromagnetic properties of semiconducting metal oxides under external stimulation.* 2019, Cardiff University.
133. Hefford, S.J., *Microwave processing in additive manufacturing.* 2019, Cardiff University.
134. Murphy, E. and S. Morgan, *The dielectric properties of insulating materials.* The Bell System Technical Journal, 1937. **16**(4): p. 493-512.
135. Pozar, D.M., *Microwave engineering.* 2011: John Wiley & Sons.
136. Smith, K.M. and P. Holroyd, *Electrical Properties of Materials.* 10th ed. 2013: OUP Oxford. 165-174.
137. Kaatze, U., *Complex permittivity of water as a function of frequency and temperature.* Journal of Chemical and Engineering Data, 1989. **34**(4): p. 371-374.
138. Sihvola, A.H., *Electromagnetic mixing formulas and applications.* 1999: Iet.
139. Levy, O. and D. Stroud, *Maxwell Garnett theory for mixtures of anisotropic inclusions: Application to conducting polymers.* Physical Review B, 1997. **56**(13): p. 8035-8046.
140. Atkins, P. and J. Paula, *The rate of chemical reactions "Atkins' physical chemistry, 9th edn"*. 2010, Oxford University Press, New York.
141. Ahmad, Z., *Polymer dielectric materials,* in *Dielectric material.* 2012, IntechOpen.
142. Gregory, A.P. and R.N. Clarke, *A review of RF and microwave techniques for dielectric measurements on polar liquids.* IEEE

- Transactions on Dielectrics and Electrical Insulation, 2006. **13**(4): p. 727-743.
143. Kawabata, H., et al. *Multi-frequency measurements of complex permittivity of dielectric plates using higher-order modes of a balanced-type circular disk resonator*. in *2006 European Microwave Conference*. 2006. IEEE.
  144. EverythingRF. *.034AG-W-P-50*. 2021 [cited 2021, February 22; Available from: <https://www.everythingrf.com/products/rf-cables/jyebao/35-136-034ag-w-p-50>].
  145. DielectricOptions. *High performance Microwave interconnect products*. 2021 [cited 2021, February 22]; Available from: [https://www.datasheetarchive.com/whats\\_new/95be5379c425607d87d2047ff0ffccd7.html](https://www.datasheetarchive.com/whats_new/95be5379c425607d87d2047ff0ffccd7.html).
  146. Cuenca, J.A., *Characterisation of powders using microwave cavity perturbation*. 2015, Cardiff University.
  147. Butcher I. *Circle fit*. 2021 [cited 2021, Jan 25]; Available from: <https://uk.mathworks.com/matlabcentral/fileexchange/5557-circle-fit>.
  148. Jasinski, W. and J. Berry, *Measurement of refractive indices of air, nitrogen, oxygen, carbon dioxide and water vapour at 3360 Mc/s*. Proceedings of the IEE-Part III: Radio and Communication Engineering, 1954. **101**(73): p. 337-343.
  149. MacBean, I., *The measurement of complex permittivity and complex tensor permeability of ferrite materials at microwave frequencies*. Proceedings of the IEE-Part B: Radio and Electronic Engineering, 1957. **104**(6S): p. 296-306.
  150. Dietrich, M., et al., *A laboratory test setup for in situ measurements of the dielectric properties of catalyst powder samples under reaction conditions by microwave cavity perturbation: Set up and initial tests*. Sensors, 2014. **14**(9): p. 16856-16868.
  151. Clark, N., N. Jones, and A. Porch, *Measurement of average particle size in metal powders by microwave cavity perturbation in the magnetic field*. Sensors and Actuators A: Physical, 2017. **259**: p. 137-143.
  152. Hartley, J., A. Porch, and M. Jones, *A non-invasive microwave method for assessing solid-state ammonia storage*. Sensors and Actuators B: Chemical, 2015. **210**: p. 726-730.
  153. Krupka, J., et al., *A dielectric resonator for measurements of complex permittivity of low loss dielectric materials as a function of temperature*. Measurement Science and Technology, 1998. **9**(10): p. 1751.

154. Clark, N., *Microwave methods for additive layer manufacturing*. 2017, Cardiff University.
155. Fisher Scientific. *Water, extra pure, deionized, ACROS Organics™*. 2019 2021, February 23]; Available from: <https://www.fishersci.co.uk/shop/products/water-extra-pure-deionized-acros-organics-2/10347071>.
156. Merck. *Sodium chloride*. 2019 2021, February 23]; Available from: [https://www.sigmaaldrich.com/catalog/substance/sodiumchloride5844764714511?lang=en&region=GB&gclid=EAIaIQobChMI6NLC-vv\\_7gIVUoFQBh3Y8AsqEAAYASAAEgK4bPD\\_BwE](https://www.sigmaaldrich.com/catalog/substance/sodiumchloride5844764714511?lang=en&region=GB&gclid=EAIaIQobChMI6NLC-vv_7gIVUoFQBh3Y8AsqEAAYASAAEgK4bPD_BwE).
157. Peyman, A., C. Gabriel, and E. Grant, *Complex permittivity of sodium chloride solutions at microwave frequencies*. Bioelectromagnetics: Journal of the Bioelectromagnetics Society, The Society for Physical Regulation in Biology and Medicine, The European Bioelectromagnetics Association, 2007. **28**(4): p. 264-274.
158. Chaplin, M. *Water and microwaves*. 2015, December 18 2021, February 23]; Available from: [http://www1.lsbu.ac.uk/water/microwave\\_water.html](http://www1.lsbu.ac.uk/water/microwave_water.html).
159. All About Circuits. *Skin Depth Calculator*. [cited 2021 July 1]; Available from: <https://www.allaboutcircuits.com/tools/skin-depth-calculator/>.